Imperial College London
Department of Mechanical Engineering

Design of Mechanically Lined Pipe for Reel-Lay Installation and Subsea Service

Aurélien Pépin

Submitted in part fulfilment of the requirements for the degree of
Doctor of Philosophy in Mechanical Engineering of Imperial College London, September 2019

Declaration of Originality

I, Aurelien Pépin, declare that this thesis is my own work and has not been submitted in any form for another diploma at any university. Data extracted from literature is appropriately referenced in the bibliography.

Copyright Declaration

The copyright of this thesis rests with the author. Unless otherwise indicated, its contents are licensed under a Creative Commons Attribution-Non Commercial-No Derivatives 4.0 International Licence (CC BY-NC-ND).

Under this licence, you may copy and redistribute the material in any medium or format on the condition that; you credit the author, do not use it for commercial purposes and do not distribute modified versions of the work.

When reusing or sharing this work, ensure you make the licence terms clear to others by naming the licence and linking to the licence text.

Please seek permission from the copyright holder for uses of this work that are not included in this licence or permitted under UK Copyright Law.

Abstract

An increasing demand for subsea transport of corrosive fluids has generated interest in mechanically lined pipes (MLP), made of carbon steel (CS) pipe lined with corrosion resistance alloy (CRA). MLP offers shorter lead times and is more economical than alternative products. Reel-lay is a cost-effective method for installing pipelines up to 18" in diameter subsea. This work examines the development of structural integrity procedures for assessment of MLPs installed by reel-lay.

The CRA liner is susceptible to wrinkling when an MLP is subjected to plastic deformation representative of reeling. This thesis discusses an approach where the liner thickness is increased to enable reel-lay of MLP using standard procedures. A framework is proposed for the numerical prediction of liner wrinkling during reeling.

In contrast to surface flaws, solutions for fracture assessment of embedded flaws in evenmatch welds subjected to reeling are overconservative. New limit load solutions are proposed. After showing that pre-strain does not degrade the toughness of undermatch welds similar to those in MLPs, a methodology for fracture assessment of undermatch welds is proposed.

Subsequently, it is demonstrated that although they include more crack initiation sites than standard pipelines, high in-service fatigue performance can be achieved with MLPs. It is proposed that fatigue assessment of MLP welds be undertaken using existing stress intensity factor solutions. Finally, it is shown that liner imperfections up to 6 mm would not compromise the in-service integrity of MLP.

Acknowledgements

First, I would like to thank the GOD of heaven for the breath of life.

I am very grateful to my academic and industry supervisors, Prof. Kamran Nikbin from Imperial College London, Prof. Noel P. O'Dowd from the University of Limerick and Dr. Tomasz Tkaczyk from TechnipFMC, for giving me the opportunity to undertake this PhD. Their support and guidance were vital to the successful completion of this programme.

I would also like to acknowledge the financial support provided by TechnipFMC. Special thanks go to Mr. Sylvain Denniel, for making funds available to cover tuition fees and experiments. The contribution of my colleagues, Dr. Daniil Vasilikis, Dr. Ludovic Pinier and Dr. Paul Sicsic, is also acknowledged.

The assistance of Dr. Catrin M. Davis, Dr. Ruth Brooker and Mr. Suresh V. Chettiar from Imperial College London with the fracture mechanics testing, David Haldane and Katerina Stoyanova from PTC with the bending trials, Emilie Buennagel and Alan Day from TWI with the resonance fatigue testing, Gilles Maîtres from A2MI with the cyclic tensile and low cycle fatigue testing and Tinashe Bare, Stephen Wells and Edward Fowkes from Exova with the cyclic fracture toughness testing, are also greatly acknowledged.

Finally, I am very grateful to my family for their unparalleled support and encouragement.

Nomenclature

a	crack depth
a_0	initial crack depth
a_e	half-height of embedded flaw
a^{eff}	effective crack depth
a_{eff}	effective crack depth (SINTEF correction)
a_s	height or depth of surface breaking flaw
$\widetilde{a}$	yield criterion parameter
A	material constant (Paris law)
b	safety factor or isotropic hardening exponent
$\widetilde{b}_1$, $\widetilde{b}_2$	yield criterion parameters
B	width of SEN(B) or SEN(T) fracture specimen
$2c$	crack length
$2c_e$	length of embedded flaw
$2c_s$	length of surface breaking flaw
c_{ijk}	constants
$\widetilde{c}$	parameter controlling yield surface distortion
$\widetilde{c}_0$, $\widetilde{c}_1$	fixed criterion parameters, sum of which provides the value of $\widetilde{c}$ at zero plastic strain
$\widetilde{c}_f$	maximum increase of $\widetilde{c}$
C	material constant in fatigue crack growth curve, or shape function in the SINTEF approach
C_1, C_2	linear kinematic hardening moduli
d	outer diameter of liner pipe or dimensionless function of n, α and ε_0
da	crack depth reduction
$\mathrm{d}a/\mathrm{d}N$	fatigue crack growth rate
$\mathrm{d}s$	length of line element
D	pipe outer diameter
D_{fat}	fatigue damage
D_{max}	maximum pipe outer diameter
D_{min}	minimum pipe outer diameter
e	pipe axial misalignment
E	elastic modulus
E'	effective elastic modulus
f	ratio between CTOD and CMOD
f_{ij}	dimensionless function of the circumferential position θ and n
f_w	finite width correction factor
F_{gb}	dimensionless function of geometry
g	liner radial insertion gap
g_{ij}	dimensionless function of the circumferential position θ and n
h	dimensionless function or height of initial liner imperfection
$h^{'}$, $h^{''}$	dimensionless functions
H	dimensionless function
i_0	dimensionless function of geometry
J	J-integral

J_c	fracture toughness under large scale yielding (J dominance conditions are not met)
J_e	elastic part of the J-integral
J_p	plastic part of the J-integral
J_E	end of Region I on a J-ε plot for materials with yield plateau
J_H	end of Region III on a J-ε plot for materials with yield plateau
J_{Ic}	fracture toughness under large scale yielding (J dominance conditions are met)
J_L	end of Region II on a J-ε plot for materials with yield plateau
J_R	fracture resistance curve
k_t	elastic stress concentration factor
K	stress intensity factor
K_c	value of K at fracture
K_{Ic}	fracture toughness under small scale yielding (K dominance conditions are met)
K_{mat}	material fracture toughness
K^p	stress intensity factor from the primary stress
K_r	fracture ratio
K^s	stress intensity factor from the secondary stress
L	pipeline length
L^1, L^2	anisotropic operators
L_r	plastic collapse ratio
L_r^{max}	limit of plastic collapse ratio
$loga$	intercept of mean S-N curve with the logN axis
m	slope of fatigue crack growth curve, inverse slope of S-N curve or weld metal mismatch at assessment strain
m_i	shape function in CTOD estimation scheme
m_y	weld metal mismatch at yield
M	bending moment, or mismatch ratio
M_b	bending stress intensity magnification factor
M_k	stress intensity magnification factor
M_m	membrane stress intensity magnification factor
M_p	plastic bending moment capacity
M_p^s, M_p^w	plastic bending moment capacity of stronger/weaker pipe
n	hardening exponent or number of specimens
n_i	outward unit normal or number of cycles for a given stress range
N	number of welds or number of cycles to failure
N_i	number of cycles to failure at given stress range
p, p_i	probability of occurrence
p_b	pressure containment resistance
p_e	external pressure
p_{el}	elastic collapse pressure
p_i	internal pressure
p_p	plastic collapse pressure
P	load or polarity tensor
P_0	reference load
P_b	primary bending stress
P_f	probability of failure
P_L	plastic limit load
$\widetilde{P}_L$	modified limit load
P_m	primary membrane stress

Q	difference between the HRR and actual stress field
Q_m	secondary membrane stress
Q_∞	isotropic hardening modulus
r	polar coordinate, or pipe mid wall radius
r_L	liner mid wall radius
R	bending radius, reel radius or fatigue stress ratio
s_{logN}	standard deviation of logN
S	stress range
S_1^i, S_2^i, S_3^i	principal values of stress tensor
t	actual or nominal pipe wall thickness
t_{CS}	carbon steel pipe wall thickness
t_l	liner wall thickness before expansion
t_L	liner wall thickness after expansion
t_{lmean}	mean liner wall thickness before expansion
t_{Lmin}	minimum reelable liner wall thickness
t_{min}	minimum reelable pipe wall thickness
t_{tol}	manufacturing pipe wall thickness tolerance
u_i	displacement vector
V_1	opening of the lower clip gauge
V_2	opening of the upper clip gauge
W	strain energy density, weld width, width of an equivalent flat plate, or thickness of SEN(B) or SEN(T) fracture specimen
w_h	wrinkle height
Y	dimensionless geometry factor
Y/T	yield to tensile strength ratio
z_1	attachment height of the lower clip gauge
z_2	attachment height of the upper clip gauge

Greek

α	parameter of a Ramberg-Osgood stress-strain curve or backstress tensor
α_{ij}	constants in minimum reelable liner thickness formula
α_u	safety factor
$\alpha^{'}$	flaw height to thickness ratio in new limit load solution for embedded flaws
$\alpha^{''}$	flaw height to thickness ratio in BS7910 limit load solution for embedded flaws
$\alpha^{'''}$	flaw height to thickness ratio in R6 limit load solution for embedded flaws
β	reliability index, half-crack angle or biaxiality ratio
β_{ij}	constants in crack depth adjustment formula
$\beta_{ijk}^{'}$, $\beta_{ijk}^{''}$	constants in crack driving force estimation scheme
γ	function of geometry which relates $\widetilde{P}_L$ to P_L, or mismatch limit load ratio
γ_c	saturation coefficient for $\widetilde{c}$
γ_m	material resistance factor
γ_{SC}	safety class resistance factor
γ_1	kinematic hardening exponent
Γ	counterclockwise contour encircling the crack tip
δ	ovality, or crack tip opening displacement
δ_0	initial (manufacturing) ovality

ΔM, ΔM_i	plastic moment mismatch
Δa	crack growth
ΔK	stress intensity range
$\Delta\varepsilon_a$	axial strain range
$\Delta\varepsilon_h$	hoop strain range
$\Delta\sigma$	stress amplitude
ε	strain, or bending strain
ε_0	elastic strain associated with σ_0
ε_a	axial strain
ε_{app}	remote applied strain
ε_h	hoop strain
ε_{ij}	strain tensor
ε_L	total strain at the end of a Lüders plateau
ε_L^{pl}	plastic part of ε_L
ε_{nom}	maximum nominal reeling strain
ε_{off}	correction factor
ε_p	length of a Lüders plateau
ε^{pl}	plastic part of ε
ε_{ref}	reference strain
ε_{weld}	welding residual strain
$\hat{\varepsilon}$	strain which includes the effect of strain concentration
$\hat{\varepsilon}_{ref}$	adjusted reference strain
θ	polar coordinate
κ	pipe or bending curvature
λ	half wavelength of wrinkle or eigenmode/geometrical imperfection
ν	Poisson's ratio
ρ	plasticity correction factor
σ	stress or stress tensor
σ_0	normalising stress or yield stress of the parent material
σ_{app}	remote applied stress
σ^b	primary bending stress
σ_{eq}	equivalent stress
σ_g	grip force
σ_h	hoop stress
σ_{ij}	stress tensor
σ_p	true stress at the end of a yield plateau
σ_{ref}	reference stress
σ_t	tensile stress
σ_u	ultimate tensile stress
σ_u^{min}	specified minimum ultimate tensile stress at the design temperature
σ_y	yield strength
σ_y^{min}	specified minimum yield strength at the design temperature
$\hat{\sigma}$	stress which includes the effect of strain concentration
ζ	shape function in CTOD estimation scheme
ψ_1, ψ_2	stress potentials

Abbreviations

AE	As-Expanded
API	American Petroleum Institute
AR	As-Received
ASME	American Society of Mechanical Engineers
BS	British Standard
AUT	Automatic Ultrasonic Testing
CRA	Corrosion Resistant Alloy
CCT	Centre Crack Tension
CS	Carbon Steel
CT	Compact Tension
CTOD	Crack Tip Opening Displacement
DIC	Digital Image Correlation
DNVGL	Det Norske Veritas Germanischer Lloyd
DPI	Dye Penetrant Inspection
ECA	Engineering Critical Assessment
ECT	Eddy Current Testing
EDM	Electro-Discharge Machining
EPRI	Electric Power Research Institute
FAD	Failure Assessment Diagram
FCG	Fatigue Crack Growth
FE	Finite Element
FEA	Finite Element Analysis
FL	Fusion Line
FNC	French Nuclear Code
FORM	First Order Reliability Method
FPSO	Floating Production Storage and Offloading
GMAW	Gas Metal Arc Welding
GTAW	Gas Tungsten Arc Welding
GW	Girth Welded
HAZ	Heat Affected Zone
HFW	High Frequency Welding
HISC	Hydrogen Induced Stress Cracking
HRB	Hot-Roll Bonded
HWU	Heriot Watt University
ID	Inner Diameter
IJOPE	International Journal of Offshore and Polar Engineering
ISOPE	International Society of Offshore and Polar Engineers
JIP	Joint Industrial Project
JCO	J-ing C-ing O-ing
JPVT	Journal of Pressure Vessel Technology
LSY	Large Scale Yielding
LoF	Lack of Fusion
MLP	Mechanically Lined Pipe
MMC(T)	Modified Middle Cracked Tension

NDE	Non-Destructive Examination
NSSMC	Nippon Steel and Sumitomo Metal Corporation
OD	Outer Diameter
OMAE	Offshore Mechanics and Arctic Engineering
PTC	Pipeline Technology Centre
PVP	Pressure Vessels and Piping
RT	Radiography Testing
SF	Safety Factor
SCF	(elastic) Stress Concentration Factor
SCR	Steel Catenary Riser
SEN(B)	Single Edge Notch Bending
SEN(T)	Single Edge Notch Tension
SMYS	Specified Minimum Yield Strength
SP	Single Pipe
SSY	Small Scale Yielding
TFP	Tight Fit Pipe
TWI	The Welding Institute
UOE	U-ing O-ing Expansion
WCL	Weld Centre Line
WT	Wall Thickness
YS	Yield Strength
2D	Two-Dimensional
3D	Three-Dimensional

Contents

Declaration of Originality **1**

Copyright Declaration **2**

Abstract **3**

Acknowledgements **4**

1 Introduction to Subsea Mechanically Lined Pipelines **32**

1.1 Subsea Pipelines 32

1.1.1 Introduction to Subsea Pipelines 32

1.1.2 Fabrication of Subsea Pipelines 33

1.1.3 Installation of Subsea Pipelines 34

1.1.4 Operation of Subsea Pipelines 36

1.2 Subsea Mechanically Lined Pipelines 36

1.2.1 Introduction to Subsea Mechanically Lined Pipelines 36

1.2.2 Manufacturing of Mechanically Lined Pipelines 37

1.2.3 Installation and Operation of Mechanically Lined Pipelines 40

1.3 Thesis Outline 42

1.4 Figures 43

2 Review of Design Rules for Reeled Subsea Pipelines 51

2.1 Buckling of Backing Pipe 51

2.1.1 Minimum Reelable Wall Thickness 51

2.1.2 Reliability Assessment 52

2.1.3 Reeling Induced Ovality 54

2.1.4 In-Service Buckling 54

2.2 Wrinkling of Liner Pipe 55

2.2.1 Contact Interference Stress 55

2.2.2 Wrinkling under Axial Compression 56

2.2.3 Wrinkling under Monotonic Bending 59

2.2.4 Wrinkling under Cyclic Bending 68

2.3 Fracture of Pipeline Welds 71

2.3.1 Engineering Critical Assessment 71

2.3.2 Strain-Based Fracture Assessment of Evenmatch Girth Welds 76

2.3.3 Strain-Based Fracture Assessment of Undermatch Girth Welds 82

2.3.4 Fracture Assessment of Interface between Liner and Overlay Welds in MLP 84

2.4 Fatigue of Subsea Pipelines 86

2.4.1 Fatigue Design Approaches 86

2.4.2 High Cycle Fatigue Performance of MLP 89

2.4.3 Low Cycle Fatigue Performance of MLP 90

2.5 Other Service Considerations 90

2.6 Summary of Literature Review 91
2.6.1 Manufacturing 91
2.6.2 Installation 92
2.6.3 Subsea Operation 94
2.7 Figures 96

3 Guideline for Design Against Liner Wrinkling 116

3.1 Introduction 116
3.2 Liner Wrinkling Criteria 117
3.3 Experimental Work 117
3.3.1 Tensile Testing 117
3.3.2 Large Scale Bend Tests 120
3.4 Numerical Simulation 126
3.4.1 Flow Behaviour 126
3.4.2 Wrinkling Parametric Study 127
3.4.3 Numerical Framework for Prediction of Liner Wrinkling during High Strain Cyclic Bending 130
3.4.4 Validation of Framework for Prediction of Liner Wrinkling during High Strain Cyclic Bending 132
3.5 Recommendations for the Design of MLP Against Liner Wrinkling 138
3.6 Tables and Figures 141

4 Guideline for Design Against Fracture of Mechanically Lined Pipe Welds 181

4.1 Introduction 181

4.2 Fracture Assessment of Embedded Flaws in Evenmatch Girth Welds 182

4.2.1 Objective 182

4.2.2 Limit Load Analysis 183

4.2.3 J-Estimation Scheme for Embedded Flaws in Pipeline Girth Welds . . . 186

4.2.4 Fracture Testing – Determination of Limit Load 189

4.2.5 Recommendations for Fracture Assessment of Embedded Flaws in Evenmatch Pipeline Girth Welds 193

4.3 Fracture Assessment of Undermatch Girth Welds 194

4.3.1 Effect of Pre-Strain on Fracture Toughness of Undermatch Girth Welds . 194

4.3.2 Fracture Assessment of Surface Flaws in Undermatch Welds 198

4.3.3 Fracture Assessment of Embedded Flaws in Undermatch Girth Welds . . 205

4.4 Recommendations for Design of Mechanically Lined Pipe Welds Against Fracture 208

4.4.1 Liner Seam Weld 208

4.4.2 Triple Point Interface 208

4.4.3 Overlay Welds 208

4.4.4 Girth Welds 209

4.5 Tables and Figures 210

5 Guideline for Design of Mechanically Lined Pipeline Against Fatigue 253

5.1 Introduction 253

5.2 High Cycle Low Stress Fatigue Design 254

5.2.1 Objective 254

5.2.2 Large Scale Testing 254

5.2.3 Fatigue Crack Growth Assessment of Mechanically Lined Pipe with Triple Point Interface Flaws . . . 260

5.2.4 Case Study . . . 262

5.3 Low Cycle High Stress Fatigue Design . . . 264

5.3.1 Objective . . . 264

5.3.2 Numerical Simulation . . . 264

5.3.3 Experimental Work . . . 268

5.4 Recommendations for Fatigue Design of MLP . . . 270

5.4.1 High Cycle Fatigue Design . . . 270

5.4.2 Low Cycle Fatigue Design . . . 272

5.5 Tables and Figures . . . 274

6 Conclusions and Further Work **291**

6.1 Conclusions . . . 291

6.2 Further Work . . . 295

Bibliography **297**

List of Tables

3.1 Liner Wrinkling Criteria 141

3.2 Liner Tensile Test Pipes 141

3.3 Liner Tensile Test Matrix 141

3.4 Summary of Liner Tensile Test Results 142

3.5 Specification of Mechanically Lined Pipes for Bending Trials 142

3.6 10” Bend Test Pipes 142

3.7 10” Bend Test Regime 142

3.8 Test Pipe “10-1”: Largest Imperfections Measured in Middle of Pipe during Strain Capacity Tests 143

3.9 Test Pipe “10-1”: Largest Imperfections Measured at Anchor Side during Strain Capacity Tests 143

3.10 Test Pipe “10-2.GW”: Largest Imperfections Measured during Strain Capacity Tests 144

3.11 Test Pipe “10-3.GW”: Largest Imperfections Measured during Strain Capacity Tests 144

3.12 12” Bend Test Pipes 145

3.13 12” Bend Test Regime 145

3.14 Test Pipe “12-1”: Largest Imperfections Measured during Strain Capacity Tests 145

3.15 Test Pipe "12-2.GW": Largest Imperfections Measured at Anchor Side during Strain Capacity Tests 146

3.16 Test Pipe "12-2.GW": Largest Imperfections Measured at Pull Side during Strain Capacity Tests 146

3.17 Test Pipe "12-3.GW": Largest Imperfections Measured during Strain Capacity Tests 147

3.18 Test Pipe "10-1": Largest Liner Imperfections – Measurements vs. Numerical Predictions 147

3.19 Test Pipe "10-2": Largest Liner Imperfections – Measurements vs. Numerical Predictions 148

3.20 Test Pipe "10-3": Largest Liner Imperfections – Measurements vs. Numerical Predictions 148

3.21 Test Pipe "12-1": Largest Liner Imperfections – Measurements vs. Numerical Predictions 149

3.22 Test Pipe "12-2.GW": Largest Liner Imperfections – Measurements vs. Numerical Predictions 150

3.23 Test Pipe "12-3.GW": Largest Liner Imperfections – Measurements vs. Numerical Predictions 151

4.1 Limit Load Analysis: FEA Case Matrix – Crack Geometries 210

4.2 Parameters of Assumed Stress-Strain Curve 210

4.3 Values of β'_{ijk} for $n = 16.8$ 210

4.4 Values of β''_{ijk} for $n = 16.8$ 210

4.5 Range of Application of New J-Estimation Scheme 211

4.6 Embedded Flaw Test Matrix 211

4.7 Test Results – Reference Load 211

4.8 Fracture Toughness Testing – Weld Metal Mismatch 211

4.9 Surface Flaws in Undermatch Welds: Parametric FEA Matrix of Cases – Crack Geometries 212

4.10 Parametric FEA – Stress-Strain Curve Parameters for Materials with Yield Plateau, E=210 GPa, σ_y=450 MPa, n=16.8 (Y/T=0.9) 212

4.11 Parametric FEA – Stress-Strain Curve Parameters for Materials with Continuous Hardening, E=210 GPa, σ_y=450 MPa, n=5.7 (Y/T=0.6) 212

4.12 Parametric FEA Matrix of Cases – Tensile Properties 212

4.13 New Crack Depth Adjustment Formula – Values of β_{ij} for Material Exhibiting Continuous Hardening 213

4.14 New Crack Depth Adjustment Formula – Range of Application 213

4.15 Validation of New ECA Approach for Undermatch Welds – Pipe Sizes 213

4.16 Validation of New ECA Approach for Undermatch Welds – Effective Undermatch for Material with Yield Plateau 214

4.17 Validation of New ECA Approach for Undermatch Welds – Effective Undermatch for Material with Continuous Hardening 214

5.1 Fatigue Test Regime 274

5.2 FEA Matrix of Cases – Carbon Steel Crack Geometries 274

5.3 FEA Matrix of Cases – CRA Crack Geometries 274

5.4 Selected Results for Cracks in Single Carbon Steel Pipe 274

5.5 Selected Results for Cracks in Single Liner Pipe 275

5.6 Selected Results for Cracks in Carbon Steel Pipe of MLP 275

5.7 Selected Results for Cracks in Liner Pipe of MLP 275

List of Figures

1.1 Overview of Subsea Oil Field Architecture 43

1.2 Low Strain Installation Methods for Subsea Pipelines 44

1.3 Reel-Lay Installation 45

1.4 Reel-Lay Installation: Moment-Curvature Plot 46

1.5 Illustration of Mechanically Lined Pipe 46

1.6 Main Steps of Manufacturing of Mechanically Lined Pipe 47

1.7 Liner Expansion during Manufacturing of Mechanically Lined Pipe at: (a) Cladtek, (b) Kuroki, (c) Proclad/Butting 48

1.8 Effect of Manufacturing Imperfections in Liner Seam Weld: (a) Lack of Fusion Flaws, (b) Liner Burst during Expansion 49

1.9 Manufacturing Imperfections in Liner Body 50

2.1 Effect of High Plastic Moment Mismatch during Reel-Lay Installation: (a) Bulging, (b) Buckling 96

2.2 Mises, Tresca and Haythornthwaite Yield Surfaces (from Martinez *et al.* [46]) . . 97

2.3 Wrinkling Modes under Axial Compression: (a) Standalone Liner, (b) Liner Inside Backing Pipe, (c) Mechanically Lined Pipe (from Focke *et al.* [54]) 98

2.4 Large Scale Bending Rig: (a) Overview, (b) Zoom on Reeling Former (from Focke *et al.* [53]) 99

2.5 Laser Inspection Tool (from Focke *et al.* [63]) 100

2.6 Definition of Liner Imperfection Height from Laser Measurements (from Focke [63]) 100

2.7 Liner Wrinkling during Bending of Tight Fit Pipe: (a) Low Grip, (b) High Grip (from Focke *et al.* [63]) 100

2.8 Four-Point Bending of Mechanically Lined Pipe: (a) Bending Rig, (b) FE Model (from Hilberink *et al.* [64, 66]) 101

2.9 Liner Wrinkling during Four-Point Bending of Mechanically Lined Pipe: (a) Experimental Result, (b) Numerical Prediction (from Hilberink *et al.* [64]) 102

2.10 Numerical Prediction of Bending Moment-Curvature Diagram of Standalone and Confined Liner under Pure Bending (from Hilberink *et al.* [65]) 102

2.11 Liner Wrinkling during Pure Bending of MLP (from Hilberink *et al.* [66]) 103

2.12 FEA Model for Simulation of Bending of MLP (from Vasilikis *et al.* [68]) 103

2.13 Numerical Prediction of Liner Separation during Bending of Loose Fit Pipe (SFP) and Tight Fit Pipe (TFP) – Identification of 1st Bifurcation Point (from Vasilikis *et al.* [68]) 103

2.14 Numerical Prediction of Liner Wrinkling during Bending of MLP – Illustration of 1st Bifurcation Point: (Left) Half-Wavelength, (Right) Full Length Pipe (from Vasilikis *et al.* [68]) 104

2.15 Numerical Prediction of Liner Separation during Bending of Loose Fit Pipe – Identification of 1st and 2nd Bifurcation Points (from Vasilikis *et al.* [68]) 104

2.16 Numerical Prediction of Liner Wrinkling during Bending of MLP – Illustration of 2nd Bifurcation Point: (Left) Single Wavelength, (Right) Full Length Pipe (from Vasilikis *et al.* [68]) 104

2.17 Liner Wrinkling during Bending of Lined Pipe – Illustration of 3rd Bifurcation Point: (Left) Numerical Prediction, (Right) Test Result (from Vasilikis *et al.* [71]) 105

2.18 Liner Wrinkling during Bending of Lined Pipe – Comparison between Numerical Predictions and Test Results (from Vasilikis *et al.* [71]) 105

2.19 FEA Model for Simulation of Bending of Lined Pipe (from Yuan *et al.* [72]) . . . 105

2.20 Liner Imperfection Modes: (a) Axisymmetrical, (b) Asymmetrical (from Yuan [72]) 106

2.21 Numerical Prediction of Liner Wrinkling during Bending of Lined Pipe: (Top) Uniform Wrinkling, (Bottom) Diamond-Type Wrinkling (from Yuan *et al.* [72]) . . . 106

2.22 Topology of Inner Surface of Liner in As-Manufactured 12" Lined Pipe with Seamless Backing Pipe (from Harrison *et al.* [76]) 107

2.23 Comparison between Natural and Idealised Harmonic Circumferential Imperfections in Liner of As-Manufactured 12" MLP with Seamless Backing Pipe (from Harrison *et al.* [76]) 107

2.24 Heriot Watt University Bending Rig (now transferred to the Pipeline Technology Centre (PTC)) 107

2.25 Liner Wrinkling during Cyclic Plastic Bending of 12.75" Lined Pipe at HWU . . 108

2.26 FEA Model for Simulation of Cyclic Plastic Bending of MLP at HWU (from Tkaczyk *et al.* [82]) 108

2.27 Liner Wrinkling during Cyclic Plastic Bending of 12.75" Lined Pipe: Comparison between Experimental and Numerical Results (from Tkaczyk *et al.* [82]) 108

2.28 CladTek Bending Rig 109

2.29 Kuroki Bending Rig 109

2.30 Fracture Toughness Resistance Curve 109

2.31 SENT Fracture Toughness Test Specimen 110

2.32 Effect of Pre-Strain on Fracture Toughness of Overmatch Weld (from Tkaczyk [96]) 110

2.33 Pipe and Surface Flaw Geometry 110

2.34 Failure Assessment Diagram 111

2.35 Embedded Flaw Geometry 111

2.36 DNVGL Reclassification Criterion for Embedded Flaws 111

2.37 Typical Tensile Response for Material with Yield Plateau (from Tkaczyk *et al.* [121]) 112

2.38 Evolution of J-integral vs. Applied Strain for Material with Yield Plateau (from Tkaczyk *et al.* [121]) 112

2.39 Definition of Girth Weld Overmatching Clad/Lined Parent Pipe (from DNVGL [81]) 113

2.40 Definition of Girth Weld Partially Overmatching Clad/Lined Parent Pipe (from DNVGL [81]) 113

2.41 CRA Flaw at MLP Triple Point Interface (from Tkaczyk *et al.* [128]) 113

2.42 FE Model of MLP with CRA Flaw at Triple Point Interface (from Tkaczyk [128]) 114

2.43 Illustration of Tangency Approach: (a) Ductile Tearing Instability, (b) Tearing Limited to 0.5 mm (from Tkaczyk *et al.* [128]) 114

2.44 Fatigue Crack Initiation Sites: (a) Standard Pipeline, (b) Mechanically Lined Pipeline (from Tkaczyk *et al.* [128]) 115

2.45 CladTek Rig in 4-Point Bending Configuration (from Tkaczyk *et al.* [82]) 115

3.1 Liner Tensile Test Specimen 152

3.2 Tensile Testing of CRA Liners at A2MI: (a) Specimen Instrumented and Gripped on Test Frame, (b) Anti-Buckling System Mounted, (c) Test Machine 153

3.3 CRA Liner Stress-Strain Curves in As-Received Condition: (a) 316L, (b) 625 . . 154

3.4 CRA Liner Stress-Strain Curves in As-Expanded Condition: (a) 316L, (b) 625 . 155

3.5 Effect of Hoop Expansion on CRA Liner Tensile Behaviour: (a) 316L, (b) 625 . 156

3.6 Effect of Cyclic Plastic Straining on CRA Liner Tensile Behaviour: (a) 316L, (b) 625, (c) Tension vs Compression Load Mode 157

3.7 Test Pipe “10-1”: Longitudinal Profile of Liner Imperfections at 9 o’clock after Bending on 6.4 m Former 158

3.8 Test Pipe “10-1”: Bending on 5.5 m Former 158

3.9 Test Pipe “10-1”: Onset of Liner Periodic Imperfection Mode Shape during Bending on 5.5 m Former 159

3.10 Test Pipe “10-1”: Evolution of Largest Liner Imperfection during Third Bending Cycle 159

3.11 Test Pipe “10-2.GW”: Longitudinal Profile of Liner Imperfections at 9 o’clock after Four Bending Cycles 160

3.12 Test Pipe “10-3.GW”: Longitudinal Profile of Liner Imperfections at 9 o’clock after Four Bending Cycles 160

3.13 Test Pipe “12-1”: Longitudinal Profile of Liner Imperfections at 9 o’clock before and after First Bending Event (on 6.4 m Former) 161

3.14 Test Pipe “12-1”: Longitudinal Profile of Liner Imperfections after Fourth Bending Event (on 5.5 m Former) 161

3.15 Test Pipe “12-2”: Longitudinal Profile of Liner Imperfections before Test and after Third Bending Cycle 162

3.16 Test Pipe “12-2”: Longitudinal Profile of Liner Imperfections after Fourth Bending Event (on 5.5 m Former) 162

3.17 Test Pipe “12-3”: Longitudinal Profile of Liner Imperfections before and after Testing 163

3.18 Comparison between Test Results and Numerical Prediction of Liner Behaviour during Cyclic Plastic Straining: (a) 316L, (b) 625 164

3.19 As-Received Stress-Strain Curves Used in Numerical Simulation of Bending of MLP 165

3.20 Manufacturing Imperfections in Mechanically Lined Pipe: (a) Seamless Backing Pipe Inner Surface, (b) Impressions on Liner Inner Surface 165

3.21 Liner Eigenmode Analysis: (a) Finite-Element Analysis Model, (b) Contour Plot of Eigenmode Radial Displacements 166

3.22 Finite-Element Analysis Model for Wrinkling Parametric Study: (a) Typical Mesh and Boundary Conditions, (b) Contour Plot of Liner Separation from Backing Pipe 166

3.23 Effect of Imperfection Height on Liner Separation from Backing Pipe during Bending 167

3.24 Effect of Imperfection Mode Shape on Liner Separation during Bending 167

3.25 Effect of Residual Gap between Liner and Backing Pipe on Liner Separation during Bending 168

3.26 Effect of Liner Yield Strength on Liner Separation during Bending: (a) Assumed Stress-Strain Curves, (b) Liner Separation 169

3.27 Effect of Liner Strain Hardening on Liner Separation during Bending: (a) Assumed Stress-Strain Curves, (b) Liner Separation 170

3.28 Finite-Element Analysis Model for Simulating a Bending Trial 171

3.29 Finite-Element Analysis Model for Simulating Reel-Lay Installation: MLP Submodel in Span between Reel and Aligner 172

3.30 Flowchart for Finite-Element Simulation of Reel-Lay Installation of MLP 173

3.31 Eigenmode for Seeding Liner Imperfections in Three-Dimensional Finite-Element Analysis Model for Cyclic Plastic Bending of MLP 173

3.32 Test Pipe “10-1”: Numerical Prediction of Evolution of Liner Imperfections during Cyclic Bending 173

3.33 Test Pipe “10-1”: Largest Liner Imperfections – Measurements vs. Numerical Predictions: (a) 3 o’clock, (b) 9 o’clock, (c) Largest Imperfection Regardless of Clock Position 174

3.34 Test Pipes “10-2.GW” and “10-3.GW”: Largest Liner Imperfections – Measurements vs. Numerical Predictions: (a) 3 o’clock, (b) 9 o’clock, (c) Largest Imperfection Regardless of Clock Position 175

3.35 Test Pipe "12-1": Largest Liner Imperfections – Measurements vs. Numerical Predictions: (a) 3 o'clock, (b) 9 o'clock, (c) Largest Imperfection Regardless of Clock Position 176

3.36 Numerical Prediction of Evolution of Liner Imperfections during Cyclic Bending: (a) Test Pipe "12-2.GW", (b) Test Pipe "12-3.GW" 177

3.37 Test Pipe "12-2.GW": Largest Liner Imperfections – Measurements vs. Numerical Predictions: (a) 3 o'clock, (b) 9 o'clock, (c) Largest Imperfection Regardless of Clock Position 178

3.38 Test Pipe "12-3.GW": Largest Liner Imperfections – Measurements vs. Numerical Predictions: (a) 3 o'clock, (b) 9 o'clock, (c) Largest Imperfection Regardless of Clock Position 179

3.39 12" Test Pipes: Largest Liner Imperfections – Measurements vs. Numerical Predictions with von Mises and Martinez *et al.* Yield Criteria: (a) "12-2.GW", (b) "12-3.GW" 180

4.1 Embedded Flaw Geometry 215

4.2 Illustration of Ligament Collapse Criterion 215

4.3 Finite-Element Analysis Model of Pipe with Embedded Flaw 215

4.4 Limit Load Analysis Results – Effect of Normalised Embedment Depth: (a) $2c/W = 0.02$, (b) $2c/W = 0.05$, (c) $2c/W = 0.10$ 216

4.5 Limit Load Analysis Results – Effect of Normalised Crack Height: (a) $2c/W = 0.02$, (b) $2c/W = 0.05$, (c) $2c/W = 0.10$ 217

4.6 Limit Load Analysis Results – Effect of Normalised Crack Length: (a) $2a/t = 0.05$, (b) $2a/t = 0.15$, (c) $2a/t = 040$ 218

4.7 Comparison Between Limit Load Solutions: (a) $2a/t = 0.05$, (b) $2a/t = 0.15$, (c) $2a/t = 040$ 219

4.8 J-Estimation Scheme for Embedded Flaws – Assumed Stress-Strain Curve . . . 220

4.9 J-Estimation Scheme for Embedded Flaws – Comparison between Analytical and Numerical SIF: (a) $2a/t = 0.05$, (b) $2a/t = 0.40$ 220

4.10 Comparison of J-Estimation Schemes for $2a/t = 0.05$: (a) $p^A/t = 1.5$, (b) $p^A/t = 9.0$ 221

4.11 Comparison of J-Estimation Schemes for $2a/t = 0.40$: (a) $p^A/t = 1.0$, (b) $p^A/t = 1.5$ 222

4.12 Schematic Illustration of MMCT Specimen with Through Thickness Embedded Flaw 223

4.13 Examples of Speckle Patterns Applied on Test Specimens 223

4.14 Embedded Flaw Test Setup 223

4.15 Test Setup for Establishment of Reference Load 224

4.16 Test Results – Stress-Strain Curves Obtained with Uncracked Specimens 224

4.17 Test Results – Illustration of Lüders' Banding Process: (a) Strain-Time Curves, (b) Stress-Strain Curves 225

4.18 Test Results – Load versus Time Curves: (a) $2a = 4.0$ mm and $p^A = 1.0$ mm, (b) $2a = 6.0$ mm and $p^A = 1.5$ mm 226

4.19 Summary of Test Results 227

4.20 Regression Analysis 227

4.21 Strain and Displacement Contours from Digital Image Correlation – Specimens with $2a = 4.0$ mm $\times$ $p^A = 1.0$ mm Flaw: (a) Yield Plateau, (b) Continuous Hardening 228

4.22 Strain and Displacement Contours from Digital Image Correlation – Specimens with $2a = 6.0$ mm $\times$ $p^A = 4.5$ mm Flaw: (a) Yield Plateau, (b) Continuous Hardening 229

4.23 Finite-Element Analysis Model for Simulation of Embedded Flaw Tests 230

4.24 Comparison between FEA and Embedded Flaw Test Results for Specimen with $2a = 4.0$ mm $\times$ $p^A = 1.0$ mm: (a) Yield Plateau, (b) Continuous Hardening . . 230

4.25 Comparison between FEA and DIC Results for Material with Continuous Hardening: (a) $2a = 4.0$ mm $\times$ $p^A = 2.0$ mm, (b) $2a = 6.0$ mm $\times$ $p^A = 1.5$ mm . . . 231

4.26 Comparison between FEA and DIC Contour Plots for Material with Yield Plateau: (a) $2a = 4.0$ mm $\times$ $p^A = 1.0$ mm, (b) $2a = 6.0$ mm $\times$ $p^A = 1.5$ mm 232

4.27 Comparison between FEA and DIC Contour Plots for Material with Continuous Hardening: (a) $2a = 4.0$ mm $\times$ $p^A = 1.0$ mm, (b) $2a = 6.0$ mm $\times$ $p^A = 3.0$ mm 233

4.28 Comparison between FEA and Test Based Limit Load Solutions 234

4.29 Fracture Toughness Testing – Profile of Weld Bevel and Weld Passes 234

4.30 Fracture Toughness Testing – Specimen Used for Material Characterisation . . . 235

4.31 Fracture Toughness Testing – Material Stress-Strain Curves 235

4.32 Fracture Toughness Test Specimen: (a) General Overview, (b) Side Groove Detail236

4.33 Fracture Toughness Testing – Geometrical Construction Used to Estimate CMOD and CTOD 237

4.34 Fracture Toughness Testing – Example of Load-CMOD and Load-CTOD Curves 237

4.35 Fracture Toughness Testing: (a) Setup for Tensile Straining Event, (b) Setup for Compressive Straining Event, (c) Acquisition of Silicon Impression of Crack . . . 238

4.36 Fracture Toughness Testing – Silicon Replica 239

4.37 Fracture Toughness Testing – Example of Fracture Face Showing EDM, Pre-Crack and Tearing 239

4.38 Fracture Toughness Testing – Results Summary 240

4.39 Surface Flaws in Undermatch Welds – Weld Geometry: (a) Actual, (b) Equivalent240

4.40 Parametric FEA – Stress-Strain Curves with Yield Plateau, E=210 GPa, σ_y=450 MPa, n=16.8 241

4.41 Parametric FEA – Stress-Strain Curves with Continuous Hardening, E=210 GPa, σ_y=450 MPa, n=5.7 241

4.42 Parametric FEA – Typical Model 242

4.43 Parametric FEA Results – Effect of Yield Plateau on Crack Driving Force in Evenmatch Weld 242

4.44 Parametric FEA Results – Effect of Undermatch on Crack Driving Force 243

4.45 Parametric FEA Results – Effect of Undermatch and Crack Depth on Normalised Crack Depth Adjustment in Material Exhibiting Continuous Hardening 243

4.46 Parametric FEA Results – Effect of Undermatch and Crack Length on Normalised Crack Depth Adjustment in Material Exhibiting Yield Plateau 244

4.47 Validation of New ECA Procedure for Undermatch Welds – Stress-Strain Curves with Yield Plateau 244

4.48 Validation of New ECA Procedure for Undermatch Welds – Stress-Strain Curves with Continuous Hardening 245

4.49 Validation of New ECA Procedure for Undermatch Welds – Equivalent Stress-Strain Curve 245

4.50 Validation of New ECA Procedure for Undermatch Welds – Results for 168.3 mm OD × 7.11 mm WT Pipe with Yield Plateau 246

4.51 Validation of New ECA Procedure for Undermatch Welds – Results for 323.9 mm OD × 15.9 mm WT Pipe with Continuous Hardening 247

4.52 Validation of New ECA Procedure for Undermatch Welds – Results for 323.9 mm OD × 25.4 mm WT Pipe with Continuous Hardening 248

4.53 Validation of New ECA Procedure for Undermatch Welds – Results for 406.4 mm OD × 25.4 mm WT Pipe with and without Yield Plateau 249

4.54 Adjustment Scheme for Embedded Flaws in Undermatch Welds 250

4.55 Validation of New ECA Procedure for Embedded Flaws in Undermatch Welds – CTOD Versus Strain Curves for: (a) 168.3 mm OD × 7.11 mm WT Pipe with Yield Plateau, (b) 323.9 mm OD × 15.9 mm WT Pipe with Yield Plateau, (c) 406.4 mm OD × 25.4 mm WT Pipe with Continuous Hardening 251

4.56 Validation of New ECA Procedure for Embedded Flaws in Undermatch Welds – Normalised CTOD Versus Crack Length Curves for: (a) 168.3 mm OD × 7.11 mm WT Pipe with Yield Plateau, (b) 323.9 mm OD × 15.9 mm WT Pipe with Yield Plateau, (c) 406.4 mm OD × 25.4 mm WT Pipe with Continuous Hardening 252

5.1 Uncontrolled Galling during Liner Insertion: (a) Scratches and Nuggets, (b) Liner Dents 276

5.2 Fatigue String Weld Profiles: (a) Seal, (b) Clad Overlay, (c) Girth Weld 277

5.3 Fatigue String Instrumentation 278

5.4 TWI Resonant Rig 278

5.5 DPI Inspection Tool 279

5.6 ECT Inspection Tool: (a) Probe, (b) Calibration Block with 3 mm Deep Notch . 279

5.7 Post-Mortem Examination: (a) DPI Indication, (b) Macro-Section 280

5.8 Fatigue Test Results versus DNVGL-RP-C203 SN Curves 280

5.9 MLP Triple Point Interface Flaws: (a) CS Flaw (b) CRA Flaw 281

5.10 Fatigue Crack Growth Curve 282

5.11 Fatigue Crack Growth Assessment Results – Normalised Number of Cycles to Failure 283

5.12 Low Cycle Fatigue of MLP – 3D FEA Model for Simulation of Manufacturing and Reeling of MLP 284

5.13 Low Cycle Fatigue of MLP – 3D FEA Model for Simulation of In-Service Operation of MLP 284

5.14 Low Cycle Fatigue of MLP – Liner Strip Model Extracted from 3D FEA Model of MLP: Contour Plot of Liner Lift-off from Host Pipe 285

5.15 8” MLP with 316L Liner – Wrinkle Height 285

5.16 8” MLP with 316L Liner – In-Service Stress Ranges 286

5.17 8” MLP with 316L Liner – In-Service Strain Ranges 286

5.18 Stress Ranges in Alloy 316L Liner – 3D Pipe Model vs Strip Model 287

5.19 Strain Ranges in Alloy 316L Liner – 3D Pipe Model vs Strip Model 287

5.20 Small Scale Fatigue Test Specimen 288

5.21 Small Scale Fatigue Test Machine 288

5.22 Load-Life Line 289

5.23 Crack Initiation Site 289

5.24 Small Scale Fatigue Test Results 290

Chapter 1

Introduction to Subsea Mechanically Lined Pipelines

1.1 Subsea Pipelines

1.1.1 Introduction to Subsea Pipelines

Subsea pipelines are used to transport large volumes of oil and/or gas from a well to an offshore storage and processing facility (the pipeline is referred to as a gathering or infield line), or from an offshore facility to another offshore/onshore facility (the pipeline is referred to as an export line). Other pipelines such as water/gas injection lines are used to re-pressurise reservoirs. There are two main categories of offshore storage and processing facilities: (i) platforms, which are usually fixed and suitable for shallow to moderately deep water depths (typically less than 1000 m) and (ii) floating production storage and offloading (FPSO) vessels, suitable for deeper waters. Petroleum fluids processed in offshore platforms are often transmitted via export lines, while those processed in FPSOs are typically offloaded into tankers, and then transported to a designated onshore facility. A subsea pipeline can be split into two parts: (i) a flowline, which lies on a seabed and (ii) a riser, which is suspended between a seabed and an anchoring point on an FPSO or a platform. Risers are subjected to dynamic loading, whereas flowlines typically experience static loads. Figure 1.1 illustrates a subsea field architecture.

1.1.2 Fabrication of Subsea Pipelines

There are two categories of subsea pipelines: (i) rigid and (ii) flexible pipelines. Rigid pipelines, which are considered in this work, are generally more economical, while flexible pipelines are more versatile. The former are made of tubular joints, typically 12 m long, which are circumferentially welded together to achieve a required length. Circumferential welding of pipe joints, termed "girth" welding, is performed at an onshore spoolbase or on a pipelay vessel offshore.

Most often, pipe joints are produced from cylinders, called "billets", or from plate. In the latter case, the plate is trimmed to achieve the desired width and then rounded. The rounding process usually involves bending into a "U" shape, then into an "O" shape and finally Expansion (hence "UOE" pipes). Subsequently, the rounded plate is longitudinally welded using a consumable, to produce a "seam-welded" pipe. The UOE process is generally used to produce large diameter (above 400 mm typically) thick walled (above 18 mm typically) pipes. Smaller (down to 350 mm typically) and thinner (down to 16 mm typically) seam-welded pipes can also be manufactured using a high frequency welding (HFW) process, whereby a coil is unwounded from a drum, rounded in a continuous process and welded through an induction welding process. The seam weld is then ground flush and subjected to a non-destructive examination (NDE), such as automatic ultrasonic testing (AUT). Finally, the pipe may be heat-treated to relieve stresses.

Seam-welded pipes exhibit a more uniform distribution of wall thickness (WT) compared to "seamless" pipes, manufactured from billets. During fabrication, a seamless pipe is heated in a furnace and pierced through to extrude the excess material. The pipe is then sized to achieve the required dimensions in terms of outer diameter (OD) and WT. Finally, the pipe is heat-treated in a furnace. The seamless process is generally used for small to medium size pipes (up to 460 mm OD typically) and offers a wider range of WTs and higher strain hardening compared to the cold-worked seam-welded process. Consequently, seamless pipes are more frequently used subsea. The selection of material grade for a subsea pipeline is dictated by project constraints, such as procurement, installation and operational (maintenance) costs. Most pipelines currently in operation subsea were made of medium grade carbon steels (CS), such as API 5L X52, X60 or X65 [1], supplied by Tenaris [2] or Vallourec [3].

1.1.3 Installation of Subsea Pipelines

Installation Methods for Subsea Pipelines

There are two categories of installation methods for subsea pipelines: (i) low strain installation methods, where the pipeline generally remains within the elastic regime, and (ii) high strain installation methods, involving plastic deformation. The former include S-lay and J-lay [4], illustrated in Figure 1.2. The S-lay method is often used for installing pipelines in shallow water (typically up to 300 m). Pipe joints are loaded on a lay barge onshore and transported to the offshore field. Upon arrival at the installation site the pipeline is (i) welded, inspected and coated (for insulation and/or corrosion protection) in a horizontal plane, (ii) bent over a stinger as it exits the vessel, (iii) nearly straightened by gravity when it enters into the water, (iv) reverse/sag bent as it approaches a touchdown point and finally (v) laid on a seabed, resulting in an 'S' catenary shape, see Fig. 1.2(a). The pipeline typically sees the highest installation strain on the stinger. Consequently, the stinger radius is designed not to exceed the maximum allowable bending strain, which is typically 0.4%.

As the installation strain generally increases with the water depth, the J-lay method is preferred to the S-lay method for deeper waters. Here, the pipeline is welded, inspected and deployed in a nearly vertical plane, as shown in Fig. 1.2(b). Consequently, the highest installation strain occurs at the sag-band, and this can be controlled by applying appropriate laying tension. Although larger diameter pipes (up to 1500 mm OD typically) can be installed using low strain installation methods, the installation process is typically much slower than that for high strain methods such as reel-lay. Furthermore, welding and inspection are more challenging offshore. Consequently, reel-lay is often preferred.

The reel-lay process, illustrated in Fig. 1.3, involves welding, inspecting and coating at an onshore spoolbase, shown in Fig. 1.3(a). Thus, productivity and quality can be optimised in a controlled environment. The pipeline is assembled into lengths of approximately 1 km, referred to as "stalks", and stored in a dedicated area at the spoolbase. When the reel-lay vessel arrives at the spoolbase a first stalk is spooled onto a large diameter reel mounted on the vessel, see

Fig. 1.3(a). Subsequently, a "tie-in" weld is performed between the trailing end of the first stalk and the leading end of a second stalk, and spooling-on is resumed. This process is repeated until a pipeline section, several kilometres long, is loaded on the vessel. The latter then sails to the offshore field where the pipeline is deployed, as detailed in Fig. 1.3(b).

Reel-Lay Installation

A standard reel-lay installation involves two symmetrical plastic strain cycles, illustrated in Figure 1.4. The symbols M and κ in Fig. 1.4 respectively denote applied bending moment and pipe curvature at a given location during reeling, while the numbers '1' to '7' indicate the sequence of loading. During spooling-on the pipeline is plastically bent onto a reel which has a curvature 'a' in Fig. 1.4. Upon arrival of the pipelay vessel at the installation site the pipeline is reverse bent to a curvature 'b' in Fig. 1.4, during partial straightening in the span between the reel and the aligner (see Fig. 1.3). Subsequently, the pipeline conforms to a curvature 'c' in Fig. 1.4 when it is once again plastically deformed over the aligner. Finally, when passing through the straightener the pipeline is plastically deformed to a negative curvature 'd' in Fig. 1.4, resulting in the deployment of a straight pipe into the seabed following elastic recovery. The maximum nominal bending strain, ε_{nom} seen by a pipe during reeling, is determined from

$$\varepsilon_{nom} = \frac{D}{D + 2R} \tag{1.1}$$

where D and R are the pipe OD and the reel hub radius, respectively. R is typically in the order of 7.5 to 10.5 m, and ε_{nom} can be up to 2.5% for 18" (457 mm) OD pipes, which represent the upper bound size for reeled pipelines [5].

Plastic deformation during reeling can cause high ovalisation of a slender pipeline. This phenomenon, known as the Brazier effect [6], may be magnified by a bending strength mismatch between consecutive joints, resulting from inherent wall thickness and yield strength (YS) variations. Fracture may also be a concern if (i) a pipeline contains large flaws such as lack of fusion (LoF) at the heat affected zone (HAZ) or pores/inclusions in the weld, (ii) there is significant pipe wall misalignment (referred to as "hilo") or axial misalignment at the weld, (iii) the yield

strength mismatch between parent metal (PM) and weld metal (WM) is high, or (iv) the weld's fracture toughness is poor. All these need to be properly managed to ensure a safe reel-lay installation.

1.1.4 Operation of Subsea Pipelines

Following subsea installation rigid pipelines are pre-commissioned prior to start of operation. This involves hydrotesting the pipeline and running a gauge pig through it, to verify that pressure containment and flow assurance, respectively, have not been compromised.

Subsea pipelines are subjected to a combination of environmental and operational loads during service. The former generally include external pressure and bending resulting from wave/current loads, while the latter involve temperature and internal pressure. Collapse under external pressure or combined external pressure and bending is primarily governed by the pipeline's as-laid ovality, diameter to thickness ratio (D/t) and yield strength. Cyclic elastic bending from wave/current loads may trigger high cycle fatigue of girth welds. The pipeline may also be at risk of burst if the operating internal pressure is too high. Finally, high internal pressure in combination with high temperature may trigger lateral or upheaval buckling, which may promote girth weld fracture and/or low cycle fatigue.

1.2 Subsea Mechanically Lined Pipelines

1.2.1 Introduction to Subsea Mechanically Lined Pipelines

The demand for subsea pipelines which can operate under high temperature and pressure and transport highly corrosive fluids is increasing. Carbon manganese steels used to produce the vast majority of pipelines installed subsea to date, often do not meet the corrosion requirements and therefore more expensive corrosion resistant alloy (CRA) materials, such as 13% Cr martensitic steel, have also been used. Furthermore, high operating pressures often require the use of heavy wall pipes, which significantly increases the pipeline's cost. Moreover, small diameter

CRA pipes (e.g. 6.625" in diameter) are often supplied in 6 m joints and consequently, there is a significant cost associated with additional girth welding. Finally, solid CRA pipes may be susceptible to hydrogen induced stress cracking (HISC) and are often not readily available.

An alternative to the solid CRA pipe is the bi-metal pipe, which comprises of a carbon steel pipe hosting a thin (usually 2.5 – 3.0 mm thick) layer of corrosion resistant material such as alloy 316L [7, 8]. Here, the CS host pipe provides strength while the CRA layer provides corrosion protection and also strength [7, 9, 10]. The bond between both layers can be either (i) metallurgical, in which case the bi-metal pipe is referred to as hot-roll bonded (HRB) metallurgically clad pipe (or simply clad pipe), or (ii) mechanical, in which case the bi-metal pipe is called mechanically lined pipe (MLP, or simply lined pipe). In contrast to solid CRA pipes, bi-metal pipes experience much less reduction in tensile strength at elevated temperatures (termed temperature de-rating) and are not susceptible to HISC. Mechanically lined pipe, illustrated in Figure 1.5, offer shorter lead times than either solid CRA or clad pipe. Furthermore, small diameter lined pipes can be supplied in 12 m lengths, unlike clad or CRA pipes, and therefore additional girth welding cost can be avoided. Finally, the lined pipe is generally significantly cheaper in terms of procurement compared to equivalent clad and CRA pipes. Consequently, mechanically lined pipe is becoming a preferred solution for the transport of corrosive fluids.

1.2.2 Manufacturing of Mechanically Lined Pipelines

Manufacturing Approaches for Mechanically Lined Pipelines

There are three main approaches for manufacturing mechanically lined pipes, the primary difference between them being the process used to form the CRA liner and apply interference fit (also referred to as "grip force") between the liner and the CS host pipe. The CRA liner and CS host pipe are fabricated separately, typically according to API 5LC [11] and API 5L [1], respectively, and assembled following the steps shown in Figure 1.6.

Cladtek [12], based in Indonesia, follows fabrication approach "A" where the CRA liners are individually fabricated from a flat plate using the JCO process (i.e. the plate is bent into a 'J'

then 'C' and finally 'O' shape, similarly to a UOE process) and seam welded with consumable. The seam-welded liner is then heat-treated as required and calibrated. The host pipe inner surface is cleared of debris and shot blasted. Subsequently, the liner is inserted into the host pipe and mechanically expanded using an internal mandrel, shown in Figure 1.7(a). After a seal weld is completed between the end of the liner and the host pipe inner diameter (ID) to prevent water/moisture ingress in the annulus, the pipe is filled with water and pressurised until the target expansion of the host pipe is achieved. When pressure is removed the carbon steel host pipe springs back more than the liner, resulting in the establishment of an interference fit between the host pipe and the liner. Finally, weld overlay (also called "overlay cladding") is completed between the liner and the host pipe at both pipe ends (the cladding eases girth welding, NDE and cut/repair). Cladtek has been manufacturing MLP since the early 2000s.

In the late 1970s Kawasaki Heavy Industries developed a mechanically lined pipe product referred to as tight fight pipe (TFP). A decade later the license for manufacturing of TFP was transferred to Nippon Steel and Sumitomo Metal Corporation (NSSMC), who rebranded it "C-II" pipe. Production of "C-II" pipe stopped in 1995, due to a shortage of demand, and Kuroki was granted an exclusive license for the TFP in 1999. Kuroki [13], based in Japan, follows fabrication approach "B", illustrated in Figure 1.7(b), where the liner is fabricated by roller forming of a coil and seam welded with or without consumable depending on the liner grade. The seam weld cap is ground flush and the liner is heat-treated, calibrated and cut to length. The host pipe inner surface is cleared of debris and shot blasted. It is then heated in a furnace. At the same time, the liner is placed in a hydraulic expansion system which is in line with the furnace. When the host pipe reaches the target temperature, the furnace is shut down and moved forward so that the host pipe slides over the liner which is cooled from the inside with water. The liner is then hydraulically expanded with pressure which induces a hoop stress in the host pipe wall of approximately 80% of its specified minimum yield strength (SMYS). Pressure is then reduced and the liner continuously water cooled from the inside until the host pipe temperature falls to a pre-defined level. Subsequently, pressure is released, the furnace is opened and the lined pipe cooled in air. Finally, the liner is cut back and overlay cladding completed between the liner and the host pipe at both joint ends [14].

Finally, Proclad [15] and Butting [16], based in UAE and Germany, respectively, follow fabrication approach "C", illustrated in Figure 1.7(c). The liner is formed from a coil into a continuous tubular by roller forming, and seam welded with or without consumable depending on the liner grade. The seam weld cap is then ground flush and the liner heat-treated as required, calibrated and cut into the required individual lengths. The host pipe inner surface is cleared of debris and shot blasted. Subsequently, the liner is inserted into the host pipe and its ends swaged. Proclad, who has been manufacturing mechanically lined pipes for over a decade, uses tightly fitted polymer rings to seal the annulus between the liner and the host pipe prior to expansion. In contrast, Butting seals the annulus by welding. In this case, a relief valve is installed into the carbon steel pipe to allow venting of air trapped in the annulus during hydroforming. Subsequently, hydraulic pressure is applied to the liner inner surface until the target expansion of the host pipe is achieved. Following pressure release the liner (and the host pipe in the Butting process) is cut back. Finally, overlay cladding is completed between the liner and the host pipe at both joint ends. Having started in the mid-1990s, Butting is now well established as the world's leading supplier of mechanically lined pipe. Gieminox [17], based in Italy, also follows a fabrication approach "C" where the CRA liners are individually fabricated from a flat plate using the JCO process, and the MLP assembled broadly as per the Butting process.

Manufacturing Imperfections in Mechanically Lined Pipelines

To enable insertion of the liner into the carbon steel host pipe during manufacturing of mechanically lined pipe, a radial gap is required between the liner outer diameter and the host pipe inner diameter. A large gap makes insertion easier but increases hoop strain in the liner during expansion which renders the liner seam weld prone to fracture. Figure 1.8 shows an example of seam weld flaws which caused liner burst during expansion inside the host pipe. A small radial insertion gap in the order of 3 – 5 mm is typically specified to limit the expansion strain to 5%. Thus, some amount of liner scoring is inherent to the manufacturing process of mechanically lined pipe. Light scoring is typical of a well-controlled insertion process. Uncontrolled galling of the liner may occur if: (i) the host pipe and the CRA liner are axially misaligned during liner insertion or (ii) the pipe diameter or straightness tolerances are too high. Liner galling

may result in balling up of the CRA material in the annulus between the liner and the host pipe. This material build-up can indent the liner during expansion, as shown in Figure 1.9.

Contact Interference Stress in Mechanically Lined Pipelines

The interference stress developed during manufacturing depends on the flow behaviour of the CS host pipe and CRA liner, as well as the insertion gap between the two pipes prior to expansion. The contact stress reduces when (i) the insertion gap between the CS host pipe and the CRA liner increases, and/or (ii) the hoop stress in the host pipe at the end of the expansion process decreases or that in the liner increases. Usually, a higher interference stress is achieved in the manufacturing process which involves heating of the host pipe before liner insertion (i.e. fabrication approach B). However, the interference stress may be significantly reduced due to stress relaxation during the pipe coating process at high temperatures.

1.2.3 Installation and Operation of Mechanically Lined Pipelines

In early 1991, Nippon Steel and Sumitomo Metal Corporation (NSSMC) were contracted by Shell USA to supply 4.25" (108.0 mm) inner diameter C-II mechanically lined pipes with 3 mm thick alloy 825 liner. Since the operational temperature and pressure were expected to be very high, there was a possibility that the pipeline would buckle during service. To control the magnitude of the buckling strain it was proposed to install the pipeline subsea in a horizontal "zig-zag" configuration [18]. Prior to subsea installation, mechanically lined pipes with the outer diameter in the range between 5.51" (140 mm) and 6.625" (168.1 mm) were manufactured by NSSMC and tested in a four-point bending rig, to demonstrate suitability of the C-II pipe for the intended "zig-zag" lay [19, 20]. Although the carbon steel host pipe did not buckle, the 3 mm thick liner wrinkled when the mechanically lined pipe was bent to a curvature, $\kappa = 0.47$ (i.e. bending radius of ca. 2 m), which was well above the intended "zig-zag" curvature. Further tests carried out to determine the implosion and burst pressure of the bi-metal pipe were also successful [19, 20]. Later that year the 4.25" (108.0 mm) inner diameter C-II mechanically lined pipeline was laid subsea in the Fairway field in the Gulf of Mexico, from an S-lay barge.

Two years later NSSMC performed further bending trials, where 7.28" (184.9 mm) outer diameter mechanically lined pipes were plastically bent on a former with an 8.26 m radius, to simulate reel-lay installation with TechnipFMC's Apache II reel-lay vessel. No wrinkles were found during a subsequent post-mortem examination. Building upon the success of this trial another series of tests was undertaken, during which 10.75" (273.1 mm) outer diameter C-II pipes were tested [21]. As the liner wrinkled during these trials, it was concluded that mechanically lined pipelines with a 3 mm liner and outer diameter greater than 7.28" (184.9 mm) were not suitable for reel-lay installation. In the subsequent years a number of mechanically lined pipelines were installed subsea using low strain installation methods such as S-lay, see [22, 23, 24] for example.

A strong drive to reduce the cost of subsea pipelines has recently re-ignited interest in reel-lay installation of mechanically lined pipelines. Two approaches for reel-lay installation of mechanically lined pipelines without the risk of liner wrinkling have been proposed and patented: (i) pressurised reeling [25, 26, 27, 28] and (ii) non-pressurised (ambient) reeling [29, 30]. The first approach, where internal pressure is applied to the pipe to prevent the CRA liner from separating from the CS host pipe during reeling, allows installing large diameter mechanically lined pipelines with a nominal liner thickness of ca. 3 mm. However, pressurised reeling introduces additional considerations (e.g. accidental depressurisation during installation or insertion of mid-line structures offshore), with associated constraints and time/cost repercussions. The second approach, where the liner thickness is increased to mitigate the risk of liner wrinkling during non-pressurised reel-lay installation, is well suited for mechanically lined pipelines with a diameter up to 10" – 12" typically, which represent the majority of reeled subsea pipelines, and requires no modification to the standard reeling operation. Consequently, the ambient reeling approach is considered in this work.

CRA consumables suitable for girth welding of mechanically lined pipelines may undermatch the CS parent metal with regards to the tensile behaviour. This is particularly relevant for high strength carbon steels, such as API 5L X65 or X70. As a result, the risk of girth weld fracture during reel-lay installation may be higher for mechanically lined pipelines than for carbon steel pipelines. The triple-point interface between CRA liner, overlay cladding and carbon steel

is also a potential crack initiation site during reeling. In contrast, the liner seam weld sees significantly lower strain during reel-lay installation than when the liner is expanded during manufacturing. Consequently, the risk of seam weld fracture during reel-lay installation is low.

Concerns have also been expressed that liner imperfections such as small dents or wrinkles, introduced during manufacturing, installation or service, may compromise the integrity of a mechanically lined pipeline subjected to high in-service cyclic loading, resulting from lateral or upheaval buckling for example.

1.3 Thesis Outline

Following a literature review detailed in Chapter 2, a framework for the numerical prediction of the liner separation from the host pipe and subsequent wrinkling during reeling is proposed in Chapter 3, and validated against large scale bend tests.

Limit load solutions for the direct fracture assessment of embedded flaws in evenmatch girth welds are developed through a combined analytical and experimental work, detailed in Chapter 4. Subsequently, small scale tests are carried out to demonstrate that pre-strain (during the first tensile straining event of the reeling process) does not degrade the fracture toughness in undermatch girth welds, similar to those in mechanically lined pipelines. A new approach for the fracture assessment of surface flaws in undermatch welds is then proposed, and extended to embedded flaws.

Following demonstration through large scale testing that high in-service fatigue performance can be achieved with reeled mechanically lined pipelines without breaching the CRA barrier, it is proposed in Chapter 5 that fatigue crack growth assessment of triple point interface flaws can be conveniently performed using existing stress intensity factor solutions for standalone pipes. Subsequently, a combined numerical and experimental work is undertaken to determine the maximum acceptable flaws sizes in mechanically lined pipes subjected to low cycle fatigue during operation.

Finally, conclusions from the research work are drawn in Chapter 6, and areas for further work are identified. Papers presented at (i) the American Society of Mechanical Engineers' (ASME) conference on Pressure Vessels and Piping (PVP), (ii) the ASME conference on Ocean, Offshore and Arctic Engineering (OMAE), and (iii) the International Society of Offshore and Polar Engineers' (ISOPE) conference, and published in (iv) the International Journal of Offshore and Polar Engineering (IJOPE) and (v) the Journal of Pressure Vessel Technology (JPVT), are included in Appendix.

1.4 Figures

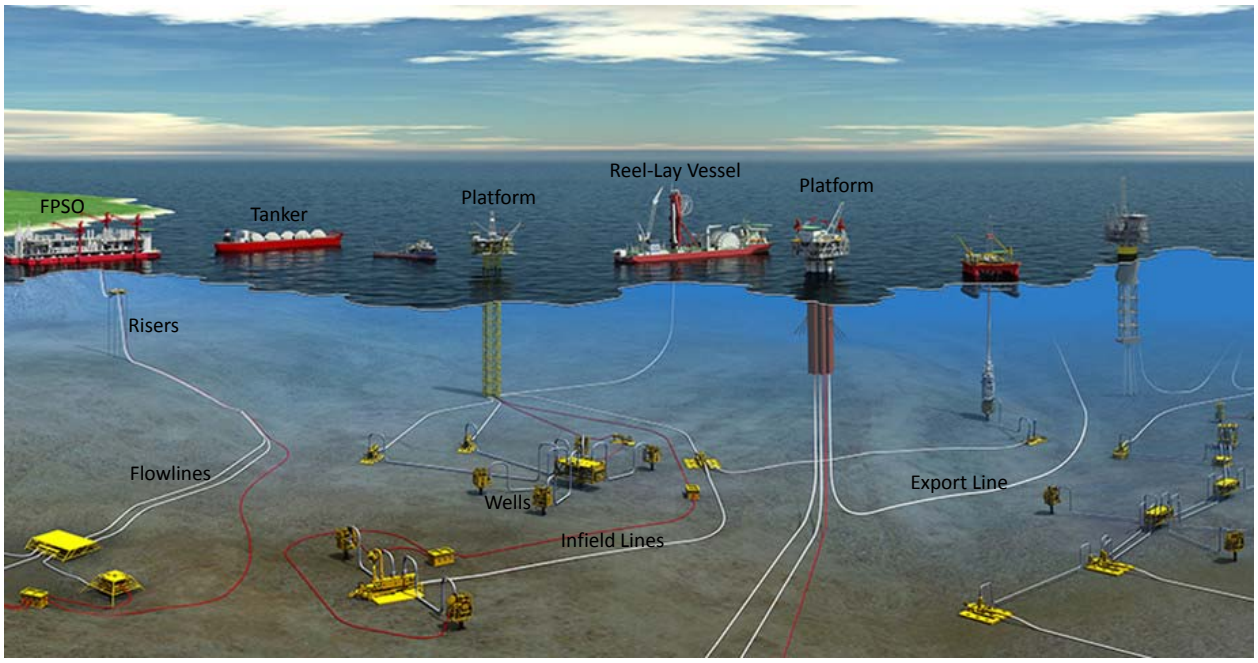


Figure 1.1: Overview of Subsea Oil Field Architecture

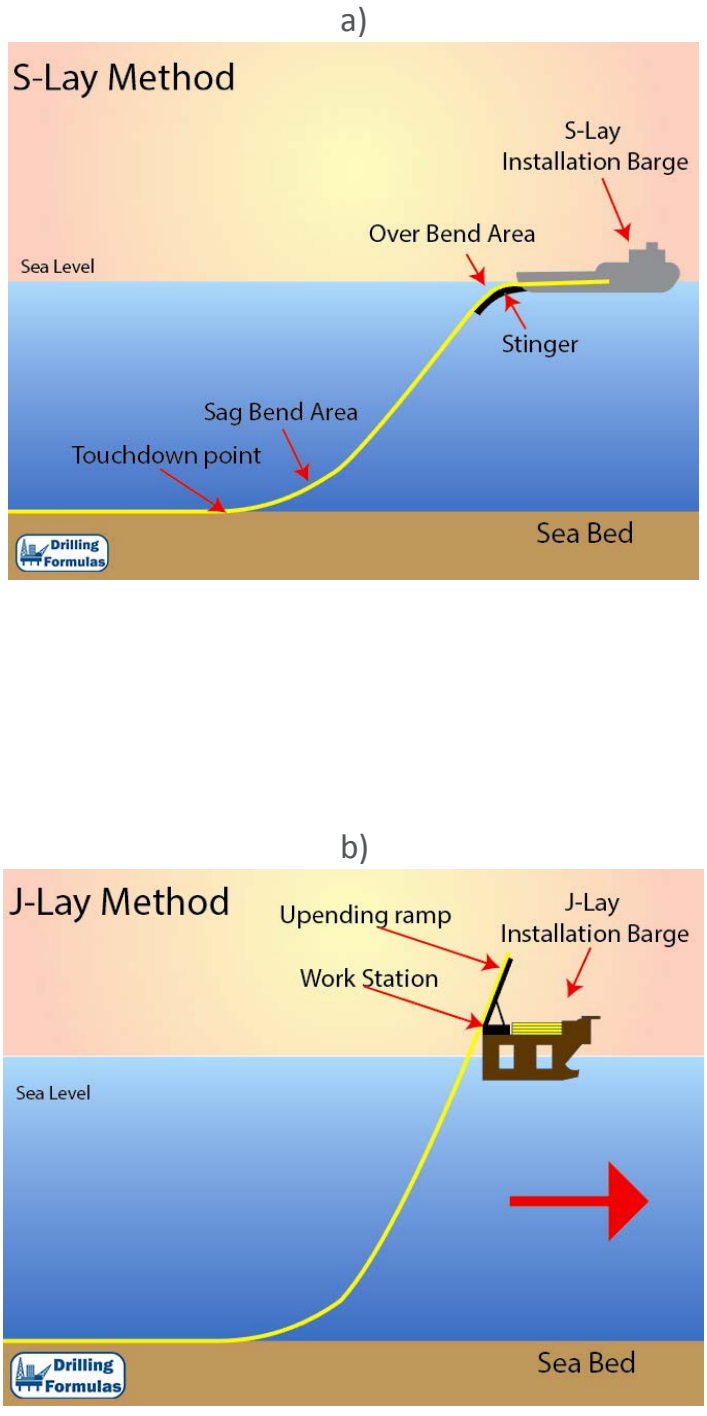


Figure 1.2: Low Strain Installation Methods for Subsea Pipelines: (a) S-Lay, (b) J-Lay (from drillingformulas.com [31])



Figure 1.3: Reel-Lay Installation: (a) Onshore Operations, (b) Offshore Operations

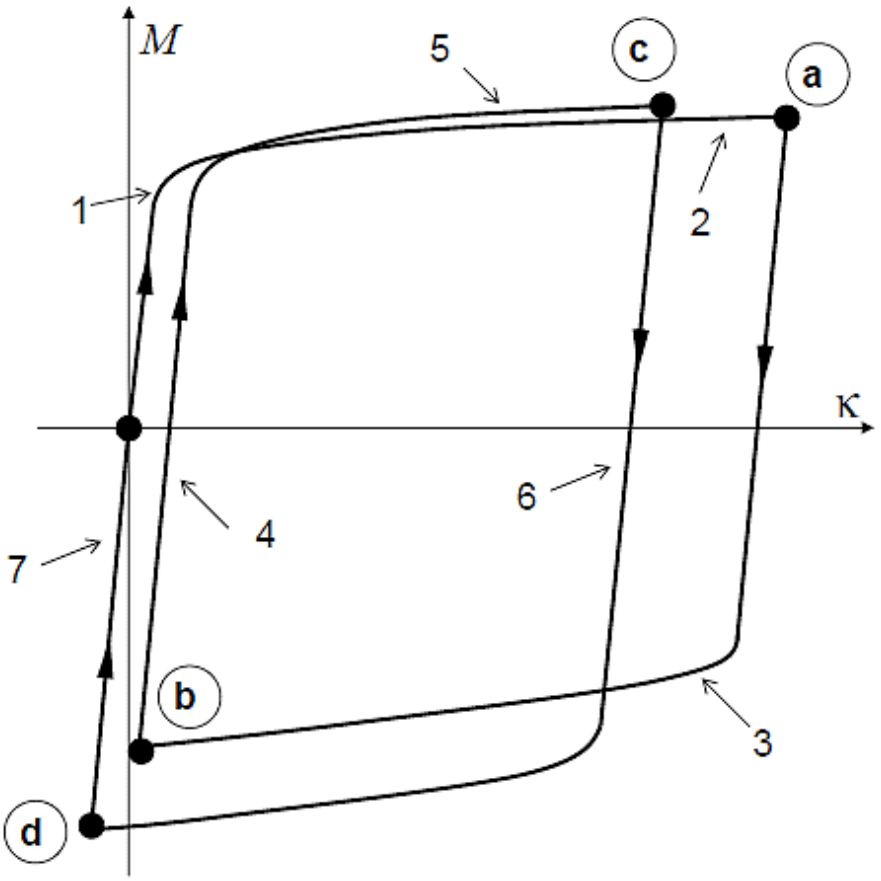


Figure 1.4: Reel-Lay Installation: Moment-Curvature Plot

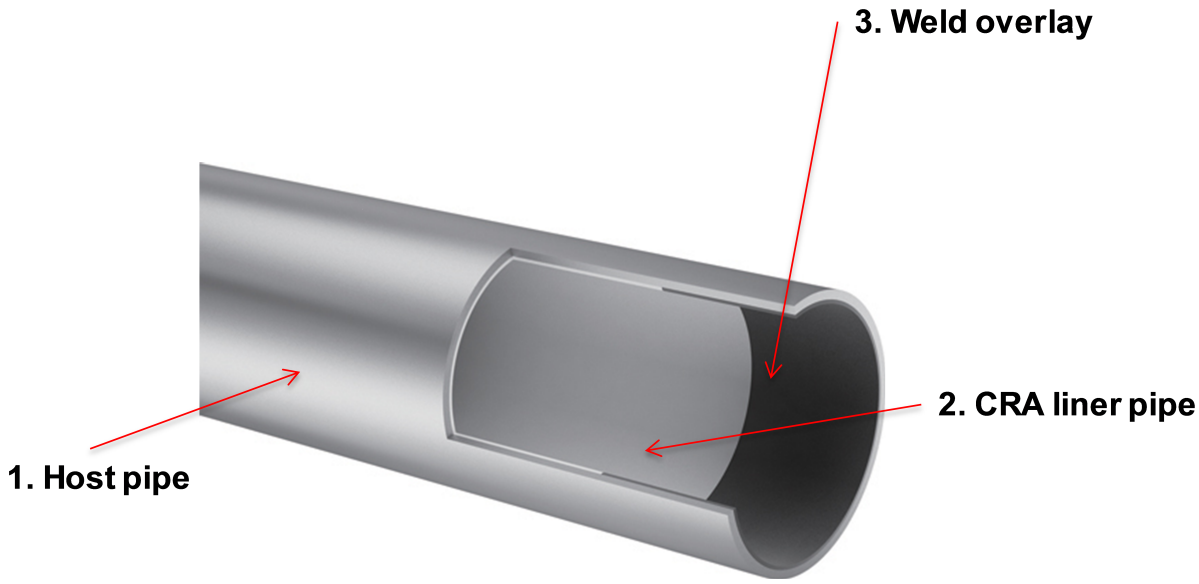


Figure 1.5: Illustration of Mechanically Lined Pipe

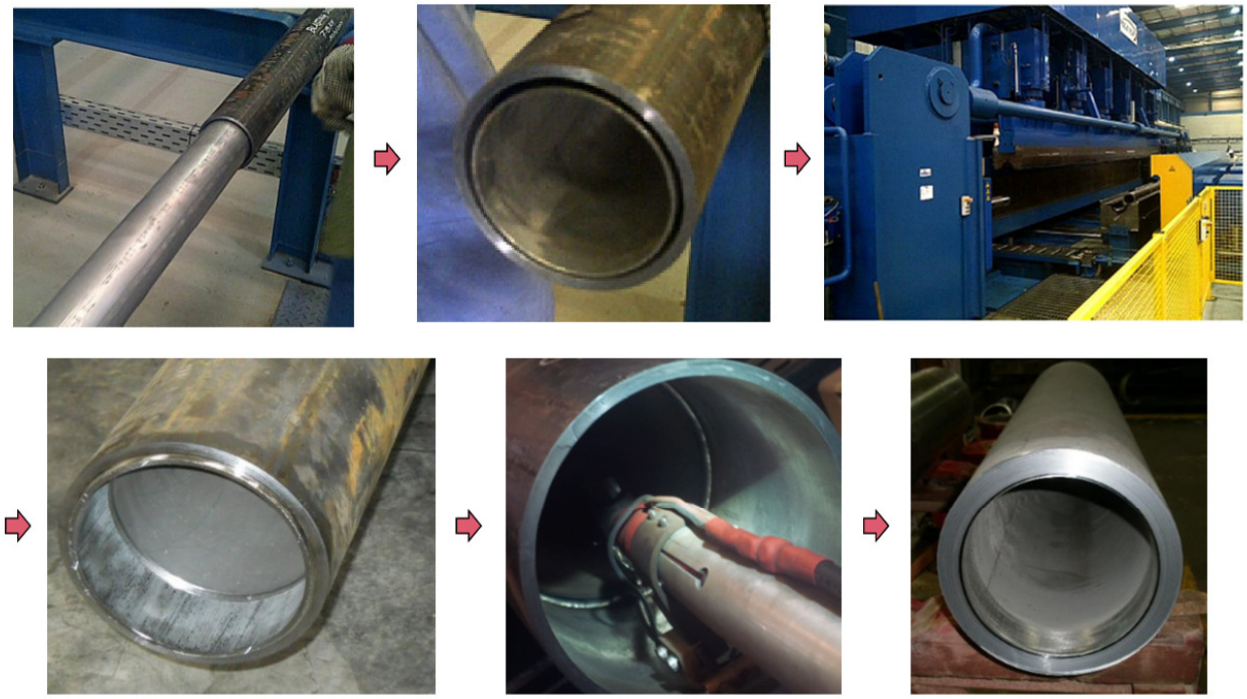


Figure 1.6: Main Steps of Manufacturing of Mechanically Lined Pipe

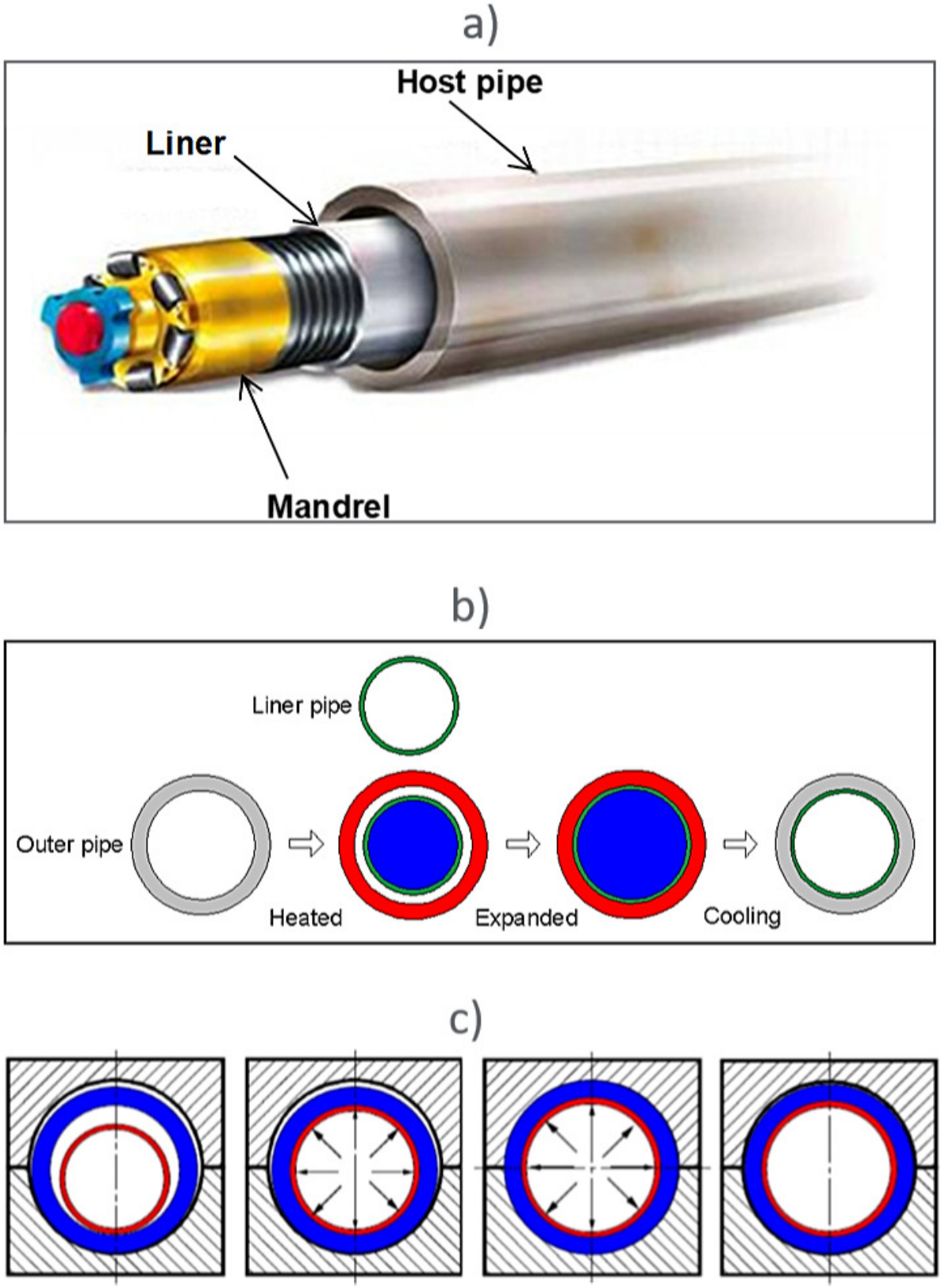


Figure 1.7: Liner Expansion during Manufacturing of Mechanically Lined Pipe at: (a) Cladtek, (b) Kuroki, (c) Proclad/Butting

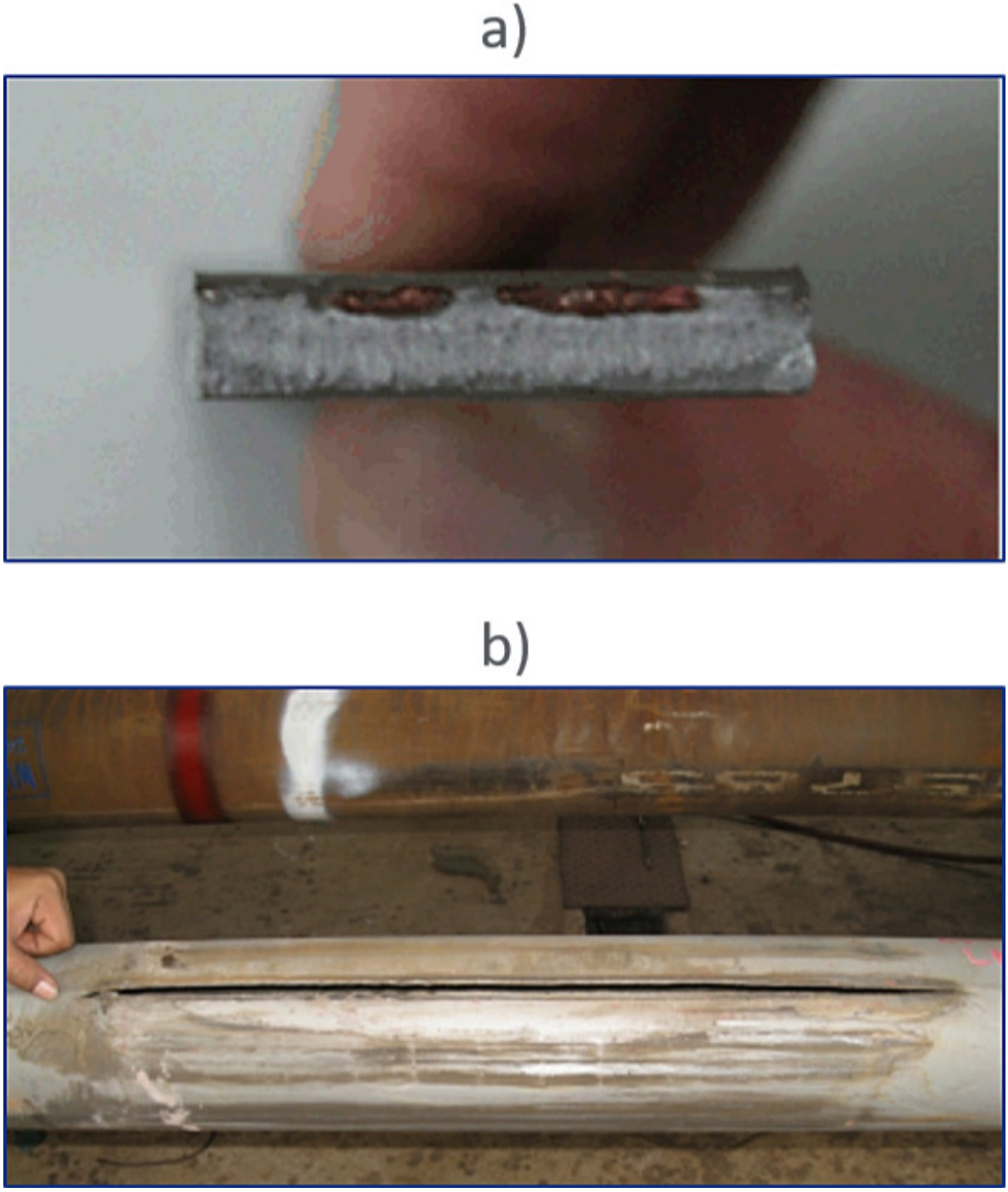


Figure 1.8: Effect of Manufacturing Imperfections in Liner Seam Weld: (a) Lack of Fusion Flaws, (b) Liner Burst during Expansion

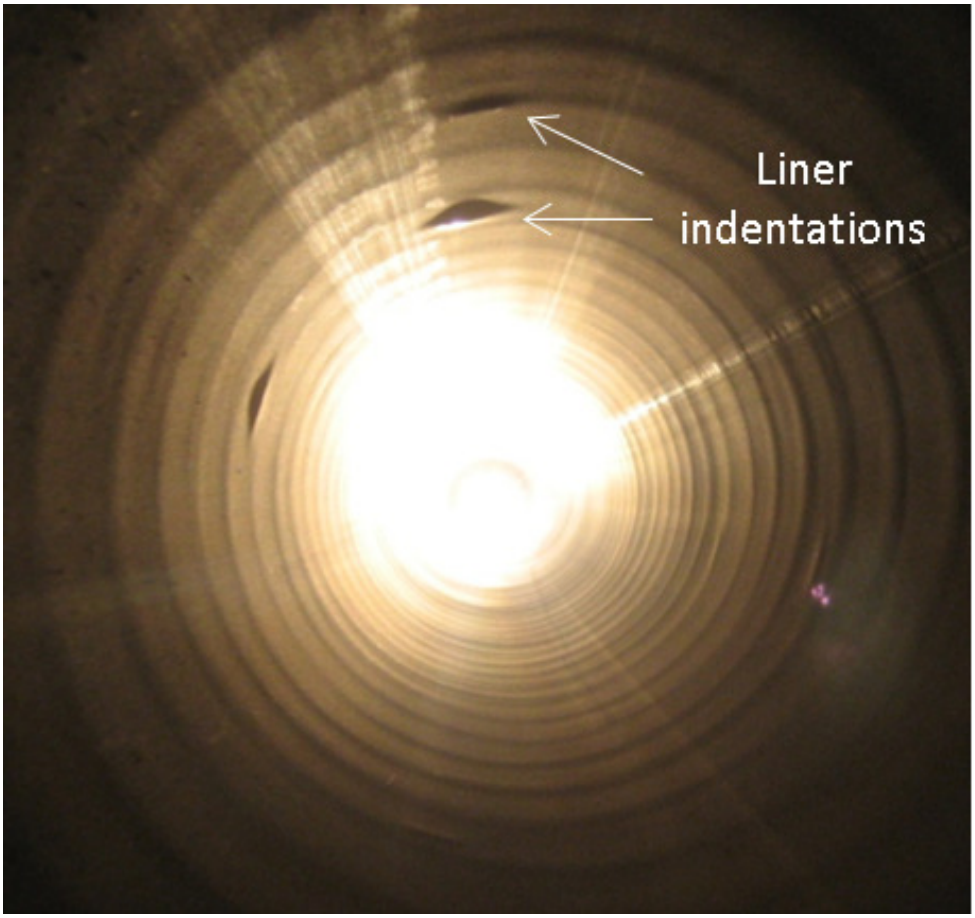


Figure 1.9: Manufacturing Imperfections in Liner Body

Chapter 2

Review of Design Rules for Reeled Subsea Pipelines

2.1 Buckling of Backing Pipe

2.1.1 Minimum Reelable Wall Thickness

Buckling of tubes has been the subject of numerous studies over the past decades. Most studies focused on the behaviour of slender single skinned pipes (SP) under axial compression or bending, see [32, 33, 34, 35, 36] for example. Buckling of elastic-plastic pipes subjected to bending is considered to have occurred when the plastic bending moment capacity is reached

$$M_p = \frac{\sigma_y \left(D^3 - (D - 2t)^3\right)}{6} \tag{2.1}$$

Here, σ_y, D and t are the yield strength (YS), outer diameter and wall thickness of the pipe, respectively. Similarly, the buckling strain is that corresponding to the curvature at which the maximum bending moment is reached. Using the above definition, the minimum nominal wall thickness (i.e. excluding manufacturing tolerances) required to bend a pipe without buckling, t_{nom}, can be estimated using an empirical formula proposed by Murphey and Langner [32]

$$t_{min} = 2bD\varepsilon_{nom} \tag{2.2}$$

where ε_{nom} is the nominal bending strain calculated from Eq. 1.1 and b is a safety factor which accounts for manufacturing tolerances. In the context of reel-lay installation, b may be determined from [37]

$$b = \frac{1}{1 - t_{tol}} \tag{2.3}$$

Here, t_{tol} is the absolute value of the negative wall thickness tolerance of the pipe, e.g. 12.5%. Due to inherent wall thickness and yield strength variations there may be a high plastic moment mismatch between consecutive pipe joints during reel-lay installation

$$\Delta M = \frac{\left(M_p^s - M_p^w\right)}{2\left(M_p^s + M_p^w\right)} \tag{2.4}$$

where M_p^s and M_p^w are the plastic bending moment capacities of the stronger and weaker joint, respectively. High plastic moment mismatch may lead to a local increase in ovality. The peak ovality is usually observed in the weaker joint, one pipe outer diameter away from the weld between weak and strong pipe joints. In extreme cases, bulging or even buckling of the weaker pipe joint may occur during reel-lay installation, as shown in Figure 2.1. Consequently, a reelability assessment needs to be carried out to verify the suitability of t_{nom} for reeling.

2.1.2 Reliability Assessment

The DNVGL report No. 2014-0185 [38] provides a methodology for determining the probability of failure of a pipeline during reel-lay installation. First, a failure criterion, in terms of peak ovality and strain, is defined and several finite-element analyses (FEA) are carried out to determine a failure boundary in a unit normal space. Then, a reliability index, β, which is the closest distance from the origin to the failure boundary in the unit normal space, is used to determine the probability of failure, $P_f = \text{func}(\beta)$.

Alternatively, a similar but more practical approach which employs a first order reliability method (FORM), can be used [39, 40]. A commercially available software such as Opensees [41], licensed by the Berkeley University, which automates first order reliability principles, is used to calculate probabilities of occurrence, p_i, corresponding to a range of mismatch levels, ΔM_i, where $i = 1$ to n. To determine p for a given ΔM in Opensees, a performance function and random variables must be defined. The random variables in this problem, i.e. the wall thickness and yield strength of strong and weak pipe joints, are assumed to have normal distributions with mean values equal to the average of relevant properties. To determine the corresponding standard deviations, tolerance ranges are adjusted (reduced) to account for cross-section property variations using appropriate averaging factors [42]. Then, the adjusted tolerances are divided by 6 to obtain standard deviations, following the three-sigma rule [43]. The performance function, F, for a given mismatch value, ΔM, is defined by $F = \mathrm{G}(\Delta M)$ - $\Delta M = 0$, where G is a mismatch function that depends on the random variables.

After determining the probabilities of occurrence at a single girth weld (p_i) for a range of mismatch levels (ΔM_i), the system effect is accounted for using the geometric distribution. For a given pipeline length, L, the number of girth welds, N, can be estimated by dividing L by a joint length (typically 12 m). The probability for the whole pipeline with N welds, P_i, corresponding to, p_i, is obtained from

$$P_i = 1 - (1 - p_i)^N \tag{2.5}$$

The most likely combination of wall thickness and yield strength for the weak and strong pipe joints (i.e. the design point, ΔM_0, corresponding to a probability, P_0), are the output from Opensees. DNVGL-ST-F101 [7] requires that the probability of failure of a pipeline during installation does not exceed 10^{-2}. This corresponds to a low safety class and serviceability limit state, i.e. the pipeline is not suitable for use but is integral; any dry buckle is to be repaired. Consequently, $P_0 = 10^{-2}$ is normally assumed. The thus obtained design point is used in a finite-element (FE) reeling analysis. A pipeline is considered reelable if: (i) it does not buckle, (ii) the local peak ovality does not exceed 10% [38], as per the DNVGL-ST-F101

definition [7], and (iii) the compressive axial peak strain averaged over a representative area does not exceed 5% [38]. Furthermore, the nominal ovality must not exceed 3% as per the DNVGL definition or 1.5% as per the American Petroleum Institute (API) definition

$$\delta_{DNVGL} = \frac{D_{max} - D_{min}}{D} \tag{2.6}$$

$$\delta_{API} = \frac{D_{max} - D_{min}}{D_{max} + D_{min}} \tag{2.7}$$

where D_{min} and D_{max} are respectively the minimum and maximum pipe outer diameter for a given cross section. The mismatch calculation may also be performed analytically, following the approach detailed in [44].

2.1.3 Reeling Induced Ovality

Martinez *et al.* [45, 46] showed that reeling induced ovality can be signicantly overestimated when a classical metal plasticity model is used in a finite-element analysis in combination with a fixed yield criterion shape such as the von Mises criterion, indicated by a solid blue line in Figure 2.2. A history dependant yield criterion with the initial yield surface (indicated by a solid green line in Fig. 2.2) lying between the Tresca (indicated by a long grey dashed line in Fig. 2.2) and Mises yield surfaces, was proposed for carbon steel pipes. The yield surface evolves towards the Haythornthwaite surface (indicated by a short grey dashed line in Fig. 2.2) when the pipe is subjected to cyclic plastic deformation, which results in the reduction in the ovality increment. User defined material subroutines were then written by Martinez *et al.* for use with the classical metal plasticity models in the finite-element analysis software ABAQUS [47].

2.1.4 In-Service Buckling

High temperatures and pressures during operation may promote the build-up of large axial loads in the pipeline, which would lead to global (lateral or upheaval) buckling during ex-

pansion. The latter can be controlled by (i) using buckle initiators at critical locations, (ii) deploying the pipeline in a "snake" configuration, (iii) reducing the submerged weight of the pipeline at relevant locations using buoys, or (iv) laying the pipeline with a residual curvature. The buckling strain, which is determined by FEA following the guideline provided in SAFEBUCK [48] and DNVGL-RP-F110 [49], is typically lower than the reeling strain.

2.2 Wrinkling of Liner Pipe

Wrinkling of a CRA liner inside a CS host pipe has been extensively studied over the past decade, primarily through doctoral research works and joint industrial projects (JIP).

2.2.1 Contact Interference Stress

As part of her research on the reeling of tight fit pipe (TFP), summarised in her PhD thesis [50], E. S. Focke developed a two-dimensional (2D) analytical model of the Kuroki mechanically lined pipe manufacturing process, to determine the residual stress state in the tight fit pipe after manufacturing [51]. The analytical predictions generally agreed well with those from a 2D axis-symmetrical model of tight fit pipe, built in the FEA software MARC [52].

To validate the 2D models, predictions of the residual compressive hoop stress in the CRA liner were compared against measurements taken on six TFPs, manufactured by Kuroki [53]. The MLPs had (i) an OD in the range between 4.5" (114.3 mm) and 10.75" (273.1 mm), (ii) a backing pipe of grade C95 or API 5L X65, with a WT in the range between 8.9 mm and 11.5 mm, and (iii) a liner pipe of grade SUS 304, UNS N08031 or UNS N08825 with a WT ranging from 1.6 mm to 2.5 mm. One hundred millimetres long rings were cut from a TFP and used to determine the contact interference stress in the as-manufactured condition. Biaxial strain gauges were attached to the inner surface of the liner and connected to a data logging system. The backing pipe was then cut longitudinally to release the liner, while change in axial and hoop strain in the latter was recorded. The grip stress in the liner was determined from [8]

$$\sigma_g = \frac{E}{1-\nu^2}\left(\frac{\sum_{i=0}^{n}\Delta\varepsilon_h^i}{n} + \nu\frac{\sum_{i=0}^{n}\Delta\varepsilon_a^i}{n}\right) \tag{2.8}$$

where E and ν are the Young's modulus and Poisson ratio of the liner, n is the number of sets of biaxial strain gauges and $\Delta\varepsilon_h^i$ and $\Delta\varepsilon_a^i$ are the hoop and axial strain ranges, respectively. The residual compressive hoop stress in the CRA liner ranged from 119 MPa to 195 MPa. Such high stress is characteristic of the Kuroki thermo-hydraulic manufacturing process.

The analytical and numerical predictions did not agree well with the factory test results. The analytical equations were then modified and a three-dimensional (3D) model of 1/72nd of an MLP was built in the FEA software MARC [52]. Although some of the analytical and numerical predictions agreed well with the measured data, there was still a significant scatter. It was concluded that the as-manufactured grip stress could not be predicted accurately because it was also influenced by other unknown parameters.

2.2.2 Wrinkling under Axial Compression

Focke *et al.* undertook large scale axial compression tests to determine the strain capacity of (i) standalone liner, (ii) liner inside backing pipe and (iii) mechanically lined pipe [54]. The experimental work was conducted with a 10.75" (273.1 mm) OD × 9.3 mm WT carbon steel backing pipe manufactured to API 5L X65, lined with a 2.45 mm thick alloy 304L pipe. First, short sections of pipe, with the length ranging from 50 mm to 200 mm, were cut from a mechanically lined pipe and employed to estimate the grip stress using the residual compressive hoop stress method [8], described earlier. The grip stress, which was not influenced by the specimen length, was 181 MPa in average. Push-out tests were also carried out, and the load required to push the liner out of the backing pipe increased with the specimen length. This is because the contact area between the liner and host pipe also increases with the length.

Compression tests were then carried out. Each 100/200 mm long specimen was instrumented with strain gauges, mounted on a test machine, fitted with displacement metres, and loaded in compression until the liner wrinkled or the backing pipe buckled. Liner wrinkling was examined

by visual inspection. The standalone liner wrinkled outwardly, axis-symmetrically, while the confined liner wrinkled inwardly, in a non-symmetrical mode, as shown in Figure 2.3. The average wrinkling strain for the standalone liner was 0.3%, which agreed well with analytical predictions from Gerard [55], Batterman [56] and Gresnigt [57]. The wrinkling strain of the liner inside the backing pipe was significantly higher than that for the standalone liner, due to the outer lateral constraint. The wrinkling strain, which was similar for 100 mm and 200 mm long specimens, was 1.6% when the load was applied to the liner only and 1.0% when the load was applied to the mechanically lined pipe. It was argued that the wrinkling strain was higher for the former configuration than for the latter because some of the load applied to the liner was transferred to the backing pipe. The wrinkle wavelength was shorter for the confined liner than for the standalone liner. Similar results were obtained with 12.75" (323.9 mm) tight fit pipes, as detailed in [58].

In continuation of Focke's work, A. Hilberink also studied the mechanical behaviour of lined pipe [59]. Axial compression of a 295.74 mm OD $\times$ 2.93 mm WT alloy 316L pipe was simulated numerically in ABAQUS [60]. First, the behaviour of the standalone liner pipe was investigated. J_2 flow theory [4] with an isotropic hardening plasticity scheme was used to model the tensile behaviour of the CRA liner. The pipe was modelled with first order four-node shell elements with full or reduced integration (S4R and S4, respectively, in ABAQUS [47]). The model length was 107 mm, which was approximately three times half of the elastic buckling wavelength. A symmetrical imperfection, corresponding to one and a half wavelengths of an eigenmode, was applied to a perfect shell mesh to initiate buckling. Kinematic couplings were used to connect the nodes at either end of the liner to reference nodes in the middle of the pipe. One reference node was held in place while axial displacement was applied to the other one, to load the pipe in compression. Large deformation theory [4] was employed.

The liner expanded uniformly under small compressive strains within the elastic regime. When the applied strain exceeded a certain threshold (0.5% typically) a symmetrical surface topology, corresponding to the imposed eigenmode imperfection, developed as the liner buckled outwardly. Further increase in the compressive strain resulted in a uniform increase of the imperfection height, followed by the localisation of deformation at one of the peaks of the eigenmode. The

buckling strain decreased when the initial imperfection height increased. The strain capacity was 0.61%, 0.47% and 0.28% for imperfection heights equal to 0.03%, 0.34% and 3.41% of the liner thickness, respectively. These agreed reasonably well with the analytical predictions from Batterman [56].

Axial compression of the above-mentioned liner pipe, loosely fitted inside a 12.75" (323.9 mm) OD × 14.48 mm WT carbon steel backing pipe manufactured to API 5L X65, was then simulated. Both backing pipe and liner were modelled with first order eight-node solid elements with reduced integration (C3D8R in ABAQUS [47]). A quarter of the MLP was modelled with appropriate boundary conditions. The model length was approximately six times the liner OD and the liner and backing pipe had three elements through the thickness and sixty elements around a quarter of the circumference. The element length ranged from ca. 100 mm at one end to ca. 5 mm at the other end, where a symmetrical imperfection corresponding to the half-wavelength of an eigenmode, was imposed to initiate buckling. A reference node at one end of the pipe was held in place while axial displacement was applied to the other one, to load the pipe in compression. Damping was applied to ease numerical convergence.

Similarly to the standalone liner, the confined liner expanded outwardly uniformly under moderate compressive strains. When the applied strain reached 1.7% the liner buckled inwardly following the imposed eigenmode, while the backing pipe continued to expand outwardly. The buckling strain was significantly higher for the confined liner (2.08%, 1.74% and 1.34% for imperfection heights equal to 0.03%, 0.34% and 3.41% of the liner thickness, respectively) than for the standalone liner. In addition, the strain capacity of the confined liner increased with the coefficient of friction between the liner and backing pipe, whereas the imperfection mode shape had no effect on the buckling behaviour. A sensitivity analysis showed that the strain capacity of both standalone and confined liner increased with the liner thickness, but was not significantly influenced by the tensile properties of the liner. Finally, the numerical predictions were compared to Focke's experimental results in [61]. Good agreement was found between tests and FEA results when an imperfection height equal to 0.34% of the liner thickness was assumed in the analysis.

2.2.3 Wrinkling under Monotonic Bending

In preparation for large scale testing Focke *et al.* built a small scale bending rig, and carried out monotonic bending trials with 11 pipes with an OD of 22 mm and a WT in the range between 1.3 mm and 4.3 mm [62]. The test results were used to design a large scale bending rig shown in Figure 2.4.

Large scale bending tests were first performed with a single pipe [63]. The test string, made of a 12.75" (323.9 mm) OD × 21.77 mm WT carbon steel pipe welded to a weaker 12.75" OD × 18.65 mm WT carbon steel pipe, was bent onto a reeling former shown in Fig. 2.4(b). This simulated the scenario of a high plastic bending moment mismatch between consecutive joints during the spooling-on phase of a reel-lay installation. Following successful bending onto a 9 m radius former, the latter was replaced with a smaller (8 m radius) reeling former and bending resumed in the same direction (i.e. monotonic bending). This was repeated until the pipe was bent onto the smallest reeling former, which had a radius of 5 m. Bending of a pipe to an increasingly tighter radius is termed "sequential" bending in this work. The applied loads, reaction forces and movements of the rig equipment and the pipe ovalisation were monitored during bending. The test was then simulated numerically using the FEA software ABAQUS [47]. The experimental and numerical results were used to adjust the rig settings prior to testing of mechanically lined pipes.

Seven (7) tight fit pipes, each 3.44 m long and comprising of a 12.75" (323.9 mm) OD × 14.3 mm WT seam-welded API 5L X65 carbon steel pipe and a 3 mm thick alloy 316L liner, were manufactured by Kuroki: (i) 5 off "non-welded" pipes and (ii) 2 off "girth-welded" pipes. The welded pipes had a CRA girth weld in the middle, produced using a duplex consumable. The as-manufactured grip stress, measured from samples extracted from each pipe following the procedure detailed above, was 53 MPa (low grip) for 2 non-welded TFPs and 189 MPa (high grip) for the remaining pipes. A 2.5 m long carbon steel piece was welded at one end of each tight fit pipe while a flange was attached to the other end, for connection with a pull head. Following installation on the rig strain gauges and curvature metres were affixed to the assembled test string, which was subsequently bent following the "sequential" procedure

described earlier, to determine the strain at the onset of liner wrinkling. A laser inspection tool, shown in Figure 2.5, was used to measure the size of bending induced liner imperfections. Wrinkling was determined to have occurred when the local separation of the liner from the backing pipe, illustrated in Figure 2.6, exceeded a certain threshold.

The liner in every test string wrinkled at some point during bending. The largest wrinkle was 14 mm in height. The wrinkles in pipes with stronger mechanical bond were fewer and smaller than those in pipes with lower initial grip stress, see Figure 2.7. The relationship between liner wrinkle height and applied bending strain was linear for pipes with low manufacturing grip force, and nearly exponential for pipes with high contact interference stress. It was suggested that the wrinkles were smaller in the pipes with stronger mechanical bond because the latter restricts liner feeding into wrinkles. The longitudinal seam weld of the carbon steel backing pipe had no influence on the wrinkling process. In contrast, the CRA girth weld in the middle of two test pipes had a detrimental effect on wrinkling. The liner in those pipes, which had a high manufacturing grip force, behaved in a similar manner to that in non-welded pipes with a low mechanical bond. The largest wrinkles in pipes subjected to a "sequential" bending regime were similar to those in pipes subjected to a single bending event on the smallest former. This proved that "sequential" bending is suitable for determination of the strain at the onset of liner wrinkling. Grip stress tests carried out after the large scale bending trials showed that the contact interference stress had significantly reduced for both low and high grip pipes.

Focke concluded that reeling of tight fit pipe could be enabled by minimising ovalisation and wrinkling of the liner pipe during the reeling process. This could be achieved by reducing the bending curvature or decreasing the diameter to thickness ratio of the pipe (by increasing either the liner pipe or the outer pipe wall thickness). Although increasing the as-manufactured contact interference stress (e.g. by heating the carbon steel pipe to higher temperature during manufacturing) would be beneficial, further investigations would need to be carried out to verify the in-service integrity of a liner with significantly lower as-laid grip stress [50].

Few years later, Hilberink *et al.* undertook pure bending trials to investigate the buckling behaviour of a 293.1 mm OD $\times$ 3 mm WT alloy 316L liner confined inside a 324.7 mm

OD × 14.3 mm WT API 5L X65 seamless or seam-welded pipe [64, 65, 66]. Three scenarios were simulated: (i) bending of as-received TFP, (ii) bending of TFP subjected to a thermal cycle to simulate coating application and (iii) pressurised bending of as-received TFP. Each pipe was mounted on the rig shown in Figure 2.8 and instrumented with strain gauges, curvature and ovalisation metres. Subsequently, the pipe was held at fixtures in the middle of the rig while its ends were pulled upwards using hydraulic cylinders indicated in Fig. 2.8(a), to impose a constant bending moment between fixtures. A laser tool, as per Figure 2.5, was used to scan the inner surface of the liner pipe at 20 mm intervals during testing.

The laser measurements indicated that the liner cross-section deformed uniformly when the as-received TFP was subjected to curvatures below 0.05 m^{-1} (0.8% bending strain). Further bending resulted in the onset of localised separation of the liner from the backing pipe in-between the fixtures in Fig. 2.8(a). The liner wrinkle heights, measured from the test data as per Figure 2.6, increased linearly with the applied curvature up to 0.11 m^{-1} (1.8% bending strain). Subsequently, the wrinkle heights grew exponentially, leading to the buckling of the liner into a diamond-type mode shape, shown in Figure 2.9. Wrinkling initiated sooner in the heated pipe. This is because a thermal cycle representative of coating application at a high temperature relaxes the contact interference stress between the liner and backing pipe. In contrast, pressurisation of the pipe delayed the onset of wrinkling [59]. Although the wrinkle heights grew slightly faster in the seam-welded pipe compared to the seamless pipe, the moment-curvature diagrams for both pipes were similar, suggesting that the longitudinal seam weld had a small effect on the lined pipe behaviour. The large scale bend test results were then compared to those from Focke's reeling tests in [59]. Reeling was shown to be more onerous than pure bending. This is because the contact load between the pipe and the reel increases the ovalisation of both backing pipe and liner, resulting in an earlier onset of wrinkling.

Subsequently, pure bending of standalone liner, standalone backing pipe and mechanically lined pipe was simulated numerically using a half-symmetrical FEA model [65, 66]. The numerical modelling technique employed was broadly similar to that adopted for the simulation of axial compression tests in [60]. A focused mesh was used to trigger buckling/wrinkling in the middle of the pipe (as observed during the large scale bending tests) without a geometrical imperfection.

FE analyses were also run with a coarse pipe mesh to simulate failure by localized ovalisation (the Brazier effect [6]). Symmetry boundary conditions were applied in the middle of the pipe, while rotation was applied to reference nodes at either end of the pipe to simulate pure bending [65, 66]. Wrinkling was predicted to have initiated when contact was re-established between the liner and backing pipe at the intrados, following uniform liner separation [66].

Failure of the standalone backing pipe was shown to be governed by localized ovalisation, whereas that of the standalone and confined liner resulted from a combination of ovalisation and wrinkling. The critical bending curvature of the confined liner (0.12 m^{-1}, corresponding to 1.9% bending strain) was twice as high as that of the standalone liner (0.05 m^{-1}, corresponding to 0.8% bending strain). Initially, the confined liner ovalized together with the backing pipe during bending. When the pipe was bent to a curvature of ca. 0.04 m^{-1} (0.6% bending strain, and indicated by a downwards arrow in Fig. 2.10) the liner began separating from the backing pipe uniformly. Liner wrinkling initiated at a curvature of 0.11 m^{-1} (1.8% bending strain, and indicated by an upwards arrow in Fig. 2.10). This was later followed by buckling of the liner into a diamond-type mode shape shown in Fig. 2.9(b), and buckling of the backing pipe from localised ovalisation. The bending moment capacity of the confined liner is indicated by a caret symbol in Figure 2.10. Sensitivity analyses showed that the bending strain capacity of the liner pipe is mainly driven by its thickness. Furthermore, high interference stress can delay the onset of liner wrinkling. Moreover, although the contribution of the liner was small compared to that of the backing pipe failure of the later occurred shortly after liner buckling. The strain capacity of MLP under pure bending was therefore similar to that of the confined liner, which was higher than the strain at the onset of wrinkling.

The numerical predictions were then compared to the experimental results in [66]. Lower bending moment capacity was predicted in FEA than measured during testing. The authors argued that the discrepancy could be attributed to the variation of tensile and geometrical properties along the test pipe. Good agreement was found between numerical and test results in terms of the liner deformation for bending curvatures below 0.05 m^{-1} (0.8% bending strain). Further bending resulted in the onset of a localised separation of the liner from the backing pipe in the tests, while the liner separated uniformly in the FEA. The liner wrinkle height,

measured from the test data as per Figure 2.6, was on the order of 2 mm when contact was re-established between the liner and backing pipe at the intrados in the FEA (defined as the onset of wrinkling in [66]). It was suggested that underestimation of the wrinkle height was due to the absence of initial imperfection in the FEA model. Subsequently, the wrinkle grew faster in FEA than measured, resulting in an earlier failure of the liner, see Figure 2.11.

Hilberink concluded that reeling of mechanically lined pipe could be made possible if (i) an acceptance criterion for liner wrinkles is established, (ii) a numerical model for the simulation of the complete reeling process is developed and validated, and (iii) further sensitivity analyses are run to investigate effects such as mismatches resulting from variations in geometrical and tensile properties. She also suggested that wrinkling mitigation methods such as pressurisation of the liner bore during reeling could be explored [59].

In continuation of Hilberink's work, D. Vasilikis studied the structural behaviour of the liner of MLP subjected to bending under atmospheric or external overpressure [67]. First, a wrinkling parametric study of lined pipe subjected to bending was undertaken using ABAQUS [68]. An MLP made of a 12.75" (323.9 mm) OD $\times$ 14.3 mm WT carbon steel backing pipe manufactured to API 5L X65 and a 3 mm thick alloy 316L liner, was considered. J_2 flow theory with an isotropic hardening plasticity scheme were employed. The liner and backing pipe were modelled with first-order shell elements with reduced integration (S4R in ABAQUS [47]) and second order solid elements with reduced integration (C3D20R in ABAQUS [47]), respectively. A frictionless contact scheme was used. The model length was assumed equal to the half-wavelength of a wrinkle. Half of the pipe cross-section was modelled with appropriate symmetry boundary conditions. The liner had 20 elements along the pipe axis and 100 elements around half-circumference, while the backing pipe had 4 elements in the longitudinal direction and 48 elements around half-circumference. Kinematic couplings were used to connect the nodes on the right-hand side of the model in Figure 2.12 to a reference node in the middle of the pipe. Rotation was applied to the latter to bend the pipe. Finite strain theory was employed.

Initially, the liner separated uniformly from the backing pipe under pure bending, due to the Brazier effect [6]. The as-manufactured contact interference stress was lost in the very early

stages. A loosely fitted liner separated from the backing pipe almost immediately, while a pipe with high grip (166 MPa) separated at a curvature of 0.025 m^{-1} (0.4% bending strain). At the onset of a first bifurcation point, indicated by arrows in Figure 2.13, the liner started closing in on the backing pipe on the left-hand side of the model in Fig. 2.12, while separating further at the other end. This resulted in the development of a uniform/periodic wavy pattern, shown in Figure 2.14. The wrinkling curvature was respectively 0.032 m^{-1} (0.5% bending strain) and 0.042 m^{-1} (0.7% bending strain) for the loosely and tightly fitted pipes. The corresponding wrinkle height, defined in Fig. 2.14 as the difference in liner separation at both ends of the pipe, was less than 5% of the liner wall thickness. The strain at the onset of liner wrinkling was shown to be sensitive to the model length (assumed equal to half of the wrinkle wavelength). The critical half-wavelength, corresponding to the model length for which the wrinkling strain was lowest, was 44 mm for both loosely and tightly fitted pipes.

Increasing the model length to a full wavelength allowed the capture of a second bifurcation point observed during the Focke [50] and Hilberink [59] large scale tests (see Figure 2.9 for example). The first and second bifurcation points are indicated in Figure 2.15. The bending curvature at the onset of the second bifurcation point was 0.042 m^{-1} (0.8% bending strain), and the corresponding wrinkle height and maximum liner separation were in the order of 40% and 100% of the liner thickness, respectively, for the loose fit pipe. Shortly after the onset of the second bifurcation point the liner buckled into a diamond-type mode shape, see Fig. 2.16.

Similar results were obtained when the numerical work was repeated with an MLP with thinner liner (2.5 mm thick as opposed to 3.0 mm) in [69, 70]. The bending curvature at the onset of the first and second bifurcation points was 0.015 m^{-1} (0.2% bending strain) and 0.026 m^{-1} (0.4% bending strain), respectively, for a loose fit pipe. The wrinkle height and maximum liner separation at the onset of the second bifurcation point were in the order of 20% and 60% of the liner thickness, respectively, for a loose fit pipe. The strain at the onset of either bifurcation point was shown to be very sensitive to eigenmode imperfections with height up to 5% of the liner thickness. The wrinkling strain decreased hyperbolically when the imperfection height increased, and the diamond-type eigenmode was more critical than the periodic mode shape corresponding to the first bifurcation point.

A further increase of the model length to five times a full wavelength allowed the capture of a third bifurcation point, illustrated in Figure 2.17 [71]. The numerical predictions of the normalised liner wrinkle height were compared to the Focke [50] and Hilberink [59] large scale test results. Very good agreement was found between FEA and test results when eigenmode imperfections with height up to 9% of the liner thickness were introduced in the numerical model, see Figure 2.18 [70, 71]. It was also shown that external pressure delays the onset of wrinkling by maintaining contact between the liner and backing pipe [68].

Finally, Vasilikis suggested that the secondary bifurcation point could be considered as a wrinkling limit state, because it is associated with wrinkles that are large enough to be easily detected. He recommended that the research be continued towards defining an acceptance criterion for wrinkles. In addition, the cyclic loading response of the liner, including fatigue/ratcheting phenomena could be investigated [67].

The Structural Integrity of Offshore Pipelines JIP, sponsored by several major oil and gas operators and contractors, has been run by the University of Texas at Austin, USA, for decades, under the supervision of Prof. S. Kyriakides. The subject of liner wrinkling was added to the JIP programme in 2012. First, manufacturing of lined pipes as per the Butting process (refer to Sec. 1.2.2), followed by pure bending with or without internal pressure, was simulated numerically in ABAQUS [72, 73]. API 5L X65 carbon steel host pipe with the WT = 17.9 mm and the OD in the range between 8.625" (219.1 mm) and 14" (355.6 mm), and alloy 825 liner with the WT between 2 mm and 4.5 mm, were modelled using first order solid elements (C3D8 in ABAQUS [47]) and first order shell elements (S4 in ABAQUS [47]), respectively. Large deformation J_2 flow theory and a frictionless contact scheme were employed. Half of the pipe was modelled with appropriate boundary conditions. The model length was equal to twenty times the half-wavelength of an elastic wrinkle under axial compression, λ, given by [4]

$$\lambda = \frac{\pi\sqrt{r_L t_L}}{\left(12(1-\nu^2)\right)^{0.25}} \tag{2.9}$$

where r_L, t_L and ν are the mid-wall radius, wall thickness and Poisson ratio of the liner. The backing pipe had 4 elements through the thickness and, together with the liner, 108

elements around half-circumference. The axial mesh density ranged from 30 elements over a span of 16λ on the right-hand side to 56 elements over 4λ on the left end of the model in Figure 2.19, where geometrical imperfections were introduced in the liner to initiate wrinkling. The geometrical imperfection was a combination of axisymmetric and asymmetric mode shapes, shown in Figure 2.20. Symmetry boundary conditions were applied on the left-hand side of the model while the nodes on the right-hand side were coupled to a reference node in the middle of the pipe. MLP manufacturing was simulated separately in a simplified model, and the resulting stress state was transferred to the model in Fig. 2.19, before applying rotation to the reference node to bend the pipe. A comprehensive set of sensitivity analyses was run.

Internal pressure applied to the liner during simulation of the manufacturing process halved the initial imperfection heights. The mechanism of liner wrinkling during subsequent pure bending was qualitatively the same as that described by Vasilikis in [67]. The liner separated from the backing pipe, then wrinkled uniformly before buckling into a diamond-type mode shape, shown in Figure 2.21. The strain at the onset of periodic wrinkling increased with the liner thickness and with the internal pressure. In contrast, the wrinkling strain reduced when (i) the insertion gap between liner and backing pipe increased; this was partly because increasing the gap reduced the as-manufactured grip stress, or (ii) the liner thickness was maintained and the backing pipe OD increased, i.e. the D/t ratio of the liner increased. Furthermore, while the number of circumferential waves in the diamond-type imperfection (between 6 and 10) and the value of λ (between 0.8 and 1.2 times that given by Eq. 2.9) had a negligible effect on the wrinkling process, the imperfection height was found to have the dominant effect on the strain at the onset of wrinkling. The latter reduced significantly when the imperfection height increased. The axisymmetric and asymmetric imperfections had similar effect on the liner wrinkling process. Similar trends were found when the scenario of MLP subjected to axial compression was assessed in [74].

A plastic bifurcation analysis was then run to establish the onset of periodic wrinkling [75]. The numerical modelling technique was similar to that detailed above, the main difference being the use of deformational plasticity as opposed to flow theory. The strain at the onset of periodic wrinkling was 0.6% for the 12.75" pipe. The corresponding wavelength was nearly identical

to that given by Eq. 2.9, i.e. 36 mm. The wrinkling mode was identical to that predicted by Vasilikis in [68], and shown in Fig. 2.13(Right). Subsequently, the obtained mode shape was applied as initial imperfection to the liner and sensitivity analyses were run as per [72, 73], using large deformation J_2 flow theory. The results were qualitatively similar to those reported in [72, 73]. The following scenarios were found to be increasingly onerous with regards to the liner integrity: (i) axial compression of confined liner, (ii) bending of confined liner, (iii) bending of standalone liner and (iv) axial compression of standalone liner. Additionally, it was shown that axisymmetric imperfections as per Figure 2.20 are slightly more critical than the periodic bifurcation buckling mode in Fig. 2.13(Right). Furthermore, the strain at the onset of liner collapse was more than three times higher than the strain at the onset of periodic wrinkling. Moreover, the liner separation for the latter was very benign. Consequently, it was suggested that the onset of periodic bifurcation would be an overly conservative failure criterion.

Subsequently, a laser tool similar to that shown in Figure 2.5 was built and liner imperfections in as-manufactured 8" and 12" lined pipes with a seamless backing pipe were measured [76]. The topology of the inner surface of the liner exhibited periodic circumferential and axial variations inherent to the seamless pipe manufacturing process. The largest imperfection heights were up to 2% and 22% of the liner thickness in the axial and circumferential direction, respectively, see Figure 2.22. Fourier-type harmonic series were fitted to the measurements and imperfections imposed to a perfect liner in a 12.75" (323.9 mm) OD $\times$ 14.3 + 2.7 mm WT lined pipe. Subsequently, pure bending of the lined pipe was simulated using the FEA model shown in Fig. 2.19. The numerical modelling technique was the same as that detailed above [73]. Sensitivity analyses were run to assess the effect of the shape of the dominant imperfection. The wrinkling process was qualitatively similar to that described above [72, 73, 75]. The liner collapsed when the test pipe was subjected to 0.8% bending strain. The corresponding liner separation was well above the liner thickness. Furthermore, although the measured imperfections differed significantly from idealised eigenmode type imperfections (see Figure 2.23), their effect on the liner behaviour was qualitatively the same [76].

Finally, it was also shown that a seal weld between liner and backing pipe at the end of a mechanically lined pipe may have a similar effect on the liner behaviour to that of geometrical

imperfections in the main body of the lined pipe [77, 78]. This is because the weld locally prevents liner separation, creating an axially periodic disturbance to the liner which grows with the applied bending strain and eventually leads to a diamond-shaped collapse mode. It was suggested that the numerical modelling and analysis technique developed during the JIP could be used to undertake a cost-performance analysis to select the optimal liner thickness for a given application.

2.2.4 Wrinkling under Cyclic Bending

During Phase III of the Clad and Lined Pipeline Materials JIP, DNVGL undertook a numerical wrinkling parametric study. Two MLPs were considered: (i) 305 mm OD × 17.5 mm WT host pipe manufactured to API 5L X60, lined with 3 mm thick alloy 316L and (ii) 406.4 mm OD × 19.1 mm WT backing pipe manufactured to API 5L X60, lined with 3 mm thick alloy 316L. The numerical modelling technique and liner wrinkling criteria adopted were broadly similar to those employed by Vasilikis in [71]. It was shown that the wrinkling strain significantly increases with the liner imperfection height. Increasing the backing pipe wall thickness has only a moderate beneficial effect. Furthermore, a significant increase in the liner yield strength leads to a small reduction of the strain at the onset of wrinkling [79].

Three 12" MLPs with 3 mm thick alloy 316L liner were then manufactured: (i) one non-welded pipe, and (ii) two girth-welded pipes. Following insertion of a crawler equipped with a camera and a laser head, each specimen was installed on a four-point rig similar to that shown in Fig. 2.8(a), and subjected to cyclic bending. One non-welded and one girth-welded pipe were tested at atmospheric pressure whereas an internal pressure of 6 bar was applied to the remaining girth-welded pipe during bending [80].

The liner in each test pipe wrinkled during the first bending event. The wrinkling strain, defined as the bending strain at which wrinkles appeared in the test pipes, ranged from 0.27% for the girth-welded specimen tested at elevated pressure to 0.85% for the girth-welded specimen tested at ambient pressure. The corresponding wrinkle heights were 0.5 mm and 1.0 mm, respectively. Further bending resulted in a significant increase in the wrinkle heights. The wrinkles at the

pipe intrados were nearly flattened when the pipe was reverse bent. However, wrinkling initiated at the opposite clock position. Cyclic plastic bending eventually caused buckling of the liner in a diamond mode shape [80].

It was suggested that the liner in the pressurised MLP wrinkled earlier than that in the non-pressurised pipes because a 1 mm gap was left between the liner and backing pipe adjacent to the cladding, after manufacturing. It was argued that a gap of 0.1 mm would be representative of project pipes. Finally, following calibration of the numerical model against experimental data supplied by JIP sponsors, it was proposed that the wrinkling strain could be determined from [81]

$$\varepsilon_w = \frac{Dt_L}{2\left(D - 2t_{CS}\right)^2} \tag{2.10}$$

where D and t_{CS} are the backing pipe OD and WT, and t_L is the liner thickness.

To qualify mechanically lined pipe for reel-lay installation Tkaczyk *et al.* undertook an extensive numerical modelling and experimental testing programme [82, 83]. First, two MLPs with 12.75" (323.9 mm) OD × 15.1 mm WT API 5L X65 host pipe and 2.8 mm thick alloy 316L liner, manufactured by CladTek, were subjected to five reverse bending cycles (equivalent to 2.5 times a standard reel-lay installation) at Heriot Watt University (HWU) in Edinburgh, UK. The HWU rig, shown in Figure 2.24, was equipped with a 7.84 m radius reeling former, resulting in a bending strain of 2.0% for each cycle. The inner surface of each specimen was subjected to a video and laser inspection at various stages during testing.

Very large wrinkles were produced during cyclic bending. As observed during the DNVGL JIP trials the wrinkles produced at the pipe intrados during the first bending event were nearly flattened when the pipe was reverse bent. However, wrinkling initiated at the opposite clock position. Cyclic plastic bending eventually caused buckling of the liner in a diamond mode shape shown in Figure 2.25. The ability of internal hydrotest pressure to remove wrinkles, which were produced during bending, was also examined. An internal pressure of 39 MPa reduced the wrinkle heights by more than 50%, but could not return the liner surface to its as-manufactured condition. Nevertheless, no cracks or other damage were found during post-mortem examination of the wrinkled liners.

The large scale bend tests were then simulated numerically in ABAQUS [47]. First-order shell elements with reduced integration (S4R in ABAQUS [47]) were used to model both the liner and backing pipe. The Gauss integration scheme with 5 and 7 integration points through the thickness was employed for the host pipe and liner, respectively. J_2 flow theory, finite strain and non-linear kinematic hardening plasticity schemes were employed to model the flow behaviour of the liner and host pipe. The parameters of the kinematic hardening model were chosen to obtain a good fit to cyclic stress-strain curves representative of API 5L X65 and alloy 316L materials. A finite-sliding hard contact formulation, where the contact constraint is enforced with a Lagrange multiplier, and the classical Coulomb friction model were applied to model the interaction between the liner and backing pipe. A coefficient of friction of 0.1 was considered. To predict the onset of wrinkling and subsequent wrinkle growth, geometrical imperfections in the order of 5% of its thickness were imposed on the liner. The FEA model was 15D long and comprised of over 20,000 elements, see Figure 2.26. Due to symmetry, only a quarter of the lined pipe was modelled with appropriate boundary conditions. The pipe end to the right in Fig. 2.26 was coupled to a reference node while symmetry boundary conditions were applied to the other pipe end. The reeling and straightening formers were modelled using rigid surfaces with appropriate radii. The pipe was loaded by applying a suitable rotation to the reference node and appropriate displacements to the rigid surfaces.

Good agreement was found between the numerical predictions and the tests results, as shown in Figure 2.27. The calibrated FEA model was then used to run a wrinkling parameter study, to examine the effect of backing pipe and liner geometry, yield strength/wall thickness variations and manufacturing/installation parameters on liner wrinkling. Subsequently, it was proposed that the minimum reelable liner thickness could be determined from

$$t_{Lmin} = 0.16 + \alpha_{ij} \left(\varepsilon_{nom} D^{0.75}\right)^i g^j \tag{2.11}$$

Here, ε_{nom} is the reeling strain, D is the outer diameter of the lined pipe, g is the liner radial insertion gap and α_{ij} are constants given in Table 1 in [29].

Subsequently, twelve MLPs with the liner thickness as per Eq. 2.11 were produced: (i) three 6.625" pipes with API 5L X65 backing pipe and alloy 904L liner, (ii) six 8.625" pipes with

API 5L X60 backing pipe and alloy 316L liner and (iii) three 12.75" pipes with API 5L X65 backing pipe and alloy 625 liner. The 6.625" and 12.75" CladTek pipes were tested in a vertical bending rig, shown in Figure 2.28, equipped with 8.3 and 10.5 m reeling formers, respectively. In contrast, the 8.625" Kuroki pipes were subjected to bending in a horizontal bending rig in Figure 2.29, equipped with an 8.23 m reeling former. The non-welded and girth-welded test specimens were subjected to three to six reverse bending cycles (i.e. 1.5 to 3 times a standard reeling operation). No wrinkles were found during inspection undertaken during the trials [82, 83]. Only manufacturing imperfections as per Fig. 1.9 were found during post-mortem examination. This validated the concept of increasing the liner thickness to suppress wrinkling.

2.3 Fracture of Pipeline Welds

2.3.1 Engineering Critical Assessment

Background

Traditionally, subsea pipeline welds were inspected by radiography testing (RT), which can only size a flaw length (but not its height/depth). Due to this limitation, flaw heights were assumed equal to a weld pass (3 mm typically) and workmanship criteria were used to deem flaw acceptability. Following the development of the Automated Ultrasonic Testing (AUT) inspection technique, DNVGL introduced a requirement to use that technique to inspect subsea pipeline welds, because it allowed sizing both the height/depth of a flaw, "a" or "$2a$" depending on the flaw type, and its length, "$2c$". Engineering Critical Assessment (ECA) of pipeline welds then became mandatory, to prove acceptability of detected flaws.

An ECA generally involves a fracture and/or a fatigue assessment (the latter is discussed in a separate section). Fracture is deemed to have initiated when the crack driving force (CDF) is greater than the material's resistance, or when the applied load exceeds the bearing capacity of the cracked structure.

Most flaws in pipeline welds are embedded. Unlike the former, surface breaking flaws may be easily repaired by welding or grinding and flapping. Planar flaws such as surface/embedded

lack of fusion flaws are typically assessed in an ECA. The acceptability of other types of flaws, such as laminations and volumetric flaws (e.g. pores) is usually sanctioned by workmanship criteria provided in industry standards, such as DNVGL-ST-F101 [7].

Crack Driving Force

Under Small Scale Yielding (SSY) conditions, when the plastic zone remains confined to a small region surrounding the crack tip, the crack driving force can be conveniently expressed in terms of the stress intensity factor (SIF). For a cracked body subjected to a remotely applied stress, σ, the mode I stress intensity factor, K, can be estimated from

$$K = Y\sigma\sqrt{\pi a} \tag{2.12}$$

where a is the crack depth or height and Y is a dimensionless function of the geometry and load mode. Under Large Scale Yielding (LSY), the crack driving force may be expressed in terms of the J-integral, proposed by Rice [84]

$$J = \int_{\Gamma}(Wn_i - \sigma_{ij}\, n_j\, \partial u_i/\partial x_j)\mathrm{d}s \qquad\qquad i,j = 1,2,3 \tag{2.13}$$

Here, Γ is any counter clockwise contour encircling the crack tip, u_i is the displacement vector, n_i is the outward unit normal to Γ, $\mathrm{d}s$ is the length of the line element and W is the strain energy density

$$W = \int_0^{\varepsilon_{ij}} \sigma_{ij}\mathrm{d}\varepsilon_{ij} \tag{2.14}$$

Hutchinson [85], and Rice and Rosengren [86] also proposed to use the J-integral as a non-linear SIF for materials with power-law stress-strain behaviour

$$\frac{\varepsilon}{\varepsilon_0} = \alpha\left(\frac{\sigma}{\sigma_0}\right)^n \tag{2.15}$$

where σ is stress, ε is strain, σ_0 is a normalising stress (often the yield stress) and $\varepsilon_0 = \sigma_0/E$ is the elastic strain. The J-integral can therefore be considered as both an energy release rate and a non-linear SIF. Under linear elastic conditions, J and K are related through

$$J_e = \frac{K^2}{E'} \tag{2.16}$$

where E' is the effective elastic modulus, $E' = E$ in plane stress and $E' = E/(1-\nu^2)$ in plane strain, and ν is the Poisson ratio. The crack driving force may also be expressed in terms of the Crack Tip Opening Displacement (CTOD), δ, proposed by Wells [87]. For power-law materials, the relationship between J-integral and CTOD is of the form [88]

$$\delta = d(\alpha\varepsilon_0, n)\frac{J}{\sigma_0} \tag{2.17}$$

where d is a dimensionless function of n and $\alpha\varepsilon_0$. Therefore, J and δ are equivalent crack driving force estimation parameters.

Fracture Toughness

Under small scale yielding conditions, fracture toughness can be measured in terms of a single K value, K_{Ic}. Likewise, critical values of J and δ, J_{Ic} and δ_c, respectively, can be determined under large scale yielding conditions. In contrast to the latter, the former requires that J-dominance conditions are met, i.e. (i) the deformation model of plasticity (non-linear elasticity) accurately models the small strain behaviour of real elastic-plastic material under monotonic loading and (ii) the microscopic damage process zone, where large strains are seen, is well contained within the small strain solution region. However, free surfaces are often present near crack tips in reeled pipelines and as a result the latter condition may not be satisfied.

Consequently, the J-integral may not describe the crack tip stress field as large scale yielding develops. The constraint effect on the near crack tip fields may be quantified by the J-Q analysis, where Q is the difference between the HRR stress field (Hutchinson [85], Rice and Rosengren [86]) and the actual stress field in a real geometry (see O'Dowd [89] for example). As the stress at the crack tip decreases with decreasing crack tip constraint (lower Q values), higher values of the fracture toughness, J_c, are found in less constrained structures.

As the constraint in reeled pipelines is generally low, Single Edge Notched Tension (SEN(T)) specimens (see Figure 2.31) can be conveniently used to determine the fracture toughness, as opposed to highly constrained Single Edge Notched Bending (SEN(B)) specimens. A significant extra fracture resistance is gained if small amounts of stable crack growth are permitted in materials with high tearing resistance. Consequently, in a reeling ECA fracture toughness is often expressed in terms of a J-R or δ-R resistance curve, established as per BS8571 [90], see Figure 2.30. In contrast, δ_c established from SENB testing as per BS EN ISO 15653 [91] (supersedes BS7448) may still be used for the operational phase, to account for internal pressure.

The fracture toughness of a reeled pipeline is governed by that of its welds (including Heat Affected Zones (HAZ)), which usually contain flaws. Welding introduces inhomogeneity of the material and residual stresses, which may influence the crack tip constraint (see Østby *et al.* [92] for example), due to differential cooling. When the weld metal (WM) overmatches the parent metal (PM) in terms of the stress-strain curve the constraint ahead of the crack tip may be reduced. In contrast, WM undermatch has the opposite effect. In addition, the crack tip constraint may depend on the crack position and mismatch magnitude (see Fu and Shi [93] and Boothman *et al.* [94] for example).

Residual stresses may strongly influence the fracture response when the CDF is low. However, this effect reduces significantly with the plastic deformation, and is therefore less important under large scale yielding. The effect of pre-strain on the fracture toughness of welded pipes was investigated experimentally by Pisarski *et al.* [95]. The fracture toughness of welds that had undergone straining to simulate reeling was similar to that of the as-received welds when the WM overmatched the PM. However, the validity of this conclusion was questionable because pre-straining was performed on uncracked samples, which were subsequently notched and fracture tested under monotonic loading.

More recently, Tkaczyk *et al* [96, 97] investigated the effect of pre-strain on the fracture toughness of overmatch girth welds in API 5L X70 pipes. Cross-weld SENT specimens, with the initial crack depth to specimen width ratio, $a/W = 0.25$ and 0.50, were subjected to a tension-compression-tension cycle representative of loading experienced by reeled pipelines. The nor-

malised crack depth had a negligible effect on the fracture toughness in terms of J or δ. No significant difference was observed between the fracture resistance curves obtained for the weld material in the as-received and strained conditions for the crack growth during pre-strain in the range between 0.2 mm and 1.1 mm, see Figure 2.32. The experimental results were confirmed by a numerical analysis detailed in [98]. It was concluded that the fracture toughness of overmatch welds is unaffected by prior tension-compression cycles. Similar results were found during subsequent work by Østby *et al.* [99].

Pisarski *et al.* [95] also showed that pre-strain may have a detrimental effect on the fracture toughness of undermatch welds. The fracture resistance of welds with moderate undermatch (10% in terms of the yield strength) significantly reduced when the pre-strain exceeded 4%. For lower pre-strains (which are more representative of reeling) reductions of the fracture toughness were minimal. However, the validity of these results remains questionable because pre-straining was performed on uncracked samples. Furthermore, although similar trends were found by Tang and Shi [100] and Lin *et al.* [101] for weld centre line (WCL) flaws in SENB specimens, this may not hold for flaws in low constraint SENT specimens.

Limit Load Solutions

Industry standards such as BS7910 [102]) and R6 [103] provide a comprehensive set of limit load solutions for the assessment of surface and embedded flaws in evenmatch and undermatch pipeline welds. Consequently, the robustness of a fracture assessment procedure often relies on its ability to accurately predict the crack driving force.

Load-Controlled vs Displacement-Controlled

Fracture assessment procedures can be classified into two categories: (i) stress-based approaches, such as that proposed by the Electric Power Research Institute (EPRI) for power-law materials in [104], and generalised by Ainsworth in [105], and (ii) strain-based schemes, such as the SINTEF [106, 107] and DNVGL [7] procedures. The former is typically used for the

assessment of structures loaded within the elastic regime (load-controlled scenarios), while the latter is best-suited to displacement-controlled load modes, such as reeling.

2.3.2 Strain-Based Fracture Assessment of Evenmatch Girth Welds

DNVGL-ST-F101 Procedure

Outline of assessment procedure Most often, reeling ECA of even/overmatch pipeline girth welds is carried out following the guidance provided in DNVGL-ST-F101 [7]. The assessment procedure, which is detailed in DNVGL-RP-F108 [108], follows the BS7910 [102] option 2 approach (equivalent to option 2 in R6 [103]).

Maximum acceptable flaw sizes, expressed in terms of crack depth and length, are determined through ductile tearing assessments. Each tensile straining event of the reeling process is assessed separately, using an appropriate parent metal stress-strain curve and a material fracture resistance curve (typically a J-R curve). An as-received stress-strain curve (i.e. a curve exhibiting a yield plateau for seamless pipes) is used for the assessment of the first event, while a pre-strained stress-strain curve (i.e. a curve exhibiting continuous hardening for seamless pipes) is used for the second event.

The nominal strain at the pipe extrados, ε_{app}, determined from Eq. 1.1, is converted (using the relevant stress-strain curve) into a remote applied stress, σ_{app}, which is accounted for as a primary membrane stress, P_m. A primary bending stress, P_b, resulting from misalignment at the girth weld (hilo), is determined using the Neuber approach [109]

$$\begin{aligned} \hat{\sigma}_{app}\,\hat{\varepsilon}_{app} &= k_t^2\,\sigma_{app}\,\varepsilon_{app} \\ P_b &= \hat{\sigma}_{app} - \sigma_{app} \end{aligned} \tag{2.18}$$

where $\hat{\sigma}_{app}$ and $\hat{\varepsilon}_{app}$ are the elevated stress/strain and k_t is an appropriate elastic stress concentration factor defined in DNVGL-RP-F108 [108].

A local applied stress (Ainsworth's reference stress [105]), σ_{ref}, which accounts for the reduced cross-sectional area in the defective weld, is estimated using an appropriate limit load solution

$$\sigma_{ref} = \frac{P}{P_0}\sigma_0 = \frac{P_0}{P_L}\sigma_{app} \tag{2.19}$$

where P is the applied load, P_L is the plastic limit load, P_0 is a reference/normalising load (typically the yield load of the uncracked structure) and σ_0 is the stress corresponding to P_0 (i.e. typically the yield stress). The proximity to failure by plastic collapse is assessed by the load ratio, L_r, determined from

$$L_r = \frac{\sigma_{ref}}{\sigma_y} \tag{2.20}$$

Similarly, the proximity to failure by fracture is evaluated through the fracture ratio, K_r, determined from

$$K_r = \frac{K}{K_{mat}} + \rho \tag{2.21}$$

where ρ is a plasticity correction factor defined in Annex R of BS7910, K_{mat} is the material fracture toughness and K is estimated using an appropriate SIF solution. Welding residual stresses, which are considered as a secondary membrane stress, Q_m, are assumed equal to the yield stress of the parent metal, and allowed to relax according to

$$Q_m = \min \begin{cases} \sigma_y \\ \left(1.4 - \dfrac{\sigma_{ref}}{\sigma_y + \sigma_t}\right)\sigma_y \end{cases} \tag{2.22}$$

Alternatively, a welding residual strain, $\varepsilon_{weld} = \sigma_y/E$, may be added to ε_{app} prior to determining σ_{app}. The assessment point, (L_r, K_r), is then plotted in a BS7910 (R6) failure assessment diagram (FAD), which boundary is constructed from

$$K_r = \left(\frac{J}{J_e}\right)^{-0.5} = \left(\frac{E\epsilon_{ref}}{L_r\sigma_y} + \frac{1}{2}\frac{L_r^3\sigma_y}{E\epsilon_{ref}}\right)^{-0.5} \tag{2.23}$$

where ε_{ref} is the strain corresponding to σ_{ref} on the assumed stress-strain curve. The cut-off value for L_r, i.e. L_{rmax}, is the tensile to yield ratio, as recommended in DNVGL-RP-F108 [108].

Eq. 2.23 implies that the crack driving force is of the form

$$J = \frac{K^2}{E'}\left(\frac{E\varepsilon_{ref}}{\sigma_{ref}} + \frac{1}{2}\frac{\sigma_{ref}^3}{\sigma_0^2 E\varepsilon_{ref}}\right) \tag{2.24}$$

A ductile tearing assessment is carried out by iteratively increasing the crack depth (assuming a certain amount of tearing occurs) until the assessment point falls within the FAD, as shown in Figure 2.34. For each tearing increment, the material fracture toughness expressed in terms of J, i.e. J_{mat}, is determined from the resistance curve, and then converted into K_{mat} through

$$K_{mat} = \left(\frac{EJ_{mat}}{1-\nu^2}\right)^{0.5} \tag{2.25}$$

The stable grown flaw size from the first tensile straining event is used as a starting point for the assessment of the second event. The initial (as-welded) flaw is deemed acceptable for reeling if stable growth is predicted to occur during both tensile straining events, and the accumulated tearing does not exceed 10% of the pipe wall thickness [108].

Surface breaking flaws DNVGL-RP-F108 [108] recommends deriving σ_{ref} from the Kastner *et al.* solution [110], which considers local plastic collapse of cylinders loaded in tension

$$\sigma_{ref} = P_m \frac{\pi(1-a/t) + 2(a/t)\sin(c/r)}{(1-a/t)(\pi-(c/r)(a/t))} + \frac{2}{3}P_b\left(1 - \frac{a/t}{1+t/c}\right)^{-2} \tag{2.26}$$

where a, $2c$, t and r are crack depth, crack length, pipe wall thickness, and pipe mid-wall radius, respectively (see Figure 2.33 for definitions of a, $2c$, t and r). The SIF, K, is to be estimated from the Raju and Newman [111] solution for a surface flaw in a flat plate

$$K = \left(f_w(M_{km}M_mP_m + M_{kb}M_bP_b) + M_{km}M_mQ_m\right)\sqrt{\pi a} \tag{2.27}$$

The expressions for the finite width correction factor, f_w, and the stress intensity magnification factors, M_{km}, M_m, M_{kb} and M_b, are given in BS7910 [102]. The width of an equivalent flat plate is taken as $W = 2\pi r$, where r is defined in Fig. 2.33.

Embedded flaws As for surface breaking flaws, the SIF for embedded flaws in pipeline girth welds can be evaluated using the Raju and Newman [111] solution in Eq. 2.27, with appropriate shape functions given in BS7910 [102]. The proximity to failure by ligament collapse can be assessed using a BS7910 modified Willoughby and Davey [112] limit load solution for embedded flaws in plates [102]

$$\sigma_{ref} = \frac{P_b + 3P_m\alpha'' + \left(\left(P_b + 3P_m\alpha''\right)^2 + 9P_m^2\left[\left(1-\alpha''\right)^2 + 4\left(p^A\alpha''/t\right)\right]\right)^{0.5}}{3\left[\left(1-\alpha''\right)^2 + 4\left(p^A\alpha''/t\right)\right]} \tag{2.28}$$

where $2a$, $2c$ and p^A are the height, length and embedment depth of the flaw, t is the pipe thickness, W is the plate width or pipe mid-wall circumference (see Figure 2.35 for the definition of $2a$, $2c$, p^A, t and W), and α'' is the height to thickness ratio adjusted (reduced) to account for the load bearing capacity of the uncracked material on either side of the flaw, which is not included in Willoughby and Davey's 2D analysis in [112]

$$\alpha'' = \begin{cases} \dfrac{2a/t}{1+(t/c)} & \text{for} \quad W \geq 2(c+t) \\ (2a/t)\,(2c/W) & \text{for} \quad W < 2(c+t) \end{cases} \tag{2.29}$$

However, the reference stress solution given in Eq. 2.28 is too conservative when used for the assessment of embedded flaws in pipeline girth welds (see Yi *et al.* [113] for example). Furthermore, embedded flaws are perceived to be less critical than surface breaking flaws. Consequently, DNVGL-RP-F108 [108] recommends using the surface breaking flaw acceptable criteria for embedded flaws provided that $p^A \geq a$. Furthermore, an embedded flaw must remain buried during the whole pipeline life. Otherwise, the embedded flaw should be reclassified as a surface breaking flaw

$$\begin{aligned} a_s &= 2a_e + p^A \\ 2c_s &= 2c_e + p^A \end{aligned} \tag{2.30}$$

Here, a_s and $2a_e$ are the surface and embedded flaw heights, and $2c_s$ and $2c_e$ the surface and embedded flaw lengths, respectively. The DNVGL reclassification criterion for embedded flaws is illustrated in Figure. 2.36.

Improved Crack Driving Force Estimation Scheme

Tkaczyk *et al.* [114] compared fracture assessment schemes proposed in the literature for the treatment of surface breaking flaws in evenmatch pipeline girth welds subjected to reeling strains. API 5L X65 pipes with the OD in the range between 10.75" (273.1 mm) and 18" (457.0 mm), with the corresponding minimum reelable WT (between 8.7 mm and 25.4 mm) determined from Eq. 2.2 assuming $R = 9750$ mm, were considered. For a critical fracture toughness, $J_c = 400\ N/mm$ (mid-range SEN(T) toughness for ductile tearing between 0.2 mm and 0.5 mm including blunting), and a range of crack lengths between 25 mm and 200 mm, the maximum acceptable crack depths were determined for each pipe size. The crack driving force from four different estimation schemes were compared to the results of a finite-element analysis: (i) the DNVGL-ST-F101 scheme [7, 108], (ii) the SINTEF procedure [106, 107], (iii) the reference strain method [115] and (iv) the South West Research Institute (SwRI) FlawPRO procedure [116]. The SINTEF approach yielded the best agreement with the FEA results. However, since its range of application in terms of pipe geometries and materials was rather limited, the authors recommended using the DNVGL approach with the Kastner solution (other limit load solutions, e.g. the Miller solution [117] gave less accurate predictions).

Subsequently, to improve the DNVGL crack driving force estimation scheme Tkaczyk *et al.* [118] proposed a modified reference stress solution for pipes with surface breaking flaws, following the approach laid out by Kim and Budden in [119]

$$P_L^{TTK} = \gamma^{TTK} P_L^{DNVGL} \tag{2.31}$$

where P_L^{DNVGL} is the limit load corresponding to the Kastner reference stress solution in Eq. 2.26 and γ^{TTK} is a dimensionless function of the crack geometry and the hardening index of the material stress-strain curve

$$\gamma^{TTK} = c_{ijk}(2c/\pi D)^i (a/t)^j n^k \tag{2.32}$$

Here, c_{ijk} are constants fitted to the results of a 3D parametric FEA study, and tabulated in [118].

To account for seamless pipe with a yield plateau in the as-received condition the approach of Boothman *et al.* [120] was followed. An idealised true stress-strain curve (a modified Ramberg-Osgood relationship) representative of a material exhibiting a yield plateau was considered [121]

$$\begin{aligned} \frac{\varepsilon}{\varepsilon_0} &= \frac{\sigma}{\sigma_0} && \text{for} \quad 0 \leq \varepsilon \leq \varepsilon_0 \\ 1 + (\varepsilon - \varepsilon_0) &= \frac{\sigma}{\sigma_0} && \text{for} \quad \varepsilon_0 < \varepsilon < \varepsilon_0 + \varepsilon_p \\ \frac{\varepsilon}{\varepsilon_0} + (\alpha - 1) - \frac{\varepsilon_p}{\varepsilon_0} &= \alpha \left(\frac{\sigma}{\sigma_p} \right)^n && \text{for} \quad \varepsilon \geq \varepsilon_0 + \varepsilon_p \end{aligned} \tag{2.33}$$

where α and n are material parameters describing a true stress-strain curve, ε_0 ($= \sigma_0/E$) is the yield strain, ε_p is the plastic strain at the end of the plateau (i.e. the Lüders strain) and σ_p is the true stress at $\varepsilon = \varepsilon_0 + \varepsilon_p$, see Figure 2.37. The J-strain curve was split into four regions, illustrated in Figure 2.38, where the tension and bending load modes are indicated by solid and dashed lines, respectively: (i) Region I: small scale yielding, (ii) Region II: net ligament/net section yielding, (iii) Region III: saturation of J and (iv) Region IV: global yielding [121, 98]. The Tkaczyk *et al.* crack driving force estimation scheme was validated experimentally in [122].

Other Fracture Assessment Procedures for Evenmatch Welds

Surface breaking flaws Other crack driving force estimation schemes have been proposed in the literature for the assessment of surface flaws in even/overmatch pipeline girth welds, see Nourpanah and Taheri [123] and Parise *et al.* [124, 125], for example. However, these are generally not suitable for the assessment of small to medium size seamless pipes with a yield plateau.

Embedded flaws R6 [103] provides local and global limit load solutions for embedded flaws in plates. The suitability of the local solution for the assessment of flaws in pipeline girth welds will be investigated in the next chapter. Global limit load solutions will not be assessed because they are less accurate for the prediction of the plastic collapse of the smaller ligament of length p^A in Fig. 2.35.

2.3.3 Strain-Based Fracture Assessment of Undermatch Girth Welds

DNVGL-ST-F101 Procedure

The DNVGL clad and lined pipe JIP guidance report No. 2017-3114 [81], which supersedes DNVGL-RP-F108 [108] for the assessment of flaws in metallurgically clad and mechanically lined pipes, classifies pipeline girth welds which do not meet all the criteria listed in Figure 2.39 as either: (i) "partial-overmatching" if they meet all the requirements in Figure 2.40 or (ii) "undermatching" if they fail to meet any of the criteria in Fig. 2.40. For simplicity, in this work "partial-overmatching" and "undermatching" welds are referred to as "undermatch" welds. Flaws in such welds cannot be directly assessed with the standard DNVGL-RP-F108 [108] ECA approach described in Sec. 2.3.2. First, a 3D FEA must be carried out to:

1. Demonstrate that the CDF predicted by FEA is lower than that estimated using the standard DNVGL-RP-F108 ECA procedure,

2. Prove that the CDF predicted by FEA where representative stress-strain curves are assigned to all materials is lower than that estimated by FEA for the same model where the parent pipe stress-strain curve is assigned to all materials, or

3. Demonstrate that the DNVGL-RP-F108 ECA approach can be modified (e.g. by adjusting the stress-strain curve, applied strain or flaw geometry, such that the CDF is overestimated) and safely used to determine acceptable flaw sizes.

Then, a standard/adjusted DNVGL-RP-F108 ECA approach as per Sec. 2.3.2 may be undertaken if any of the conditions listed above is met. Otherwise, a full 3D FEA-based ECA must be carried out (e.g. an option 3 ECA as per BS7910 [102] or R6 [103]).

SINTEF Procedure

The most versatile assessment procedure for undermatch welds was proposed by SINTEF in [106, 107]. In this approach the elastic regime is ignored, and it is argued that the CTOD, δ,

is a linear function of the applied strain and the pipe WT in a full plastic regime

$$\delta = t\,\varepsilon\,C \tag{2.34}$$

Here, C is a function (established by fitting coefficients of polynomials to the results of parametric FEA of pipes with constant depth surface cracks, loaded in tension) of the pipe and flaw geometries and the weld metal mismatch at yield, m_y, determined from

$$m_y = 1 - \frac{\sigma_y^{WM}}{\sigma_y^{PM}} \tag{2.35}$$

where σ_y^{PM} and σ_y^{WM} are the parent and weld metal yield stresses, respectively. Eq. 2.35 implies that $m_y > 0$ for undermatch and $m_y < 0$ for overmatch. The effect of the mismatch on the acceptable flaw sizes is introduced by the definition of an effective crack depth

$$a_{\mathit{eff}} = a - m_y H \tag{2.36}$$

where H is half of the equivalent weld width, a is the flaw depth in the even/overmatch weld and a_{eff} is the flaw depth in the undermatch weld.

The SINTEF scheme is valid for: (i) pipes with $20 < D/t < 40$, (ii) normalised crack depth, $a/t \leq 0.35$; if $a/t < 0.1$ then it is assumed that $a/t = 0.1$, (iii) crack length, $2c \leq 300$ mm, (iv) wall thickness, 15 mm $\leq t \leq 35$ mm, (v) continuously hardening material with yield to tensile strength ratio, $0.82 < \ Y/T \ < 0.93$. Therefore, it is not strictly applicable for most reeled pipes with D/t usually below 20, and mechanically lined pipes which exhibit a yield plateau in the as-received condition. Similar crack driving force estimation schemes have been proposed more recently (see Yi *et al.* [113] and Zhang *et al.* [126] for example). However, their applicability is very limited.

SINTAP Procedure

When the SINTAP procedure is used, undermatch welds can be assessed at Level 2 or Level 3. The Level 3 assessment, which is essentially the R6 procedure [103], is considered in this work,

because it is the most accurate analytical assessment method. Section III.8 of the R6 code Revision 4 includes a procedure for undermatch welds, whereby an equivalent stress-strain curve is used in the assessment [127]. The equivalent stress-strain curve is derived from [127]

$$\sigma_{eq}\left(\varepsilon^{pl}\right) = \frac{(\gamma-1)\sigma^{WM} + (M-\gamma)\sigma^{PM}}{M-1} \tag{2.37}$$

The mismatch ratio, M, and the mismatch limit load ratio, γ, are determined from

$$\begin{aligned} M\left(\varepsilon^{pl}\right) &= \frac{\sigma^{WM}}{\sigma^{PM}} \\ \gamma\left(\varepsilon^{pl}\right) &= \frac{P_L^M}{P_L^{PM}} \end{aligned} \tag{2.38}$$

where σ^{PM} is the parent metal stress, σ^{WM} is the weld metal stress, P_L^M is the mismatch limit load and P_L^{PM} is the parent metal limit load. Traditionally, limit loads are determined assuming elastic-perfectly plastic stress-strain response. As a result, they are usually conservative and independent of the applied strain. For mismatched structures, M has a significant effect on P_L^M. However, if the weaker (in terms of yield strength) component of a mismatched structure has significantly higher strain hardening than the stronger component, the actual limit load of the structure could be significantly higher than predicted assuming elastic-perfectly plastic stress-strain response. To account for this effect in Eq. 2.37, M is calculated for each increment of plastic strain, ε^{pl}, and so are σ^{PM}, σ^{WM} and P_L^M. It will be shown in the next chapter that the acceptable flaw sizes in reeled pipes with undermatch welds can be significantly overestimated using this approach.

2.3.4 Fracture Assessment of Interface between Liner and Overlay Welds in MLP

Tkaczyk *et al.* [128] proposed a strain-based fracture assessment procedure for flaws at the interface between liner and overlay cladding, referred to as "CRA interface flaws" in this work. First, an extensive FE study was undertaken to examine the effect of the following parameters on the crack driving force: (i) the geometry of host pipe and liner, (ii) the crack size and (iii) the

tensile behaviour of clad overlay weld and liner. Reelable MLPs with outer diameter, D, in the range from 6.625" (168.3 mm) to 12.75" (323.9 mm), made of API 5L X65 host pipe lined with alloy 316L, nickel alloys 825 or 625, and terminated with alloy 625 cladding, were considered. The liner thickness was chosen based on the assumption that the MLP would be installed from the Deep Blue reel-lay vessel with a 9.75 m reel hub radius. CRA interface flaws, illustrated in Figure 2.41, with normalised crack depth, a/t, in the range between 0.10 and 0.65, and height to length ratio, $a/2c$, from 0.02 to 0.23, were considered.

A parametric elastic-plastic FE analysis of MLPs with part circumferential interface cracks was performed using ABAQUS [47]. J_2 flow theory with non-linear kinematic hardening plasticity and small strain kinematics were employed. Figure 2.42 depicts a typical FE mesh made of up to 170,000 eight-node linear hexahedral elements with reduced integration (C3D8R in ABAQUS [47]). Due to symmetry, only a quarter model of the pipe was built. The crack tip region, shown in Fig. 2.42(c), had a focused mesh, composed of 5 rings and 17 to 29 layers depending on crack and pipe geometries. The smallest element size at the crack tip was of the order of 1% of the crack depth, a. A total of 112 FE analyses (16 geometries with 7 different material tensile responses) were performed for cracked pipes subjected to bending.

The crack driving force in the CRA interface flaw, expressed in terms of the CTOD, δ, increased with the liner yield strength. Following fitting of polynomial functions to the numerical results for alloy 625 liner, which were most onerous, it was proposed that the crack driving force could be estimated from

$$\delta = (m_0 + m_1\,\zeta + m_2\,\zeta^2)\,t \tag{2.39}$$

where ζ, m_0, m_1 and m_2 are given by

$$\begin{aligned} \zeta =& (a/t)^{1.4}\ (2c/t)^{0.65} \\ m_0 =& -12.6\,\varepsilon^2 + 94.7\times 10^2\,\varepsilon - 42.9\times 10^4 \\ m_1 =& -94.0\,\varepsilon^2 + 43.3\times 10^1\,\varepsilon - 28.0\times 10^4 \\ m_2 =& \quad 7.60\,\varepsilon^2 - 31.6\times 10^2\,\varepsilon + 12.8\times 10^4 \end{aligned} \tag{2.40}$$

Here, ε is the applied strain measured on the liner OD. For all cases considered, δ from Eq. 2.39 overestimated FE predictions by 15% on average. SEN(T) testing was then carried out to establish a fracture toughness resistance curve for alloy 625 overlay welds deposited inside a 10.75" (273.1 mm) OD carbon steel pipe manufactured to API 5L X65. Subsequently, maximum acceptable flaw sizes for 6.625" (168.3 mm) to 12.75" (323.9 mm) OD MLPs were determined using the tangency approach, illustrated in Figure 2.43.

The crack driving force and ductile tearing resistance, both expressed in terms of the CTOD, δ, were plotted against the crack depth and crack growth, respectively. Only stable ductile crack growth was allowed (i.e. crack driving force below tangency point in Fig. 2.43(a)). The spooling-on and aligning stages of the reeling process were assessed separately. Tearing was limited to 0.5 mm for each tensile straining event, see Fig. 2.43(b). In addition, the minimum CRA ligament at the end of the reeling process was set to 1 mm. For regular CRA interface flaws (i.e. flaws with $2c \leq 30$ mm), the normalised maximum acceptable flaw height, a/t, was above 0.5 for all pipe sizes and increased with the pipe OD. No other fracture assessment procedure for interface flaws in MLP was found in the literature.

2.4 Fatigue of Subsea Pipelines

2.4.1 Fatigue Design Approaches

Fatigue design of subsea pipelines is generally undertaken following the S-N approach or the fracture mechanics-based fatigue crack growth (FCG) approach.

S-N Approach

This approach is often used when the size of pipeline flaws is not known, but the pipeline (including welds) is expected to be of a certain quality [7]. The design progresses in two stages. First, large scale fatigue tests are carried out to establish a reference S-N fatigue class curve. Several test pipes with girth welds are filled with a fluid (typically water), pressurised and

subjected to representative stress ranges until failure (loss of internal pressure) occurs. The test results in terms of stress range (S) versus the number of cycles to failure (N) are entered in a log-log plot. N is then reduced by a number of standard deviations (typically 2) and a design S-N curve is fitted to the data in the form

$$logN = loga - d\, s_{logN} - m\, log\Delta\sigma \tag{2.41}$$

where $\Delta\sigma$ is the stress range, N is the number of cycles to failure, $loga$ is the intercept of the mean S-N curve with the $logN$ axis, s_{logN} is the standard deviation of $logN$ and m is the inverse slope of the S-N curve.

Subsequently, the fatigue damage resulting from the project specific applied loads is determined using the Miner rule [7]

$$D_{fat} = SF\frac{n_i}{N_i} \leq 1 \tag{2.42}$$

Here, SF is a safety factor (e.g. SF = 10 for high safety class in DNVGL-ST-F101 [7]), n_i is the number of cycles corresponding to a given stress range and N_i is the number of cycles to failure at the same stress range.

Industry standards such as DNVGL-RP-C203 [129] and BS 7608 [130] provide a comprehensive set of reference S-N curves for standard subsea pipelines. Thus, only a limited number of project pipes (e.g. 6) need to be tested to deem that a certain fatigue class has been reached.

Mechanically lined pipeline girth welds include two more fatigue crack initiation sites than standard pipeline girth welds, indicated in Figure 2.44. Furthermore, the breach of the CRA barrier must be classified as failure, because exposure of the CS backing pipe to corrosive fluids would promote premature environmentally assisted fatigue. Consequently, the reference fatigue class curves in industry standards may not be suitable for mechanically lined pipelines.

Fatigue Crack Growth Approach

This fracture mechanics approach is used to determine the maximum acceptable flaw sizes. As for the S-N approach, the assessment is carried out in two stages. First, small scale tests are performed to establish a representative FCG rate curve, following BS ISO 12108 [131]. Most often, Compact Tension (CT) and Centre Crack Tension (CCT) specimens are used for thick (e.g. backing pipe of MLP) and thin (e.g. liner) structures, respectively. Several samples are subjected to cyclic loads while measuring the crack advance (e.g. by optical means). The effect of residual stresses, which were relaxed when the specimen was machined from a welded structure, or inexistent if the sample was extracted from a parent pipe, is accounted for by setting the ratio between minimum and maximum stress (stress ratio), $R > 0.5$. The test results in terms of the rate of crack growth per cycle, da/dN, versus the applied stress intensity range, ΔK, are presented in a log-log plot. The rate of crack growth, da/dN is increased by two standard deviations to derive a representative FCG rate curve in the form of the Paris law

$$\frac{da}{dN} = A\left(\Delta K\right)^m \tag{2.43}$$

Here, A and m are constants which depend on the material and environment (e.g. sea water). In the absence of project specific FCG curve, a BS7910 [102] curve may be used.

A fatigue crack growth assessment is then undertaken, where ΔK corresponding to each entry of a project specific stress range histogram is estimated using an appropriate SIF solution (e.g. the Raju and Newman solution in Eq. 2.27), and the individual crack growths associated to each ΔK are calculated separately and summed to determine the total crack growth.

Shorter life is usually predicted by FCG compared to the S-N approach, because the crack initiation time, which may represent a significant part of the total life, is not accounted for. Furthermore, the precision of the FCG prediction relies on the accuracy of the K solution and FCG rate curve. Suitability of the available K solutions and FCG curves for the assessment of flaws in MLP will be investigated in a subsequent chapter.

2.4.2 High Cycle Fatigue Performance of MLP

Tkaczyk *et al.* [128, 132] undertook resonance fatigue testing of 10.75" (273.1 mm) OD × 26.5 mm WT MLPs made of API 5L X65 backing pipe and nickel alloy 625 liner. The pipes were subjected to two bending cycles in one plane followed by two bending cycles in a perpendicular plane. This installation procedure, referred to as "perpendicular reeling", is representative of a scenario where a pipeline is first spooled onto a storage carousel, then trans-spooled from the carousel to the reel-lay vessel following delivery at the offshore field location and finally deployed subsea from the reel-lay vessel. Visual inspection carried out on completion of the bending trials confirmed no signs of damage to the liner. Subsequently, the test strings were fatigue tested at $R > 0$ until failure (loss of internal pressure) occurred or until the run-out condition (the DNVGL-RP-C203 class C target curve) was achieved. Fatigue cracks initiated from lack of fusion flaws, similar to that shown in Fig. 2.41, in three test pipes. The lack of fusion flaws were approximately 1 mm in height. The post-mortem examination of fracture faces suggested that the anti-corrosion barrier was not breached until after the crack had reached the carbon steel outer surface. The fourth failure initiated from a blemish at the pipe outer surface. Specimens tested at the lowest stress range reached the run-out condition without failure. Overall, the fatigue life was above the DNVGL-RP-C203 class D target curve.

Toguyeni and Banse [133] tested three API 5L X65 carbon steel pipes lined with alloy 625, to qualify MLPs reeled at elevated pressure for steel catenary riser (SCR) service. The MLPs had an outer diameter $D = 8.625$" (219.1 mm) and a total wall thickness $t = 21.3$ mm. The test strings were internally pressurised to 30 bar and subjected to bending to simulate pressurised reeling. Subsequently, the pipes were fatigue tested at $R > 0$ until the DNVGL-RP-C203 class F1 target curve was achieved. No failure (pressure loss) occurred in the test, and no through thickness cracks were found during subsequent post-mortem examination.

Since then, several MLPs have been fatigue tested successfully, see Togyeni *et al.* [134] and DNVGL [81], for example. However, it is yet to be demonstrated that a high fatigue performance can be achieved before the CRA barrier is breached and the CS backing pipe exposed to corrosive fluids.

2.4.3 Low Cycle Fatigue Performance of MLP

Tkaczyk *et al.* [82] performed large scale service testing of four reeled CladTek MLPs: (i) two 6.625" pipes with API 5L X65 backing pipe and alloy 904L liner and (ii) two 12.75" pipes with API 5L X65 backing pipe and alloy 625 liner. The CladTek rig in a four-point bending configuration, shown in Figure 2.45, was used. To reproduce the conditions that a pipeline experiences during lateral/upheaval buckling, each test pipe was first internally heated to 150°C. After reaching the test temperature, the internal pressure of 10 bar was applied and the pipe was bent until an axial compressive strain of 0.5% was reached at the pipe intrados. Then, the test pipe was unloaded to 0.3% compressive strain. Finally, the internal pressure was released and the pipe was returned to a straight configuration. This was repeated twenty times with the liner temperature maintained at 150°C. As the pipes were pressurised with air, it was safer to limit the test pressure to a conservative level of 10 bar, which is well below the design pressure of a typical flowline. At the end of the service test, the pipes were cooled down to ambient temperature, visually inspected and then sectioned for post-mortem examination. Only manufacturing imperfections (as per Fig. 1.9) up to 2 mm in height were found. This demonstrated that wrinkling initiation during operation is unlikely. However, since only 20 cycles were simulated, it is not certain that such imperfections would not compromise the liner integrity under a representative number of cycle, e.g. 300.

2.5 Other Service Considerations

DNVGL [81] recommends accounting for the liner when determining the burst capacity of an MLP

$$p_i - p_e \leq \frac{p_b}{\gamma_m \gamma_{SC}} \tag{2.44}$$

where γ_m, γ_{SC} and α_u are partial safety factors, p_i and p_e are the internal and external pressures, and p_b is the pressure containment resistance determined from

$$p_b = \frac{2\left(t_{bs}\sigma_{cb} + t_l\sigma_{lb}\right)}{D - t_{bs} - t_l}\frac{2}{\sqrt{3}} \tag{2.45}$$

Here, σ_{cb} and σ_{lb} are the characteristic yield strengths of the host pipe and liner, given by

$$\sigma_{cb} = \min \left[\left(\sigma_{y/bs}^{min} - \sigma_{y/bs}^{temp} \right) \alpha_u \ , \ \frac{\left(\sigma_{u/bs}^{min} - \sigma_{u/bs}^{temp} \right) \alpha_u}{1.15} \right] \tag{2.46}$$

$$\sigma_{lb} = \left[\sigma_{y/l}^{min} - \sigma_{y/l}^{temp} \right] \tag{2.47}$$

where, $\sigma_{u/bs}^{min}$ and $\sigma_{u/bs}^{temp}$ are the specified minimum ultimate tensile stress (SMTS) and the de-rated (reduced to account for the effect of temperature) nominal ultimate tensile strength (UTS) of the backing pipe, respectively, $\sigma_{y/bs}^{min}$ and $\sigma_{y/l}^{min}$ are the specified minimum yield stress (SMYS) of the backing pipe and liner, and $\sigma_{y/bs}^{temp}$ and $\sigma_{y/l}^{temp}$ are the respective temperature de-rated nominal yield strengths. The backing pipe and liner thicknesses in Eq. 2.45, t_{bs} and t_l, should be the minimum values.

In contrast, as no advantage can be taken of the liner with regards to other design considerations (e.g. collapse under external pressure), the standard DNVGL-ST-F101 [7] rules apply.

2.6 Summary of Literature Review

2.6.1 Manufacturing

The MLP manufacturing process requires a liner (manufactured to API 5LC [11], for example) and a backing pipe (manufactured to API 5L [1], for instance). First, the liner is inserted into the host pipe and expanded by applying internal pressure until it contacts the host pipe. Then, expansion of both pipes continues until a target expansion level is achieved. Once pressure is released, the liner and the host pipe spring back so that interference stress (mechanical bond) develops between the two pipes. Subsequently, the liner ends are cut back to leave a required length of unlined CS pipe and clad overlay welding is carried out to seal the liner ends. The level of residual contact interference stress in the as-manufactured pipe is function of a number of parameters, such as the manufacturing approach (ref. Section 1.2.2) and the relative tensile

strength of the liner and backing pipe. Following non-destructive examination, the MLP may be subjected to a thermal cycle during application of an insulation coating, which can significantly reduce the residual mechanical bond (ref. Section 2.2.1).

2.6.2 Installation

During reel-lay installation MLP is subjected to cyclic plastic bending under high radial contact loads. This is translated into a predominantly membrane and radial load on the pipe wall, which can trigger local buckling and fracture of welds. Industry standards provide robust design rules to prevent buckling of the standalone pipeline wall. In contrast, there is little guidance on the design of a pipe wall against confined buckling.

When an MLP is subjected to bending the confined liner ovalizes together with the backing pipe initially. Then, the liner starts separating uniformly from the backing pipe. This results in a partial or complete loss of the residual contact stress. At the onset of a first bifurcation point (see Fig. 2.13), the liner begins closing in on the backing pipe at discrete locations while separating further elsewhere. This results in the development of a periodic wavy pattern (see Fig. 2.14). When further bending is applied the imperfection height increases moderately (see Fig. 2.11). This is followed by a rapid increase of the liner lift-off from the host pipe, leading to the onset of a second bifurcation point (see Fig. 2.16), and subsequently buckling of the liner into a diamond mode shape (see Fig. 2.21). The latter typically occurs when the liner separation from the host pipe exceeds its thickness. The wrinkles at the pipe intrados can be nearly flattened when the pipe is reverse bent. However, wrinkling may initiate at the opposite clock position.

High mechanical bond can delay wrinkling initiation and reduce the height of liner lift-off. However, this residual grip stress is significantly reduced during coating application and plastic bending. The as-manufactured liner imperfections have a significant effect on the wrinkling process. The higher the initial imperfection height the lower the wrinkling strain. Internal pressure applied to the liner during numerical simulation of the manufacturing process can significantly reduce the initial imperfection heights. Although the actual liner imperfections

may differ significantly from idealised eigenmode type imperfections, their effect on the liner behaviour is qualitatively the same.

Increasing the liner thickness can help suppress wrinkling. However, an acceptance criterion for wrinkles needs to be proposed and validated. The onset of periodic bifurcation would be an overly conservative failure criterion for the liner, because the corresponding liner separation is very benign. The secondary bifurcation point could be considered as a wrinkling limit state, because it is associated with wrinkles that are large enough to be easily detected. Definition of a wrinkling criterion should be supplemented by a guidance on the numerical prediction of the liner lift-off and subsequent wrinkling during cyclic plastic bending.

Most flaws in pipeline welds are embedded. Unlike the former, surface breaking flaws may be easily repaired. Planar flaws such as lack of fusion flaws are normally assessed in an ECA. The acceptability of other types of flaws, such as volumetric flaws, is typically sanctioned by workmanship criteria provided in industry standards. An ECA normally includes an assessment, where fracture is deemed to have initiated if the crack driving force is greater than the material's toughness, or the applied load exceeds the bearing capacity of the cracked structure. The robustness of the ECA procedure relies on the accuracy of the assessment solutions.

In the context of reeling, the crack driving force is typically expressed in terms of: (i) the J-integral for the assessment of evenmatch (or overmatch) girth welds, or (ii) the CTOD for the assessment of undermatch girth welds and the interface between clad overlay welds and liner in MLP. Similarly, the fracture toughness is expressed in terms of: (i) a J-R curve derived from tests carried out using SENT specimens, for the assessment of evenmatch welds, or (ii) a CTOD-R curve established from tests performed using the same type of specimens, for the assessment of undermatch welds and the triple point interface in MLP. Welding residual stresses are typically assumed equal to the parent metal's yield strength (or the elastic strain corresponding to its yield stress), and allowed to relax as the plastic deformation increases.

A strain-based ECA scheme was proposed in the literature for the assessment of flaws at the interface between liner and overlay cladding in MLP (ref. Sec. 2.3.4). Accurate limit load solutions and crack driving force estimation schemes are also available for the assessment of planar

surface breaking flaws in evenmatch pipeline girth welds subjected to reeling (ref. Sec. 2.3.2). In contrast, the solutions available for the fracture assessment of embedded flaws are so conservative that they are not used for reeling currently. Instead, they are treated as surface breaking flaws (ref. Sec. 2.3.2). A new solution needs to be developed to enable a direct ECA of embedded flaws in evenmatch girth welds.

Cyclic plastic straining associated to reeling has a negligible effect on the fracture toughness of evenmatch girth welds. Consequently, an R-curve based on tests performed with as-received specimens is suitable for the assessment of the whole reeling process. However, this is yet to be demonstrated for undermatch welds (ref. Sec. 2.3.1). Finally, the range of application of analytical solutions for the assessment of surface flaws in undermatch welds is rather limited (ref. Sec. 2.3.3). This range needs to be expanded and then extended to embedded flaws.

2.6.3 Subsea Operation

Subsea pipelines are subjected to a variety of environmental and operational loads during service. Cyclic elastic bending from wave and/or current loads may trigger high cycle fatigue of welds, especially for risers. In contrast, high internal pressure in combination with high temperature may trigger global lateral or upheaval buckling of a flowline lying on a seabed. If not properly managed, in-service buckling may promote fracture of welds and/or low cycle fatigue of an imperfect liner.

Methodologies for the fracture assessment of welds during reeling can generally also be applied during operation. Fatigue design of subsea pipeline welds is normally performed following the fatigue crack growth approach or the S-N approach. In the former case the crack driving force is expressed in terms of the stress intensity factor range, and residual stresses are accounted for by using a representative fatigue crack growth rate curve, established from tests undertaken under a stress ratio above 0.5. In contrast, as industry standards provide several reference S-N curves for carbon steel pipelines, only a few project pipes need to undergo large scale testing to prove that a pipeline is fit for a given in-service fatigue loading.

It was shown experimentally that although MLPs include two additional fatigue crack initiation sites compared to carbon steel pipelines, a high fatigue class as per BS7608 [130] or DNVGL-RP-C203 [129] can still be achieved. However, no evidence has been provided that the CRA barrier remains integral until failure, indicated by the loss of internal pressure during testing. Furthermore, no stress intensity factor solution is available in the literature for fatigue crack growth assessment of triple point flaws in MLP, refer to Section 2.4.2.

Finally, scoring of the liner during insertion inside the backing pipe during manufacturing of MLP is inevitable. It was demonstrated experimentally that the risk of liner wrinkling or crack initiation from CRA nuggets up to 2 mm in height is negligible. However, since only 20 cycles were applied during testing, it remains uncertain whether such imperfections and/or reeling induced imperfections could compromise the liner integrity under a representative number of service cycle or not, refer to Section 2.4.3.

2.7 Figures

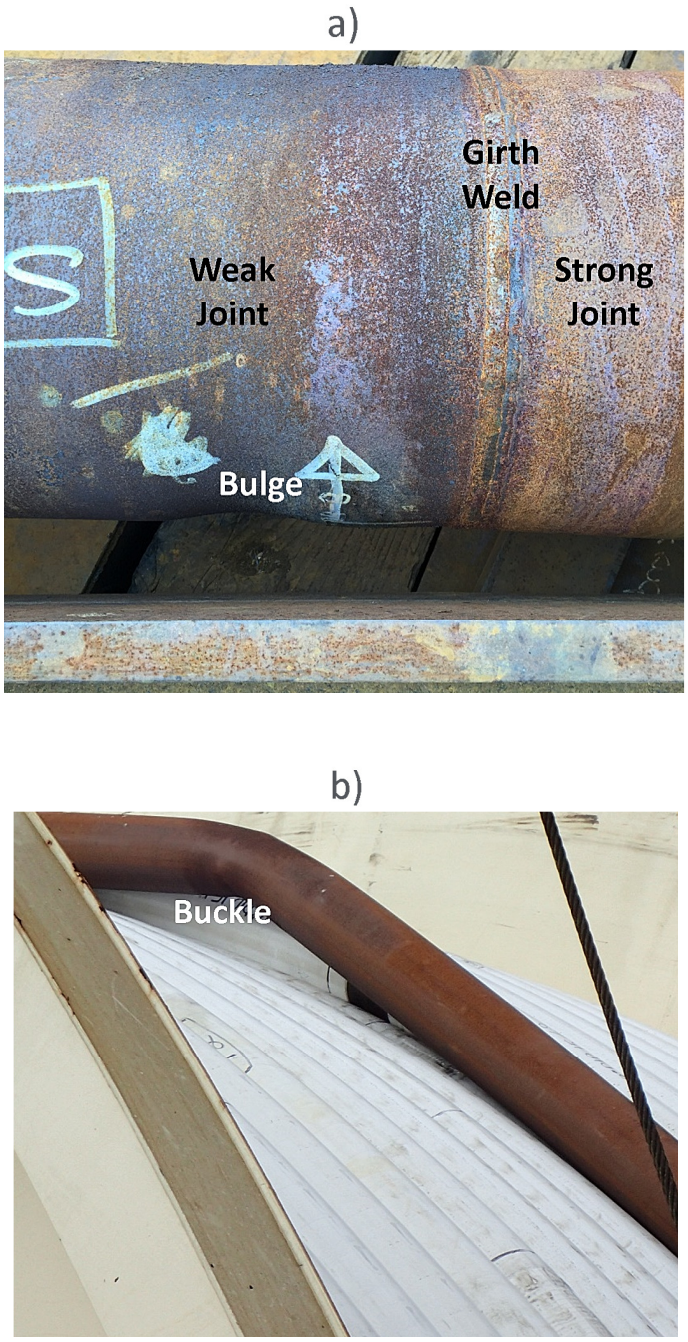


Figure 2.1: Effect of High Plastic Moment Mismatch during Reel-Lay Installation: (a) Bulging, (b) Buckling

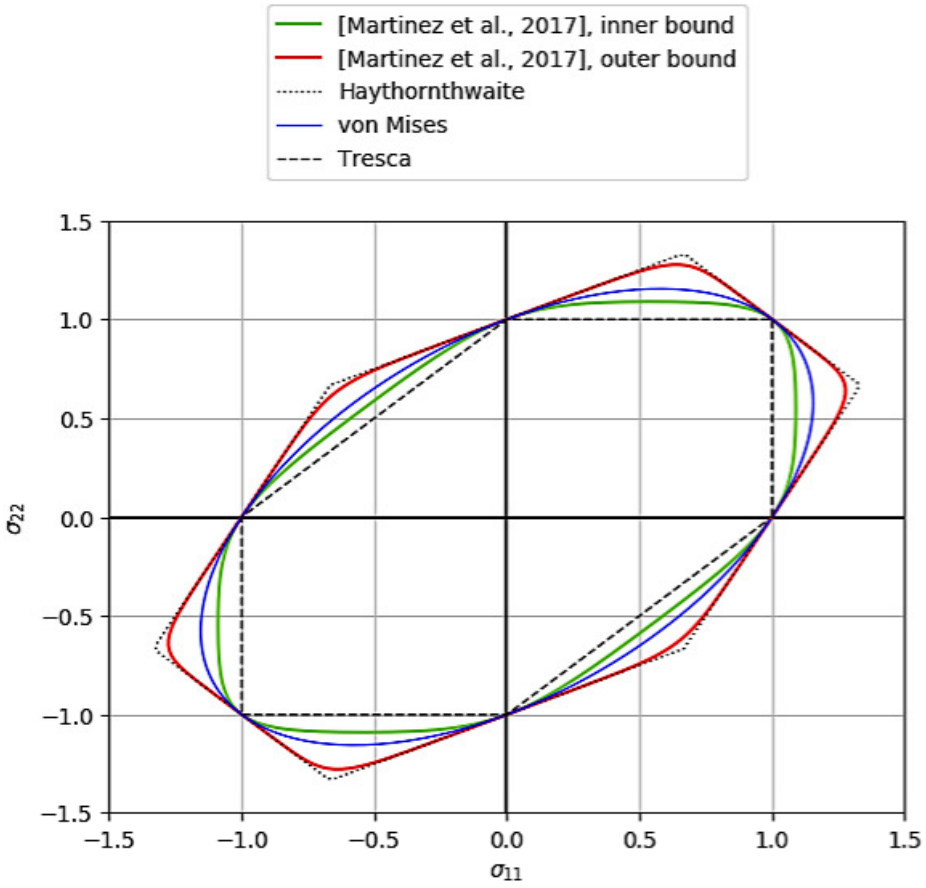


Figure 2.2: Mises, Tresca and Haythornthwaite Yield Surfaces (from Martinez *et al.* [46])

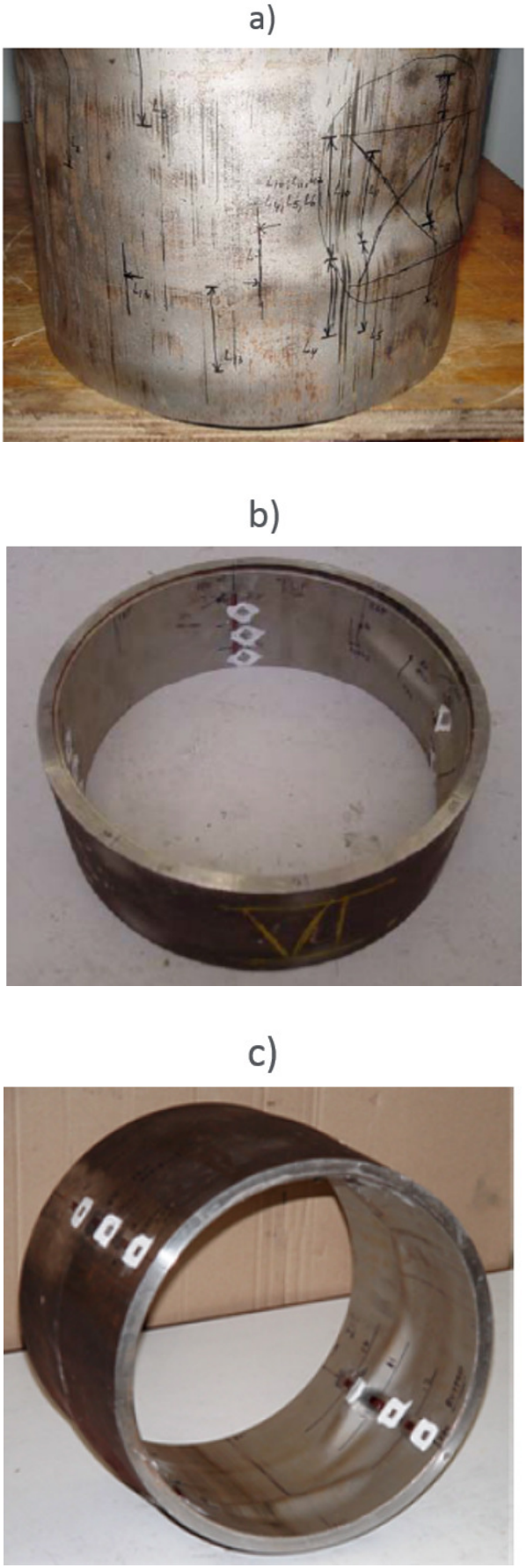


Figure 2.3: Wrinkling Modes under Axial Compression: (a) Standalone Liner, (b) Liner Inside Backing Pipe, (c) Mechanically Lined Pipe (from Focke *et al.* [54])

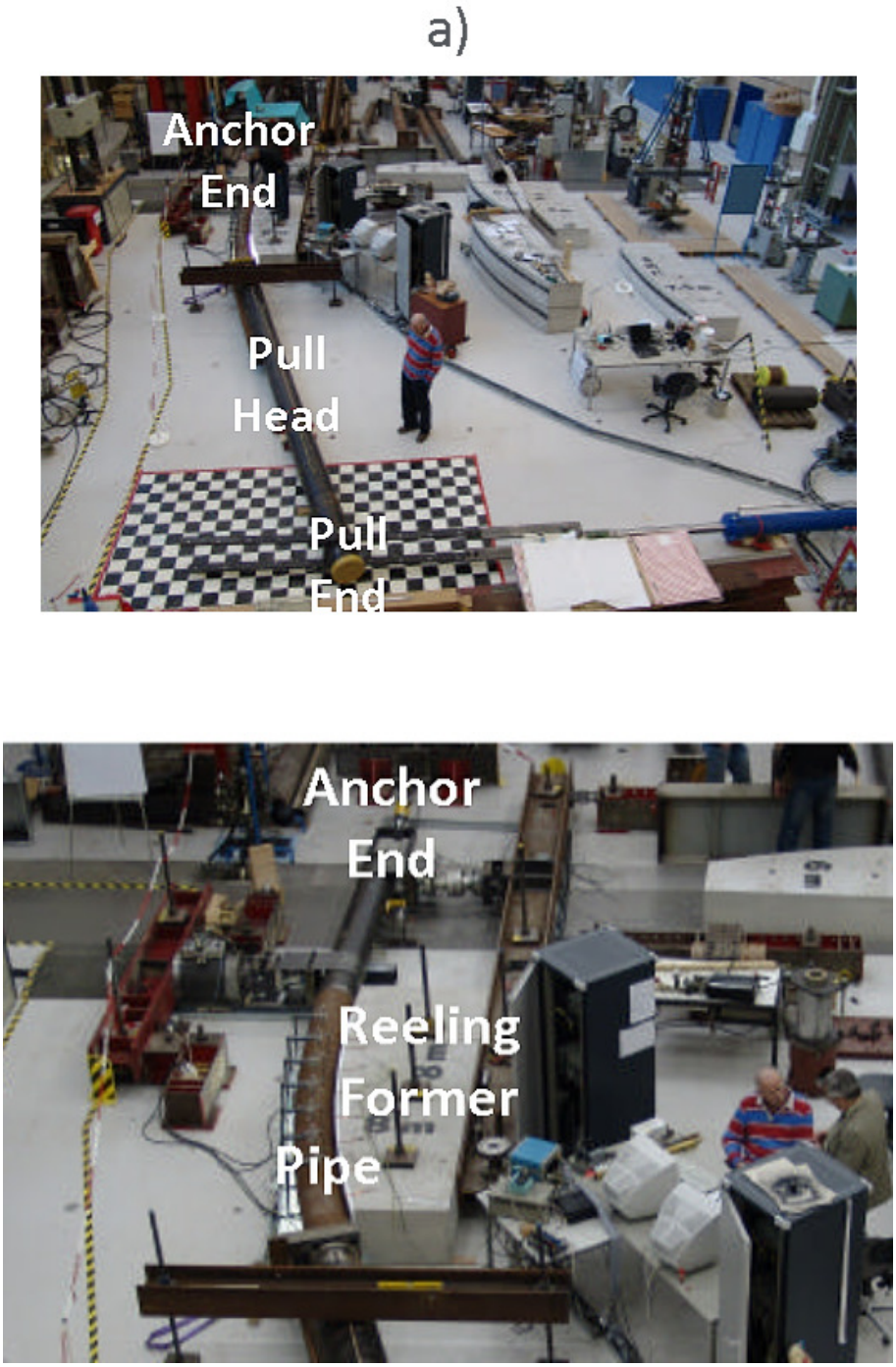


Figure 2.4: Large Scale Bending Rig: (a) Overview, (b) Zoom on Reeling Former (from Focke *et al.* [53])

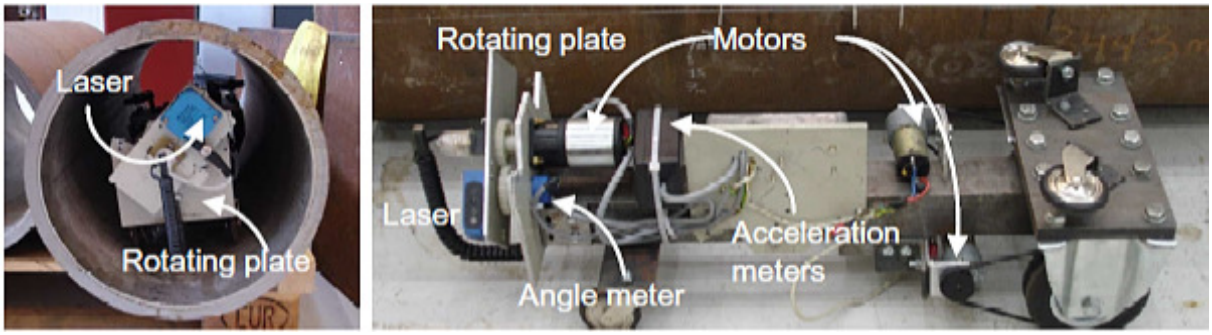


Figure 2.5: Laser Inspection Tool (from Focke *et al.* [63])

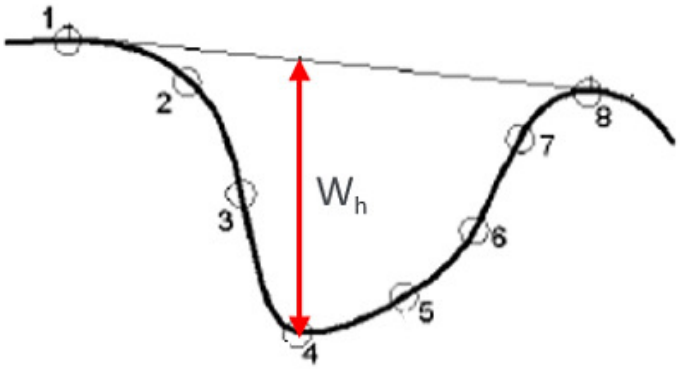


Figure 2.6: Definition of Liner Imperfection Height from Laser Measurements (from Focke [63])

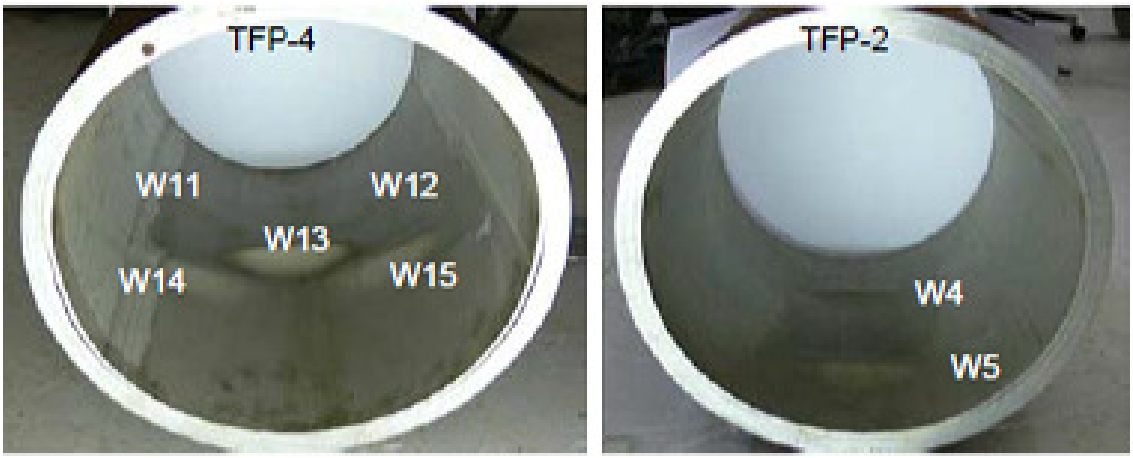


Figure 2.7: Liner Wrinkling during Bending of Tight Fit Pipe: (a) Low Grip, (b) High Grip (from Focke *et al.* [63])

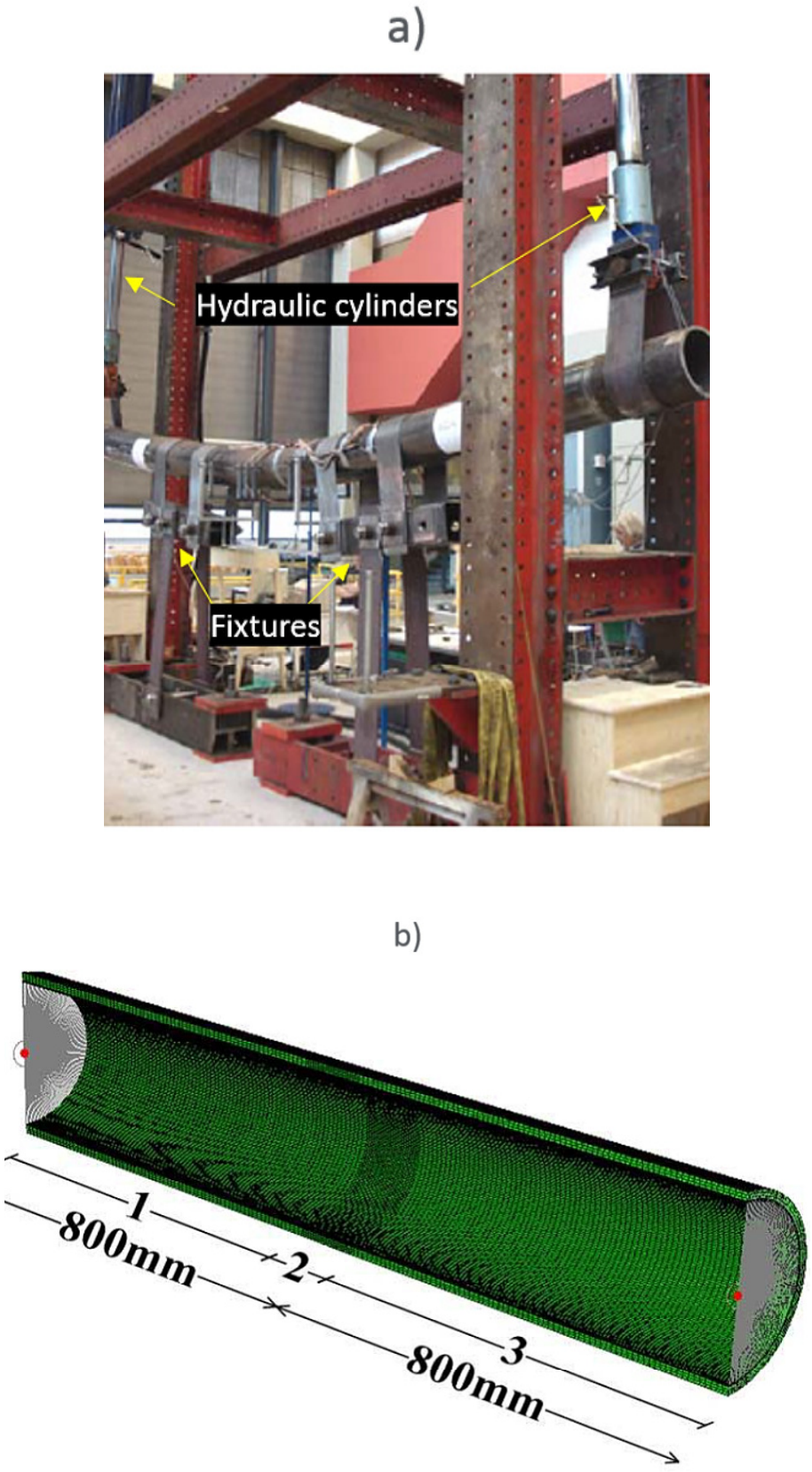


Figure 2.8: Four-Point Bending of Mechanically Lined Pipe: (a) Bending Rig, (b) FE Model (from Hilberink *et al.* [64, 66])

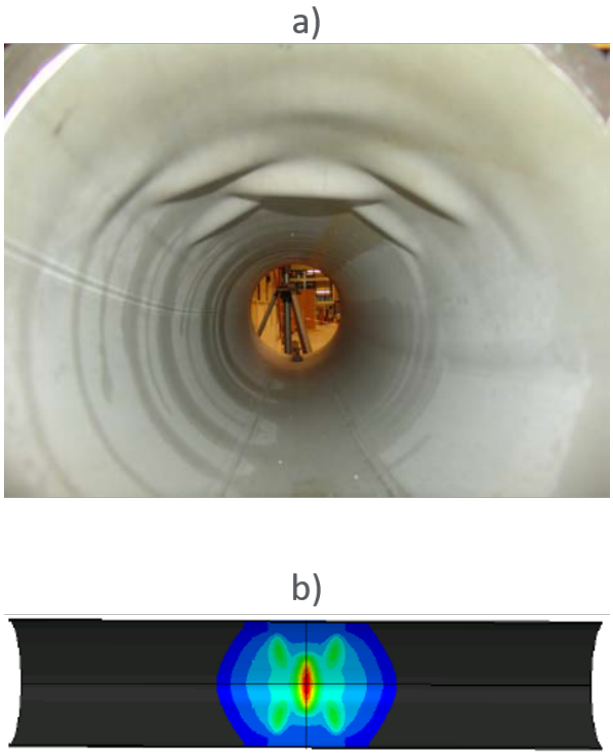


Figure 2.9: Liner Wrinkling during Four-Point Bending of Mechanically Lined Pipe: (a) Experimental Result, (b) Numerical Prediction (from Hilberink *et al.* [64])

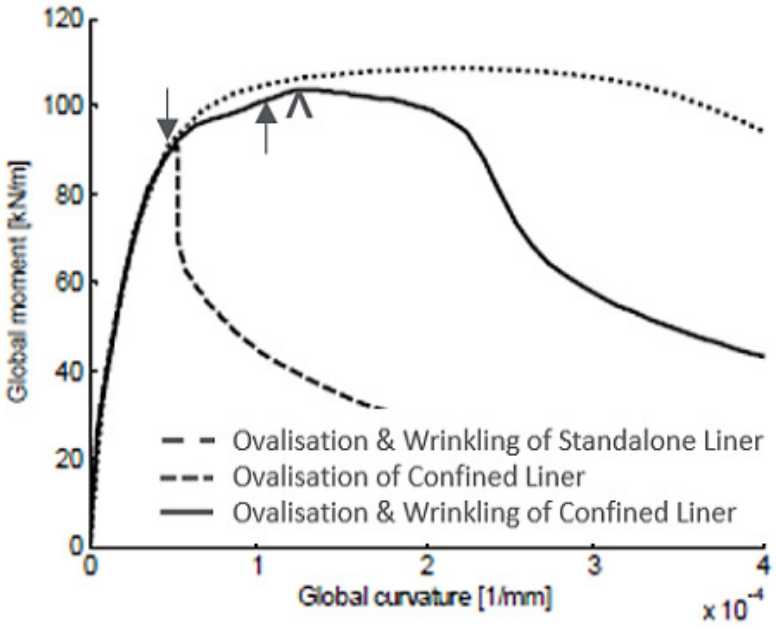


Figure 2.10: Numerical Prediction of Bending Moment-Curvature Diagram of Standalone and Confined Liner under Pure Bending (from Hilberink *et al.* [65])

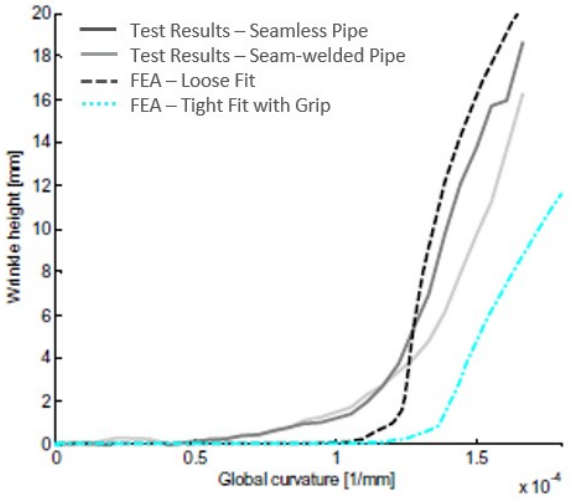


Figure 2.11: Liner Wrinkling during Pure Bending of MLP (from Hilberink *et al.* [66])

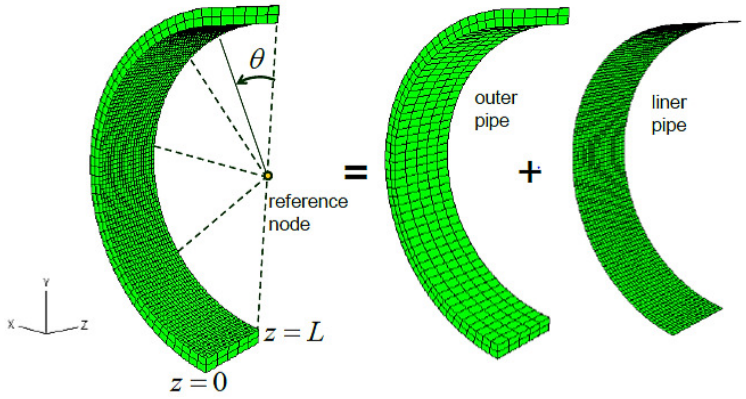


Figure 2.12: FEA Model for Simulation of Bending of MLP (from Vasilikis *et al.* [68])

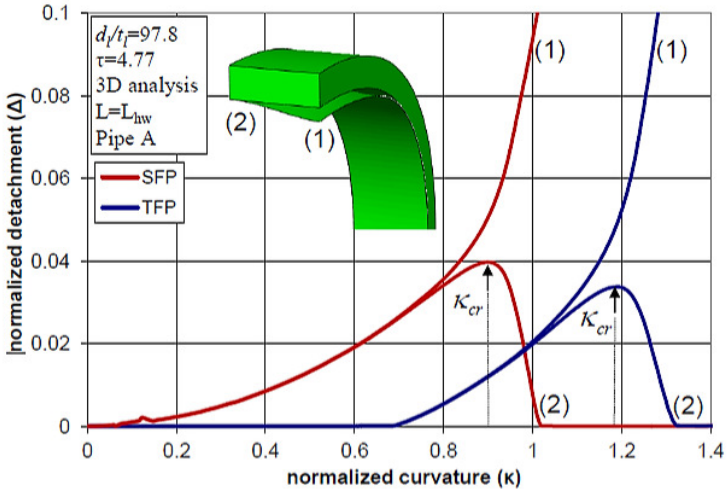


Figure 2.13: Numerical Prediction of Liner Separation during Bending of Loose Fit Pipe (SFP) and Tight Fit Pipe (TFP) – Identification of 1st Bifurcation Point (from Vasilikis *et al.* [68])

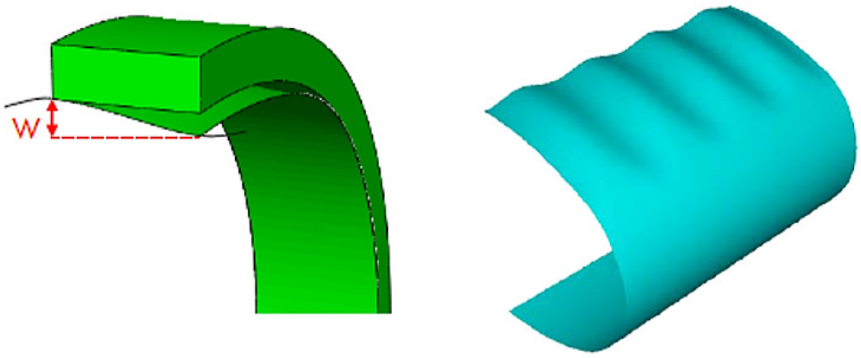


Figure 2.14: Numerical Prediction of Liner Wrinkling during Bending of MLP – Illustration of 1st Bifurcation Point: (Left) Half-Wavelength, (Right) Full Length Pipe (from Vasilikis *et al.* [68])

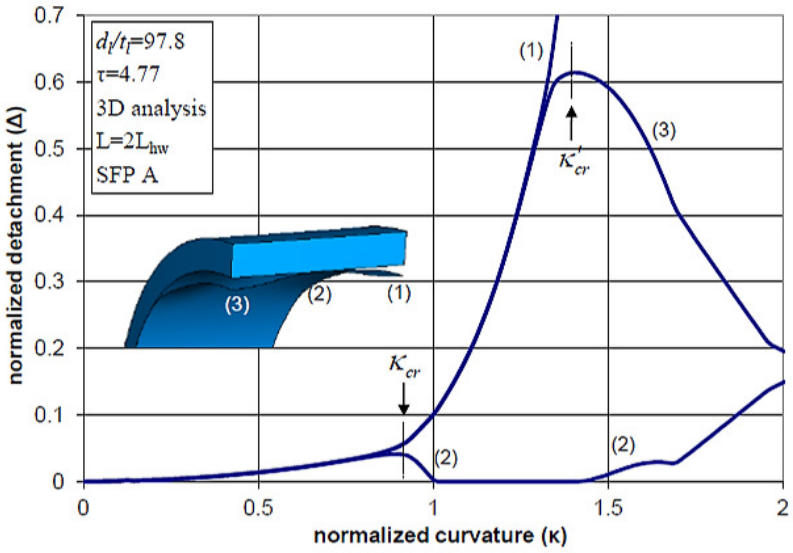


Figure 2.15: Numerical Prediction of Liner Separation during Bending of Loose Fit Pipe – Identification of 1st and 2nd Bifurcation Points (from Vasilikis *et al.* [68])

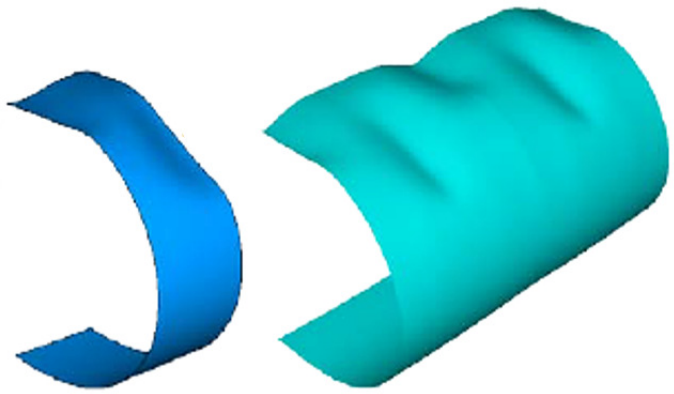


Figure 2.16: Numerical Prediction of Liner Wrinkling during Bending of MLP – Illustration of 2nd Bifurcation Point: (Left) Single Wavelength, (Right) Full Length Pipe (from Vasilikis *et al.* [68])

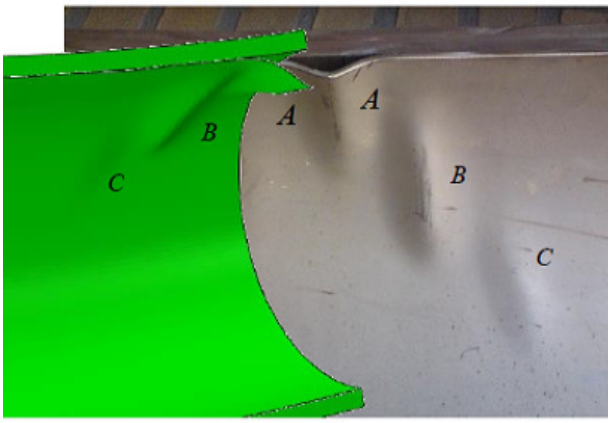


Figure 2.17: Liner Wrinkling during Bending of Lined Pipe – Illustration of 3rd Bifurcation Point: (Left) Numerical Prediction, (Right) Test Result (from Vasilikis *et al.* [71])

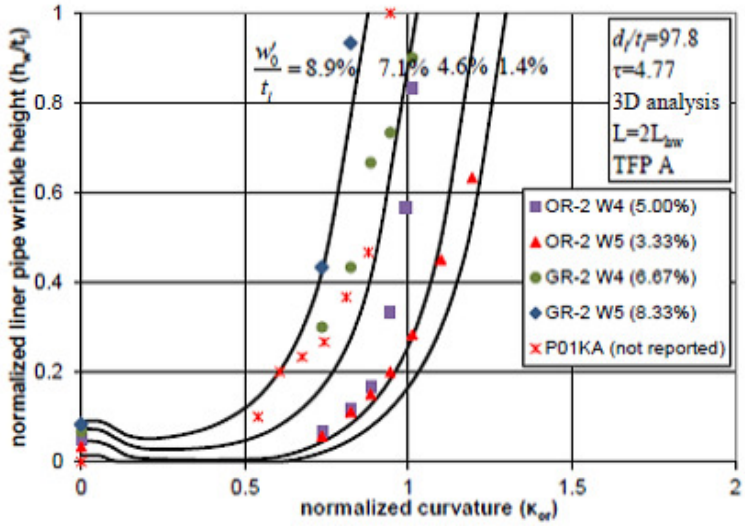


Figure 2.18: Liner Wrinkling during Bending of Lined Pipe – Comparison between Numerical Predictions and Test Results (from Vasilikis *et al.* [71])

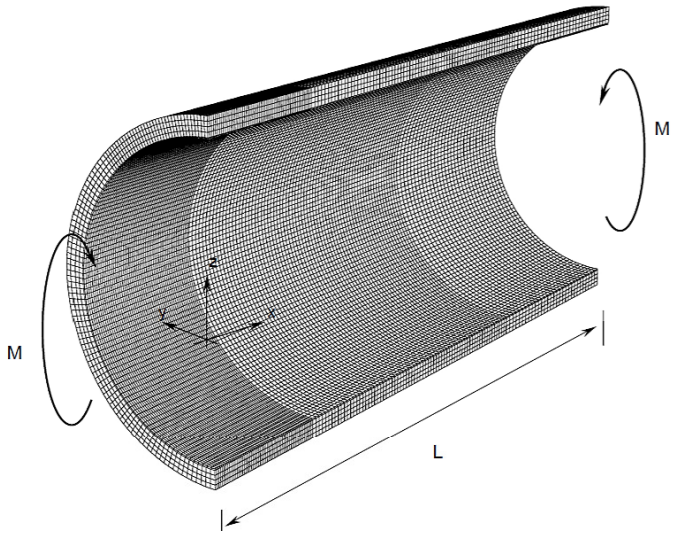


Figure 2.19: FEA Model for Simulation of Bending of Lined Pipe (from Yuan *et al.* [72])

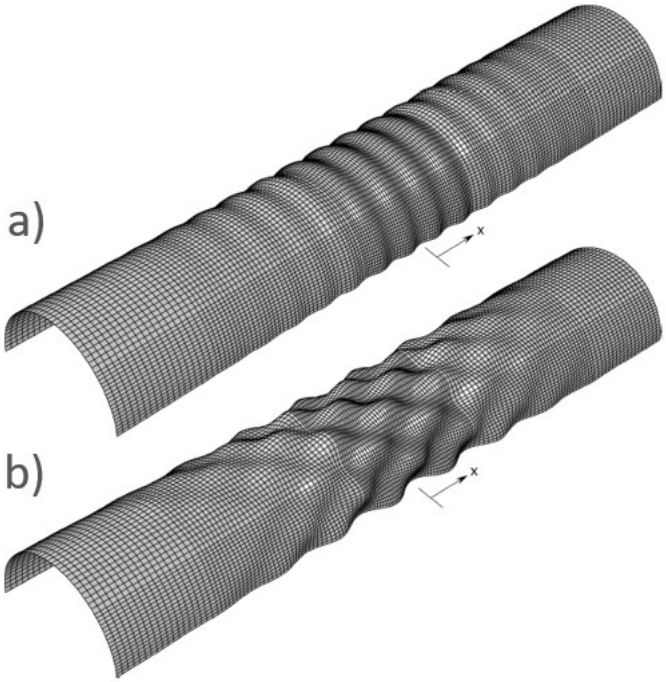


Figure 2.20: Liner Imperfection Modes: (a) Axisymmetrical, (b) Asymmetrical (from Yuan [72])

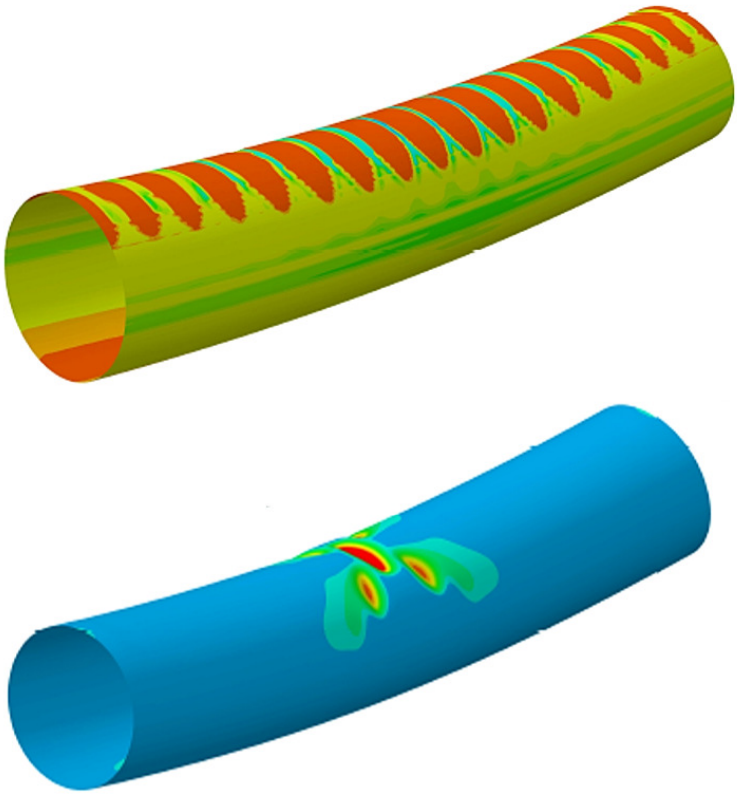


Figure 2.21: Numerical Prediction of Liner Wrinkling during Bending of Lined Pipe: (Top) Uniform Wrinkling, (Bottom) Diamond-Type Wrinkling (from Yuan *et al.* [72])

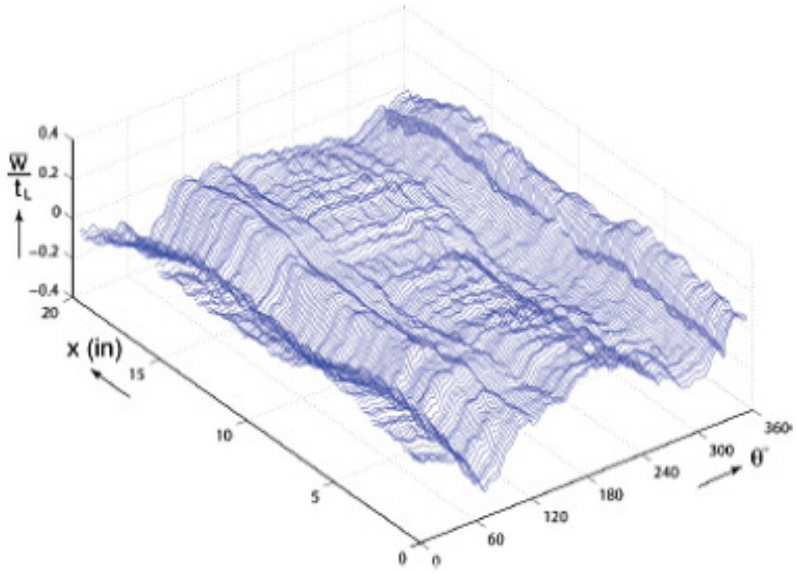


Figure 2.22: Topology of Inner Surface of Liner in As-Manufactured 12" Lined Pipe with Seamless Backing Pipe (from Harrison *et al.* [76])

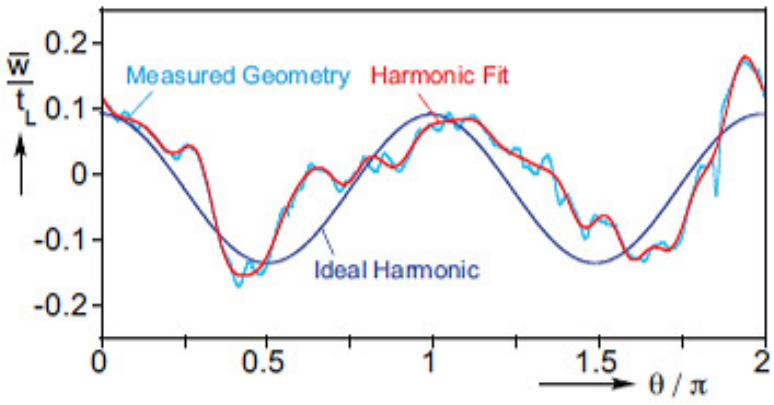


Figure 2.23: Comparison between Natural and Idealised Harmonic Circumferential Imperfections in Liner of As-Manufactured 12" MLP with Seamless Backing Pipe (from Harrison *et al.* [76])



Figure 2.24: Heriot Watt University Bending Rig (now transferred to the Pipeline Technology Centre (PTC))

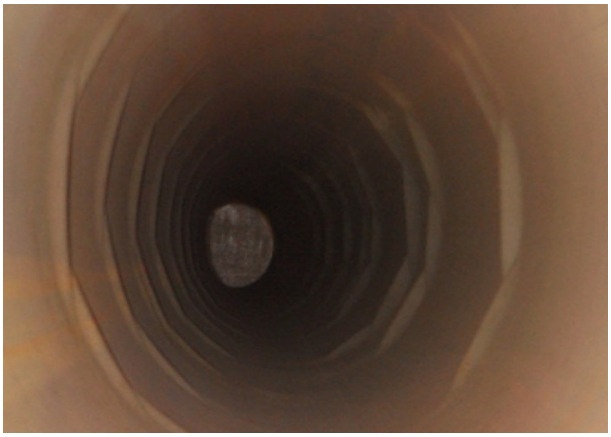


Figure 2.25: Liner Wrinkling during Cyclic Plastic Bending of 12.75" Lined Pipe at HWU

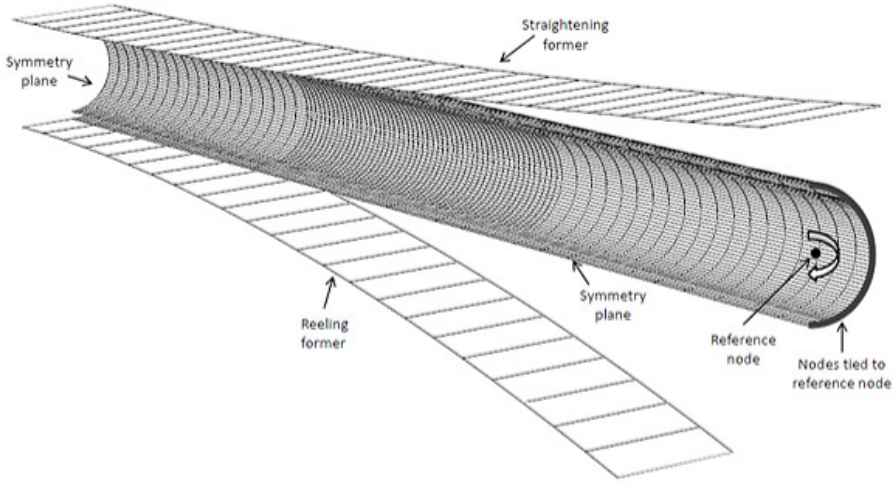


Figure 2.26: FEA Model for Simulation of Cyclic Plastic Bending of MLP at HWU (from Tkaczyk *et al.* [82])

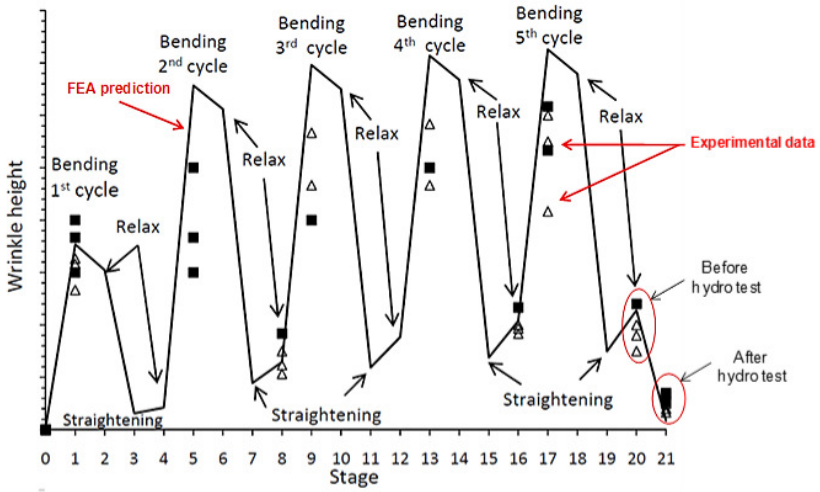


Figure 2.27: Liner Wrinkling during Cyclic Plastic Bending of 12.75" Lined Pipe: Comparison between Experimental and Numerical Results (from Tkaczyk *et al.* [82])



Figure 2.28: CladTek Bending Rig



Figure 2.29: Kuroki Bending Rig

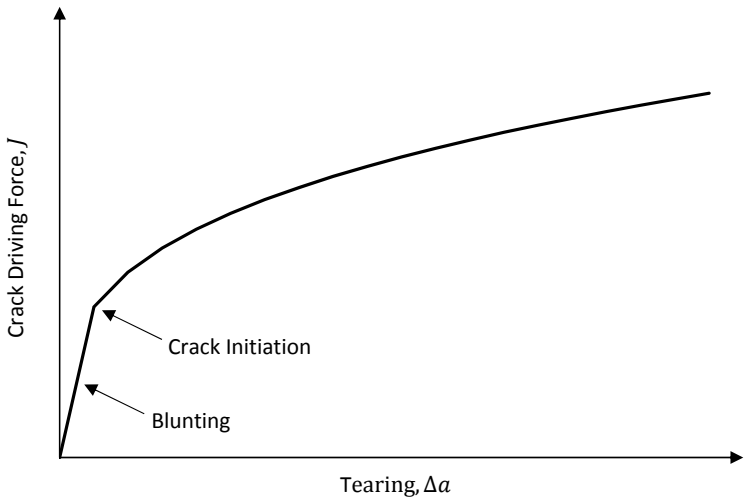


Figure 2.30: Fracture Toughness Resistance Curve

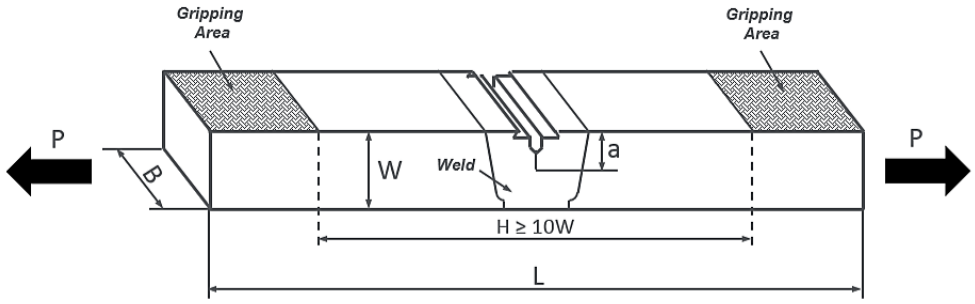


Figure 2.31: SENT Fracture Toughness Test Specimen

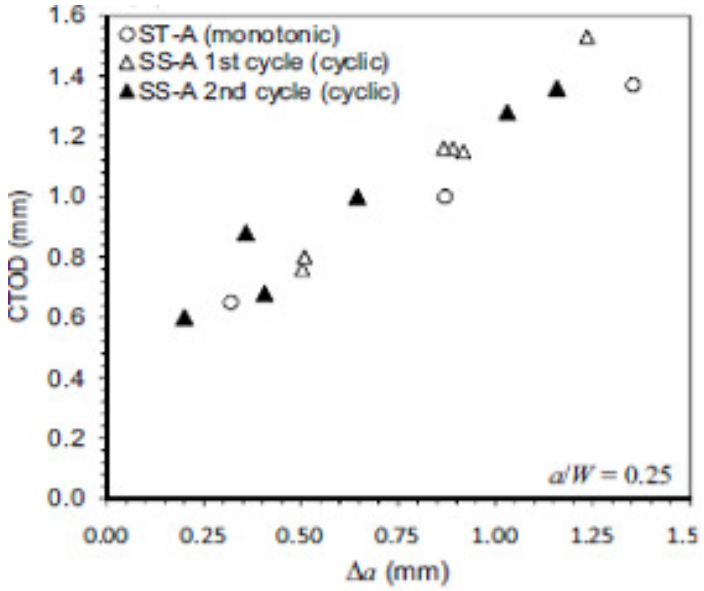


Figure 2.32: Effect of Pre-Strain on Fracture Toughness of Overmatch Weld (from Tkaczyk [96])

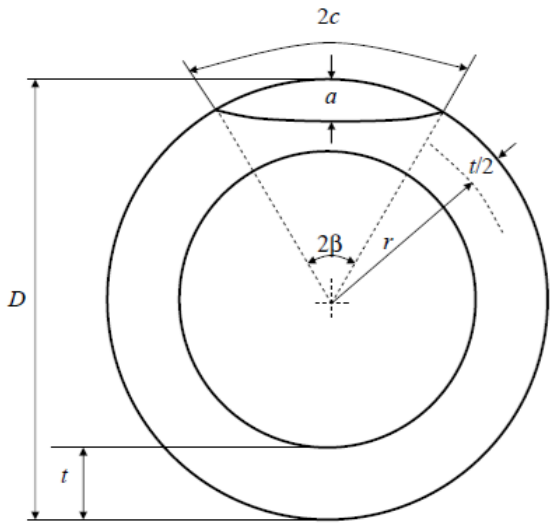


Figure 2.33: Pipe and Surface Flaw Geometry

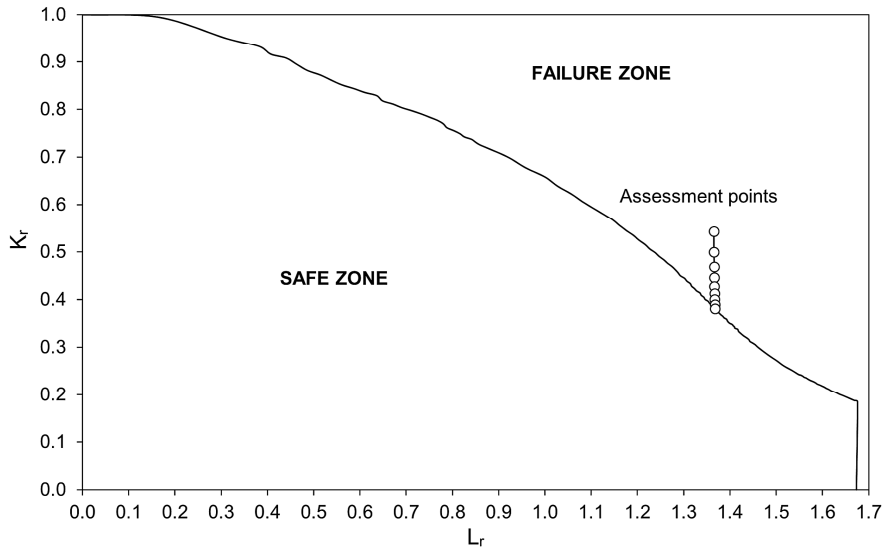


Figure 2.34: Failure Assessment Diagram

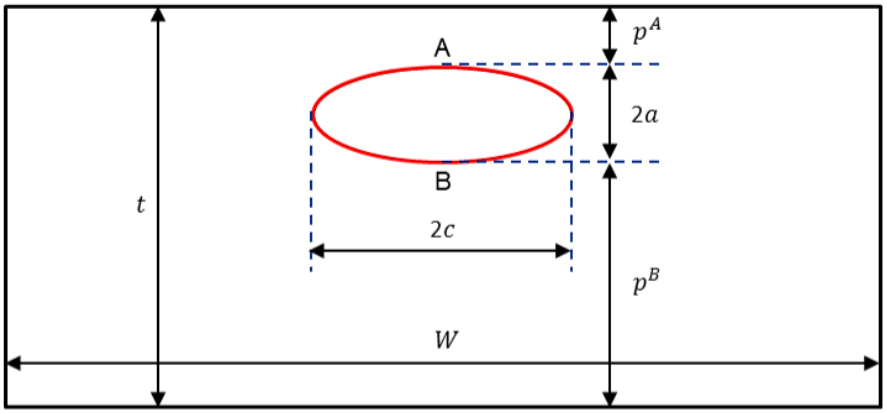


Figure 2.35: Embedded Flaw Geometry

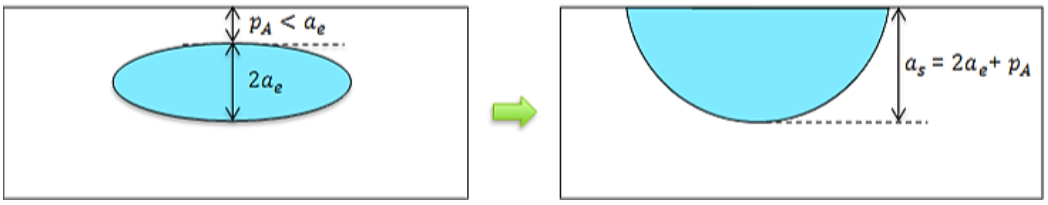


Figure 2.36: DNVGL Reclassification Criterion for Embedded Flaws

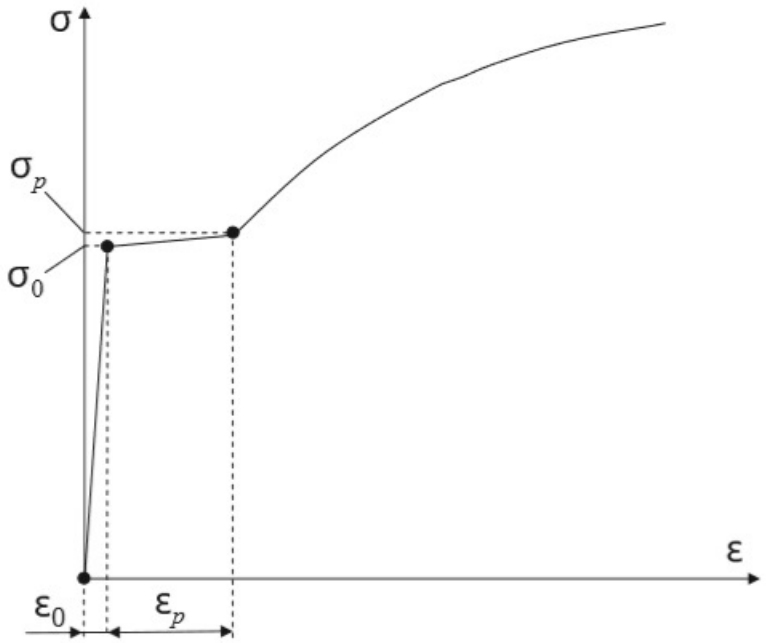


Figure 2.37: Typical Tensile Response for Material with Yield Plateau (from Tkaczyk *et al.* [121])

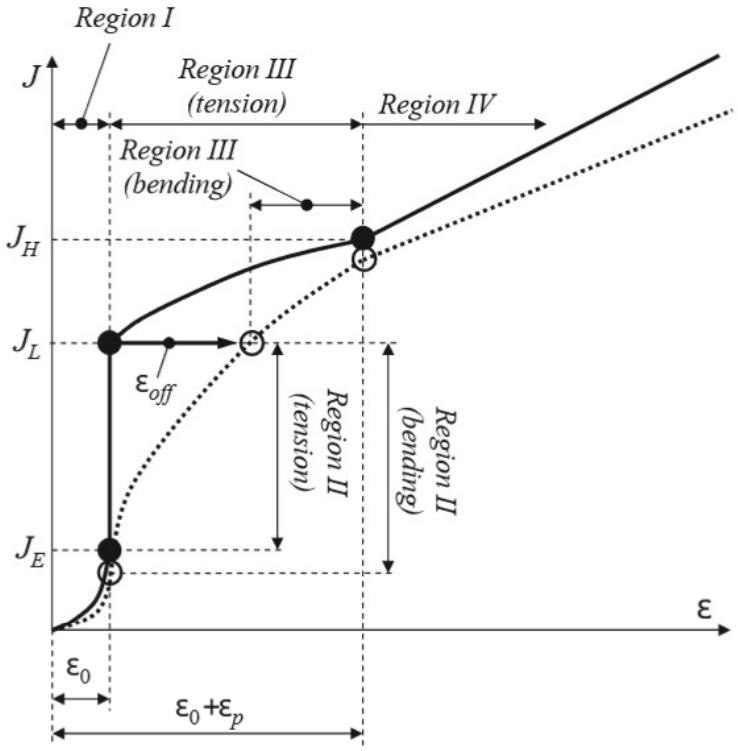


Figure 2.38: Evolution of J-integral vs. Applied Strain for Material with Yield Plateau (from Tkaczyk *et al.* [121])

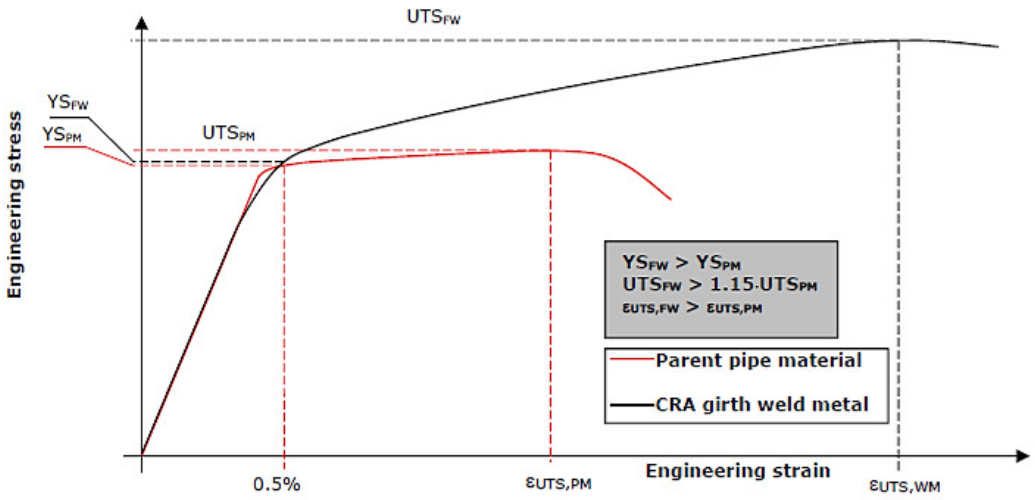


Figure 2.39: Definition of Girth Weld Overmatching Clad/Lined Parent Pipe (from DNVGL [81])

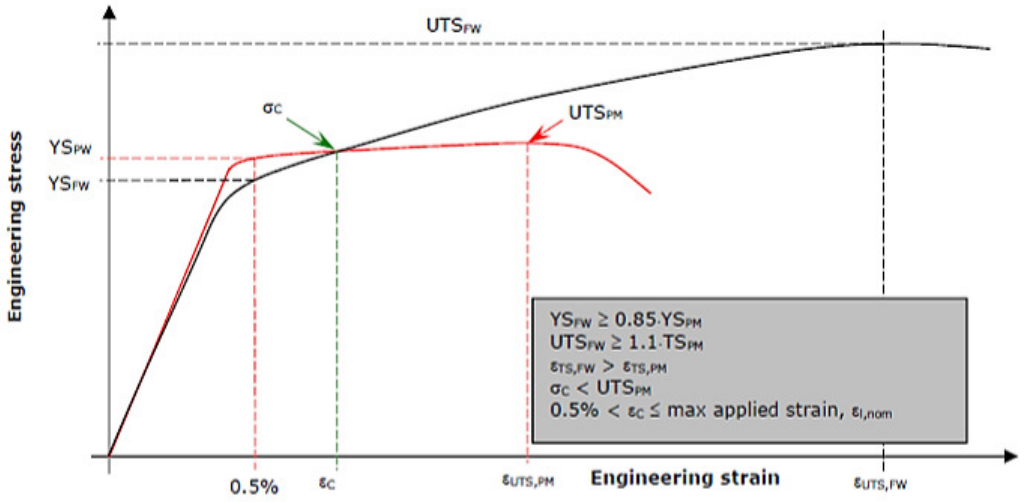


Figure 2.40: Definition of Girth Weld Partially Overmatching Clad/Lined Parent Pipe (from DNVGL [81])

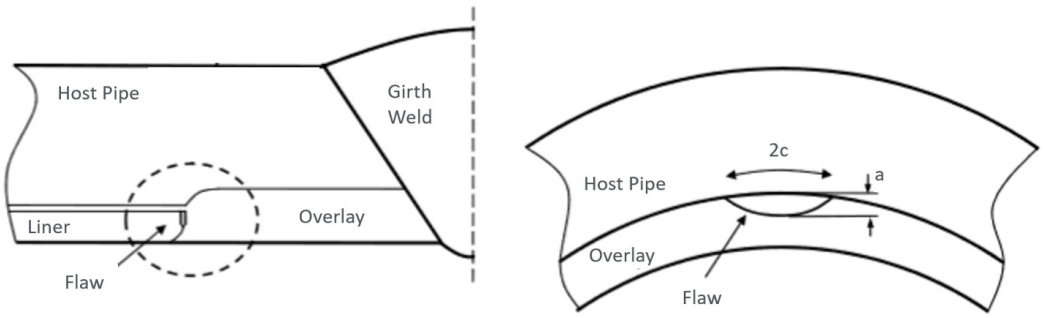


Figure 2.41: CRA Flaw at MLP Triple Point Interface (from Tkaczyk *et al.* [128])

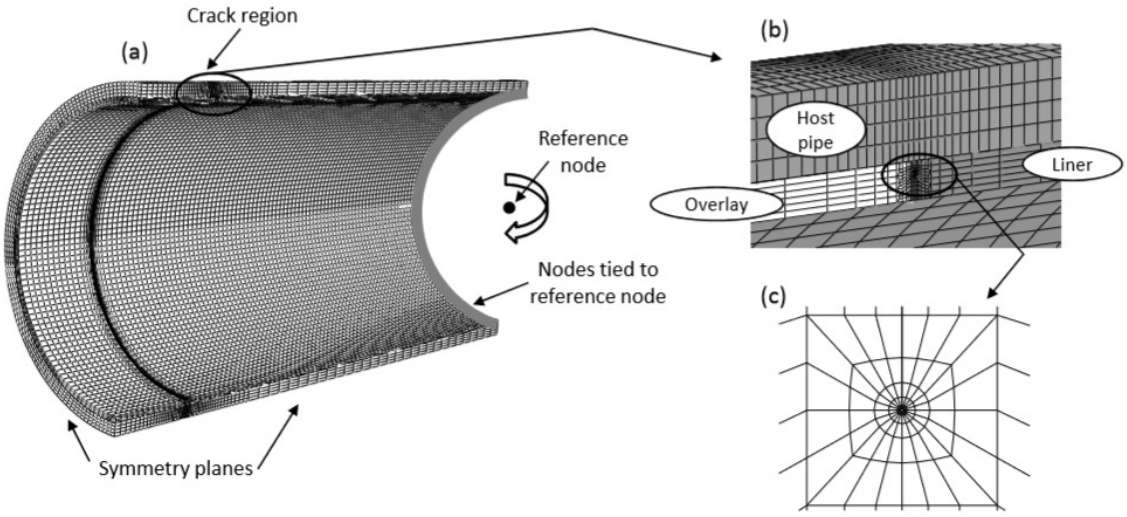


Figure 2.42: FE Model of MLP with CRA Flaw at Triple Point Interface (from Tkaczyk [128])

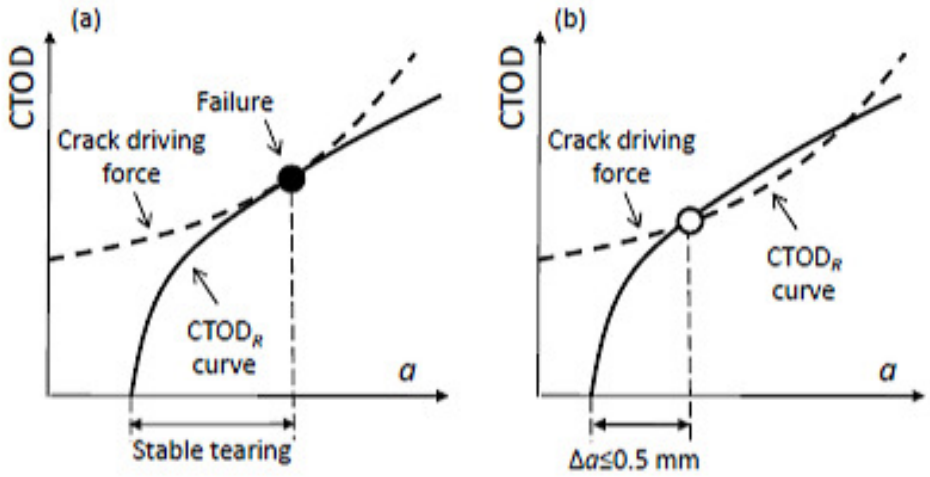


Figure 2.43: Illustration of Tangency Approach: (a) Ductile Tearing Instability, (b) Tearing Limited to 0.5 mm (from Tkaczyk *et al.* [128])

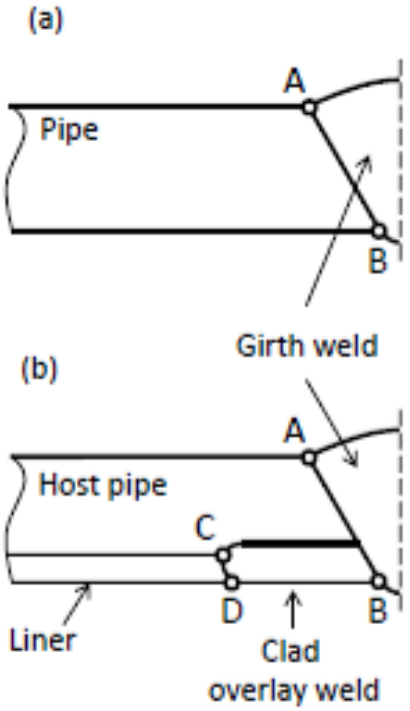


Figure 2.44: Fatigue Crack Initiation Sites: (a) Standard Pipeline, (b) Mechanically Lined Pipeline (from Tkaczyk *et al.* [128])



Figure 2.45: CladTek Rig in 4-Point Bending Configuration (from Tkaczyk *et al.* [82])

Chapter 3

Guideline for Design Against Liner Wrinkling

3.1 Introduction

This chapter aims at providing guidance for the design of mechanically lined pipe against liner wrinkling during reeling. The reel-lay installation strategy, where the mechanically lined pipeline is installed subsea under atmospheric pressure following the standard reeling procedure described in Sec. 1.1.3, is considered. The concept of increasing the liner thickness to suppress wrinkling during high strain bending is adopted. The residual contact interference stress introduced between the liner and backing pipe during manufacturing of MLP is neglected, because it is significantly reduced during coating application at high temperature, and completely removed during plastic deformation during reeling (ref. Sec. 2.6).

First, a quantitative definition of the onset of liner wrinkling during reeling is proposed in Section 3.2. Experiments are then undertaken, as detailed in Section 3.3. Mechanical tests are carried out to characterise the effect of hoop expansion (during MLP manufacturing) and axial cyclic plastic straining (during reeling) on the tensile behaviour of the liner, as no such data were found in the literature. This is followed by large scale cyclic bent tests, where the liner behaviour before and after the onset of wrinkling as defined in Section 3.2, is examined. Subsequently, a

numerical work is discussed in Section 3.4. Finite-element analyses are carried out to identity the parameters that govern liner wrinkling during bending. A numerical modelling technique is then proposed for the prediction of liner lift-off from the backing pipe and subsequent wrinkling during bending. Finally, following validation of the proposed numerical modelling technique against the large scale bend test results, recommendations for the design of mechanically lined pipelines against liner wrinkling are made in Section 3.5.

3.2 Liner Wrinkling Criteria

Liner wrinkling is deemed to have initiated when the local separation of the liner from the backing pipe, w_h, as defined in Fig. 2.6, exceeds any of the following values: (i) 100% of the liner thickness at any stage during reeling or cyclic bending, (ii) 50% of the liner thickness once all loads have been relaxed at the end of reeling or cyclic bending, or (iii) 50% of the liner thickness at any stage during monotonic bending.

The criteria in Table 3.1 imply that only a periodic bifurcation, as illustrated in Figs. 2.14 and 2.21, may be allowed. The maximum allowable liner lift-off of 50% liner WT at the end of reeling ensures that any residual liner imperfection is no larger than other common imperfections in subsea pipelines. For instance, the maximum allowable girth weld root penetration is typically 3 mm. Therefore, there is also no risk of excessive reduction of the pipeline's bore. Furthermore, there is no higher risk of erosion compared to that for a hot-roll bonded clad pipeline. It will be shown in Chapter 5 that as-laid liner imperfections of such sizes would not compromise the in-service integrity of the liner.

3.3 Experimental Work

3.3.1 Tensile Testing

Cyclic tensile tests were carried out at A2MI [135] in Fraisses, France, to establish the flow behaviour of alloys 316L and 625 in as-received (AR) and as-expanded (AE) condition. The

tests were run by Gilles Maîtres, following a procedure established by myself. The specification of the CRA liner pipes from which the test specimens were extracted is given in Table 3.2.

Tensile Test Procedure

Dumbbell tensile test specimens, see Figure 3.1, were extracted from each of the liner pipes in Table 3.2. Following instrumentation with an MTS 632-13C-20 type extensometer, shown in Figure 3.2(a), the specimens were mounted on a SCHENCK RMC100 machine, shown in Fig. 3.2(c), and tested at room temperature following BS EN ISO 6892-1 [136].

Two loading scenarios were considered: (i) Cyclic compression and (ii) Cyclic tension. The former consisted of subjecting a specimen to 3% strain in compression and then 3% strain in tension (i.e. one cycle), whereas the latter involved applying 3% strain in tension and then 3% strain in compression, three times. To prevent buckling of the sample under compression, a four-sided anti-buckling system, shown in Fig. 3.2(b) was used.

For each liner pipe in Table 3.2, three specimens were tested in cyclic tension while the remaining two specimens were tested in cyclic compression. In total, twenty (20) specimens were tested, as detailed in Table 3.3.

Tensile Test Results

As-Received Material The results in Figure 3.3(a) show that in the as-received condition the alloy 316L liner has very similar yield strength in tension (indicated by the dashed lines in Fig. 3.3(a)) and compression (indicated by the solid lines in Fig. 3.3(a)). The average YS is 340 MPa and 350 MPa in tension and compression, respectively. In addition, the test data are very consistent. The main difference in the tensile behaviour is the strain hardening, which is higher in compression than in tension.

As for the 316L material, the yield surface of the alloy 625 liner is nearly isotropic in the as-received condition. The average YS is 440 MPa and 460 MPa in tension and compression (indicated by the dashed and solid lines in Fig. 3.3(b)), respectively.

As-Expanded Material The results in Figure 3.4(a) show that as for the as-received material, the as-expanded 316L liner has very similar yield strength in tension and compression (indicated by the dashed and solid lines in Fig. 3.4(a), respectively). The average YS is 460 MPa and 475 MPa in tension and compression, respectively.

In contrast to the 316L material, the as-expanded alloy 625 liner shows a small amount of yield anisotropy (ca. 8%). The average YS is 505 MPa and 545 MPa in tension and compression (indicated by the dashed and solid lines in Fig. 3.4(b)), respectively.

Effect of Liner Expansion It can be seen in Figure 3.5(a) that liner expansion during manufacturing of MLP induces significant isotropic hardening. On average, the yield strength of the alloy 316L material increases by 120 MPa and 125 MPa in tension (indicated in Fig. 3.5(a) by the thin dashed line and thin solid line for the as-received and as-expanded material, respectively) and compression (indicated in Fig. 3.5(a) by the thick dashed line and thick solid line for the as-received and as-expanded material, respectively).

Likewise, significant isotropic hardening is evidenced for the alloy 625 material in Figure 3.5(b). However, the magnitude is nearly half of that for the alloy 316L material. In addition, the yield strength increases more in compression (85 MPa; indicated in Fig. 3.5(b) by the thick dashed line and thick solid line for the as-received and as-expanded material, respectively) than in tension (65 MPa; indicated in Fig. 3.5(b) by the thin dashed line and thin solid line for the as-received and as-expanded material, respectively).

Effect of Cyclic Plastic Straining The test results in Figure 3.6(a) show that the liner hardens predominantly kinematically when subjected to cyclic plastic straining. The yield strength reduces when the loading direction is reversed (this is known as the Bauschinger effect). In addition, some amount of isotropic hardening is evidenced, as the stresses in the fully plastic regime (e.g. stress at 2% total strain) increase with the number of cycles. This effect is more pronounced for the as-received material (indicated by the dashed line in Fig. 3.6(a)) than for the as-expanded material (indicated by the solid line in Fig. 3.6(a)), as expected.

Similar trends are observed for the alloy 625 liner in Fig. 3.6(b). Finally, the cyclic behaviour is qualitatively the same whether the liner be loaded in tension or compression first. This is shown in Fig. 3.6(c), where the results for alloy 316L are indicated by the thin and thick solid lines for the tension and compression load modes, respectively, while those for alloy 625 are indicated by the thin and thick dashed lines for the tension and compression load modes, respectively.

Summary of Tensile Test Results The yield behaviour of the alloy 316L and 625 liner pipes in tension and compression is similar. Liner hoop expansion during manufacturing of MLP induces significant isotropic hardening. The yield strength of the 316L and 625 alloy increases by ca. 120 MPa and 75 MPa, respectively, when the liner is subjected to 5% hoop expansion. A small amount of yield surface anisotropy (less than 10%) is also introduced for the case of alloy 625. The liner tensile behaviour during subsequent cyclic plastic straining, representative of conditions experienced by the pipe during reeling, is predominantly kinematic.

No tensile tests were carried out for the carbon steel backing pipe because its behaviour is well established. The tensile behaviour of the former does not significantly change during MLP manufacturing because it is subjected to no or little plastic straining. The behaviour of the carbon steel pipe during subsequent cyclic plastic straining is similar to that of the liner, i.e. predominantly kinematic. The CRA tensile test results are summarised in Table 3.4.

3.3.2 Large Scale Bend Tests

Bending trials were carried out at Heriot Watt University in Edinburgh, UK, to determine the strain at the onset of liner wrinkling for 10” and 12” mechanically lined pipes. The tests were managed by David Haldane and Katerina Stoyanova, following a procedure established by myself.

Pipe Sizes and Material Grades

The 10” and 12” carbon steel pipes, with the nominal dimensions in Table 3.5, were procured from stockists. A liner radial insertion gap of 3.0 mm and 3.3 mm for the 10” and 12” pipes,

respectively, was determined using a TechnipFMC in-house formula. The minimum liner thickness after expansion, t_{Lmin}, required to prevent wrinkling during reeling on TechnipFMC's Deep Blue vessel, which has a minimum reel hub radius, $R = 9.75$ m, was estimated to be 4.7 mm and 6.8 mm, respectively, using Eq. 2.11. Alloy 625 and 316L liners, with the selected minimum wall thickness after expansion, t_L in Table 3.5, were procured for the 10" and 12" pipes, respectively. The corresponding minimum liner thickness before expansion, t_l, was somewhat higher (typically 0.1/0.2 mm depending on the level of hoop expansion), and so was the average thickness before expansion, t_{lmean}, which is typically 5% higher than t_l. MLPs were then manufactured following the procedures described in Sec. 1.2.2.

Bend Testing of 10" Pipes

Test Strings Three 10" MLP test pipes with 5.1 mm thick (before expansion) alloy 625 liner, listed in Table 3.6, were subjected to bending strain capacity testing: one non-welded pipe (labelled "10-1") and two welded pipes (labelled "10-2.GW" and "10-3.GW"). The length of these pipes was 11.7 m and 11.0 m, respectively. The former had a 5.7 m long lined section whereas the latter included two lined sections, each 2.5 m long. Both ends of each lined section were terminated with a 50 mm long clad overlay weld. The girth-welded test pipes had a CRA weld between the lined sections. Carbon steel extension pieces were welded to either side of the lined sections to achieve the required length of a test string. The test pipe ends were marked "End A" and "End B". The 3, 6, 9 and 12 o'clock positions were marked when looking from "End A" towards "End B". The liner seam weld was located at the 6 o'clock position. The pipe dimensions in Table 3.6 correspond to average values measured prior to liner expansion.

Bending Trials Each test pipe was mounted in the Heriot Watt University bending rig, shown in Fig. 2.24. "End A" was located at the pull end (to the left in Fig. 2.24) while "End B" was located at the anchor end (to the right in Fig. 2.24). The 3 o'clock position marked on the pipe faced the straightening former while the 9 o'clock position faced the reeling former. The rig was equipped with a 9.75 m radius (reel hub radius of TechnipFMC's Deep Blue vessel) reeling former for the case of Test Pipe "10-1" and an 8.23 m radius (reel hub radius of the

TechnipFMC's Apache II vessel, which is the smallest for the TechnipFMC fleet) reeling former for the case of Test Pipes "10-2.GW" and "10-3.GW". A 40.2 m radius straightening former was used for all test pipes. Prior to strain capacity testing, a video inspection was carried out to examine the surface condition of the liner. A laser inspection was then undertaken to measure the initial imperfections in the test pipes. The laser tool was inserted from the anchor end and the middle section of the pipe was scanned at 10 mm interval. For each scan, the zero of the tool was at the bottom of the pipe (6 o'clock), where the liner seam weld was located. Scanning progressed clockwise, so that the 9 o'clock position (straightener side) was at 90° while the 3 o'clock position (reel side) was at 270°. The cross-sectional measurements were used to create longitudinal 2D profiles of the inside of the liner, from which imperfections were measured. All imperfections found were less than 0.4 mm in height, except CRA girth weld root in welded test pipes, which were typically 2.5 mm in height.

Subsequently, the pipes were subjected to a test regime detailed in Table 3.7. During strain capacity testing, the 9 o'clock position was under compression when a test pipe was on the reeling former. Test Pipe "10-1" was monotonically bent on the 7.84 m, 7.00 m and 6.40 m reeling formers without being straightened. Subsequent visual inspection revealed several small bending-induced imperfections which were sized with a laser tool. The largest imperfection of 1.4 mm in height was produced at the 9 o'clock position, see Figure 3.7. Bending of the test pipe onto a 5.5 m reeling former, as per Figure 3.8, resulted in the increase of the imperfection height at the 9 o'clock position to 2.0 mm, and the onset of a periodic mode shape, shown in Figure 3.9. Finally, the liner wrinkled (i.e. the imperfection height measured on the reeling former was larger than the liner WT, refer to wrinkling criteria in Table 3.1) at several locations at this clock position when the pipe was subjected to three reverse bending cycles on a 4.45 m former (during reverse bending, a pipe is straightened after each bending event; three reverse bending cycles simulate a contingency retraction operation where a pipe section that has already undergone a full reeling operation is returned to the aligner before being deployed again). The largest bending-induced imperfection, observed in test pipe "10-1" during the entire strain capacity trial, was reduced from 12.2 mm on the reeling former to 3.7 mm after straightening, see Figure 3.10. The symbols "B3" and "RS3" in Fig. 3.10 denote "3^{rd}

bending" and "relaxation after 3^{rd} straightening" event, respectively. The heights of largest imperfections found during laser inspection are summarised in Tables 3.8 and 3.9. The 9 and 3 o'clock position in Tables 3.8 and 3.9 is at the pipe intrados when the pipe is on the reeling and straightening former, respectively. Imperfections larger than 50% and 100% of the liner WT are boldened and underlined, respectively. An empty cell indicates that only visual inspection was carried out.

Test Pipes "10-2.GW" and "10-3.GW" were subjected to four reverse bending cycles on a 6.1 m radius former (this simulates a contingency retraction operation where a pipe section that has already undergone a full reeling operation is returned into the span between the reel and aligner before being deployed again). Although the local separation of the liner from the host pipe grew during bending, it remained below half of the liner thickness (refer to wrinkling criteria in Table 3.1). As with test pipe "10-1", the largest imperfections were always found at the 9 o'clock position which faced the reeling former. The largest imperfection in "10-2.GW" grew from 0.9 mm during the first bending event to 2 mm during the fourth (last) bending event, and finally reduced to 0.8 mm when the pipe was relaxed after straightening, see Figure 3.11. The largest imperfection in test pipe "10-3.GW" grew from 1 mm after the first bending event to 1.2 mm when the pipe was straightened and relaxed at the end of the fourth (last) bending cycle, see Figure 3.12. The heights of largest imperfections found during laser inspection are summarised in Tables 3.10 and 3.11 for test pipes "10-2.GW" and "10-3.GW", respectively. The 9 and 3 o'clock position in Tables 3.10 and 3.11 is at the pipe intrados when the pipe is on the reeling and straightening former, respectively. Imperfections larger than 50% and 100% of the liner WT are boldened and underlined, respectively. An empty cell indicates that only visual inspection was carried out.

Bend Testing of 12" Pipes

Test Strings Three 12" MLP test pipes with 6.7 mm thick (prior to expansion) alloy 316L liner, listed in Table 3.12, were subjected to bending strain capacity testing: one non-welded pipe (labelled "12-1") and two welded pipes (labelled "12-2.GW" and "12-3.GW"). All test

pipes were 12 m in length. The non-welded pipes had an 11.2 m long lined section whereas the welded pipes included two lined sections, each 5.6 m long. The girth-welded test pipes had a CRA weld between the lined sections which were terminated with a 150 mm long overlay weld at the string centre. The remaining ends of each lined section were terminated with a short seal weld. Carbon steel extension pieces were welded to either side of the lined sections to achieve the required length of a test string. The test pipe ends were marked "Anchor End" and "Pull End". The 3, 6, 9 and 12 o'clock positions were marked when looking from "Anchor End" towards "Pull End".

Bending Trials Each test pipe was mounted in the HWU bending rig, shown in Fig. 2.24, such that "End A" was located at the pull end (to the left in Fig. 2.24) while "End B" was located at the anchor end (to the right in Fig. 2.24). The 3 o'clock position marked on the pipe faced the straightening former while the 9 o'clock position faced the reeling former. The 9 o'clock position was under compression when a test pipe was bent on the reeling former during strain capacity testing. A 55.84 m radius straightening former was used for all test pipes. In contrast, different reeling former radii were used at various stages of the tests, as detailed in Table 3.13. Prior to testing, each test pipe was laser inspected to size initial liner imperfections. All manufacturing imperfections were less than 0.4 mm in height, except CRA girth weld roots. Subsequently, the pipes were subjected to the test regime detailed in Table 3.13.

Bending-induced liner imperfections, up to 1.4 mm in height at the 9 o'clock position, were found after test pipe "12-1" had been bent onto a 6.4 m reeling former for the first time (see Figure 3.13). Two other reverse bending cycles on the same reeling former were then applied, and the pipe was straightened and relaxed. All bending-induced imperfections found were less than 1 mm in height. When the pipe was bent on a 5.5 m reeling former during the fourth bending event, the height of largest bending-induced imperfections increased to 3.8 mm and 1.6 mm at 9 o'clock and 3 o'clock, respectively (refer to Figure 3.14). The largest residual imperfection height was 1.9 mm after the pipe was relaxed following six bending cycles (three on a 6.4 m former and three on a 5.5 m former), see Table 4 6. Residual imperfections at the 3 o'clock position were smaller than those observed at the 9 o'clock.

Bending-induced imperfections, up to 1.4 mm in height at the 9 o'clock position, were found in Test Pipe "12-2.GW" following bending on a 6.4 m reeling former for the first time. When the pipe was straightened after two other bending cycles on the same former, the largest imperfection of 1.3 mm in height was measured at the 3 o'clock position, see Figure 3.15. Bending-induced imperfections, up to 3.1 mm in height, were produced when the pipe was bent onto a 5.5 m reeling former during the fourth bending event (refer to Figure 3.16), with the largest imperfection found at the 9 o'clock position. Finally, the largest residual imperfection after the same bending regime as that for test pipe "12-1" was 2.8 mm in height, see Table 3.14. Imperfections larger than 50% of the liner WT are boldened. The 9 and 3 o'clock positions in the table are at the pipe intrados when the pipe is on the reeling and straightener straightening former, respectively. An empty cell indicates that only visual inspection was carried out.

After five reverse bending cycles on an 8.23 m former, a 1.1 mm high bending-induced imperfection was measured at 3 o'clock in Test Pipe "12-3.GW". It was measured at the very location where the largest manufacturing imperfection had been found prior to bend testing, see Figure 3.17. All other imperfections were less than 1 mm in height. The imperfection at the 3 o'clock position did not grow when the pipe was bent onto a 6.4 m former. However, other bending-induced imperfections, up to 1.9 mm in height, were produced at the 9 o'clock position. The highest residual bending-induced imperfections after bending on a 5.5 m reeling former and straightening were 1.5 mm and 1.2 mm at the 3 and 9 o'clock position, respectively (refer to Figure 3.17). The bending strain capacity results for test pipe "12-2.GW" are summarised in Tables 3.15 and 3.16 while those for test pipe "12-3.GW" are given in Table 3.17. The 9 and 3 o'clock positions in these tables are at the pipe intrados when the pipe is on the reeling and straightener straightening former, respectively. An empty cell indicates that only visual inspection was carried out.

Summary of Bending Trials

The 10" and 12" MLPs with the liner WT selected for reeling from TechnipFMC's Deep Blue vessel did not wrinkle when subjected to more bending cycles than a standard reel-lay installation, on radii tighter than typical for reeling. Liner wrinkling, as defined in Table 3.1, initiated

when the pipes were bent on a former with a radius smaller than 6.1 m. Since the Deep Blue pipelay vessel has a reel hub radius of 9.75 m, it can be concluded that MLPs with the liner thickness as per Eq. 2.11 have an inherent safety factor on the bending strain of at least 1.6. The largest bending-induced liner imperfections at any time during strain capacity testing were at the 9 o'clock position which was under compression when on the reeling former. A straightening event reduced the largest imperfection in a given test pipe when on the reeling former by a factor of at least 2 typically. Following cycling bending, the largest residual imperfection was at either 3 o'clock or 9 o'clock, on the bending plane.

3.4 Numerical Simulation

3.4.1 Flow Behaviour

It was shown in Section 3.3.1 that the liner hardens predominantly isotropically during hoop expansion and kinematically during subsequent cyclic plastic straining representative of reeling. Such complex behaviour cannot be modelled with classical incremental metal plasticity models available in ABAQUS [47], because the associated hardening behaviour does not change with the plastic strain history. To overcome this issue while employing classical metal plasticity, a work-around approach is used whereby the as-received stress-strain curve is altered through an iterative process, such that following hoop expansion the predicted cyclic stress-strain hysteresis agrees with the behaviour observed during testing.

First, an FEA model comprising of a single shell element is subjected to 5% strain in one direction. Finite-strain J_2 flow theory with a combined isotropic and kinematic hardening plasticity scheme is employed, where the uni-axial stress-strain relationship is given by [47]

$$\sigma\left(\varepsilon^{pl}\right) = \sigma_0 + \frac{C_1}{\gamma_1}\left(1 - e^{-\gamma_1 \varepsilon^{pl}}\right) + C_2\varepsilon^{pl} + Q_\infty\left(1 - e^{-b\varepsilon^{pl}}\right) \tag{3.1}$$

Here, ε^{pl} is the plastic strain, σ_0 is the stress at zero plastic strain, C_1 and C_2 are the linear kinematic hardening moduli, γ_1 is the kinematic hardening exponent, Q_∞ is the isotropic hardening modulus and b is the isotropic hardening exponent. Following relaxation, the finite element is

cyclically loaded in a perpendicular direction to replicate the tensile test. Subsequently, the stress-strain hysteresis is extracted and compared to the test result. If needed, the parameters of the combined hardening plasticity model are modified until good agreement is found between numerical and test results.

It can be seen in Figures 3.18(a) and 3.18(b) that the stress-strain hysteresis from cyclic tests (indicated by the solid lines in the figures) performed on as-expanded alloys 316L and 625, respectively, can be well replicated numerically (indicated by the dashed lines in the figures). The corresponding as-received stress-strain curves, which have a yield stress (stress at 0.5% total elongation) of 370 MPa and 470 MPa for alloy 316L and 625, respectively, are shown in Figure 3.19. It is assumed that alloy 625 cladding has similar cyclic behaviour to that of alloy 625 liner. Consequently, the as-received stress-strain curve of alloy 625 cladding is derived by lowering the yield stress of the alloy 625 liner by 75 MPa (refer to Sec. 3.3.1). This curve is also shown in Fig. 3.19, together with a stress-strain curve representative of API 5L X65 CS.

3.4.2 Wrinkling Parametric Study

Liner Imperfections

Liner wrinkling is strongly influenced by initial imperfections (refer to Section 2.6.2). Most liner imperfections are introduced during manufacturing of the MLP when the liner conforms to the shape of the backing steel pipe inner surface. Seamless backing pipes are characterised by a spiral surface topology (visible on the pipe inner surface in Figure 3.20(a)) which is introduced during the piercing process. This topology is transferred to the liner during expansion, as shown in Fig. 3.20(b). Such imperfections have qualitatively the same effect on the liner wrinkling as idealised harmonic imperfections (refer to Section 2.6.2). Consequently, imperfections derived from a buckling/wrinkling eigenmode analysis are applied to the liner in this study.

The length of the liner model in the eigenmode analysis is equal to half of the wavelength of a liner wrinkle under axial compression, λ, from Eq. 2.9. A quarter of the liner is modelled with first-order shell elements with reduced integration (S4R in ABAQUS [47]) and appropriate

symmetry boundary conditions, see Figure 3.21(a). A compression load mode is preferred over a bending load mode because it yields eigenmodes that are symmetrical with respect to the pipe axis. These are suitable for modelling reverse bending as experienced during the reeling process. Fig. 3.21(b) shows ten eigenmodes obtained from this analysis.

Finite-Element Modelling

The wrinkling parametric study is undertaken using an FEA model adapted from that proposed by Vasilikis in [68]. The same MLP size, i.e. 325.0 mm OD × 14.3 mm WT carbon steel pipe lined with 3 mm thick liner, is considered. The model length is the same as that in the eigenmode analysis. Both the liner and the backing pipe are modelled with first-order shell elements with reduced integration (S4R in ABAQUS [47]). A quarter of the MLP with appropriate symmetry boundary conditions is modelled. A finite-sliding, hard contact formulation with Coulomb friction (friction coefficient of 0.1 assumed because friction has a negligible effect on the liner behaviour in the absence of grip stress, refer to Sec. 3.1) is employed to model interaction between the liner and the backing pipe. A selected eigenmode is scaled so that the required initial imperfection height is seeded onto the liner, as explained below. Liner expansion is not simulated here because it would reduce the size of initial imperfections (refer to Sec. 2.2.3). The nodes to the right hand side of the model in Figure 3.22(a) are connected to a reference node through kinematic coupling. The MLP is bent by applying rotation to the reference node.

Sensitivity Analyses

In the base case, eigenmode 3 in Fig. 3.21(b) is chosen because it is best suited, as will be shown in a subsequent section. The normalised initial imperfection height, $h/t = 5\%$ and the radial insertion gap, $g = 0.1$ mm (ref. Sec. 2.2.4) are selected. Sensitivity analyses are then carried out to assess the effect of the following parameters on the liner separation from the host pipe on the left hand side of the model in Figure 3.22(b):

1. Imperfection height
2. Imperfection mode shape

3. Residual gap between liner and backing pipe

4. Liner yield strength and strain hardening

5. Mesh discretisation

Other parameters, such as the grip force or friction, are not considered here because their effect on liner wrinkling is deemed sufficiently documented (refer to Section 2.2 for more details). Where applicable, the FEA results are expressed in terms of the liner separation from the host pipe normalised by the liner thickness, versus the normalised bending curvature, κ/κ_0, determined from

$$\kappa/\kappa_0 = \kappa \times d^2/t \tag{3.2}$$

where d and t are the liner mid-wall diameter and wall thickness, respectively.

Results

Effect of Imperfection Height Figure 3.23 shows the effect of the normalised imperfection height, h/t, on the liner separation at $\kappa/\kappa_0 = 2.5$. The predicted liner separation is very sensitive to the imperfection height for h/t up to 5% only. Consequently, $h/t = 5\%$ is appropriate.

Effect of Imperfection Mode Shape The numerical results in Figure 3.24 show that Eigen-mode 3 in Fig. 3.21(b) is the best suited imperfection shape, because it is symmetrical with respect to the neutral bending axis, and yields the separation no lower than the other modes.

Effect of Residual Gap between Liner and Backing Pipe It can be seen in Figure 3.25 that the residual gap between the liner and backing pipe has a similar effect on the normalised liner separation as the normalised imperfection height. The predicted liner separation is very sensitive to the residual gap for g up to 0.1 mm. Consequently, $g = 0.1$ mm is appropriate.

Effect of Liner Tensile Behaviour The numerical results in Figure 3.26 show that a 50 MPa increase in the yield strength (i.e. range of 100 MPa, which is typical for reeling) results in a 7% increase in the normalised liner separation. In contrast, a 50% increase in the strain hardening,

expressed in terms of the tangent modulus of the stress-strain curve in the fully plastic regime, marginally reduces the normalised liner separation, see Figure 3.27.

Mesh Discretisation Finally, the liner and backing pipe with: (i) axial element length in the order of 4 mm and 10 mm, respectively, (ii) at least 60 and 90 elements around half-circumference, respectively, and (iii) at least 5 integration points though the thickness, are suitable to predict liner wrinkling during reeling.

3.4.3 Numerical Framework for Prediction of Liner Wrinkling during High Strain Cyclic Bending

Finite-Element Modelling

A three-dimensional finite-element analysis model is used to simulate liner expansion during MLP manufacturing followed by reel-lay installation or a bending trial. First-order shell elements with reduced integration and first-order pipe/beam elements (S4R and PIPE31 in ABAQUS [47]) are used to model the liner, the overlay cladding and the host pipe. For shell elements, the Gauss' integration scheme with 5 and 7 integration points through the thickness is employed for the host pipe and the liner/overlay cladding, respectively. The shell section is preceded and followed by a pipe/beam mesh. All beam elements are 0.5 m long and have 24 integration points around the pipe circumference. Kinematic couplings are used to connect shell to beam elements. Due to symmetry, only half of a pipe is modelled with appropriate boundary conditions. The model length is 12 m when simulating a bending trial, see Figure 3.28, and maybe up to a few hundred meters when simulating reel-lay installation, see Figure 3.29.

When designing a reeled pipe, the maximum statistical plastic moment mismatch between consecutive pipe joints is considered, refer to Section 2.1.2. In this scenario, a weaker joint is assumed to be welded to a stronger joint. As an MLP is bent, strain concentrates in the weaker joint. This location is most susceptible to liner wrinkling. Therefore, a liner section along the weaker joint, close to overlay cladding on the left-hand side of a girth weld in the FEA model in

Fig. 3.29 has a highly-refined shell mesh. As plastic mismatch is not considered when simulated bending trials, a liner shell mesh is highly refined at the centre of the shell mesh in Fig. 3.28. The pipe mesh discretisation is as per Section 3.4.2 in the refined area, and coarser elsewhere.

Finite-sliding contact formulation with a soft behaviour and Coulomb's friction law is used to model liner to host pipe interaction and host pipe to vessel equipment/bending formers interaction. In contrast, the overlay cladding is tied to the host pipe. Since a small amount of local sliding is possible, tube-to-tube contact elements (ITT31 in ABAQUS [47]) are used to model interaction between liner and host pipe beam nodes. J_2 flow theory and a combined isotropic and kinematic hardening plasticity scheme are used to model the flow behaviour of the liner and cladding, while a non-linear kinematic hardening plasticity model is employed for the carbon steel host pipe. The corresponding CS and CRA material stress-strain curves are shown in Fig. 3.19. These curves can be adjusted to meet project specific requirements (e.g. in terms of yield strength).

Rigid bending formers are utilised to replicate the reel, the aligner, the straightener and the free span between the reel and the aligner when simulating a bending trial. These formers are connected through their reference nodes to the beam mesh end nodes with kinematic couplings. The liner is first subjected to internal pressure to simulate manufacturing of the MLP. After releasing the pressure, the pipe is bent onto a relevant former (representing the reel, the "free span", the aligner or the straightener) by rotating the reference node on the left-hand side of the model in Fig. 3.28 while constraining all degrees of freedom but in-plane rotation and horizontal displacement for the reference node to the right.

In the context of a full-cycle reeling analysis, all vessel equipment is explicitly modelled as rigid surfaces. The analysis progresses in two stages. First, a full-cycle reeling beam-mesh analysis, where a long pipeline section is modelled with beam elements only, is performed to determine the optimum straightening settings. The settings are altered and the analysis is re-started until a straight pipe (i.e. the maximum deviation from a straight line is no more than 0.15%, refer to DNVGL-ST-F101 [7]) is obtained at the end of the analysis. Then, the results of this analysis (displacements and rotations of representative nodes, and pipe section forces) are used to drive

a sub-model, meshed with a combination of beam elements and shell elements in Fig. 3.29, following simulation of manufacturing of MLP. The finite-element analysis flowchart is shown in Fig. 3.30.

Liner Imperfections

Geometrical imperfections are seeded onto the highly refined liner shell mesh in Figs. 3.28 and 3.29 to correctly predict wrinkling initiation. This time, the eigenmode analysis is carried out with a host pipe shell mesh identical to that used in the 3D FEA model. A representative eigenmode, shown in Figure 3.31, which corresponds to eigenmode 3 in Fig. 3.21(b), is selected and imposed onto a perfect host pipe in the 3D model, to create imperfections with the height, $h = 7.5\%\ t_l$. These geometrical imperfections are later imposed onto the liner when it conforms to the host pipe surface topology during expansion. This procedure allows controlling the shape and size of liner imperfections after expansion. When pressure is released, h/t_l is somewhat below 7.5% due to elastic recovery, but remains above 5%.

3.4.4 Validation of Framework for Prediction of Liner Wrinkling during High Strain Cyclic Bending

Approach

The large scale bend tests are simulated numerically to demonstrate that the proposed numerical analysis technique is suitable to conservatively predict liner separation from the host pipe and subsequent wrinkling during reeling. First, imperfections obtained from an eigenmode analysis are seeded in the host pipe and then imprinted onto the liner when it is expanded during simulated MLP manufacturing. The expansion pressure is 80 MPa for the 10" MLPs and 66 MPa for the 12" MLPs. Then, the bending strain capacity tests are simulated using the FEA model in Fig. 3.28. The classical incremental metal plasticity in ABAQUS [47], where the flow behaviour is described by a combined isotropic and kinematic hardening as per Sec. 3.4.1,

is used throughout. In the base case, the von Mises yield criterion (indicated by a solid blue line in Fig. 2.2) is employed. Finally, to illustrate the effect of the bending-induced ovality on the liner behaviour, the Martinez *et al.* yield criterion is assumed for the host pipe and the bending trial simulation is repeated for the 12" Test Pipes. Here, the equivalent stress, σ_{eq}, is of the form [46]

$$\sigma_{eq}(\sigma-\alpha) = \left((\mathbf{1}-\widetilde{\mathbf{c}})\psi_{\mathbf{1}}^{\widetilde{\mathbf{a}}/\widetilde{\mathbf{b_1}}} + \widetilde{\mathbf{c}}\psi_{\mathbf{2}}^{\widetilde{\mathbf{a}}/\widetilde{\mathbf{b_2}}}\right)^{\mathbf{1}/\widetilde{\mathbf{a}}} \tag{3.3}$$

where, σ and α are the stress and backstress tensors, $\widetilde{a}$, $\widetilde{b_1}$ and $\widetilde{b_2}$ are fixed criterion parameters, ψ_1 and ψ_2 are stress potentials, and $\widetilde{c}$ is a weighting function given by [46]

$$\psi_1 = \frac{1}{2}\left(|{S_1}^1 - {S_2}^1|^{\widetilde{b_1}} + |{S_2}^1 - {S_3}^1|^{\widetilde{b_1}} + |{S_3}^1 - {S_1}^1|^{\widetilde{b_1}}\right) \tag{3.4}$$

$$\psi_2 = \frac{3^{\widetilde{b_2}}}{2^{\widetilde{b_2}}+2}\left(|{S_1}^2|^{\widetilde{b_2}} + |{S_2}^2|^{\widetilde{b_2}} + |{S_3}^2|^{\widetilde{b_2}}\right) \tag{3.5}$$

$$\widetilde{c} = \begin{cases} \widetilde{c_0} + \left(\widetilde{c_1} + \widetilde{c_f}(1-e^{-\gamma_c \varepsilon^{pl}})\right)||P||\left(\dfrac{\varepsilon^{pl}}{\varepsilon_L^{pl}}\right), & \text{if} \quad \varepsilon^{pl} \le \varepsilon_L^{pl} \\ \widetilde{c_0} + \left(\widetilde{c_1} + \widetilde{c_f}(1-e^{-\gamma_c \varepsilon^{pl}})\right)||P||, & \text{if} \quad \varepsilon^{pl} > \varepsilon_L^{pl} \end{cases} \tag{3.6}$$

Here, L^1 and L^2 are anisotropic operators and $({S_1}^1, {S_2}^1, {S_3}^1)$ and $({S_1}^2, {S_2}^2, {S_3}^2)$ are principal values of the modified stress tensors $L^1:(\sigma-\alpha)$ and $L^2:(\sigma-\alpha)$, '$\widetilde{c_0}+\widetilde{c_1}$' and $\widetilde{c_f}$ are the initial value and the maximum allowable increase in $\widetilde{c}$, respectively, γ_c is the saturation coefficient for $\widetilde{c}$, ε_L^{pl} is the plastic strain at the end of the Lüders plateau and P is a polarity tensor, which norm ranges between 0 and 1 [46].

In this work, $L^1 = L^2 = L$ is the deviatoric operator, and the criterion parameters are such that the obtained yield surface always lies between the lower and upper bound criteria illustrated in Fig. 2.2. Several combinations of parameters will yield a given yield criterion shape. For example, the Mises yield criterion can be obtained by setting $\widetilde{a} = \widetilde{b_2} = 2$, $\widetilde{c_0} = 1.0$ and $\widetilde{c_1} = \widetilde{c_f} = 0$. At the beginning of the FE analysis the yield surface of the host pipe is described by the lower bound criterion indicated by a green solid line in Fig. 2.2. The corresponding

criterion parameters, which were calibrated from large scale bend test results [46], are $\widetilde{a} = 2$, $\widetilde{b_1} = 8$, $\widetilde{b_2} = 16$, $\gamma_c = 30$, $\widetilde{c_0} = 0.3$, $\widetilde{c_1} = 0.4$, $\widetilde{c_f} = 0.3$ and $\varepsilon_L^{pl} = 0.015$.

von Mises Yield Criterion – Results for 10" Pipes

Non-Welded Test Pipe "10-1" Figure 3.32 illustrates the evolution of bending-induced liner imperfections during cyclic straining predicted numerically. The FEA estimates are compared in Table 3.18 and Figure 3.33 to the imperfections found during testing for bending events when liner imperfections were measured. One reverse bending cycle in Fig. 3.33 includes bending onto the reeling former, relaxing, bending onto the straightening former and relaxing, which represents half of a standard reeling operation. The 9 and 3 o'clock position in Table 3.18 is at the pipe intrados when the pipe is on the reeling and straightening former, respectively. Imperfections larger than 50% t_L and 100% t_L are respectively boldened and underlined.

In line with the experiment, larger imperfections are predicted to occur when the pipe is on the reeling former (i.e. when the 9 o'clock position is under compression) compared to those on the straightening former (i.e. when the 3 o'clock position is under compression) during the same bending cycle. Furthermore, the numerical predictions agree very well with the experimental results at the 9 o'clock position, which is under compression first, see Fig. 3.33(b). The ratio between the former and the latter ranges between 1.1 and 2.1, with an average of 1.6, see Table 3.18. Moreover, as the largest liner imperfections were found at this clock position at every stage during testing, this also means that the largest FEA predictions at 9 o'clock agree very well with the largest imperfections found during the bending tests, see Fig. 3.33(b).

The numerical predictions and test results diverge, however, at the 3 o'clock position which faces the straightening former. Nevertheless, predictions of residual imperfections are conservative at this clock position as it is in compression during a "straightening event", which results in overestimation of experimental observations. Finally, although imperfections at the pipe extrados (i.e. the clock position under tension) may be underestimated by the FEA, especially during a "reeling event" (ref. Fig. 3.33(a)), they are smaller than other imperfections and as such are insignificant from the design point of view.

Welded Test Pipes "10-2.GW" and "10-3.GW" The FEA estimates are compared in Tables 3.19 and 3.20 and Figure 3.34 to the imperfections found during testing for bending events when liner imperfections were measured. Liner lift-offs larger than 50% t_L and 100% t_L are respectively boldened and underlined in Tables 3.19 and 3.20.

As for the non-welded test pipe and in line with the experiment, larger imperfections are predicted to occur when the pipe is on the reeling former compared to those on the straightening former during the same bending cycle. The numerical predictions of largest bending-induced imperfections at the 9 o'clock position are in good agreement with the test results (but slightly more conservative than for the non-welded pipe) during the first two bending cycles, representative of one standard reeling operation (ref. Fig. 3.34(b)). The numerical prediction of the largest imperfection at this clock position is typically 2 times higher than measured during testing, see Tables 3.19 and 3.20. This ratio significantly increases subsequently, when the liner separation exceeds 50% of its thickness and starts to localise close to the girth weld, due to a strength mismatch between lined and overlay sections of the welded MLP.

Finally, as observed for the non-welded pipe: (i) the numerical predictions and test results diverge at the 3 o'clock position which faces the straightening former, but the predictions of residual imperfections are conservative at this clock position, and (ii) although imperfections at the pipe extrados (i.e. the clock position under tension) may be underestimated by the FEA, especially during a "reeling event" (ref. Fig. 3.34(a)), they are smaller than other imperfections and as such are insignificant from the design point of view.

von Mises Yield Criterion – Results for 12" Pipes

Non-Welded Test Pipe "12-1" Table 3.21 and Figure 3.35 compare the numerical predictions to the imperfections found during testing for bending events when liner imperfections were measured. Liner lift-offs larger than 50% t_L and 100% t_L are respectively boldened and underlined in Table 3.21. As for the 10" non-welded pipe and in line with the experiment, larger imperfections are predicted to occur when the pipe is on the reeling former (i.e. when the 9 o'clock position is under compression) compared to those on the straightening former (i.e. when the 3 o'clock position is under compression) during the same bending cycle. The nu-

merical predictions of largest bending-induced imperfections at 9 o'clock are in good agreement with the test results (but slightly more conservative than for the non-welded 10" pipe) during the first three bending cycles (ref. Fig. 3.35(b)). The FEA estimate of the largest imperfection at this clock position is typically 1.9 times higher than measured during testing, see Table 3.21. This ratio increases considerably subsequently, when the MLP is bent onto a tighter radius and the liner separation exceeds 50% t_L. The same observations are made as for the non-welded 10" pipe with regards to the liner separation at 3 o'clock and more generally at the pipe extrados.

Welded Test Pipes "12-2.GW" and "12-3.GW" It can be seen in Figure 3.36 that in the case of the 12" welded pipes the liner separation localises close to the weld sooner than observed for the 10" pipes, especially for test pipe "12-2.GW", which is bent on a tighter radius than typical for reeling. The effect of the strength mismatch between lined and overlay sections is more pronounced for the 12" pipes than for the 10" pipes because they are slenderer. Tables 3.22 and 3.23 and Figures 3.37 and 3.38 compare the numerical predictions to the imperfections found during testing of "12-2.GW" and "12-3.GW", respectively. Liner lift-offs larger than 50% t_L and 100% t_L are respectively boldened and underlined in Tables 3.22 and 3.23.

The numerical predictions for test pipe "12-2.GW" agree with the numerical predictions only during the first bending cycle, see Table 3.22 and Fig. 3.37. Subsequently, the liner separation rapidly localises close to the girth weld, due to strength mismatch, leading to a significant overestimation of the liner imperfection. Such effect was not observed during testing probably because some amount of tension, which has a significant effect on the local deformation of the pipe in case of strength mismatch, was applied to the pipe.

In contrast, the FEA estimates of the liner separation for test pipe "12-3.GW" agree well with the measurements. As for the 10" welded pipes, larger imperfections are predicted to occur when the pipe is on the reeling former (i.e. when the 9 o'clock position is under compression) compared to those on the straightening former (i.e. when the 3 o'clock position is under compression) during the same bending cycle. The numerical predictions of largest bending-induced imperfections agree well with the test results at both clock positions during the first five bending cycles (representative of a contingency re-reeling operation), when the test pipe is bent on

a radius typical of reeling (ref. Fig. 3.38). The FEA estimate of the largest imperfection after five bending cycles is 2.3 times higher than measured during testing, see Table 3.23. This ratio increases considerably subsequently, when the MLP is bent onto a tighter radius.

von Mises Yield Criterion – Results Summary

The FEA can predict the evolution of liner separation from the host pipe during "bending events" when the MLP is subjected to bending on the reeling former. Predictions do not agree as well with the test results for "straightening events" when the pipe is bent on the straightening former. Nevertheless, the numerical predictions of bending-induced liner imperfections are always conservative compared to experiment at the pipe intrados, i.e. the clock position subjected to compression. This is the most critical location around the pipe circumference, relevant to the reeled MLP design, where the wrinkling evaluation is to be undertaken during bending trial simulation or reelability assessment, i.e.: (i) 100% t_L check on the reel and the aligner and (ii) 50% t_L check after straightening.

The FEA prediction at the clock position which sees compression first during a bending trial or reeling provides a good estimate of the largest measured liner imperfection at any stage, regardless of whether the pipe is under compression (i.e. at the intrados) at that clock position or not. The FEA conservatism, in terms of the factor on the height of bending-induced liner imperfections, is typically on the order of 2 when the MLP is subjected to: (i) multiple bending cycles (in excess of a standard reeling operation) on a radius typical of reeling, or (ii) two bending cycles (a standard reeling operation) on a radius tighter than typical of reeling. The numerical prediction generally becomes over-conservative when an MLP is subjected to a more severe bending regime. A safety factor in the order of 1.5 – 2.0 on the estimate of the liner imperfection may account for uncertainties relates to pipe properties, measurement errors, etc.

The conservatism of the numerical prediction increases with the number of bending cycles and with the applied strain. This is most likely because the use of von Mises yield criterion may lead to an overestimation of the pipe ovalisation, as shown by Martinez *et al.* [45, 46]. To verify this, the numerical work is repeated in the following section, where a history dependant yield criterion is used to limit pipe ovalisation during bending.

Martinez *et al.* Yield Criterion

To illustrate the effect of bending-induced ovality on liner wrinkling, the numerical work is repeated with a user defined material subroutine (developed by Martinez *et al.*) assigned to the CS backing pipe only. The 12" pipe bending strain capacity tests are then simulated numerically using the same input data (pipe sizes, material stress-strain curves, etc.). It can be seen in Figure 3.39 that the bending induced ovality has a significant effect on the liner separation. The heights of largest imperfections are reduced by a third when the Martinez *et al.* yield criterion is used (indicated by the solid lines in Fig. 3.39) instead of the von Mises yield criterion (indicated by the dashed lines in Fig. 3.39). It is anticipated that the use of the von Mises yield criterion for the liner also results in the overestimation of the CRA liner ovality and thus of the liner wrinkles. Therefore, further work similar to that undertaken by Chouman [137], should be carried out to validate the use of a history dependant yield criterion for the CRA liner. This would allow reducing the level of conservatism within the proposed numerical modelling framework.

3.5 Recommendations for the Design of MLP Against Liner Wrinkling

In this chapter, it was established experimentally that the liner hardens predominantly isotopically when expanded inside the host pipe during MLP manufacturing, and kinematically during subsequent cyclic plastic straining representative of reeling. Such behaviour, which was not reported in the literature, cannot be simulated using classical incremental metal plasticity models available in ABAQUS [47], because the associated hardening behaviour does not change with the plastic strain history. To overcome this issue while employing classical metal plasticity, a work-around approach was proposed herein. A quantitative definition of liner wrinkling was proposed and large scale bending trials were undertaken, to investigate the behaviour of the liner before and after the onset of liner wrinkling during cyclic plastic straining representative of reeling. A framework for the numerical prediction of the liner separation from the host pipe

during cyclic bending was proposed, and validated against the experiment. The results from this chapter have been accepted for presentation at the 38^{th} OMAE conference in Glasgow, UK, in June 2019, and will appear in the conference proceedings.

The design recommendations provided herein assume that both CS and CRA material grades were chosen based on the outcome of a project specific material selection exercise. The process detailed below should be followed to design the liner wall thickness against wrinkling:

1. Selection of carbon steel wall thickness
2. Estimation of liner radial insertion gap
3. Preliminary selection of liner wall thickness and cladding length
4. Reelability assessment
5. Cost evaluation

The CS pipe WT is selected following client specifications and/or industry standards such as DNVGL-ST-F101 [7]. When the design is governed by reeling, Eq. 2.2 is used to determine the lowest allowable nominal WT of the CS pipe, t_{min}.

Industry standards do not provide recommendations for the selection of the radial insertion gap between liner and host pipe. A large gap makes insertion easier and reduces the risk of liner scoring/galling. However, the hoop strain applied to the liner during expansion increases with a greater gap, rendering the liner seam weld more prone to fracture. Therefore, sizing of the insertion gap is a compromise between the risk of galling and fracture. A fitment gap in the order of 3 – 5 mm typically is selected following recommendations from an MLP supplier.

The preliminary minimum liner thickness after hoop expansion, t_L, is estimated from Eq. 2.11. Alternatively, t_L may be determined from Eq. 2.10. The mean liner thickness before expansion, t_{lmean}, is then established by increasing t_L by: (i) an allowance for thinning during expansion (e.g. 0.1-0.2 mm), and (ii) an allowance for wall thickness variations (e.g. -0/+10%). Subsequently, the preliminary cladding length (e.g. 50 mm) is selected based on project specific requirements, such as NDE limitations and the anticipated number of girth welds cut-outs.

A reelability assessment is then carried out as detailed in Sec. 2.1.2, using a vessel specific FEA model (ref. Sec. 3.4.3), to confirm or optimise the required minimum liner thickness. As liner wrinkling may occur unnoticed prior to dry buckling of the host pipe, a higher mismatch than for a standard pipeline, corresponding to a lower probability of occurrence (e.g. 10^{-3} instead of 10^{-2}) is used to determine the properties of weaker and stronger MLP joints. In the absence of project specific stress-strain data, those provided in Sec. 3.4.1 are used in the analysis. If needed, the liner WT, the host pipe WT and/or installation parameters such as the back tension to be applied during pipeline installation may be adjusted to optimise the design and meet the acceptance criteria in Sec. 2.1.2 and Table 3.1. A history dependant yield criterion, such as that proposed by Martinez *et al.* [45, 46] should be used for the CS backing pipe (and liner if available).

3.6 Tables and Figures

Table 3.1: Liner Wrinkling Criteria

Test Regime	Stage	Maximum Allowable Liner Separation
Monotonic Bending	Any	50% t_L
Reeling / Cyclic Bending	Any	100% t_L
	End	50% t_L

Table 3.2: Liner Tensile Test Pipes

Pipe Id (-)	Diameter D (mm)	Thickness t (mm)	Material Grade (-)	Material Condition (-)	Hoop Pre-Strain (%)
316L-AR	273.1	6.5	316L	As-Received	0
316L-AE				As-Expanded	5
625-AR	149.1	3.5	625	As-Received	0
625-AE				As-Expanded	5

Table 3.3: Liner Tensile Test Matrix

Pipe Id	Load Scenario	Test Regime	Number of Cycles	Number of Specimens
316L-AR	Cyclic Compression	-/+ 3%	1	2
	Cyclic Tension	+/- 3%	3	3
316L-AE	Cyclic Compression	-/+ 3%	1	2
	Cyclic Tension	+/- 3%	3	3
625-AR	Cyclic Compression	-/+ 3%	1	2
	Cyclic Tension	+/- 3%	3	3
625-AE	Cyclic Compression	-/+ 3%	1	2
	Cyclic Tension	+/- 3%	3	3

Table 3.4: Summary of Liner Tensile Test Results

Material Grade (-)	Load Mode (-)	YS in As-Received Condition (MPa)	YS after 5% Hoop Expansion (MPa)	YS Delta (MPa)
316L	Compression	350	475	125
	Tension	340	460	120
625	Compression	460	545	85
	Tension	440	505	65

Table 3.5: Specification of Mechanically Lined Pipes for Bending Trials

Pipe Size (")	CS Grade (-)	CS OD (mm)	CS WT (mm)	CRA Grade (-)	CRA WT from Eq. 2.11 (mm)	Selected CRA WT, t_L (mm)
10	API 5L X65	273.1	21.44	Alloy 625	4.7	5.0
12	API 5L X66	323.9	21.44	Alloy 316L	6.8	6.4

Table 3.6: 10" Bend Test Pipes

Test Pipe (-)	CS OD (mm)	CS WT (mm)	CRA OD (mm)	CRA WT t_l (mm)	Pipe Type (-)
10-1	273.1	20.6	225.3	5.1	Non-welded
10-2.GW					Girth-welded
10-3.GW					Girth-welded

Table 3.7: 10" Bend Test Regime

Bending Cycle	Test Pipe Reeling Former Radius (m)		
	10-1	10-2.GW	10-3.GW
1	7.84–7.00–6.40–5.50–4.45	6.10	6.10
2	4.45	6.10	6.10
3	4.45	6.10	6.10
4	–	6.10	6.10

Table 3.8: Test Pipe "10-1": Largest Imperfections Measured in Middle of Pipe during Strain Capacity Tests

Cycle	Bend Radius (m)	Event	Position				
			3 o'c	w_h (mm) 9 o'c	3 o'c	w_h (%) 9 o'c	
0	–	Initial	≤ 0.4	≤ 0.4	$\leq 8\%$	$\leq 8\%$	
1a	7.84	Bending					
1b	7.00	Bending					
1c	6.40	Bending	0.5	1.4	10%	28%	
1d	5.50	Bending	0.7	2.0	14%	40%	
1e	4.45	Bending	0.7	1.9	14%	38%	
		Straight	0.5	0.5	10%	10%	
2	4.45	Bending	1.9	6.9	38%	138%	
		Straight	0.7	1.9	14%	38%	
3	4.45	Bending	2.9	11.4	**58%**	228%	
		Straight	2.2	3.4	44%	**68%**	

Table 3.9: Test Pipe "10-1": Largest Imperfections Measured at Anchor Side during Strain Capacity Tests

Cycle	Bend Radius (m)	Event	Position				
			3 o'c	w_h (mm) 9 o'c	3 o'c	w_h (%) 9 o'c	
0	–	Initial	≤ 0.4	≤ 0.4	$\leq 8\%$	$\leq 8\%$	
3	4.45	Bending	3.1	12.2	**62%**	244%	
		Straight	1.0	3.7	20%	**74%**	

Table 3.10: Test Pipe "10-2.GW": Largest Imperfections Measured during Strain Capacity Tests

Cycle	Bend Radius (m)	Event	Position			
			3 o'c	9 o'c	3 o'c	9 o'c
			w_h (mm)		w_h (%)	
0	–	Initial	≤ 0.4	≤ 0.4	$\leq 8\%$	$\leq 8\%$
1	6.10	Bending	0.5	0.9	10%	18%
		Straight				
2	6.10	Bending	0.7	1.3	14%	26%
		Straight	0.3	0.5	6%	10%
3	6.10	Bending	0.8	1.7	16%	34%
		Straight				
4	6.10	Bending	0.9	2.0	18%	40%
		Straight	0.7	0.8	14%	16%

Table 3.11: Test Pipe "10-3.GW": Largest Imperfections Measured during Strain Capacity Tests

Cycle	Bend Radius (m)	Event	Position			
			3 o'c	9 o'c	3 o'c	9 o'c
			w_h (mm)		w_h (%)	
0	–	Initial	≤ 0.4	≤ 0.4	$\leq 8\%$	$\leq 8\%$
1	6.10	Bending	0.4	1.0	8%	20%
		Straight				
4	6.10	Bending				
		Straight	0.4	1.2	8%	24%

Table 3.12: 12” Bend Test Pipes

Test Pipe (-)	CS OD (mm)	CS WT (mm)	CRA OD (mm)	CRA WT (mm)	Pipe Type (-)
12-1	324.0	21.49	273.3	6.64	Non-welded
12-2.GW	325.0	21.05	273.4	6.70	Girth-welded
12-3.GW	324.0	21.55	273.7	6.78	Girth-welded

Table 3.13: 12” Bend Test Regime

Bending Cycle	Test Pipe Reeling Former Radius (m)		
	12-1	12-2.GW	12-3.GW
1	6.40	6.40	8.23
2	6.40	6.40	8.23
3	6.40	6.40	8.23
4	5.50	5.50	8.23
5	5.50	5.50	8.23
6	5.50	5.50	6.40
7	–	–	5.50

Table 3.14: Test Pipe “12-1”: Largest Imperfections Measured during Strain Capacity Tests

Cycle	Bend Radius (m)	Event	Position			
			3 o’c	9 o’c	3 o’c	9 o’c
			w_h (mm)		w_h (%)	
0	–	Initial	≤ 0.4	≤ 0.4	$\leq 6\%$	$\leq 6\%$
1	6.40	Bending	0.8	1.4	13%	22%
		Straight				
3	6.40	Bending				
		Straight	0.4	0.7	6%	11%
4	5.50	Bending	1.6	3.8	25%	**59%**
		Straight				
6	5.50	Bending				
		Straight	0.9	1.9	14%	30%

Table 3.15: Test Pipe "12-2.GW": Largest Imperfections Measured at Anchor Side during Strain Capacity Tests

Cycle	Bend Radius (m)	Event	Position			
			3 o'c	9 o'c	3 o'c	9 o'c
			w_h (mm)		w_h (%)	
0	–	Initial	≤ 0.4	≤ 0.4	$\leq 6\%$	$\leq 6\%$
1	6.40	Bending	0.9	1.3	14%	20%
		Straight				
3	6.40	Bending				
		Straight	0.9	1.0	14%	16%
4	5.50	Bending	1.4	3.1	22%	48%
		Straight				
6	5.50	Bending				
		Straight	1.4	1.3	22%	20%

Table 3.16: Test Pipe "12-2.GW": Largest Imperfections Measured at Pull Side during Strain Capacity Tests

Cycle	Bend Radius (m)	Event	Position			
			3 o'c	9 o'c	3 o'c	9 o'c
			w_h (mm)		w_h (%)	
0	–	Initial	≤ 0.4	≤ 0.4	$\leq 6\%$	$\leq 6\%$
1	6.40	Bending	1.1	1.4	17%	22%
		Straight				
3	6.40	Bending				
		Straight	1.3	0.9	20%	14%
4	5.50	Bending	1.8	2.9	28%	45%
		Straight				
6	5.50	Bending				
		Straight	2.8	1.1	44%	17%

Table 3.17: Test Pipe "12-3.GW": Largest Imperfections Measured during Strain Capacity Tests

Cycle	Bend Radius (m)	Event	Position			
			3 o'c	9 o'c	3 o'c	9 o'c
			w_h (mm)		w_h (%)	
0	–	Initial	≤ 0.4	≤ 0.4	$\leq 6\%$	$\leq 6\%$
1-4	8.23	Bending				
		Straight				
5	8.23	Bending				
		Straight	1.1	0.8	17%	13%
6	6.40	Bending	1.1	1.9	17%	30%
		Straight				
7	5.50	Bending				
		Straight	1.5	1.2	23%	19%

Table 3.18: Test Pipe "10-1": Largest Liner Imperfections – Measurements vs. Numerical Predictions

Cycle	Bend Radius (m)	Event	3 o'clock			9 o'clock			Largest
			Test (mm)	FE (mm)	FE/ Test	Test (mm)	FE (mm)	FE/ Test	FE/ Test
0	–	Initial	0.2	0.3	1.5	0.4	0.3	0.7	0.7
1a	7.84	Bending		0.1			1.1		
1b	7.00	Bending		0.1			1.4		
1c	6.40	Bending	0.5	0.1	0.2	1.4	1.6	1.1	1.1
1d	5.50	Bending	0.7	0.1	0.1	2.0	2.1	1.1	1.1
1e	4.45	Bending	0.7	0.2	0.3	1.9	**3.9**	2.1	2.1
		Straight	0.5	1.7	3.4	0.5	0.9	1.8	3.4
2	4.45	Bending	1.9	0.2	0.1	6.9	11.2	1.6	1.6
		Straight	0.7	5.7	8.1	1.9	**2.7**	1.4	3.0
3	4.45	Bending	**3.1**	1.5	0.5	12.2	20.5	1.7	1.7
		Straight	2.2	15.2	6.9	**3.7**	5.8	1.6	4.1

Table 3.19: Test Pipe "10-2": Largest Liner Imperfections – Measurements vs. Numerical Predictions

Cycle	Bend Radius (m)	Event	3 o'clock Test (mm)	3 o'clock FE (mm)	3 o'clock FE/ Test	9 o'clock Test (mm)	9 o'clock FE (mm)	9 o'clock FE/ Test	Largest FE/ Test
0	–	Initial	0.1	0.3	3.0	0.1	0.3	3.0	3.0
1	6.10	Bending	0.5	0.1	0.2	0.9	1.9	2.1	2.1
		Straight		0.8			0.6		
2	6.10	Bending	0.7	0.2	0.3	1.3	**2.8**	2.2	2.2
		Straight	0.3	1.3	4.3	0.5	0.9	1.8	2.6
3	6.10	Bending	0.8	0.3	0.4	1.7	**4.0**	2.4	2.4
		Straight		2.0			1.4		
4	6.10	Bending	0.9	0.5	0.6	2.0	8.1	4.1	4.1
		Straight	0.7	2.4	3.4	0.8	**2.8**	3.5	3.5

Table 3.20: Test Pipe "10-3": Largest Liner Imperfections – Measurements vs. Numerical Predictions

Cycle	Bend Radius (m)	Event	3 o'clock Test (mm)	3 o'clock FE (mm)	3 o'clock FE/ Test	9 o'clock Test (mm)	9 o'clock FE (mm)	9 o'clock FE/ Test	Largest FE/ Test
0	–	Initial	0.3	0.3	1.0	0.1	0.3	3.0	1.0
1	6.10	Bending	0.4	0.1	0.3	1.0	1.9	1.9	1.9
		Straight		0.8			0.6		
2	6.10	Bending		0.2			**2.8**		
		Straight		1.3			0.9		
3	6.10	Bending		0.3			**4.0**		
		Straight		2.0			1.4		
4	6.10	Bending		0.5			8.1		
		Straight	0.4	2.4	6.0	1.2	**2.8**	2.3	2.3

Table 3.21: Test Pipe "12-1": Largest Liner Imperfections – Measurements vs. Numerical Predictions

Cycle	Bend Radius (m)	Event	3 o'clock Test (mm)	3 o'clock FE (mm)	3 o'clock FE/ Test	9 o'clock Test (mm)	9 o'clock FE (mm)	9 o'clock FE/ Test	Largest FE/ Test
0	–	Initial	0.2	0.4	2.0	0.3	0.4	1.3	1.3
1	6.40	Bending	0.8	0.1	0.1	1.4	2.3	1.6	1.6
		Straight		0.7			0.6		
2	6.40	Bending		0.1			3.2		
		Straight		0.8			1.0		
3	6.40	Bending		0.1			**4.6**		
		Straight	0.4	0.9	2.3	0.7	1.5	2.1	2.1
4	5.50	Bending	1.6	0.1	0.1	**3.8**	13.6	3.6	3.6
		Straight		1.5			3.2		
5	5.50	Bending		0.2			21.9		
		Straight		3.7			**5.8**		
6	5.50	Bending		0.6			23.9		
		Straight	0.9	14.1	15.7	1.9	8.2	4.3	7.4

Table 3.22: Test Pipe "12-2.GW": Largest Liner Imperfections – Measurements vs. Numerical Predictions

Cycle	Bend Radius (m)	Event	3 o'clock Test (mm)	3 o'clock FE (mm)	3 o'clock FE/ Test	9 o'clock Test (mm)	9 o'clock FE (mm)	9 o'clock FE/ Test	Largest FE/ Test
0	–	Initial	0.3	0.4	1.3	0.1	0.4	4.0	1.3
1	6.40	Bending	1.1	0.2	0.2	1.4	3.1	2.2	2.2
		Straight		1.4			0.9		
2	6.40	Bending		0.4			**5.4**		
		Straight		2.2			1.6		
3	6.40	Bending		0.7			13.2		
		Straight	1.3	3.2	2.5	1.0	**3.9**	3.9	3.0
4	5.50	Bending	1.8	0.9	0.5	3.1	20.5	6.6	6.6
		Straight		7.0			**5.5**		
5	5.50	Bending		1.5			22.0		
		Straight		14.4			6.7		
6	5.50	Bending		3.2			22.4		
		Straight	2.8	18	6.4	1.3	8.4	6.5	6.4

Table 3.23: Test Pipe "12-3.GW": Largest Liner Imperfections – Measurements vs. Numerical Predictions

Cycle	Bend Radius (m)	Event	3 o'clock Test (mm)	3 o'clock FE (mm)	3 o'clock FE/ Test	9 o'clock Test (mm)	9 o'clock FE (mm)	9 o'clock FE/ Test	Largest FE/ Test
0	–	Initial	0.3	0.4	1.3	0.4	0.4	1.0	1.0
1	8.23	Bending		0.2			1.8		
		Straight		0.9			0.7		
2	8.23	Bending		0.4			2.3		
		Straight		1.3			1.0		
3	8.23	Bending		0.6			3.0		
		Straight		1.7			1.3		
4	8.23	Bending		0.8			**4.0**		
		Straight		2.2			1.6		
5	8.23	Bending		1.0			**5.5**		
		Straight	1.1	2.5	2.3	0.8	2.3	2.9	2.3
6	6.40	Bending	1.1	1.0	0.9	1.9	15.1	7.9	7.9
		Straight		**5.0**			**4.0**		
7	5.50	Bending		1.4			21.7		
		Straight	1.5	7.4	4.9	1.2	6.7	5.6	4.9

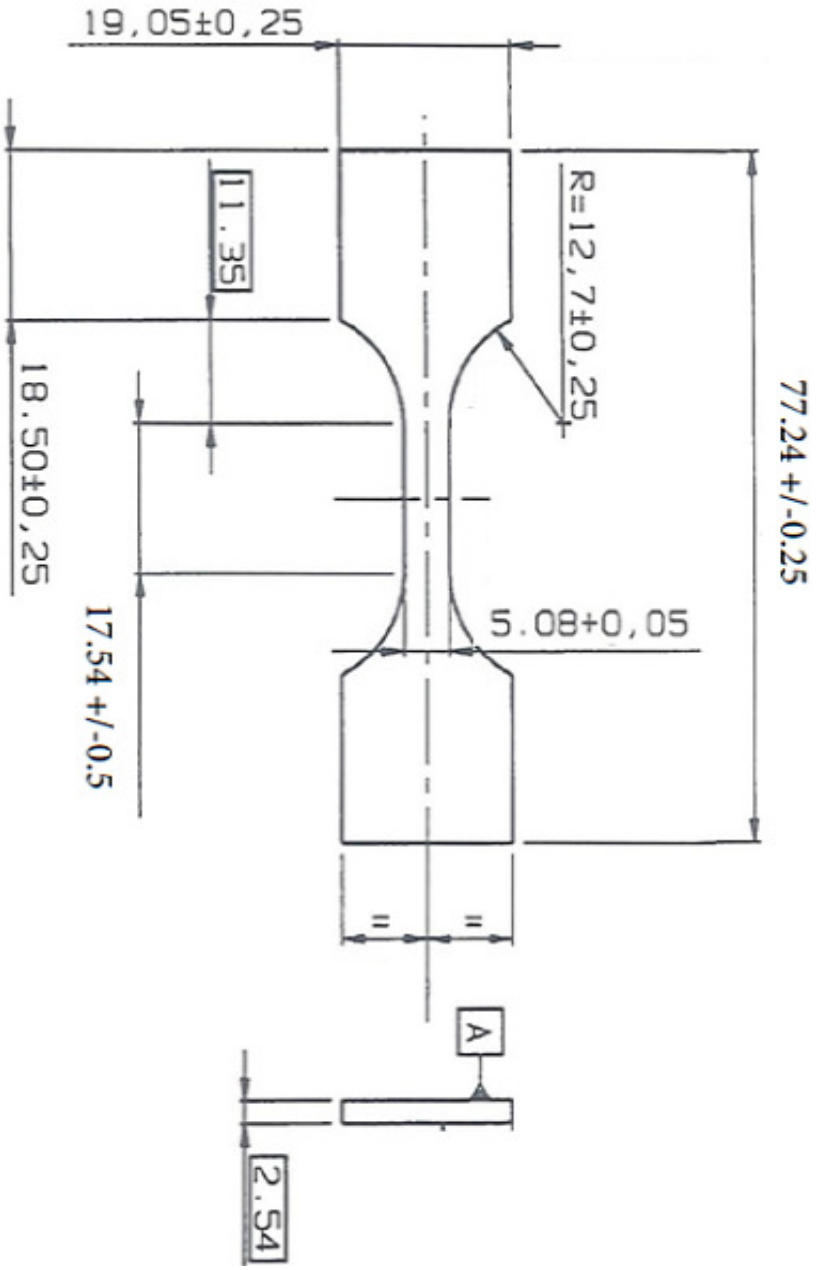


Figure 3.1: Liner Tensile Test Specimen

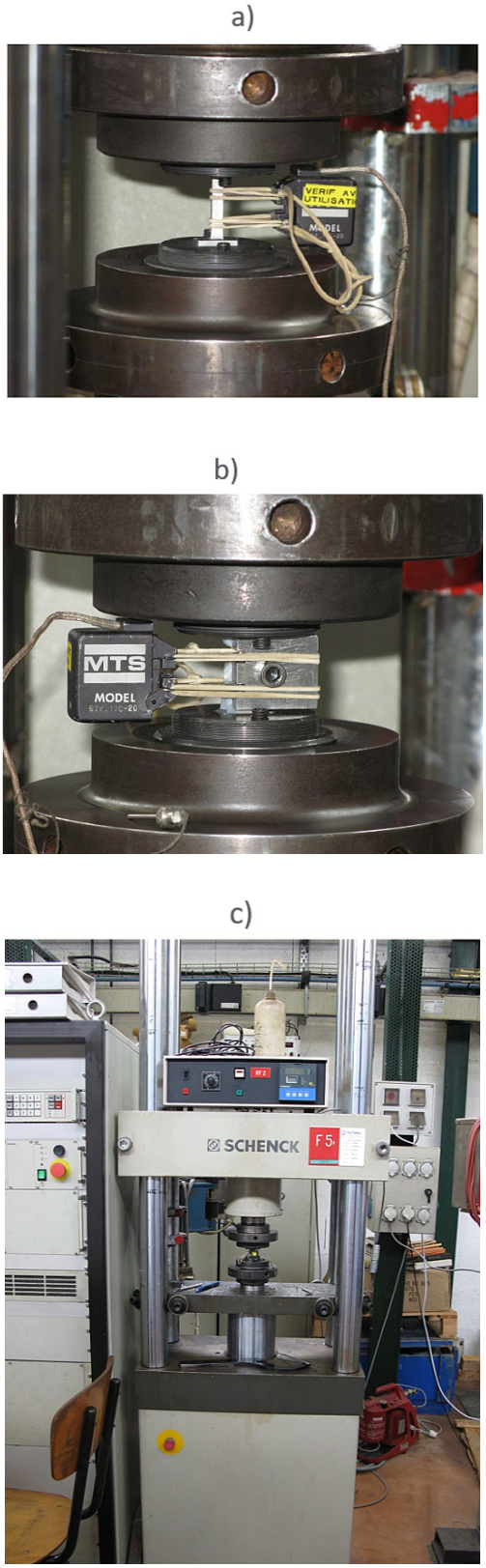


Figure 3.2: Tensile Testing of CRA Liners at A2MI: (a) Specimen Instrumented and Gripped on Test Frame, (b) Anti-Buckling System Mounted, (c) Test Machine

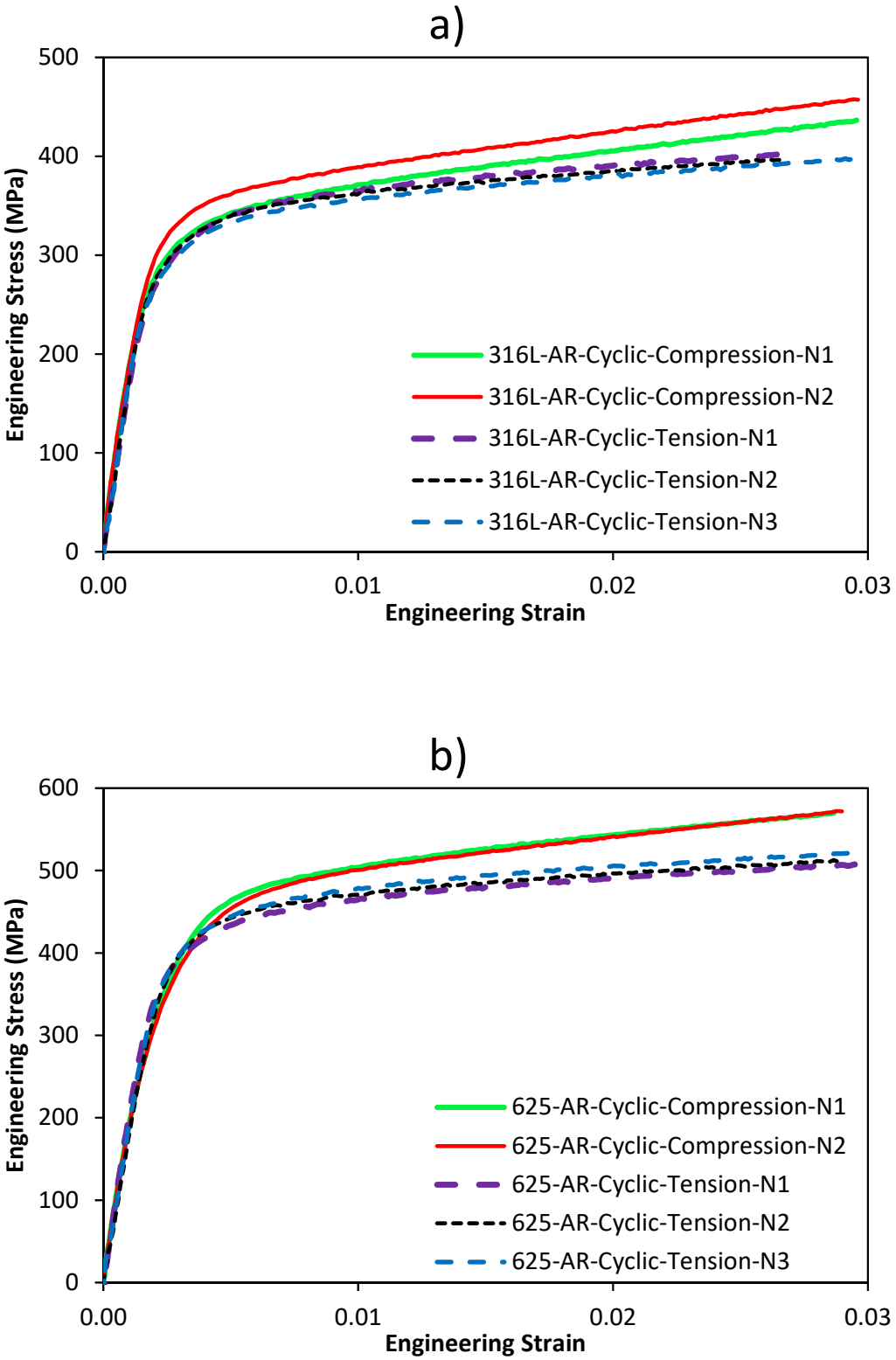


Figure 3.3: CRA Liner Stress-Strain Curves in As-Received Condition: (a) 316L, (b) 625

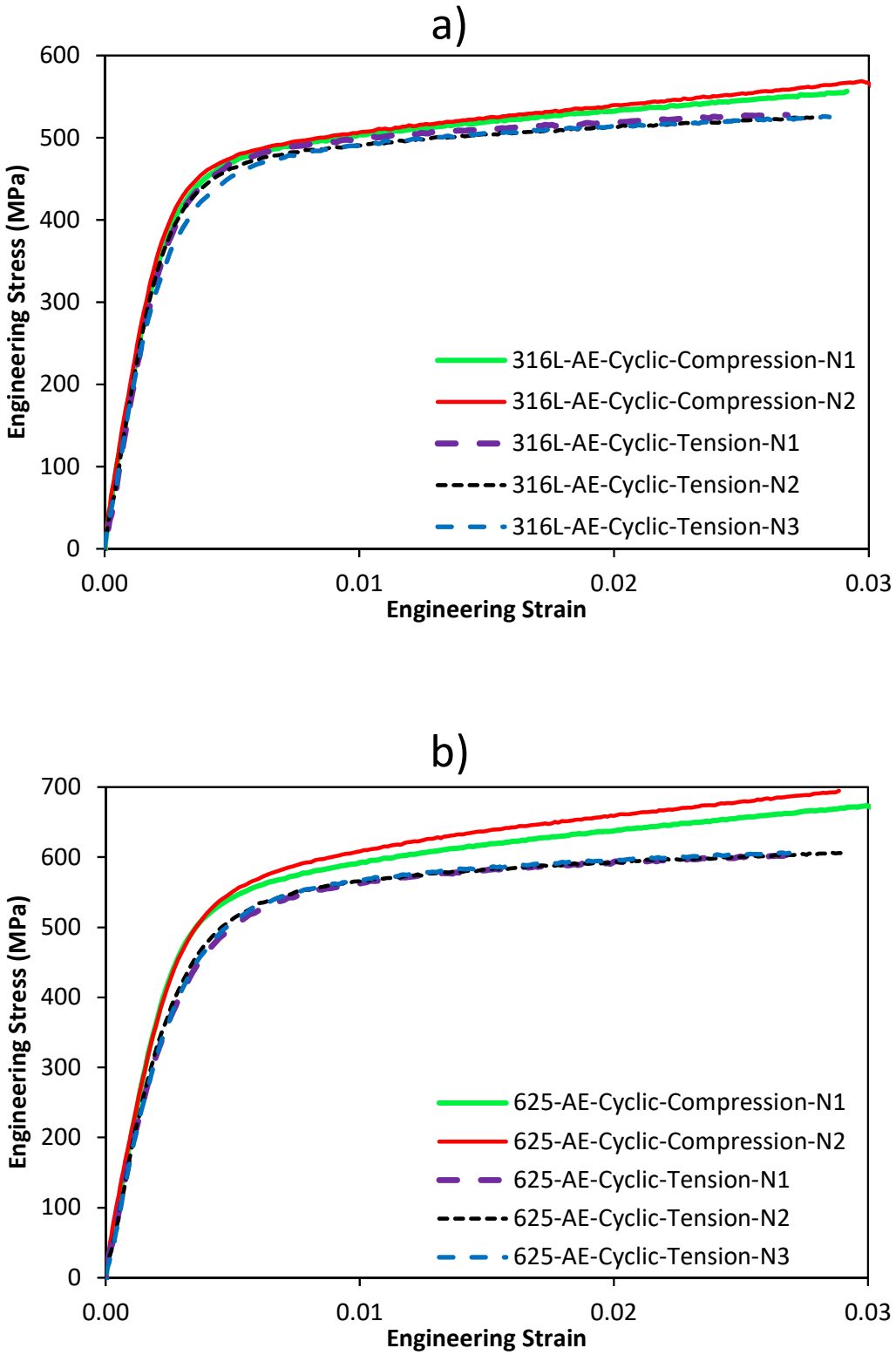


Figure 3.4: CRA Liner Stress-Strain Curves in As-Expanded Condition: (a) 316L, (b) 625

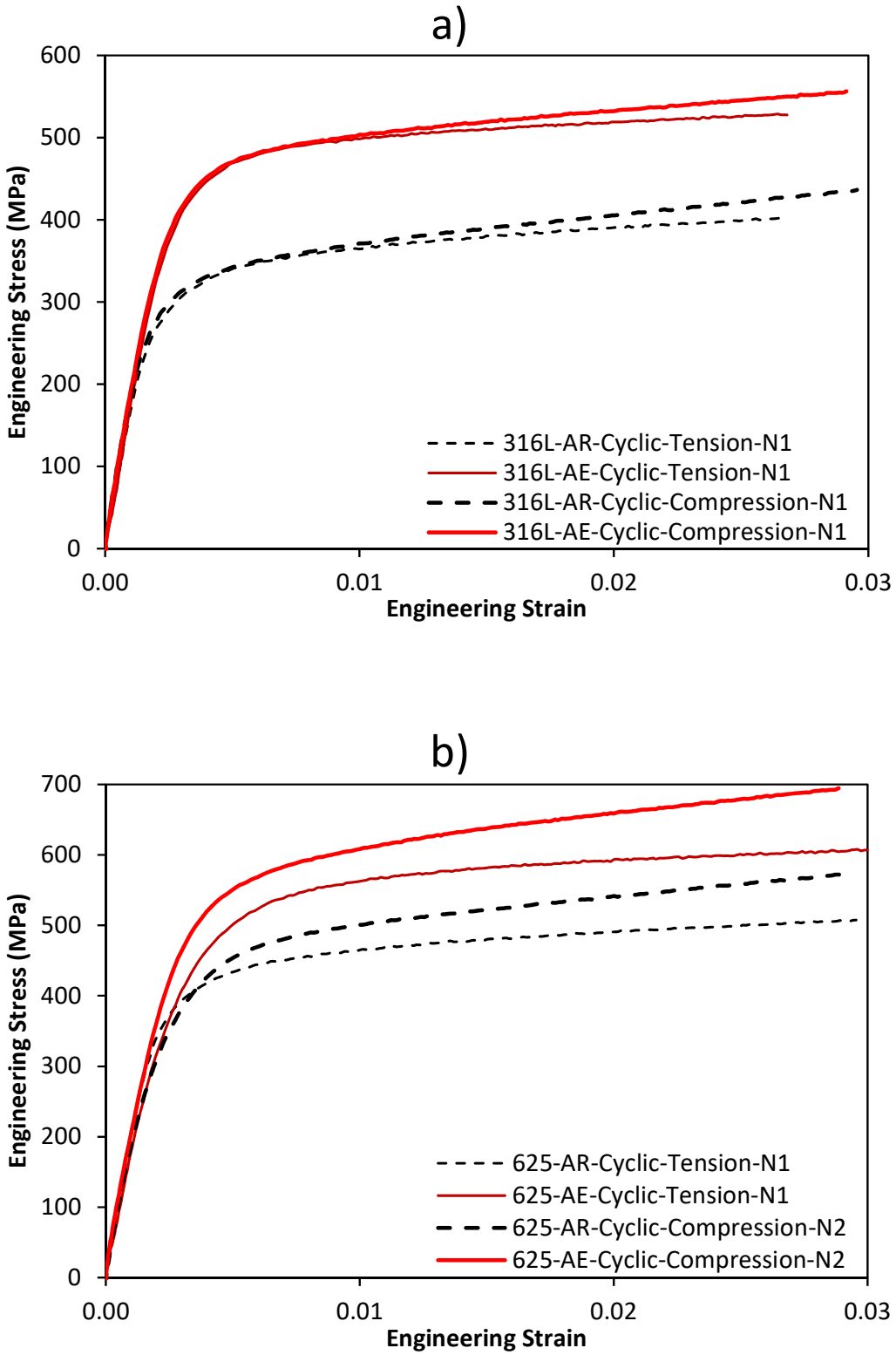


Figure 3.5: Effect of Hoop Expansion on CRA Liner Tensile Behaviour: (a) 316L, (b) 625

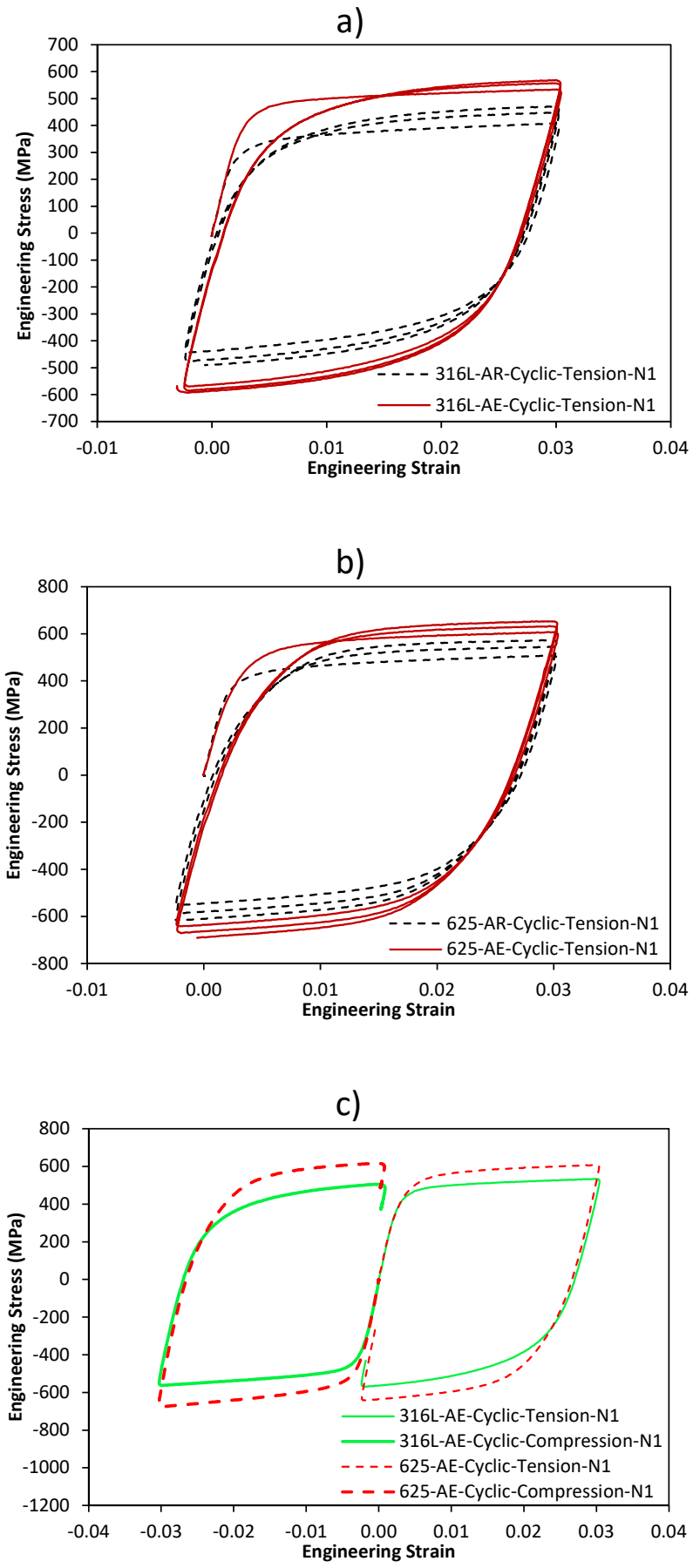


Figure 3.6: Effect of Cyclic Plastic Straining on CRA Liner Tensile Behaviour: (a) 316L, (b) 625, (c) Tension vs Compression Load Mode

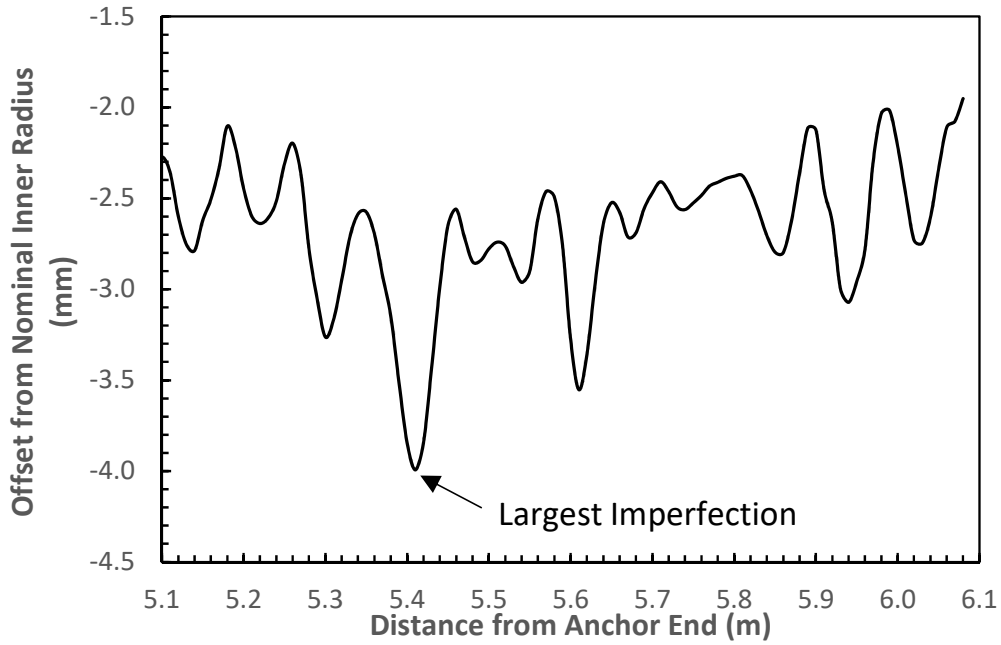


Figure 3.7: Test Pipe "10-1": Longitudinal Profile of Liner Imperfections at 9 o'clock after Bending on 6.4 m Former



Figure 3.8: Test Pipe "10-1": Bending on 5.5 m Former



Figure 3.9: Test Pipe "10-1": Onset of Liner Periodic Imperfection Mode Shape during Bending on 5.5 m Former

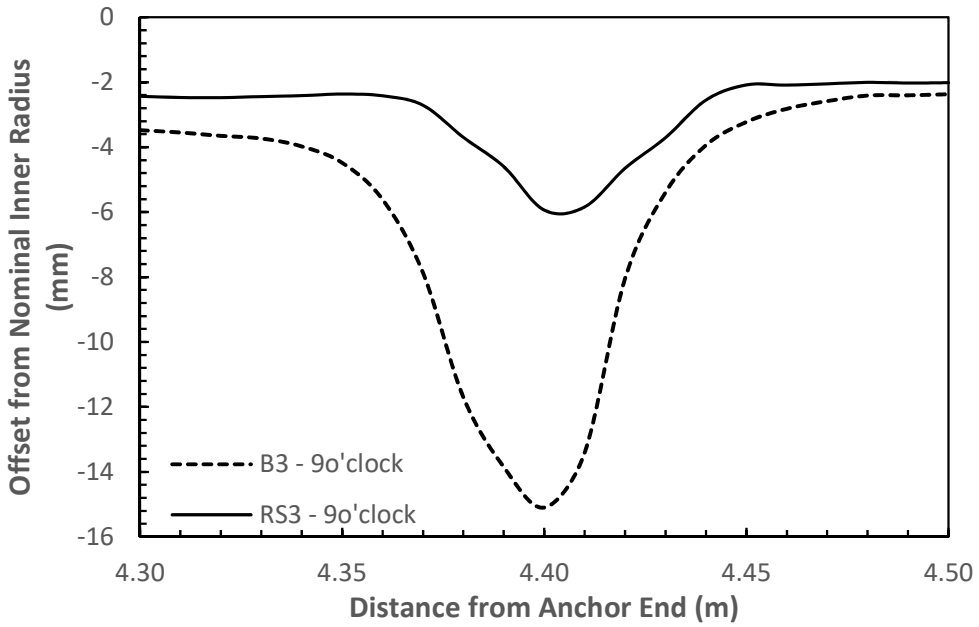


Figure 3.10: Test Pipe "10-1": Evolution of Largest Liner Imperfection during Third Bending Cycle

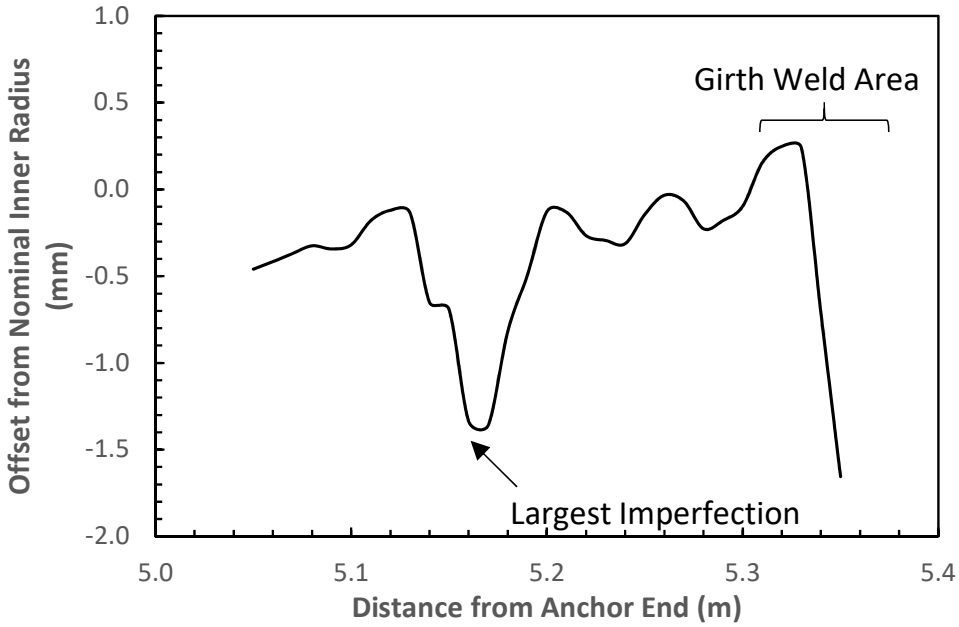


Figure 3.11: Test Pipe "10-2.GW": Longitudinal Profile of Liner Imperfections at 9 o'clock after Four Bending Cycles

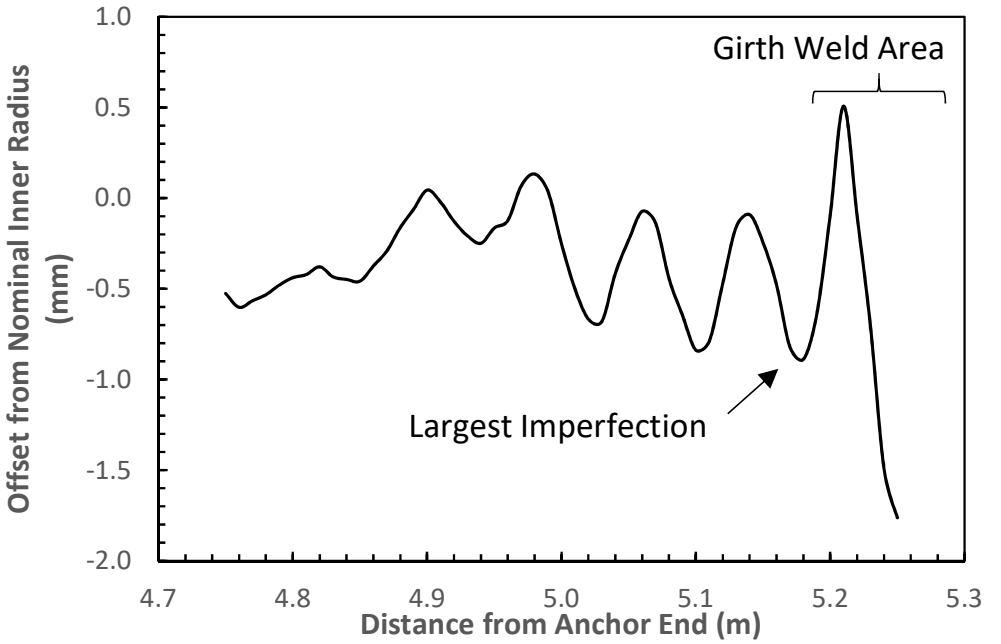


Figure 3.12: Test Pipe "10-3.GW": Longitudinal Profile of Liner Imperfections at 9 o'clock after Four Bending Cycles

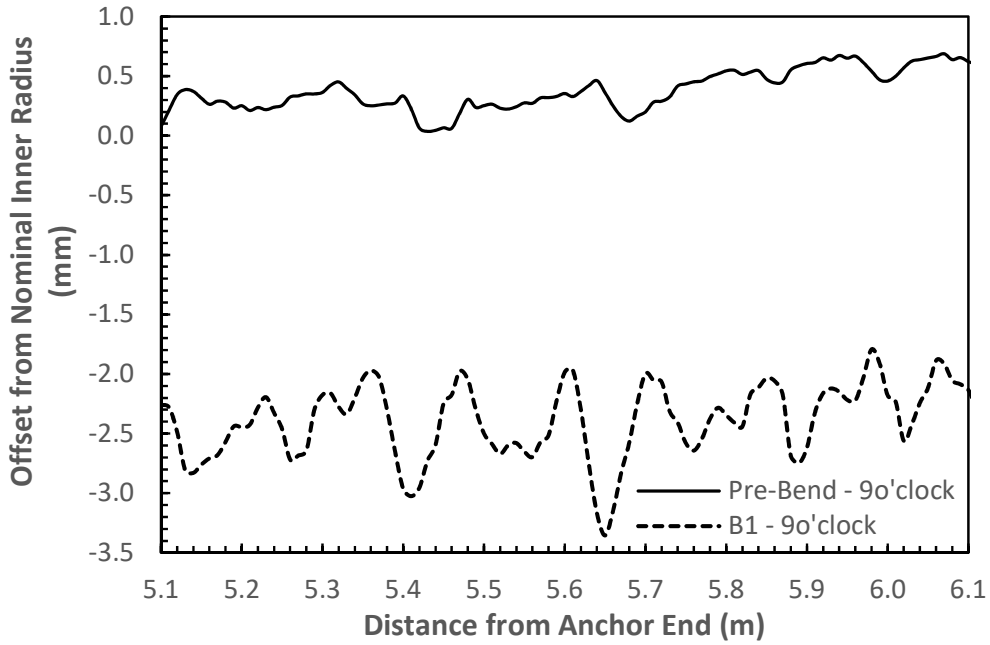


Figure 3.13: Test Pipe "12-1": Longitudinal Profile of Liner Imperfections at 9 o'clock before and after First Bending Event (on 6.4 m Former)

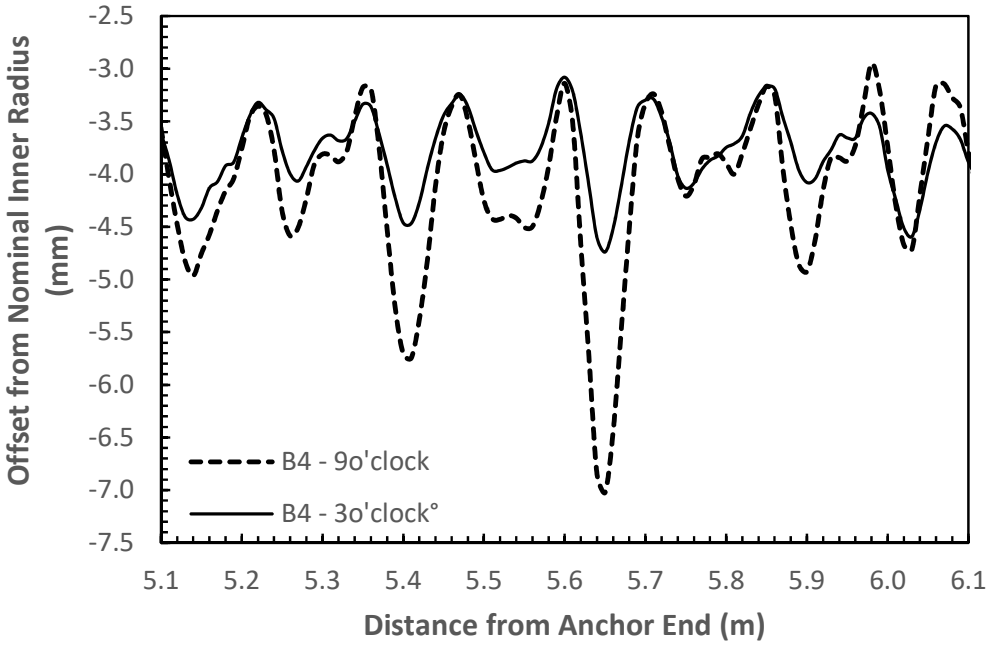


Figure 3.14: Test Pipe "12-1": Longitudinal Profile of Liner Imperfections after Fourth Bending Event (on 5.5 m Former)

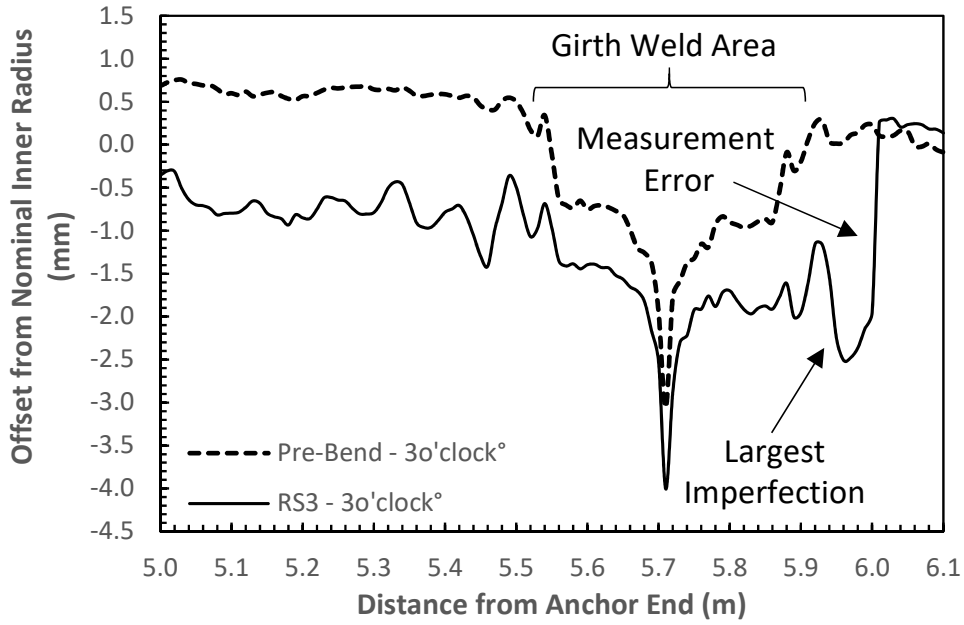


Figure 3.15: Test Pipe "12-2": Longitudinal Profile of Liner Imperfections before Test and after Third Bending Cycle

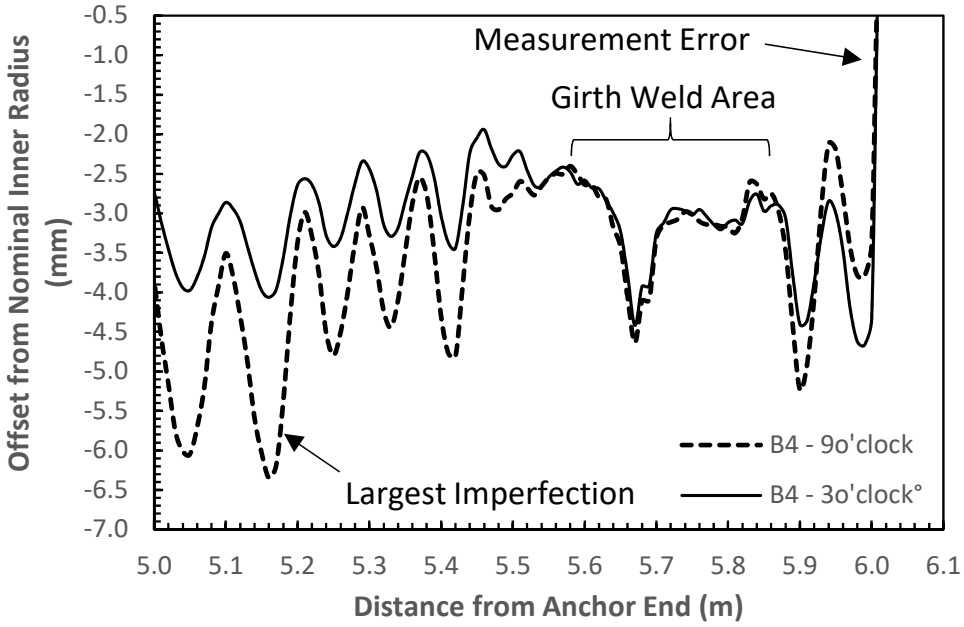


Figure 3.16: Test Pipe "12-2": Longitudinal Profile of Liner Imperfections after Fourth Bending Event (on 5.5 m Former)

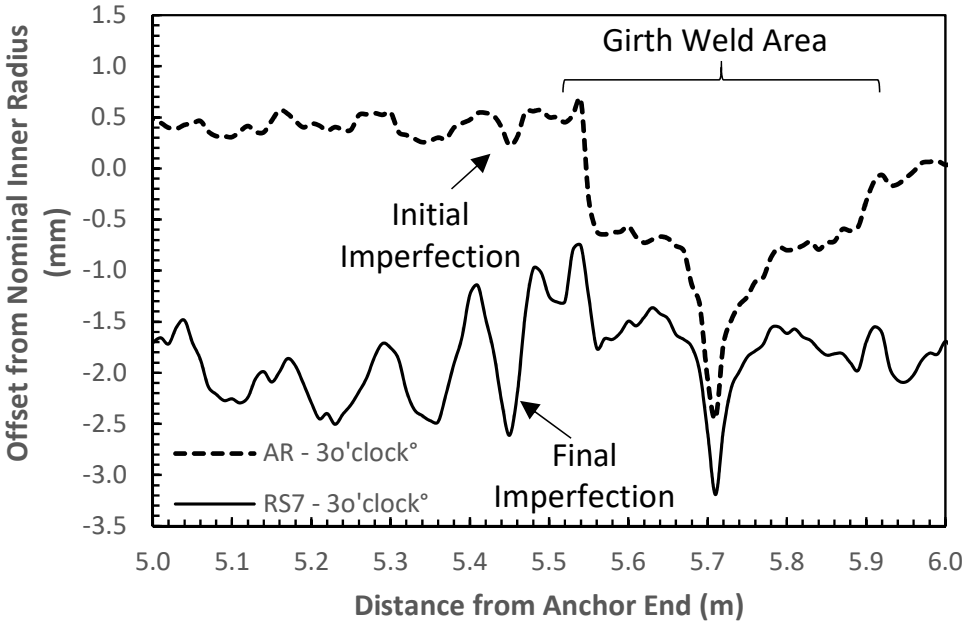


Figure 3.17: Test Pipe "12-3": Longitudinal Profile of Liner Imperfections before and after Testing

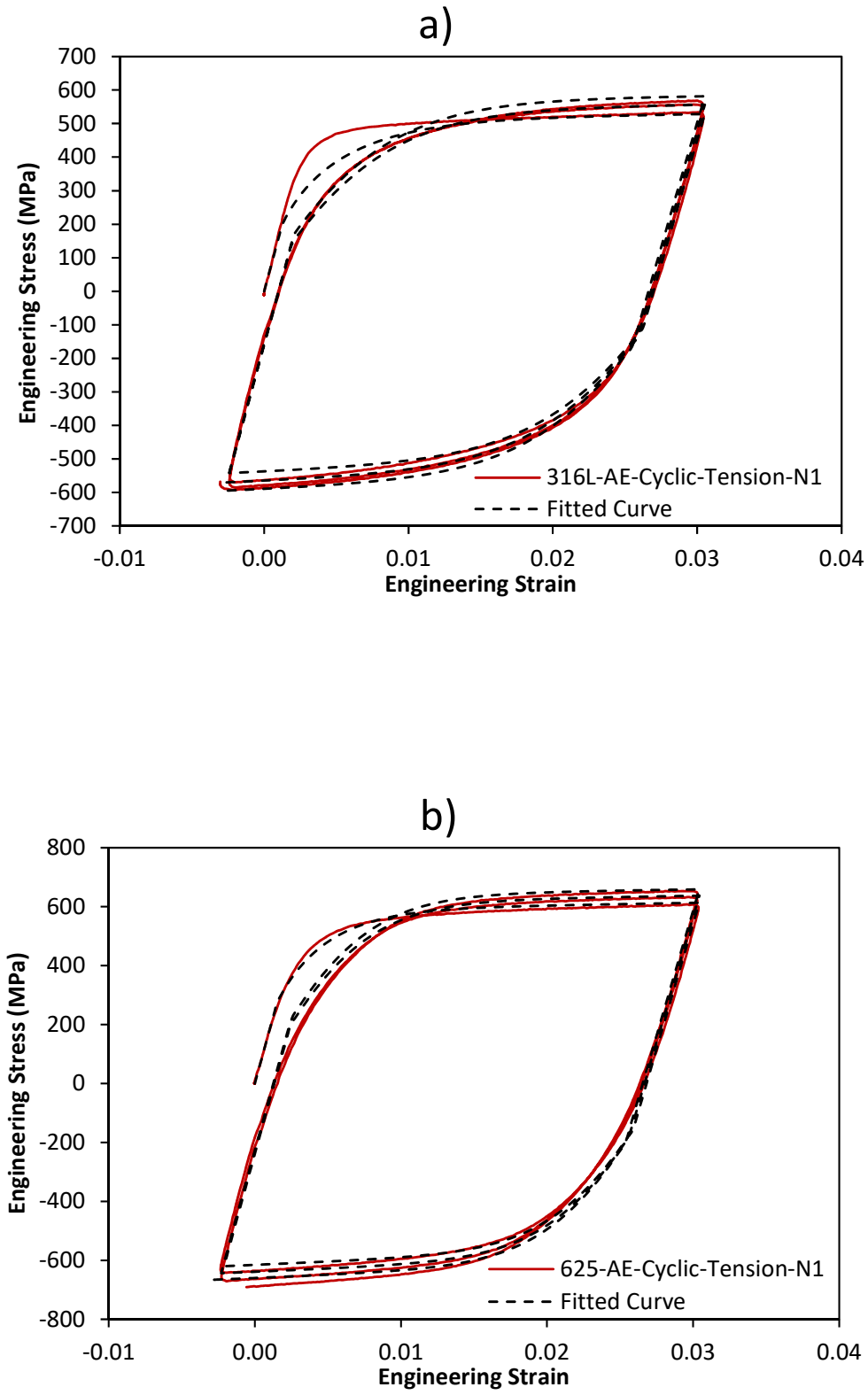


Figure 3.18: Comparison between Test Results and Numerical Prediction of Liner Behaviour during Cyclic Plastic Straining: (a) 316L, (b) 625

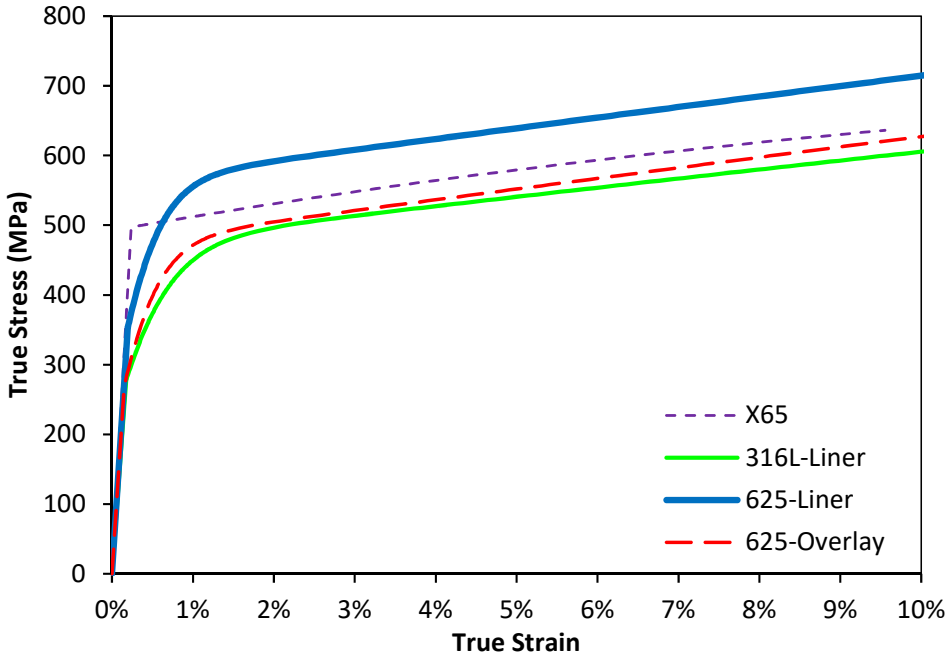


Figure 3.19: As-Received Stress-Strain Curves Used in Numerical Simulation of Bending of MLP

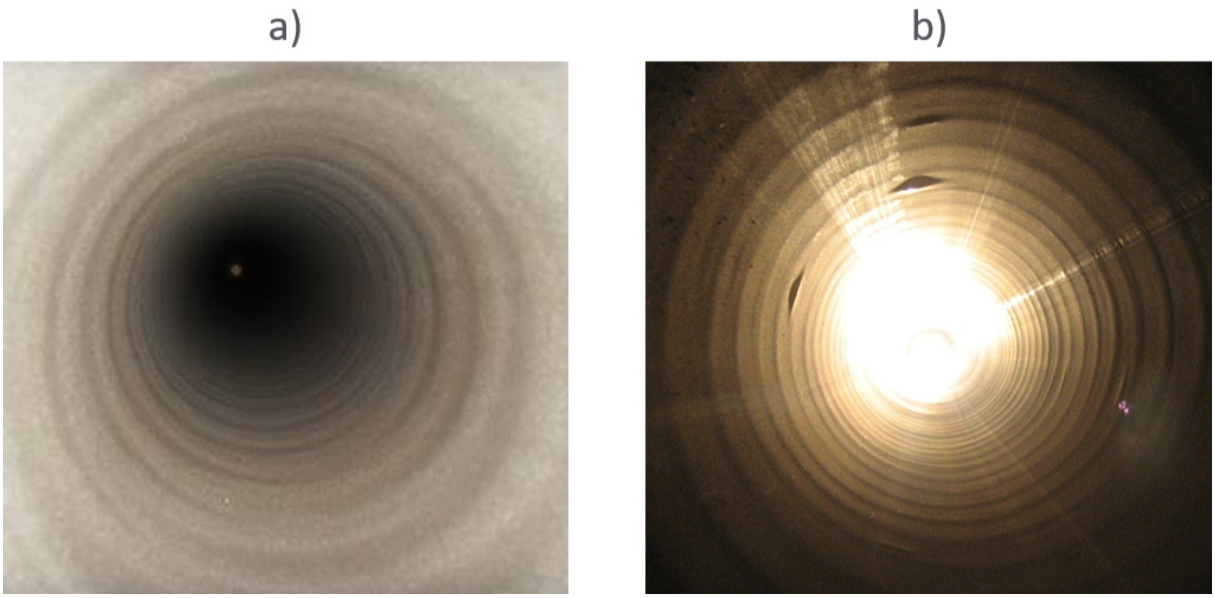


Figure 3.20: Manufacturing Imperfections in Mechanically Lined Pipe: (a) Seamless Backing Pipe Inner Surface, (b) Impressions on Liner Inner Surface

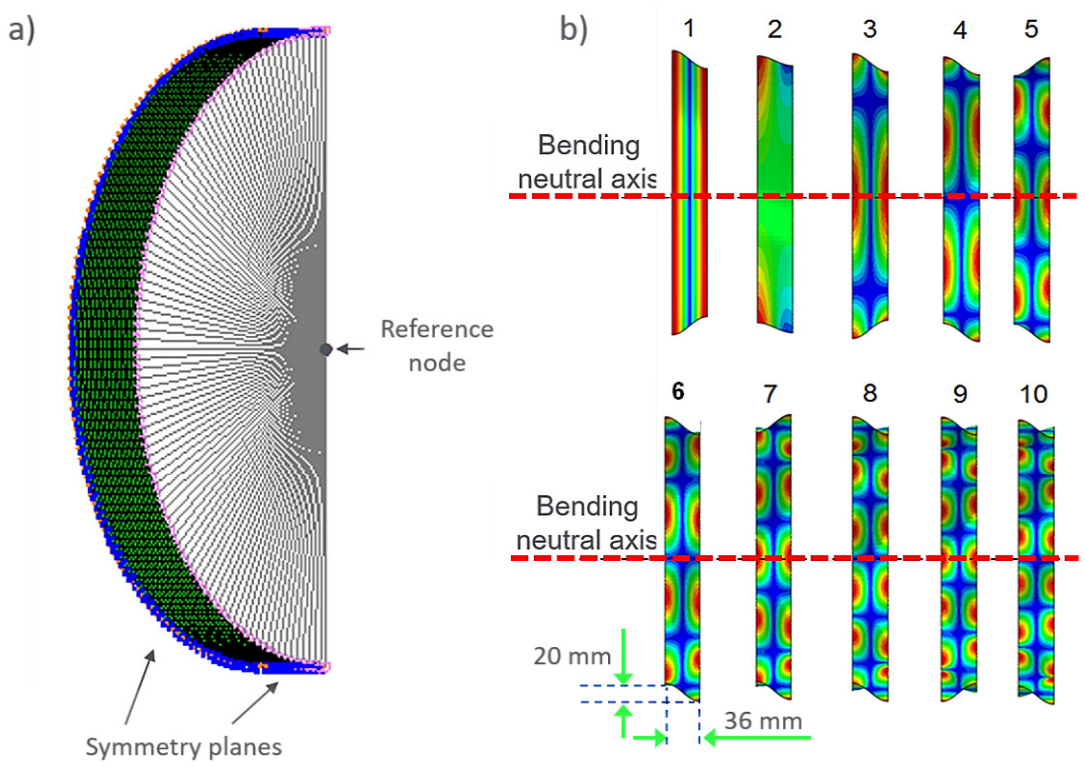


Figure 3.21: Liner Eigenmode Analysis: (a) Finite-Element Analysis Model, (b) Contour Plot of Eigenmode Radial Displacements

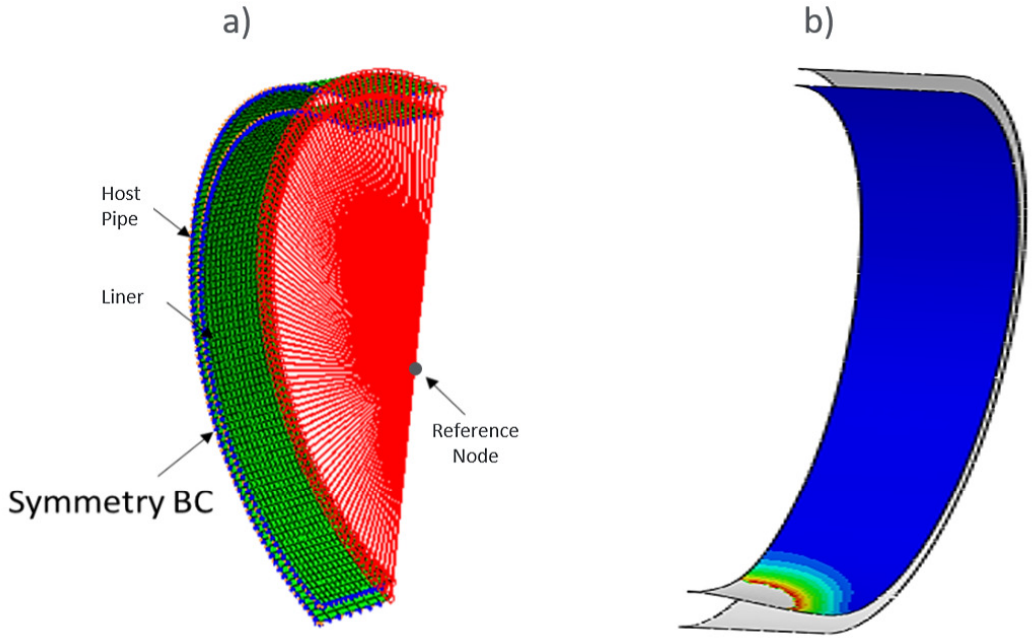


Figure 3.22: Finite-Element Analysis Model for Wrinkling Parametric Study: (a) Typical Mesh and Boundary Conditions, (b) Contour Plot of Liner Separation from Backing Pipe

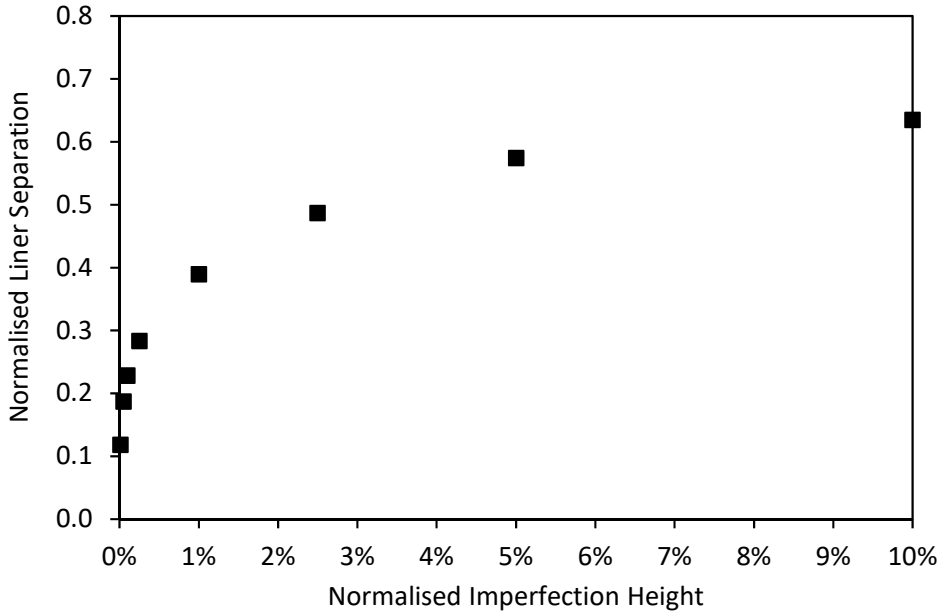


Figure 3.23: Effect of Imperfection Height on Liner Separation from Backing Pipe during Bending

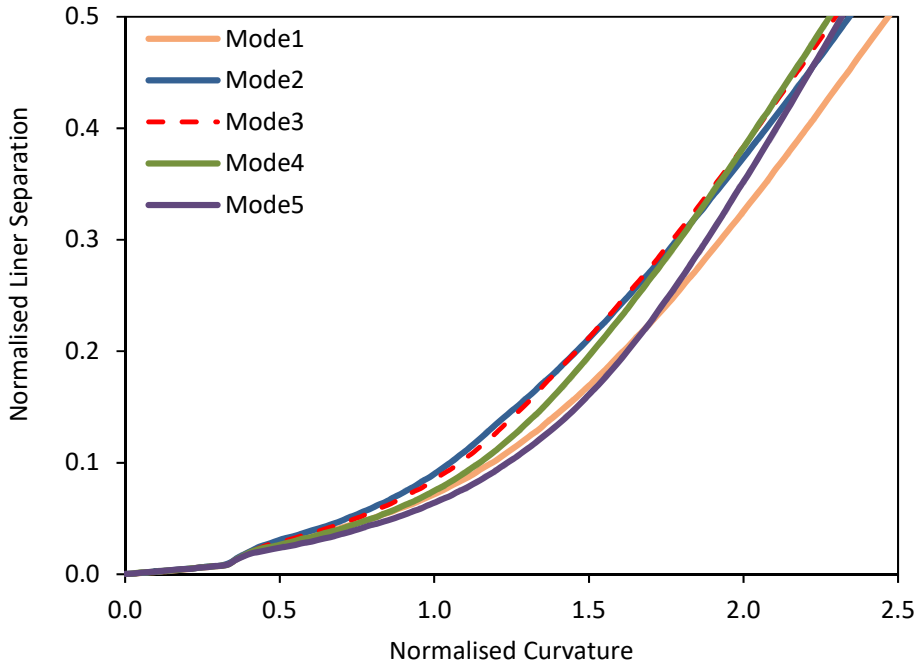


Figure 3.24: Effect of Imperfection Mode Shape on Liner Separation during Bending

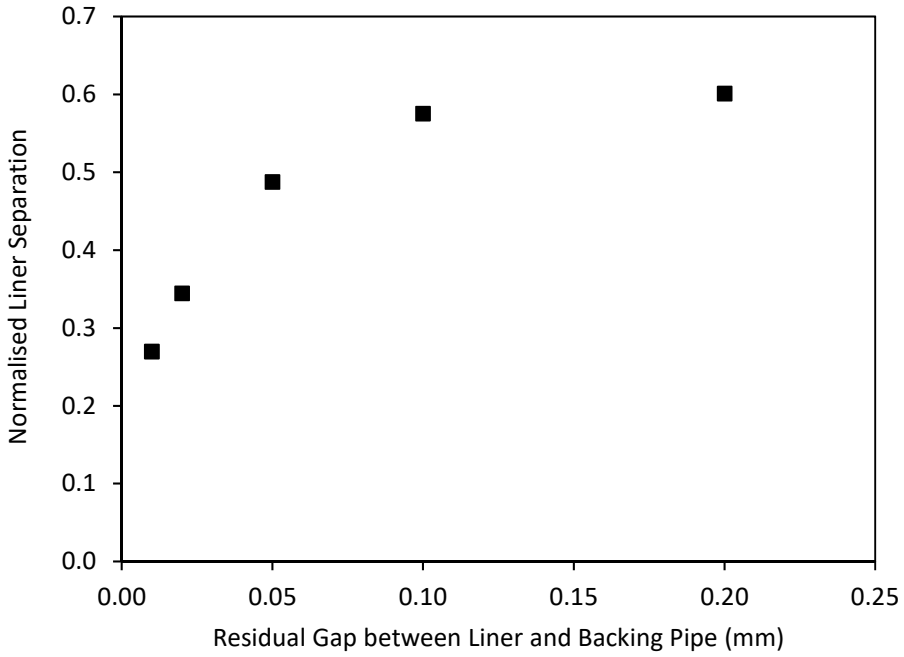


Figure 3.25: Effect of Residual Gap between Liner and Backing Pipe on Liner Separation during Bending

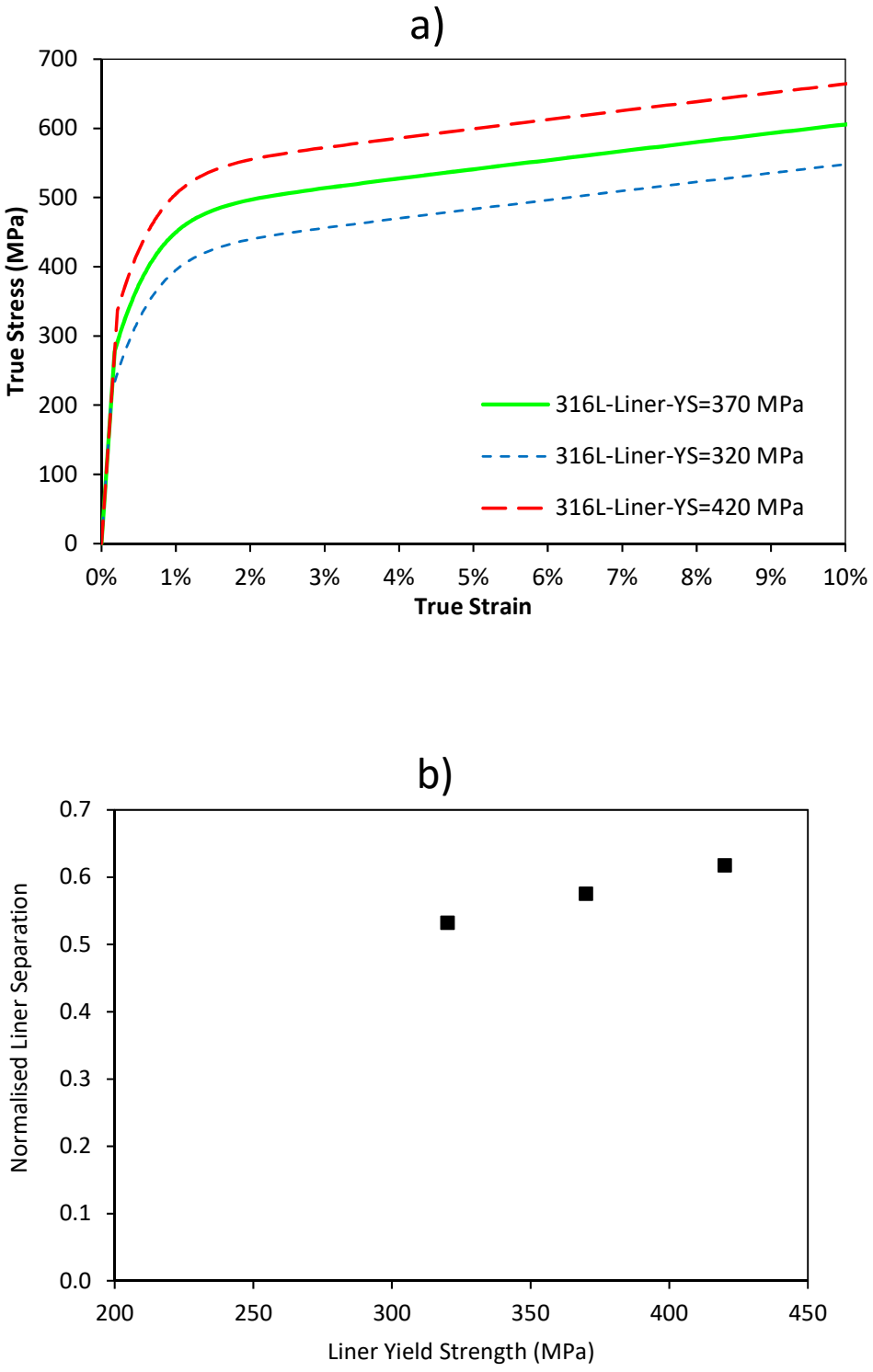


Figure 3.26: Effect of Liner Yield Strength on Liner Separation during Bending: (a) Assumed Stress-Strain Curves, (b) Liner Separation

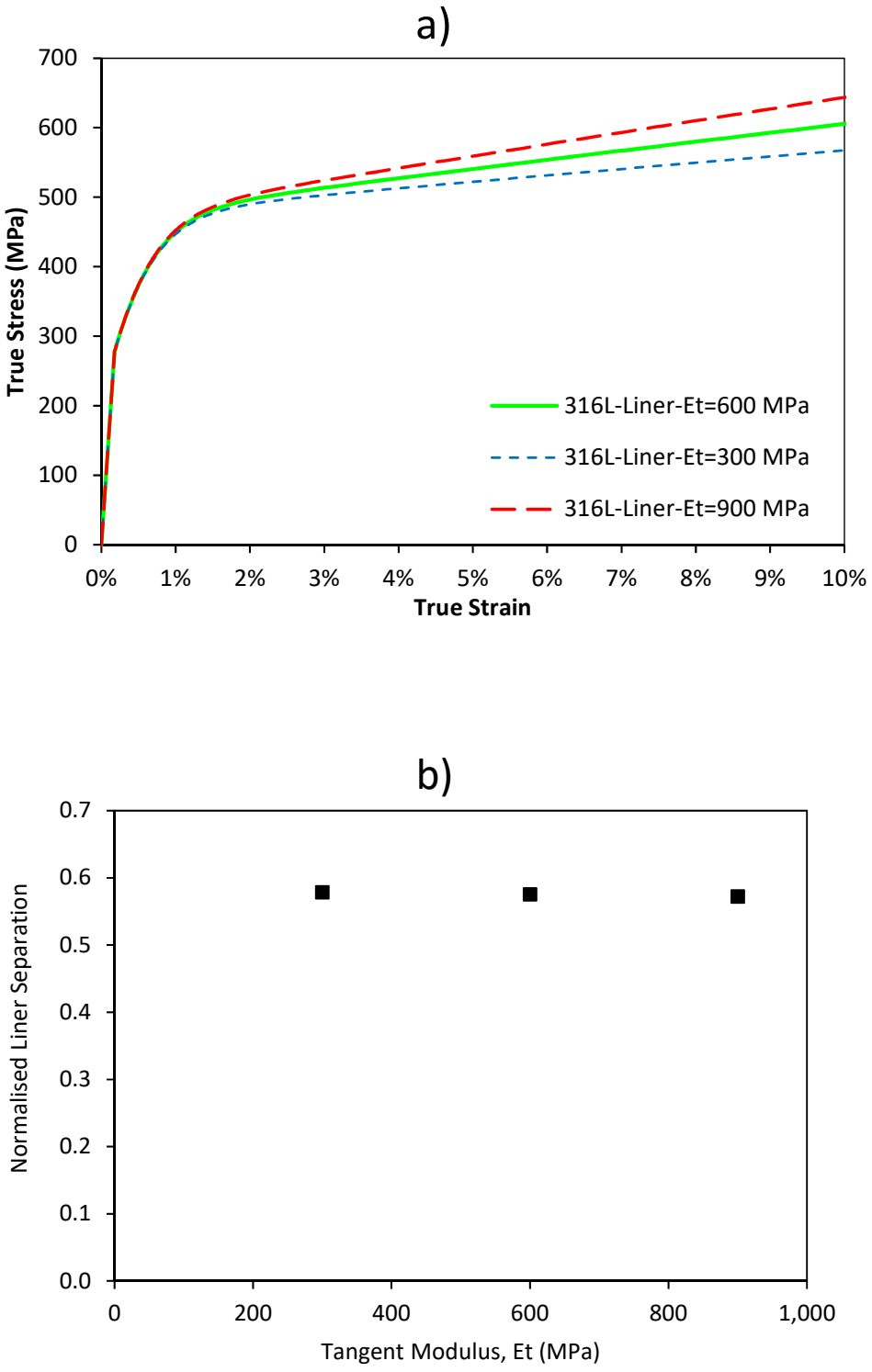


Figure 3.27: Effect of Liner Strain Hardening on Liner Separation during Bending: (a) Assumed Stress-Strain Curves, (b) Liner Separation

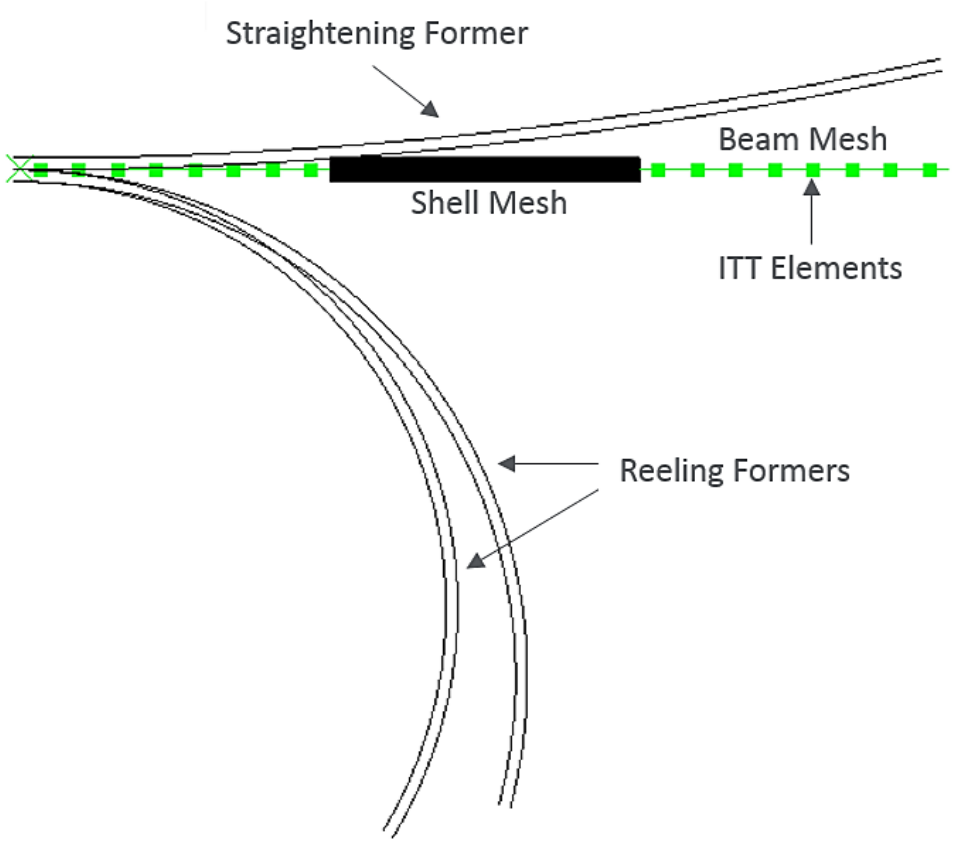


Figure 3.28: Finite-Element Analysis Model for Simulating a Bending Trial

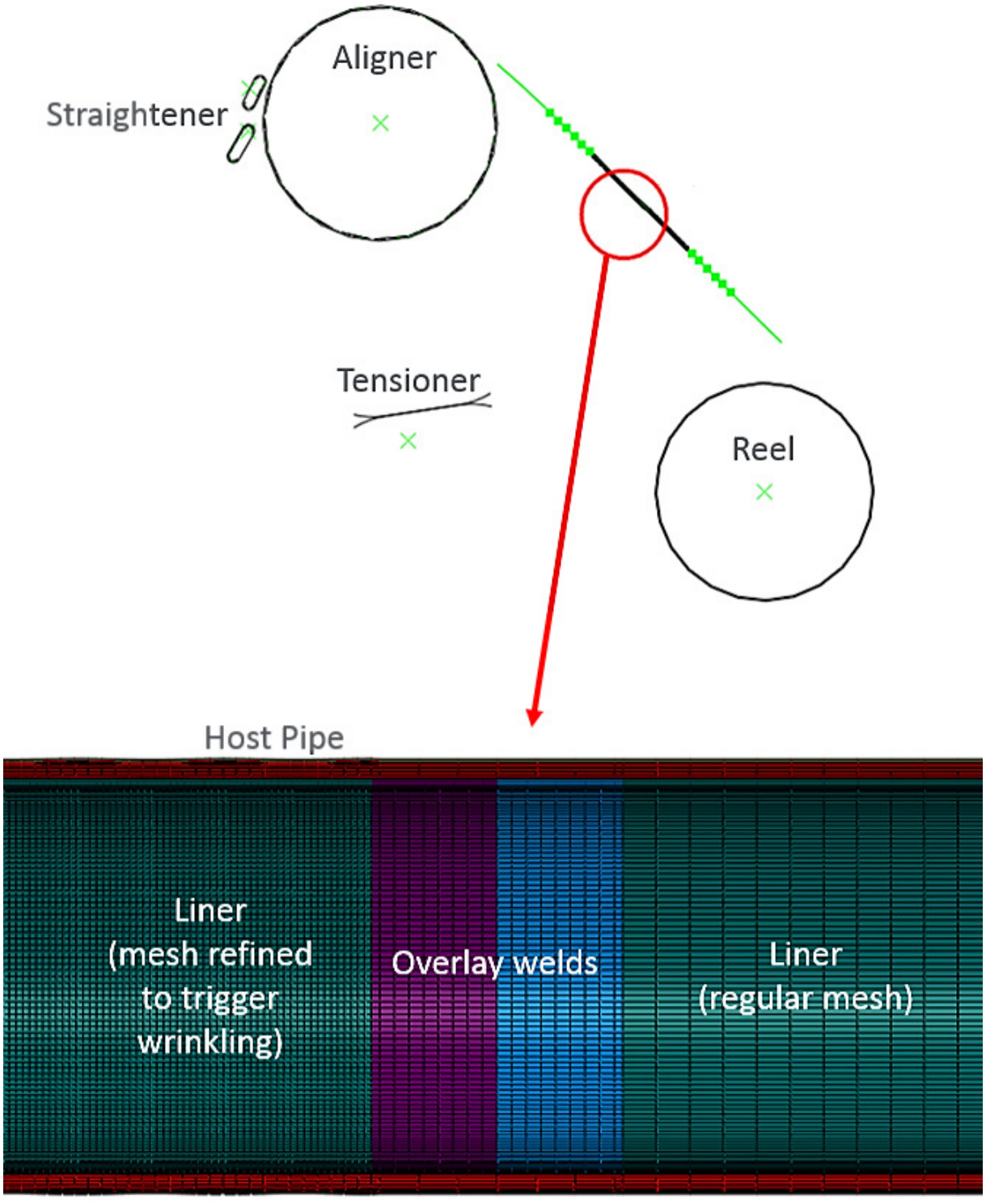


Figure 3.29: Finite-Element Analysis Model for Simulating Reel-Lay Installation: MLP Sub-model in Span between Reel and Aligner

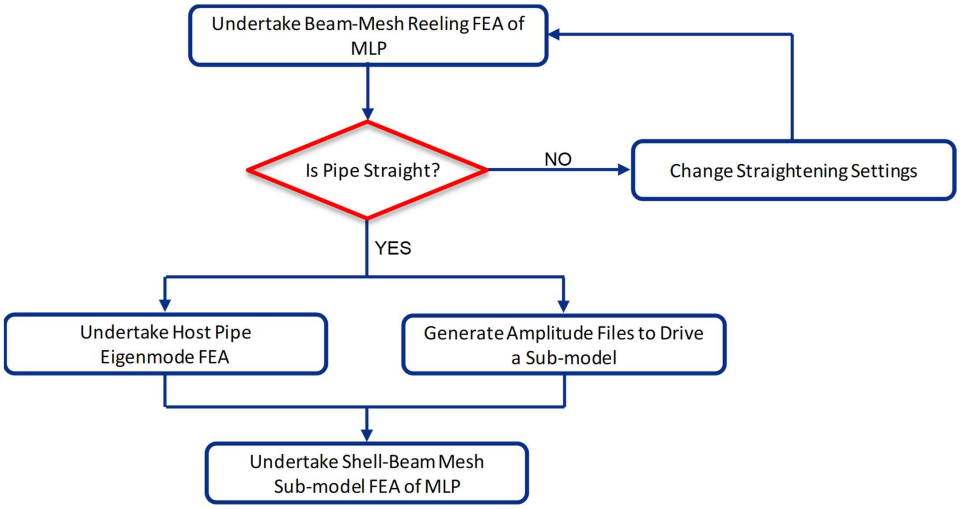


Figure 3.30: Flowchart for Finite-Element Simulation of Reel-Lay Installation of MLP

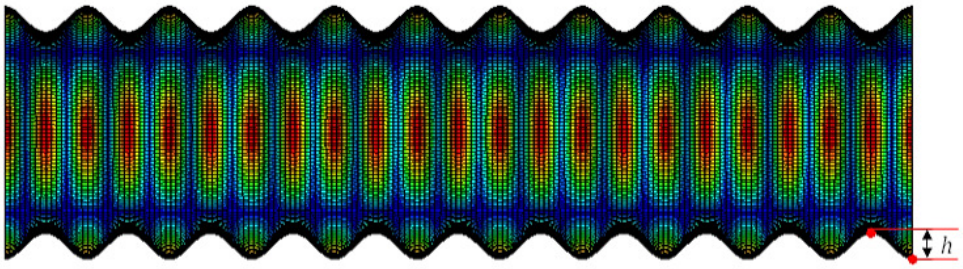


Figure 3.31: Eigenmode for Seeding Liner Imperfections in Three-Dimensional Finite-Element Analysis Model for Cyclic Plastic Bending of MLP

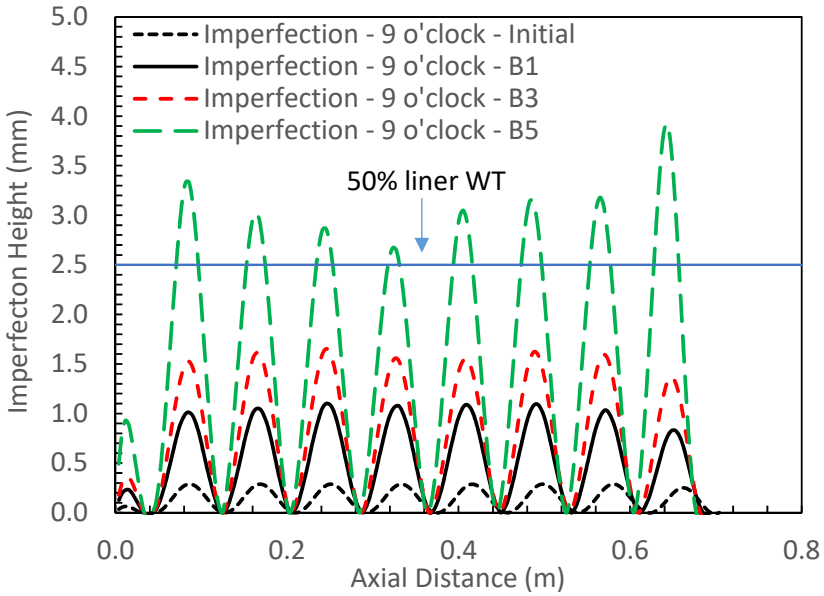


Figure 3.32: Test Pipe "10-1": Numerical Prediction of Evolution of Liner Imperfections during Cyclic Bending

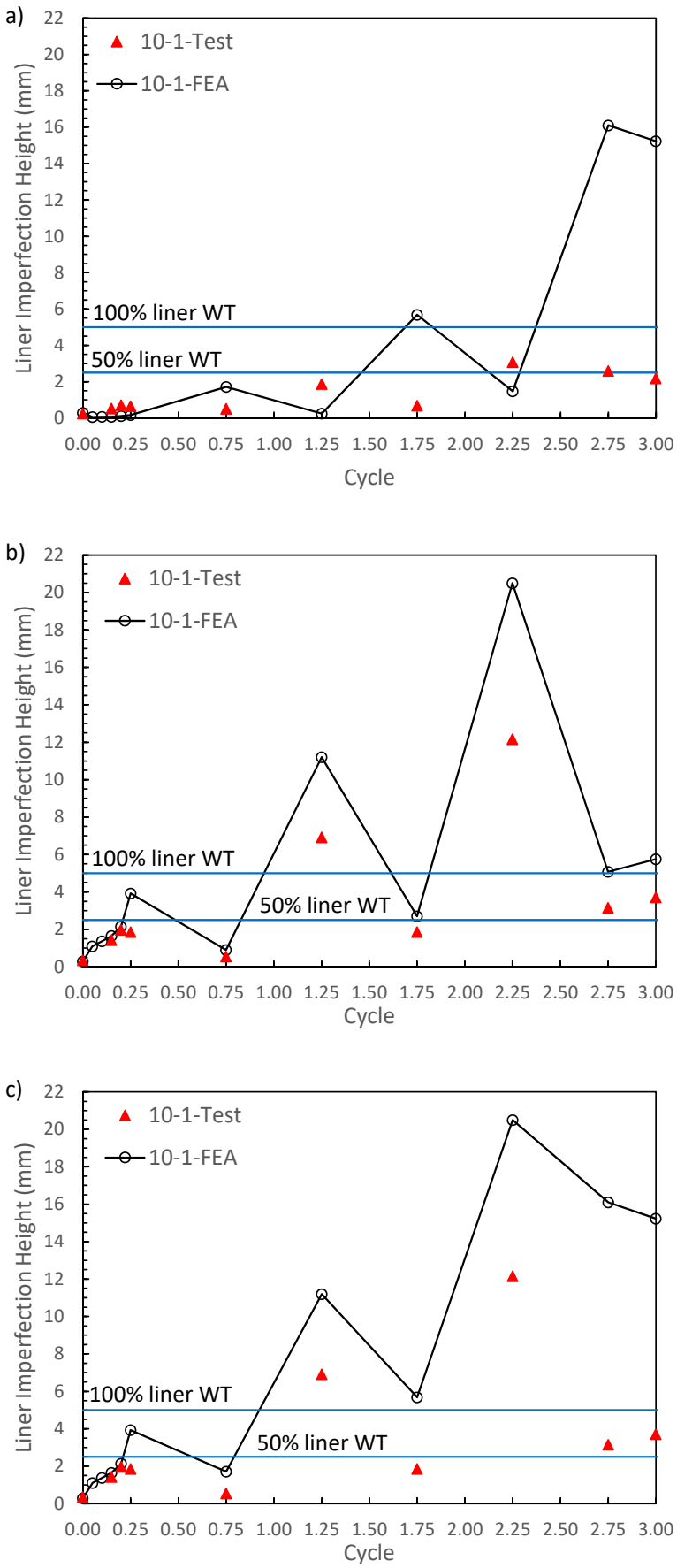


Figure 3.33: Test Pipe "10-1": Largest Liner Imperfections – Measurements vs. Numerical Predictions: (a) 3 o'clock, (b) 9 o'clock, (c) Largest Imperfection Regardless of Clock Position

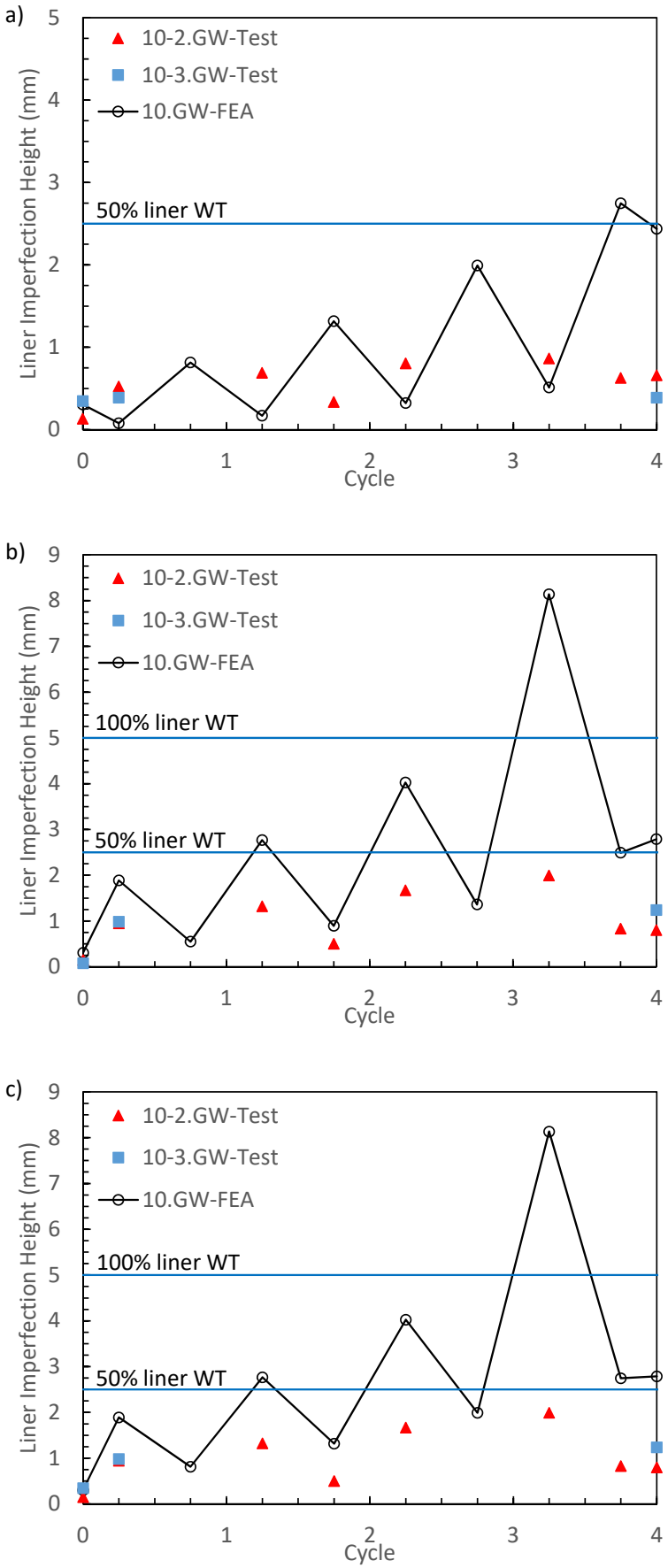


Figure 3.34: Test Pipes "10-2.GW" and "10-3.GW": Largest Liner Imperfections – Measurements vs. Numerical Predictions: (a) 3 o'clock, (b) 9 o'clock, (c) Largest Imperfection Regardless of Clock Position

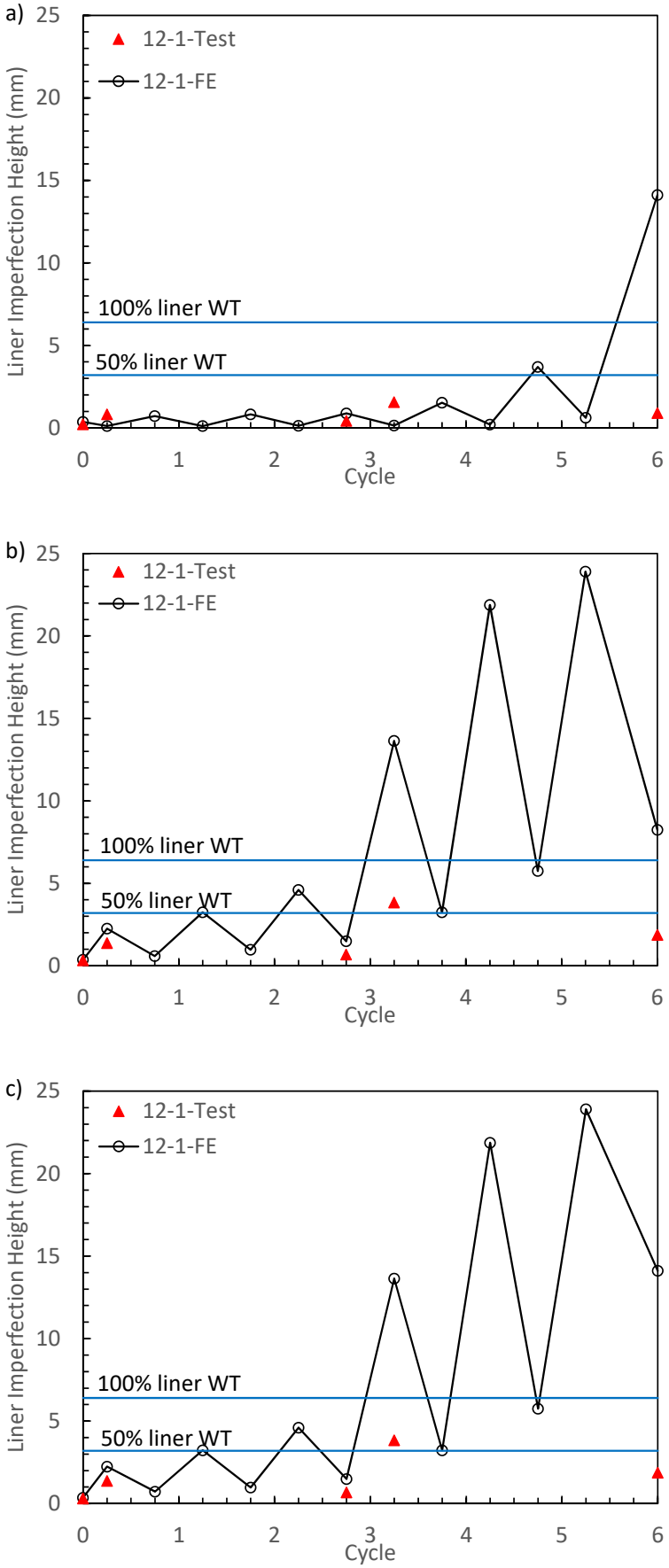


Figure 3.35: Test Pipe "12-1": Largest Liner Imperfections – Measurements vs. Numerical Predictions: (a) 3 o'clock, (b) 9 o'clock, (c) Largest Imperfection Regardless of Clock Position

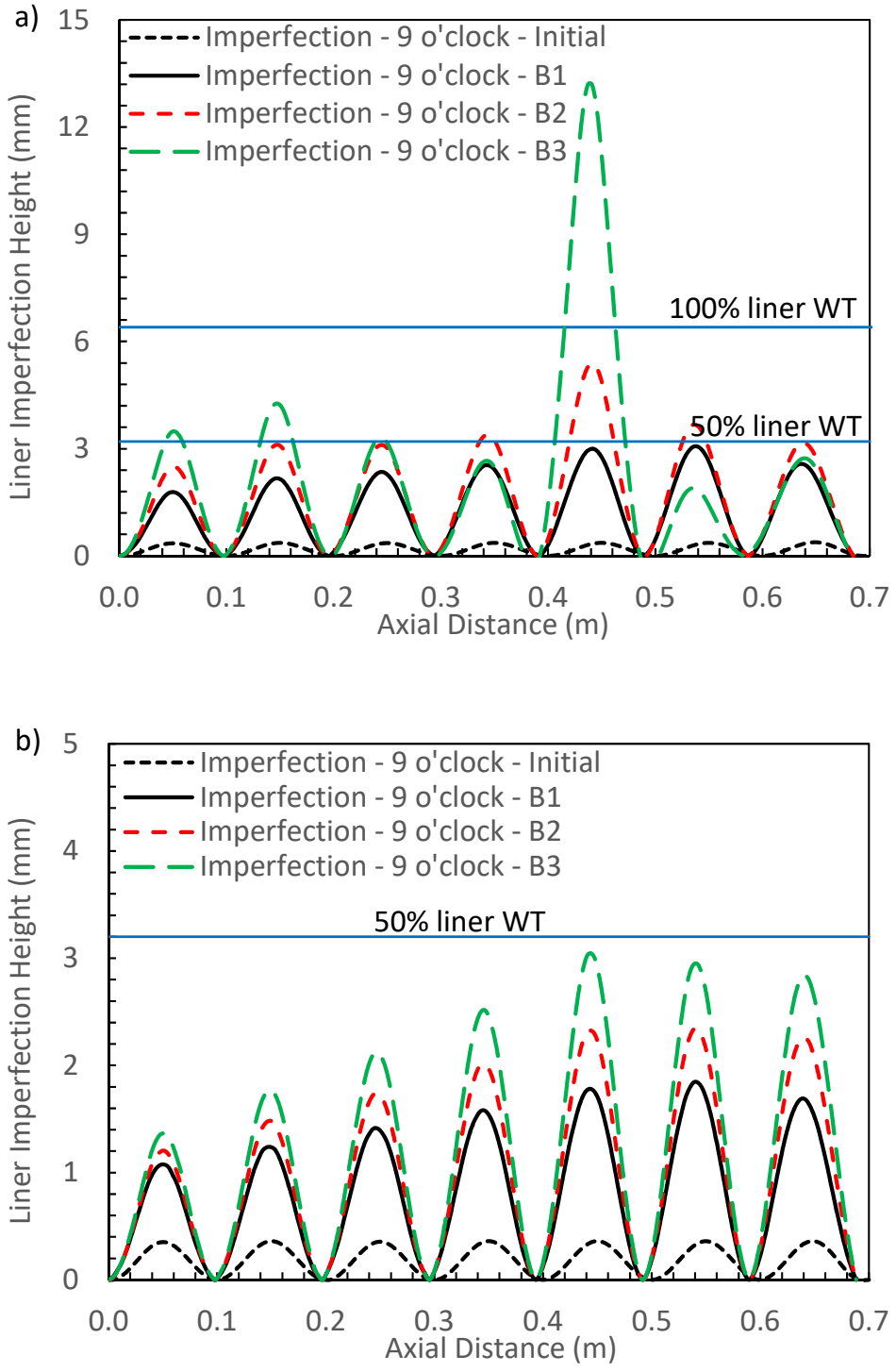


Figure 3.36: Numerical Prediction of Evolution of Liner Imperfections during Cyclic Bending: (a) Test Pipe "12-2.GW", (b) Test Pipe "12-3.GW"

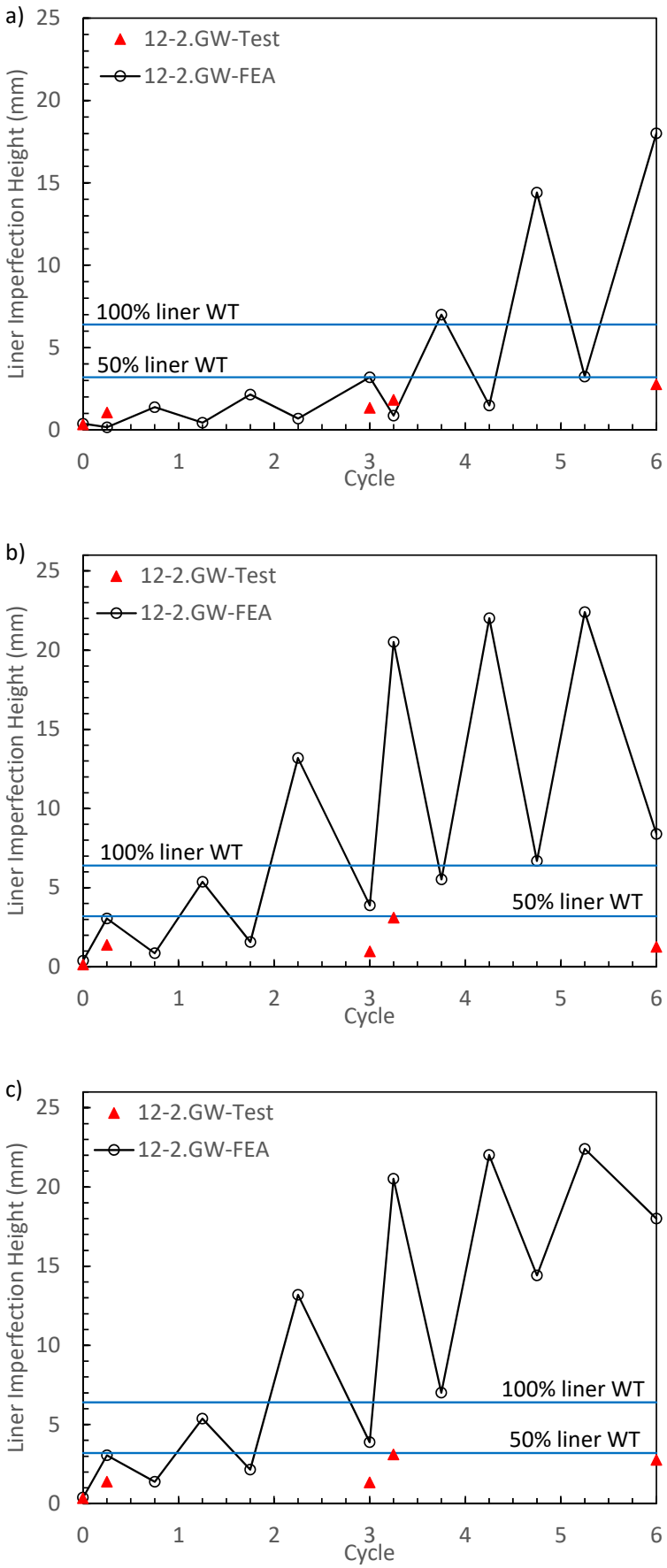


Figure 3.37: Test Pipe "12-2.GW": Largest Liner Imperfections – Measurements vs. Numerical Predictions: (a) 3 o'clock, (b) 9 o'clock, (c) Largest Imperfection Regardless of Clock Position

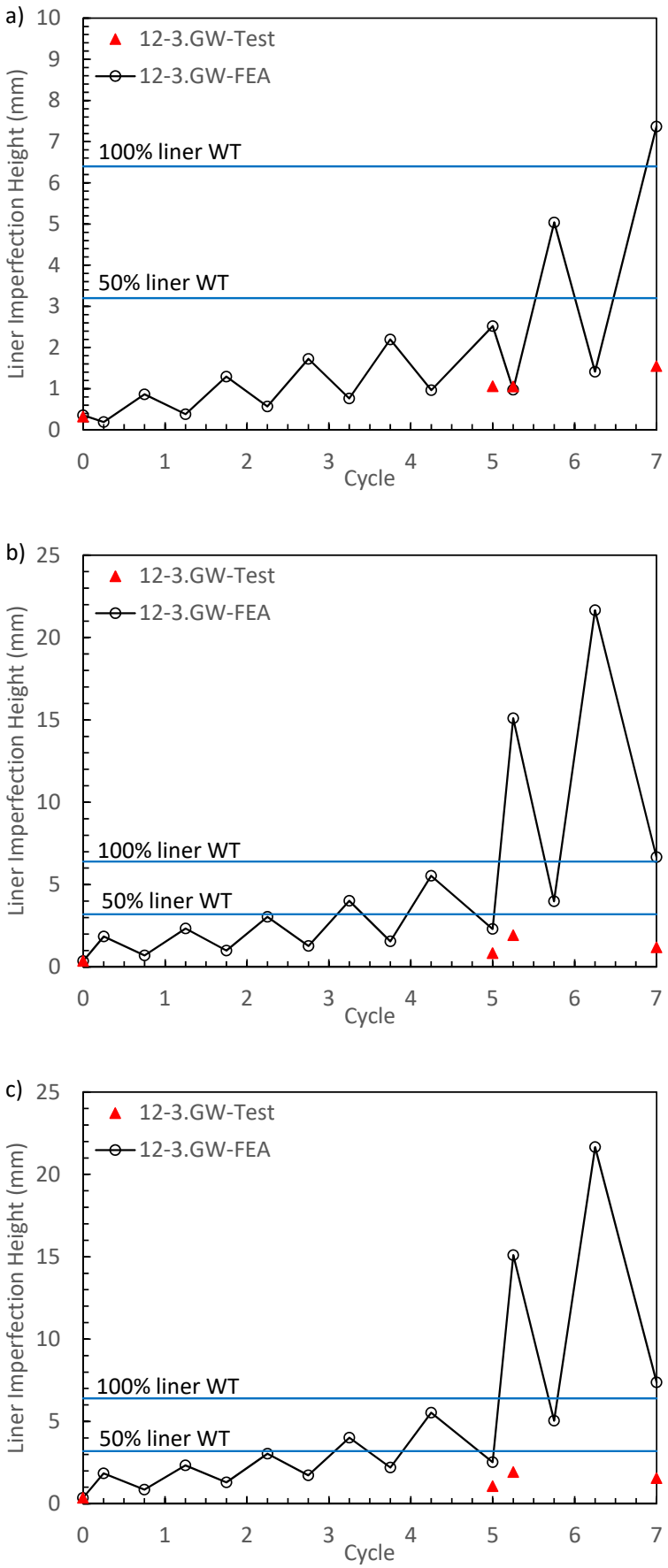


Figure 3.38: Test Pipe "12-3.GW": Largest Liner Imperfections – Measurements vs. Numerical Predictions: (a) 3 o'clock, (b) 9 o'clock, (c) Largest Imperfection Regardless of Clock Position

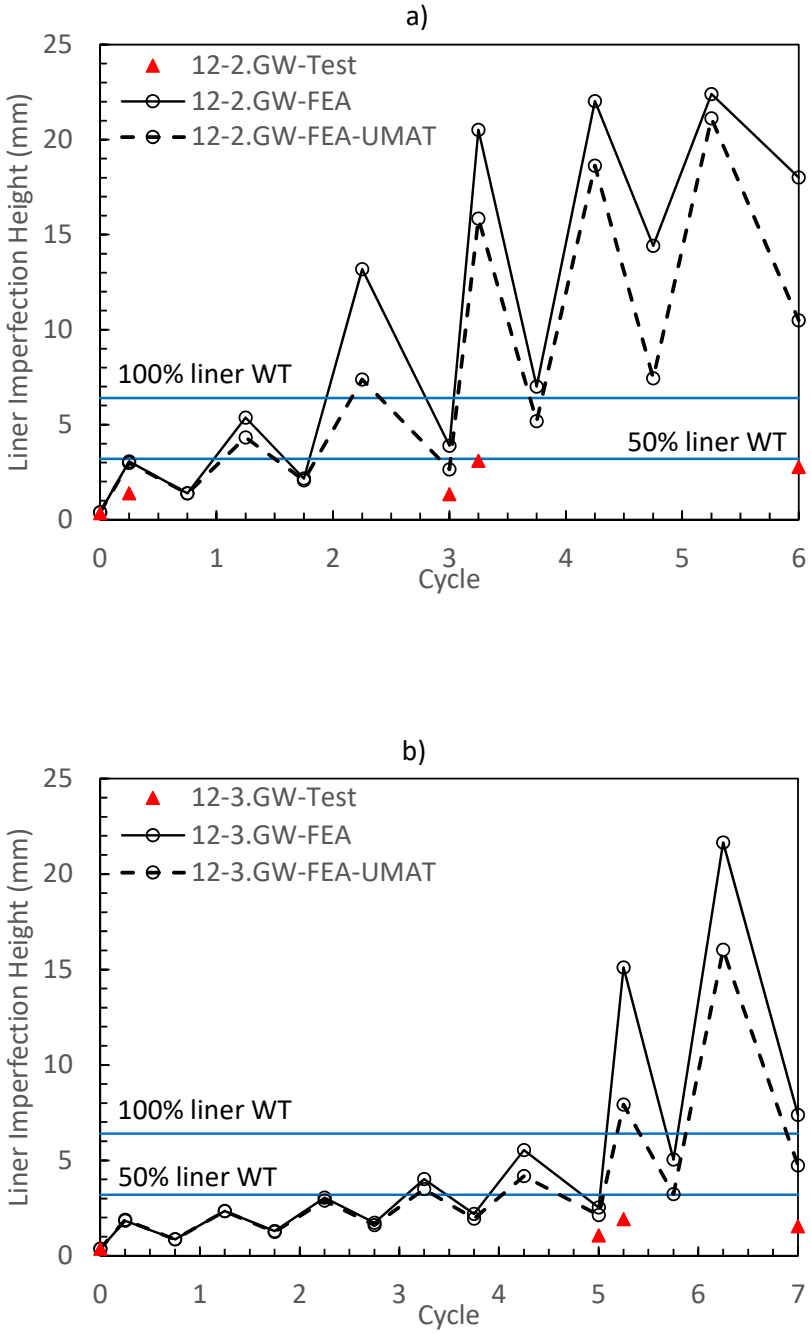


Figure 3.39: 12" Test Pipes: Largest Liner Imperfections – Measurements vs. Numerical Predictions with von Mises and Martinez *et al.* Yield Criteria: (a) "12-2.GW", (b) "12-3.GW"

Chapter 4

Guideline for Design Against Fracture of Mechanically Lined Pipe Welds

4.1 Introduction

This chapter aims at providing guidance for the fracture assessment of planar flaws in subsea mechanically lined pipelines. While such pipelines are subjected to displacement-controlled conditions during reeling, they may experience load or displacement-controlled conditions during subsea operation. As the latter are less onerous than the former, load-controlled conditions are investigated in this work. Furthermore, since subsea mechanically lined pipelines often convey fluids that are not bio-degradable, leakage is regarded as failure. Consequently, only local limit load solutions which relate to the collapse of a ligament are considered. Moreover, as it is likely that the girth weld in a mechanically lined pipeline may undermatch the parent metal, both even/over-match and undermatch scenarios are investigated.

Unlike surface breaking flaws, embedded flaws include two ligaments, i.e. two crack propagation and collapse initiation sites. Furthermore, while accurate solutions are available for the assessment of surface breaking flaws in evenmatch pipeline girth welds (ref. Sec. 2.3.2), the solutions available for the fracture assessment of embedded flaws are so conservative that they are not used currently (ref. Sec. 2.3.2). In Sec. 4.2 new solutions are proposed for the frac-

ture assessment of the shorter ligament of an embedded flaw in an evenmatch girth weld. At the onset of collapse of this ligament the embedded flaw is converted into a surface breaking flaw, which is then assessed using available solutions. Subsequently, after proving that cyclic plastic straining associated to reeling does not degrade the fracture toughness of undermatch girth welds representative of mechanically lined pipelines, the range of application of analytical solutions proposed for the assessment of surface breaking flaws in undermatch girth welds is expanded and extended to embedded flaws in Sec. 4.3. Finally, recommendations are made in Sec. 4.4 for the design of mechanically lined pipeline welds against fracture.

4.2 Fracture Assessment of Embedded Flaws in Evenmatch Girth Welds

4.2.1 Objective

The aim of this work is to provide new fracture assessment solutions for the shorter ligament of embedded flaws in evenmatch pipeline girth welds. Following collapse of this ligament the embedded flaw is reclassified as a surface breaking flaw, which is then assessed using available solutions. Here, an embedded flaw is defined by its length, $2c$, height, $2a$, its shorter ligament with associated length (embedment depth), p^A, and crack tip, 'A', and its longer ligament with associated length, p^B, and crack tip, 'B', as shown in Fig. 4.1.

First, a three-dimensional parametric finite-element study is carried out to assess the effect of p^A, $2a$ and $2c$ on the load required to cause collapse of the shorter ligament of an embedded flaw subjected to tension. The tension load mode is preferred to bending because it provides a conservative representation of the loading experienced by the pipeline wall during reeling. A closed form limit load solution is then fitted to the numerical results, and compared against available solutions for pipes subjected to tension. Subsequently, a J-based crack driving force estimation scheme is derived for a selected material behaviour. Fracture tests are then undertaken, to verify suitability of the proposed limit load solution. Finally, recommendations are made for the fracture assessment of subsea pipeline girth welds with embedded flaws.

4.2.2 Limit Load Analysis

Available Limit Load Solutions

R6 [103] provides a comprehensive set of local and global limit load solutions for various load modes. However, only a local solution for a pin-loaded tension load mode is considered in this work, because it explicitly deals with the collapse of the shorter ligament of length p^A

$$P_L^{R6} = \frac{\left(1 - \frac{2\alpha'''}{1-2k}\right)(1+\psi)}{\left(1 - \frac{2\alpha'''}{1-2k}\right) + \psi} P_0 \tag{4.1}$$

where $\alpha''' = a/t$, $\psi = c/t$ and

$$k = \frac{1}{2} - \frac{p^A + a}{t} \tag{4.2}$$

Under a tension load mode, the BS7910 recommended Willoughby and Davey limit load solution in Eq. 2.28 can be re-written as

$$P_L^{BS} = \frac{(1-\alpha'')^2 + 4p^A\alpha''/t'}{\alpha'' + (1 - 2\alpha'' + 4p^A\alpha''/t')^{0.5}} P_0 \tag{4.3}$$

The suitability of these limit load solutions for the assessment of embedded flaws in pipeline girth welds is investigated in a subsequent section.

Analysis Approach

A parametric FE study is carried out to quantify the effect of p^A, $2a$ and $2c$ on the load required to cause collapse of the ligament of length p^A. Plastic collapse is assumed to occur when the plastic zone initiating from crack tip 'A' reaches the pipe surface, see Figure 4.2. Subsequently, a closed form limit load solution is fitted to the numerical results.

Pipe and Crack Geometry

A pipe with outer diameter $D = 12.75$" (323.9 mm) and wall thickness $t = 21.4$ mm is analysed. The normalised embedment depth, p^A/a, in the range between 0.5 and 9.0, the normalised crack height, $2a/t$, in the range between 0.05 and 0.40 and the normalised crack length, $2c/W$, in the range between 0.02 and 0.10, which are typical of flaw sizes assessed in an ECA, are investigated. In total, 36 crack geometries are considered, as detailed in Table 4.1.

Flow Behaviour

An elastic-perfectly plastic stress-strain response with the Young's modulus, $E = 210$ GPa and yield strength, $\sigma_y = 500$ MPa, is assumed in the limit load study.

Finite-Element Analysis

The parametric study of stationary cracks is carried out with the FEA model shown in Figure 4.3. Due to symmetry, only a quarter model of the pipe is built with appropriate boundary conditions. The model length is three times the pipe outer diameter. Up to 50,000 eight-node first order solid elements with reduced integration (C3D8R in ABAQUS [47]) are used to model a pipe with an elliptical part-circumferential embedded flaw. Both crack tip regions in Fig. 4.3 have a focused mesh composed of 5 to 7 rings and 17 to 51 layers depending on the crack size. The smallest element size at the crack tip is up to 3% of the crack depth. J_2 incremental plasticity with large strain theory is employed. To load the pipe in tension, displacement is applied to the reference node, indicated in Fig. 4.3, which is coupled to the extreme pipe nodes at the right hand side.

Results of Parametric Study

Figure 4.4 shows the effect of the normalised embedment depth, p^A/a, on the normalised limit load, P_L^{FE}/P_0. The results for $2a/t = 0.05$, 0.10 and 0.40 are indicated by the squares, circles

and triangles, respectively. As expected, the limit load significantly decreases when the ligament decreases.

The results in Figure 4.5 show that the normalised limit load, P_L^{FE}/P_0, increases with the normalised crack height, $2a/t$. This is because p^A also increases with $2a/t$. The results for $p^A/a = 1.0$ and 1.5 are indicated by the triangles and circles, respectively, in Fig. 4.5.

Finally, the normalised crack length, $2c/W$, has a small effect on the normalised limit load, as shown in Figure 4.6, where the results for $p^A/a = 1.0$ and 1.5 are indicated by the triangles and circles, respectively.

Limit Load Solution for Embedded Flaws in Evenmatch Girth Welds

The results of the parametric FE study are used to derive an analytical limit load solution for embedded flaws in evenmatch pipeline girth welds. The BS7910 formulation is suitable for pipelines subjected to a combined bending and tension load mode. Therefore, it is adopted in this work. The new solution is derived from the BS7910 solution in Eqs. 2.28 and 4.3 by replacing the effective wall thickness, $t^{'}$, by the actual wall thickness, t, and proposing a new equation for the effective height to thickness ratio, $\alpha^{''}$

$$P_L^{NEW}(t, \alpha^{'}) = P_L^{BS}(t^{'} = t, \alpha^{''} = \alpha^{'}) \tag{4.4}$$

where $\alpha^{'}$ is an effective height to thickness ratio derived from the FEA results

$$\alpha^{'} = \left(0.1935 - 0.125\frac{2a/t}{1 + 40\frac{2c}{W}}\right)(p^A/a)^{-0.769} \tag{4.5}$$

Figure 4.7 compares analytical limit loads normalised by FEA predictions. The results obtained with the BS7910 and R6 solutions are indicated by circles and triangles, respectively, while those obtained with the new solution are indicated by rectangles. The predictions for small and large embedment depths are indicated by open and close symbols, respectively. A ratio in excess of 1 indicates that the analytical solution is non-conservative.

The results in Fig. 4.7 show that all analytical solutions are accurate for large embedment depths. However, for small embedment depths, which are the most critical, the BS7910 solution

can be very conservative, while the R6 solution can be non-conservative. In contrast, the proposed solution is very accurate for all cases considered here. The new analytical limit load, normalised by the FEA prediction, is in the range between 0.95 and 1.05, i.e. the error is within +/-5%. Finally, since bending is less severe than tension, it is safe to apply the proposed limit load solution to pipes subjected to bending or combined tension and bending.

4.2.3 J-Estimation Scheme for Embedded Flaws in Pipeline Girth Welds

Approach

A parametric FE study is undertaken to quantify the effect of p^A, $2a$, $2c$ and ε_{app} on the crack driving force at the crack tip 'A'. The FEA results are then used to derive a new J estimation scheme for embedded girth weld flaws in pipelines subjected to tension, based on the BS7910 formulation in Eq. 2.24. Subsequently, the CDF predicted using analytical solutions are compared against the numerical results.

Stress Intensity Factor Solutions

In addition to the BS7910 recommended Raju and Newman [111] K-solution in Eq. 2.27, that developed by Marie *et al.* [138] for plates containing embedded flaws, for use in the French nuclear codes (FNC) RSE-M and RCC-MR, is also considered in this work

$$K = (i_0 \; P_m + F_{gb} \; P_b) \sqrt{\pi a} \tag{4.6}$$

The values of the dimensionless functions i_0 and F_{gb} in Eq. 4.6 are given in [138] for crack tips 'A' and 'B'.

The R6 formulation is identical to that in Eq. 4.6, except that i_0 and F_{gb} are termed f_m and f_b, respectively [103]. The suitability of these K-solutions for the fracture assessment of pipeline girth welds with embedded flaws is investigated in a following section.

Limit Load Solutions

Under a tension load mode, the DNVGL recommended Kastner *et al.* [110] solution in Eq. 2.26 can be rewritten as

$$P_L^{DNVGL} = \frac{(1-a/t)(\pi(c/r)(a/t))}{\pi(1-a/t)+2(a/t)sin(c/r)}P_0 \tag{4.7}$$

In addition, (i) the Tkaczyk *et al.* solution for surface flaws in pipes, $P_L^{TTK} = \gamma^{TTK} P_L^{DNVGL}$ in Eq. 2.31, (ii) the BS7910 solution for embedded flaws in plates, given in Eq. 4.3 and (iii) the new solution for embedded flaws in pipes, given in Eq. 4.4, are also considered.

Pipe and Crack Geometry

Twenty seven crack geometries in Table 4.1, with $p^A/a \geq 1.0$, are investigated.

Material Flow Behaviour

An elastic-plastic stress-strain response with $E = 210$ GPa, $\sigma_y = 450$ MPa and $Y/T = 0.9$, representative of API 5L X65 pipe in the strained condition, shown in Figure 4.8, is used. The parameters of this curve, which follows the Ramberg-Osgood stress-strain relationship in Eq. 4.8, are given in Table 4.2

$$\varepsilon = \left(\frac{\sigma}{\sigma_0} + \left(\frac{\sigma}{\sigma_0}\right)^n\right)\varepsilon_0 \tag{4.8}$$

Finite-Element Analysis

The parametric study is carried out with the FEA model shown in Fig. 4.3. First, an elastic analysis is run and K-factors are extracted at the crack tip 'A' using the contour integral method. The numerical results are in excellent agreement with the analytical predictions, as shown in Figure 4.9, where the predictions with the BS and FNC solutions are indicated by the triangles and rectangles, respectively. Subsequently, an elastic-plastic analysis is carried out, using J_2 incremental plasticity with small strain theory, and the average J from all but the first

contour is computed for both crack tips. Further confidence in the FE analysis is gained from the path independence of J values, which are within 6% of the average value. As expected, J is higher at the crack tip 'A'. J^A/J^B varies between 1.0 and 1.2 for all cases considered.

J-Estimation Scheme for Embedded Girth Weld Flaws in Pipelines Subjected to Tension

The FEA predictions of J are significantly lower than the values obtained when the new limit load solution in Eq. 4.4 is used with the BS7910 J-scheme in Eq. 2.24 (this suggests that the new solution may still be somewhat conservative). Therefore, the analytical estimate of the crack driving force needs to be adjusted. A small error in the limit load (reference stress) can be translated into a significant error in J, especially for materials with low strain hardening. Therefore, instead of correcting the limit load, as performed by Tkaczyk *et al.* in [118], the reference strain, ε_{ref}, which is linearly proportional to J in the plastic regime, is adjusted to accurately predict J. J^A is estimated from

$$J^A = \frac{K^2(1-\nu^2)}{E}\left(\frac{E\widetilde{\varepsilon}_{ref}}{\widetilde{L}_r\sigma_y} + \frac{1}{2}\frac{\widetilde{L}_r^3\sigma_y}{E\widetilde{\varepsilon}_{ref}}\right) \tag{4.9}$$

Here, K is evaluated using the FNC solution in Eq. 4.6, because it is more accurate than the BS7910 solution. $\widetilde{L}_r$ is calculated using $\widetilde{\sigma}_{ref}$, which is the stress corresponding to $\widetilde{\varepsilon}_{ref}$. The modified reference strain, $\widetilde{\varepsilon}_{ref}$, is determined from

$$\widetilde{\varepsilon}_{ref} = \gamma^{'}\varepsilon_{ref} \tag{4.10}$$

Here, $\gamma^{'}$, $h^{'}$ and $h^{''}$ are empirical dimensionless functions fitted to the FEA results, and have a limited application range

$$\gamma^{'} = \begin{cases} 0.0025\exp(9.2\frac{2a}{t}) & \text{for} \quad 2a/t < 0.15 \ \text{ and } \ \mathrm{p^A/a} < 1.5 \\ h^{'}(\varepsilon_{app})^{h^{''}} & \text{otherwise} \end{cases} \tag{4.11}$$

$$h^{'} = \beta^{'}_{ijk}(2c/\pi D)^i(p^A/a)^j(2a/t)^k \tag{4.12}$$

$$h^{''} = \beta^{''}_{ijk}(2c/\pi D)^i(p^A/a)^j(2a/t)^k \tag{4.13}$$

The constants $\beta^{'}_{ijk}$ and $\beta^{''}_{ijk}$ in Eqs. 4.12 and 4.13 are given in Tables 4.3 and 4.4.

FEA predictions of J^A are normalised by J values obtained using analytical solutions in Figures 4.10 and 4.11. The results, obtained with the BS7910 limit load solution for embedded flaws (ref. Eq. 4.3) and with the surface flaw solution proposed by Tkaczyk *et al.* (ref. Eq. 2.31, labelled "DNVGL-TTK" in the figure), are indicated by circles and triangles, respectively. Those obtained with the adjusted embedded flaw solution proposed in this work are indicated by rectangles. The predictions for short and long crack lengths are indicated by open and close symbols, respectively. A ratio above 1 indicates that the analytical solution is non-conservative.

The results in Figs. 4.10 and 4.11 show that the BS7910 J-scheme is consistently too conservative when the Willoughby and Davey [112] limit load solution is used. The level of conservatism reduces when p^A increases. In contrast, a reasonable approximation of J^A is obtained for the near surface flaws when the Tkaczyk *et al.* limit load solution is used (i.e. the DNVGL-ST-F101 approach with an improved limit load solution). However, unlike surface breaking flaws, embedded flaws grow in two directions. Consequently, the DNVGL approach may significantly underestimate the crack growth for the near surface flaws in low toughness girth welds, as already highlighted by Oslo *et al.* [139] and Ostby *et al.* [140]. Finally, the proposed J-scheme provides a good approximation of J^A for all cases considered here. J estimates from the new analytical solution, normalised by the FEA predictions, are in the range between 0.95 and 1.10, i.e. the accuracy is generally within -5%/+10%.

Application Range

The range of application of the proposed J-scheme is summarised in Table 4.5. Further work needs to be carried out to extend the applicability to materials with a yield plateau. This may be achieved by simply enhancing the proposed limit load solution, such that it needs not be corrected to accurately predict J. This is investigated experimentally hereafter.

4.2.4 Fracture Testing – Determination of Limit Load

Machining and Notching of Test Specimen

Rectangular specimens, with B (= 17 mm) x 2B (= 34 mm) cross-section as per standard SENT test specimens, are extracted from as-received and strained (subjected to compression) 12.75"

(323.9 mm) OD × 18 mm WT seamless carbon steel pipes manufactured to API 5L X65. To generate through thickness embedded flaws, a starter hole is spark eroded through the thickness and a 0.15 mm diameter wire is threaded through the starter hole to produce a flaw of a desired height by Electro-Discharge Machining (EDM). Fatigue pre-cracking is not undertaken, to limit the amount of tearing during testing. The test specimen, which is adapted from that used by Ostby *et al.* in [140], and schematically illustrated in Figure 4.12, is referred to as a Modified Middle Crack Tension (MMCT) specimen in this work.

Instrumentation of Test Specimen

Prior to testing, a speckle pattern is applied to the side of the specimen. This is later used to estimate displacement and strain fields through digital image correlation (DIC). Figure 4.13 shows a range of patterns which are produced by spraying black paint over white paint, from a canister. In addition, strain gauges are affixed to measure remote and local strains.

Test Protocol

The fracture tests are carried out at Imperial College London under load-controlled conditions. Following installation of the test specimen on the machine, shown in Figure 4.14, strain gauges are connected to a strain indicator, and an extensometer is attached to the specimen. The specimen is then loaded in tension until the maximum load is reached. A high-resolution camera, shown in Fig. 4.14 is used to record 2D images of the speckle pattern at regular intervals during testing. The images are stored on a laptop and processed after testing.

First, specimens without a notch, shown in Figure 4.15, are tested to establish the reference load, P_0. Subsequently, notched specimens are tested to determine the limit load. In total, forty-two (42) samples are tested, as detailed in Table 4.6.

Test Results

Reference Load Figure 4.16 compares the stress-strain curves established from tests carried out with as-received (indicated by the dashed line) and strained (indicated by the solid line) samples without a notch. As expected, the as-received stress-strain curve exhibits a yield

plateau (YP), whereas the strained curve exhibits a continuous hardening (CH), which is typical of seamless materials. The reference yield strength, defined as the mean plus two standard deviations, is $\sigma_y = 497$ MPa and 407 MPa in the as-received and strained condition, respectively. This implies a Bauschinger effect (reduction in the yield strength due to a compressive pre-strain) of 18%, which is also typical. In contrast, the ultimate tensile strength is nearly the same in as-received (573 MPa) and strained condition (561 MPa), as expected. The corresponding reference load is $P_0 = 331$ kN and 324 kN in as-received and strained condition, respectively, see Table 4.7.

Figure 4.17(a) compares the strain readings from strain gauges and extensometers, which are approximately one W apart in Figure 4.15. In the linear elastic regime, when the applied strain is below 0.3%, similar readings are obtained. At the onset of yielding the readings diverge. Subsequently, when the applied strain reaches ca. 2.2%, corresponding to the end of the plateau in Fig. 4.16, the readings converge again. When the test results are expressed in terms of stress-strain curve in Fig. 4.17(b), very good agreement is obtained throughout. This illustrates the Lüders' banding process, typical of as-received seamless pipes.

Limit Load Figure 4.18(a) shows load versus time curves for samples with $2a = 4$ mm and $p^A = 1$ mm. The curves, indicated by a dashed line for the as-received material, and a solid line for the strained material, exhibit two distinctive peaks. The first peak in Fig. 4.18(a) corresponds to the maximum load of the ligament of length p^A. Shortly after this load is reached, the ligament starts necking rapidly. Some amount of ductile tearing also occurs. Meanwhile, the load is being transferred to the longer ligament. When the shorter ligament breaks the embedded flaw is converted into a surface flaw, which is then loaded until the maximum load is reached, corresponding to the second peak in Fig. 4.18(a). The second maximum load is no more than 5% higher than the first.

Likewise, the load versus time curves for specimens with $2a = 6$ mm and $p^A = 1.5$ mm exhibit two peaks. However, this time the second peak is lower than the first, see Fig. 4.18(b). For all other samples, which have higher normalised ligament length, the load-time curve exhibits only one peak, corresponding to the maximum load of the cracked sample.

In summary, the limit load of the ligament of length p^A, which is a function of the normalised crack height, $2a/W$, and the normalised ligament length, p^A/a, is nearly equal to the limit load of the cracked sample in the range tested. For a given normalised crack height, the normalised limit load is nearly linearly proportional to the normalised ligament length in the range tested, see Figure 4.19. The results for the normalised crack height $2a/W = 0.24$ and 0.35 are indicated by the squares and triangles, respectively, in Fig. 4.19. Slightly lower (less than 8%) normalised limit load is obtained for the strained material (indicated by the close symbols in the figure) compared to the as-received material (indicated by the open symbols in the figure) because the former has lower yield strength than the latter.

A linear regression analysis is carried out, as illustrated in Figure 4.20, and an empirical limit load solution for through thickness embedded flaws in plates is derived in the form

$$P_L = \left(0.85 - 0.70 \times 2a/t + 0.09 \times p^A/a\right) P_0 \tag{4.14}$$

Digital Image Correlation The high resolution images taken during testing were processed using a 2D version of the image correlation software GOM Correlate [141]. The test results in terms of longitudinal surface strains and displacements with respect to the centre of the crack, are shown in Figures 4.21 and 4.22 for specimens with $2a = 4.0$ mm $\times$ $p^A = 1.0$ mm and $2a = 6.0$ mm $\times$ $p^A = 4.5$ mm. High strain bands, initiating from the crack tip and progressing in a direction approximately 45° from the crack propagation direction, are evidenced. Although the strain contours for specimens with a small ligament show some level of noise, the displacement contours are very smooth and uniform for all samples. The latter provide an estimate of the crack opening, which is compared to the FEA predictions in a subsequent section.

Numerical Simulation of Fracture Tests

Finite-Element Analysis The fracture tests are simulated numerically in ABAQUS [47] using the 3D FEA model shown in Figure 4.23. Due to symmetry, only a quarter of the MMCT specimen is built with appropriate boundary conditions. The model length is 190 mm, which includes a grip length of 54 mm and a free span of 136 mm (equal to 8W). Up to 50,000 eight-node first order solid elements with reduced integration (C3D8R in ABAQUS [47]) are used to

model an MMCT specimen with a through thickness embedded flaw. Both crack tip regions in Fig. 4.23 have a focused mesh composed of 9 rings and 34 layers. The smallest element size at the crack tip is up to 1% of the crack depth. J_2 incremental plasticity with large strain theory and an isotropic hardening plasticity model are employed. To load the specimen in tension, displacement is applied to the reference node, indicated in Fig. 4.23, which is coupled to the sample nodes in the gripping area.

Results Figure 4.24 compares the FEA predictions (indicated by the dashed lines) to the test results (indicated by the solid lines) in terms of the engineering stress-strain curve. The strain in the FEA is measured from a surface element in the middle of the specimen, whereas that from the experiment corresponds to the extensometer reading. For both FEA and tests the engineering stress is obtained by diving the applied load by the cross-sectional area. It can be seen that the numerical predictions agree well with the experimental results initially. When the applied load approaches the limit load of the ligament of length p^A the FEA prediction starts diverging from the test result. This is because the damage process of the ligament is not captured by the classical metal plasticity model.

Figure 4.25 compares the numerical predictions of the CTOD, calculated using the 90° intercept method [88], to the crack opening estimated from the displacement contours established through DIC. It can be seen that the FEA predictions agree reasonably well with the experiments. Finally, good agreement is also obtained between numerical and DIC results in terms of strain and displacement contour plots at a load corresponding to 95% of the ligament collapse load, see Figures 4.26 and 4.27.

4.2.5 Recommendations for Fracture Assessment of Embedded Flaws in Evenmatch Pipeline Girth Welds

Figure 4.28 compares the limit load solution established from the 3D FEA detailed in Sec. 4.2.2, to that derived from the tests detailed in Sec. 4.2.4. A ratio below 1 indicates that the FEA based solution is conservative compared to the experiment. The results for $2a = 4$ mm and 6 mm

are indicated by squares and triangles, and those for $2c = 20$ mm and 200 mm are represented by the open and close symbols, respectively, in Fig 4.28.

It can be seen in Fig 4.28 that the FEA based solution is very conservative for small flaws and small ligaments. This explains why the former needed to be adjusted to accurately predict the crack driving force in Sec. 4.2.3. In contrast, the numerically based limit load solution appears to be slightly non-conservative for long ligaments and long flaws. Consequently, under load-controlled conditions the test-based limit load solution should be used. In contrast, as the ligament of length p^A would not collapse but rather stretch to accommodate the boundary conditions under displacement-controlled conditions, it is recommended that the solution yielding highest limit load between the two be used in a reeling ECA, in conjunction with the BS7910 J-estimation scheme, or that proposed in Sec. 4.2.3 if applicable.

4.3 Fracture Assessment of Undermatch Girth Welds

4.3.1 Effect of Pre-Strain on Fracture Toughness of Undermatch Girth Welds

Approach

A similar approach to that used by Tkaczyk *et al.* in [96] is followed. The effect of pre-strain on the fracture toughness is investigated by testing specimens subjected to a strain hysteresis representative of conditions experienced at the 12 o'clock position of a pipeline during reeling. Side-grooved SENT specimens with a square cross-section, as per BS8571 [90], are used. First, the SENT specimen is loaded in tension to extend the crack by a certain amount. Then, compression is applied to completely close the crack before subjecting the specimen to a final tensile straining event. The fracture toughness is expressed in terms of the CTOD at the current crack tip (i.e. the 'initial' crack length for the second tensile straining event takes into account the tearing during the first straining event), which is the standard practice for undermatch welds. The multiple specimens technique is followed here, where several specimens are tested to produce a single fracture toughness curve, in accordance with BS8571 [90].

Pipe Material and Welding Procedure

Hot-roll bonded clad pipe coupons, comprising of 3 mm thick alloy 316L metallurgically bonded to 10.75" (273.1 mm) OD × 22 mm WT backing pipe manufactured to API 5L X65, are girth welded using a mechanised gas metal arc welding (m-GMAW) process, executed in the 5G position. The root pass is deposited with a UGITECH UGIALLOY NCW consumable, and the remaining passes are executed using a Bohler UTP A 6222 Mo-3 consumable. The minimum pre-heat and maximum interpass temperature are 90°C and 150°C, respectively. In total nine (9) weld passes are deposited, as shown in Figure 4.29. No post weld heat-treatment is undertaken.

Material Flow Behaviour

Tensile tests are carried out at Element Aberdeen to determine the mechanical properties of API 5L X65 parent metal and alloy 622 weld metal. Three parent metal specimens extracted in the axial direction and three all-weld metal specimens extracted in the circumferential direction are cyclically tested in accordance with BS EN ISO 6892-1 [136]. The round bar specimen geometry, shown in Figure 4.30, is used.

Figure 4.31 shows average stress-strain curves for the parent material (indicated by a solid line) and weld material (indicated by a dashed line). The yield strength of the parent material is 482 MPa and 421 MPa in the as-received and strained condition, respectively, while that of the weld metal is 526 MPa and 373 MPa in the as-received and strained condition, respectively. Therefore, the weld metal overmatches the parent metal by 9% in the as-received condition, and undermatches the latter by 11% in the strained condition, see Table 4.8. A positive mismatch in Table 4.8 indicates that the weld metal undermatches the parent metal.

Machining and Notching of Fracture Toughness Test Specimens

Six square cross-weld SENT specimens, 460 mm long with the nominal dimensions, B × W = 18.5 × 18.5 mm, shown in Figure 4.32, are extracted from a welded pipe. The specimens are

notched from the pipe outer surface in the centre of the weld by EDM, with a wire of 0.25 mm diameter, then fatigue pre-cracked to a nominal depth $a = 3.7$ mm ($a/W = 0.2$), and finally side-grooved by 1 mm, see Fig. 4.32(b).

Fracture Toughness Testing

Cyclic fracture toughness tests are carried out at Exova Daventry, in accordance with BS8571 [90], using a servo screw driven TZ130 test machine. The test machine is operated by Tinashe Bare, following a procedure established by myself. Knife-edged 'legs' are fitted on either side of the notch on each specimen, and a double clip-gauge set-up, shown in Figure 4.35 is used to measure the crack opening at a distance of z_1= 6.5 mm and z_2= 106.5 mm above the specimen surface. These readings are used to calculate the crack mouth opening displacement (CMOD) from a geometrical construction in Figure 4.33

$$CMOD = V_1 - \frac{Z_1}{Z_2 - Z_1}(V_2 - V_1) \tag{4.15}$$

where V_1 and V_2 are displacements (openings) of the lower and upper clip gauges, see Fig. 4.33. Likewise, the CTOD is derived from

$$CTOD = V_1 - \frac{Z_1 + a}{Z_2 - Z_1}(V_2 - V_1) \tag{4.16}$$

Figure 4.34 shows an example of load versus CMOD (indicated by the dashed line) and load versus CTOD curves (indicated by the solid line) established from test data.

Each specimen is first loaded in tension to produce ductile tearing in the range between 0.2 mm and 1.0 mm, which is typical for reeling, and then relaxed. Following installation of an anti-buckling system, shown in Fig. 4.35(b), the sample is loaded in compression to close the crack. Subsequently, the load is released, the anti-buckling system is removed and the specimen is subjected to tension once again to produce similar or larger crack growth.

Ductile tearing is measured during testing using the silicon impression technique, where a semi-

viscous liquid of grade 101RF [142] is injected into the crack using a Microset [142] dispensing gun and mixing nozzle. The excess fluid is gathered on a backing slide, shown in Fig. 4.35(c), which label includes the specimen's identification and tensile straining event for later post-processing. The silicon compound then cures to produce a high resolution replica, which is removed from the crack without damage and later taken to Imperial College London, where it is measured on a microscope. EDM, fatigue pre-crack and tearing are clearly visible on the silicon replica in Figure 4.36. For some specimens, testing is interrupted, the load reduced and silicon replicas taken at several instances during tensile straining events, to increase the number of data points.

On completion of fracture toughness testing each specimen is unloaded, removed from the test machine, heat tinted, chilled in liquid nitrogen and broken open to measure the initial crack depth (including pre-cracking) and the total tearing. For some specimens, the crack growth during each tensile event can be clearly distinguished, see Figure 4.37.

Results and Conclusions

Figure 4.38 summarises the fracture toughness test results in terms of the CTOD, δ, versus the crack growth, Δa. The results for as-received specimens are indicated in Fig. 4.38 by the open symbols in a green font, whereas those for the strained material are illustrated by the close symbols in a red font. The crack growth during the first and second tensile straining events, measured from silicon replicas, ranges between 0.2 mm and 1.0 mm. The fracture toughness in terms of the CTOD is a near-linear function of the crack growth in both as-received and strained condition. All test data appear to be part of the same population. It can therefore be concluded that the fracture toughness of the undermatch weld is not affected by the pre-strain. This is in line with the results obtained by Tkaczyk *et al.* for overmatch welds [96]. Finally, very good agreement was found between the crack growth measured from silicon replicas at Imperial College London and that measured on the fracture faces at Exova Daventry. This further confirms that the silicon impression technique is suitable for the measurement of ductile tearing.

4.3.2 Fracture Assessment of Surface Flaws in Undermatch Welds

Approach

A parametric finite-element study is performed to assess the effect of weld metal undermatch on the crack driving force, expressed in terms of the CTOD. A new fracture assessment procedure is then proposed for undermatch girth welds in reeled pipelines, whereby a standard DNVGL-ST-F101 [7] ECA is performed first, under the assumption of weld metal evenmatch. Then, the depths of the acceptable flaw sizes determined under the assumption of weld metal evenmatch are reduced using an analytical formula, to account for weld metal undermatch, while the flaw lengths remain unchanged. Finally, the new ECA approach is validated and compared against existing procedures for undermatch welds in a case study.

Parametric Finite-Element Study

Pipe and Crack Geometry A pipe with 12.75" (323.9 mm) OD × 21.4 mm WT is considered. The normalised crack depth, a/t, in the range between 0.05 and 0.40 and the normalised crack length, $2c/W$, in the range between 0.02 and 0.10, are investigated. It is assumed that the flaw is located in the centre of a typical manual girth weld with 30° V-bevel and 3 mm root opening, as shown in Figure 4.39(a). The latter is idealised as a rectangular weld, illustrated in Fig. 4.39(b), which width is determined following the approach by Hertelé *et al.* [143]. In total, nine crack geometries are considered, as detailed in Table 4.9.

Material Flow Behaviour Weld metal undermatch is a concern for mechanically lined pipes and clad pipes, where the carbon steel host pipe has yield strength above 450 MPa (e.g. pipes manufactured to API 5L X65 or X70 [1]) welded using nickel based alloy consumables. Similarly, there is a risk of undermatch when 25% Cr consumables are used to weld 13% Cr steel pipelines. Two scenarios are considered in this work: (i) pipe material with a yield plateau and (ii) pipe material with continuous hardening. The former is representative of seamless lined pipes in the as-received condition whereas the latter is representative of solid CRA pipes, clad pipes and seam welded lined pipes in both as-received and strained condition, and seamless lined pipes

in the strained condition (after plastic straining on the reel). The weld material is assumed to exhibit continuous hardening, which is always the case for lined, clad and solid CRA pipelines.

The yield strength, σ_y, in the range between 450 and 700 MPa and the weld metal undermatch at yield, m_y up to 20% are considered. For parent materials with a yield plateau, the strain at the end of the yield plateau, ε_L, is assumed to be from 1% to 3%, while the upper bound yield to tensile strength ratio, $Y/T = 0.9$ is considered. In contrast, Y/T in the range between 0.6 and 0.9 is assumed for parent materials exhibiting continuous hardening.

The as-received stress-strain curve of the seamless parent material is defined by the Young's modulus, E, σ_y, ε_L, and the Ramberg-Osgood hardening index, n. There is a unique relationship between n and Y/T. The parent metal stress-strain curve (indicated 'PM' in Figure 4.40) is bi-linear for strains between 0 and ε_L and described by a power law for higher strains. The line between 0 and ε_y has a slope equal to E. The plateau is flat on an engineering stress-strain plot but has a small slope when converted to a true stress-strain plot. The power law curve is expressed by the modified Ramberg-Osgood relationship

$$\varepsilon = \begin{cases} \dfrac{\sigma}{E} & \text{for} \quad \varepsilon \leq \varepsilon_y \\ \varepsilon_y + \dfrac{\varepsilon_L - \varepsilon_y}{\sigma_y \varepsilon_L} (\sigma - \sigma_y) & \text{for} \quad \varepsilon_y \leq \varepsilon \leq \varepsilon_L \\ \left(\dfrac{\sigma}{\sigma_0} + \left(\dfrac{\sigma}{\sigma_0} \right)^n \right) \varepsilon_0 + \varepsilon_{off} & \text{for} \quad \varepsilon > \varepsilon_L \end{cases} \tag{4.17}$$

For the evenmatch weld metal stress-strain curve (indicated 'WM-EM' in Fig. 4.40), $\varepsilon_{off} = 0$ while σ_0 is chosen to achieve $\sigma = \sigma_y$ at $\varepsilon = 0.5\%$. The same hardening index, n, is used for both parent and weld metal. Undermatch weld metal stress-strain curves (indicated 'WM-UM' in Fig. 4.40) are derived by lowering σ_0 to achieve 5%, 10% and 20% undermatch. For example, the parameters defining the stress-strain curves with $\sigma_y = 450$ MPa are given in Table 4.10. The same approach is used to create parent and weld metal stress-strain curves exhibiting continuous hardening, shown in Figure 4.41. For example, the parameters defining the stress-strain curves with $\sigma_y = 450$ MPa and $n = 5.7$ are given in Table 4.11. In total, eighteen tensile properties are considered, as detailed in Table 4.12.

Finite-Element Analysis The FEA model, shown in Figure 4.42, is used to investigate the effect of weld metal undermatch on the crack driving force in stationary semi-elliptical surface breaking flaws. Due to symmetry, only a quarter model of the pipe is modelled with appropriate boundary conditions. The model length is three times the pipe outer diameter. Up to 17000 eight-node first order solid elements with full integration (C3D8 in ABAQUS) are used. The crack tip region has a focused mesh composed of 5 to 7 rings and 17 to 20 layers depending on the crack size. The smallest element size at the crack tip is up to 3% of the crack depth. J_2 incremental plasticity with large strain theory is employed. Bending is achieved by applying rotation to the reference node, indicated in Fig. 4.42, which is coupled to the extreme pipe nodes at the right hand side.

Tkaczyk *et al.* showed, in [114], that the FEA model in Fig. 4.42 is suitable for the prediction of the J-integral when C3D8I elements are used with the small strain theory. In this work, J predicted using C3D8 elements is virtually identical to that predicted using C3D8I elements. This shows that C3D8 elements are suitable for the prediction of J, when the small strain theory is used. Subsequently, J is plotted against $\sigma_y\delta$. A linear relationship is found between both quantities, which is in agreement with the results presented in [88]. When the large strain theory is used, J is no longer path independent. At low strains (below 1%), the CTOD is very similar for the small and large strain theory. At large strains, a saturation of δ is observed with the large strain theory, which is due to the ovalisation of the pipe. Finally, δ is virtually identical at low strains, and within 10% at large strains, when C3D8I elements are used. This demonstrates that the FEA model is suitable for the prediction of δ.

A parametric FE study is carried out to quantify the effect of weld metal undermatch on the crack driving force, expressed in terms of the CTOD, calculated using the 90° intercept definition [88]. First, a reference crack size, (a, $2c$) in Table 4.9, is analysed under evenmatch conditions, and the predicted CTOD is plotted against the applied strain. Subsequently, iterative analyses are carried out assuming different levels of undermatch. For each level of undermatch, the crack depth is reduced (the crack length remains unchanged) until good agreement of the CTOD-strain curve in the range between 0.75% and 2.5% strain, for the case of evenmatch and undermatch, is obtained. Thus, for each reference (evenmatch) crack size, (a, $2c$), and each

level of undermatch, a corresponding crack depth reduction, da, is found

$$a^{eff} = a - da \tag{4.18}$$

where (a^{eff}, $2c$) is the allowable crack size in the undermatch weld. This is repeated for a range of crack sizes and material properties in Tables 4.9 and 4.12. A total of 648 cases are run.

Results of Parametric Study Figure 4.43 shows the evolution of the CTOD for the case of evenmatch where the parent metal exhibits a yield plateau, $\varepsilon_L = 1\%$, 2% and 3%. The effect of the yield plateau is evident. Since the weld is rather slender here, the plastic deformation in the parent metal interacts with the plastic deformation at the crack tip. The crack driving force is a quadratic function of strain in the elastic regime. As the material yields, the relationship becomes nearly linear, up to $\varepsilon_{app} = \varepsilon_L$. (It should be noted, however, that under tension, in this region the crack driving force may increase significantly and then saturate, as shown in [120]). For strains $\varepsilon_{app} > \varepsilon_L$, there is a noticeable increase in the crack driving force, beyond which the relationship between δ and ε_{app} is again close to linear, but with a higher slope, due to global yielding of the pipe [121].

The effect of the undermatch magnitude on the CTOD is illustrated in Fig. 4.44 for the parent metal with $\varepsilon_L = 3\%$. The crack driving force significantly increases with the undermatch magnitude. This is in agreement with the results presented by Fu and Shi [93] and Boothman *et al.* [94].

The interaction between the plastic deformation at the crack tip of an undermatch weld and the plastic deformation in the background material reduces the crack driving force. When a increases, the level of interaction reduces. Consequently, the effect of the undermatch on the CTOD becomes more pronounced, hence the flaw depth reduction, da, increases, as shown in Figure 4.45.

The results in Figure 4.46 show that da/t decreases with $2c/W$. For a given a, the uncracked area decreases when c increases, while the area adjustment (increase in uncracked area due to flaw depth reduction) increases with c. Consequently, to achieve the same net (proportional) increase in uncracked area when a is reduced, da must reduce when c increases. This effect,

which is more pronounced for materials with a yield plateau, is less significant than that of the crack depth.

The normalised crack depth adjustment, da/t can increase by 30% when n increases from 5.7 to 16.8. In contrast, σ_y in the range between 450 and 700 MPa and ε_L in the range between 2% and 3% (typical for subsea seamless pipes) have a small effect on da/t.

New ECA Procedure for Surface Flaws in Undermatch Welds

Approach The SINTEF concept of crack depth adjustment (ref. Sec. 2.3.3) is adopted here. First, a DNVGL-ST-F101 – BS7910 Option 2 assessment (equivalent to Option 2 in R6 [103]) is undertaken to determine the maximum acceptable flaw sizes. The acceptable crack depths are subsequently reduced using an analytical formula, to account for weld undermatch.

Crack Depth Adjustment Formula Second order polynomials are fitted to the FEA results expressed in terms of da/t as a function of m, a/t and $2c/W$. The effect of the weld width is captured through the factor H/H_0, where H is half of the project specific weld width and H_0 is half of the reference weld width, determined for the weld geometry considered in the parametric FE study (i.e. 21.4 mm thick 30° V-bevelled weld with and 3 mm root opening, illustrated in Fig. 4.39)

$$\frac{da}{t} = (H/H_0)^{0.5} \, (m/0.0445)^{0.9} \sum_{i,j=0}^{2} \beta_{ij} (a/2c)^i (a/t)^j \tag{4.19}$$

where the mismatch, m, is evaluated at $\varepsilon = \varepsilon_{app}$, from

$$m\left(\varepsilon_{app}\right) = 1 - \frac{\sigma^{WM}}{\sigma^{PM}} \tag{4.20}$$

Four sets of constants α_{ijk} in Eq. 4.19 are produced: (i) one for parent metals with yield plateau and $n \leq 16.8$, (ii) one for parent metals with continuous hardening and $n = 16.8$, (iii) one for parent metals with continuous hardening and $n = 9.0$ and (iv) one for parent metals with continuous hardening and $n = 5.7$, given in Table 4.13.

Application to ECA of Reeled Pipelines When applying the proposed approach to reeled pipelines, the below procedure should be followed:

1. Calculate ε_{app} using Eq. 1.1.
2. Carry out a DNVGL-ST-F101 – BS7910 Option 2 ECA to determine the maximum acceptable flaw size prior to reeling, ($2c_0$, a_0), under the assumption of evenmatch.
3. Calculate m using Eq. 4.20.
4. Determine n by fitting the Ramberg-Osgood relationship in Eq. 4.17 to the parent metal stress-strain curve.
5. Calculate da using Eq. 4.19.
6. Finally, calculate the acceptable initial (as-welded) crack depth in the undermatch weld

$$a_0^{\mathit{eff}} = a_0 - da \tag{4.21}$$

Application Range The range of application of the proposed methodology is summarised in Table 4.14. It is required that the weld metal stress-strain curve exhibits continuous yielding and higher strain hardening than the parent metal. In the case of bimetal pipes, it is also required that the CRA layer does not overmatch the parent metal.

Validation of New ECA Procedure for Surface Flaws in Undermatch Welds

Approach FE analyses are carried out to determine the maximum acceptable crack depth for 15, 25 and 50 mm long flaws in undermatch welds, for a critical toughness, CTOD = 0.3 mm. Crack depths in excess of $t/2$ are disregarded because such flaws would not be allowed during fabrication of reeled pipelines. The FEA results are then compared to predictions from: (i) the SINTAP level 3 assessment detailed in Sec. 2.3.3, (ii) the SINTEF scheme presented in Sec. 2.3.3 and (iii) the new ECA approach. Since no mismatch limit load solutions are available for part-circumferential flaws in pipes subjected to bending, the one for tension, proposed by Kim *et al.* [144] is used in the SINTAP scheme.

Pipe Geometry and Material Stress-Strain Curves Typical reelable pipes with an outer diameter in the range between 6.625" (168.3 mm) and 16" (406.4 mm) and wall thickness in the range between 7.11 mm and 25.4 mm are analysed, as detailed in Table 4.15. A weld width of 14 mm, which is representative of manual welds for thin pipes and mechanised welds for thick pipes, is considered for the following four scenarios:

1. 'YP1': $\sigma_y = 487$ MPa, $\varepsilon_L = 1.7\%$, $n = 9.9$, alloy 625 weld consumable
2. 'YP2': $\sigma_y = 500$ MPa, $\varepsilon_L = 2.5\%$, $n = 16.8$, alloy 625 weld consumable
3. 'CH1': $\sigma_y = 632$ MPa, $n = 9.1$, 25% Cr weld consumable
4. 'CH2': $\sigma_y = 500$ MPa, $n = 16.8$, 25% Cr weld consumable

The undermatch at yield, m_y, is up to 10%. The corresponding stress-strain curves are shown in Figures 4.47 and 4.48 for cases with and without a yield plateau, respectively.

The SINTAP approach is used for the 'YP2', 'CH1' and 'CH2' scenarios. A simplified procedure is followed, where the maximum acceptable flaw sizes are determined by FEA. Figure 4.49 compares, for the 'CH2' scenario, the parent and weld metal stress-strain curves (indicated by thick and thin solid lines, respectively) to the equivalent stress-strain curve (indicated by a dashed line) obtained using the mismatch limit load solution for part-circumferential flaws in pipes subjected to tension [144]. The equivalent curve is very similar to the parent metal stress-strain curve. The same trend is observed for 'YP2' and 'CH1'. Consequently, the acceptance criteria derived using the equivalent curves are expected to be very similar to those derived using parent metal stress-strain curves.

Results and Discussions The analytical predictions are normalised by the FEA results and plotted against the crack length in Figures 4.50 to 4.53: (i) SINTAP predictions are represented by solid lines with diamond symbols, (ii) SINTEF predictions are illustrated by long dashed lines with rectangular symbols and (iii) predictions with the new ECA approach are represented by short dashed lines with triangular symbols. Cases with $m_y = 5\%$ and 10% are represented by open and closed symbols, respectively. The corresponding values of m are given in Tables 4.16

and 4.17. Cases with $m \leq 0$ are treated as evenmatch cases. A prediction is conservative when the normalised flaw depth is below 1 and non-conservative when it is above 1.

The results in Figs. 4.50 to 4.53 show that the SINTAP procedure is consistently non-conservative. The magnitude of crack depth overestimation reduces when m reduces. This is because an equivalent curve for pipes in tension is used. Since the prescribed load for pipes subjected to tension is a force, the corresponding applied strain would be higher for the equivalent curve (due to lower stress-strain curve) than for the parent metal stress-strain curve. Therefore, the effect of the undermatch would be captured. This is not the case for reeling, where the prescribed load is strain. The accuracy of the SINTAP procedure can be improved if an equivalent stress-strain curve with lower strain hardening than both parent and weld metal stress-strain curves is used. Such curve could be derived using a mismatch limit load solution for pipes subjected to bending. Alternatively, Eq. (2.37) could be modified. The SINTEF scheme is generally too conservative, because it does not account for the effects of the strain hardening and the crack length on the crack driving force in undermatch welds.

In contrast, the new ECA approach is the most accurate over the whole range of standard reeled pipe sizes. The acceptable crack depth is estimated with an accuracy of -15%/+6% typically. Out of the 61 cases run, the analytical predictions are within 5% of the FE results for 31 cases (51%), within 10% for 49 cases (80%) and within 15% for 57 cases (93%). The maximum error of 20% is obtained for 4 cases with short flaws: (i) the acceptable crack depth is overestimated by up to 20% for thick pipes with continuous hardening, and (ii) underestimated by up to 20% for thin large pipes with a yield plateau. The flaw length in excess of 15 mm has small effect on the accuracy, and therefore similar accuracy would be obtained for flaws longer than 50 mm.

4.3.3 Fracture Assessment of Embedded Flaws in Undermatch Girth Welds

New Procedure for Assessment of Embedded Flaws in Undermatch Girth Welds

Building upon the work undertaken for surface flaws in undermatch welds discussed in Section 4.3.2, the analysis in Section 4.2.2 and the fracture tests detailed in Section 4.2.4, the

below procedure is proposed for the assessment of embedded flaws in undermatch welds:

1. Calculate ε_{app} using Eq. 1.1.
2. Carry out a DNVGL-ST-F101 – BS7910 Option 2 ECA to determine the maximum acceptable flaw size prior to reeling, ($2c_0$, $2a_0$, p^A), under the assumption of evenmatch, using the limit load solution developed in this work.
3. Split the embedded flaw into two surface flaws, as shown in Figure 4.54.
4. Calculate m using Eq. 4.20.
5. Determine n by fitting the Ramberg-Osgood relationship in Eq. 4.17 to the parent metal stress-strain curve.
6. For each surface flaw in Fig. 4.54, calculate da using Eq. 4.19.
7. For each surface flaw in Fig. 4.54, calculate the acceptable initial crack depth in the undermatch weld, a_0^{eff}, from Eq. 4.21.
8. Finally, join the adjusted surface flaws in Fig. 4.54 to obtain the acceptable initial embedded flaw in the undermatch weld, ($2c_0$, $2a_0^{\mathit{eff}}$, $p^{A\mathit{eff}}$)

Validation of New ECA Procedure for Embedded Flaws in Undermatch Welds

Approach To validate the new ECA procedure, the exercise performed for surface flaws in Sec. 4.3.2 is repeated here for embedded flaws. The maximum acceptable surface flaws in evenmatch welds determined in Sec. 4.3.2 are assumed acceptable beneath the surface, at an embedment depth $p^A = a$. The acceptable embedded flaw in the undermatch weld is then calculated using the procedure detailed above. Subsequently, an FEA is run and the crack driving force in terms of the CTOD is plotted against the applied strain at both crack tips for the evenmatch and undermatch scenarios. Finally, the CTOD at the assessment strain in Table 4.16, predicted for the undermatch weld, is normalised by that predicted for the evenmatch weld. The new assessment scheme is deemed suitable if: (i) the normalised crack driving force is less than 1 at crack tip 'A' and (ii) the average between normalised crack

driving force at crack tips 'A' and 'B' is less than 1. This is because higher crack driving force is expected at crack tip 'A', which has smaller ligament length.

Results and Discussions Figure 4.55 compares the crack driving force versus strain curves for evenmatch and undermatch scenarios for three cases: (i) 168.3 mm OD × 7.11 mm WT pipe material exhibiting a yield plateau, referred to as 'YP1' in Fig. 4.47, (ii) 323.9 mm OD × 15.9 mm WT pipe material exhibiting a yield plateau, referred to as 'YP2' in Fig. 4.47 and (iii) 406.4 mm OD × 25.4 mm WT pipe material exhibiting continuous hardening, referred to as 'CH2' in Fig. 4.48. In the case of the 6" pipe the predicted crack driving force is higher for the undermatch weld (indicated in Fig. 4.55(a) by the thick and thin dashed lines for crack tips 'A' and 'B', respectively) than for the evenmatch weld (indicated in Fig. 4.55(a) by the thick and thin solid lines for crack tips 'A' and 'B', respectively) in the elastic regime. However, the opposite trend is observed in the plastic regime, relevant for reeling. In the case of the 10" pipe the crack driving force in the undermatch weld is lower at crack tip 'A' and higher at crack tip 'B' than that predicted for the evenmatch material. However, the average crack driving force is lower for the undermatch weld than for the evenmatch weld. Finally, for the 16" pipe the crack driving force is consistently lower for the undermatch weld than for the evenmatch weld.

Figure 4.56 presents the FEA results in terms of the crack driving force in the undermatch weld normalised by that in the evenmatch weld, for three cases: (i) 168.3 mm OD × 7.11 mm WT pipe material exhibiting a yield plateau ('YP1' in Fig. 4.47), (ii) 323.9 mm OD × 15.9 mm WT pipe material exhibiting a yield plateau ('YP2' in Fig. 4.47) and (iii) 406.4 mm OD × 25.4 mm WT pipe material exhibiting continuous hardening ('CH1' in Fig. 4.48). Although the normalised crack driving force at the assessment strain is above 1 at crack tip 'B' (indicated by the open symbols in Fig. 4.56(a)) for the 10" pipe, it is below 1 at crack tip 'A' (indicated by the close symbols in Fig. 4.56(a)) for all other cases in Fig. 4.56. In addition, out of the 61 cases analysed, the average normalised crack driving force is above 1 only for cases where the weld metal has $n > 9.0$ (i.e. $Y/T > 0.75$). In the context of MLP, the CRA weld metal typically has Y/T below 0.75. This demonstrates that the proposed approach is suitable (conservative) for the treatment of embedded flaws in undermatch welds in MLP.

4.4 Recommendations for Design of Mechanically Lined Pipe Welds Against Fracture

4.4.1 Liner Seam Weld

Tkaczyk *et al.* showed in [145] that planar flaws with normalised height $a/t_L \leq 0.2$ are not detrimental to the integrity of liner seam welds subjected to expansion strains up to 5%. The seam weld sees significantly lower strain during reeling than when the liner is expanded during manufacturing. The hoop strain during reeling is ca. 50% of the corresponding axial strain assuming a Poisson ratio of 0.5 in a fully plastic regime. As the maximum axial strain during reeling is ca. 2.5%, the maximum hoop strain is 1.25%, compared to 4 – 5% strain during expansion. Consequently, for $a/t_L \leq 0.2$ the risk of fracture during reeling is negligible.

4.4.2 Triple Point Interface

Maximum acceptable sizes for flaws growing from the OD of the CRA pipe towards the MLP inner surface (referred to as "CRA interface flaws" or simply "CRA flaws" in this work) should be determined using the approach detailed in Sec. 2.3.4. It may be challenging to establish a representative fracture toughness for CRA flaws according to BS8571 [90] when t_L is small (e.g. 3 mm). Sub-sized specimens may need to be used. Alternatively, a segment testing protocol may be developed to demonstrate that an acceptable amount of stable tearing (if any) would be produced when the flaw is subjected to a crack driving force as per Eq. 2.39.

The acceptability of flaws growing from the carbon steel pipe ID towards the MLP outer surface (referred to as "CS interface flaws" or simply "CS flaws") should be sanctioned following the standard DNVGL-ST-F101 – BS7910 Option 2 ECA approach, described in Sec. 2.3.2.

4.4.3 Overlay Welds

As for CS flaws, overlay weld flaws should be assessed following the standard DNVGL-ST-F101 – BS7910 Option 2 ECA approach, described in Sec. 2.3.2.

4.4.4 Girth Welds

Surface Flaws in Girth Welds

Surface flaws in evenmatch girth welds should be assessed following a modified DNVGL-ST-F101 – BS7910 Option 2 ECA approach, where the modified limit load solution in Eq. 2.31 and the crack driving force estimation scheme illustrated in Fig. 2.38 are used as relevant.

Following establishment of acceptable flaw sizes in evenmatch welds as described above, the flaw heights should be adjusted as per Sec. 4.3.2 to derive the maximum acceptable surface flaws in undermatch welds.

The work related to the treatment of surface flaws in undermatch welds was published in the ASME JPVT journal, refer to Appendix A for more details.

Embedded Flaws in Girth Welds

Embedded flaws in evenmatch girth welds should be assessed following a modified DNVGL-ST-F101 – BS7910 Option 2 ECA approach, where the least onerous of the limit load solutions in Eqs. 4.4 and 4.14 is used together with the standard BS7910 J-estimation scheme in Eq. 2.24. Where applicable, the J-estimation scheme in Eq. 4.9 should be used. Moreover, applicability of the J-estimation scheme in Fig. 2.38 to the treatment of embedded flaws in materials exhibiting a yield plateau should be investigated.

Following establishment of acceptable flaw sizes in evenmatch welds as described above, the flaw heights and embedment depths should be adjusted as per Sec. 4.3.3 to derive the maximum acceptable embedded flaws in undermatch welds.

The limit load analysis of embedded flaws in evenmatch pipeline girth welds was published at the ASME PVP 2015 conference, refer to Appendix B for more details.

4.5 Tables and Figures

Table 4.1: Limit Load Analysis: FEA Case Matrix – Crack Geometries

D (mm)	t (mm)	$2c/W$	$2a/t$	p^A/a
323.9	21.4	0.02 – 0.10	0.05	1.00 – 9.00
			0.10	0.75 – 3.50
			0.40	0.50 – 1.50

Table 4.2: Parameters of Assumed Stress-Strain Curve

E (GPa)	σ_y (MPa)	σ_0 (MPa)	ε_y (%)	ε_0 (%)
210	450	442	0.50	0.21

Table 4.3: Values of β'_{ijk} for $n = 16.8$

		k		
i	j	0	1	2
0	0	-0.0818	0.7358	-0.9719
0	1	0.0639	-0.6379	0.1972
0	2	-0.0032	0.0960	0.5235
1	0	0.0374	-1.1925	12.5370
1	1	-0.1416	4.3401	-34.9503
1	2	0.1177	-3.4417	23.8306

Table 4.4: Values of β''_{ijk} for $n = 16.8$

		k		
i	j	0	1	2
0	0	-0.3275	0.4911	-0.8057
0	1	0.0285	-0.1199	0.5237
0	2	-0.0014	0.0169	-0.0202
1	0	0.1505	-5.6746	6.2449
1	1	-0.1002	2.1754	1.3680
1	2	-0.0057	0.2375	-2.6416

Table 4.5: Range of Application of New J-Estimation Scheme

D/t	p^A/a	$2a/t$	$2c/W$	n	$\varepsilon_{app}(\%)$
≥15	≥1.0	≤0.4	≤0.1	16.8	0.5 – 2.5

Table 4.6: Embedded Flaw Test Matrix

Material Condition	W (mm)	2a/W (-)	p^A/a (-)	2a (mm)	p^A (mm)	Number of Specimens
As-Received	17	-	-	-	-	3
		0.24	0.5	4.0	1.0	3
		0.24	1.0	4.0	2.0	3
		0.24	2.0	4.0	4.0	3
		0.35	0.5	6.0	1.5	3
		0.35	1.0	6.0	3.0	3
		0.35	1.5	6.0	4.5	3
Strained	17	-	-	-	-	3
		0.24	0.5	4.0	1.0	3
		0.24	1.0	4.0	2.0	3
		0.24	2.0	4.0	4.0	3
		0.35	0.5	6.0	1.5	3
		0.35	1.0	6.0	3.0	3
		0.35	1.5	6.0	4.5	3

Table 4.7: Test Results – Reference Load

Material Condition	σ_y (MPa)	σ_t (MPa)	P_0 (kN)
As-Received	497	573	331
Strained	407	561	324

Table 4.8: Fracture Toughness Testing – Weld Metal Mismatch

Material Condition	PM YS (MPa)	WM YS (MPa)	Mismatch, m_y (%)
As-Received	482	526	-9
Strained	421	373	+11

Table 4.9: Surface Flaws in Undermatch Welds: Parametric FEA Matrix of Cases – Crack Geometries

D (mm)	t (mm)	a/t	$2c/W$
323.9	21.4	0.05, 0.15, 0.40	0.02, 0.05, 0.10

Table 4.10: Parametric FEA – Stress-Strain Curve Parameters for Materials with Yield Plateau, E=210 GPa, σ_y=450 MPa, n=16.8 (Y/T=0.9)

Material	m_y (%)	σ_y (MPa)	σ_0 (MPa)	ε_0 (%)	ε_L (%)	ε_{off} (%)
PM		450	450	0.21	2	1.5
WM-EM	0	450	443	0.21	2	0.0
WM-5%UM	5	428	421	0.20	2	0.0
WM-10%UM	10	405	399	0.19	2	0.0
WM-20%UM	20	360	354	0.17	2	0.0

Table 4.11: Parametric FEA – Stress-Strain Curve Parameters for Materials with Continuous Hardening, E=210 GPa, σ_y=450 MPa, n=5.7 (Y/T=0.6)

Material	m_y (%)	σ_y (MPa)	σ_0 (MPa)	ε_0 (%)
PM		450	423	0.20
WM-EM	0	450	423	0.20
WM-5%UM	5	428	395	0.19
WM-10%UM	10	405	367	0.17
WM-15%UM	15	326	340	0.16

Table 4.12: Parametric FEA Matrix of Cases – Tensile Properties

σ_y (MPa)	n	ε_L (%)
450, 575, 700	16.8	1, 2, 3
450, 575, 700	5.7, 9.0, 16.8	-

Table 4.13: New Crack Depth Adjustment Formula – Values of β_{ij} for Material Exhibiting Continuous Hardening

		n		
i	j	5.7	9.0	16.8
0	0	-0.0001	0.0012	0.0019
0	1	0.0990	0.0923	0.0871
0	2	-0.1000	-0.0914	-0.0857
1	0	0.0153	-0.0027	0.0231
1	1	0.2931	0.4581	0.4603
1	2	0.0343	-0.2657	-0.4514

Table 4.14: New Crack Depth Adjustment Formula – Range of Application

D/t	a/t	$2c/\pi D$	n	m_y	$\varepsilon_{app}(\%)$
7 – 25	$\leq$0.35	$\leq$0.10	$\leq$16.8	$\leq$10%	0.75 – 2.50

Table 4.15: Validation of New ECA Approach for Undermatch Welds – Pipe Sizes

Pipe Size (in)	D (mm)	t (mm)	D/t
6	168.3	7.11	24
6	168.3	25.4	7
12	323.9	15.9	20
12	323.9	25.4	13
16	406.4	17.6	23
16	406.4	25.4	16

Table 4.16: Validation of New ECA Approach for Undermatch Welds – Effective Undermatch for Material with Yield Plateau

Pipe Size (in)	ε_{app} (%)	Material	m_y (%)	m (%)
6	1.24	YP1	5.0	-2.0
6	1.24	YP1	10.0	3.1
6	1.24	YP2	10.0	5.2
12	2.16	YP1	5.0	-1.1
12	2.16	YP1	10.0	3.8
12	2.16	YP2	10.0	2.2
16	2.64	YP1	5.0	-0.0
16	2.64	YP1	10.0	4.8

Table 4.17: Validation of New ECA Approach for Undermatch Welds – Effective Undermatch for Material with Continuous Hardening

Pipe Size (in)	ε_{app} (%)	Material	m_y (%)	m (%)
6	1.24	CH1	5.0	5.6
6	1.24	CH1	10.0	11.1
6	1.24	CH2	10.0	10.3
12	2.16	CH1	5.0	5.6
12	2.16	CH1	10.0	11.2
12	2.16	CH2	10.0	10.4
16	2.64	CH1	5.0	5.7
16	2.64	CH1	10.0	11.3

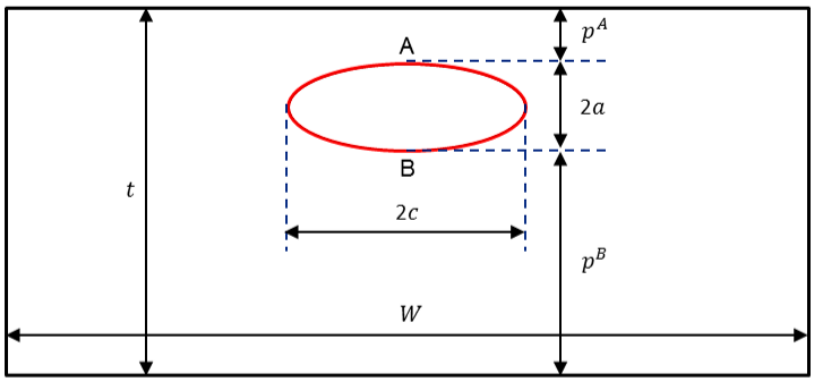


Figure 4.1: Embedded Flaw Geometry

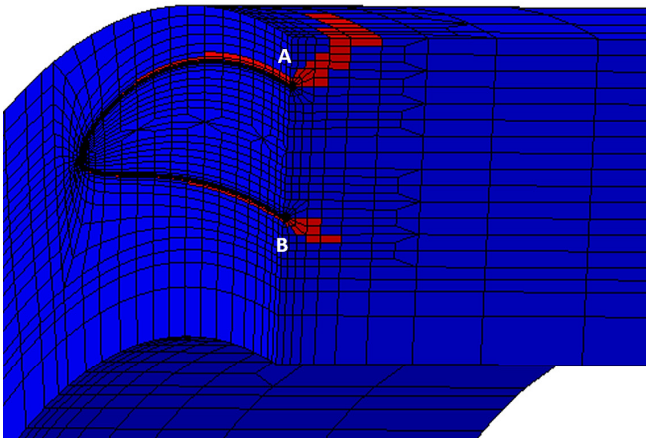


Figure 4.2: Illustration of Ligament Collapse Criterion

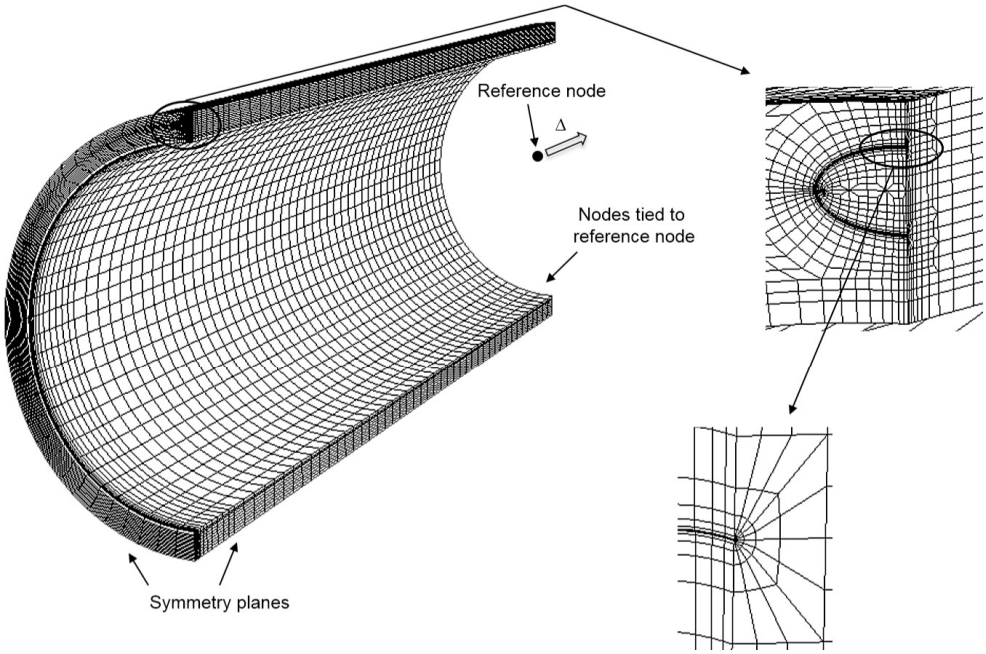


Figure 4.3: Finite-Element Analysis Model of Pipe with Embedded Flaw

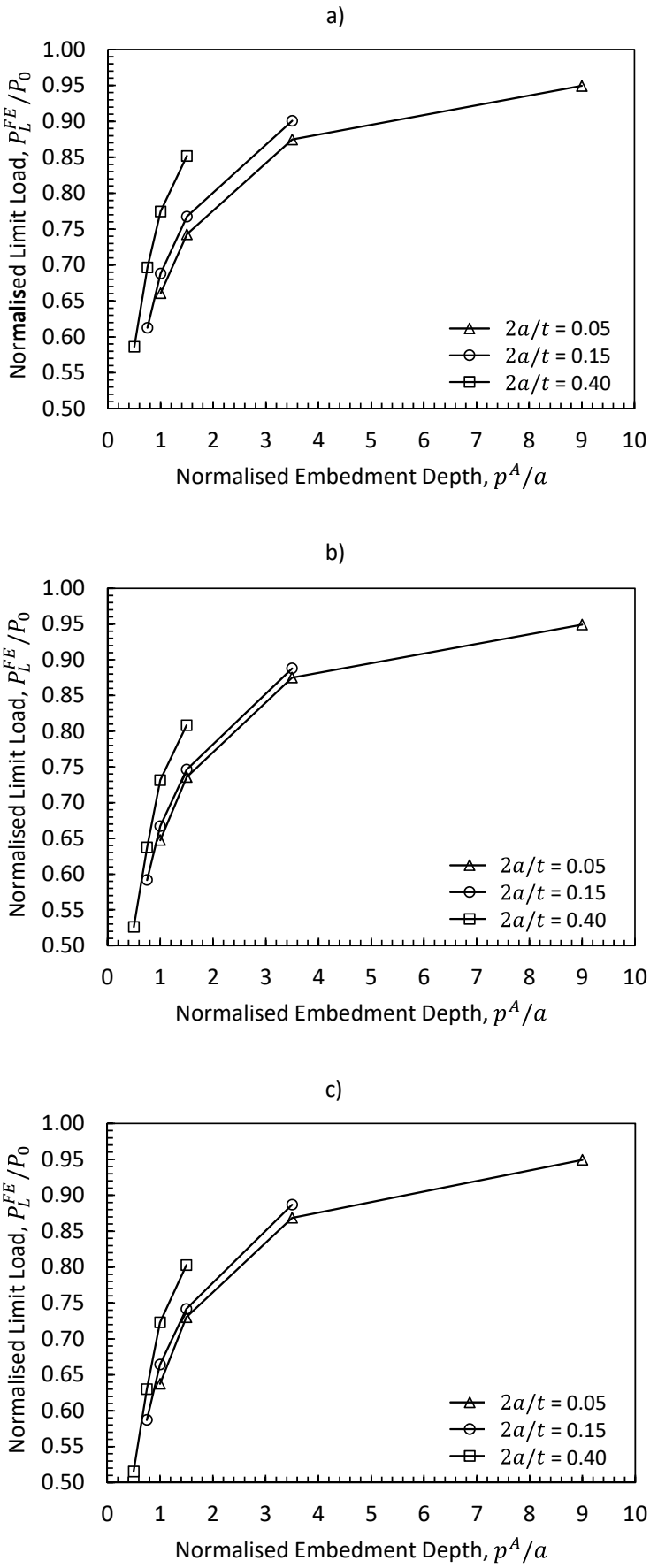


Figure 4.4: Limit Load Analysis Results – Effect of Normalised Embedment Depth: (a) $2c/W = 0.02$, (b) $2c/W = 0.05$, (c) $2c/W = 0.10$

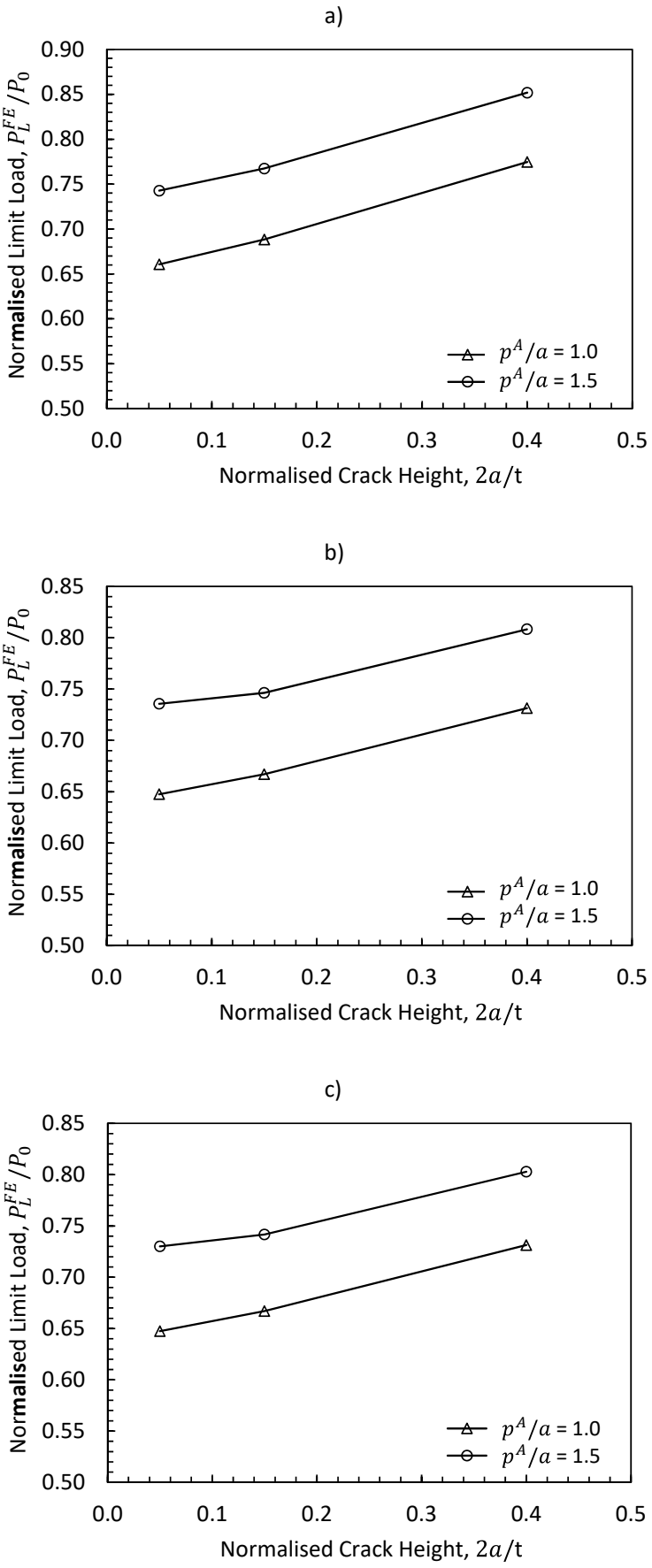


Figure 4.5: Limit Load Analysis Results – Effect of Normalised Crack Height: (a) $2c/W = 0.02$, (b) $2c/W = 0.05$, (c) $2c/W = 0.10$

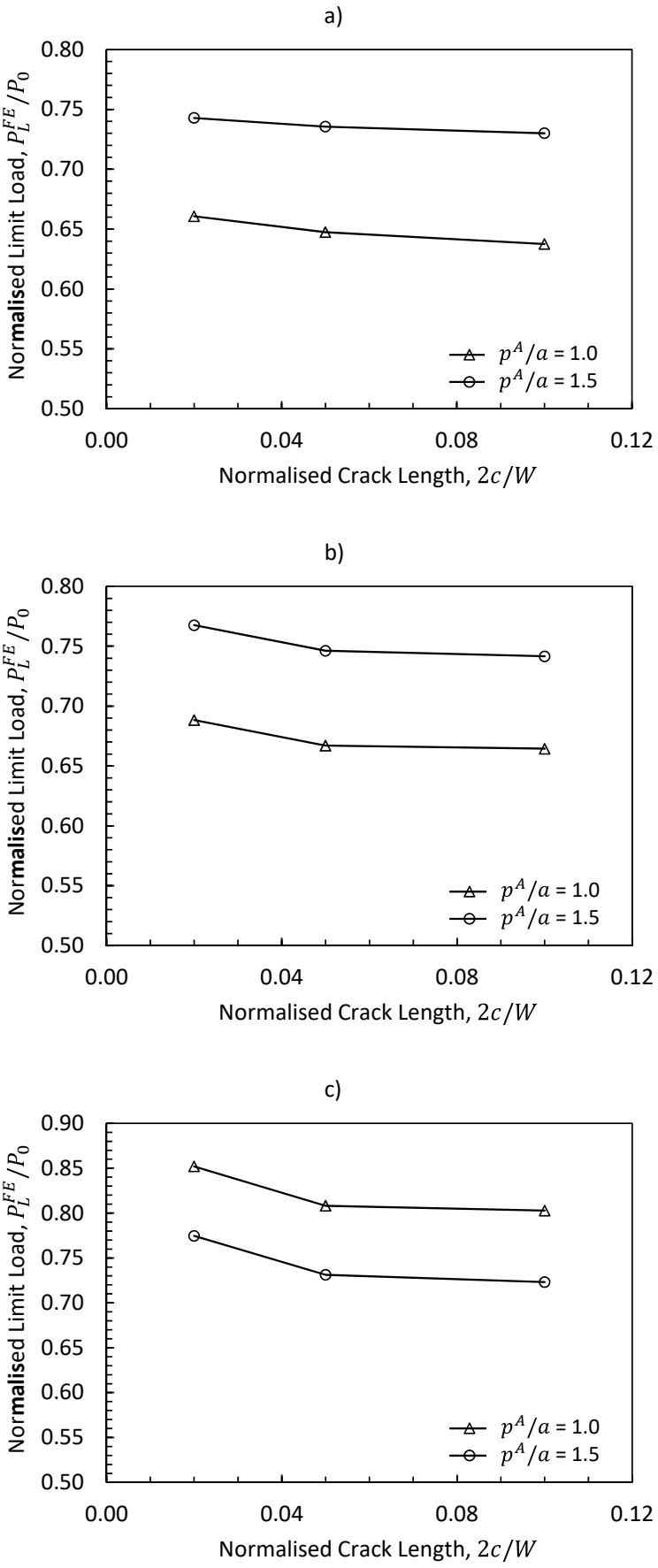


Figure 4.6: Limit Load Analysis Results – Effect of Normalised Crack Length: (a) $2a/t = 0.05$, (b) $2a/t = 0.15$, (c) $2a/t = 040$

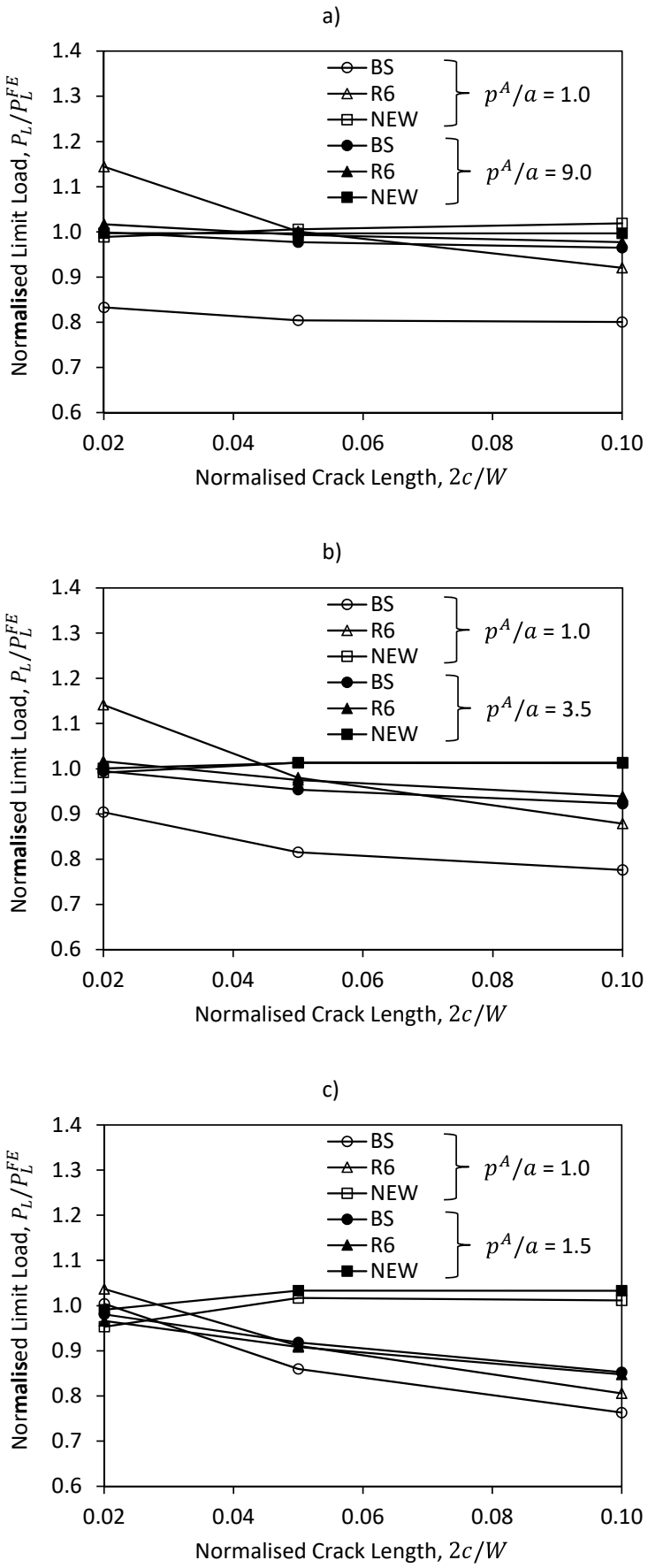


Figure 4.7: Comparison Between Limit Load Solutions: (a) $2a/t = 0.05$, (b) $2a/t = 0.15$, (c) $2a/t = 040$

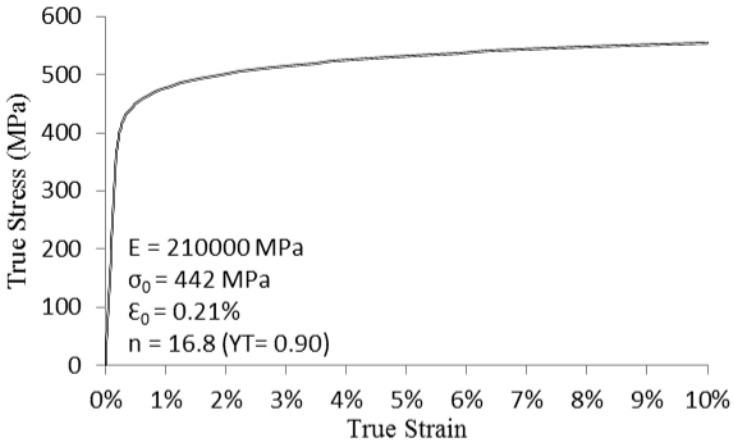


Figure 4.8: J-Estimation Scheme for Embedded Flaws – Assumed Stress-Strain Curve

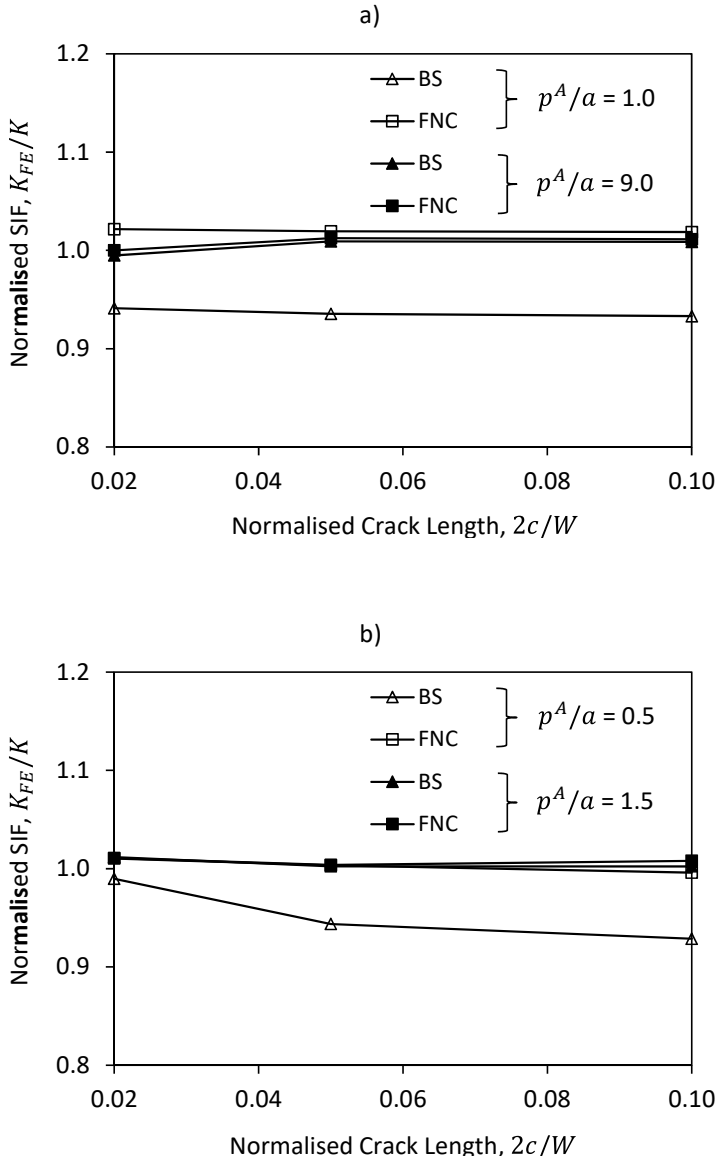


Figure 4.9: J-Estimation Scheme for Embedded Flaws – Comparison between Analytical and Numerical SIF: (a) $2a/t = 0.05$, (b) $2a/t = 0.40$

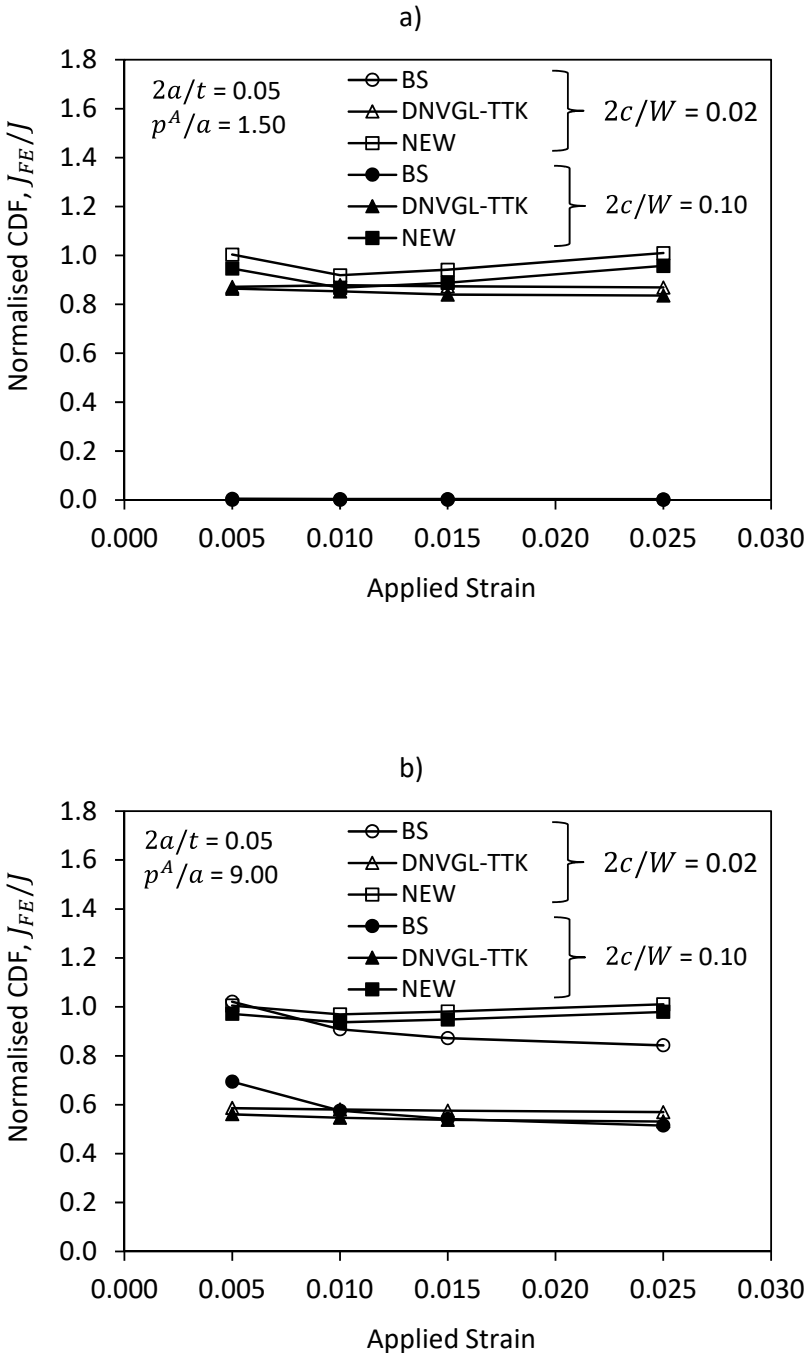


Figure 4.10: Comparison of J-Estimation Schemes for $2a/t = 0.05$: (a) $p^A/t = 1.5$, (b) $p^A/t = 9.0$

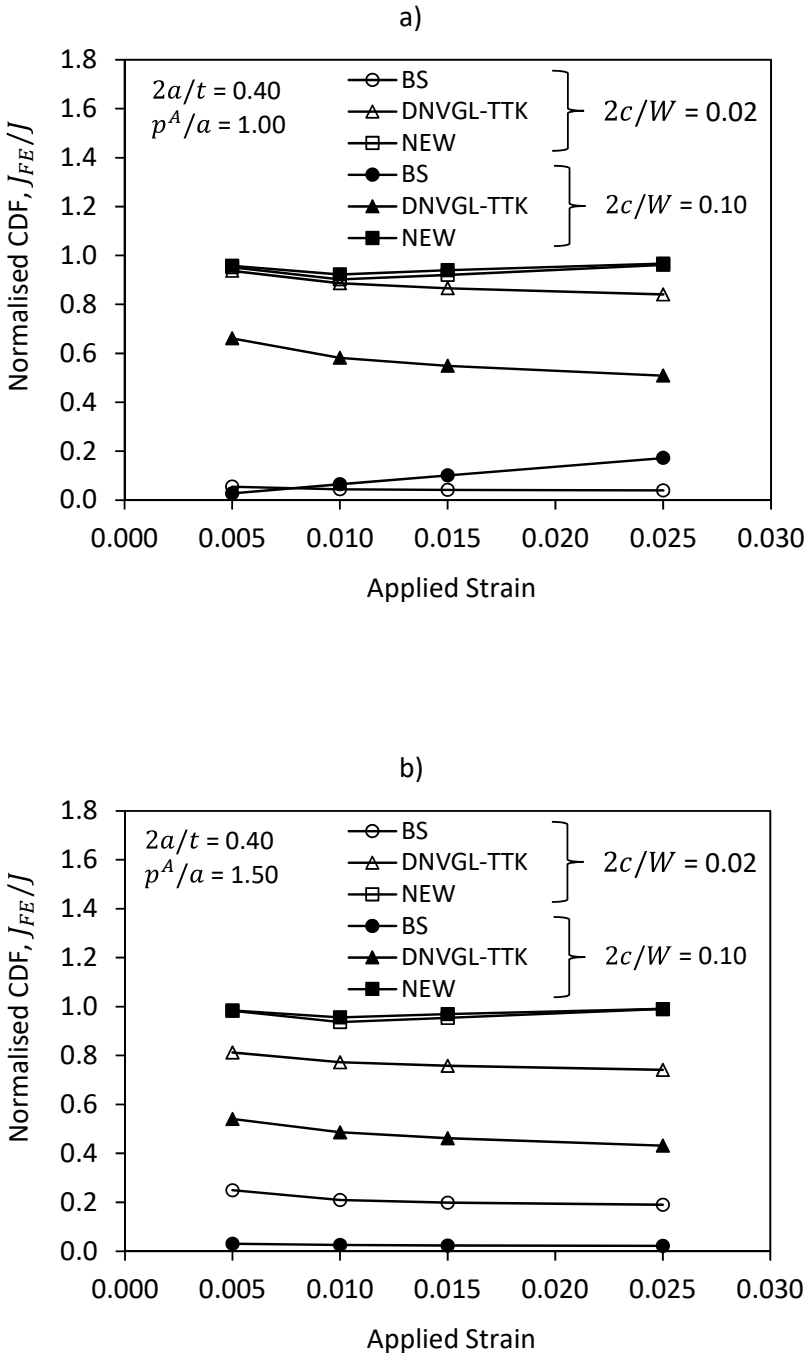


Figure 4.11: Comparison of J-Estimation Schemes for $2a/t = 0.40$: (a) $p^A/t = 1.0$, (b) $p^A/t = 1.5$

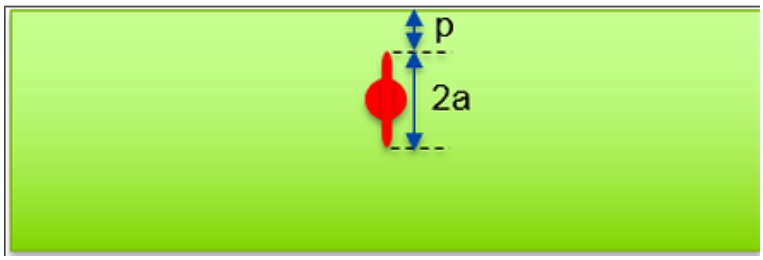


Figure 4.12: Schematic Illustration of MMCT Specimen with Through Thickness Embedded Flaw

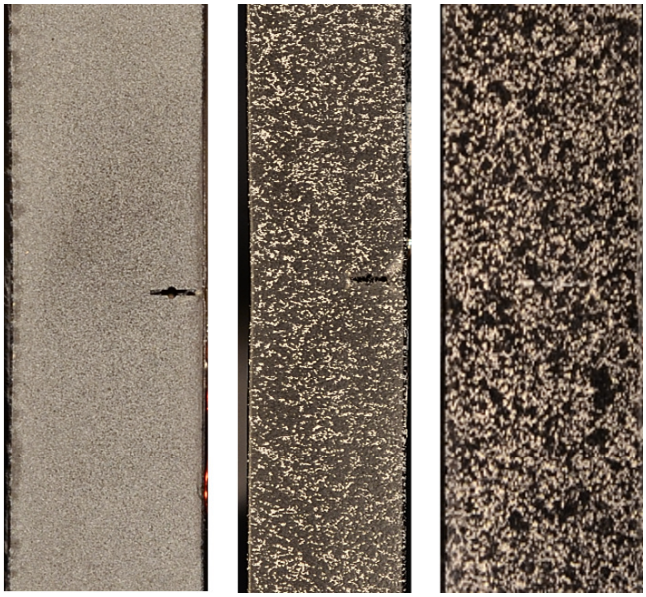


Figure 4.13: Examples of Speckle Patterns Applied on Test Specimens

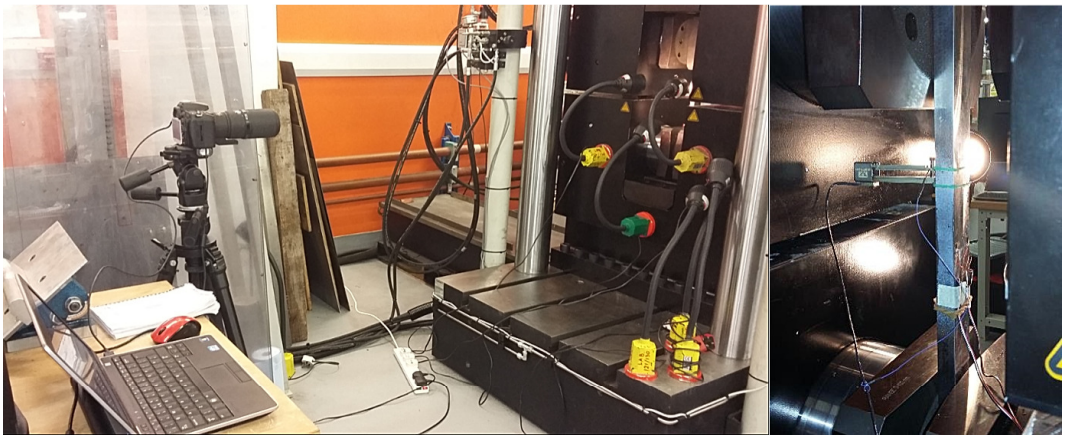


Figure 4.14: Embedded Flaw Test Setup



Figure 4.15: Test Setup for Establishment of Reference Load

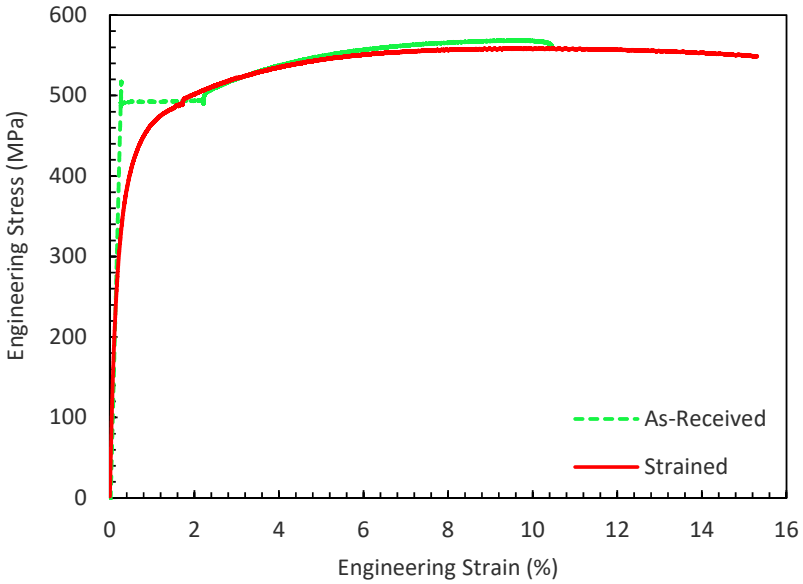


Figure 4.16: Test Results – Stress-Strain Curves Obtained with Uncracked Specimens

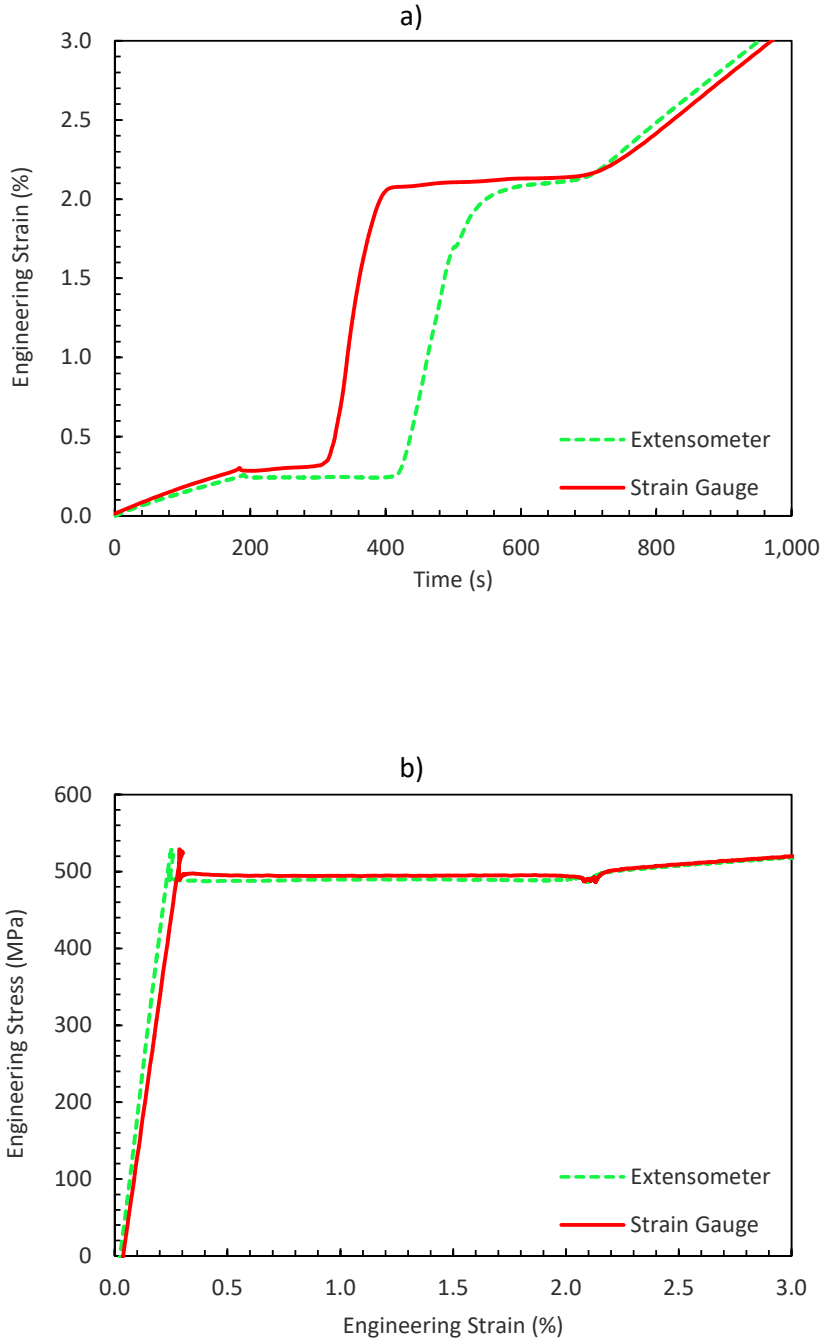


Figure 4.17: Test Results – Illustration of Lüders' Banding Process: (a) Strain-Time Curves, (b) Stress-Strain Curves

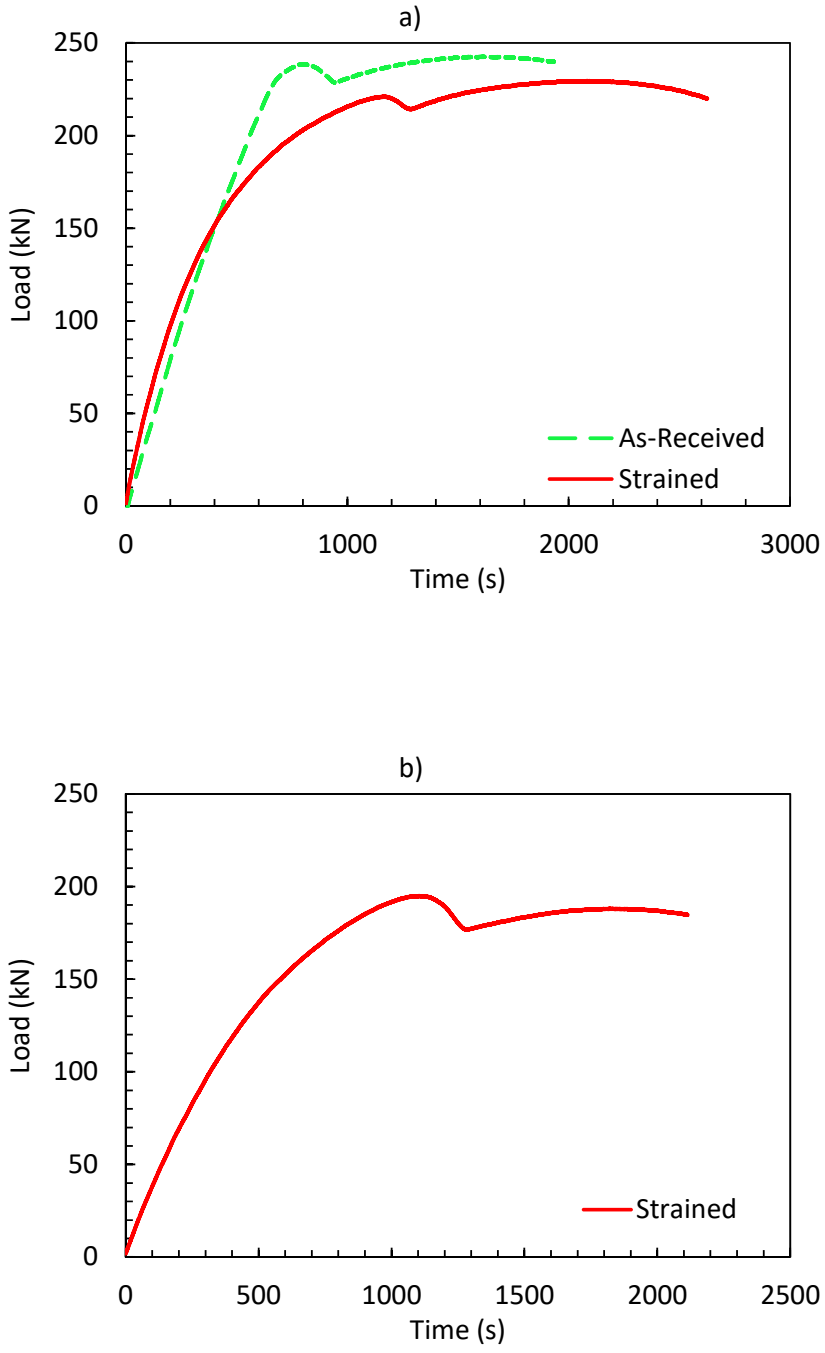


Figure 4.18: Test Results – Load versus Time Curves: (a) $2a = 4.0$ mm and $p^A = 1.0$ mm, (b) $2a = 6.0$ mm and $p^A = 1.5$ mm

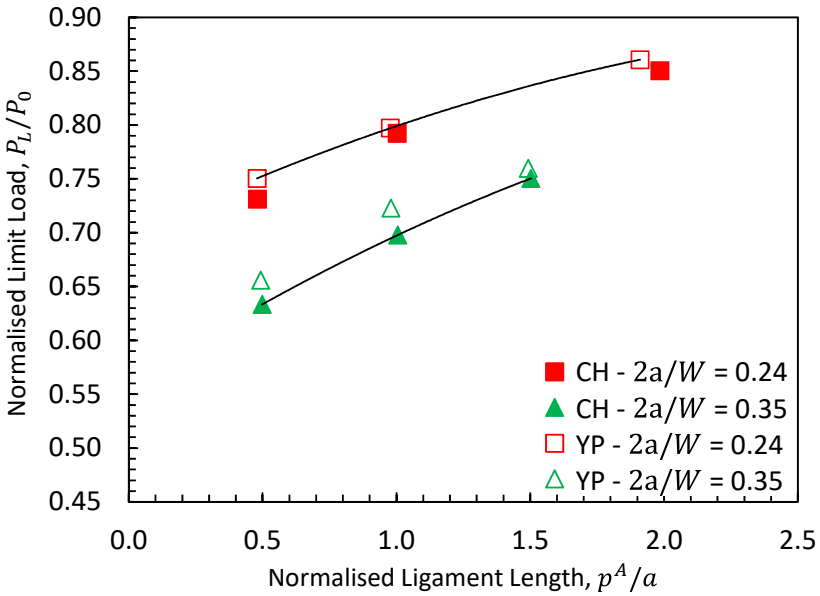


Figure 4.19: Summary of Test Results

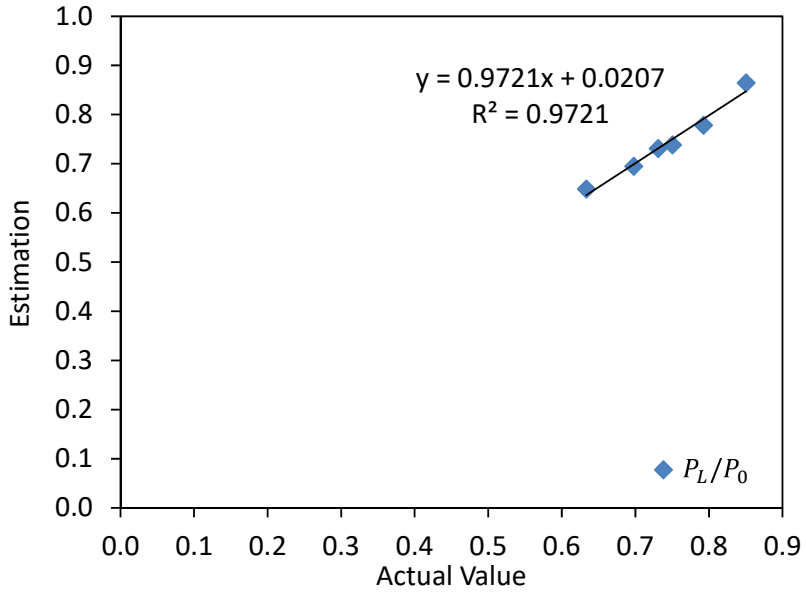


Figure 4.20: Regression Analysis

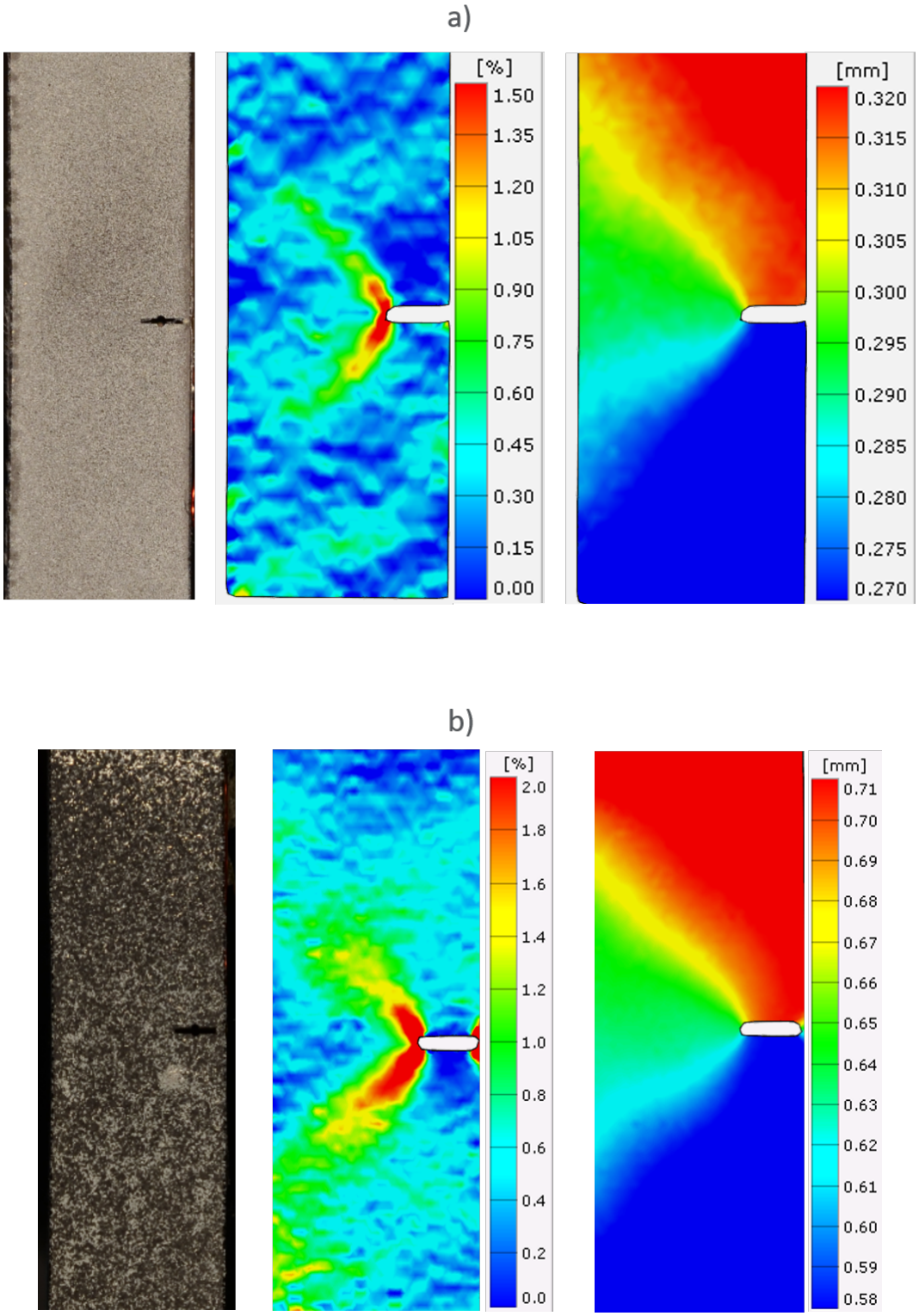


Figure 4.21: Strain and Displacement Contours from Digital Image Correlation – Specimens with $2a = 4.0$ mm $\times$ $p^A = 1.0$ mm Flaw: (a) Yield Plateau, (b) Continuous Hardening

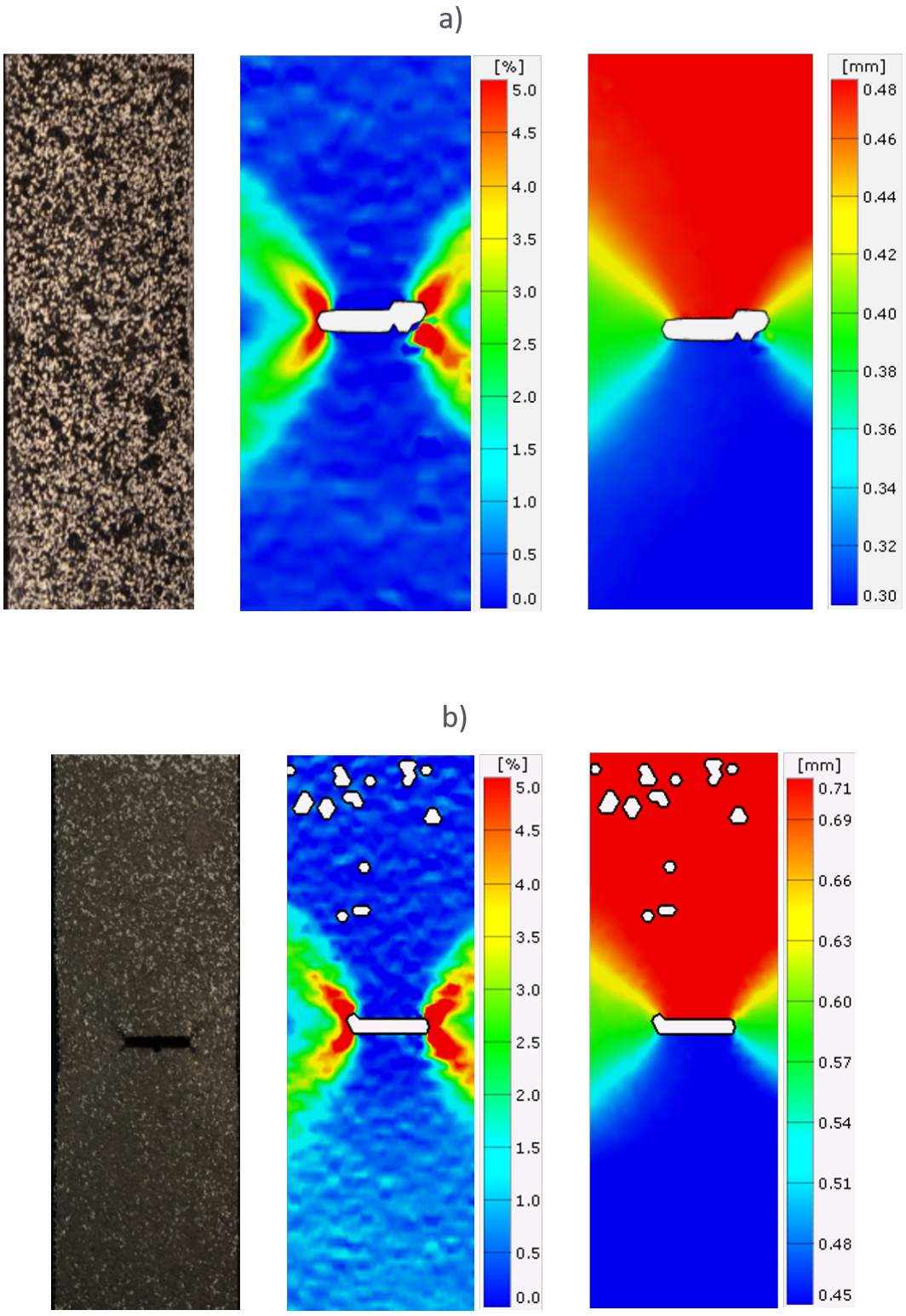


Figure 4.22: Strain and Displacement Contours from Digital Image Correlation – Specimens with $2a = 6.0$ mm $\times$ $p^A = 4.5$ mm Flaw: (a) Yield Plateau, (b) Continuous Hardening

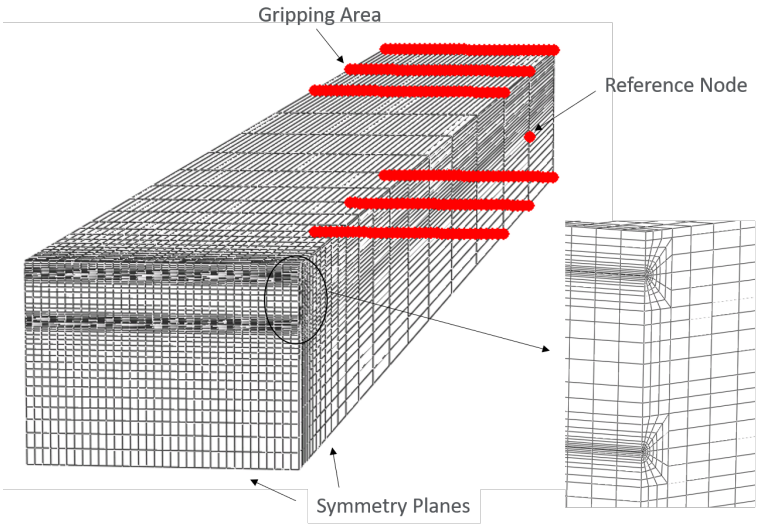


Figure 4.23: Finite-Element Analysis Model for Simulation of Embedded Flaw Tests

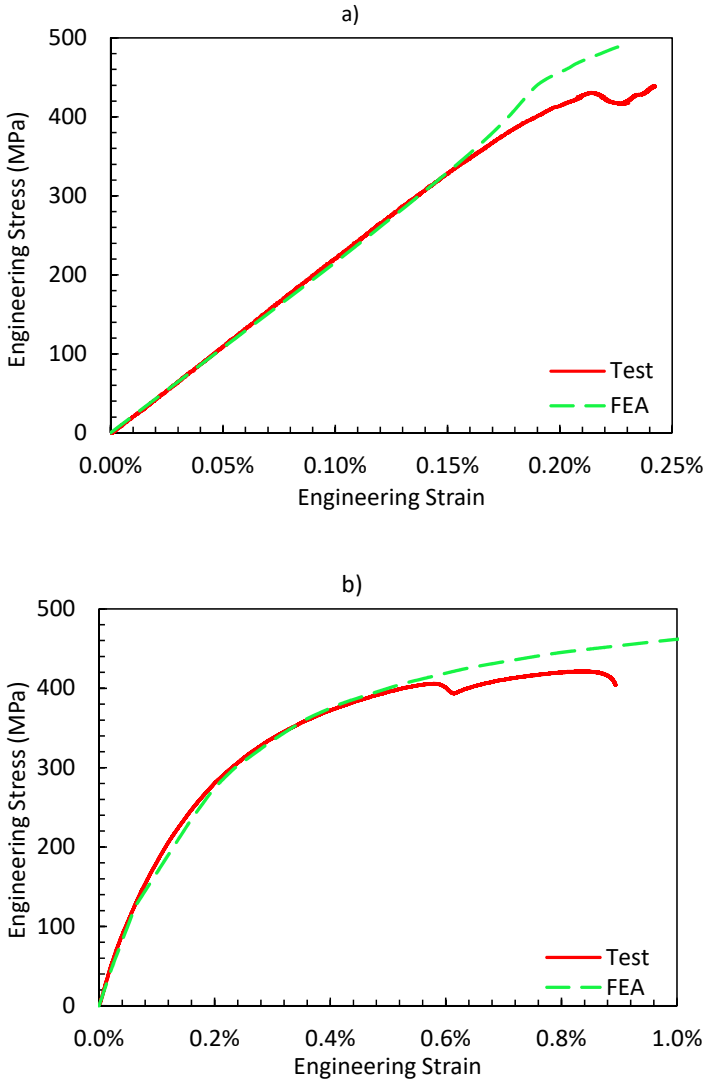


Figure 4.24: Comparison between FEA and Embedded Flaw Test Results for Specimen with $2a = 4.0$ mm $\times$ $p^A = 1.0$ mm: (a) Yield Plateau, (b) Continuous Hardening

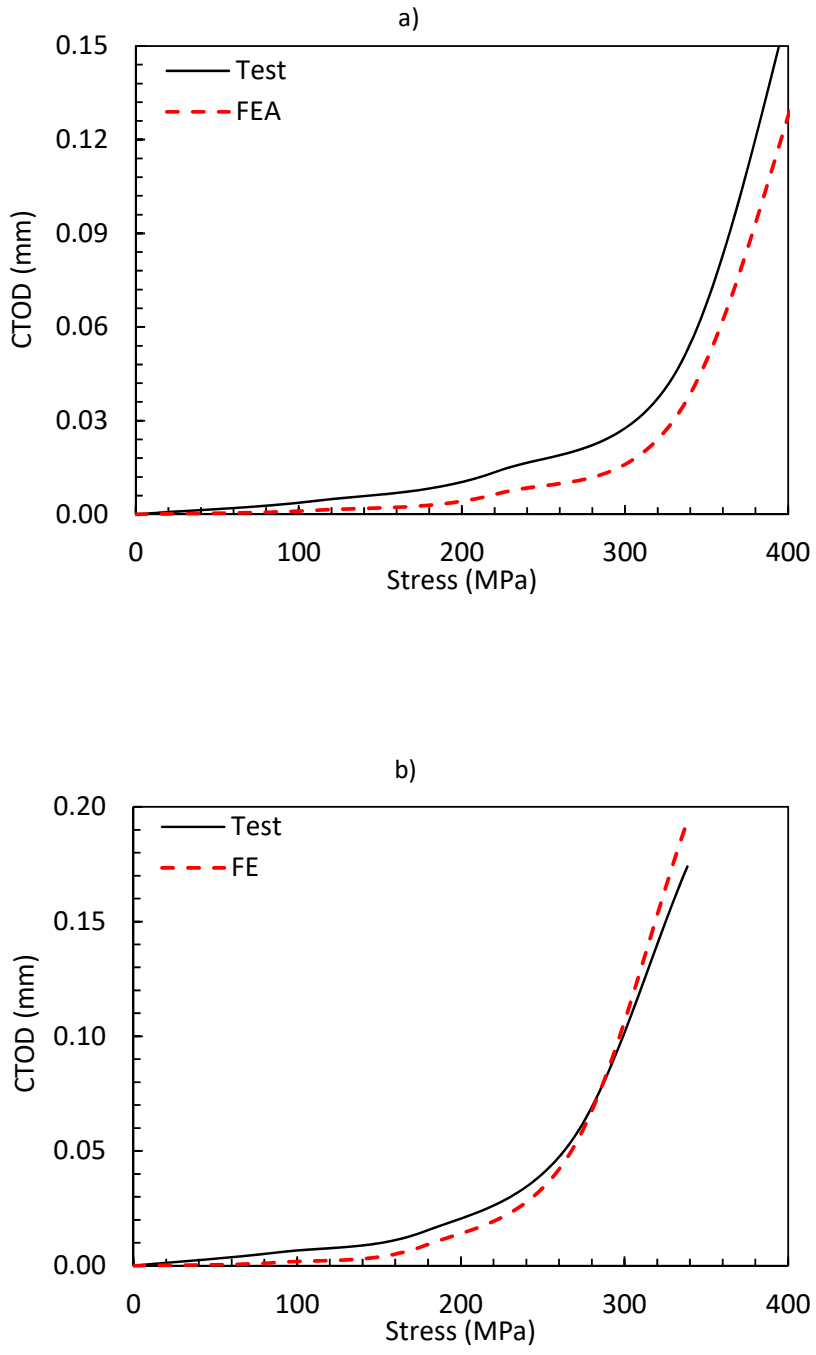


Figure 4.25: Comparison between FEA and DIC Results for Material with Continuous Hardening: (a) $2a = 4.0$ mm $\times$ $p^A = 2.0$ mm, (b) $2a = 6.0$ mm $\times$ $p^A = 1.5$ mm

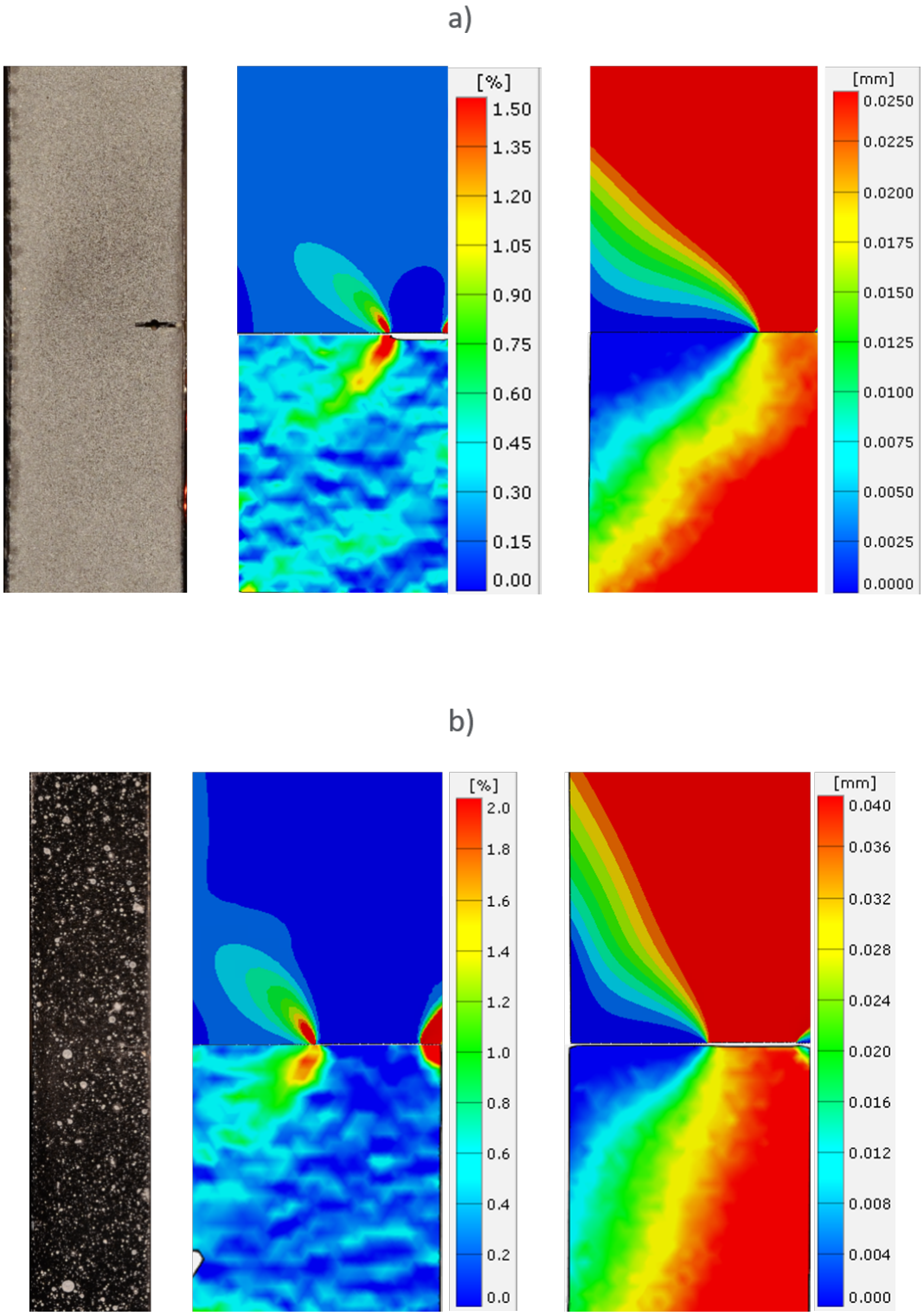


Figure 4.26: Comparison between FEA and DIC Contour Plots for Material with Yield Plateau: (a) $2a = 4.0$ mm $\times$ $p^A = 1.0$ mm, (b) $2a = 6.0$ mm $\times$ $p^A = 1.5$ mm

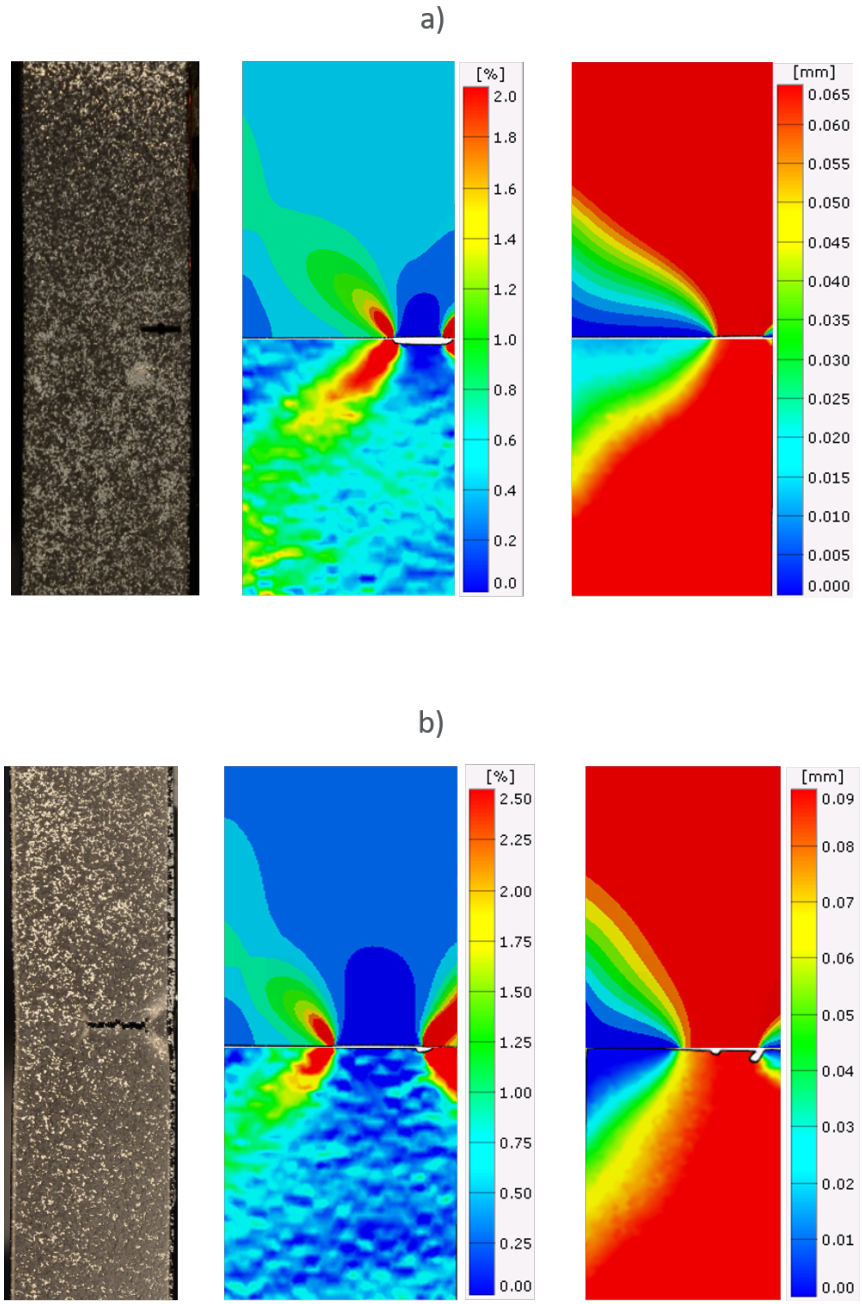


Figure 4.27: Comparison between FEA and DIC Contour Plots for Material with Continuous Hardening: (a) $2a = 4.0$ mm $\times$ $p^A = 1.0$ mm, (b) $2a = 6.0$ mm $\times$ $p^A = 3.0$ mm

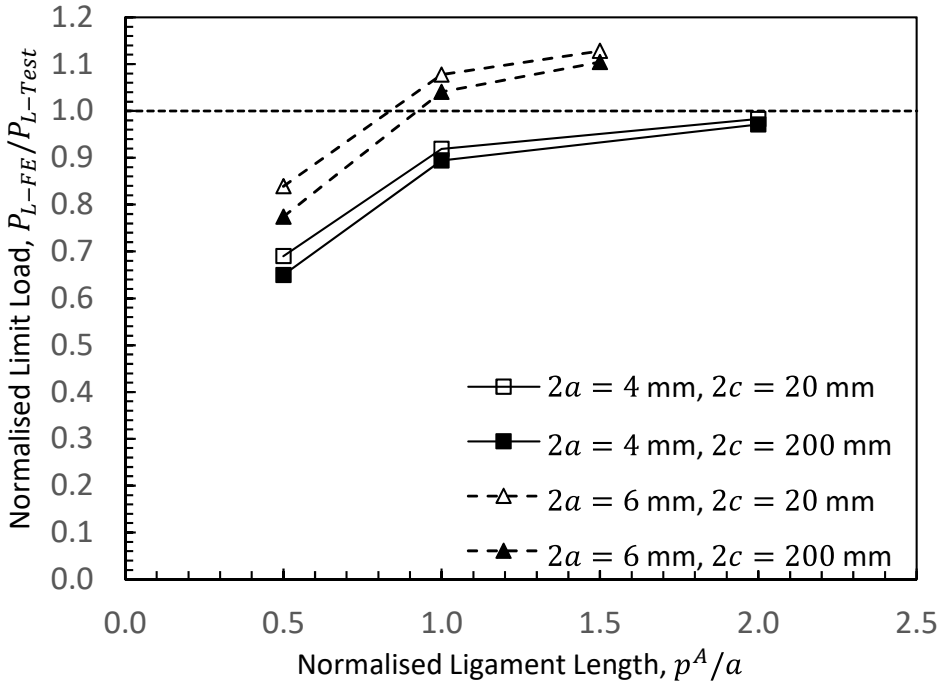


Figure 4.28: Comparison between FEA and Test Based Limit Load Solutions

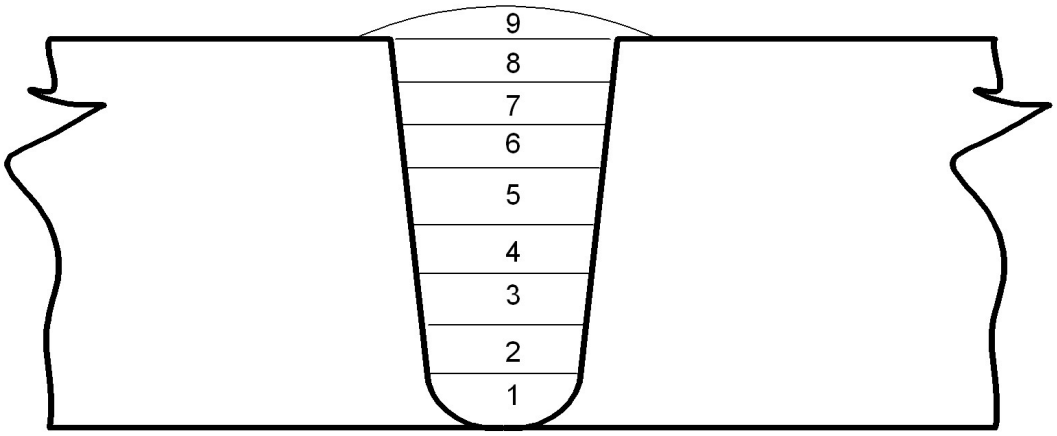


Figure 4.29: Fracture Toughness Testing – Profile of Weld Bevel and Weld Passes

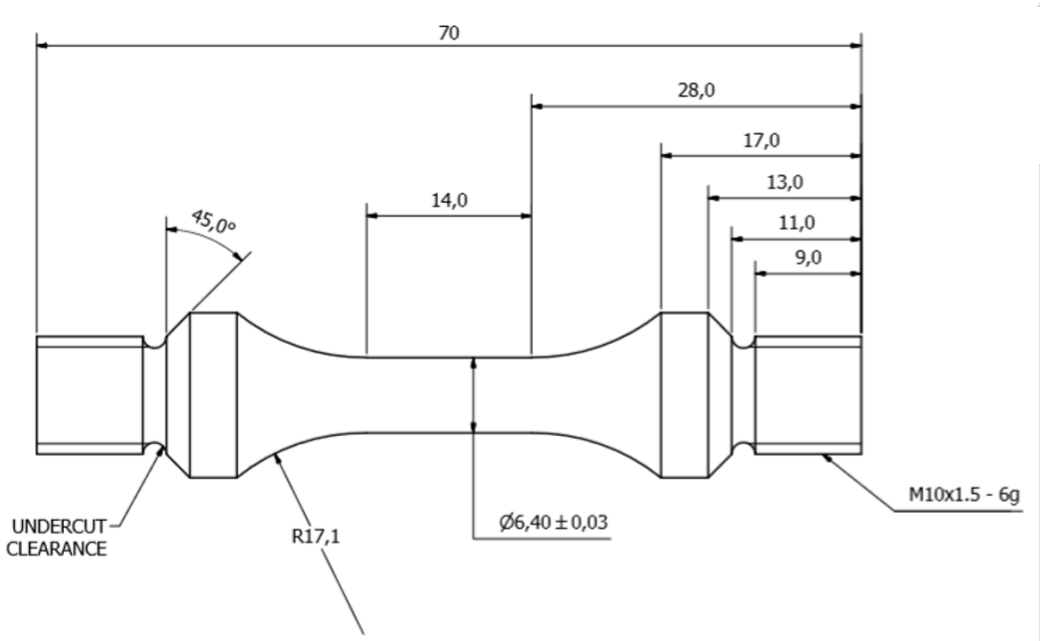


Figure 4.30: Fracture Toughness Testing – Specimen Used for Material Characterisation

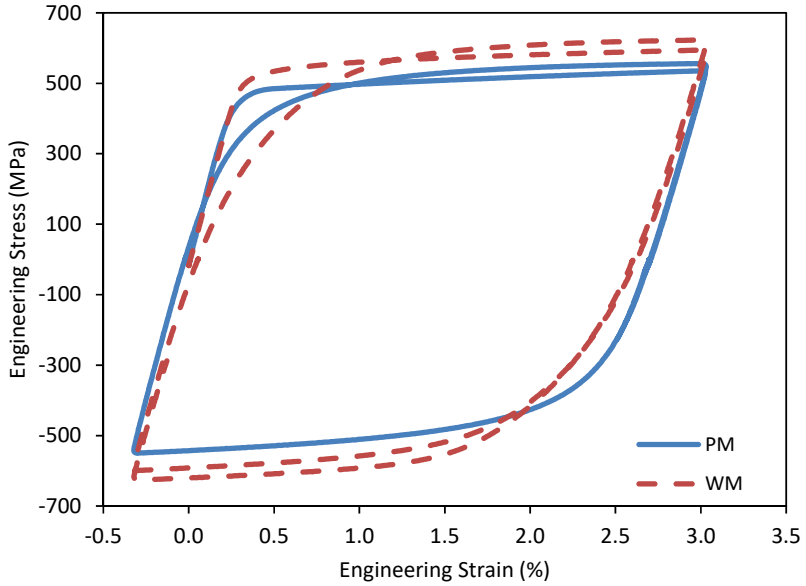


Figure 4.31: Fracture Toughness Testing – Material Stress-Strain Curves

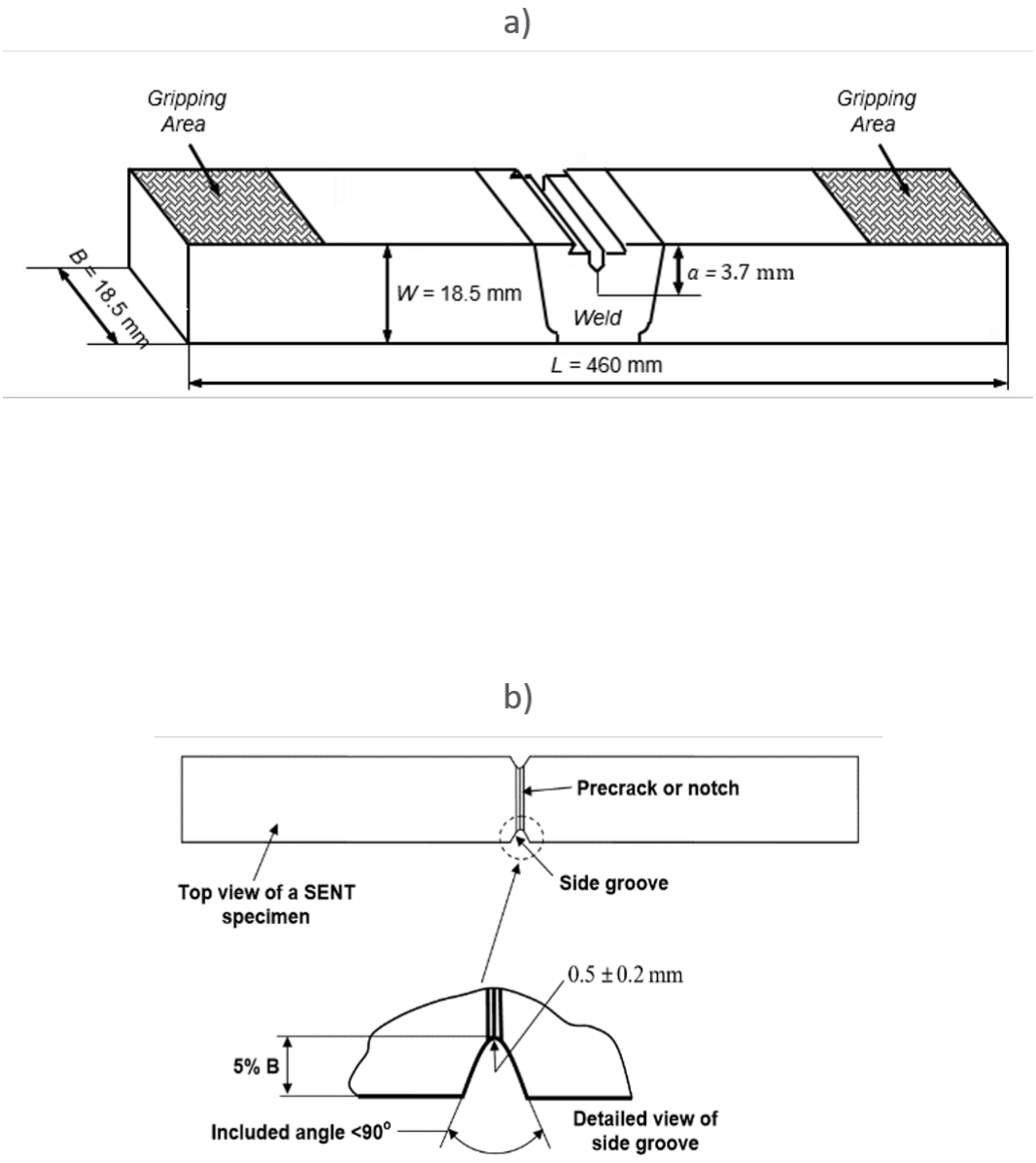


Figure 4.32: Fracture Toughness Test Specimen: (a) General Overview, (b) Side Groove Detail

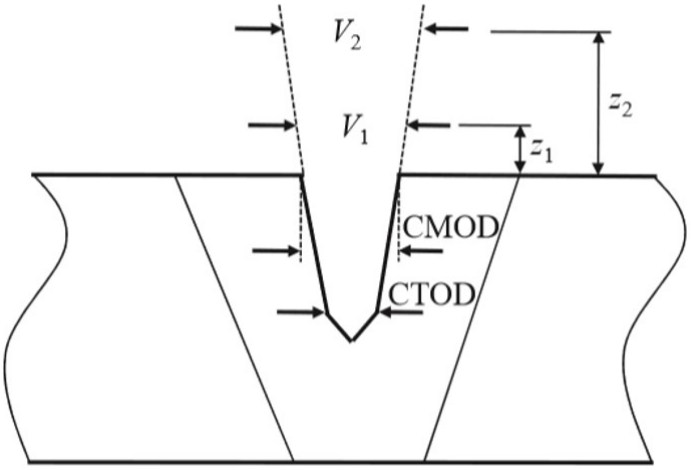


Figure 4.33: Fracture Toughness Testing – Geometrical Construction Used to Estimate CMOD and CTOD

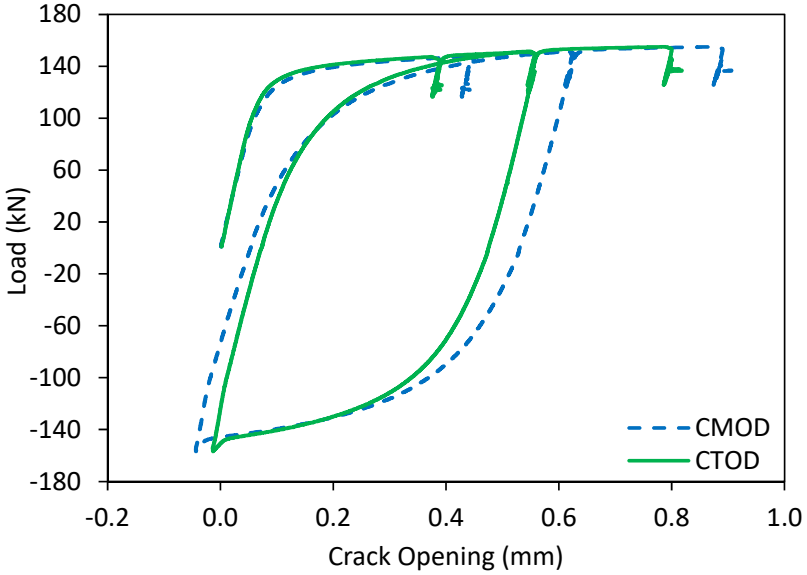


Figure 4.34: Fracture Toughness Testing – Example of Load-CMOD and Load-CTOD Curves

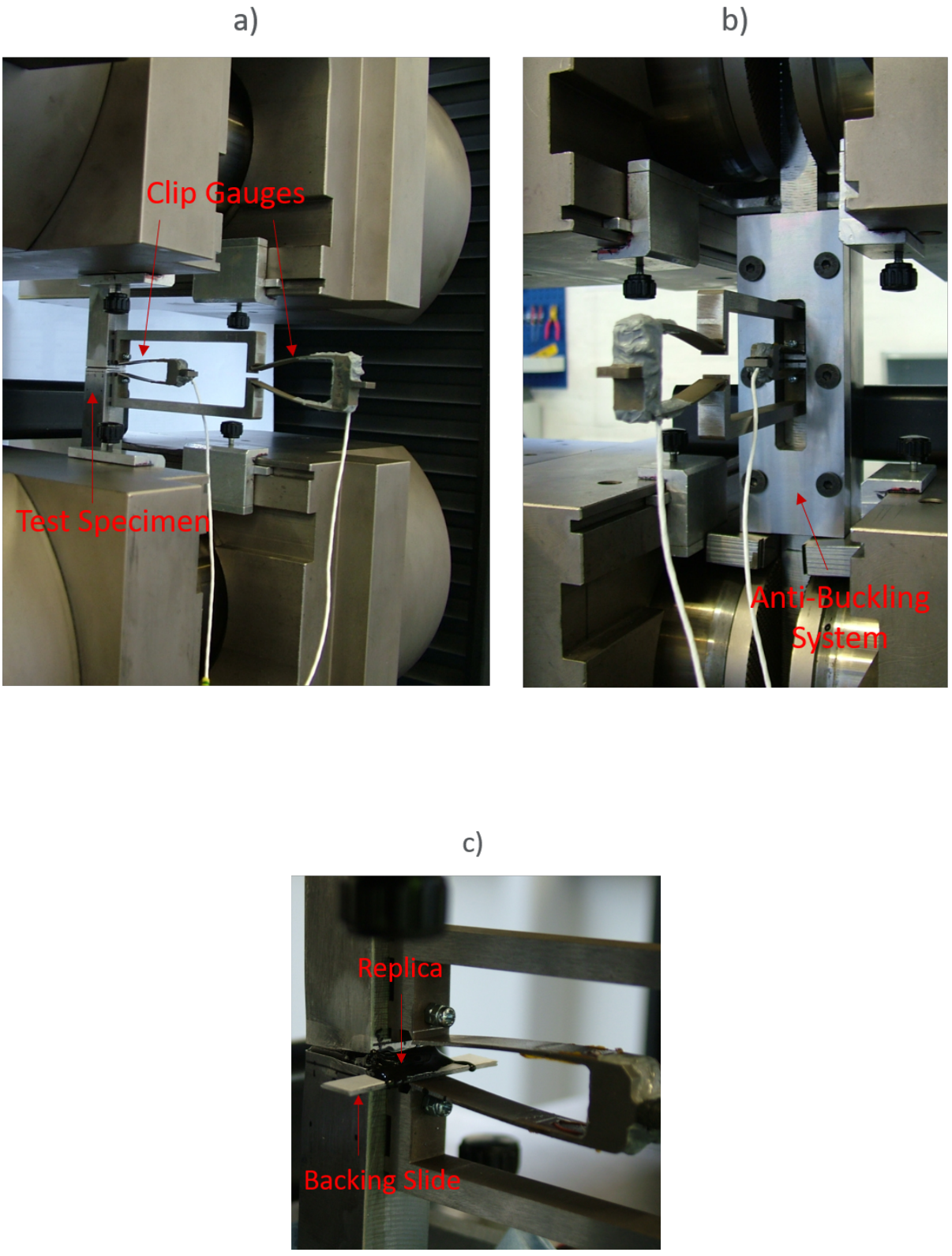


Figure 4.35: Fracture Toughness Testing: (a) Setup for Tensile Straining Event, (b) Setup for Compressive Straining Event, (c) Acquisition of Silicon Impression of Crack

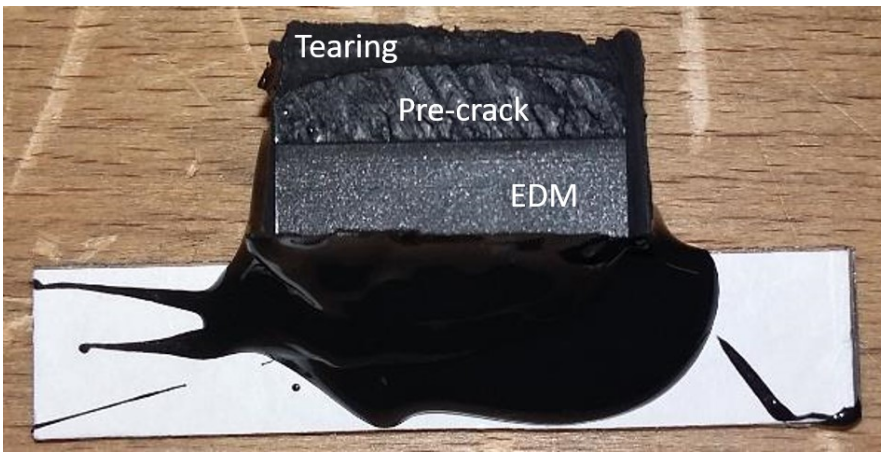


Figure 4.36: Fracture Toughness Testing – Silicon Replica

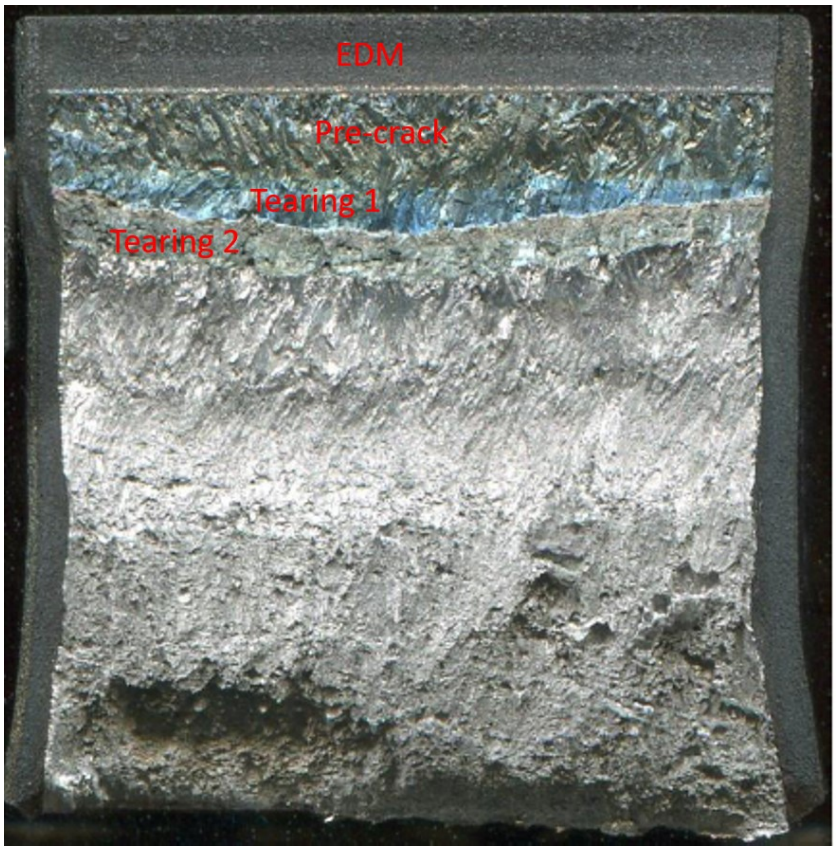


Figure 4.37: Fracture Toughness Testing – Example of Fracture Face Showing EDM, Pre-Crack and Tearing

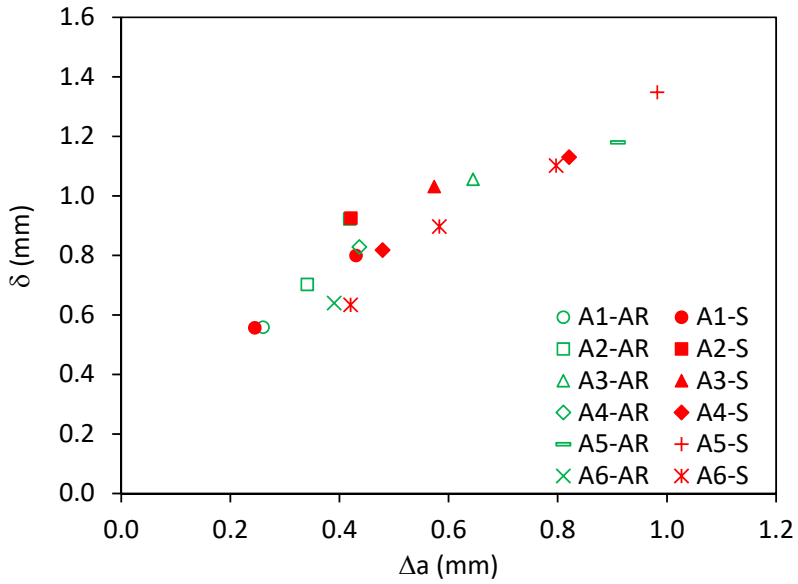


Figure 4.38: Fracture Toughness Testing – Results Summary

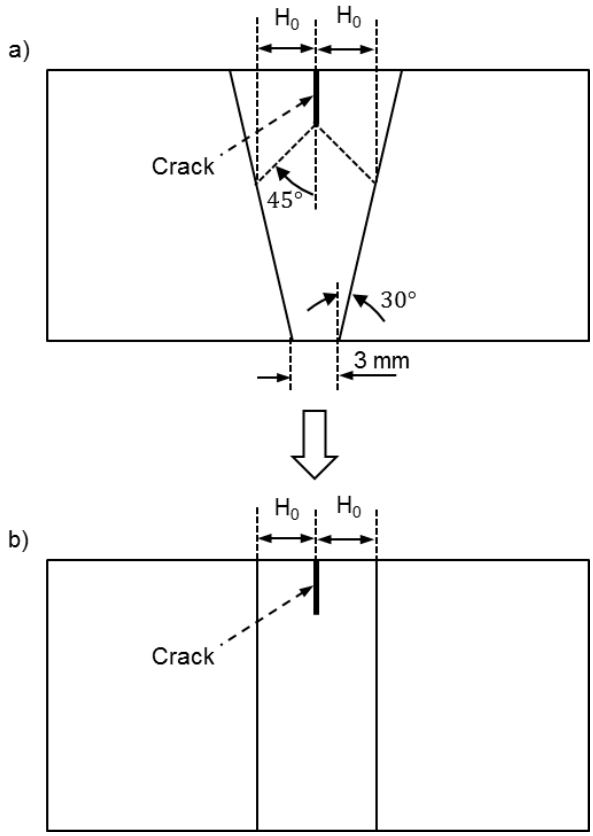


Figure 4.39: Surface Flaws in Undermatch Welds – Weld Geometry: (a) Actual, (b) Equivalent

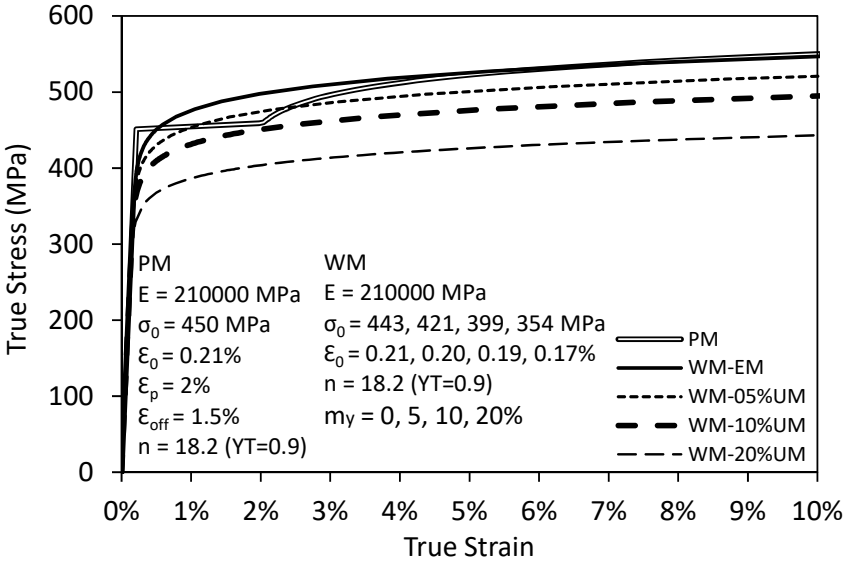


Figure 4.40: Parametric FEA – Stress-Strain Curves with Yield Plateau, E=210 GPa, σ_y=450 MPa, n=16.8

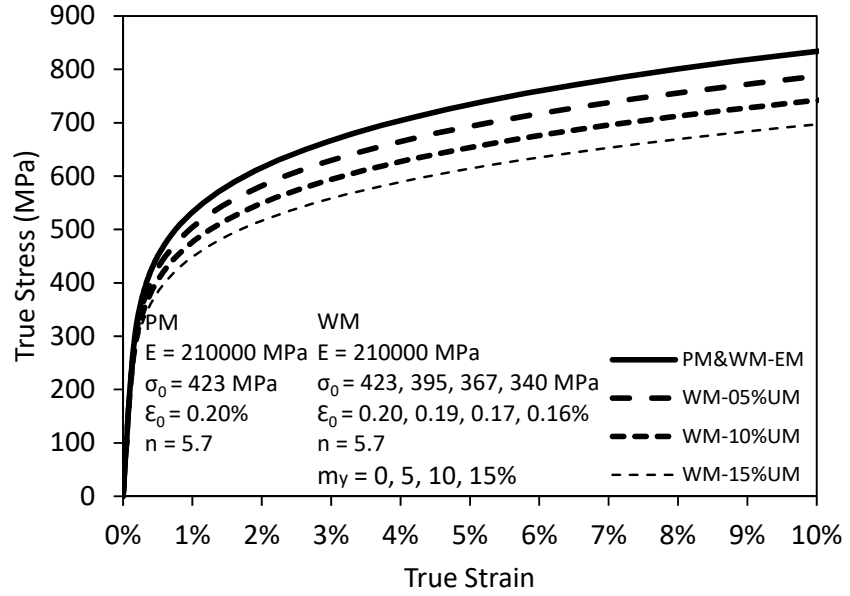


Figure 4.41: Parametric FEA – Stress-Strain Curves with Continuous Hardening, E=210 GPa, σ_y=450 MPa, n=5.7

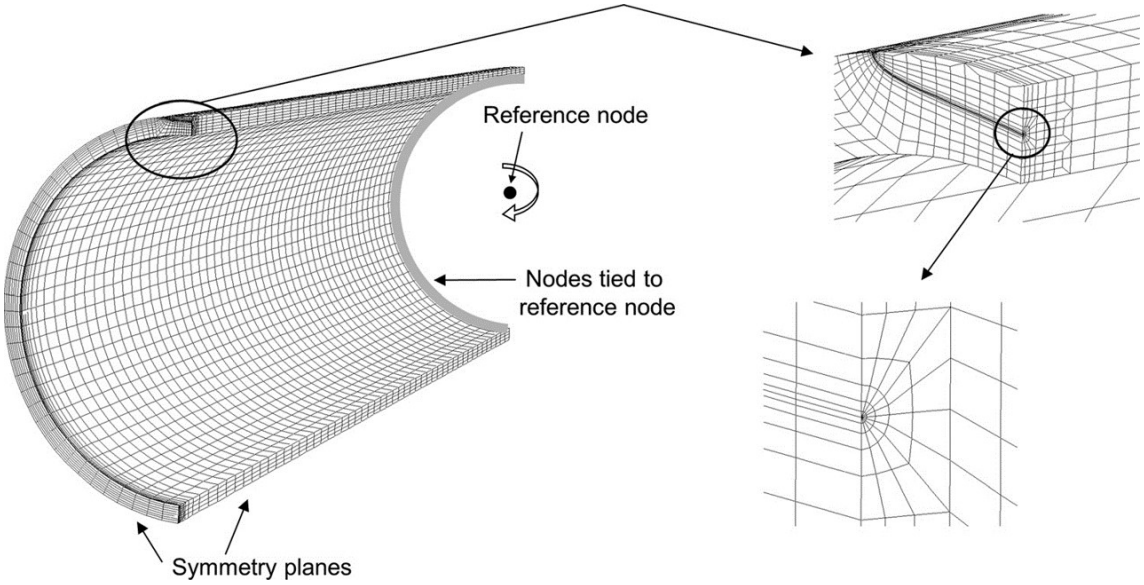


Figure 4.42: Parametric FEA – Typical Model

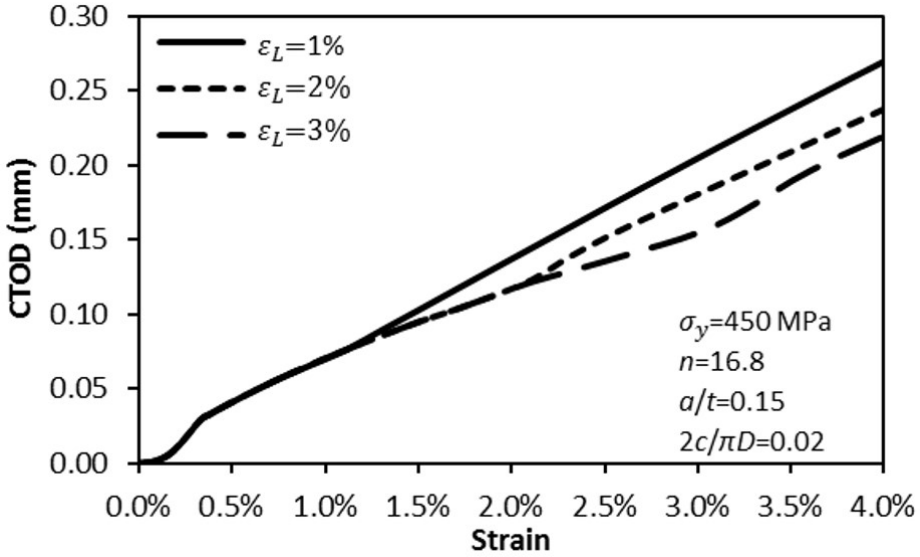


Figure 4.43: Parametric FEA Results – Effect of Yield Plateau on Crack Driving Force in Evenmatch Weld

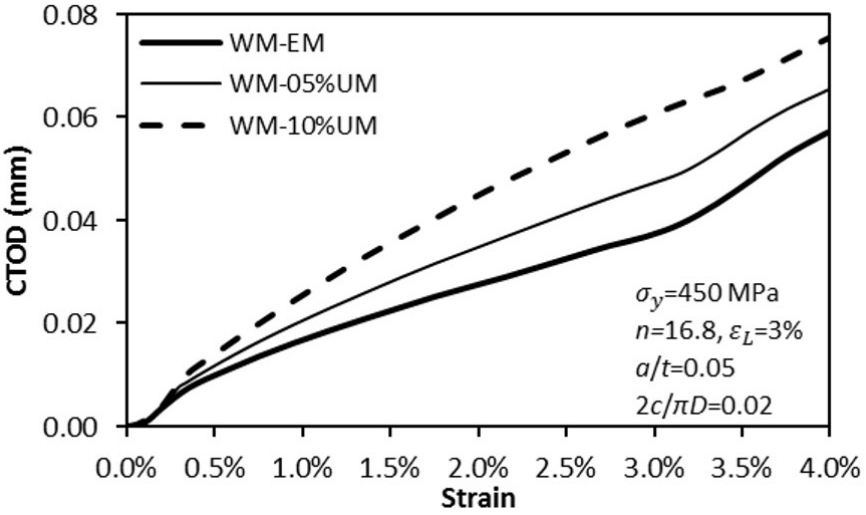


Figure 4.44: Parametric FEA Results – Effect of Undermatch on Crack Driving Force

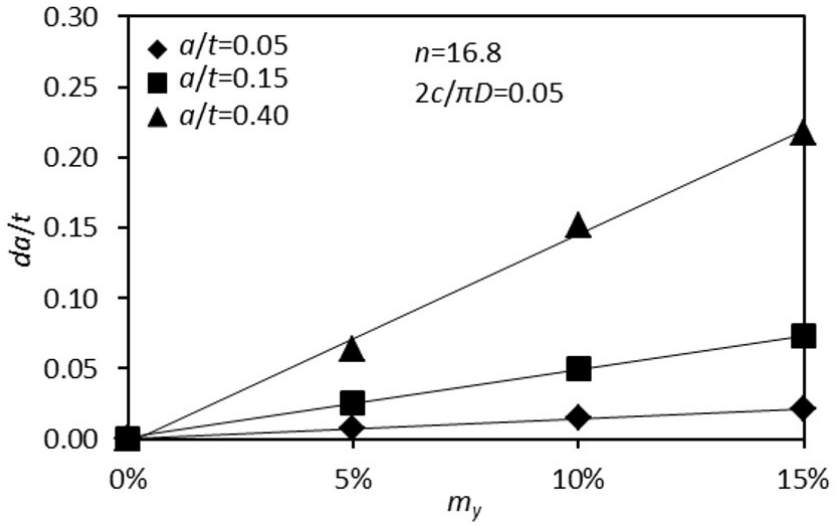


Figure 4.45: Parametric FEA Results – Effect of Undermatch and Crack Depth on Normalised Crack Depth Adjustment in Material Exhibiting Continuous Hardening

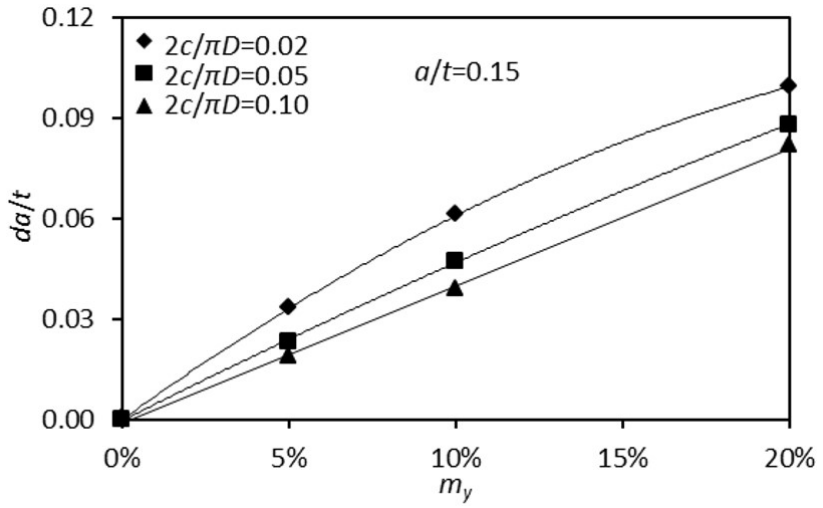


Figure 4.46: Parametric FEA Results – Effect of Undermatch and Crack Length on Normalised Crack Depth Adjustment in Material Exhibiting Yield Plateau

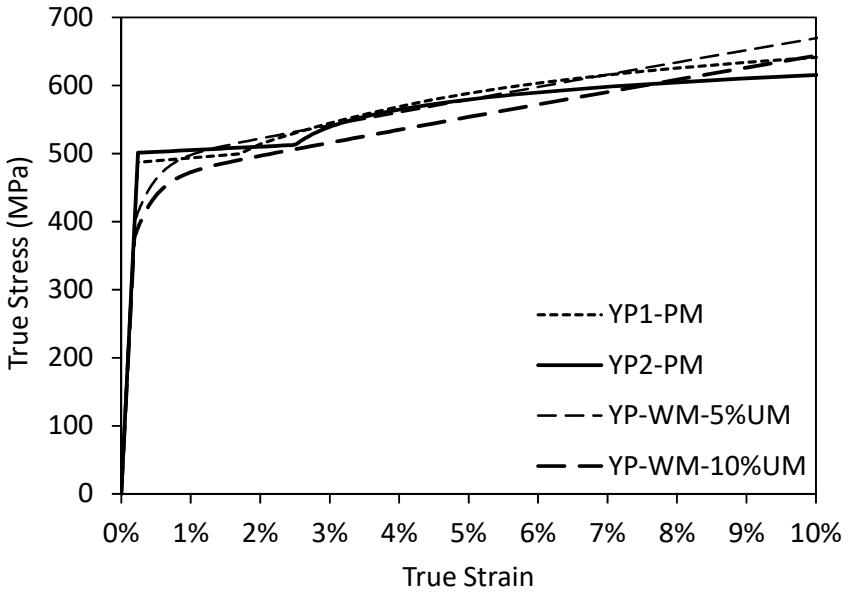


Figure 4.47: Validation of New ECA Procedure for Undermatch Welds – Stress-Strain Curves with Yield Plateau

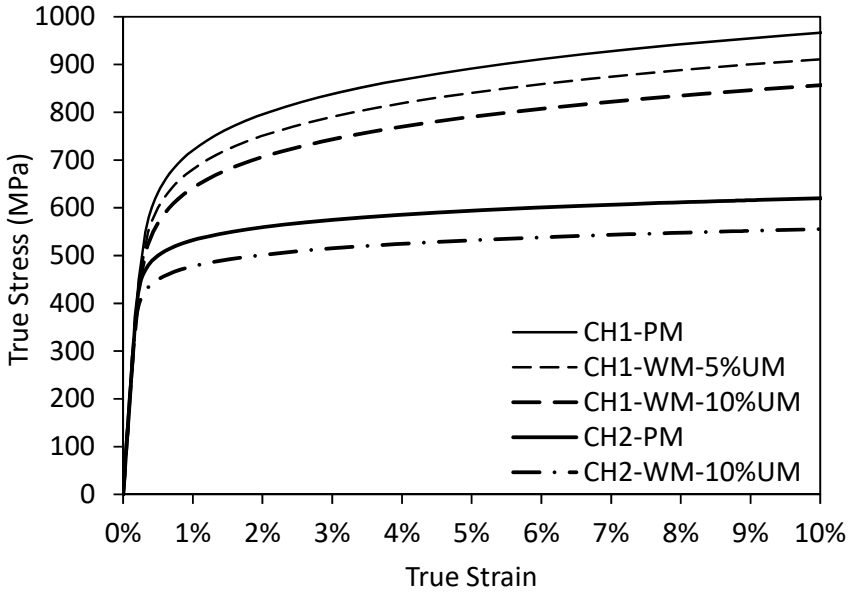


Figure 4.48: Validation of New ECA Procedure for Undermatch Welds – Stress-Strain Curves with Continuous Hardening

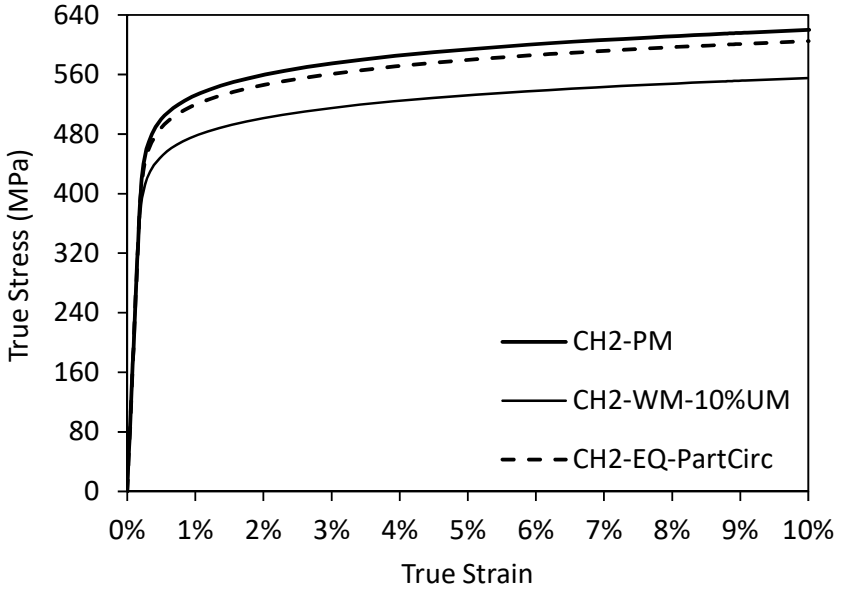


Figure 4.49: Validation of New ECA Procedure for Undermatch Welds – Equivalent Stress-Strain Curve

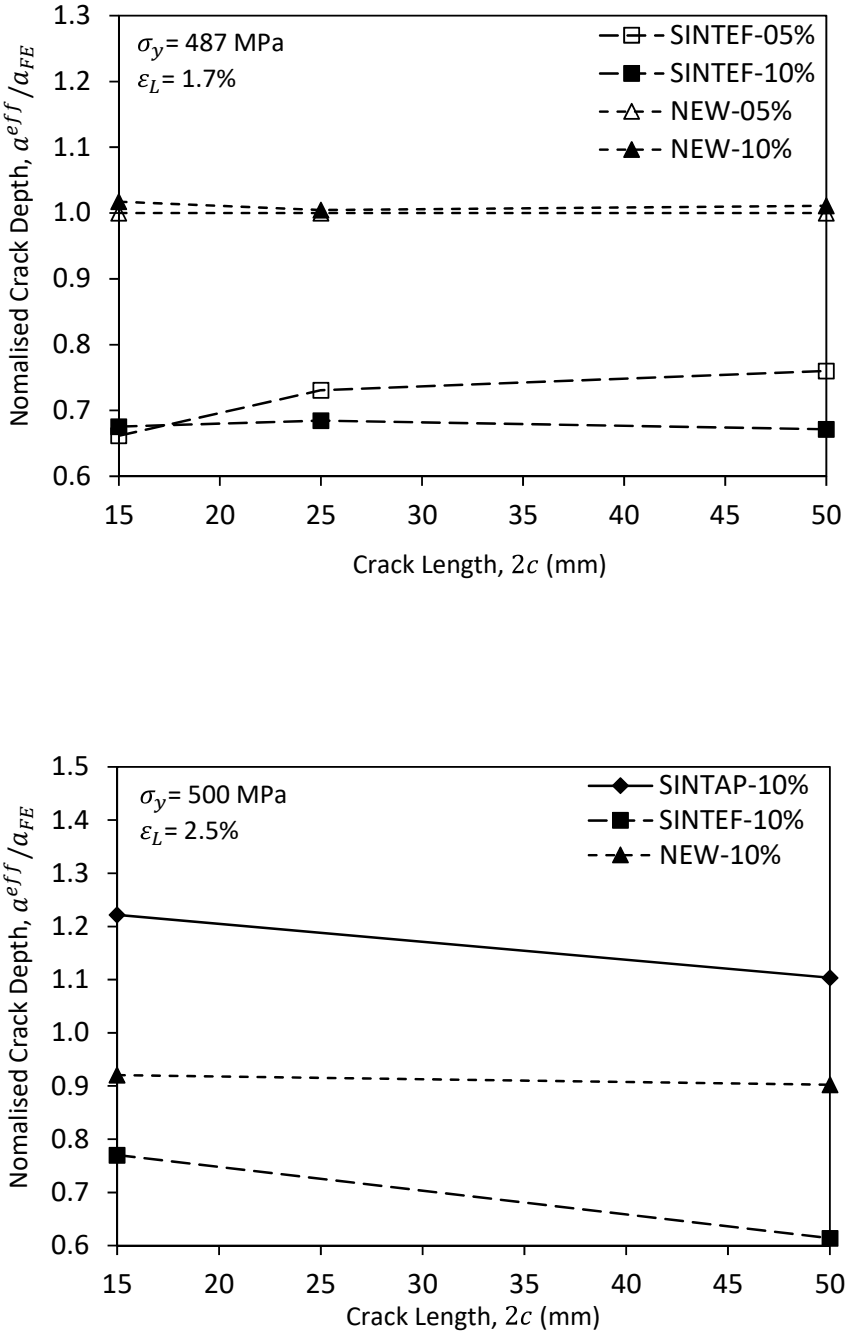


Figure 4.50: Validation of New ECA Procedure for Undermatch Welds – Results for 168.3 mm OD × 7.11 mm WT Pipe with Yield Plateau

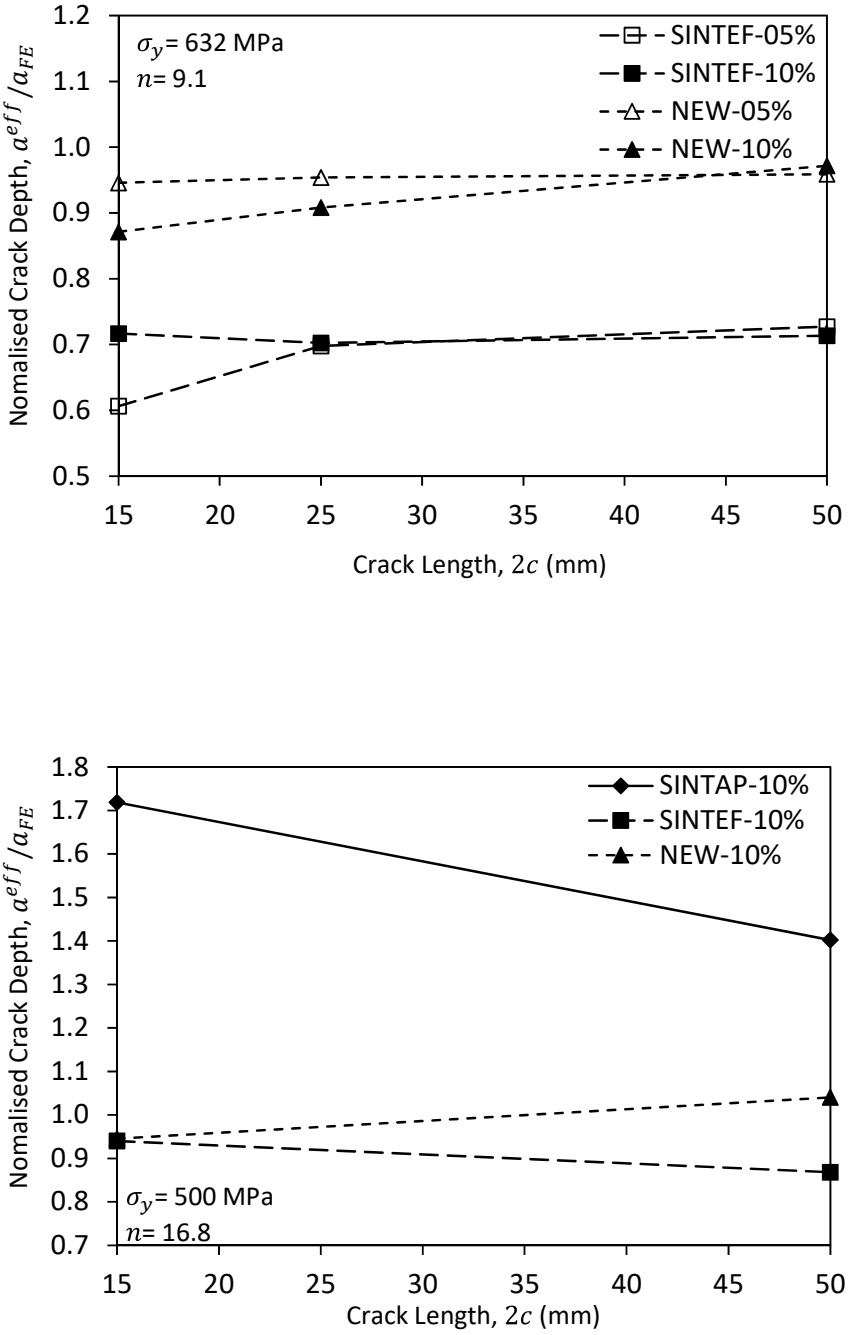


Figure 4.51: Validation of New ECA Procedure for Undermatch Welds – Results for 323.9 mm OD × 15.9 mm WT Pipe with Continuous Hardening

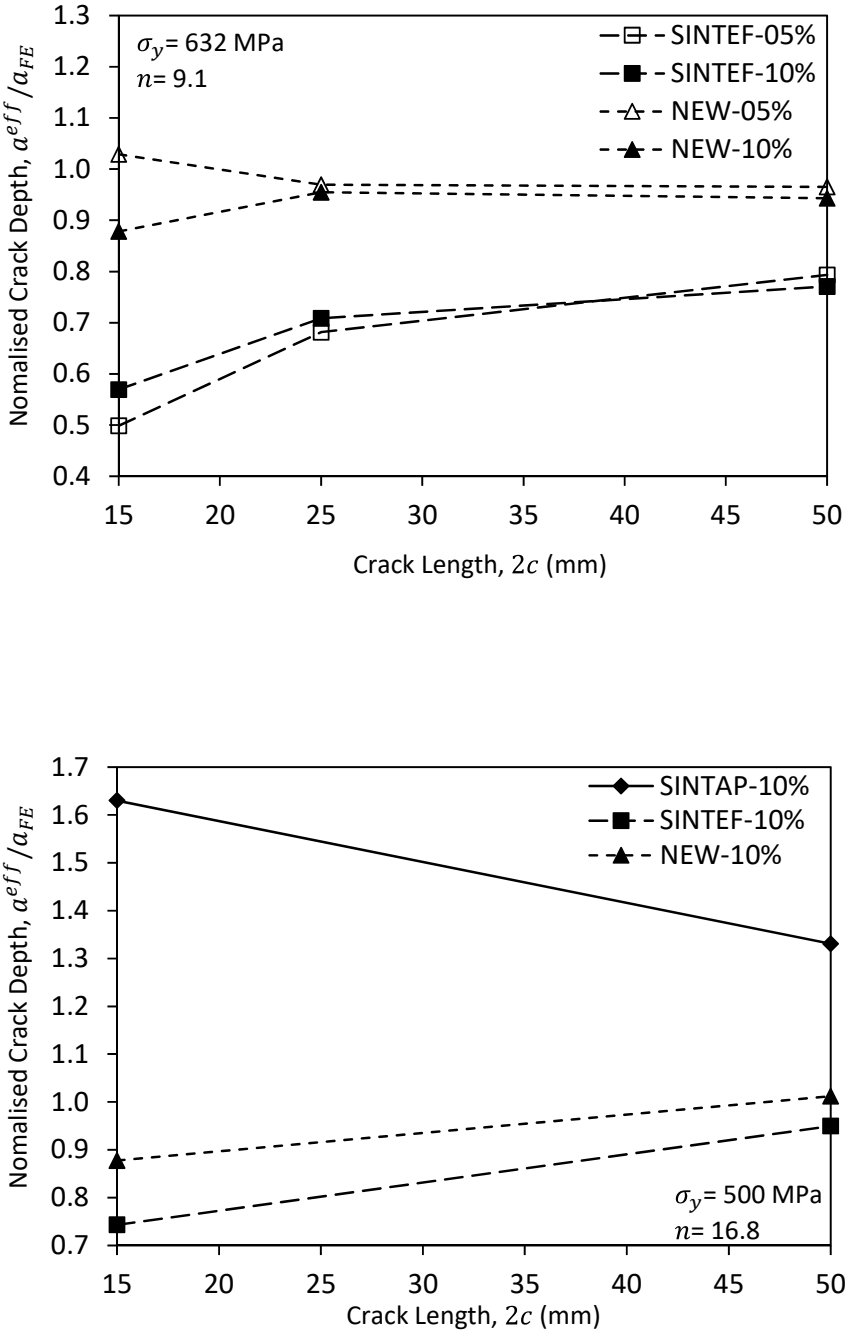


Figure 4.52: Validation of New ECA Procedure for Undermatch Welds – Results for 323.9 mm OD × 25.4 mm WT Pipe with Continuous Hardening

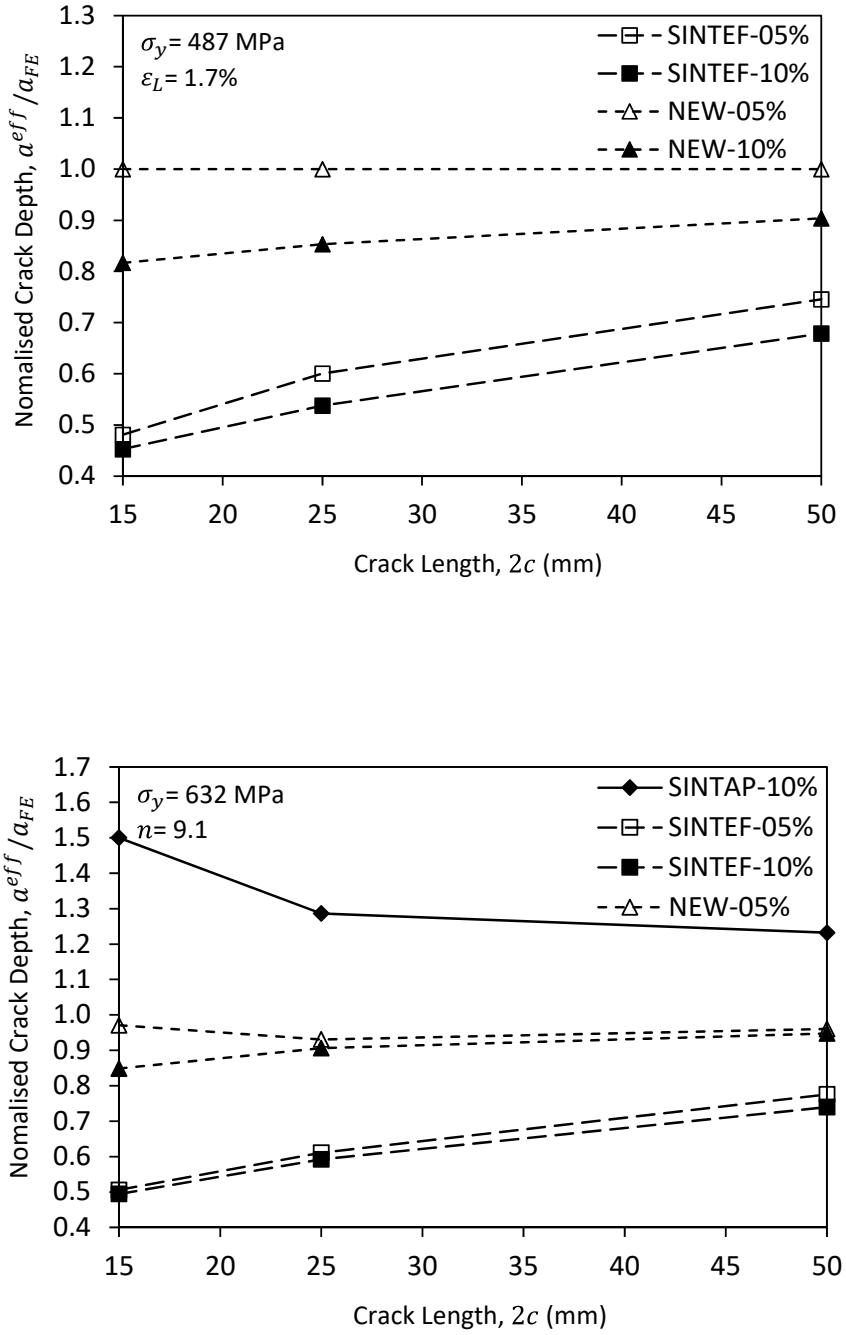


Figure 4.53: Validation of New ECA Procedure for Undermatch Welds – Results for 406.4 mm OD × 25.4 mm WT Pipe with and without Yield Plateau

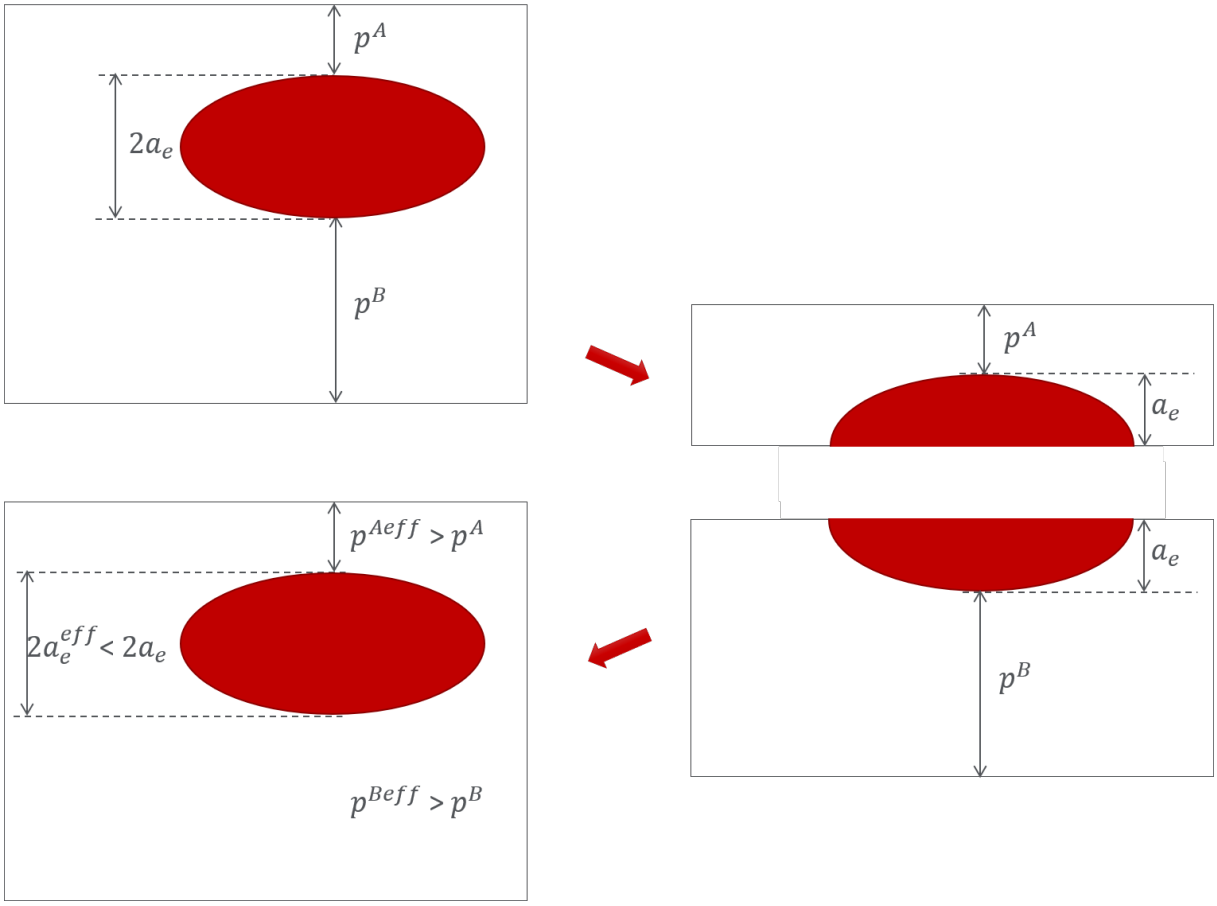


Figure 4.54: Adjustment Scheme for Embedded Flaws in Undermatch Welds

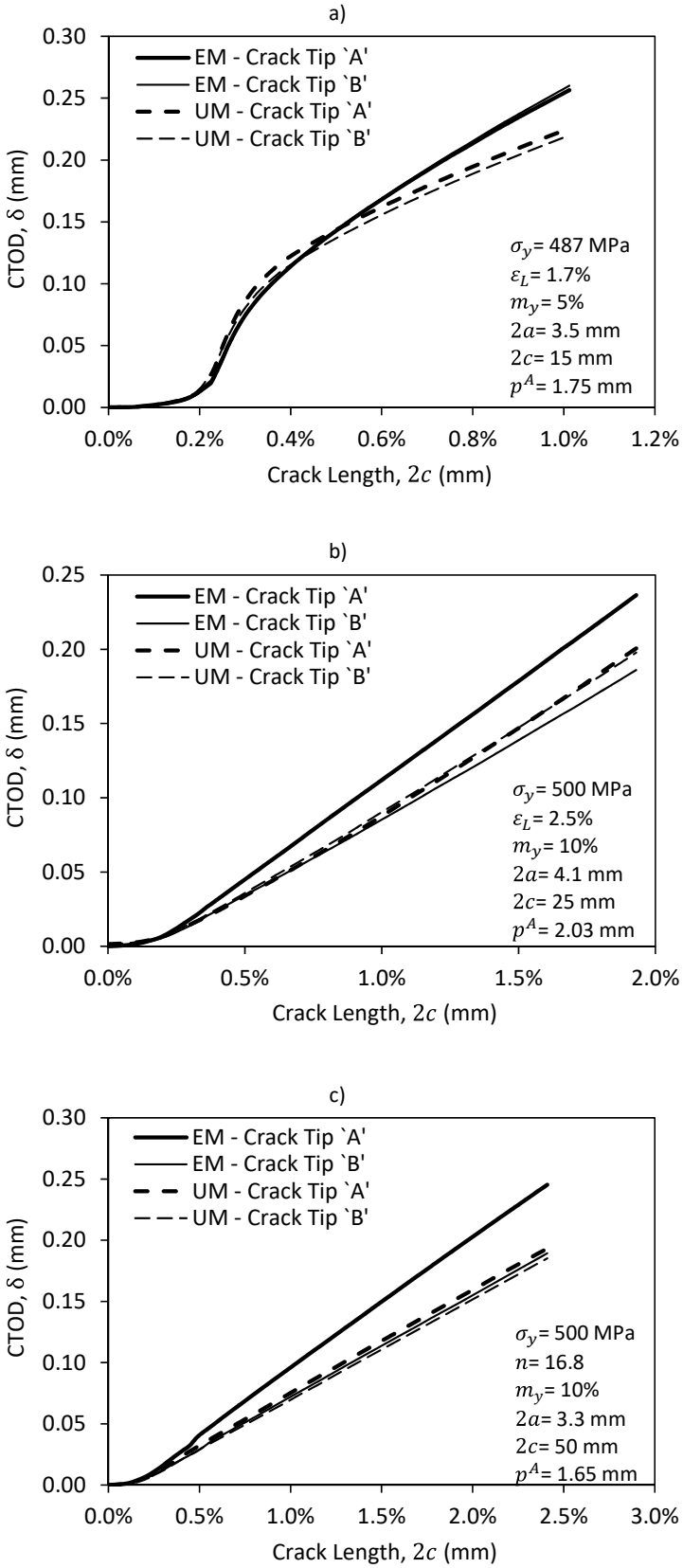


Figure 4.55: Validation of New ECA Procedure for Embedded Flaws in Undermatch Welds – CTOD Versus Strain Curves for: (a) 168.3 mm OD × 7.11 mm WT Pipe with Yield Plateau, (b) 323.9 mm OD × 15.9 mm WT Pipe with Yield Plateau, (c) 406.4 mm OD × 25.4 mm WT Pipe with Continuous Hardening

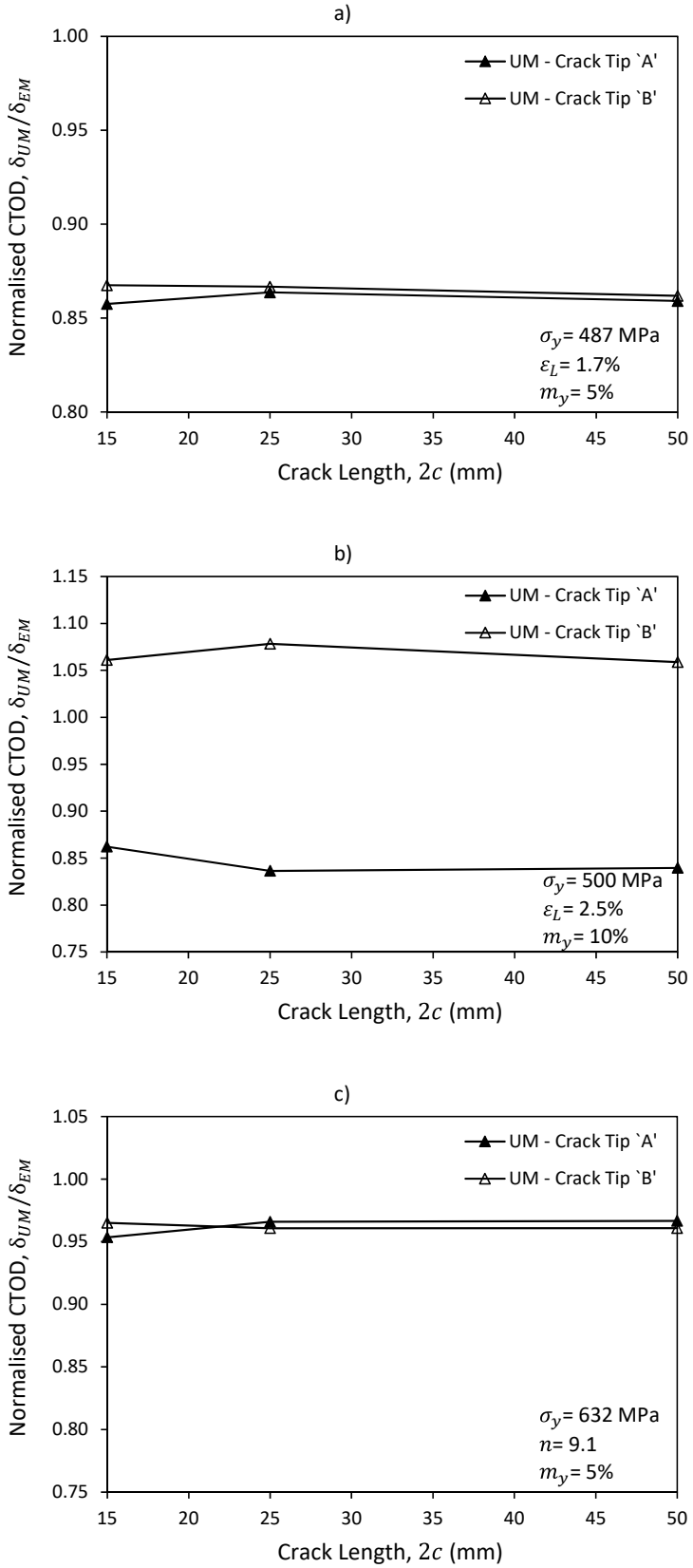


Figure 4.56: Validation of New ECA Procedure for Embedded Flaws in Undermatch Welds – Normalised CTOD Versus Crack Length Curves for: (a) 168.3 mm OD × 7.11 mm WT Pipe with Yield Plateau, (b) 323.9 mm OD × 15.9 mm WT Pipe with Yield Plateau, (c) 406.4 mm OD × 25.4 mm WT Pipe with Continuous Hardening

Chapter 5

Guideline for Design of Mechanically Lined Pipeline Against Fatigue

5.1 Introduction

This chapter aims at providing guidance for the fatigue design of mechanically lined pipeline welds and body during subsea operation. As the triple point interface was shown to be a dominant failure initiation site during high cycle fatigue testing of mechanically lined pipes (ref. Sec. 2.4.2), only this weld region is considered in this work. Cracks initiating from this interface can either grow into the carbon steel layer towards the pipeline's outer surface (these are referred to as "CS flaws" in this work) or into the CRA layer towards the pipeline's inner surface (these are referred to as "CRA flaws"). Since the CS layer is much thicker and in contact with sea water, whereas the CRA layer is thinner and exposed to corrosive fluids, CRA flaws are more critical than CS flaws. Breach of the CRA layer is considered as failure. In addition, crack initiation from scores/dents/wrinkles in the liner, introduced during manufacturing (ref. Sec. 2.4.3), installation (ref. Sec. 3.3.2) and/or subsea operation, is also investigated under low cycle service fatigue.

First, large scale fatigue testing is undertaken, during which non-destructive examination is performed with a new purpose-built inspection tool, to demonstrate that a high fatigue life can

be achieved with mechanically lined pipelines before the CRA layer is breached, see Section 5.2. This is supplemented by a parametric finite-element study, aiming at examining whether available K-solutions would be suitable to estimate the crack driving force in triple point interface flaws. Recommendations are then made for the fatigue crack growth assessment of MLPs with triple point flaws. Subsequently, a combined numerical and experimental work is undertaken, where small-scale fatigue testing is carried out using a newly established procedure detailed in Section 5.3, to determine the low cycle fatigue endurance of reeled mechanically lined pipelines with liner imperfections such as dents and wrinkles, and validate the acceptance criteria for liner wrinkles proposed in Sec. 3.2.

5.2 High Cycle Low Stress Fatigue Design

5.2.1 Objective

The objective of this work is to prove that a high fatigue life can be achieved with MLPs before the CRA layer is breached, and provide recommendations for the high cycle low stress fatigue assessment of mechanically lined pipelines with triple point interface flaws.

5.2.2 Large Scale Testing

Approach

An approach similar to that detailed in [132] is followed. The novelty here is that a bespoke non-destructive examination technique is developed and implemented at various stages during fatigue testing, to verify the integrity of the anti-corrosion barrier.

The liner thickness is designed as per Sec. 3.5 and MLP joints manufactured as per Sec. 1.2.2. Subsequently, six MLP strings are subjected to two reverse bending cycles, to simulate a standard reeling operation. After pre-straining, the specimens are subjected to fatigue testing in a resonant rig under positive stress range ratio, at three constant stress ranges.

Statistically based target S-N curves, which depend on the number of welds/specimens tested, n, are derived following recommendations in BS7608 [130]. Since the main focus is the fatigue performance of each specimen as a whole, $n = 6$ is used. Therefore, to meet the DNVGL-RP-C203 [129] class D and C design curves at the 95% confidence interval, the specimens have to achieve lives at least $f = 1.36$ times higher than those corresponding to the DNVGL D and C mean curves, respectively.

Manufacturing of Test Strings

MLP joints with a nominal outer diameter $D = 8.625$" (219.1 mm) and a wall thickness $t = 28.6 + 3.5 = 32.1$ mm are manufactured using API 5L X65 host pipes and alloy 625 liners. The joints are split into twelve pup pieces, each 2.6 m long. One end of each pup piece is terminated with a seal weld and a 150 mm long clad overlay weld. The liner at the other end is sealed 400 mm away from the pup piece end, leaving a bare backing steel pipe. Seal welding is carried out in a single pass using a mechanised pulsed gas tungsten arc welding process with a single wire in the 2F position, see Figure 5.2(a). In contrast, clad overlay welding is performed in two passes using a mechanised pulsed GTAW process with a twin wire in the 1G position, see Fig. 5.2(b). Alloy 625 (ERNiCrMo-3) consumables are used for both procedures. Subsequently, each overlay cladded pipe end is counter bored to a constant inner diameter and flapped to leave a smooth transition between the liner and clad overlay weld. The pipes are then heated in a furnace to 250°C for 5 minutes, to simulate the application of insulation coating. On completion of non-destructive examination, the pup pieces are shipped to the TechnipFMC's spoolbase in Evanton, UK, for girth welding.

Each overlay cladded pipe end is first scanned with a laser tool, and 2D cross-sectional profiles of the inner and outer pipe surfaces are produced. The profiles are then analysed and matched together to achieve a target internal hi-lo (mismatch at the pipe inner surface) of 0.5 mm, which is typical of steel catenary risers or flowlines designed for high fatigue service. Subsequently, six couples of pup pieces are girth welded together in thirty nine passes using a manual GTAW process in the 5G position, see Fig. 5.2(c). Alloy 625 welding consumables are used. After grinding flush CRA weld caps, 3 m long carbon steel pieces are girth welded to each end of

each fatigue string to produce 11.2 m long bending strings. Finally, NDE of girth welds is carried out. The maximum allowed flaw sizes are representative of the acceptance criteria for a typical SCR.

Simulation of Reel-Lay Installation

The test strings are bend tested at atmospheric pressure at Heriot-Watt University, UK. The bending rig in Figure 2.24 is equipped with an 8.23 m radius reeling former, corresponding to the smallest reel hub radius of the TechnipFMC reel-lay fleet, and a 31.1 m radius straightening former, and the strings are subjected to two reverse bending cycles to simulate reel-lay installation. The corresponding reeling strain is $\varepsilon_{nom} = 1.63\%$. On completion of bending, visual inspection is carried out. No signs of wrinkling, buckling or other damage to the liner are observed. Subsequently, the sacrificial carbon steel pup pieces are cut off to produce six 5 m long fatigue test strings, labelled 'FS01' to 'FS06', which are shipped to TWI in Cambridge, UK, for fatigue testing.

Fatigue Test Procedure

After welding end caps at both ends of each string, a vent hole, indicated in Figure 5.3, is drilled through the carbon steel layer, to allow air to escape when the pipe is filled with water. Subsequently, the specimens are instrumented with two rings of eight TML type PFL-20-11 strain gauges and connected to a data logging system. The gauges, which are located 300 mm apart and above the transitions between the liner and clad overlay weld, are equispaced around the pipe circumference as shown in Fig. 5.3. In order to detect potential liner cracking before a through-wall crack develops in the carbon steel backing pipe, the escape ports, shown in Fig. 5.3, are drilled through the carbon steel at each end of the test string. In addition, a colorant is added to the water to ease detection of a leak, should this occur.

The test strings are mounted in a resonance test machine, shown in Figure 5.4, filled with water and pressurised to achieve an axial mean stress of 90 MPa. Then, they are fatigue tested at ambient temperature, at a frequency of approximately 30 Hz. Two specimens are tested at

80 MPa, 120 MPa and 175 MPa constant amplitude stress ranges, as detailed in Table 5.1. The test is managed by Emilie Buennagel, a principal project leader in fatigue integrity at TWI.

The results of the fatigue tests undertaken by Tkaczyk *et al.* and summarised in Sec. 2.4.2 suggest that girth welded MLPs should not fail before reaching the DNVGL-RP-C203 class D and C target curves, when tested at the medium/high and low stress ranges, respectively. Therefore, the specimens 'FS03' to 'FS06' are first fatigue tested until the DNVGL class D target curve is reached. Testing is then stopped and the specimens are slowly depressurised to allow water to travel to the escape ports, if a through thickness crack has developed in the CRA layer. Subsequently, the end cap on the drive end side is cut off, the specimens are de-watered and internally inspected as detailed in the following section. After inspection and re-welding of the end cap, the specimens are filled with water and pressurised. Finally, fatigue testing is resumed; all six specimens ('FS01' to 'FS06') are tested until failure (pipe burst) or the run-out condition (the DNVGL class C target curve) is reached.

On completion of testing, a central section of each specimen is cut out. The exposed inner region containing the girth and clad overlay welds is subjected to NDE. Any cracks discovered are then extracted by cutting longitudinally, chilled in liquid nitrogen and broken open to expose the fracture faces for fractographic examination.

Non-Destructive Examination

The novelty here is that a bespoke NDE technique, including dye penetrant and Eddy current inspection, is developed and implemented at various stages during fatigue testing, to sanction breach of the CRA barrier prior to the establishment of a through thickness crack in the MLP wall, which is considered as failure in this work.

A dedicated inspection tool, shown in Figure 5.5, is built by Alan Day, to allow dye penetrant inspection (DPI) of the interface between the liner and clad overlay weld, 2.5 m away from the pipe end. The DPI is undertaken at three stages: (i) prior to fatigue testing (ii) after reaching the DNVGL class D target curve and (iii) after the test completion.

After verifying that its internal surface is clean, the specimen is rotated while the penetrant is sprayed and allowed to set for approximately 30 minutes. Then, the penetrant is removed using a cloth dampened with a solvent, and a developer is sprayed on the surface. It is allowed to set for approximately 7 minutes. Finally, a video inspection is carried out, to note the position and length of any indication found.

When suspicious indications are found with the intermediate DPI (after reaching the DNVGL class D target curve), a supplementary Eddy current testing (ECT) is carried out using a 700 kHz Hocking locator probe type 29P106 linked to a Phasec 2200 acquisition system. The Hocking 29P106 probe, shown in Figure 5.6(a), is calibrated against notches introduced in unmachined clad overlay welds, shown in Fig. 5.6(b). The ECT probe is first run by hand across a 1 mm notch in the calibration block, to verify that it is set up properly. Subsequently, the ECT probe is mounted on the leading edge of the DPI inspection tool that is positioned over the area to be inspected. The probe is then balanced and finally moved forward to scan the indication.

Fatigue Test Results

Although the initial DPI of the liner to clad overlay weld transition revealed the presence of linear indications, shown in Figure 5.7(a), the DNVGL class C target curve is achieved for specimens tested at a low stress range ('FS01–02') without any signs of pressure loss or leak. Macro-section examination shows that these indications are cold laps, shown in Fig. 5.7(b), which were not completely removed when the clad overlay welds were flapped after machining.

Similar indications are found in the medium ('FS03–04') and high ('FS06–06') stress range specimens during the intermediate DPI (after reaching the DNVGL class D target curve). The response amplitude measured with ECT is below the threshold corresponding to a 1 mm high notch for all but the test string 'FS05'. In this case the response amplitude is less than the threshold corresponding to a 2 mm notch height. This indicates that the DNVGL class D target curve has been reached for all specimens without breaching the anti-corrosion barrier.

When fatigue testing is resumed, the test string 'FS05' fails at the location indicated by the ECT before reaching the DNVGL class C target curve. The fractographic examination reveals that the failure initiated from flaws between the carbon steel and clad overlay weld and between the liner and clad overlay weld. The cracks grew both in the carbon steel pipe towards the pipe outer surface and in the CRA layer towards the pipe inner surface, seemingly reaching the inner surface before the pipe burst. The examination of strain gauge histograms suggests that the anti-corrosion barrier was breached after reaching 1.2 million cycles (i.e. 75% of the total life). The test string 'FS04' fails 300 mm away from the girth weld (i.e. 150 mm away from the nearest liner to clad overlay weld transition) before reaching the DNVGL class C target curve. An inspection of the fracture faces reveals that cracking initiated from a blemish at the pipe outer surface. In contrast, the DNVGL class C target curve is reached for the test strings 'FS03' and 'FS06' without any signs of pressure loss or leak. The post-mortem examination confirms that all indications found with the DPI during the initial and intermediate NDE are cold laps, similar to the one showed in Fig. 5.7(b), which were not completely removed when clad overlay welds were flapped after machining. No fatigue failure initiated from these features.

The fatigue test results, in terms of the number of cycles to failure versus the stress range at the pipe outer surface, are compared in Figure 5.8 with the DNVGL-RP-C203 C (labelled 'DNVGL C target') and D (labelled 'DNVGL D target') target curves. In addition, the DNVGL C and D mean curves are plotted in Fig. 5.8, indicated respectively by the thin dashed and thin solid lines. Stresses at the pipe outer surface have been calculated by interpolating between strain gauge readings; no stress concentration factor (SCF) has been included. The failure initiated at the liner to clad overlay weld transition is indicated by the solid square, while the remaining failure is indicated with the solid triangle. Finally, the run outs are indicated by the open circles.

The fatigue test results for reeled MLP lie above the DNVGL class D target curve. This demonstrates that mechanically lined pipes, designed following the rules laid out herein and reeled at atmospheric pressure, are suitable for demanding SCR and fatigue sensitive flowline service, even when they contain interface flaws.

5.2.3 Fatigue Crack Growth Assessment of Mechanically Lined Pipe with Triple Point Interface Flaws

Approach

A parametric finite-element study is undertaken to assess the effect of the pipe and crack geometry on the crack driving force for interface flaws in mechanically lined pipes subjected to low stresses in the linear elastic regime. First, the case of a single pipe with a surface breaking flaw is analysed and the predicted K-values are compared to analytical K-solutions. Subsequently, the case of an MLP with a triple point interface flaw is analysed numerically and the obtained results are compared against the FEA and analytical predictions for single pipe. Finally, a fatigue design approach for MLPs with interface flaws is proposed and a case study is undertaken to evaluate its robustness.

Stress Intensity Factor Solutions

Two K-solutions are considered in this work: (i) the Raju and Newman solution for surface flaws in plates, proposed in BS7910 [102] and recommended in DNVGL-RP-F108 [108] for the assessment of flaws in subsea pipelines, given in Eq. 2.27, and (ii) the Marie *et al.* solution for surface flaws in pipes, developed for the French Nuclear Codes, given in Eq. 4.6.

Pipe and Crack Geometry

MLPs with the nominal outer diameter, D, in the range between 168.3 mm and 323.9 mm, the carbon steel wall thickness, t_{CS} = 14.3 mm and 25.4 mm and the liner thickness, t_L = 3.0 mm and 4.1 mm are considered. The normalised crack depth, a/t, in the range between 0.035 and 0.300 and the normalised crack length, $2c/W$, in the range between 0.02 and 0.10, are assumed. Semi-elliptical part circumferential interface cracks between the carbon steel and clad overlay weld (i.e. "CS Flaws") and between the liner and clad overlay weld (i.e. "CRA Flaws"), illustrated in Figure 5.9, are analysed. In total, 48 crack geometries detailed in Tables 5.2 and 5.3 are considered.

Material Flow Behaviour

The CS and CRA materials are assumed to be elastic, with Young's modulus, E =207 GPa and 200 GPa, respectively.

Finite-Element Analysis

A parametric finite-element study is performed using ABAQUS [47]. Fig. 2.42 depicts a typical FE mesh of an MLP with an interface flaw, made of up to 300,000 eight-node linear hexahedral elements with reduced integration (C3D8R in ABAQUS). Due to symmetry, only a quarter model of the pipe is built. The model length is three times the pipe outer diameter, and the overlay welds are 150 mm long for all cases. The crack tip region, shown in Fig. 2.42(c), has a focused mesh, composed of 5 to 7 rings and 17 to 51 layers depending on crack and pipe geometries. The smallest element size at the crack tip is of the order of 3% of the crack depth, a. A 'tie' contact is used to simulate the metallurgical bond between carbon steel and overlay cladding. In contrast, a finite-sliding contact formulation with hard surface behaviour is used to model the interaction between the liner and carbon steel pipe. Symmetry boundary conditions are applied to the nodes on the left-hand side of the model. The nodes on the right-hand side of the model are coupled to a reference node. Rotation is applied to the reference node to impose bending. Single pipe (either CS backing pipe or CRA liner) and mechanically lined pipe (MLP) configurations are considered. A total of 96 FE analyses (48 geometries and 2 pipe configurations) are performed and the K values at the crack deepest point are extracted using the contour integral method.

Results

Single Pipe The FEA predictions obtained for a SP subjected to bending (indicated K_{SP}) are normalised, in Tables 5.4 and 5.5, by the BS7910 (indicated K_{BS}) and French Nuclear Code (indicated K_{FNC}) analytical results for the bending load mode. A ratio less than 1 indicates that the analytical solution overestimates the FEA prediction.

The Raju-Newman solution generally overestimates the FEA predictions. Not surprisingly there is a better agreement between the FEA results and the predictions obtained with a more

recent FNC solution, which was derived by fitting polynomial functions to the results of FE analyses. In this case, the maximum error (underestimation) is 10% for all cases considered in this work.

Mechanically Lined Pipe The FEA predictions obtained for interface flaws in MLPs subjected to bending are normalised by the numerical and analytical results for SPs with surface flaws in Tables 5.6 and 5.7. The normalised K lower than 1 indicates that either an SP FEA or an SP analytical solution is conservative.

The level of conservatism varies between 4% and 15% for all cases considered in this study. Lower K values are predicted for the MLP configuration compared to the SP configuration because the metallurgical bond between carbon steel and overlay cladding restricts opening of the crack.

The FEA predictions for MLPs subjected to bending and the FNC solutions in bending are in good agreement for all cases considered in this study. Somewhat worse agreement is obtained between the BS7910 solution and the FEA results, especially for cracks in the carbon steel backing pipe. Therefore, the fatigue assessment of MLPs with interface flaws can be conservatively performed using the FNC K-solutions for an SP with a surface flaw under bending.

5.2.4 Case Study

Approach

Most failures in the fatigue test programme detailed in [132] initiated from interface flaws ca. 1 mm high. In addition, the NDE detectability limit is near 1 mm for interface flaws. For example, Zumpano *et al.* [146] speculated that 1 mm flaws with a length of 20 mm can be found by radiography testing. Consequently, the crack depth of 1 mm is assumed in this study while the crack length is varied from 15 mm to 25 mm. Interface flaws in both carbon steel pipe and liner are considered.

Fatigue analyses are carried out for an MLP made of carbon steel pipe with $D = 219.1$ mm or 273.1 mm and $t_{CS} = 25.4$ mm lined with alloy 625 liner with $t_L = 3.0$ mm. A sensitivity

study is undertaken for $t_L = 4.0$ mm and 5.0 mm. The mechanically lined pipe is subjected to a bending stress range of 80 MPa measured at the carbon steel pipe outer surface. The corresponding stress range, measured at the liner outer surface, is 61.4 MPa and 65.1 MPa for the 8" and 10" MLP, respectively. The transition between the liner and clad overlay welds is assumed to be smooth; no stress concentration factor is applied in the fatigue assessment.

Fatigue crack growth assessment is carried out using the FNC K-solution for pipes with semi-elliptical circumferential cracks subjected to bending. The BS7910 FCG curve for steel in air, mean plus two standard deviations, for stress range ratios above 0.5, is used, see Figure 5.10. The FCG curve at $R > 0.5$ is considered to account for residual stresses in the fatigue strings. The failure criterion is defined as $a/t = 0.8$.

Results and Discussions

The predicted number of cycles to failure is normalised in Figure 5.11 by the number of cycles required to achieve the DNVGL class D target curve. The fatigue life predicted for MLP flaws in the carbon steel pipe (indicated by thick solid lines in Fig. 5.11) is between 30% to 60% of the life obtained during testing. This is a relatively good agreement. The difference is most likely due to not accounting for the crack initiation/sharpening time in the analysis.

In contrast, the life predicted for MLP flaws in the CRA layer (indicated by the dotted lines for $t_L = 3.0$ mm, the short dashed lines for $t_L = 4.0$ mm and the long dashed lines for $t_L = 5.0$ mm, in Fig. 5.11) is very low compared to those obtained during testing. The inherent conservatism of the analytical K-solution and not accounting for the crack initiation time cannot explain such significant disagreement. It therefore appears that the application of the BS7910 FCG curve for steel in air is very conservative when used for the prediction of fatigue crack growth in nickel based alloys. It is recommended that the industry makes an effort to develop suitable FCG curves for commonly used nickel based alloys such as alloy 625.

Finally, the case study results clearly show that it is extremely beneficial to increase the liner thickness. While reeling does not adversely affect the fatigue performance of MLPs (good fatigue performance was achieved during large scale testing), increasing the liner thickness to

suppress wrinkling during reeling at atmospheric pressure significantly improves the fatigue performance of the liner, compared to that of standard MLPs with a thinner liner, which can be installed by either S-lay, J-lay or reel-lay under internal pressure. The fatigue life of the liner can increase by over 50% when its thickness is increased by 1 mm.

5.3 Low Cycle High Stress Fatigue Design

5.3.1 Objective

Concerns have been expressed that liner imperfections such as small dents or wrinkles, introduced during manufacturing, installation or service, may compromise the integrity of mechanically lined pipes subjected to large variations of pressure, temperature and bending strain during operation. Therefore, this study is undertaken to examine the criticality of such flaws and determine the low cycle fatigue endurance of reeled MLPs with imperfections. First, finite-element analyses are carried out to determine the cyclic stress/strain in liners containing wrinkles/dents, associated with in-service loading. Then, the liner stress/strain condition in the MLP under in-service loading is replicated in a simple liner strip geometry subjected to cyclic axial loading. Subsequently, small scale fatigue testing on a liner with imperfections is undertaken to determine the fatigue endurance, defined as the number of high strain cycles applied before breach of the CRA layer occurs. Finally, recommendations are made for the low cycle high stress fatigue design of MLP with liner imperfections.

5.3.2 Numerical Simulation

Approach

First, buckling of a standalone host pipe is simulated to generate eigenmodes, then radial displacements, corresponding to a mode selected following the guidelines in Sec. 3.4.3, are scaled and imposed to a perfect host pipe in an MLP. Subsequently, manufacturing, installation and operation of the MLP are simulated to produce large residual imperfections (dents/wrinkles) and determine the corresponding stress/strain ranges in the liner during subsea operation of the MLP.

Liner wrinkles up to 6 mm in height (corresponding to the largest liner thickness tested in this work) are considered in order to conservatively assess the fatigue endurance of MLPs with imperfections. Such wrinkles are unlikely to be caused by galling and denting of the liner during manufacturing. Equally, it is not possible to introduce such wrinkles during ambient reeling of MLPs designed following the rules laid out herein. Therefore, bending of MLPs on a tighter radius than typical of reeling, as per the strain capacity tests in Sec. 3.3.2, is simulated in the FE analysis.

Finally, a liner strip with a wrinkle, extracted from the full scale 3D FEA model which accounts for the strain history, is subjected to cyclic axial loading. The applied axial cyclic loading is altered in an iterative manner until the stress/strain ranges in the strip FEA model correspond to those in the full scale FEA model where the MLP is subjected to in-service loading.

Pipe Materials

Three MLPs suitable for reel-lay installation at ambient pressure are considered in this work: (i) 8.625" (219.1 mm) OD carbon steel pipe lined with 4.0 mm thick alloy 316L liner, (ii) 10.75" (273.1 mm) OD carbon steel pipe lined with 5.0 mm thick alloy 625 liner, and (iii) 12.75" (323.9 mm) OD carbon steel pipe lined with 6.7 mm thick alloy 316L liner. The lined pipe manufacturing is summarised in Sec. 2.2.4 for the 8" MLPs and detailed in Sec. 3.3.2 for the 10" and 12" MLPs.

Full Scale Finite-Element Modelling

A simulation of liner expansion during manufacturing, reel-lay installation and in-service operation is performed with a half-symmetrical 3D FEA model, shown in Figure 5.12, to determine in-service cyclic loading in the liner. First-order shell elements with reduced integration and first-order pipe/beam elements (respectively S4R and PIPE31 in ABAQUS [47]) are used to model both the liner and the backing pipe. The beam mesh is connected to the shell mesh with kinematic couplings at either end of the model. The liner shell mesh has a refined central section where the eigenmode imperfections shown in Fig. 3.31 are seeded during expansion.

This central region is indented during simulated manufacturing with a rigid nugget to create a wrinkle/indent similar to those shown in Fig. 5.1(b).

The end cap, which allows application of the end cap load in-service, is modelled using elastic shell elements (S3 in ABAQUS). Rigid bending formers are utilised to replicate the reel, the aligner, the straightener and the free span between the reel and the aligner. These formers are connected through their reference nodes to the beam mesh end nodes with kinematic couplings. The finite-sliding contact formulation and Coulomb friction model is again used to model the liner-to-host pipe and pipe-to-former interactions. Frictionless contact is assumed between the host pipe and the formers. Finite strain kinematics and J_2 flow theory with a kinematic hardening plasticity model are employed.

The liner is first subjected to internal pressure to simulate manufacturing of the MLP. This creates an interference fit between the liner and the host pipe while the liner is indented at its central section, which is also seeded with imperfections with the normalised height, $5\% < h/t < 7.5\%$, ref. Sec. 3.4.3. After releasing the pressure, reel-lay installation is simulated by bending the pipe onto the reel, the "free span" former, the aligner and finally onto the straightener before the pipe is relaxed. The radius of the bending former is chosen so that the target wrinkle height (up to 6 mm in height) is obtained. On completion of the installation phase, all surfaces and elements, except from those shown in Figure 5.13, are removed from the model in Fig. 5.12. After applying symmetry boundary conditions to the nodes on the left hand side of the model, shown in Fig. 5.13, subsea operation is simulated. The MLP is hydrotested to simulate pre-commissioning and bent to 1% strain to simulate a lateral buckling event. Then, the pipe is relaxed to 0.7% residual bending strain. Finally, a severe in-service loading sequence is simulated:

1. The pipe is pressurised from 0 to a pressure corresponding to a hoop stress utilisation ratio of 0.8

2. Its temperature is increased by 150°C

3. The bending strain is increased from 0.7% to 1%

4. The pipe is depressurised

5. The pipe is cooled to ambient

6. The pipe is relaxed to 0.7% bending strain.

The results in terms of operational stress/strain ranges at the crown of the wrinkle are used in the next section.

Small Scale Finite-Element Modelling

Figure 5.14 shows a half-symmetrical liner strip model extracted from the central section of the 3D FEA model (Fig. 5.13) after simulated manufacturing, installation, and hydrotest (to account for the strain history). The size of the liner strip is representative of a dumbbell test specimen in a small scale fatigue test. Cyclic axial displacement is applied at the right end of the model, shown in Fig. 5.14, while the left end is fully constrained, to simulate a small scale fatigue test. The magnitude of displacement is altered in an iterative manner until the stress/strain range at the crown of the wrinkle in the strip FE analysis matches that obtained from the FE analysis of the MLP under operational cyclic loading.

Results of Numerical Study

To create liner imperfections up to 6 mm in height (indicated with a long-dashed line in Figure 5.15) during a standard reeling operation, a 2 mm high indent (double the height of the maximum allowable manufacturing imperfection for a project pipe), indicated with a short-dashed line in Fig. 5.15, is created during manufacturing and the MLP is bent on a 5.5 m reeling former (nearly half of a typical reel hub radius of reel-lay vessel) to maximise bending strain. The residual wrinkle after hydrotest of just over 1 mm in height is indicated with a solid line in Fig. 5.15.

Figure 5.16 shows the evolution of axial stress at the wrinkle crown during operation, obtained from the model illustrated in Fig. 5.13. It may be seen that it takes approximately 7 cycles for the stress range to stabilise although peak stresses continue to rise slightly. The maximum

stress range, $\Delta\sigma = 600$ MPa, is predicted to occur at the liner intrados, see Fig. 5.16. The three contributors to stress variations, bending, pressure and temperature, are denoted in this figure by "B", "P" and "T", respectively. The sign "+" in Fig. 5.16 indicates that bending strain, pressure or temperature increases while the opposite is indicated with the sign "–". It can be seen that temperature variations have the largest effect on the stress range at the liner intrados. Figure 5.17 shows the evolution of the corresponding axial strain at the liner intrados. It also takes approximately 7 cycles for the strain range to stabilise. The maximum (stable) strain range is $\Delta\varepsilon = 0.5\%$. It is to be noted that the mean axial strain also slowly increases with the number of cycles due to ratcheting.

Figures 5.18 and 5.19 compare the results, in terms of axial stress and strain at the liner intrados, obtained from the 3D MLP model (indicated by a dashed line) and the simple strip model (indicated by a solid line). It can be seen that the applied cyclic displacement in the strip FE model can be selected so that the stress/strain range in the MLP is conservatively reproduced. This demonstrates that the complex behaviour of the MLP in-service can be well captured in a small scale displacement-controlled fatigue test.

It may be noted that a strain range, in the order of twice that predicted with the full scale MLP model, is applied in the strip model to achieve similar stress range in both models. Higher strain range must be applied in the strip model to compensate for biaxial loading (and to some extent plastic deformation due to lateral buckling) in the MLP model.

The results presented in this section are for the 8" MLP. Similar results are obtained for the 10" and 12" pipes.

5.3.3 Experimental Work

Approach

The 8", 10" and 12" MLPs, detailed in a previous section, are manufactured and bent in a rig to simulate reel-lay installation. Some MLPs with no significant liner dents are then bent on an increasingly tight former to create liner wrinkles, while those with significant dents are

hydrotested. Subsequently, the pipes are sectioned to remove the liner. Dumbbell specimens are then extracted from the liner so that the wrinkle/dent is located centrally along the specimen. Finally, small scale tests are carried out to assess the low cycle fatigue performance of MLPs with imperfect liners. The cyclic axial displacement is selected from the numerical results presented in the previous section.

Bending Trials and Hydrotest

The 8" MLP test strings are subjected to five reverse bending cycles to simulate a contingency re-reeling operation, ref. Sec. 2.2.4. Visual inspection carried out during the bending trial reveals the presence of liner dents only, as per Fig. 1.9. Subsequently, following welding of end caps the pipes are pressurised to 64 MPa, to simulate a hydrotest.

The 10" and 12" MLP test strings are subjected to the bending strain capacity test regime detailed in Sec. 3.3.2, where the pipes are bent on an increasingly tighter radius to create a wide range of liner wrinkles. Hydrotest is not simulated. This would have resulted in a significant reduction of the wrinkle heights as shown in Fig. 5.15.

On completion of the large scale bend tests the strings are sectioned to remove the liner and fabricate specimens for small scale fatigue testing.

Small Scale Fatigue Tests

Dumbbell test specimens, as per Figure 5.20, are machined from the corrosion resistant alloy 316L and 625 liners removed from the 8", 10" and 12" MLPs after large scale testing. The largest nugget induced dent found is on the order of 0.5 mm in height. Before fatigue testing, some specimens are buckled in the test machine, shown in Figure 5.21, to increase the wrinkle height to 3 – 6 mm. Subsequently, the samples are instrumented with biaxial strain gauges. A transverse gauge is used to compensate for temperature effects. After mounting the specimen in the test machine and installing the cooling system, an extensometer with a 12.5 mm gauge length is affixed to the specimen around the crown of the wrinkle, see Fig. 5.21. The extensometer is used to control the cross-head displacement of the test machine so that the gauge

length is subjected to a global strain range of +/−0.5%. This is conservative and results in a higher strain range at the wrinkle crown compared to that reported in Fig. 5.19. The tests are conducted by Gilles Maîtres, a lab manager at A2MI.

Eighteen dumbbell specimens, six for each pipe size, are fatigue tested at a frequency of 2 Hz to determine the fatigue endurance of MLPs with imperfect liners. Although the maximum service temperature can be very high (100–150°C or above), testing is conveniently undertaken at room temperature as fatigue cracks grow slower at elevated temperature [147].

Results and Discussions

Figure 5.22 shows an example of the maximum load-life line for the alloy 316L sample tested in this programme. At the beginning of the fatigue test, a rapid decrease in peak load is observed but after a few hundred cycles the rate of load decrease stabilises at a constant low value, most likely due to ratcheting. When cracking initiates, at ca. 7600 cycles in Fig. 5.22, the load decreases rapidly again. Fatigue failure is deemed to occur when the applied load reduces by 10%, as indicated by the blue line in Fig. 5.22, which can be considered as crack initiation. Cracking consistently initiates at the liner intrados, as shown in Figure 5.23.

The test results for the 8"/316L, 10"/625 and 12"/316L MLPs (indicated respectively by the triangles, circles and squares) are compared in Figure 5.24 to the BS 7608 class C mean curve. It can be seen that all test results exceed the BS7608 class C mean curve. Furthermore, the fatigue life of the alloy 625 liner is higher than that of the alloy 316L liner. This is in line with other studies, where it has been shown that crack initiation and growth is slower in alloy 625 than in alloy 316L [147].

5.4 Recommendations for Fatigue Design of MLP

5.4.1 High Cycle Fatigue Design

Large scale bending and resonant fatigue tests were performed on 219.1 mm OD × 32.1 mm WT mechanically lined pipes with alloy 625 liner, clad overlay and girth welds. Prior to fatigue

testing, the MLPs were subjected to simulated reeling at atmospheric pressure. To demonstrate that the CRA barrier is not damaged long before the final fatigue failure defined as the pipe burst, an NDE technique was developed and implemented at various stages during testing.

All fatigue test strings reached the DNVGL-RP-C203 class D target curve without breach of the corrosion barrier. This demonstrates that reeled MLPs, designed following the rules laid out herein, are suitable for high SCR service. Four out of six specimens reached the DNVGL class C target curve without failing. Failure of the fifth test string initiated from a blemish on the carbon steel pipe, while cracks in the last specimen started from lack of fusion defects between liner and clad overlay welds and between carbon steel and clad overlay welds. The embedded lack of fusion defects grew both in the CRA layer towards the pipe inner surface and in the CS pipe towards the outer surface, and broke at the pipe inner surface before the pipe burst. It was estimated that breach of the corrosion barrier occurred after 75% of the total life was elapsed. This percentage is expected to increase when the WT of the CS pipe decreases.

Although cold laps, created during machining and flapping liner to clad overlay transitions, did not lead to the breach of CRA layer before reaching the required fatigue performance, it is recommended that for fatigue sensitive MLPs the quality of the transition is improved. One approach to achieve high quality transitions is applying a machining tool that can follow a profile of the liner inner surface, to leave a smooth transition, free of cold laps. The approach developed in this work, whereby NDE is carried out at various stages during testing, should be followed when performing fatigue tests to qualify a mechanically lined pipeline for a given fatigue class. It is expected that the DNVGL-RP-C203 and BS7608 class D curves can be consistently achieved if the pipes are designed following the rules laid out herein.

A parametric FE study showed that the Marie *el al.* K solution for semi-elliptical flaws in single pipes under bending, given in Eq. 4.6, provides a good but slightly conservative approximation of K for single pipes with surface breaking flaws and MLPs with interface flaws under bending. It is therefore recommended that the K solutions proposed in the French nuclear codes RSE-M and RCC-MR be used for the fatigue crack growth assessment of MLPs with interface, overlay

and/or girth weld flaws. Alternatively, interface flaws may be assessed using a project-specific K-solution developed using the FEA model in Fig. 2.42.

The use of the BS7910 FCG curve for steel in air for the assessment of flaws in CRAs may lead to a significant underestimation of the fatigue life. It is recommended that fatigue crack growth tests be carried out to develop curves suitable for the assessment of flaws in CRA materials such as alloy 625.

To allow reeled installation of MLPs under atmospheric pressure the liner thickness must be increased, following the recommendation in Sec. 3.5. Although the cost of the MLP increases with the liner thickness, the fatigue performance is also increased. An increase of 1 mm in the liner thickness can double the fatigue life. This must be taken into account when considering MLP for high cycle fatigue service.

The results from this section were presented at the ISOPE 2015 conference and later published in the IJOPE journal, refer to Appendix C for more details.

5.4.2 Low Cycle Fatigue Design

A numerical study was undertaken to quantify the stress/strain ranges associated with imperfect liners when the MLPs are subjected to onerous in-service loading. It was found that the axial strain range in the liner does not exceed 1% for the pressure range equal to a hoop stress utilisation ratio of 0.8, the temperature range of 150°C and the bending strain range of 0.3%. It was further demonstrated that the stress/strain range in the liner subjected to in-service loading can be reproduced in a strip geometry under cyclic axial displacement. Therefore, a simple small scale test set-up can be used in place of expensive and time consuming large scale testing to determine the fatigue endurance of the MLP in-service.

Liner dumbbell specimens were extracted from the 8", 10" and 12" MLP strings which underwent simulated reeling (bending on the former) and pre-commissioning (hydrotest). The liner specimens had wrinkles up to 6 mm in height, introduced half-way along their length prior to fatigue testing. The fatigue life obtained from these specimens was between 4,000 and 22,000

cycles, and was significantly higher for alloy 625 (13,000 to 22,000 cycles) compared to that for alloy 316L (4,000 to 10,000 cycles). The predicted life for the MLPs with large imperfections and subjected to high cyclic loading is well in excess of 3000 cycles, which corresponds to one shut-down cycle every month, for 25 years with a safety factor of 10. This demonstrates that liner imperfections (indents/wrinkles) in the range considered in this work (up to 6 mm in height) are not detrimental to the in-service integrity of MLP flowlines. This validates the wrinkling criteria defined in Table 3.1.

It is recommended that the combined numerical and experimental work detailed herein be repeated to determine acceptance criteria for liner imperfections if: (i) the service conditions or as-laid liner imperfections are outside of those assumed in this work, (ii) or the rules laid out herein are not followed when designing the MLP for reeling. The fatigue failure criterion adopted in this work (10% reduction of the maximum load) can be relaxed if further work is undertaken. For instance, fatigue tests may be interrupted after a 20% reduction in the maximum load, and NDE performed to sanction failure initiation.

The work detailed herein was presented at the OMAE 2017 conference, refer to Appendix D.

5.5 Tables and Figures

Table 5.1: Fatigue Test Regime

String Number (-)	Mean Stress (MPa)	Stress Range (MPa)	Stress Ratio (-)
FS01-02	90	80	0.38
FS03-04	90	120	0.20
FS05-06	90	175	0.01

Table 5.2: FEA Matrix of Cases – Carbon Steel Crack Geometries

D (mm)	t_{CS} (mm)	t_L (mm)	a/t	$2c/W$
168.3 219.1 323.9	14.3, 25.4	3.0	0.035, 0.100, 0.300	0.02, 0.07, 0.20

Table 5.3: FEA Matrix of Cases – CRA Crack Geometries

D (mm)	t_{CS} (mm)	t_L (mm)	a/t	$2c/W$
168.3 219.1 323.9	25.4	3.0, 4.1	0.035, 0.100, 0.300	0.02, 0.07, 0.20

Table 5.4: Selected Results for Cracks in Single Carbon Steel Pipe

D (mm)	t_{CS} (mm)	a (mm)	$2c$ (mm)	K_{SP}/K_{BS} (-)	K_{SP}/K_{FNC} (-)
168.3	14.3	0.50	105.7	0.85	1.04
		1.43	37.00	0.85	1.03
		4.29	105.7	0.83	1.03
323.9	25.4	0.89	203.5	0.86	1.04
		2.54	71.20	0.86	1.03
		7.62	203.5	0.84	1.03

Table 5.5: Selected Results for Cracks in Single Liner Pipe

d (mm)	t_{CS} (mm)	a (mm)	$2c$ (mm)	K_{SP}/K_{BS} (-)	K_{SP}/K_{FNC} (-)
		0.11	26.40	1.02	1.06
117.5	3.0	0.30	37.00	1.03	1.09
		0.90	105.6	0.98	1.03
		0.14	41.40	1.01	1.06
168.3	4.1	0.41	48.20	1.02	1.08
		1.23	137.6	0.99	1.05

Table 5.6: Selected Results for Cracks in Carbon Steel Pipe of MLP

D (mm)	t_{CS} (mm)	a (mm)	$2c$ (mm)	K_{MLP}/K_{SP} (-)	K_{MLP}/K_{BS} (-)	K_{MLP}/K_{FNC} (-)
		0.50	105.7	0.92	0.78	0.92
168.3	14.3 + 3.0	1.43	37.00	0.92	0.78	0.92
		4.29	105.7	0.93	0.77	0.93
		0.89	203.5	0.93	0.80	0.93
323.9	25.4 + 3.0	2.54	71.20	0.93	0.80	0.93
		7.62	203.5	0.95	0.80	0.95

Table 5.7: Selected Results for Cracks in Liner Pipe of MLP

d (mm)	t_{CS} (mm)	a (mm)	$2c$ (mm)	K_{MLP}/K_{SP} (-)	K_{MLP}/K_{BS} (-)	K_{MLP}/K_{FNC} (-)
		0.11	26.40	0.87	0.88	0.93
168.3	25.4 + 3.0	0.30	37.00	0.88	0.91	0.96
		0.90	105.6	0.84	0.83	0.88
		0.14	41.40	0.88	0.88	0.92
323.9	25.4 + 4.1	0.41	48.20	0.89	0.91	0.96
		1.23	137.6	0.85	0.83	0.89

a)



b)

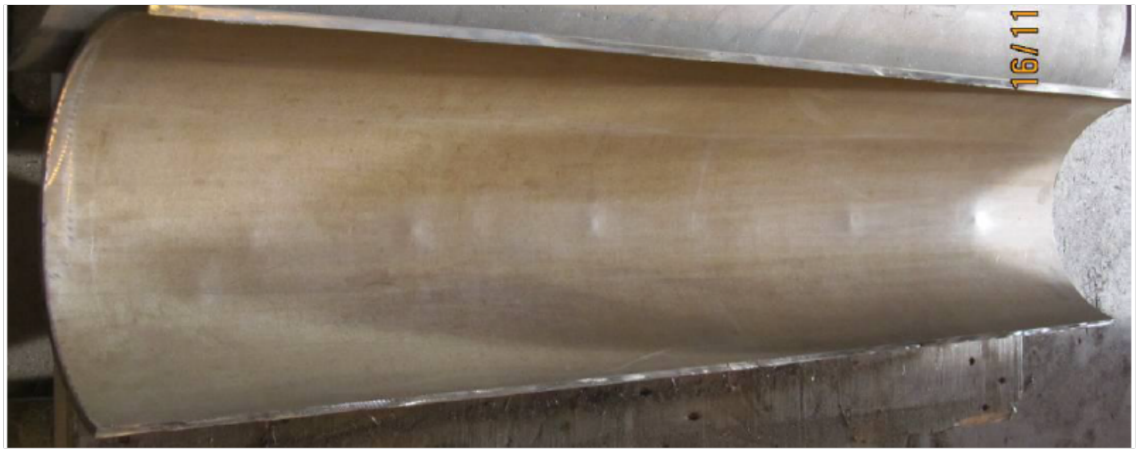


Figure 5.1: Uncontrolled Galling during Liner Insertion: (a) Scratches and Nuggets, (b) Liner Dents

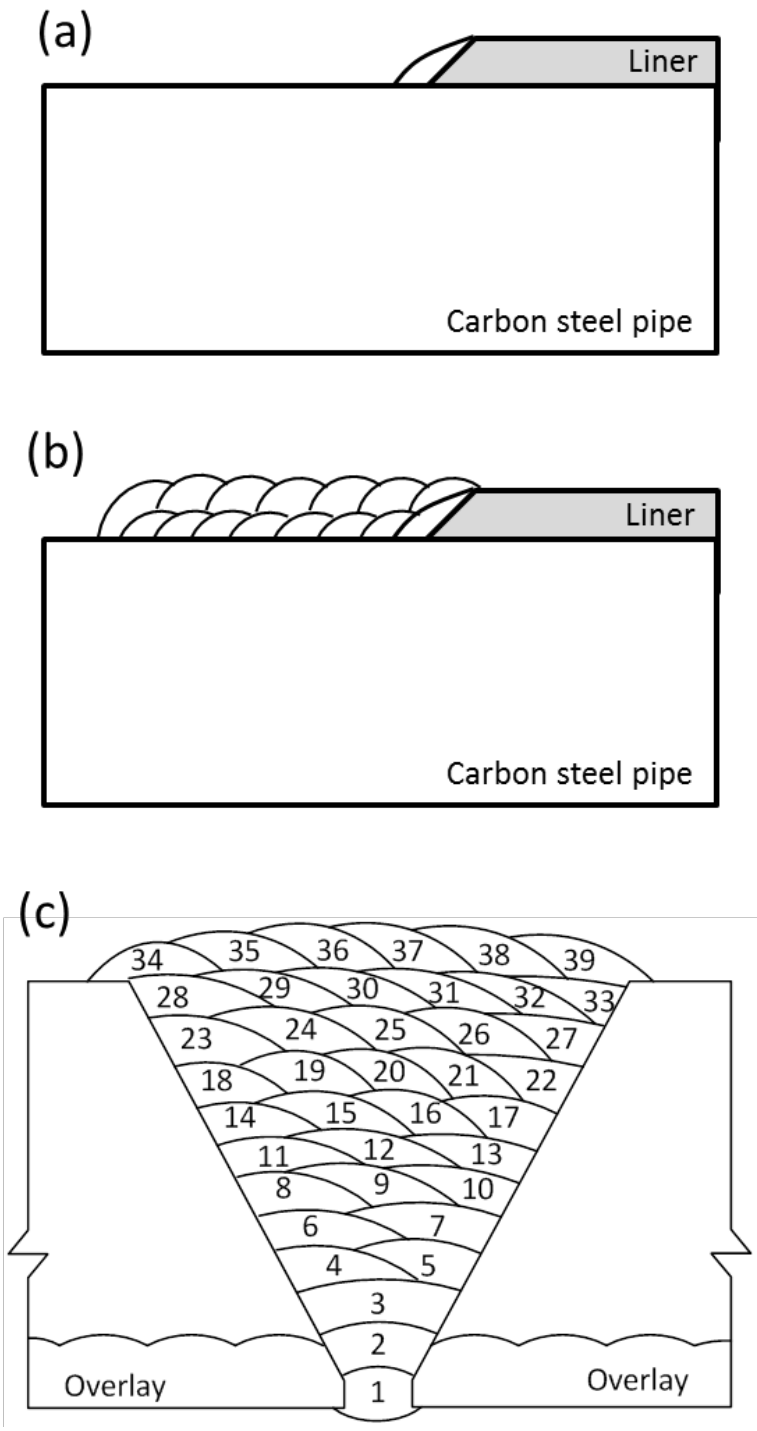


Figure 5.2: Fatigue String Weld Profiles: (a) Seal, (b) Clad Overlay, (c) Girth Weld

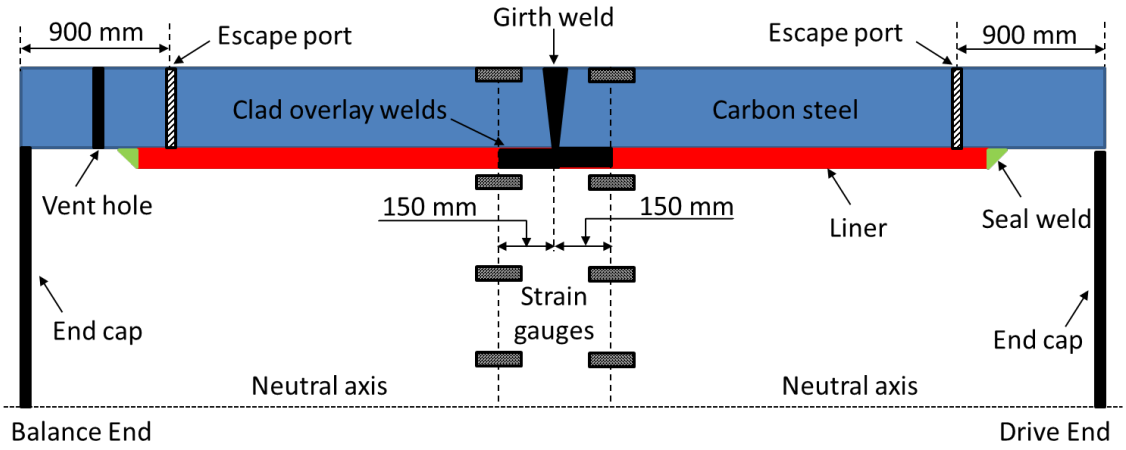


Figure 5.3: Fatigue String Instrumentation



Figure 5.4: TWI Resonant Rig

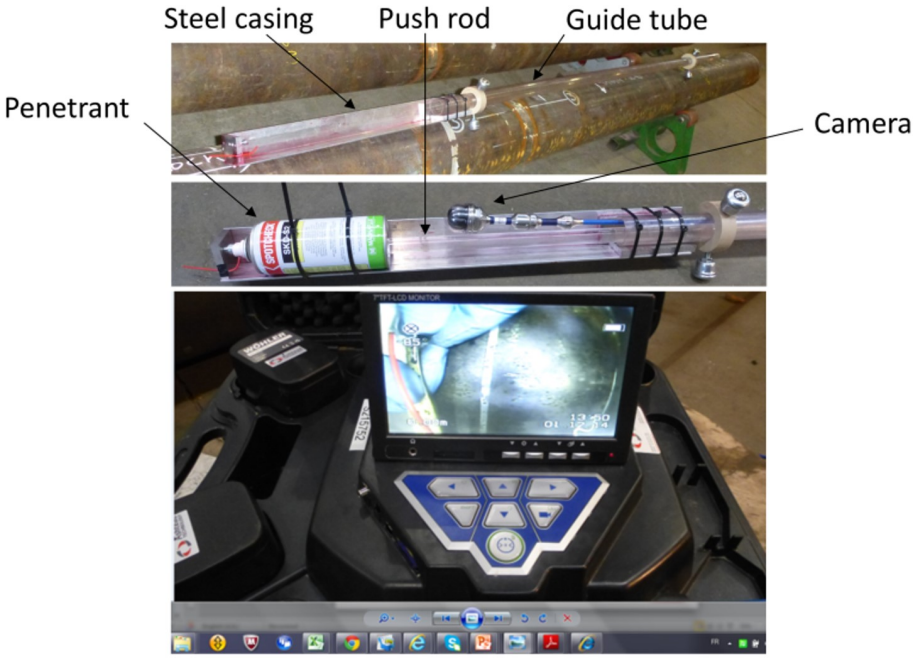


Figure 5.5: DPI Inspection Tool

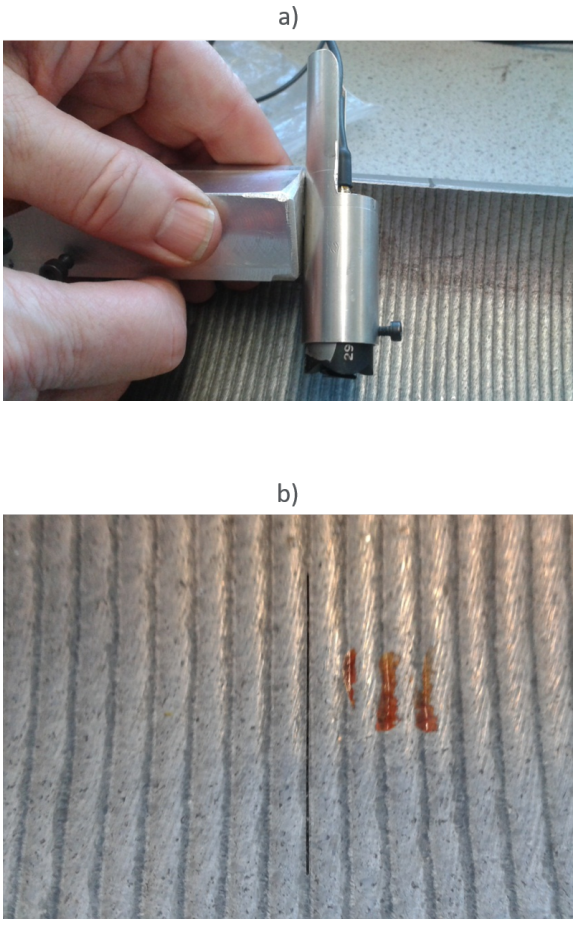


Figure 5.6: ECT Inspection Tool: (a) Probe, (b) Calibration Block with 3 mm Deep Notch

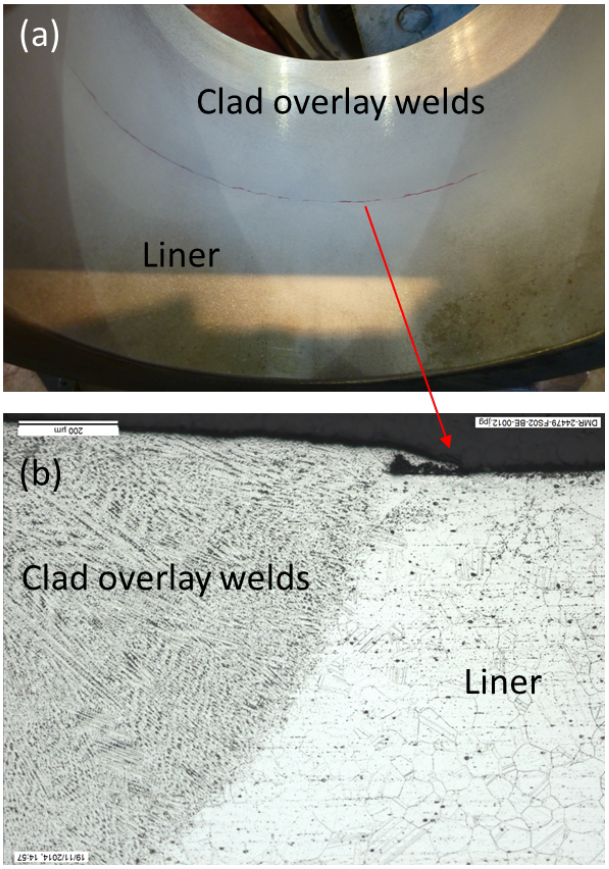


Figure 5.7: Post-Mortem Examination: (a) DPI Indication, (b) Macro-Section

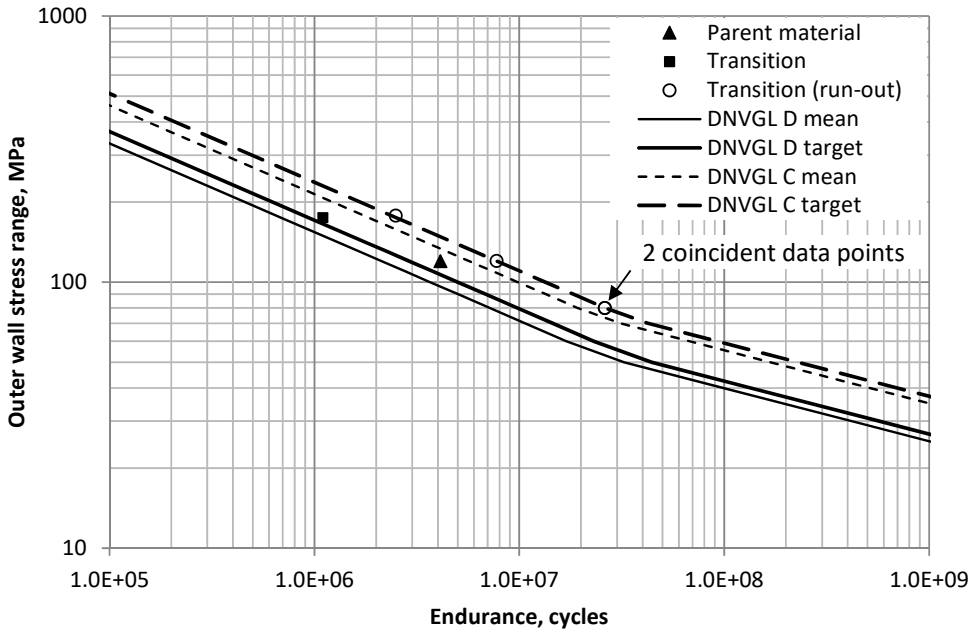


Figure 5.8: Fatigue Test Results versus DNVGL-RP-C203 SN Curves

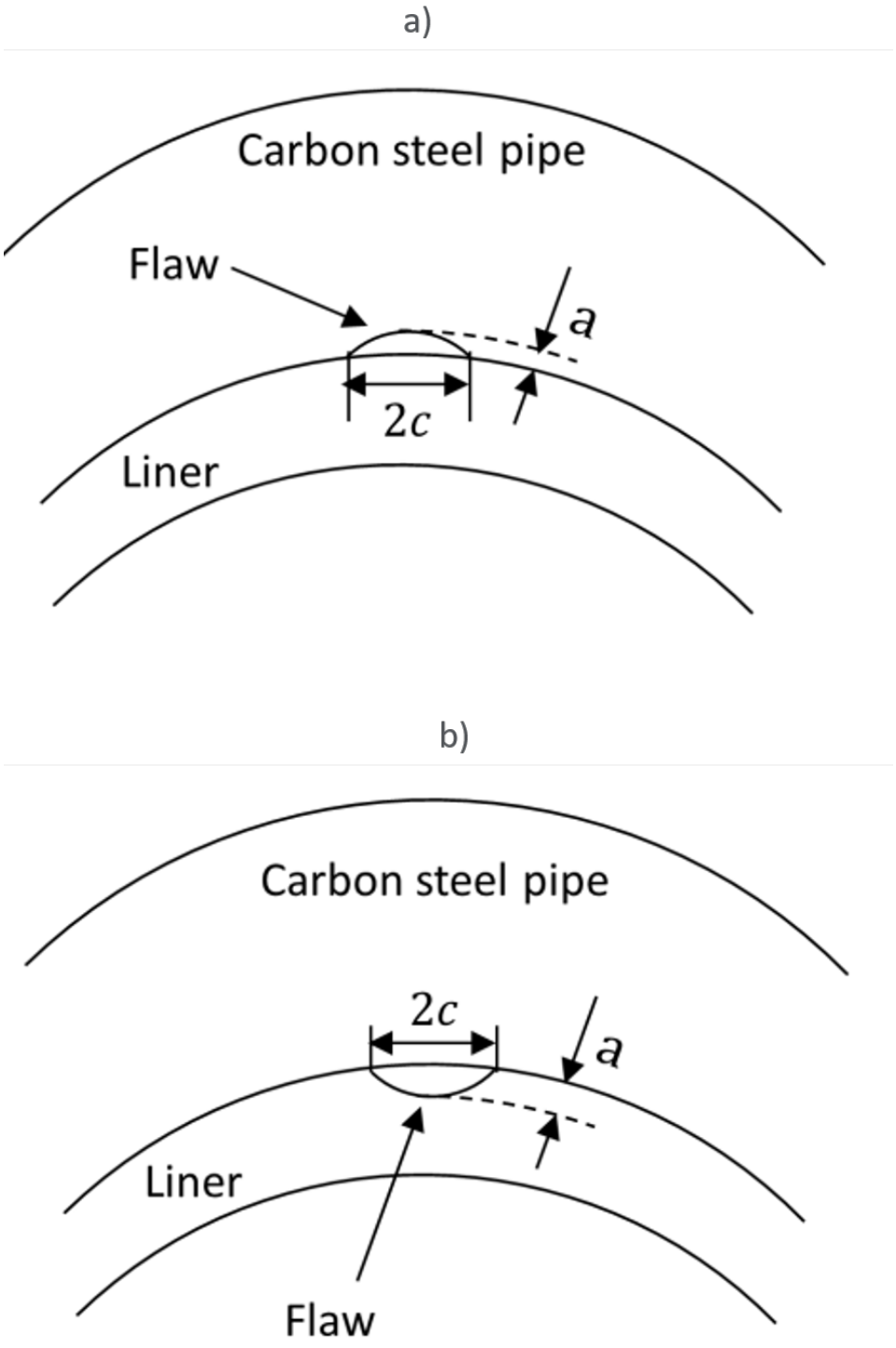


Figure 5.9: MLP Triple Point Interface Flaws: (a) CS Flaw (b) CRA Flaw

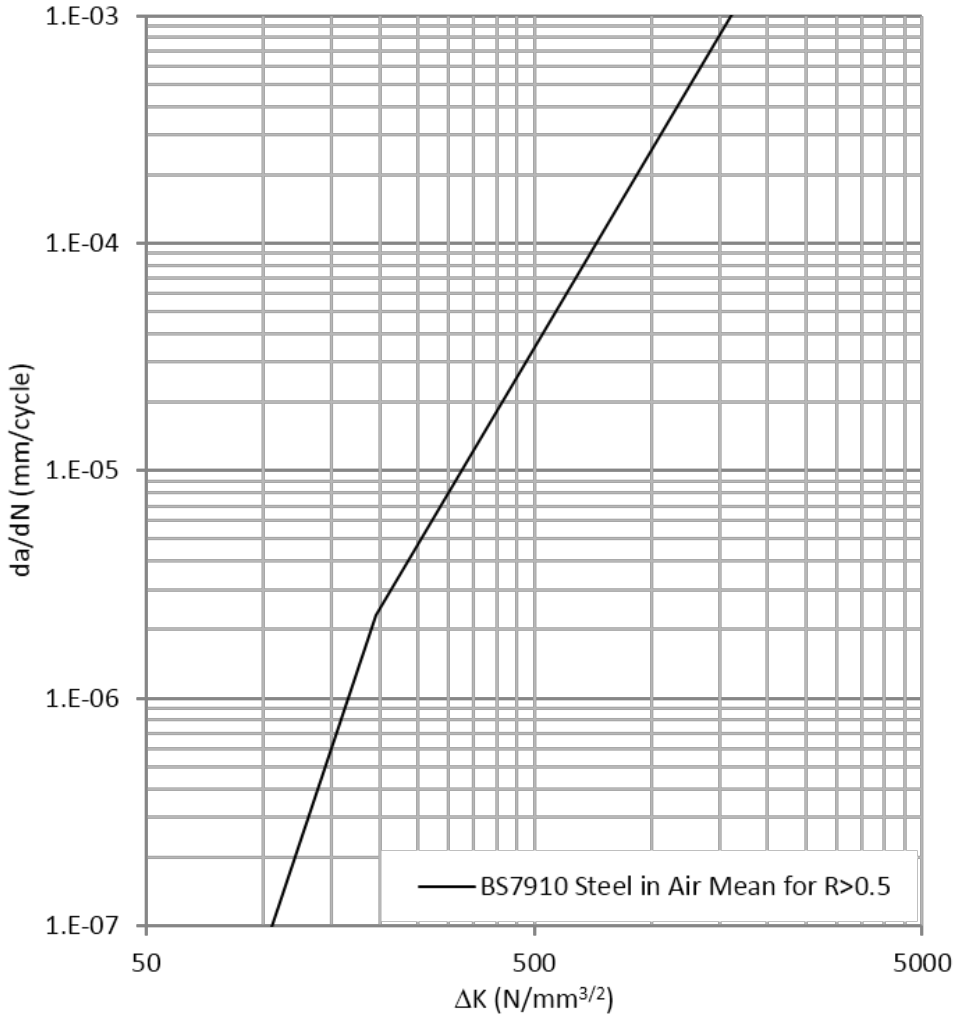


Figure 5.10: Fatigue Crack Growth Curve

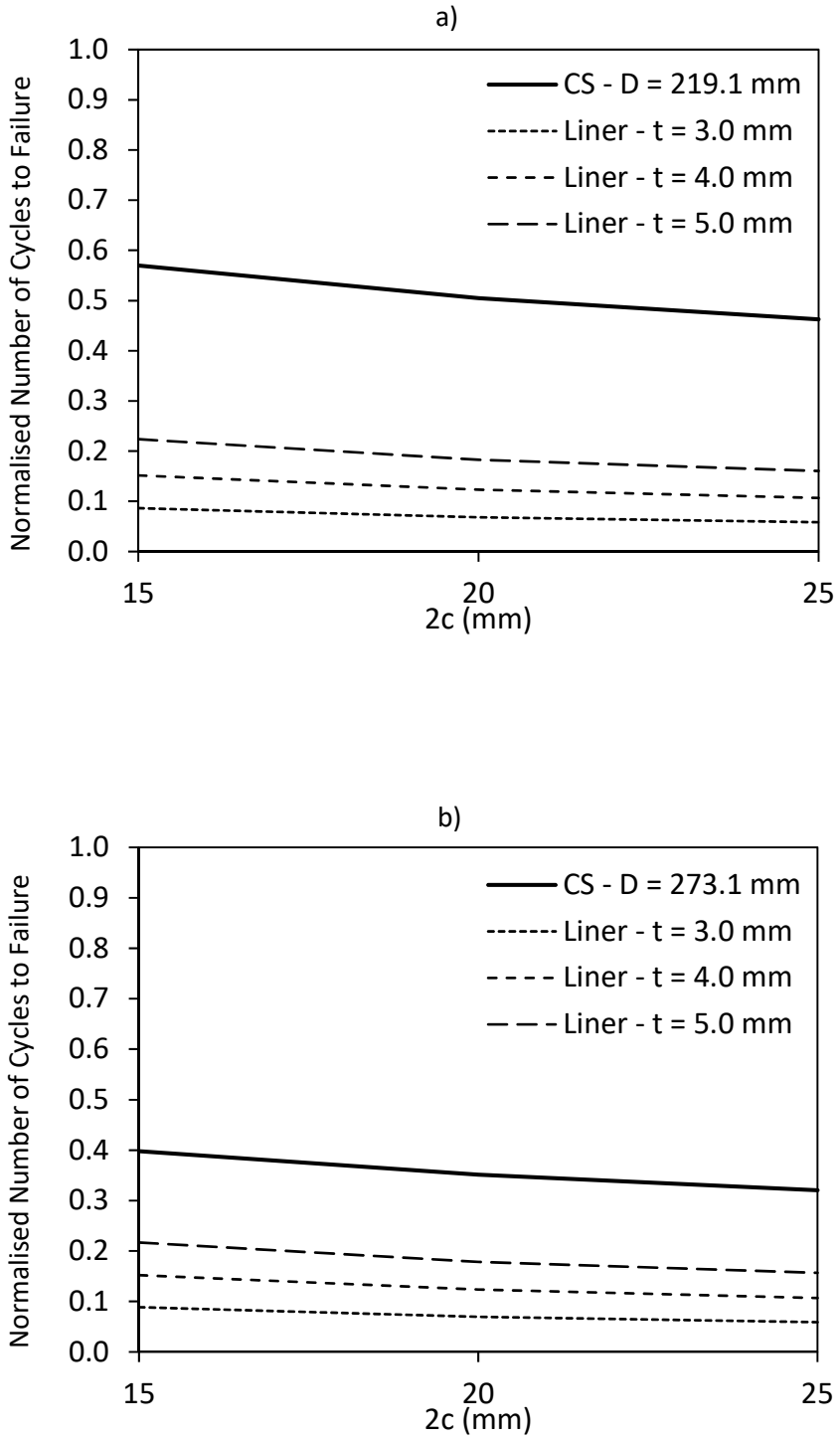


Figure 5.11: Fatigue Crack Growth Assessment Results – Normalised Number of Cycles to Failure

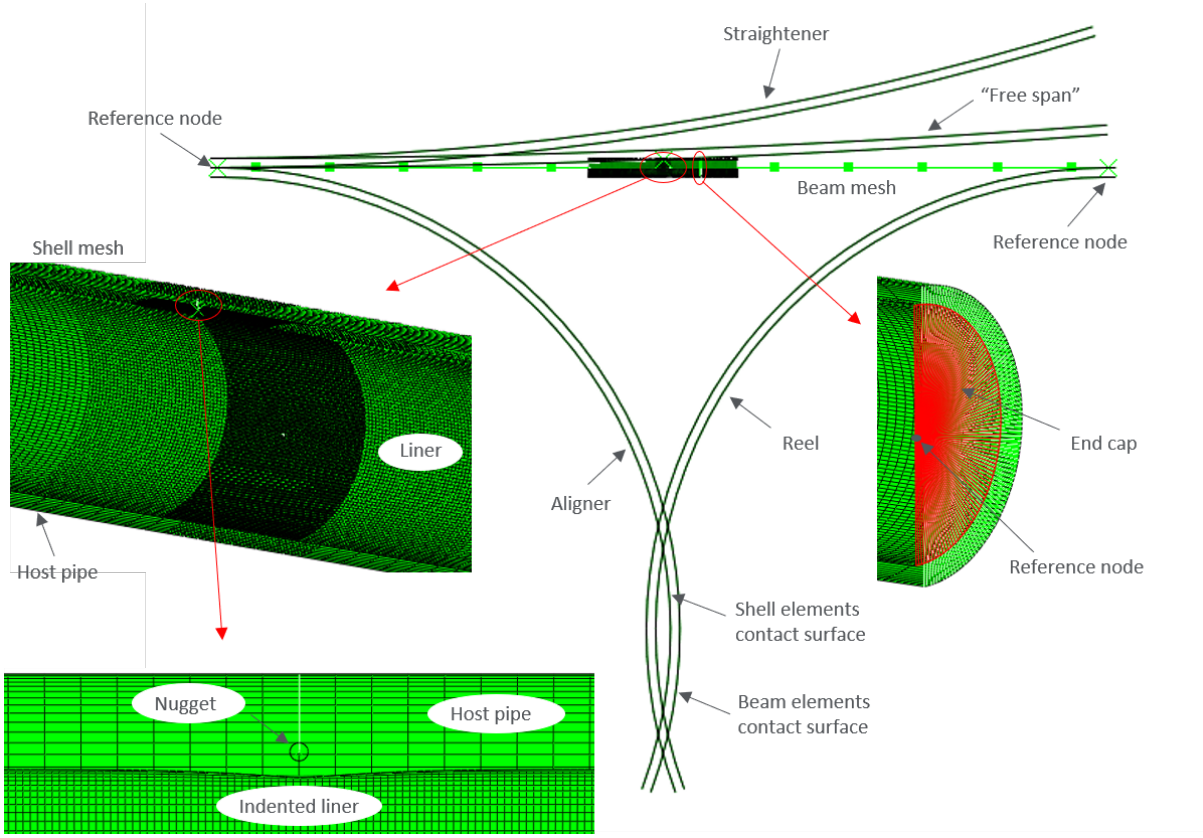


Figure 5.12: Low Cycle Fatigue of MLP – 3D FEA Model for Simulation of Manufacturing and Reeling of MLP

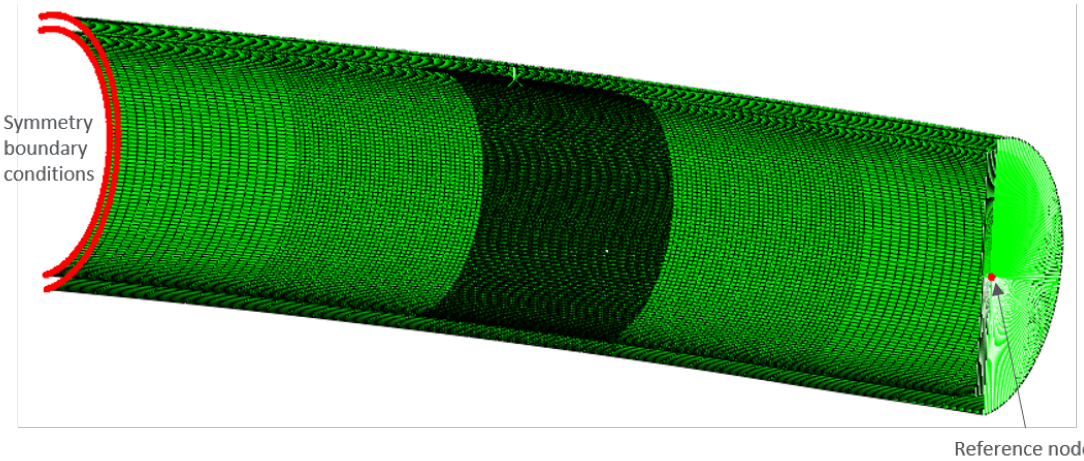


Figure 5.13: Low Cycle Fatigue of MLP – 3D FEA Model for Simulation of In-Service Operation of MLP

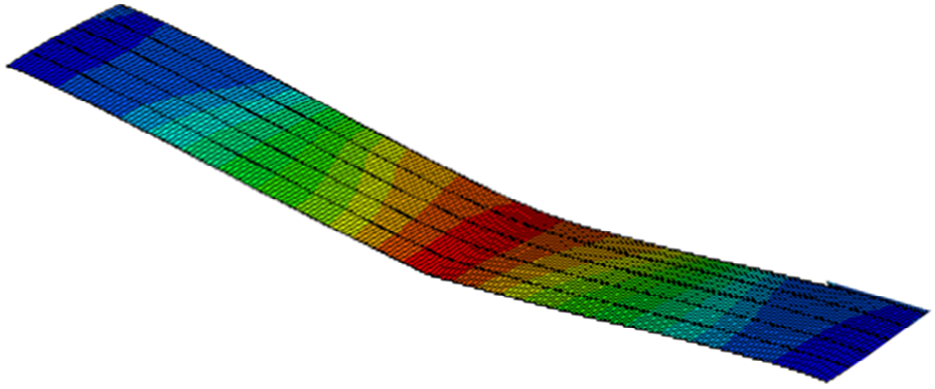


Figure 5.14: Low Cycle Fatigue of MLP – Liner Strip Model Extracted from 3D FEA Model of MLP: Contour Plot of Liner Lift-off from Host Pipe

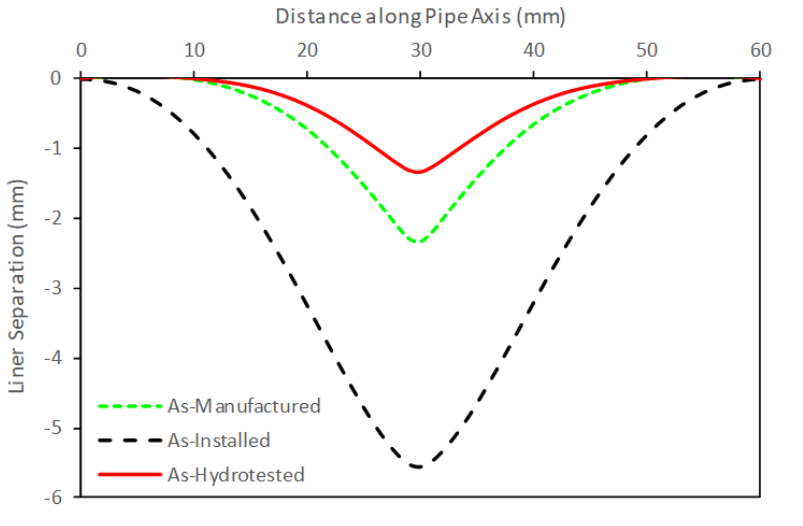


Figure 5.15: 8” MLP with 316L Liner – Wrinkle Height

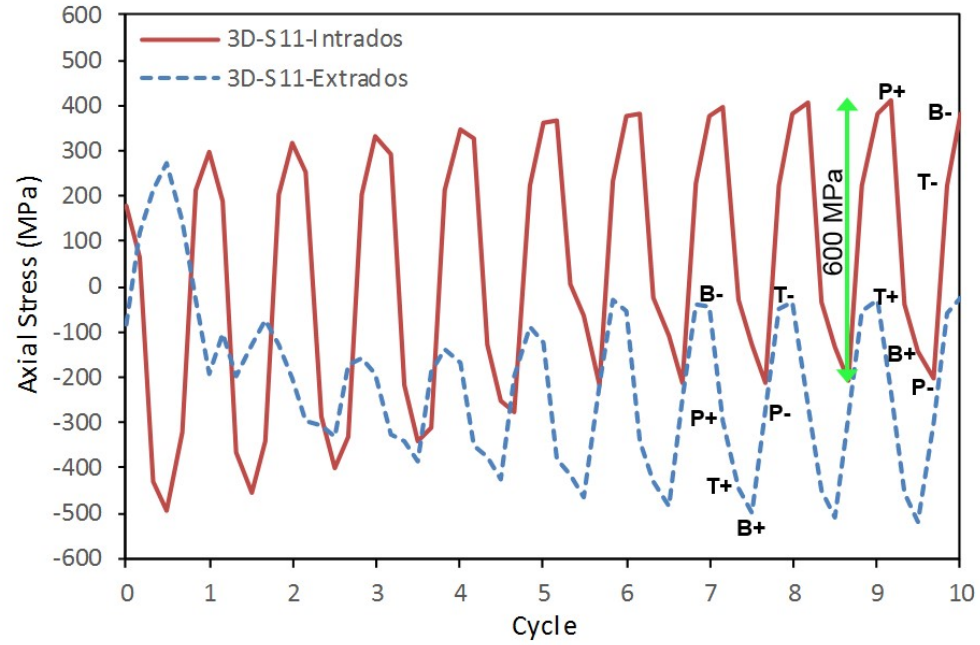


Figure 5.16: 8" MLP with 316L Liner – In-Service Stress Ranges

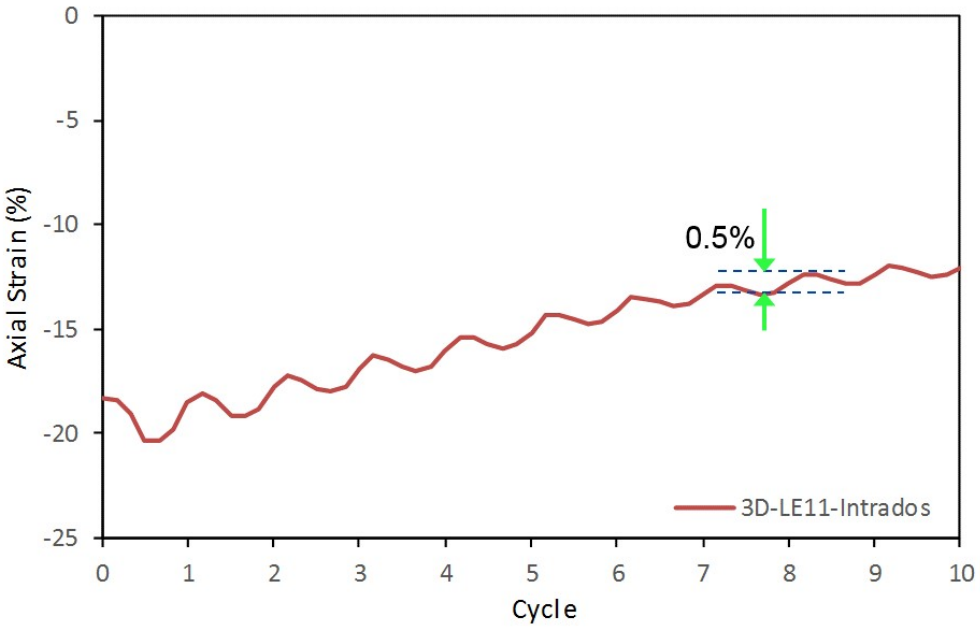


Figure 5.17: 8" MLP with 316L Liner – In-Service Strain Ranges

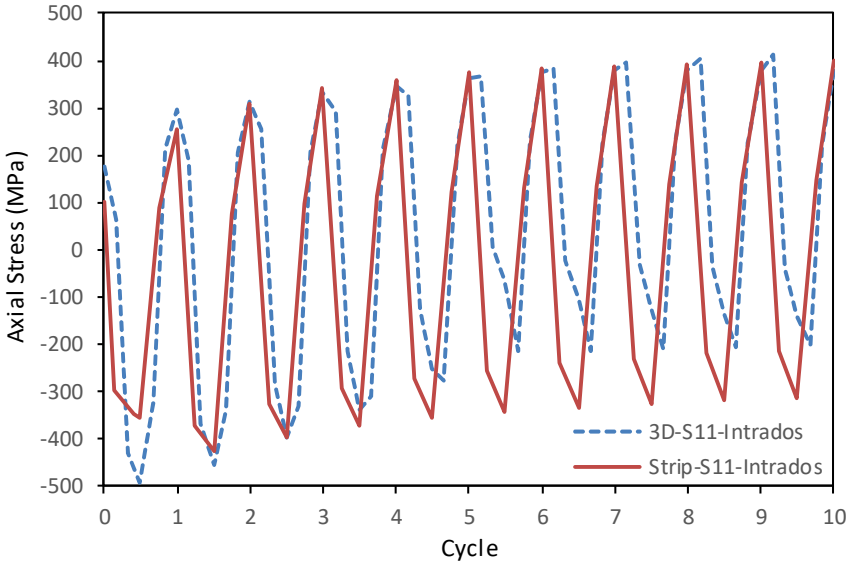


Figure 5.18: Stress Ranges in Alloy 316L Liner – 3D Pipe Model vs Strip Model

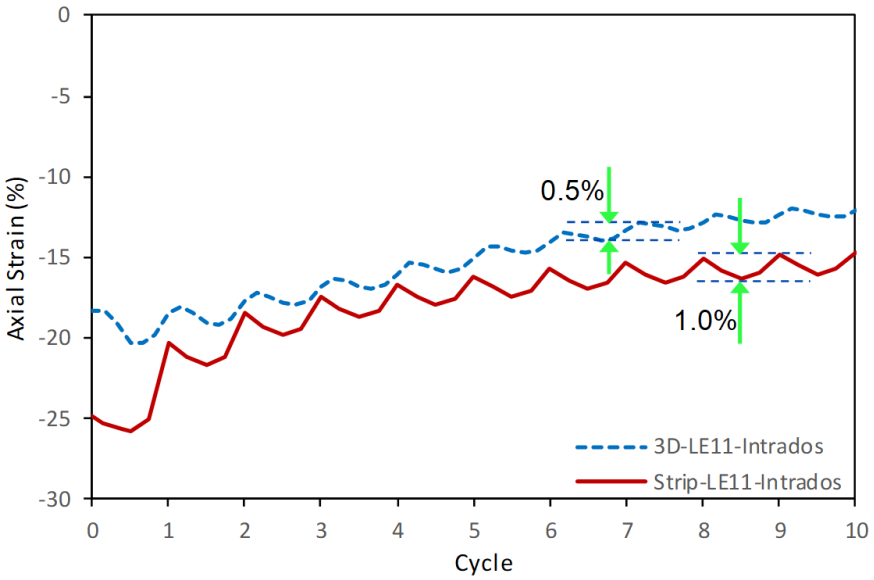


Figure 5.19: Strain Ranges in Alloy 316L Liner – 3D Pipe Model vs Strip Model

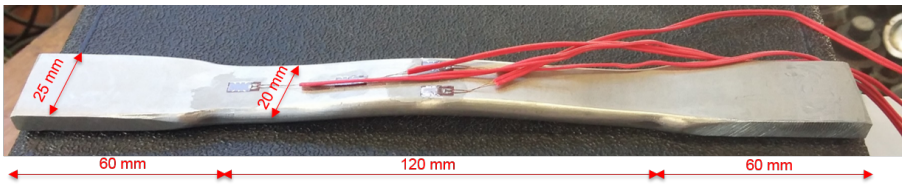


Figure 5.20: Small Scale Fatigue Test Specimen

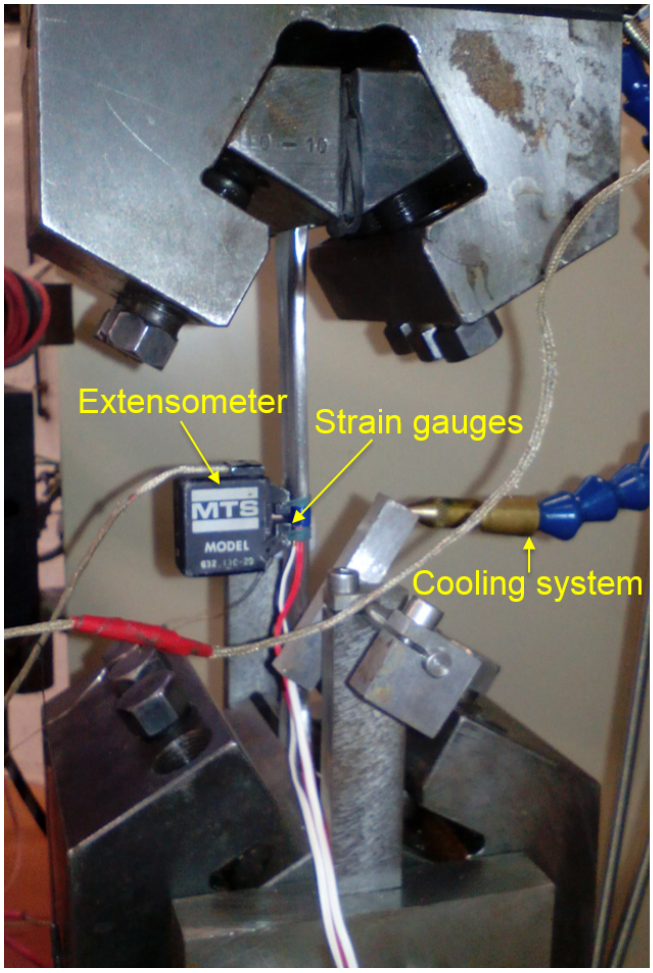


Figure 5.21: Small Scale Fatigue Test Machine

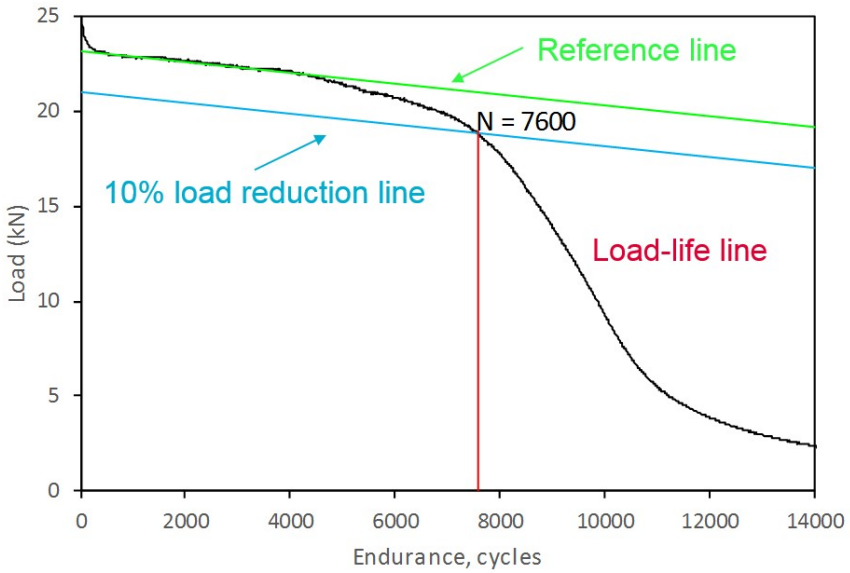


Figure 5.22: Load-Life Line



Figure 5.23: Crack Initiation Site

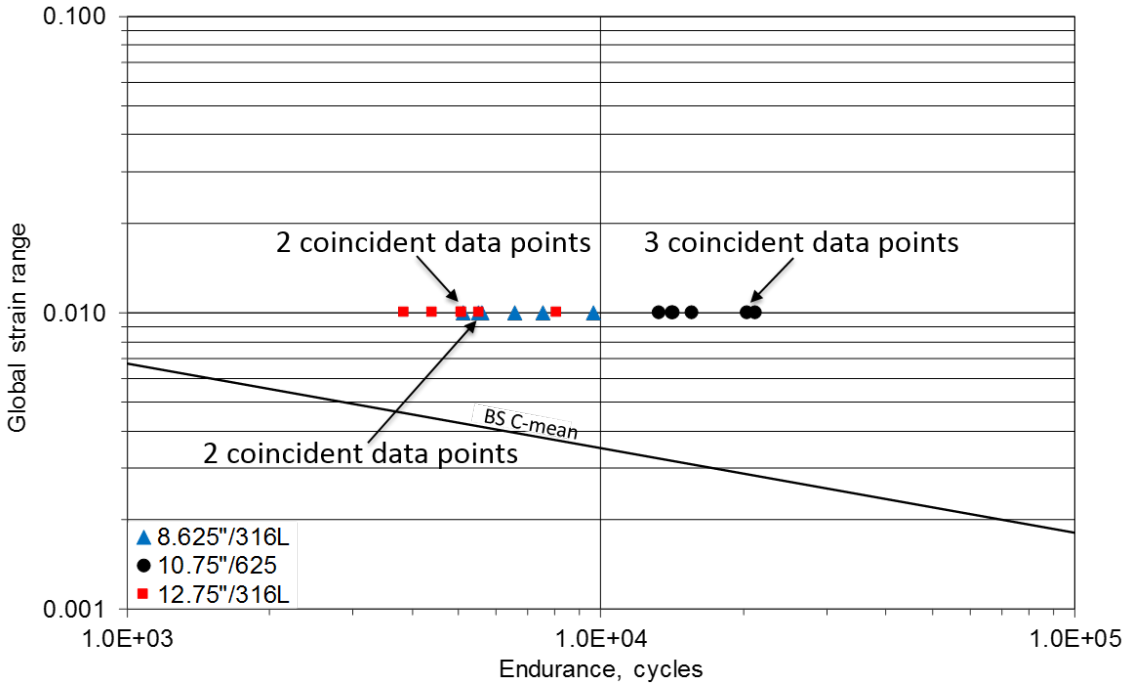


Figure 5.24: Small Scale Fatigue Test Results

Chapter 6

Conclusions and Further Work

6.1 Conclusions

A growing demand for transport of corrosive fluids subsea has engendered interest in solid CRA and bi-metal pipes. The latter, which include HRB clad and mechanically lined pipes, are made of a CS pipe lined with a CRA layer. Mechanically lined pipe, which has been the focus of this thesis, is manufactured by inserting the CRA liner into the CS host pipe and expanding it plastically until it contacts the host pipe. Expansion continues until the host pipe achieves a target expansion level. Once pressure is released, grip develops between the liner and the host pipe. Finally, clad overlay welding is performed to seal the liner ends. Mechanically lined pipes offer shorter lead times and are more economical than equivalent solid CRA and HRB clad pipes. The three main methods used for the installation of pipelines subsea are S-lay, J-lay and reel-lay. The latter, which is a cost-effective method for installing subsea pipelines up to 18" (457.2 mm) in diameter, was considered in this thesis. In contrast to S-lay and J-lay, where the pipeline typically remains within the elastic regime, a standard reel-lay installation process involves four plastic strain events. The CRA liner is susceptible to wrinkling when a mechanically lined pipe is subjected to plastic deformation representative of reeling. Two approaches were proposed in the industry to enable safe installation of reeled MLPs: pressurised and ambient reeling. This thesis focused on the latter approach, where the WT of the CRA liner is increased to enable reel-lay of MLPs at atmospheric pressure using standard reeling procedures.

Mechanical tests performed to establish the tensile behaviour of commonly used CRA liner grades showed that they strain harden predominantly isotropically during hoop expansion, representative of MLP manufacturing, and kinematically during subsequent cyclic plastic bending, representative of reeling. Such behaviour cannot be modelled with classical incremental metal plasticity models, because the associated hardening behaviour does not change with the plastic strain history. To overcome this issue while employing classical metal plasticity, a workaround approach was used, whereby the as-received stress-strain curve of the liner in the FEA was altered, to match the observed stress-strain hysteresis during cyclic bending following liner expansion. Wrinkling criteria were proposed, and 10" and 12" MLPs sized for ambient reeling were manufactured and subjected to large scale testing to examine the liner behaviour before and after the onset of wrinkling during cyclic bending at ambient pressure. The liner in the MLPs wrinkled when bent on a former with a radius less than 6.1 m, which is much lower than a typical reel hub radius (8.23 – 10.5 m in the TechnipFMC fleet), and makes provision for a safety factor. A framework was proposed for the numerical prediction of the liner separation from the host pipe and subsequent wrinkling during high strain bending. The numerical predictions of the evolution of liner separation from the host pipe, obtained using a classical metal plasticity model with a fixed yield criterion shape (e.g. the von Mises yield criterion), agreed well (though somewhat conservative) with the measurements taken at the pipe intrados during bending. This is the location, where largest liner separation was always observed, and therefore governs the design of reeled MLPs. Applying a classical metal plasticity model with a history dependant yield criterion, where the shape of the yield surface evolves with the plastic deformation, to accurately predict ovalisation of the CS host pipe during bending, reduced the level of conservatism and improved the numerical predictions in terms of liner separation.

Accurate fracture assessment procedures for surface breaking flaws in evenmatch pipeline girth welds subjected to reeling have been proposed in the literature (e.g. the DNVGL-ST-F101 procedure). In contrast, the solutions available for the assessment of embedded flaws, which represent the vast majority of weld flaws, are so conservative that they are not used currently. Instead, embedded flaws are treated as surface breaking flaws in a fracture assessment as per DNVGL-ST-F101. Consequently, a limit load solution for embedded flaws in pipeline girth

welds was derived by fitting a closed form solution to the results of a 3D FEA study. Small scale fracture tests were then carried out using modified middle crack tension specimens with through thickness embedded flaws, under load-controlled conditions, to verify suitability of the proposed analytical solution. The FEA based solution was very conservative for small flaws and small ligaments and appeared to be slightly non-conservative for long ligaments and long flaws. Consequently, under load-controlled conditions the test-based limit load solution should be used. In contrast, as the smallest ligament would not collapse but rather stretch to accommodate the boundary conditions under displacement-controlled conditions, it is recommended that the solution yielding highest limit load between the two be used for a direct ECA of embedded flaws. The ECA should be carried out as per DNVGL-ST-F101, using the BS7910 Option 2 approach (equivalent to R6 Option 2). The results of cyclic fracture tests carried out with SENT specimens, following the recommendations in BS8571, showed that pre-strain (during the first reeling tensile straining event) does not degrade the fracture toughness in undermatch pipeline girth welds, similar to those in mechanically lined pipelines. This is in-line with earlier results obtained by Tkaczyk *et al.* with overmatch welds. A crack depth adjustment formula, to account for the effect of undermatch on the crack driving force in pipeline girth welds as per the SINTEF approach, was established based on the results of an extensive 3D parametric FEA study. A new procedure for the ECA of surface flaws in undermatch welds was then proposed, whereby a DNVGL-ST-F101 – BS7910 Option 2 assessment is performed to determine the maximum acceptable flaw sizes under the assumption of evenmatch, and the acceptable crack depths are subsequently reduced to account for weld undermatch. This approach was then extended to the treatment of embedded flaws in undermatch welds.

Six 8.625” (219.1 mm) MLPs with alloy 625 liner, clad overlay and girth welds were sized, manufactured, bend tested to simulate reeling at atmospheric pressure and then fatigue tested on a resonant rig. To demonstrate that the CRA barrier was not damaged long before the final fatigue failure, NDE was carried out at various stages during testing. All fatigue test strings reached the DNVGL-RP-C203 class D target curve without breach of the corrosion barrier. Four out of six specimens reached the DNVGL class C target curve without failing. Failure of the fifth test string initiated from a blemish on the CS pipe, while cracks in the

last specimen started from lack of fusion defects at the triple point interface. The embedded defects grew both in the CRA layer and in the CS pipe, and broke at the pipe inner surface before the pipe burst. It was estimated that breach of the corrosion barrier occurred after 75% of the total life was elapsed. Cold laps, created during machining and flapping liner to clad overlay transitions, did not lead to the breach of CRA layer before reaching the required fatigue performance. This demonstrated that reeled MLPs, designed following the rules laid out herein, are suitable for high SCR service. A parametric FEA study showed that the Marie *et al.* K solution for semi-elliptical flaws in single pipes under bending, provides a good but slightly conservative approximation of K for single pipes with surface breaking flaws and MLPs with interface flaws under bending. Increasing the liner thickness to suppress wrinkling during reeled installation of MLPs under atmospheric pressure resulted in a significant increase in the fatigue life. It was shown numerically that during pipeline operation the axial strain range in the liner does not exceed 1% for the pressure range equal to a hoop stress utilisation ratio of 0.8, the temperature range of 150°C and the bending strain range of 0.3% under high stress low cycle loading. It was further demonstrated that the stress/strain range in the liner subjected to in-service loading can be reproduced in a strip geometry under cyclic axial displacement. Liner dumbbell specimens were extracted from 8", 10" and 12" MLP strings which underwent simulated reeling and pre-commissioning. The liner specimens with wrinkles up to 6 mm in height, introduced half-way along their length, were subjected to small scale fatigue testing. The predicted life, which was significantly longer for alloy 625 than for alloy 316L, was well in excess of 3000 cycles, which corresponds to one shut-down cycle every month, for 25 years with a safety factor of 10. This demonstrated that liner imperfections (dents/wrinkles) up to 6 mm in height, are not detrimental to the in-service integrity of MLP flowlines, and validated the proposed wrinkling criteria.

Design rules developed during this PhD were applied to three pipelines: (i) the world's first MLP reeled at ambient, comprising of 7" flowline and riser installed in the Gulf of Mexico in 2015, as part of the Deep Gulf Energy Kodiak project, and (ii) 10" and 12" flowlines to be reeled in Brazil in 2019, as part of the Equinor Peregrino II project.

6.2 Further Work

It is recommended that further work be carried out to develop a history dependant yield criterion for the CRA liner, to further improve the accuracy of the FEA for predicting liner ovalisation, subsequent separation from the host pipe and wrinkling during high strain bending. This will allow conservatism in the design to be reduced, and enable further optimisation of the minimum reelable liner thickness in MLPs for ambient reel-lay installation. Although this may be worth investigating it is anticipated that developing a metal plasticity model, capable of yielding isotropic hardening during a plastic hoop pre-strain and kinematic hardening during a subsequent cyclic plastic axial straining, would be very difficult. Investigations may also be undertaken to understand why the numerical predictions do not agree well with the experiment at the location that is at the pipe extrados (i.e. subjected to tension) during the first bending event, although this is not critical from a design point of view.

Although the proposed limit load solution for embedded flaws in evenmatch girth welds, established from load-controlled tests, is a significant improvement compared to existing ones, further work should be undertaken to extend it to part-through wall flaws. In addition, for displacement-controlled loadings such as reeling, the image correlation results produced during this PhD programme could be revisited and a new ligament collapse criterion proposed in terms of the critical ligament necking, which is related to the normalised crack opening. A 3D parametric FEA study of pipe with a part-circumferential embedded flaw subjected to tension or bending could then be undertaken to establish a new ligament collapse criterion for pipes. Moreover, further work should be carried out, to assess whether the J-estimation scheme proposed by Tkaczyk *et al.* for the treatment of surface breaking flaws in materials whose stress-strain curves exhibit a yield plateau, could be applied to embedded flaws for the same condition. Furthermore, it is anticipated that it may be challenging to establish a representative fracture toughness for CRA triple point flaws in MLPs whose liner thickness is small (e.g.$\leq$ 3 mm). It is therefore recommended that a segment testing protocol be developed.

The use of the BS7910 fatigue crack growth curve for steel in air for the assessment of CRA triple point flaws in MLP with nickel alloy cladding may lead to a significant underestimation of the fatigue life. It is therefore recommended that fatigue crack growth tests be carried out to develop curves suitable for the assessment of flaws in CRA materials such as alloy 625. The effect of the service environment on the fatigue crack growth rate may also be investigated. Furthermore, a generic K-solution for CRA triple point flaws should be developed using the FEA model presented in this work, to further reduce the conservatism. Moreover, it is recommended that high strain low cycle fatigue testing of MLP be undertaken to provide further confidence in the acceptance criteria for liner imperfections, proposed in this thesis. The fatigue failure criterion adopted herein (10% reduction in the maximum load) could be relaxed if fatigue tests are interrupted and NDE performed at various stages to assess whether the CRA barrier has been breached.

Bibliography

[1] *API 5L: Specification for Line Pipe.* American Petroleum Institute, 46th edition, 2018.

[2] *www.tenaris.com.*

[3] *www.vallourec.com.*

[4] S. Kyriakides, E. Corona. *Mechanics of Offshore Pipelines, Vol. I: Buckling and Collapse.* Elsevier, Oxford, UK, 2007.

[5] G.Brown, P. Thomson, M. Fryer. World's First 18" Reeled Pipe Installation. In *Proceedings of the 4th International Conference on Pipeline Technology*, Ostend, Belgium, 2004.

[6] L. G. Brazier. On the flexure of thin cylindrical shells and other thin sections. In *Proceedings of the Royal Society A*, Vol. 116, issue 773, pages 104-114, 1927.

[7] *DNVGL-ST-F101: Submarine Pipeline Systems.* Det Norske Veritas Germanischer Lloyd, 2017.

[8] *API 5LD: Specification for CRA Clad or Lined Steel Pipe.* American Petroleum Institute, 4th edition, 2017.

[9] M. Johnsrud, L. Collberg, K. Rasmussen and S. L. Bjerke. Design Guideline for Clad and Lined Pipelines. In *Proceedings of the Rio Pipeline Conference*, Rio de Janeiro, 2009.

[10] *DNVGL Report No. 2011-3167/Rev02: Design and Construction of Clad and Lined Pipelines.* Det Norske Veritas Germanischer Lloyd, Issue 2013-08-20, 2013.

[11] *API SPEC 5LC: CRA Line Pipe.* American Petroleum Institute, 4th edition, 2015.

[12] *www.cladtek.com.*

[13] *www.kuroki.co.jp/ktp/index.html.*

[14] A. C. de Koning, H. Nakasugi, L. Ping. TFP and TFT back in town (Tight Fit CRA Lined Pipe and Tubing). In *Stainless Steel World*, 2004.

[15] *www.procladgroup.com.*

[16] *www.butting.com.*

[17] *www.gieminox.com.*

[18] G. A. Lanan, D. W. Barry. Mobile Bay Corrosive Gas Flow Lines Use New Material, Design. In *Oil and Gas Journal*, 90:71, 1992.

[19] M. Mizumura, H. Mimura, H. Naoi and H. Higashiyama. Behaviour of mechanical bonded double-wall pipe under various loading conditions. In *Proceedings of the 2nd International Offshore and Polar Engineering Conference*, 1992.

[20] M. Mizumura, H. Mimura, H. Naoi and H. Higashiyama. Behaviour of mechanical bonded double-wall pipe under various loading conditions. In *International Journal of Offshore and Polar Engineering*, 4:142–150, 1994.

[21] *TechnipFMC Report No. OE006124-R-001: Reeling of Clad Steel Pipe Summary Report.* Rigid Pipeline and Installation Technology, 2006.

[22] M. A. Spence, C. V. Roscoe, K. Schafer, J. Hutchison, A. Foxton and C. Barraclough. Bi-metal, CRA-lined Pipe Employed for North Sea Field Development. In *Oil and Gas Journal*, 1999.

[23] I. Rommerskirchen. New Progress Caps 10 Years of Work with BuBi Pipes. In *World Oil*, 2005.

[24] A. Dale and G. Robertson. Tyrihans Production Pipeline: From Fairytale to Reality. In *Proceedings of the Offshore Pipeline Technology Conference*, 2008.

[25] G. Endal, E. Levold and H. Ilstad. Method for Laying a Pipeline Having an Inner Corrosion Proof Cladding. *Patent No. PCT/NO2007/000427*, 2007.

[26] G. Endal, E. Levold and H. Ilstad. Method of Spooling a Bi-Metallic Pipe. *Patent No. WO 2010/010390 A2*, 2010.

[27] J. A. Mair. Reeling and unreeling an internally clad metal pipeline. *Patent No. GB2479379B*, 2010.

[28] T. Tkaczyk, M. Chalmers and A. Pépin. Reel-Lay Installation Approaches for Mechanically Lined Pipes. In *Proceedings of the Offshore Technology Conference Asia*, Kuala-Lumpur, 2016, OTC-26440-MS.

[29] T. Tkaczyk, A. Pépin. Methods of Reel-Laying a Mechanically Lined Pipe. *Patent No. PCT/GB2010/051787*, 2010.

[30] A. Pépin, T. Tkaczyk. Mechanically Lined Pipe. *Patent No. WO 2014/080281A2*, 2014.

[31] *www.drillingformulas.com.*

[32] C. E. Murphey and C. G. Langner. Ultimate pipe strength under bending, collapse and fatigue. In *Proceedings of Offshore Mechanics and Arctic Engineering*, pages 467–473, 1985.

[33] S. Kyriakides and G. T. Ju. Bifurcation and Localization Instabilities in Cylindrical Shells under Bending: Part I - Experiments. *Journal of Solids and Structures*, 29:1117–1142, 1992.

[34] S. Kyriakides and G. T. Ju. Bifurcation and Localization Instabilities in Cylindrical Shells under Bending: Part II - Predictions. *Journal of Solids and Structures*, 29:1143–1171, 1992.

[35] F. C. Bardi and S. Kyriakides. Plastic Buckling of Circular Tubes under Axial Compression: Part I – Experiments. *International Journal of Mechanical Sciences*, 48:830–841, 2006.

[36] F. C. Bardi and S. Kyriakides. Plastic Buckling of Circular Tubes under Axial Compression: Part II – Analysis. *International Journal of Mechanical Sciences*, 48:842–854, 2006.

[37] S. Manouchehri, B. Howard, S. Denniel. A Discussion of the Effect of the Reeled Installation Process on Pipeline Limit States. In *Proceedings of the International Offshore and Polar Engineering Conference*, Vancouver, BC, Canada, 2008.

[38] L. Collberg and M. HØgberget. Guideline for Installation of Rigid Pipelines Limit State Criteria. Det Norske Veritas Germanischer Lloyd, DNVGL Report No. 2014-018, 2015.

[39] G. Brown, T. Tkaczyk, B. Howard. Reliability Based Assessment of Minimum Reelable Wall Thickness for Reeling. In *Proceedings of the International Pipeline Conference*, Calgary, Alberta, Canada, 2004.

[40] S. Denniel, T. Tkaczyk, B. Howard, E. Levold and O. Aamlid. The Development of a Refined Assessment Procedure for the Pipeline Reeling Process Using Reliability and Finite Element Techniques. In *Proceedings of Offshore Mechanics and Arctic Engineering*, OMAE2009, Honolulu, USA, 2009.

[41] *www.opensees.berkeley.edu*.

[42] S. Denniel, T. Tkaczyk, B. Howard, E. Levold and O. Aamlid. On the Influence of Mechanical and Geometrical Property Distribution on the Safe Reeling of Rigid Pipelines. In *Proceedings of Offshore Mechanics and Arctic Engineering*, OMAE2009, Honolulu, USA, 2009.

[43] T. Sotberg, R. Bruschi, K. Mark. The SUPERB Project: Reliability-based Design Guideline for Submarine Pipelines. In *Proceedings of Offshore Technology Conference*, OTC1996, Houston, Texas, USA, 1996.

[44] D. Smith, T. Tkaczyk, S. Denniel. Reliability Based Assessment of Minimum Wall Thickness for Reeling – a Focus on Cold Worked Pipe. In *Proceedings of Offshore Mechanics and Arctic Engineering*, OMAE2011, Rotterdam, The Netherlands, 2011.

[45] M. Martinez and G. Brown. Effect of Lüders Bands on the Bending Capacity of Steel Tubes. In *Proceedings of the 24th International Conference on Offshore Mechanics and Arctic Engineering*, OMAE2005, Halkidiki, Greece, 2005.

[46] M. Martinez, A. Pépin., P. Sicsic. Ovality Prediction of Reeled Seamless and SeamWelded Pipes. In *Proceedings of the 27th International Offshore and Polar Engineering Conference*, ISOPE2017, San Francisco, California, USA, 2017.

[47] *www.3ds.com/products-services/simulia/products/abaqus.*

[48] *Safe Design of Pipelines with Lateral Buckling: Design Guideline.* Safebuck Joint Industrial Project, 2015.

[49] *DNVGL-RP-F110: Global Buckling of Submarine Pipelines.* Det Norske Veritas Germanischer Lloyd, 2018.

[50] E. S. Focke. Reeling of Tight Fit Pipe. *Ph.D. Thesis*, Delft University of Technology, Delft, The Netherlands, 2007.

[51] E. S. Focke, A. M. Gresnigt, J. Meek, H. Nakasugi. The 2-Dimensional Modelling of the Manufacturing Process of Tight Fit Pipe (TFP). In *Proceedings of the 14th International Offshore and Polar Engineering Conference*, ISOPE2004, Toulon, France, 2004.

[52] *www.mscsoftware.com/product/marc.*

[53] E. S. Focke, A. M. Gresnigt, J. Meek, H. Nakasugi. The Influence of Heating of the Liner Pipe during the Manufacturing Process of Tight Fit Pipe. In *Proceedings of the 16th International Offshore and Polar Engineering Conference*, ISOPE2006, San Francisco, California, USA, 2006.

[54] E. S. Focke, A. M. Gresnigt, J. Meek, H. Nakasugi. Experimental Research on Local Buckling Behaviour of Tight Fit Pipe. In *Proceedings of the 15th International Offshore and Polar Engineering Conference*, ISOPE2005, Seoul, South Korea, 2005.

[55] G. Gerard. Compressive and Torsional Buckling of Thin Walled Cylinders in the Yield Region. In *National Advisory Committee for Aeronautics Journal*, NACA Technical Report No. 3726, Washington, USA, 1956.

[56] S. C. Batterman. Plastic buckling of axially compressed cylindrical shells. In *American Institute of Aeronautics and Astronautics Journal*, 3:316–325, 1965.

[57] A. M. Gresnigt. Plastic design of buried steel pipes in settlement areas. In *Heron Journal*, 31:1-113, ISSN 0046-7316, 1986.

[58] E. S. Focke, A. M. Gresnigt. Local Buckling of Tight Fit Liner Pipe. In *Proceedings of the ASME 2009 Pressure Vessels and Piping Conference*, ASMEPVP2009, Prague, Czech Republic, 2009.

[59] A. Hilberink. Mechanical Behaviour of Lined Pipe. *Ph.D. Thesis*, Delft University of Technology, Delft, The Netherlands, 2011.

[60] A. Hilberink, A. M. Gresnigt, L. J. Sluys. A Finite Element Method Approach on Liner Wrinkling of Snug Fit Lined Pipe. In *Proceedings of the 20th International Offshore and Polar Engineering Conference*, ISOPE2010, Beijing, China, 2010.

[61] E. S. Focke, A. M. Gresnigt, A. Hilberink. Local Buckling of Tight Fit Liner Pipe. In *Journal of Pressure Vessel Technology*, 133:011207-1–011207-9, 2011.

[62] E. S. Focke, A. M. Gresnigt, J. Meek. Small Scale Reeling Tests. In *Proceedings of the 16th International Offshore and Polar Engineering Conference*, ISOPE2006, San Francisco, California, USA, 2006.

[63] E. S. Focke, E. Karjadi, A. M. Gresnigt, J. Meek, H. Nakasugi. Reeling of Tight Fit Pipe. In *Proceedings of the 26th International Conference on Offshore Mechanics and Arctic Engineering*, OMAE2007, San Diego, California, USA, 2007.

[64] A. Hilberink, A. M. Gresnigt, L. J. Sluys. Liner Wrinkling of Lined Pipe under Compression, A Numerical and Experimental Investigation. In *Proceedings of the 29th Inter-*

national Conference on Ocean, Offshore and Arctic Engineering, OMAE2010, Shanghai, China, 2010.

[65] A. Hilberink, A. M. Gresnigt, L. J. Sluys. A Finite Element Method Approach on Liner Wrinkling of Lined Pipe during Bending. In *Proceedings of the 21st International Offshore and Polar Engineering Conference*, ISOPE2011, Maui, Hawaii, USA, 2011.

[66] A. Hilberink, A. M. Gresnigt, L. J. Sluys. Mechanical Behaviour of Lined Pipe during Bending, Numerical and Experimental Results Compared. In *Proceedings of the 30th International Conference on Ocean, Offshore and Arctic Engineering*, OMAE2011, Rotterdam, The Netherlands, 2011.

[67] D. Vasilikis. Structural Behaviour and Stability of Cylindrical Steel Shells with Lateral Confinement. *Ph.D. Thesis*, University of Thessaly, Volos, Greece, 2012.

[68] D. Vasilikis, S. A. Karamanos. Buckling of Clad Pipes under Bending and External Pressure. In *Proceedings of the 30th International Conference on Ocean, Offshore and Arctic Engineering*, OMAE2011, Rotterdam, The Netherlands, 2011.

[69] D. Vasilikis, S. A. Karamanos. Wrinkling of Lined Pipes under Bending. In *Proceedings of the 22nd International Offshore and Polar Engineering Conference*, ISOPE2012, Rhodes, Greece, 2012.

[70] D. Vasilikis, S. A. Karamanos. Mechanical Behaviour and Wrinkling of Lined Pipes. In *International Journal of Solids and Structures*, 49:3432-3446, 2012.

[71] D. Vasilikis, S. A. Karamanos. Wrinkling of Lined Steel Pipes under Bending. In *Proceedings of the 32nd International Conference on Ocean, Offshore and Arctic Engineering*, OMAE2013, Nantes, France, 2013.

[72] L. Yuan, S. Kyriakides. Wrinkling Failure of Lined Pipe under Bending. In *Proceedings of the 32nd International Conference on Ocean, Offshore and Arctic Engineering*, OMAE2013, Nantes, France, 2013.

[73] L. Yuan, S. Kyriakides. Liner Wrinkling and Collapse of Bi-Material Pipe under Bending. In *International Journal of Solids and Structures*, 51:599-611, 2014.

[74] L. Yuan, S. Kyriakides. Liner Wrinkling and Collapse of Bi-Material Pipe under Axial Compression. In *International Journal of Solids and Structures*, 60-61:48-59, 2015.

[75] L. Yuan, S. Kyriakides. Plastic Bifurcation Buckling of Lined Pipe under Bending. In *European Journal of Mechanics A/Solids*, 47:288-297, 2014.

[76] B. Harrison, L. Yuan, S. Kyriakides. Measurement of Lined Pipe Liner Imperfections and the Effect on Wrinkling and Collapse under Bending. In *Proceedings of the 35th International Conference on Ocean, Offshore and Arctic Engineering*, OMAE2016, Busan, South Korea, 2016.

[77] L. Yuan, S. Kyriakides. Wrinkling and Collapse of Girth-Welded Lined Pipe under Bending. In *Proceedings of the 33rd International Conference on Ocean, Offshore and Arctic Engineering*, OMAE2014, San Francisco, CA, USA, 2014.

[78] L. Yuan, S. Kyriakides. Liner Wrinkling and Collapse of Girth-Welded Bi-Material Pipe under Bending. In *Applied Ocean Research*, 50:209-216, 2015.

[79] *DNVGL Report No. 2010-1509/RevA: Wrinkling in Lined Pipe during Laying and Operation.* Det Norske Veritas Germanischer Lloyd, Issue 2010-10-11, 2010.

[80] *DNVGL Report No. 2011-3044/RevA: Full Scale Bend Testing of Lined Pipes.* Det Norske Veritas Germanischer Lloyd, Issue 2011-01-24, 2011.

[81] *DNVGL Report No. 2017-3114/Rev1: Guideline for Design and Construction of Lined and Clad Pipelines.* Det Norske Veritas Germanischer Lloyd, Issue 2018-06-07, 2018.

[82] T. Tkaczyk, A. Pépin, and S. Denniel. Integrity of Mechanically Lined Pipes Subjected to Multi-Cycle Plastic Bending. In *Proceedings of the 30th International Conference on Ocean, Offshore and Arctic Engineering*, OMAE2011, Rotterdam, The Netherlands, 2011.

[83] A. Pépin, T. Tkaczyk, and S. Denniel. Cost Efficient Solution for the Transport of Highly Corrosive Fluids. In *Proceedings of the Offshore Pipeline Technology Conference*, OPT2011, Amsterdam, The Netherlands, 2011.

[84] J. R. Rice. A path independent integral and the approximate analysis of strain concentration by notches and cracks. *Journal of Applied Mechanics*, 35:379–386, 1968.

[85] J. W. Hutchinson. Singular behaviour at the end of a tensile crack tip in a hardening material. *Journal of Mechanics and Physics of Solids*, 16:13–31, 1968.

[86] J. R. Rice and G. F. Rosengren. Plane strain deformation near a crack tip in a power law hardening material. *Journal of Mechanics and Physics of Solids*, 16:1–12, 1968.

[87] A. A. Wells. Unstable crack propagation in metals: cleavage and fast fracture. In *Proceedings of Crack Propagation Symposium*, volume 1, pages 210–230, Cranfield, UK, 1961.

[88] C. F. Shih. Relationship between the j-integral and the crack tip opening displacement for stationary and extending cracks. *Journal of the Mechanics and Physics of Solids*, 29:305–326, 1981.

[89] N. P. O'Dowd. Application of Two Parameter Approach in Elastic-Plastic Fracture Mechanics. *Journal of Engineering Fracture Mechanics*, 52:445–465, 1995.

[90] *British Standard BS8571:2014, Method of test for determination of fracture toughness in metallic materials using single edge notched tension (SENT) specimens.* BSI, 2014.

[91] *British Standard BS EN ISO 15653:2018, Metallic materials – Method of test for the determination of quasistatic fracture toughness of welds.* BSI, 2018.

[92] E. Østby, C. Thaulow, and Z. L. Zhang. Numerical simulations of specimen size and mismatch effects in ductile crack growth – part I: Tearing resistance and crack growth paths. *Engineering Fracture Mechanics*, 74:1770–1792, 2007.

[93] J.Q. Fu and Y.W. Shi. Effect of cracked weld joint and yield strength dissimilarity on crack tip stress triaxiality. *Theoretical and Applied Fracture Mechanics*, 25:51–57, 1996.

[94] D.P. Boothman, M.M.K. Lee and A.R. Luxmoore. The effects of weld mismatch on J-integrals and Q-values for semi-elliptical surface flaws. *Engineering Fracture Mechanics*, 64:433–458, 1999.

[95] H. G. Pisarski, R. Phaal, I. Hadley, and R. Francis. Integrity of steel pipe during reeling. In *Proceedings of the 13th Conference on Offshore Mechanics and Arctic Engineering*, volume 5, pages 189–198, Houston, TX, 1994.

[96] T. Tkaczyk, N.P. O'Dowd, K. Nikbin, and B.P. Howard. The effect of pre-strain on ductile fracture toughness of reeled pipeline steels. In *Proceedings of the Pressure and Piping Conference*, Prague, Czech Republic, 2009.

[97] T. Tkaczyk, N.P. O'Dowd and K. Nikbin. The effect of Prestrain on Ductile Fracture Toughness of Reeled Pipeline Steels. In *Journal of Pressure Vessel Technology*, 133(3), 031701, 2011.

[98] T. Tkaczyk. Development of Fracture Mechanics Based Criteria for Failure of Reeled Pipelines. *Ph.D. Thesis*, Imperial College London, London, UK, 2011.

[99] E. Østby, P.A. Kane, B. Nyhus. Small-scale Studies of the Effects of Pre-deformation And Ageing On the Ductile Tearing Resistance. In *Proceedings of the 22nd International Offshore and Polar Engineering Conference*, ISOPE2012, Rhodes, Greece, 2012.

[100] W. Tang and Y.W. Shi. Influence of strength matching and crack depth on fracture toughness of welded joints. *Engineering Fracture Mechanics*, 51:649–659, 1995.

[101] G. Lin, X.G. Meng, A. Cornec and K-H. Schwalbe. The effect of strength mismatch on mechanical performance of weld joints. *International Journal of Fracture*, 96:37–54, 1999.

[102] *BS7910:2013, Guide to Methods for Assessing the Acceptability of Flaws in Metallic Structures.* British Standard Institution, 2013.

[103] *R6: Assessment of the Integrity of Structures Containing Defects, Revision 4.* British Energy Generation Limited, 2013.

[104] V. Kumar, M. D. German, and C. F. Shih. An engineering approach for elastic-plastic fracture analysis. Technical Report EPRI NP-1931, Electric Power Research Institute, Palo Alto, CA, 1981.

[105] R. A. Ainsworth. The assessment of defects in structures of strain hardening materials. *Engineering Fracture Mechanics*, 19(4):633–642, 1984.

[106] E. Østby. Fracture Control Offshore Pipelines JIP: New strain-based fracture mechanics equations including the effects of biaxial loading, mismatch and misalignment. In *Proceedings of the 24th International Conference on Offshore Mechanics and Arctic Engineering*, OMAE2005, Halkidiki, Greece, 2005.

[107] E. Østby. Fracture Control Offshore Pipelines JIP: Proposal for strain-based fracture assessment procedure. In *Proceeding of the 17th International Offshore and Polar Engineering Conference*, ISOPE2007, Lisbon, Portugal, 2007.

[108] *DNVGL-RP-F108: Assessment of flaws in pipeline and riser girth welds.* Det Norske Veritas Germanischer Lloyd, 2017.

[109] H. Neuber. Theory of stress concentration for shear strained prismatical bodies with arbitrary non-linear stress-strain law. *Journal of Applied Mechanics*, 28:544–550, 1961.

[110] W. E. Kastner, E. Röhrich, W. Schmitt, and R. Steinbuch. Critical crack sizes in ductile piping. *International Journal of Pressure Vessels and Piping*, 9(3):197–219, 1981.

[111] I. S. Raju and J. C. Newman. Stress intensity factors for a wide range of semi-elliptical surface cracks in finite thickness plates. *Engineering Fracture Mechanics*, 11(4):817–829, 1979.

[112] A. A. Willoughby and T. G. Davey. Plastic Collapse in Part-Wall Flaws in Plates. *Fracture Mechanics: Perspectives and Directions (Twentieth Symposium), American Societey of Testing and Materials*, ASTM STP 1020, 390–409, 1989.

[113] D. Yi, Z. M. Xiao, S. Idapalapati, S. B. Kumar. Fracture analysis of girth welded pipelines with 3D embedded cracks subjected to biaxial loading conditions. *Engineering Fracture Mechanics*, 96:570–587, 2012.

[114] T. Tkaczyk, N. P. O'Dowd, and B. P. Howard. Comparison of crack driving force estimation schemes for weld defects in reeled pipelines. In *Proceedings of the 17th International Offshore and Polar Engineering Conference*, Lisbon, Portugal, 2007.

[115] D. Linkens, C. L. Formby, and R. A. Ainsworth. A strain-based approach to fracture assessment – example applications. In *Proceedings of the conference on engineering structural integrity assessment, EMAS*, Cambridge, 2000.

[116] R. C. McClung, G. G. Chell, Y. D. Lee D. A. Russell, and G. E. Orient. Development of a practical methodology for elastic-plastic and fully plastic fatigue crack growth. Technical Report NASA/CR–1999-209428, National Aeronautics and Space Administration, 1999.

[117] A. G. Miller. Review of limit loads of structures containing defects. *International Journal of Pressure Vessels and Piping*, 32:191–327, 1988.

[118] T. Tkaczyk, N. P. O'Dowd, and K. Nikbin. Fracture assessment procedures for steel pipelines using an improved reference stress solution. *International Journal of Pressure Vessel Technology*, 191, 2009.

[119] Y-J. Kim and P. J. Budden. Reference stress approximations for J and COD of circumferential through-wall cracked pipes. *International Journal of Fracture*, 116(3):195–218, 2002.

[120] D. P. Boothman, M. M. K. Lee, A. R. Luxmoore, and J. D. G. Sumpter. J-estimation for semi-elliptical surface cracks in wide plates under direct tension. *Fatigue and Fracture of Engineering Materials and Structures*, 21(3):333–346, 1998.

[121] T. Tkaczyk, N. P. O'Dowd, K. Nikbin, and B. P. Howard. A non-linear fracture assessment procedure for pipeline materials with a yield plateau. In *Proceedings of the 19th International Offshore and Polar Engineering Conference*, ISOPE2009, Osaka, Japan, 2009.

[122] T. Tkaczyk, N. P. O'Dowd, K. Nikbin, and B. P. Howard. Fracture assessment of elastic-plastic steel pipelines subject to multi-cycle bending. In *Proceedings of the 19th International Offshore and Polar Engineering Conference*, ISOPE2009, Osaka, Japan, 2009.

[123] N. Nourpanah, F. Taheri. Development of a reference strain approach for assessment of fracture response of reeled pipelines. *Engineering Fracture Mechanics*, 77:2337–2353, 2010.

[124] L. F. S. Parise, C. Ruggieri, N. P. O'Dowd. Fully-Plastic Strain-Based J Estimation Scheme for Circumferential Surface Cracks in Pipes Subjected to Reeling. In *Proceedings of the ASME 2013 Pressure Vessels and Piping Conference*, ASMEPVP2013, Paris, France, 2013.

[125] L. F. S. Parise, C. Ruggieri, N. P. O'Dowd. Fully-Plastic Strain-Based J Estimation Scheme for Circumferential Surface Cracks in Pipes Subjected to Reeling. In *Journal of Pressure Vessel Technology*, 137(4), 41204(8), ISSN:0094-9930, 2015.

[126] Y. M. Zhang, Z. M. Xiao, W. G. Zhang. On 3-D crack problems in offshore pipeline with large plastic deformation. *Theoretical and Applied Fracture Mechanics*, 67-68:22–28, 2013.

[127] Y.J. Kim, M. Koçak, R.A. Ainsworth and U.F. Zerbst. SINTAP defect assessment procedure for strength mismatched structures. *Engineering Fracture Mechanics*, 68:529–546, 2000.

[128] T. Tkaczyk, A. Pépin., S. Denniel. Fatigue and Fracture Performance of Reeled Mechanically Lined Pipes. In *Proceedings of the 22nd International Offshore and Polar Engineering Conference*, ISOPE2012, Rhodes, Greece, 2012.

[129] *DNVGL-RP-C203: Fatigue Design of Offshore Steel Structures.* Det Norske Veritas Germanischer Lloyd, 2016.

[130] *BS7608: Guide to Fatigue Design and Assessment of Steel Products.* British Standard Institution, 2014.

[131] *BS ISO 12108: Metallic materials: Fatigue testing – Fatigue crack growth method.* British Standard Institution, 2018.

[132] T. Tkaczyk, A. Pépin, and S. Denniel. Fatigue and Fracture of Mechanically Lined Pipes Installed by Reeling. In *Proceedings of the 31st International Conference on Ocean, Offshore and Arctic Engineering*, OMAE2012, Rio de Janeiro, Brazil, 2012.

[133] G.A. Toguyeni and J. Banse. Mechanically Lined Pipe: Installation by Reel-Lay. In *Proceedings of the Offshore Technology Conference*, Houston, Texas, USA, 2012, OTC-23096.

[134] G.A. Toguyeni, R. Jones, N. Pepe, D. Zhou, J. Mair, J. Banse. Reeling and Fatigue Endurance of Mechanically Lined Pipe. In *Proceedings of IBC Energy's 37th Offshore Pipeline Technology Conference*, Amsterdam, The Netherlands, 2014.

[135] *www.a2m-industrie.fr.*

[136] *British Standard BS EN ISO 6892-1:2016, Metallic materials – Tensile testing – Method of test at room temperature.* BSI, 2016.

[137] M. Chouman. Plasticité Cyclique et Phénomène de Rochet: Amélioration de la Prédiction de l'Ovalisation des Tubes en Acier durant le Cintrage Cyclique par Modélisation de la Distorsion de la Surface de Charge. *Ph.D. Thesis*, Université Paris 13, France, 2010.

[138] S. Marie, S. Chapuliot, Y. Kayser, M.H. Lacire, B. Drubay, B. Barthelet, P. Le Delliou, V. Rougier, C. Naudin, P. Gilles and M. Triay. French RSE-M and RCC-MR Code Appendices for Flaw Analysis: Presentation of the Fracture Parameters Calculation – Part II: Cracked Plates. In *International Journal of Pressure Vessels and Piping*, 84:614–658, 2007.

[139] E. Oslo, E. Berg, K. Holthe, B. Nyhus, B. Skallerud, C. Thaulow and E. Ostby. Effect of Embedded Defects in Pipelines Subjected to Plastic Strains during Operation. In *Proceedings of the 18th International Offshore and Polar Engineering Conference*, ISOPE2008, Vancouver, BC, Canada, 2008.

[140] E. Ostby, B. Nyhus, C. Thaulow. Small-scale Testing of the Effect of Embedded Defect Position in the Thickness Direction of an X65 UOE Pipe. In *Proceedings of the 21st International Offshore and Polar Engineering Conference*, ISOPE2011, Maui, Hawaii, USA, 2011.

[141] *www.gom-correlate.com*.

[142] *www.microset.co.uk*.

[143] S. Hertelé, W. De Waele, M. Verstraete, R. Denys and N.P. O'Dowd. J-integral analysis of heterogeneous mismatched girth welds in clamped single-edge notched tension specimens. *International Journal of Pressure Vessels and Piping*, 119:95–107, 2014.

[144] J.S. Kim, T.K. Song, Y.J. Kim and T.E. Jin. Strength mis-match effect on limit loads for circumferential surface cracked pipes. *Engineering Fracture Mechanics*, 76:1074–1086, 2009.

[145] *TechnipFMC Report No. OED-COR-A-02-R-002: Mechanically Lined Pipe Seam Weld Flaws – CRA Liner Burst and Notched Tensile Test Assessment*. Rigid Pipeline and Installation Technology, 2015.

[146] P.J. Zumpano, G. Zanon, A.G. Galiani, L.A. Braga, M.R. Ronald, E.O. Valente, P.C. Nunez and E.J. Hippert. Challenges about Testing, Welding and NDT of CRA Pipelines in Brazilian Pre-Salt. In *Proceedings of the 31st International Conference on Ocean, Offshore and Arctic Engineering*, OMAE2012, Rio de Janeiro, Brazil, 2012.

[147] C. Johnston, C. Nageswaran, and T. London. Investigations into the Fatigue Strength of CRA Lined Pipe. In *Proceedings of the 2016 Offshore Technology Conference*, OTC2016, Houston, Texas, USA, 2016.

Appendix A

Paper No. 1 – Methodology for Assessment of Surface Defects in Undermatched Pipeline Girth Welds

Aurélien Pépin
Offshore Engineering Division,
Technip,
Westhill, Aberdeen AB32 6TQ, UK
e-mail: apepin@technip.com

Tomasz Tkaczyk
Offshore Engineering Division,
Technip,
Westhill, Aberdeen AB32 6TQ, UK
e-mail: ttkaczyk@technip.com

Noel O'Dowd
Department of Mechanical,
Aeronautical and Biomedical Engineering,
Materials and Surface Science Institute,
University of Limerick,
Limerick, Ireland
e-mail: noel.odowd@ul.ie

Kamran Nikbin
Department of Mechanical Engineering,
Imperial College,
London SW7 2AZ, UK
e-mail: k.nikbin@imperial.ac.uk

Methodology for Assessment of Surface Defects in Undermatched Pipeline Girth Welds

The demand for subsea transport of highly corrosive constituents has noticeably increased in recent years. This has driven the requirement for high strength pipelines with enhanced corrosion resistance such as chromium stainless steel or bimetal pipes. The latter are carbon steel pipes with a corrosion resistant alloy lining. Reeling is a cost effective installation method for small to medium size subsea pipelines, up to 457.2 mm (18 in.) in diameter. However, plastic straining associated with reeling has an effect on weld defect acceptance criteria. The maximum acceptable defect sizes are typically developed using engineering critical assessment (ECA), based on the reference stress method, which requires that the weld metal is equal to or stronger than the parent metal in terms of the stress–strain curve. However, evenmatch/overmatch cannot always be achieved in the case of subsea stainless or bimetal pipelines. In this work, a parametric finite-element (FE) study was performed to assess the effect of weld metal undermatch on the crack driving force, expressed in terms of the crack tip opening displacement (CTOD). Subsequently, the fracture assessment methodology for reeled pipes was proposed, where the ECA as per BS7910 is first carried out. These acceptable defect sizes are then reduced, using an analytical formula developed in this work, to account for weld undermatch.
[DOI: 10.1115/1.4029190]

1 Introduction

Traditionally, girth welds of subsea pipelines were inspected by radiography testing, which can only size a defect length. Due to this limitation, workmanship criteria were used to deem defect acceptability. The introduction of a requirement for automatic ultrasonic testing of subsea reeled pipelines, by Det Norske Veritas (DNV), made ECA necessary.

Most often, ECA of subsea pipeline girth welds is carried out following the guidance in DNV-OS-F101 [1], using the solutions provided in BS7910 [2]. The DNV ECA procedure, summarized in Ref. [3], assumes that the weld metal is equal to or stronger than the parent metal in terms of stress–strain curve, i.e., the overmatched welds are required. The undermatched parent metal tensile properties with statistically highest yield stress and lowest strain hardening are conservatively used in the assessment.

Bimetal pipes are made of a carbon manganese steel pipe with an internal corrosion resistance alloy (CRA) layer, which is either metallurgically bonded to the outer pipe (clad pipe) or held in place by interference stress (lined pipe). Bimetal pipelines, welded with nickel based alloy consumables, and 13% Cr stainless steel pipelines, welded with 25% Cr stainless steel consumables, often have undermatched welds in terms of the yield strength. Although a number of ECA procedures have been proposed in the literature to address this issue, they have significant limitations.

Therefore, a new fracture assessment procedure is proposed in this work. First, a DNV-OS-F101 ECA is performed, using the BS7910 option 2 approach (equivalent to option 2 in R6 [4]), because it is the most accurate analytical assessment procedure, commonly used for the integrity assessment of subsea pipelines. Then, the depths of the acceptable defect sizes determined under the assumption of weld evenmatch are reduced using an analytical formula, to account for weld undermatch, while the defect lengths remain unchanged.

2 Reeling Installation

A typical reeling installation, illustrated in Fig. 1, involves four plastic straining events. First, a pipe is plastically deformed when it is spooled onto a large diameter reel. After the reel-lay vessel arrives at the installation site the pipe is plastically deformed in the free span between the reel and the aligner, then when it passes over the aligner and finally when it travels through the straightener. The 12 o'clock position, which is the most critical location, experiences two tensile straining events: (i) on the reel and (ii) on the aligner. The maximum strain seen by the pipe, ε^{app}, is

$$\varepsilon^{app} = \frac{D}{D + 2R} \tag{1}$$

where D is the nominal outer diameter of the pipe and R is the bending radius of the reel or the aligner. Typically, ε^{app} does not exceed 2.5%, and is much less for small diameter pipes.

3 DNV-OS-F101—BS7910 Option 2 Reeling ECA

Acceptable defect sizes, expressed in terms of depth and length, are determined through ductile tearing assessments. Each tensile straining event is assessed separately, using a dedicated parent metal stress–strain curve (DNV requirement) and a material fracture resistance curve (J as function of tearing). An as-received stress–strain curve is used for the assessment of the first event, while a prestrained stress–strain curve is used for the second event. The applied strain, ε^{app}, is converted into a remote applied stress, σ_{app}, using the relevant stress–strain curve. A local applied stress (also called reference stress), σ_{ref}, which accounts for the reduced cross-sectional area in the defective weld, is estimated using an appropriate reference stress solution in BS7910 (e.g.,

Contributed by the Pressure Vessel and Piping Division of ASME for publication in the Journal of Pressure Vessel Technology. Manuscript received April 1, 2014; final manuscript received November 4, 2014; published online February 27, 2015. Assoc. Editor: Xian-Kui Zhu.

 Copyright © 2015 by ASME

Downloaded from https://asmedigitalcollection.asme.org/pressurevesseltech/article-pdf/137/5/051402/4014518/pvt_137_05_051402.pdf by Imperial College London user on 21 September 2019

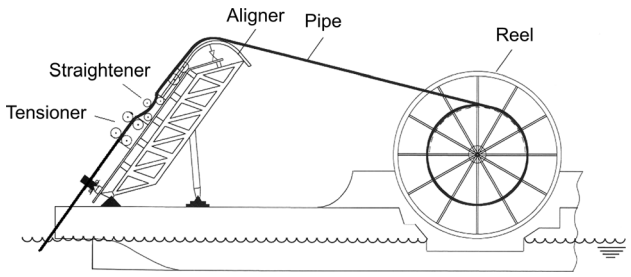


Fig. 1 Illustration of reeling installation

Kastner's [3]). The proximity to failure by plastic collapse is assessed by the load ratio, L_r, while the proximity to failure by fracture is evaluated through the fracture ratio, K_r, determined from

$$L_r = \frac{\sigma_{ref}}{\sigma_y} \tag{2}$$

$$K_r = \frac{K}{K_{mat}} \tag{3}$$

where σ_y is the yield strength, K is the stress intensity factor calculated using an appropriate solution in BS7910 (e.g., Raju and Newman's [3]), and K_{mat} is the material fracture toughness expressed in the same terms. The assessment point, (L_r, K_r), is plotted in a BS7910 (R6) failure assessment diagram (FAD), which boundary is constructed using

$$K_r = \left(\frac{E\varepsilon_{ref}}{L_r\sigma_y} + \frac{1}{2}\frac{L_r^3\sigma_y}{E\varepsilon_{ref}}\right)^{-0.5} \tag{4}$$

where ε_{ref} is the strain corresponding to σ_{ref} on the assumed stress–strain curve. The cut-off value for L_r, i.e., L_{rmax}, is the tensile to yield ratio, as recommended in DNV-OS-F101. A ductile tearing assessment is carried out by iteratively increasing the crack depth (assuming a certain amount of tearing occurs) until the assessment point falls within the FAD, as shown in Fig. 2. For each tearing increment, the material fracture toughness expressed in terms of J, i.e., J_{mat}, is determined from the resistance curve, and then converted into K_{mat} through

$$K_{mat} = \left(\frac{EJ_{mat}}{1-\nu^2}\right)^{0.5} \tag{5}$$

where E is the Young's modulus and ν is the Poisson ratio. The stable grown defect size from the first tensile straining event is used as a starting point for the assessment of the second event. The initial (as-welded) defect size is deemed acceptable for reeling if stable growth is predicted to occur during both tensile straining events.

4 Effect of Weld Metal Undermatch

The fracture behavior of welded structures with strength mismatch has been extensively investigated both analytically and experimentally. Research on the effect of the mismatch between weld and parent metal stress–strain curves has focused on: (i) the stress triaxiality at the crack tip, (ii) the fracture toughness, and (iii) the crack driving force. Here, mismatch refers to an absolute value. Undermatch is a positive mismatch (parent metal stronger than weld metal), whereas overmatch refers to a negative mismatch.

4.1 Stress Triaxiality at Crack Tip. Fu and Shi [5] carried out 2D elastic–plastic FE analyses to study the effect of mismatch on stress triaxiality at the tip of a crack located in the weld center line (WCL) of a center crack tension specimen. The large strain theory with a power law material formulation was used. Specimens with rectangular welds were subjected to axial tension and the stress triaxiality was evaluated. The authors found that the stress triaxiality increased with the undermatch magnitude. When the applied load increased, the effect of the mismatch also increased, until a critical load was reached, and then the effect decreased. This critical load generally increased with the normalized crack depth. The effect of mismatch was insignificant only for deep defects subjected to small loads.

Boothman et al. [6] studied, by 3D FE analyses, the effect of mismatch on the crack driving force and stress triaxiality for semi-elliptical surface flaws in the WCL of wide flat plates. The J_2 incremental plasticity with the small strain theory and the piecewise power law material formulation was used. A plate with a rectangular weld was subjected to tension or bending, and both the crack driving force and the stress triaxiality were evaluated. It was found that the crack driving force increased with the

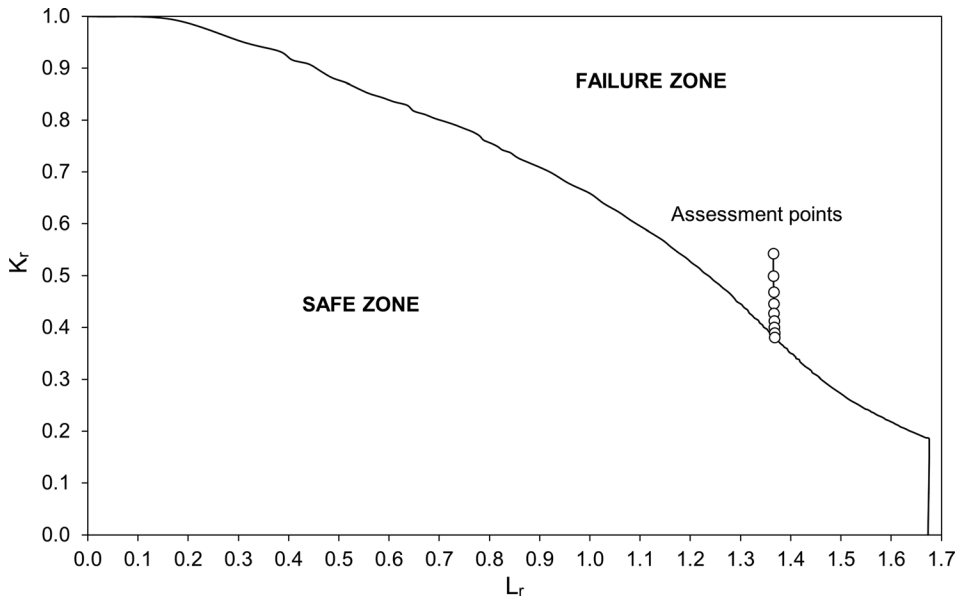


Fig. 2 FAD

Downloaded from https://asmedigitalcollection.asme.org/pressurevesseltech/article-pdf/137/5/051402/4014518/pvt_137_05_051402.pdf by Imperial College London user on 21 September 2019

undermatch magnitude and the weld width. A 30% undermatch had little effect on the constraint when the crack depth was smaller than half of the weld width. However, a significant effect was observed for deeper defects, as plastic deformation spread to the parent metal. Finally, the authors also showed that high constraint leads to low fracture toughness, consistent with earlier work on homogeneous materials, e.g., Refs. [7] and [8]. It is therefore expected that fracture toughness will decrease when undermatch increases.

4.2 Fracture Toughness. Tang and Shi [9] investigated, both numerically and experimentally, the effect of mismatch and crack depth on the fracture toughness of single edge notch bending specimens extracted from welded joints. The specimens with rectangular welds and WCL defects were subjected to three-point bending. Two-dimensional elastic–plastic FE analyses were carried out to replicate these tests. The fracture toughness generally decreased when undermatch increased. The fracture toughness increased with the crack depth up to a critical depth and then decreased with the crack depth. The peak fracture toughness was obtained for a rather shallow crack depth (less than 20% of the specimen thickness), which was a function of the mismatch magnitude. Numerical and experimental results followed similar trends.

Lin et al. [10] carried out 2D FE analyses with a cohesive zone model, to assess the effect of mismatch on the growth of WCL cracks in single edge pure bending specimens. The J_2 incremental plasticity with the small strain theory was employed. It was found that for a given weld thickness, the crack growth resistance decreased when the undermatch magnitude increased. In addition, for a given level of undermatch, reducing the weld thickness also caused a reduction of the fracture toughness. The authors argued that this effect was due to the fact that as the weld thickness reduces, plastic deformation spreads to the parent metal, which elevates crack tip stresses.

Similar conclusions were reported by SINTEF, who performed 2D FE analyses to investigate the effect of mismatch on the ductile tearing resistance of undermatched welds, in Ref. [11]. It was also found that the fracture toughness decreased with the increase of the undermatch magnitude. The decrease was a function of both the mismatch level and the weld slenderness.

4.3 Crack Driving Force. SINTEF showed numerically, in Ref. [12], that the crack driving force increased with the undermatch magnitude. This is in agreement with the results presented by Fu and Shi [5] and Boothman et al. [6]. Furthermore, a V-weld can be simplified by an equivalent rectangular weld geometry. The width of the equivalent weld, $2H = H_1 + H_2$, shown in Fig. 3, depends on the pipe wall thickness, the bevel angle and the crack depth, consistent with recent work from Hertelé et al. [13]. Finally, in the case of weld undermatch, the crack driving force is similar for WCL and fusion line defects.

5 ECA Procedures for Undermatched Welds

5.1 SINTAP Procedure. ECA procedures for undermatched welds were proposed by SINTAP and SINTEF. When the SINTAP procedure is used, undermatched welds can be assessed at level 2 or level 3. The level 3 assessment, which is essentially the R6 procedure [4], is considered in this work, because it is the most accurate analytical assessment method. Section III.8 of the R6 code Revision 4 includes a procedure for undermatched welds, whereby an equivalent stress–strain curve is used in the assessment [14]. The equivalent stress–strain curve is derived from [14]

$$\sigma_{\mathrm{eq}}(\varepsilon_{\mathrm{p}}) = \frac{(\gamma-1)\sigma^{\mathrm{WM}} + (M-\gamma)\sigma^{\mathrm{PM}}}{M-1} \tag{6}$$

The mismatch ratio, M, and the mismatch limit load ratio, γ, are determined from

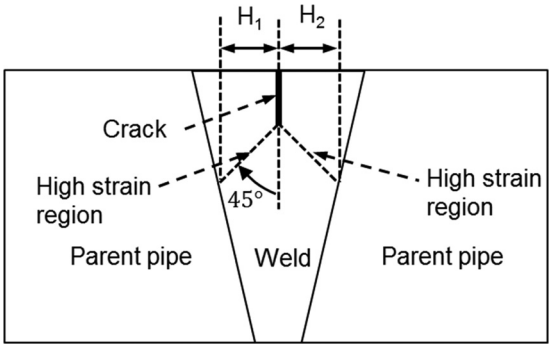


Fig. 3 Equivalent width for V-bevel weld with center line defect

$$M(\varepsilon_{\mathrm{p}}) = \frac{\sigma^{\mathrm{WM}}}{\sigma^{\mathrm{PM}}} \tag{7}$$

$$\gamma(\varepsilon_{\mathrm{p}}) = \frac{P_{\mathrm{L}}^{\mathrm{M}}}{P_{\mathrm{L}}^{\mathrm{PM}}} \tag{8}$$

where σ^{PM} is the parent metal stress, σ^{WM} is the weld metal stress, $P_{\mathrm{L}}^{\mathrm{M}}$ is the mismatch limit load, and $P_{\mathrm{L}}^{\mathrm{PM}}$ is the parent metal limit load. Traditionally, limit loads are determined assuming elastic-perfectly plastic stress–strain response. As a result, they are usually conservative and independent of the applied strain. For mismatched structures, M has a significant effect on $P_{\mathrm{L}}^{\mathrm{M}}$. However, if the weaker (in terms of yield strength) component of a mismatched structure has significantly higher strain hardening than the stronger component, the actual limit load of the structure could be significantly higher than predicted assuming elastic-perfectly plastic stress–strain response. To account for this effect in Eq. (6), M is calculated for each increment of ε_{p}, and so are σ^{PM}, σ^{WM}, and $P_{\mathrm{L}}^{\mathrm{M}}$.

Since no mismatch limit load solutions are available for part-circumferential defects in pipes subjected to bending, the one for tension, proposed in Ref. [15], is used in this work. It will be shown in Sec. 8 that the acceptable defect sizes in reeled pipes with weld undermatch can be significantly over-estimated using this approach.

5.2 SINTEF Approach. Østby proposed, in Refs. [16] and [17], a strain based defect assessment procedure. In this approach, the nonlinear elastic regime is ignored, and it is argued that the CTOD, δ, is a linear function of the applied strain, $\varepsilon^{\mathrm{app}}$, and the pipe wall thickness, t, in a full plastic regime

$$\delta = Ct\varepsilon^{\mathrm{app}} \tag{9}$$

The function C depends on the pipe and defect geometries and the weld metal mismatch at yield, m_{y}, determined from

$$m_{\mathrm{y}} = 1 - \frac{\sigma_{\mathrm{y}}^{\mathrm{WM}}}{\sigma_{\mathrm{y}}^{\mathrm{PM}}} \tag{10}$$

where $\sigma_{\mathrm{y}}^{\mathrm{PM}}$ and $\sigma_{\mathrm{y}}^{\mathrm{WM}}$ are the parent and weld metal yield stresses, respectively. This equation implies that $m_{\mathrm{y}} > 0$ for undermatch, $m_{\mathrm{y}} = 0$ for evenmatch, and $m_{\mathrm{y}} < 0$ for overmatch. This definition of mismatch (rather than Eq. (7)) is used throughout the paper. The effect of the mismatch on the acceptable defect sizes is introduced by the definition of an effective defect depth

$$a_{\mathrm{eff}} = a - m_{\mathrm{y}}H \tag{11}$$

where H is half of the equivalent weld width, a is the defect depth in the evenmatched weld, and a_{eff} is the defect depth in the undermatched weld. This notation is slightly different from that used in Ref. [16].

Downloaded from https://asmedigitalcollection.asme.org/pressurevesseltech/article-pdf/137/5/051402/4014518/pvt_137_05_051402.pdf by Imperial College London user on 21 September 2019

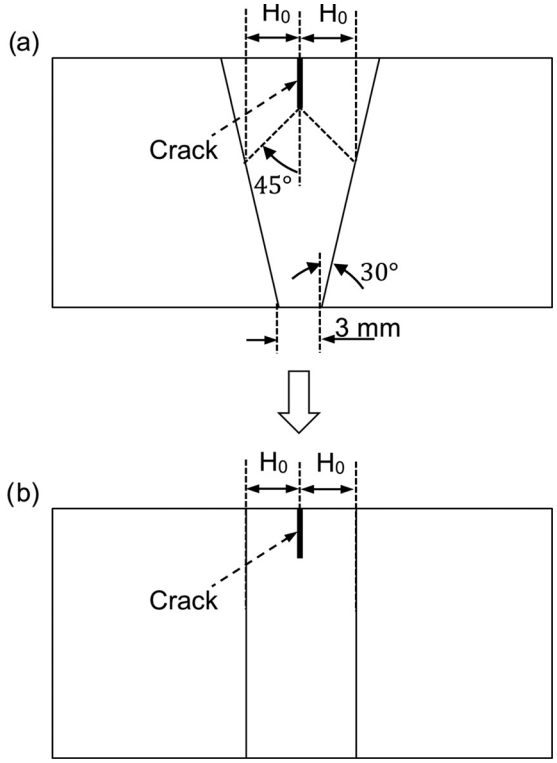


Fig. 4 Weld geometry: (*a*) actual and (*b*) equivalent

The SINTEF procedure is applicable to pipes with $20 < D/t < 40$, which stress–strain curves are continuous with engineering yield to tensile strength ratio, $0.82 < Y/T < 0.93$. Therefore, it is not suitable for most reeled pipes with D/t usually below 20, and lined pipes which exhibit a yield plateau in the as-received condition.

6 Parametric FE Study

6.1 Pipe and Crack Geometry. A pipe with a 323.9 mm (12.75 in.) outer diameter and 21.4 mm wall thickness was analyzed. The normalized crack depth, a/t, in the range between 0.05 and 0.40 and the normalized crack length, $2c/\pi D$, in the range between 0.02 and 0.10, were investigated. It was assumed that the defect was located in the center of a 30 deg V-bevel weld with a 3 mm root opening, as shown in Fig. 4(*a*). The latter was modeled as an equivalent rectangular weld, illustrated in Fig. 4(*b*). In total, nine crack geometries were considered, as detailed in Table 1.

6.2 Material Flow Behavior. Weld metal undermatch is a concern for lined and clad pipes, where the carbon steel host pipe has yield strength above 450 MPa (e.g., pipes manufactured to API 5 L X65 or X70 [18]) welded using nickel based alloy consumables. Similarly, there is a risk of undermatch when 25% Cr consumables are used to weld 13% Cr steel pipelines. Two scenarios were considered in this work: (i) pipe material with a yield plateau and (ii) pipe material with continuous yielding. The former is representative of seamless lined pipes in the as-received condition whereas the latter is representative of solid CRA pipes, clad pipes, and seam welded lined pipes in both as-received and strained

Table 1 FE matrix of cases: Crack geometries

D (mm)	t (mm)	a/t	$2c/\pi D$
323.9	21.4	0.05, 0.15, 0.40	0.02, 0.05, 0.10

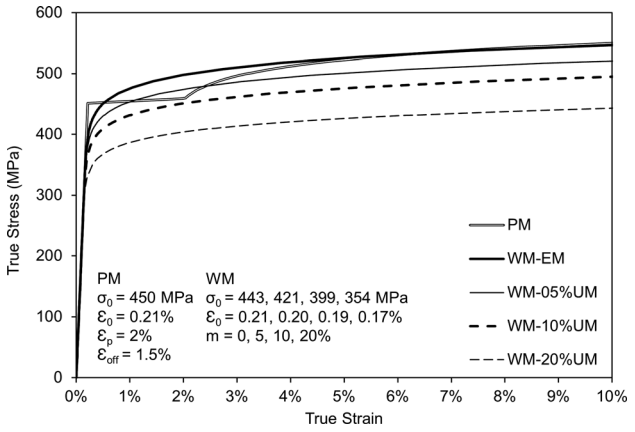


Fig. 5 Stress–strain curves with yield plateau, $E = 210$ GPa, $\sigma_y = 450$ MPa, and $n = 16.8$

condition, and seamless lined pipes in the strained condition (after plastic straining on the reel). The weld material was assumed to exhibit continuous yielding.

The yield strength, σ_y, in the range between 450 and 700 MPa and the weld undermatch up to 20% were considered. For parent materials with a yield plateau, the strain at the end of the yield plateau, ε_L, was assumed to be from 1% to 3%, while the upper bound yield to tensile strength ratio, $Y/T = 0.9$ was considered. In contrast, Y/T in the range between 0.6 and 0.9 was assumed for parent materials exhibiting continuous yielding.

The as-received stress–strain curve of the seamless parent material was defined by the Young's modulus, E, σ_y, ε_L, and the Ramberg–Osgood hardening index, n. There is a unique relationship between n and Y/T. The parent metal stress–strain curve (indicated "PM" in Fig. 5) is bilinear for strains between 0 and ε_L and described by a power law for higher strains. The line between 0 and ε_y has a slope equal to E. The plateau is flat on an engineering stress–strain plot but has a small slope when converted to a true stress–strain plot. The power law curve is expressed by the modified Ramberg–Osgood relationship

$$\varepsilon = \begin{cases} \dfrac{\sigma}{E} & \text{for} \quad \varepsilon \le \varepsilon_y \\ \varepsilon_y + \dfrac{\varepsilon_L - \varepsilon_y}{\sigma_y \varepsilon_L}(\sigma - \sigma_y) & \text{for} \quad \varepsilon_y \le \varepsilon \le \varepsilon_L \\ \left(\dfrac{\sigma}{\sigma_0} + \left(\dfrac{\sigma}{\sigma_0}\right)^n\right)\varepsilon_0 + \varepsilon_{off} & \text{for} \quad \varepsilon > \varepsilon_L \end{cases} \tag{12}$$

For the evenmatched weld metal stress–strain curve (indicated "WM-EM" in Fig. 5), $\varepsilon_{off} = 0$ while σ_0 was chosen to achieve $\sigma = \sigma_y$ at $\varepsilon = 0.5\%$. The same hardening index, n, was used for both parent and weld metal. Undermatched weld metal stress–strain curves (indicated "WM-UM" in Fig. 5) were derived by lowering σ_0 to achieve 5%, 10%, and 20% undermatch. For example, the parameters defining the stress–strain curves with $\sigma_y = 450$ MPa are given in Table 2. The same approach was used to create parent and weld metal stress–strain curves exhibiting

Table 2 Parameters for materials with yield plateau, $E = 210$ GPa, $\sigma_y = 450$ MPa, and $n = 16.8$ ($Y/T = 0.9$)

Material	m_y (%)	σ_y (MPa)	σ_0 (MPa)	ε_0 (%)	ε_L (%)	ε_{off} (%)
PM		450	450	0.21	2	1.5
WM-EM	0	450	443	0.21	2	0.0
WM-5% UM	5	428	421	0.20	2	0.0
WM-10% UM	10	405	399	0.19	2	0.0
WM-20% UM	20	360	354	0.17	2	0.0

Downloaded from https://asmedigitalcollection.asme.org/pressurevesseltech/article-pdf/137/5/051402/4014518/pvt_137_05_051402.pdf by Imperial College London user on 21 September 2019

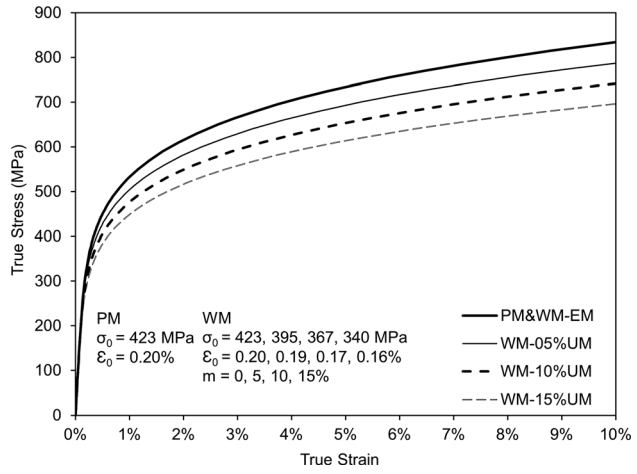


Fig. 6 Stress–strain curves with continuous yielding, $E = 210$ GPa, $\sigma_y = 450$ MPa, and $n = 5.7$

Table 3 Parameters for materials with continuous yielding, $E = 210$ GPa, $\sigma_y = 450$ MPa, and $n = 5.7$ ($Y/T = 0.6$)

Material	m_y (%)	σ_y (MPa)	σ_0 (MPa)	ε_0 (%)
PM		450	423	0.20
WM-EM	0	450	423	0.20
WM-5% UM	5	428	395	0.19
WM-10% UM	10	405	367	0.17
WM-15% UM	15	326	340	0.16

Table 4 FE matrix of cases: Tensile properties

σ_y (MPa)	n	ε_L (%)
450, 575, 700	16.8	1, 2, 3
450, 575, 700	5.7, 9.0, 16.8	

continuous yielding, shown in Fig. 6. For example, the parameters defining the stress–strain curves with $\sigma_y = 450$ MPa and $n = 5.7$ are given in Table 3. In total, eighteen tensile properties were considered, as detailed in Table 4.

6.3 FE Analysis. The FE model, shown in Fig. 7, was used to investigate the effect of weld metal undermatch on the crack driving force in stationary semi-elliptical surface breaking defects. Due to symmetry, only a quarter model of the pipe was modeled with appropriate boundary conditions. The model length was three times the pipe outer diameter. Up to 17000 eight-node first order solid elements with full integration (C3D8 in ABAQUS) were used. The crack tip region had a focused mesh composed of 5 to 7 rings and 17 to 20 layers depending on the crack size. The smallest element size at the crack tip was up to 3% of the crack depth. The J_2 incremental plasticity with the large strain theory was used. Bending was achieved by applying rotation to the reference node, indicated in Fig. 7, which was coupled to the extreme pipe nodes at the right hand side.

Tkaczyk et al. showed, in Ref. [19], that the FE model in Fig. 7 is suitable for the prediction of the J-integral when C3D8I elements are used with the small strain theory. In this work, J predicted using C3D8 elements was virtually identical to that predicted using C3D8I elements. This showed that C3D8 elements were suitable for the prediction of J, when the small strain theory was used. Subsequently, J was plotted against $\sigma_y\delta$. A linear relationship was found between both quantities, which is in agreement with the results presented in Ref. [20]. When the large strain theory was used, J was no longer path independent. At low strains (below 1%), the CTOD was very similar for the small and large strain theory. At large strains, a saturation of δ was observed with the large strain theory, which was due to the ovalisation of the pipe. Finally, δ was virtually identical at low strains, and within 10% at large strains, when C3D8I elements were used. This demonstrated that the FE model was suitable for the prediction of δ.

A parametric FE study was carried out to quantify the effect of weld metal undermatch on the crack driving force, expressed in terms of the CTOD, calculated using the 90 deg intercept definition [20]. First, a reference crack size, $(a, 2c)$ in Table 1, was analyzed under evenmatch conditions, and the predicted CTOD was plotted against the applied strain. Subsequently, iterative analyses were carried out assuming different levels of undermatch. For each level of undermatch, the crack depth was reduced (the crack length remained unchanged) until good agreement of the CTOD-strain curve in the range between 0.75% and 2.5% strain, for the case of evenmatch and undermatch, was obtained. Thus, for each reference (evenmatch) crack size, $(a, 2c)$, and each level of undermatch, a corresponding crack depth reduction, da, was found

$$a^{\text{eff}} = a - da \tag{13}$$

where $(a^{\text{eff}}, 2c)$ is the allowable crack size in the undermatch weld. This was repeated for a range of crack sizes and material properties in Tables 1 and 4. A total of 648 cases were run.

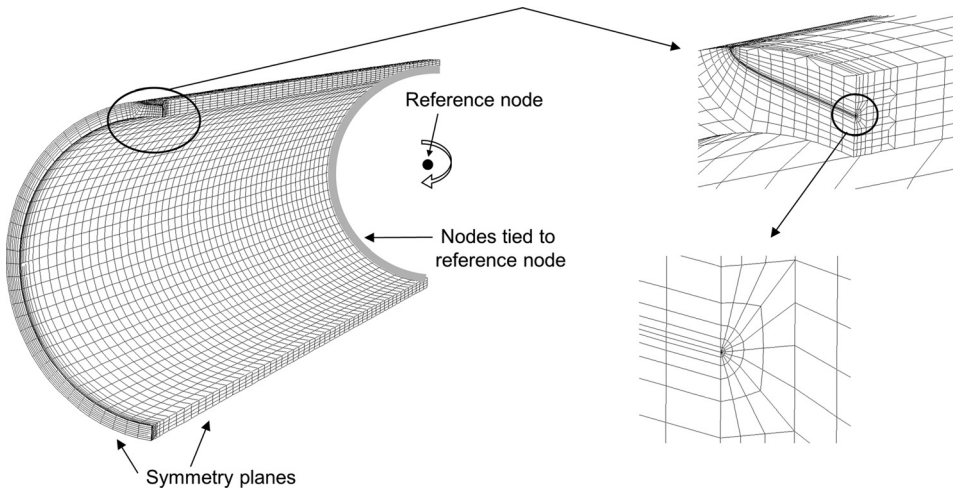


Fig. 7 Typical FE model

Downloaded from https://asmedigitalcollection.asme.org/pressurevesseltech/article-pdf/137/5/051402/4014518/pvt_137_05_051402.pdf by Imperial College London user on 21 September 2019

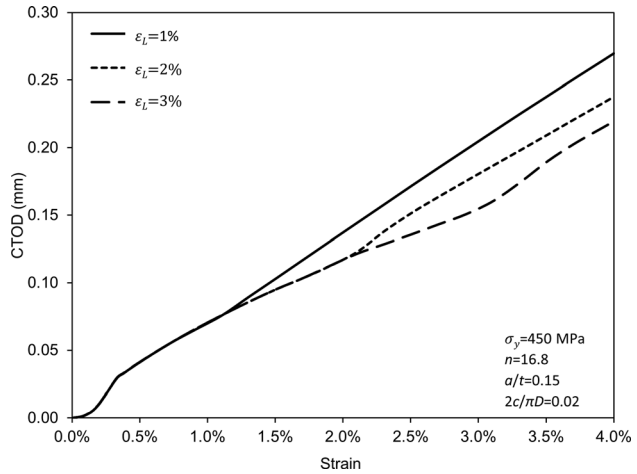


Fig. 8 Effect of yield plateau on crack driving force: Evenmatch case

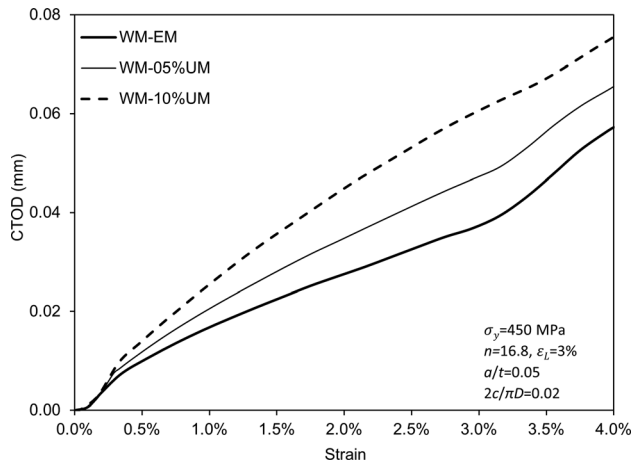


Fig. 9 Effect of undermatch on crack driving force: Yield plateau scenario

6.4 Results of Parametric Study. Figure 8 shows the evolution of the CTOD for the case of evenmatch where the parent metal exhibits a yield plateau, $\varepsilon_L = 1\%$, 2%, and 3%. The effect of the yield plateau is evident. Since the weld is rather slender here,

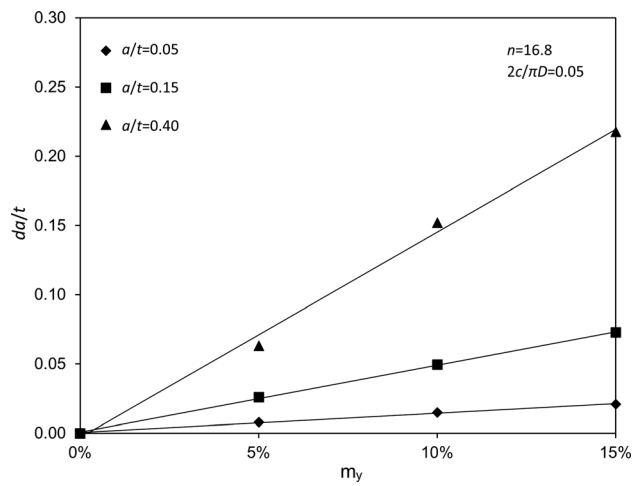


Fig. 10 Effect of undermatch and defect depth: Materials with continuous yielding

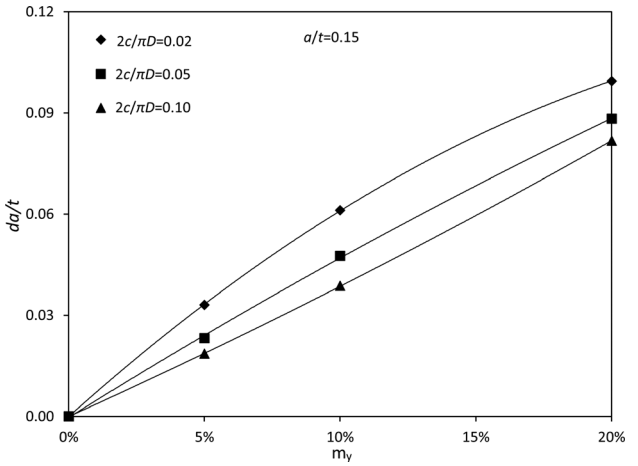


Fig. 11 Effect of undermatch and defect length: Materials with yield plateau

Table 5 Values of α_{ijk} for $n = 5.7$

		k		
i	j	0	1	2
1	0	6.40×10^{-3}	-5.51×10^{-1}	2.30
1	1	1.83	17.4	−88.8
1	2	9.31	−239	1.12×10^{3}
2	0	0.12	−1.56	2.93
2	1	−4.86	39.1	4.08
2	2	0.94	−4.14	4.71

Table 6 Range of application

D/t	a/t	$2c/\pi D$	n	m_y	ε_{app}(%)
7–25	≤0.35	≤0.10	≤16.8	≤10%	0.75–2.50

the plastic deformation in the parent metal interacts with the plastic deformation at the crack tip. The crack driving force is a quadratic function of strain in the elastic regime. As the material yields, the relationship becomes nearly linear, up to $\varepsilon^{app} = \varepsilon_L$. (It should be noted, however, that under tension, in this region the crack driving force may increase significantly and then saturate, as shown in Ref. [21]). For strains $\varepsilon^{app} > \varepsilon_L$, there is a noticeable increase in the crack driving force, beyond which the relationship between δ and ε^{app} is again close to linear, but with a higher slope, due to global yielding of the pipe [22].

The effect of the undermatch magnitude on the CTOD is illustrated in Fig. 9 for the parent metal with $\varepsilon_L = 3\%$. The crack driving force significantly increases with the undermatch magnitude.

As mentioned earlier, the interaction between the plastic deformation at the crack tip of an undermatched weld and the plastic deformation in the background material reduces the crack driving

Table 7 Pipe sizes

Pipe size (in.)	D (mm)	t (mm)	D/t
6	168.3	7.11	24
6	168.3	25.4	7
12	323.9	15.9	20
12	323.9	25.4	13
16	406.4	17.6	23
16	406.4	25.4	16

Downloaded from https://asmedigitalcollection.asme.org/pressurevesseltech/article-pdf/137/5/051402/4014518/pvt_137_05_051402.pdf by Imperial College London user on 21 September 2019

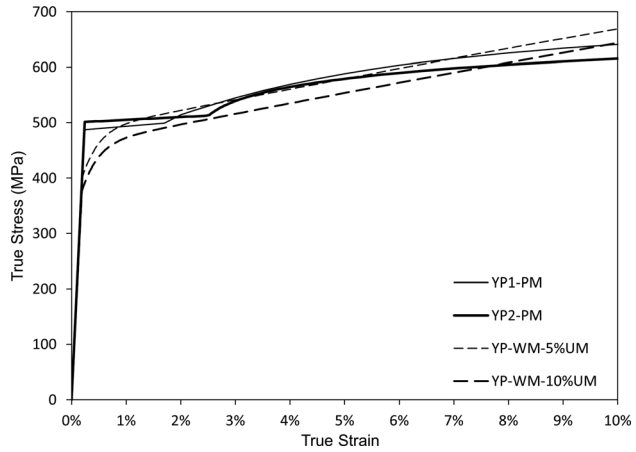


Fig. 12 Parent metal stress–strain curves with yield plateau

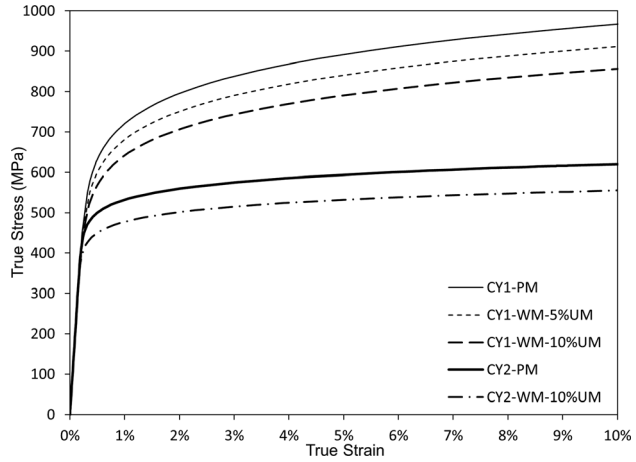


Fig. 13 Parent metal stress–strain curves with continuous yielding

force. When a increases, the level of interaction reduces. Consequently, the effect of the undermatch on the CTOD becomes more pronounced, hence the defect depth reduction, da, increases, as shown in Fig. 10.

The results in Fig. 11 show that da/t decreases with $2c/\pi D$. For a given a, the uncracked area decreases when c increases, while

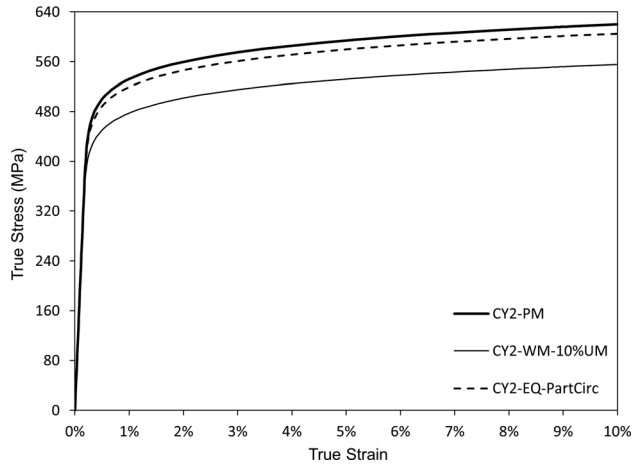


Fig. 14 Equivalent stress–strain curve

Table 8 Effective undermatch for material with yield plateau

Pipe size (in.)	ε^{app} (%)	Material	m_y (%)	m (%)
6	1.24	YP1	5.0	−2.0
6	1.24	YP1	10.0	3.1
6	1.24	YP2	10.0	5.2
12	2.16	YP1	5.0	−1.1
12	2.16	YP1	10.0	3.8
12	2.16	YP2	10.0	2.2
16	2.64	YP1	5.0	−0.0
16	2.64	YP1	10.0	4.8

Table 9 Effective undermatch for material with continuous yielding

Pipe size (in.)	ε^{app} (%)	Material	m_y (%)	m (%)
6	1.24	CY1	5.0	5.6
6	1.24	CY1	10.0	11.1
6	1.24	CY2	10.0	10.3
12	2.16	CY1	5.0	5.6
12	2.16	CY1	10.0	11.2
12	2.16	CY2	10.0	10.4
16	2.64	CY	5.0	5.7
16	2.64	CY1	10.0	11.3

the area adjustment (increase in uncracked area due to defect depth reduction) increases with c. Consequently, to achieve the same net (proportional) increase in uncracked area when a is reduced, da must reduce when c increases. This effect, which is more pronounced for materials with a yield plateau, is less significant than that of the defect depth.

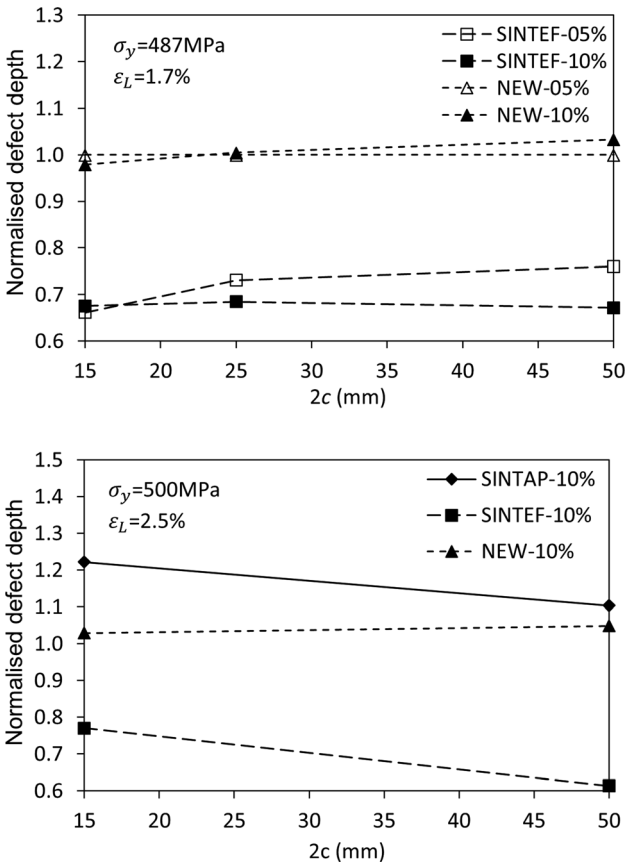


Fig. 15 Normalized maximum acceptable defect depths: 168.3 mm × 7.11 mm pipe material with yield plateau

Downloaded from https://asmedigitalcollection.asme.org/pressurevesseltech/article-pdf/137/5/051402/4014518/pvt_137_05_051402.pdf by Imperial College London user on 21 September 2019

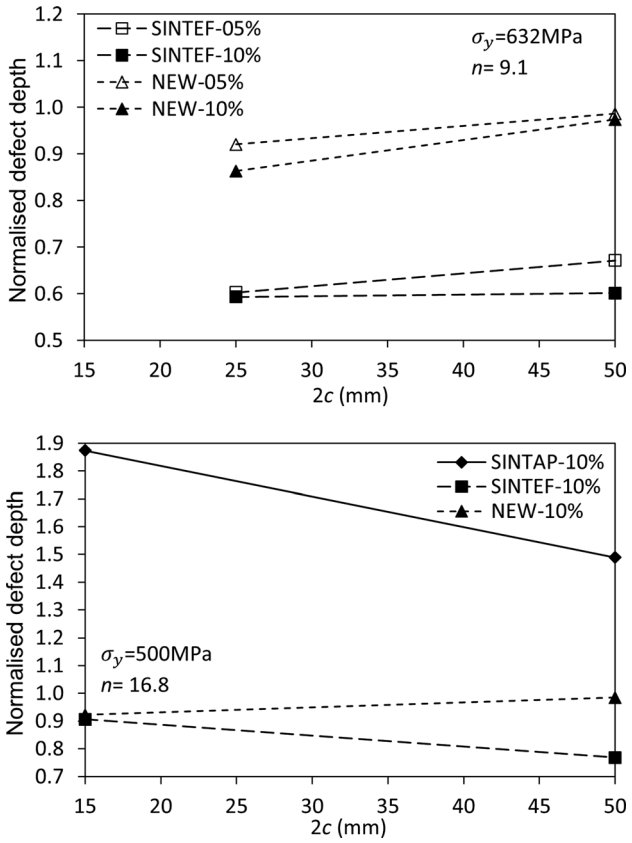


Fig. 16 Normalized maximum acceptable defect depths: 168.3 mm × 7.11 mm pipe material with continuous yielding

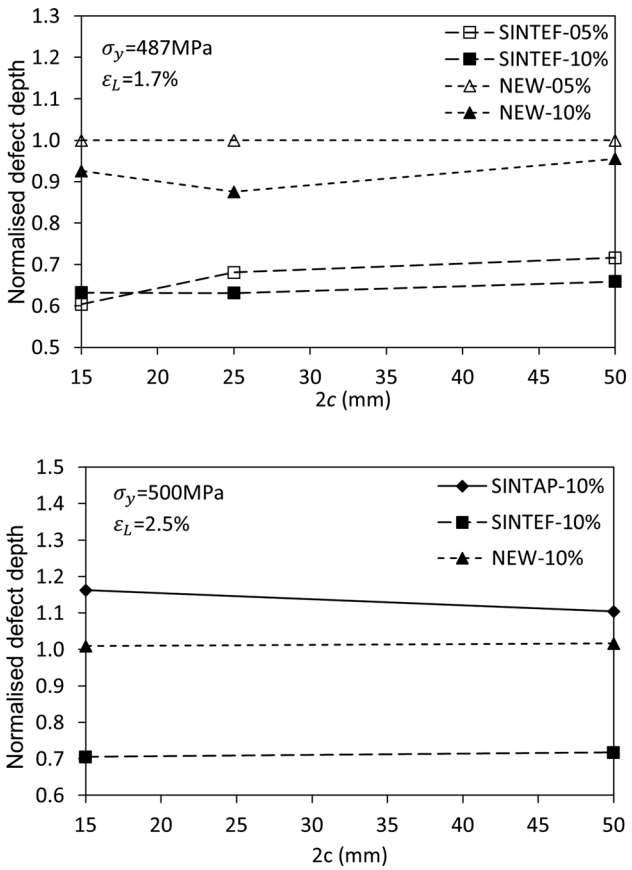


Fig. 17 Normalized maximum acceptable defect depths: 323.9 mm × 15.9 mm pipe material with yield plateau

The normalized defect depth adjustment, da/t can increase by 30% when n increases from 5.7 to 16.8. In contrast, σ_y in the range between 450 and 700 MPa and ε_L in the range between 2% and 3% (typical for subsea seamless pipes) have a small effect on da/t.

7 New ECA Procedure for Undermatched Welds

7.1 Approach. The SINTEF concept of defect depth adjustment is adopted here. First, DNV-OS-F101—BS7910 option 2 assessment (equivalent to option 2 in R6 [4]) is carried out to determine the maximum acceptable defect sizes. The acceptable defect depths are subsequently reduced using an analytical formula, to account for weld undermatch.

7.2 Defect Depth Adjustment Formula. Second order polynomials were fitted to the FE results expressed in terms of da/t as a function of m, a/t, and $2c/\pi D$. The effect of the weld width was captured through the factor H/H_0, where H is half of the project specific weld width and H_0 is half of the reference weld width, determined for the weld geometry considered in the parametric FE study (i.e., 21.4 mm thick 30 deg V-beveled weld with 3 mm root opening, illustrated in Fig. 4)

$$\frac{da}{t} = (H/H_0)^{0.5} \sum_{i,j,k=0}^{2} \alpha_{ijk} (2c/\pi D)^k (a/t)^j m^i \tag{14}$$

where the mismatch, m, is evaluated at $\varepsilon = \varepsilon^{\text{app}}$, from

$$m(\varepsilon^{\text{app}}) = 1 - \frac{\sigma^{\text{WM}}}{\sigma^{\text{PM}}} \tag{15}$$

Four sets of constants α_{ijk} in Eq. (14) were produced: (i) one for parent metals with yield plateau and $n \leq 16.8$, (ii) one for parent

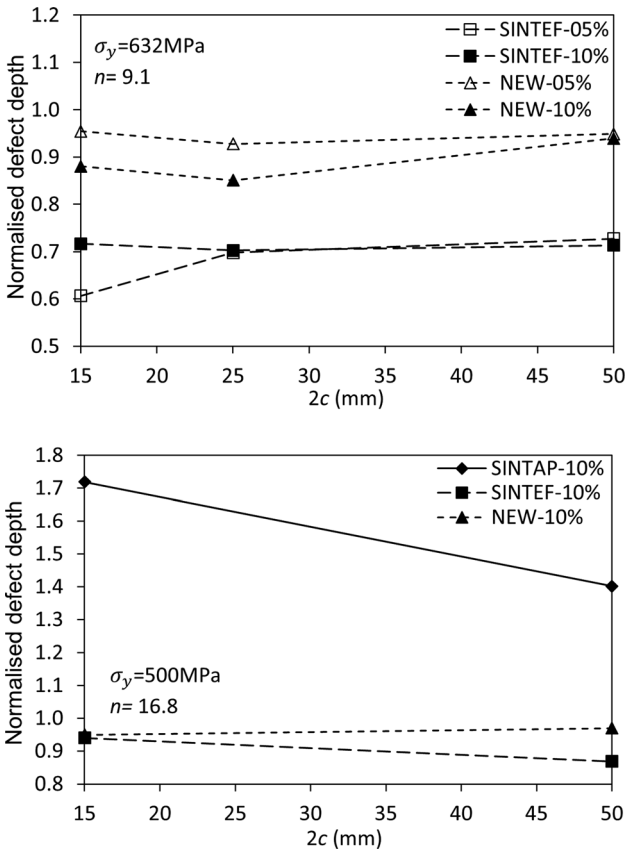


Fig. 18 Normalized maximum acceptable defect depths: 323.9 mm × 15.9 mm pipe material with continuous yielding

Downloaded from https://asmedigitalcollection.asme.org/pressurevesseltech/article-pdf/137/5/051402/4014518/pvt_137_05_051402.pdf by Imperial College London user on 21 September 2019

metals with continuous yielding and $n = 16.8$, (iii) one for parent metals with continuous yielding and $n = 9.0$, and (iv) one for parent metals with continuous yielding and $n = 5.7$, given in Table 5.

7.3 Application to ECA of Reeled Pipelines. When applying the proposed approach to reeled pipelines, the following procedure should be applied:

(1) Calculate ε^{app} using Eq. (1)
(2) Carry out a DNV-OS-F101—BS7910 option 2 ECA to determine the maximum acceptable defect size prior to reeling, $(2c_0, a_0)$, under the assumption of evenmatch
(3) Calculate m using Eq. (15)
(4) Determine n by fitting the Ramberg–Osgood relationship in Eq. (12) to the parent metal stress–strain curve
(5) Calculate da using Eq. (14)
(6) Finally, calculate the acceptable initial (as-welded) defect depth in the undermatched weld, a_0^{eff}, from

$$a_0^{eff} = a_0 - da \tag{16}$$

7.4 Application Range. The range of application of the proposed methodology is summarized in Table 6. It is required that the weld metal stress–strain curve exhibits continuous yielding and higher strain hardening than the parent metal. In the case of bimetal pipes, it is also required that the CRA layer does not overmatch the parent metal.

8 Validation of Adjustment Formula

8.1 Approach. FE analyses are carried out to determine the maximum acceptable depth for 15, 25, and 50 mm long defects in undermatched welds, for the critical toughness, CTOD = 0.3 mm. Defect depths in excess of $t/2$ are disregarded because such defects would not be allowed during production. These FE results are then compared to predictions from: (i) the SINTAP level 3 assessment, (ii) the SINTEF scheme, and (iii) the proposed ECA approach. It is assumed that the FE results are exact.

8.2 Pipe Geometry and Material Stress–Strain Curves. Typical reelable pipes with an outer diameter in the range between 6.625 in. (168.3 mm) and 16 in. (406.4 mm) and wall thickness in the range between 7.11 mm and 25.4 mm were considered, as detailed in Table 7. A weld width of 14 mm, which is representative of manual welds for thin pipes and mechanized welds for thick pipes, was considered for the following four scenarios:

(1) "YP1": $\sigma_y = 487$ MPa, $\varepsilon_L = 1.7\%$, $n = 9.9$, alloy 625 weld consumable
(2) "YP2": $\sigma_y = 500$ MPa, $\varepsilon_L = 2.5\%$, $n = 16.8$, alloy 625 weld consumable
(3) "CY1": $\sigma_y = 632$ MPa, $n = 9.1$, 25% Cr weld consumable
(4) "CY2": $\sigma_y = 500$ MPa, $n = 16.8$, 25% Cr weld consumable

The undermatch at yield, m_y, was up to 10%. The corresponding stress–strain curves are shown in Figs. 12 and13 for cases with and without yield plateau, respectively.

The SINTAP approach was used for the YP2, CY1, and CY2 scenarii. A simplified procedure was followed, where the maximum acceptable defect sizes were determined by finite-element analysis (FEA). Figure14 compares, for the CY2 scenario, the parent and weld metal stress–strain curves (indicated by thick and thin solid lines, respectively) to the equivalent stress–strain curve (indicated by a dashed line) obtained using the mismatch limit load solution for part-circumferential defects in pipes subjected to tension [15]. The equivalent curve is very similar to the parent metal stress–strain curve. The same trend was observed for YP2

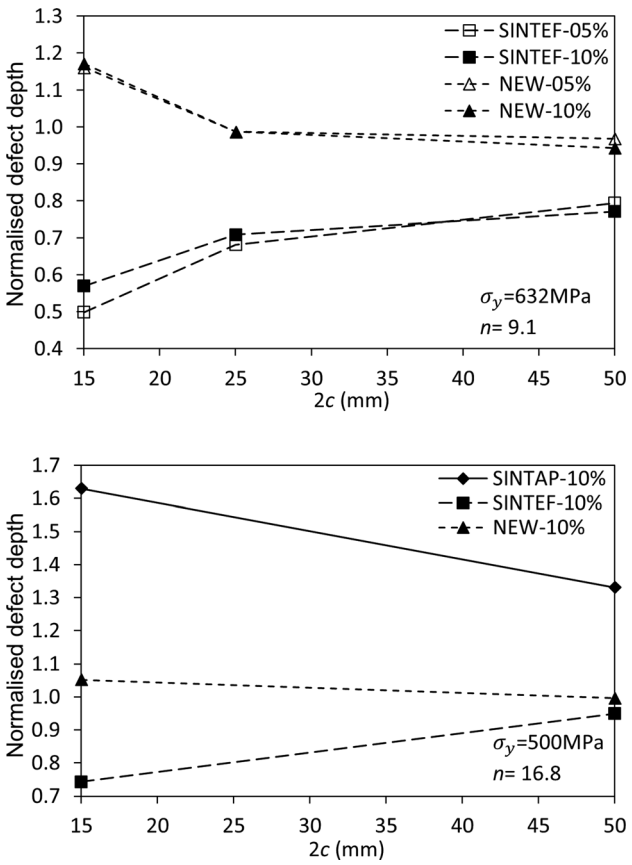


Fig. 19 Normalized maximum acceptable defect depths: 323.9 mm × 25.4 mm pipe material with continuous yielding

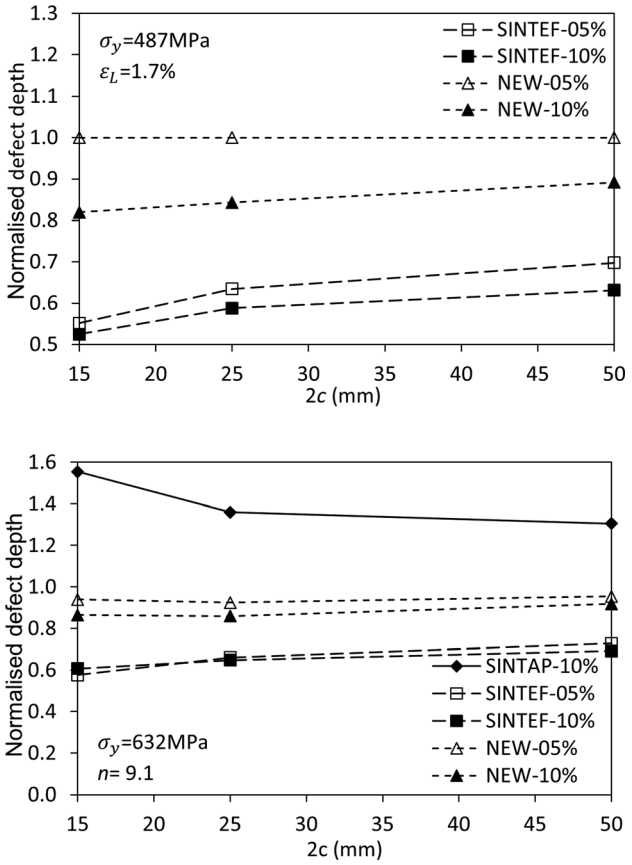


Fig. 20 Normalized maximum acceptable defect depths: 406.4 mm × 17.6 mm pipes

Downloaded from https://asmedigitalcollection.asme.org/pressurevesseltech/article-pdf/137/5/051402/4014518/pvt_137_05_051402.pdf by Imperial College London user on 21 September 2019

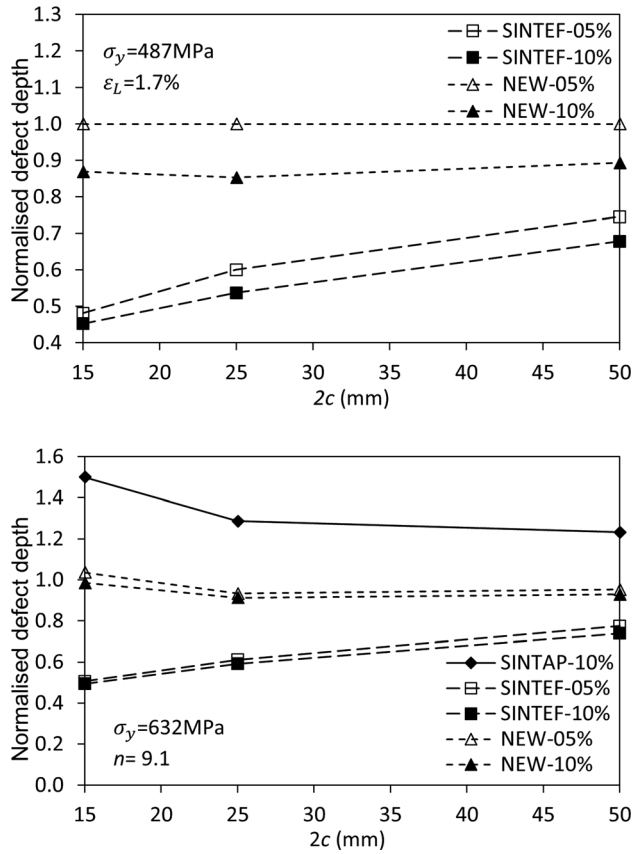


Fig. 21 Normalized maximum acceptable defect depths: 406.4 mm × 25.4 mm pipes

and CY1. Consequently, the acceptance criteria derived using the equivalent curves were expected to be very similar to those derived using parent metal stress–strain curves.

8.3 Results and Discussions. The analytical predictions are normalized by the FE results and plotted against the defect length in Figs. 15–21: (i) SINTAP predictions are represented by solid lines with diamond symbols, (ii) SINTEF predictions are illustrated by long dashed lines with rectangular symbols, and (iii) predictions with the proposed ECA approach are represented by short dashed lines with triangular symbols. Cases with $m_y = 5\%$ and 10% are represented by open and closed symbols, respectively. The corresponding values of m are given in Tables 8 and 9. Cases with $m \leq 0$ are treated as evenmatch cases. A prediction is conservative when the normalized defect depth is below 1 and nonconservative when it is above 1.

The results in Figs.15–21 show that the SINTAP procedure is consistently nonconservative. The magnitude of defect depth overestimation reduces when m reduces. This is due to the fact that an equivalent curve for pipes in tension was used. Since the prescribed load, for pipes subjected to tension, is a force, the corresponding applied strain would be higher for the equivalent curve (due to lower stress–strain curve) than for the parent metal stress–strain curve. Therefore, the effect of the undermatch would be captured. This is not the case for reeling, where the prescribed load is strain. The accuracy of the SINTAP procedure can be improved if an equivalent stress–strain curve with lower strain hardening than both parent and weld metal stress–strain curves is used. Such curve could be derived using a mismatch limit load solution for pipes subjected to bending. Alternatively, Eq. (6) could be modified. The SINTEF scheme is generally too conservative, because it does not account for the effects of the strain hardening and the defect length on the crack driving force in undermatched welds.

In contrast, the proposed ECA approach is the most accurate over the whole range of standard reeled pipe sizes. Out of the 61 cases run, the analytical predictions are within 5% of the FE results for 31 cases (51%), within 10% for 49 cases (80%), and within 15% for 57 cases (93%). The maximum error of 20% is obtained for four cases with short defects: (i) the acceptable defect depth is overestimated by up to 20% for thick pipes with continuous yielding, and (ii) underestimated by up to 20% for thin large pipes with a yield plateau. The defect length in excess of 15 mm has small effect on the accuracy, and therefore similar accuracy would be obtained for defects longer than 50 mm.

9 Conclusion

In this work, a new assessment procedure for undermatched welds subjected to plastic straining has been developed, whereby an ECA is first carried out in accordance with DNV-OS-F101 to determine the acceptable defect sizes assuming the evenmatch condition. The defect depths are subsequently reduced to account for the undermatch, while the defect lengths remain unaltered. The defect depth reduction is estimated using an analytical formula developed in this work and shown to be generally accurate within $-15\%/+6\%$. The novel approach is applicable to surface defects only. Ongoing work aims at extending the applicability to embedded defects.

Acknowledgment

Thanks go to Ludovic Krauss and Sylvain Denniel from Technip for their valuable contribution.

References

[1] Det Norske Veritas, 2013, *DNV-OS-F101 2013: Submarine Pipeline Systems*, Oslo, Norway.
[2] British Standard Institution, 2013, *BS7910: Guide to Methods for Assessing the Acceptability of Defects in Metallic Structures*.
[3] Tkaczyk, T., O'Dowd, N. P., and Howard, B. P., 2007, "Comparison of Crack Driving Force Estimation Schemes for Weld Defects in Reeled Pipelines," International Offshore and Polar Engineering Conference, ISOPE 2007.
[4] R6, 2013, "Assessment of the Integrity of Structures Containing Defects," EDF Energy Nuclear Generation Ltd., R6-Revision4.
[5] Fu, J. Q., and Shi, Y. W., 1996, "Effect of Cracked Weld Joint and Yield Strength Dissimilarity on Crack Tip Stress Triaxiality," Theor. Appl. Fract. Mech., **25**(1), pp. 51–57.
[6] Boothman, D. P., Lee, M. M. K., and Luxmoore, A. R., 1999, "The Effects of Weld Mismatch on J-Integrals and Q-Values for Semi-Elliptical Surface Flaws," Eng. Fract. Mech., **64**(4), pp. 433–458.
[7] O'Dowd, N. P., 1995, "Applications of Two-Parameter Approaches in Elastic–Plastic Fracture Mechanics," Eng. Fract. Mech., **52**(3), pp. 445–465.
[8] Ainsworth, R. A., and O'Dowd, N. P., 1995, "Constraint in the Failure Assessment Diagram Approach for Fracture Assessment," ASME J. Pressure Vessel Technol., **117**(3), pp. 260–267.
[9] Tang, W., and Shi, Y. W., 1995, "Influence of Strength Matching and Crack Depth on Fracture Toughness of Welded Joints," Eng. Fract. Mech., **51**(4), pp. 649–659.
[10] Lin, G., Meng, X. G., Cornec, A., and Schwalbe, K.-H., 1999, "The Effect of Strength Mismatch on Mechanical Performance of Weld Joints," Int. J. Fract., **96**(1), pp. 37–54.
[11] SINTEF, 2012, "Fracture Control of Offshore Pipelines JIP, Phase II, Task 1.1.2: Axisymmetrical FE Modelling of the Effect of Materials Mismatch on Ductile Tearing Resistance," SINTEF Report No. 23101.
[12] SINTEF, 2012, "Fracture Control of Offshore Pipelines JIP, Phase II, Task 1.1.1: The Effect of Materials Mismatch and Weld Geometry on the Crack Driving Force—Axisymmetrical FE Modelling," SINTEF Report No. 23100.
[13] Hertelé, S., De Waele, W., Verstraete, M., Denys, R., and O'Dowd, N. P., 2014, "J-Integral Analysis of Heterogeneous Mismatched Girth Welds in Clamped Single-Edge Notched Tension Specimens," Int. J. Pressure Vessels Piping, **119**, pp. 95–107.
[14] Kim, Y.-J., Koçak, M., Ainsworth, R. A., and Zerbst, U., 2000, "SINTAP Defect Assessment Procedure for Strength Mismatched Structures," Eng. Fract. Mech., **67**, pp. 529–546.
[15] Kim, J.-S., Song, T. K., Kim, Y.-J., and Jin, T. E., 2009, "Strength Mis-Match Effect on Limit Loads for Circumferential Surface Cracked Pipes," Eng. Fract. Mech., **76**(8), pp. 1074–1086.

Downloaded from https://asmedigitalcollection.asme.org/pressurevesseltech/article-pdf/137/5/051402/4014518/pvt_137_05_051402.pdf by Imperial College London user on 21 September 2019

[16] Østby, E., 2005, "Fracture Control, Offshore Pipelines JIP—New Strain-Based Fracture Mechanics Equations Including the Effects of Biaxial Loading, Mismatch and Misalignment," ASME Paper No. OMAE2005-67518.
[17] Østby, E., 2007, "Fracture Control, Offshore Pipelines JIP—Proposal for Strain-Based Fracture Assessment Procedure," International Offshore and Polar Engineering Conference, ISOPE 2007.
[18] American Petroleum Institute, 2007, *API 5L 2007: Specification for Line Pipe*, 44th ed.
[19] Tkaczyk, T., O'Dowd, N. P., and Nikbin, K., 2009, "Fracture Assessment Procedures for Steel Pipelines Using a Modified Reference Stress Solution," ASME J. Pressure Vessel Technol., **131**(3), p. 031409.
[20] Shih, C. F., 1981, "Relationships Between the J-integral and the Crack Opening Displacement for Stationary and Extending Cracks," J. Mech. Phys. Solids, **29**(4), pp. 305–326.
[21] Boothman, D. P., Lee, M. M. K., Luxmoore, A. R., and Smpter, J. D. P., 1998, "J-estimation of Semi-Elliptic Surface Cracks in Wide Plates Under Direct Tension," Fatigue Fract. Eng. Mater. Struct., **21**(3), pp. 333–346.
[22] Tkaczyk, T., O'Dowd, N. P., Nikbin, K., and Howard, B. P., 2009, "A Non-Linear Fracture Assessment Procedure for Pipeline Materials With a Yield Plateau," International Offshore and Polar Engineering Conference, ISOPE 2009, Osaka, Japan, June 21–26.

Downloaded from https://asmedigitalcollection.asme.org/pressurevesseltech/article-pdf/137/5/051402/4014518/pvt_137_05_051402.pdf by Imperial College London user on 21 September 2019

Appendix B

Paper No. 2 – Limit Load Solution and Crack Driving Force Estimation Scheme for Embedded Flaws in Pipeline Girth Welds

Proceedings of PVP 2015
ASME 2015 Pressure Vessels and Piping Division Conference
July 19-23, 2015, Boston, Massachusetts, USA

PVP2015-45702

LIMIT LOAD SOLUTION AND CRACK DRIVING FORCE ESTIMATION SCHEME FOR EMBEDDED FLAWS IN PIPELINE GIRTH WELDS

Aurélien Pépin*
Offshore Engineering Division
Technip
Westhill, Aberdeen, AB32 6TQ
United Kingdom
Email: apepin@technip.com

Tomasz Tkaczyk
Offshore Engineering Division
Technip
Westhill, Aberdeen, AB32 6TQ
United Kingdom
Email: ttkaczyk@technip.com

Noel O'Dowd
Department of Mechanical, Aeronautical and Biomedical Engineering
Materials and Surface Science Institute, University of Limerick
Limerick
Ireland
Email: noel.odowd@ul.ie

Kamran Nikbin
Department of Mechanical Engineering
Imperial College
London, SW7 2AZ
United Kingdom
Email: k.nikbin@imperial.ac.uk

ABSTRACT

The acceptability of flaws in a subsea rigid pipeline is usually sanctioned based on the results of an engineering criticality assessment (ECA), carried out considering all loads seen by the pipeline from fabrication to the end of service life. Reel-lay is an efficient installation method, frequently used for installing subsea pipelines. Unlike surface breaking flaws, embedded flaws are not directly assessed in a reeling ECA because the available assessment solutions are too conservative. A work around approach is often used, whereby acceptable surface breaking flaw sizes are deemed acceptable beneath the surface, provided that the embedment depth is equal to or greater than half of the flaw height. However, the results of more recent research work suggest that this approach could be non-conservative in some cases.

In this work, a parametric finite-element (FE) study was carried out to assess the effect of the embedment depth, the crack length and the crack height on the load required to cause collapse of the shorter ligament of an embedded flaw. Subsequently, a closed form limit load solution was developed, and compared against available solutions for pipes subjected to tension. A *J*-based crack driving force (CDF) estimation scheme was developed for a selected material behaviour. Finally, recommendations were made for the direct reeling ECA of subsea pipelines with embedded flaws.

INTRODUCTION

Most flaws in pipeline girth welds are embedded. Therefore, accurate prediction of acceptable embedded flaw sizes is needed. Flaw acceptance criteria can be determined through ECA. Most often, ECA of subsea pipeline girth welds is carried out following the guidance in DNV-OS-F101 [1], using the solutions provided in BS7910 [2]. All loads seen by the pipeline from fabrication to the end of service life need to be considered in the DNV ECA procedure.

Reel-lay is an efficient installation method, frequently used for installing subsea pipelines. A standard reel-lay installation involves two tensile straining events, which are assessed separately in the BS7910 Option 2 ECA (equivalent to Option 2 in R6 [3]). The nominal reeling strain, ε_{app}, which typically does

*Address all correspondence to this author.

Copyright © 2015 by ASME

not exceed 2.5%, and is much less for small diameter pipes, is converted into a remote applied stress, σ_{app}, using a relevant stress-strain curve. A local stress, called the reference stress, σ_{ref}, which accounts for the reduced cross-sectional area in the defective weld, is estimated from

$$\sigma_{ref} = \frac{P_0}{P_L}\sigma_y \tag{1}$$

where σ_y is the yield strength and P_0 and P_L are the limit loads of the uncracked and cracked pipes, respectively. The proximity to failure by plastic collapse is expressed by the load ratio, L_r, while the proximity to failure by fracture is indicated by the fracture ratio, K_r, determined from

$$L_r = \frac{\sigma_{ref}}{\sigma_y} \tag{2}$$

$$K_r = \frac{K}{K_{mat}} \tag{3}$$

where K is the stress intensity factor (SIF) calculated using an appropriate solution in BS7910, and K_{mat} is the material fracture toughness in terms of K. The assessment point, (L_r, K_r), is plotted on a failure assessment diagram (FAD), where the failure assessment curve has the form

$$K_r = \left(\frac{J}{J_e}\right)^{-0.5} = \left(\frac{E\varepsilon_{ref}}{L_r\sigma_y} + \frac{1}{2}\frac{L_r^3\sigma_y}{E\varepsilon_{ref}}\right)^{-0.5} \tag{4}$$

where E is Young's modulus, J_e is the elastic part of the total crack driving force, J, and ε_{ref} is the strain corresponding to σ_{ref} on the assumed stress-strain curve. The cut-off value for L_r, i.e. $L_{r,max}$, is the tensile to yield strength ratio, as defined in DNV-OS-F101. A ductile tearing assessment is carried out by iteratively increasing the flaw height until the assessment point falls within the FAD, as shown in Fig. 1. For each tearing increment, the material fracture toughness expressed in terms of J, i.e. J_{mat}, is determined from a resistance curve, and then converted into K_{mat} using

$$K_{mat} = \left(\frac{EJ_{mat}}{1-\nu^2}\right)^{0.5} \tag{5}$$

where ν is the Poisson ratio. The crack size at the end of the first tensile straining event is used as a starting point for the assessment of the second event. The initial flaw size is deemed acceptable for reeling if stable growth is predicted to occur during both tensile straining events.

Unlike surface breaking flaws, embedded flaws are not directly assessed in a DNV-OS-F101 reeling ECA, primarily because the relevant BS7910 limit load solution is too conservative. A work around approach is often used, whereby acceptable surface breaking flaw sizes are also deemed acceptable beneath the surface, provided that the embedment depth is equal to or greater than half of the flaw height. Olsø *et al.* [4] carried out FE analyses to evaluate the criticality of embedded flaws in pipelines subjected to biaxial loading. Pipes with outer diameter, $D = 401.6$ mm, wall thickness $t = 23$ mm, yield strength, $\sigma_y = 494$ MPa and yield to tensile ratio, $Y/T = 0.85$, containing flaws, were internally pressurised to 20 MPa and subjected to tension. Flaws with height in the range between 3 mm and 5 mm, and length in the range between 50 mm and 200 mm were analysed, and the CDF was computed in terms of the crack tip opening displacement (CTOD). For applied strains in excess of 1%, the predicted CTOD was smaller for surface breaking flaws than for subsurface flaws with embedment depth equal to half of the crack height. This suggests that the current DNV-OS-F101 approach for assessing the criticality of embedded flaws can be non-conservative in some cases.

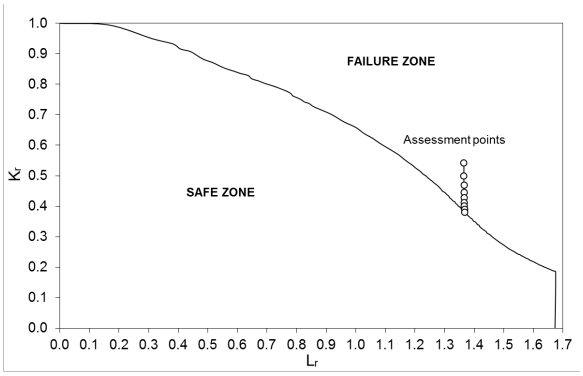


FIGURE 1. BS7910 FAILURE ASSESSMENT DIAGRAM

In this work a parametric finite-element (FE) study was carried out to assess the effect of the embedment depth, the crack length and the crack height on the load required to cause collapse of the shorter ligament of an embedded flaw. Subsequently, a closed form limit load solution was developed, and compared against available solutions for pipes subjected to tension. A J-based CDF estimation scheme was then developed for a selected material behaviour. Finally, recommendations were made for the reeling ECA of subsea pipelines with embedded flaws.

FRACTURE ASSESSMENT OF EMBEDDED GIRTH WELD FLAWS IN PIPELINES SUBJECTED TO PLASTIC STRAINS

Fracture assessment of embedded girth weld flaws in pipelines subjected to plastic strains may be carried out using the available SIF, limit load and crack driving force estimation schemes. Here, an embedded flaw is defined by its length, $2c$, height, $2a$, its shorter ligament with associated length (embedment depth), p^A, and crack tip, 'A', and its longer ligament with associated length, p^B, and crack tip, 'B', as shown in Fig. 2.

Copyright © 2015 by ASME

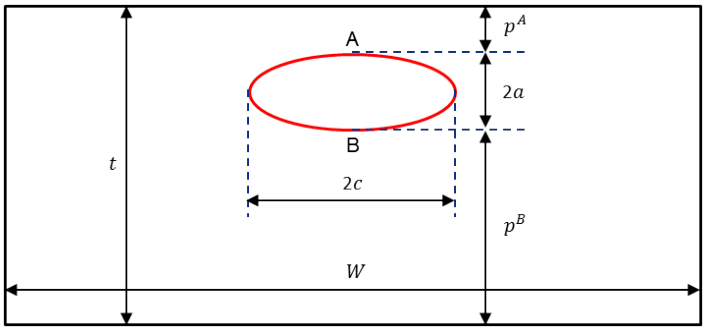


FIGURE 2. EMBEDDED FLAW GEOMETRY

Stress Intensity Factor Solutions

Design standards such as BS7910, R6 and the French nuclear codes (FNC) RSE-M and RCC-MR provide SIF solutions for plates containing embedded flaws, but none for the pipe geometry.

In BS7910 [2], the SIF in plates with embedded flaws can be estimated using the Newman and Raju K-solution for cracks in three-dimensional finite bodies subjected to tension and bending loads, [5],

$$K_{\mathrm{I}} = f_w \left(M_m \, P_m + M_b \, P_b\right) \sqrt{\pi a} \tag{6}$$

where P_m and P_b are the applied membrane and bending stresses, whereas f_w, M_m and M_b are dimensionless functions of the geometry and the location along the crack front.

A similar formulation is given in the RSE-M and RCC-MR codes, [6],

$$K_{\mathrm{I}} = \left(i_0 \, P_m + F_{gb} \, P_b\right) \sqrt{\pi a} \tag{7}$$

The values of the dimensionless functions i_0 and F_{gb} in Eqn. 7 are given in [6] for crack tips 'A' and 'B' in Fig. 2.

The R6 formulation is identical to that in Eqn. 7, except that i_0 and F_{gb} are termed f_m and f_b, respectively [3]. The suitability of the K-solutions in Eqns. 6 and 7 for the fracture assessment of pipeline girth welds with embedded flaws is investigated in the following sections.

Limit Load Solutions

No limit load solutions for pipes with embedded flaws were found in the literature. Solutions for the plate geometry are provided in R6 and BS7910 for various load modes. However, only pin-loaded tension load mode is considered in this work.

According to R6, a local limit load can be determined from

$$P_L^{R6} = \frac{\left(1 - \frac{2\alpha}{1-2k}\right)\left(1+\psi\right)}{\left(1 - \frac{2\alpha}{1-2k}\right) + \psi} P_0 \tag{8}$$

where $\alpha = a/t$, $\psi = c/t$ and

$$k = \frac{1}{2} - \frac{p^A + a}{t} \tag{9}$$

R6 also provides global solutions (e.g. the Lei and Budden solutions [7]), which are not discussed here because they are less accurate for the prediction of the plastic collapse of the ligament of length p^A.

The BS7910 limit load solution, derived from a 2D analysis detailed in [8], is expressed as follows

$$P_L^{BS} = \frac{(1-\alpha'')^2 + 4p^A\alpha''/t'}{\alpha'' + \left(1 - 2\alpha'' + 4p^A\alpha''/t'\right)^{0.5}} P_0 \tag{10}$$

where $t' = 2a + 2p^A$, W is the plate width or pipe mid-wall circumference and α'' is the height to thickness ratio adjusted (reduced) to account for the load bearing capacity of the uncracked material on either side of the flaw, which is not included in the 2D analysis, [8],

$$\alpha'' = \begin{cases} \frac{2a/t'}{1+(t'/c)} & \text{for} \quad W \geq 2(c+t') \\ (2a/t')\,(2c/W) & \text{for} \quad W < 2(c+t') \end{cases} \tag{11}$$

As will be shown in a subsequent section, the limit load solution given in Eqn. 10 is too conservative when used for the assessment of embedded flaws in pipeline girth welds. In addition, embedded flaws are perceived to be less critical than surface flaws. Therefore, DNV suggested using the surface breaking flaw acceptable criteria for embedded flaws if $p^A \geq a$. Furthermore, DNV-OS-F101 recommends using the Kastner *et al.* [9] limit load solution for the assessment of surface flaws in pipeline girth welds

$$P_L^{DNV} = \frac{(1-a/t)(\pi(c/r)(a/t))}{\pi(1-a/t) + 2(a/t)sin(c/r)} P_0 \tag{12}$$

where a is the surface flaw height and r is the pipe mid-wall radius. The limit load solutions given in Eqns. 8 to 12 are compared in the following sections to the solution for pipes with embedded flaws subjected to tension, developed in this work.

Crack Driving Force Estimation Schemes

BS7910 and R6 propose a stress-based crack driving force estimation scheme in the form

$$J = \frac{K^2(1-\nu^2)}{E}\left(\frac{E\varepsilon_{ref}}{L_r\sigma_y} + \frac{1}{2}\frac{L_r^3\sigma_y}{E\varepsilon_{ref}}\right) \tag{13}$$

where σ_{ref} is derived from Eqn. 1 with $P_L = P_L^{BS}$ or $P_L = P_L^{R6}$. The J-scheme in Eqn. 13 is generic and can be used for any crack geometry and material behaviour.

Copyright © 2015 by ASME

TABLE 1. FE CASE MATRIX: CRACK GEOMETRIES

D (mm)	t (mm)	$2c/W$	$2a/t$	p^A/a
			0.05	1.00 – 9.00
323.9	21.4	0.02 – 0.10	0.10	0.75 – 3.50
			0.40	0.50 – 1.50

DNV-OS-F101 recommends using the J-scheme in Eqn. 13 together with the limit load solution in Eqn. 12 for the fracture assessment of pipeline girth welds with surface breaking flaws. However, after performing a comparison of available CDF estimation schemes for the assessment of weld flaws in reeled pipelines [10], the authors concluded that a modified reference stress solution was needed to improve the accuracy of the DNV approach. Subsequently, following the approach laid out by Kim and Budden in [11] the authors proposed a new limit load solution for pipes with surface breaking flaws [12]

$$P_L^{TTK} = \gamma P_L^{DNV} \tag{14}$$

where γ is a dimensionless function of the crack geometry and the hardening index of the material stress-strain curve.

Strain-based CDF estimation schemes have also been proposed in the literature for the assessment of pipeline girth welds with surface (see [13–15], for example) or embedded (see [16, 17], for example) flaws. However, these schemes cannot readily be used for the assessment of pipe materials with a yield plateau, which represent the majority of reeled pipelines. Consequently, these CDF schemes are not considered in this study. The suitability of the J-scheme in Eqn. 13 for the reeling ECA of pipeline girth welds with embedded flaws is investigated in the following sections.

LIMIT LOAD ANALYSIS OF PIPE WITH EMBEDDED FLAWS

Approach

A parametric FE study was carried out to quantify the effect of p^A, $2a$ and $2c$ on the load required to cause collapse of the ligament of length p^A. Plastic collapse was assumed to occur when the plastic zone, initiating from crack tip 'A' (see Fig. 2), reached the pipe surface. Subsequently, a closed form limit load solution was developed, and compared against the solutions given in Eqns. 8 to 12.

Pipe and Crack Geometry

A pipe with outer diameter $D = 12.75$" (323.9 mm) and wall thickness $t = 0.84$" (21.4 mm) was analysed. The normalised embedment depth, p^A/a, in the range between 0.5 and 9.0, the normalised crack height, $2a/t$, in the range between 0.05 and 0.40 and the normalised crack length, $2c/W$, in the range between 0.02 and 0.10, which are typical of flaw sizes assessed in ECA, were investigated. In total, 36 crack geometries were considered, as detailed in Table 1.

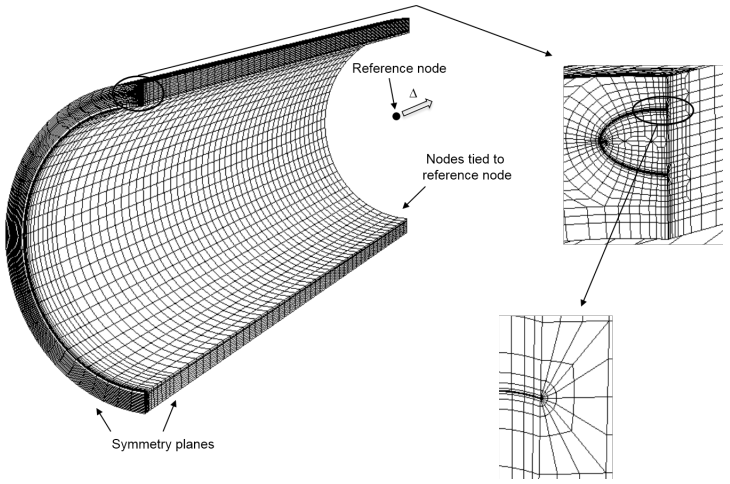


FIGURE 3. FE MODEL

Material Flow Behaviour

An elastic-perfectly plastic stress-strain response with $E = 210$ GPa and $\sigma_y = 500$ MPa, was assumed in the limit load study.

Finite-Element Analysis

The parametric study of stationary cracks was carried out with the FE model shown in Fig. 3. Due to symmetry, only a quarter model of the pipe was modelled with appropriate boundary conditions. The model length was three times the pipe outer diameter. Up to 50,000 eight-node first order solid elements with reduced integration (C3D8R in ABAQUS [18]) were used. Both crack tip regions had a focused mesh composed of 5 to 7 rings and 17 to 51 layers depending on the crack size. The smallest element size at the crack tip was up to 3% of the crack depth. The J_2 incremental plasticity with the large strain theory was used. To load the pipe in tension, displacement was applied to the reference node, indicated in Fig. 3, which was coupled to the extreme pipe nodes at the right hand side.

Results of Parametric Study

Fig. 4 shows the effect of the normalised embedded depth, p^A/a, on the normalised limit laod, P_L^{FE}/P_0, for the case of a normalised crack length, $2c/W = 0.05$. As expected, the limit load significantly decreases when the ligament decreases. The results in Fig. 5 show that P_L^{FE}/P_0 increases with the $2a/t$. This is because p^A also increases with $2a/t$. Finally, the normalised crack length has a small effect on the normalised limit load, as shown in Fig. 6.

Copyright © 2015 by ASME

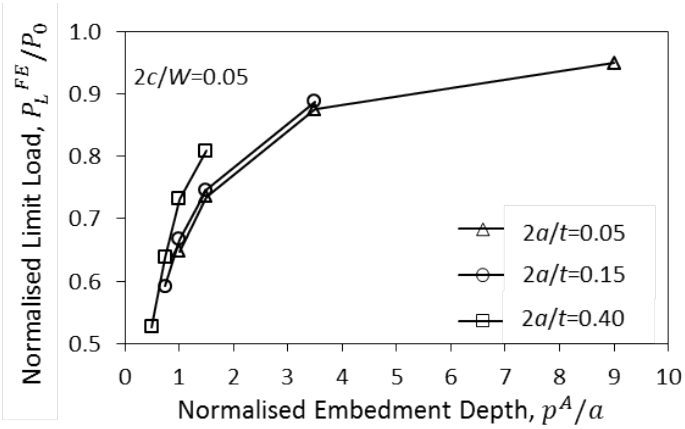


FIGURE 4. EFFECT OF NORMALISED EMBEDMENT DEPTH ON NORMALISED LIMIT LOAD

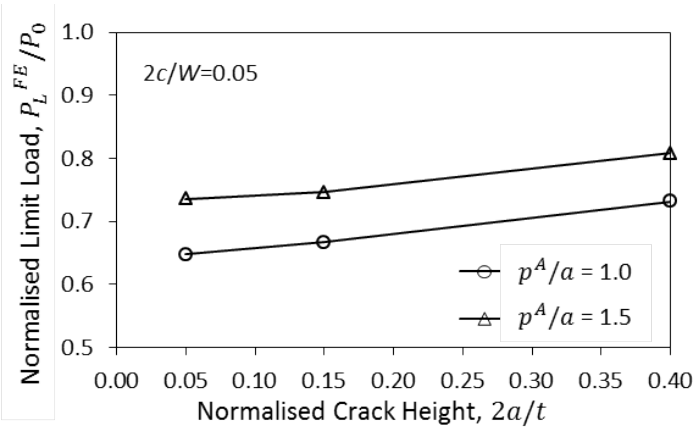


FIGURE 5. EFFECT OF NORMALISED CRACK HEIGHT ON NORMALISED LIMIT LOAD

Limit Load Solution for Embedded Girth Weld Flaws in Pipelines Subjected to Tension

The results of the parametric FE study were used to derive an analytical limit load solution for embedded flaws in pipeline girth welds. The BS7910 formulation is suitable for pipelines subjected to a combined bending and tension load mode. Therefore, it was adopted in this work

$$P_L^{NEW}(t,\alpha') = P_L^{BS}(t' = t, \alpha'' = \alpha') \tag{15}$$

where α' is an effective height to thickness ratio derived from the FE results

$$\alpha' = \left(0.1935 - 0.125\frac{2a/t}{1+40\frac{2c}{W}}\right)(p^A/a)^{-0.769} \tag{16}$$

Figs. 7 to 9 compare analytical limit loads normalised by FE

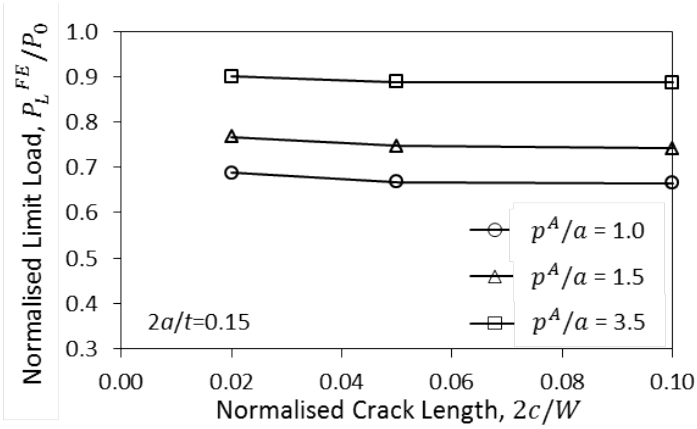


FIGURE 6. EFFECT OF NORMALISED CRACK LENGTH ON NORMALISED LIMIT LOAD

predictions. The results obtained with the BS7910 and R6 solutions are indicated by circles and triangles, respectively, while those obtained with the proposed solution are indicated by rectangles. The predictions for small and large embedment depths are indicated by open and solid symbols, respectively. A ratio in excess of 1 indicates that the analytical solution is non-conservative.

The results in Figs. 7 to 9 show that all analytical solutions are accurate for large embedment depths. However, for small embedment depths, which are the most critical, the BS7910 solution can be very conservative, while the R6 solution can be non-conservative. In contrast, the proposed solution is very accurate for all cases considered here. The error is within +/-5%. Finally, since bending is less severe than tension, it is safe to apply the proposed limit load solution to pipes subjected to bending or combined tension and bending.

J-ESTIMATION SCHEME FOR EMBEDDED GIRTH WELD FLAWS IN PIPELINES

Approach

A parametric FE study was carried out to quantify the effect of p^A, $2a$, $2c$ and ε_{app} on J at the crack tip 'A'. The FE results were then used to derive a new CDF estimation scheme for embedded girth weld flaws in pipelines subjected to tension. Subsequently, the CDF predicted using the analytical solutions in Eqns. 10 to 16 was compared against the numerical results. Finally, recommendations were made for the reeling ECA of pipeline girth welds with embedded flaws.

Pipe and Crack Geometry

Twenty seven crack geometries in Table 1, with $p^A/a \geq 1.0$, were considered.

Copyright © 2015 by ASME

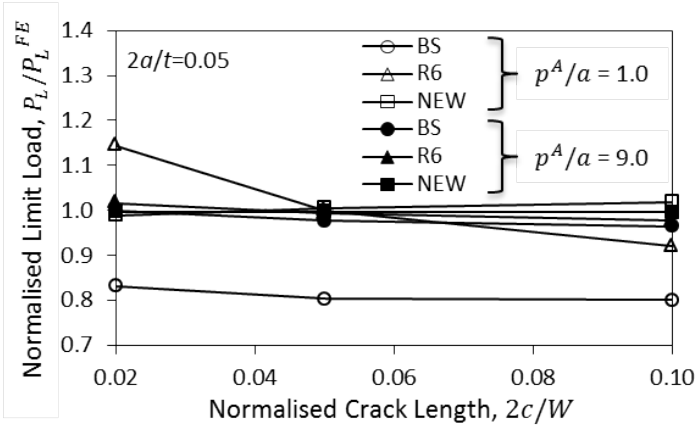


FIGURE 7. COMPARISON OF ANALYTICAL LIMIT LOAD SOLUTIONS: $2a/t = 0.05$

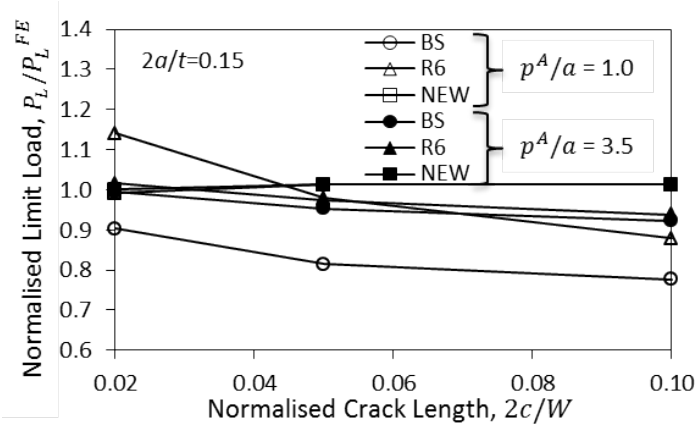


FIGURE 8. COMPARISON OF ANALYTICAL LIMIT LOAD SOLUTIONS: $2a/t = 0.15$

Material Flow Behaviour

Most reeled pipeline materials exhibit a yield plateau in the as-received condition. However, the yield plateau is usually removed during plastic deformation on the reel (first plastic strain event). In this work, an elastic-plastic stress-strain response with $E = 210$ GPa and $\sigma_y = 450$ MPa, representative of API 5L X65 [19] pipe in the strained condition, was used. The stress-strain curve, shown in Fig. 10, was expressed by the Ramberg-Osgood relationship

$$\varepsilon = \left(\frac{\sigma}{\sigma_0} + \left(\frac{\sigma}{\sigma_0}\right)^n\right)\varepsilon_0 \tag{17}$$

where $\sigma_0 = 442$ MPa and $\varepsilon_0 = \sigma_0/E$. The hardening index, $n = 16.8$ corresponds to $Y/T = 0.9$, which is typical of upper bound stress-strain curves used in DNV ECAs. The parameters, defining the stress-strain curves, are given in Table 2.

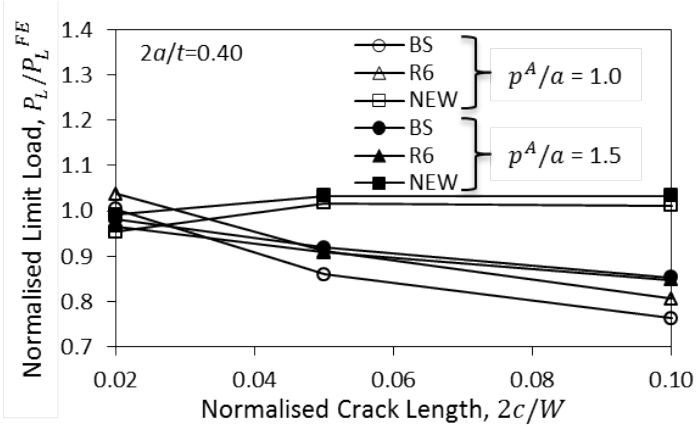


FIGURE 9. COMPARISON OF ANALYTICAL LIMIT LOAD SOLUTIONS: $2a/t = 0.40$

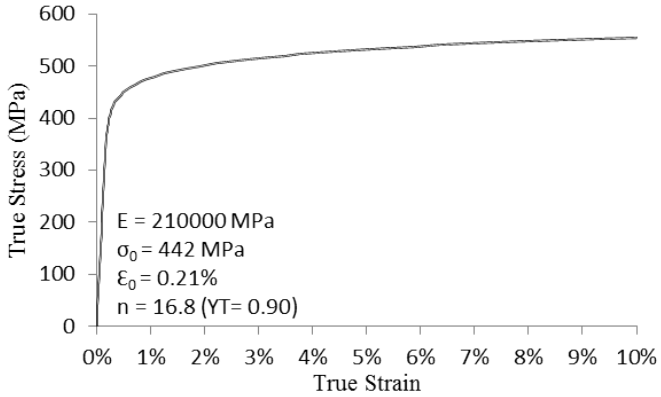


FIGURE 10. ASSUMED STRESS-STRAIN CURVE: E=210 GPa, σ_y=450 MPa, n=16.8

TABLE 2. PARAMETERS OF ASSUMED STRESS-STRAIN CURVE

E (GPa)	σ_y (MPa)	σ_0 (MPa)	ε_y (%)	ε_0 (%)
210	450	442	0.50	0.21

Finite-Element Analysis

The parametric study was carried out with the FE model shown in Fig. 3. First, an elastic analysis was carried out and K-factors were extracted at the crack tip 'A' using the contour integral method. The numerical results were in excellent agreement with the analytical results, as shown in Figs. 11 and 12. Subsequently, an elastic-plastic analysis was carried out, using the J_2 incremental plasticity with the small strain theory, and the average J from all but the first contour was computed for both crack tips. Further confidence in the FE analysis was gained from

Copyright © 2015 by ASME

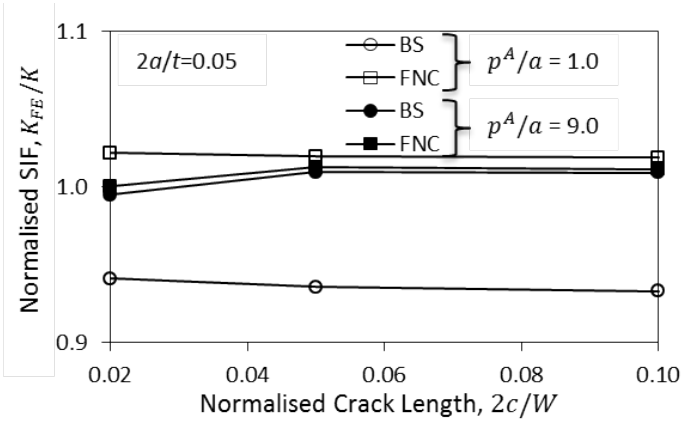


FIGURE 11. COMPARISON BETWEEN ANALYTICAL AND NUMERICAL SIF: $2a/t = 0.05$

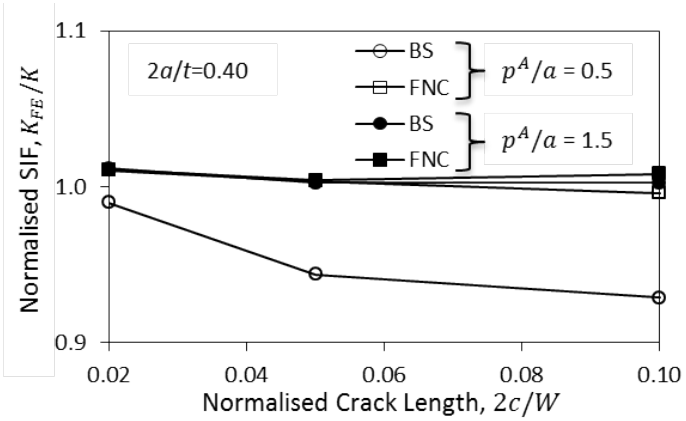


FIGURE 12. COMPARISON BETWEEN ANALYTICAL AND NUMERICAL SIF: $2a/t = 0.40$

the path independence of J values, which were within 6% of the average value. As expected, J was higher at the crack tip 'A'. J^A/J^B varied between 1.0 and 1.2 for all cases considered.

J-Estimation Scheme for Embedded Girth Weld Flaws in Pipelines Subjected to Tension

The FE predictions of J were significantly lower than the values obtained when the proposed limit load solution was used with the J-scheme in Eqn. 13. Therefore, the analytical estimate of the crack driving force needed to be adjusted. A small error in the limit load (reference stress) can be translated into a significant error in J, especially for materials with low strain hardening. Therefore, instead of correcting the limit load, as performed by the authors in [12], the reference strain, ε_{ref}, which is linearly proportional to J in the plastic regime, was adjusted to accurately predict J. J^A is estimated from

$$J^A = \frac{K^2(1-\nu^2)}{E}\left(\frac{E\tilde{\varepsilon}_{ref}}{\tilde{L}_r\sigma_y} + \frac{1}{2}\frac{\tilde{L}_r^3\sigma_y}{E\tilde{\varepsilon}_{ref}}\right) \tag{18}$$

where K is evaluated using the FNC solution in Eqn. 7. $\tilde{L}_r$ is calculated using $\tilde{\sigma}_{ref}$, which is the stress corresponding to $\tilde{\varepsilon}_{ref}$. The modified reference strain, $\tilde{\varepsilon}_{ref}$, is determined from

$$\tilde{\varepsilon}_{ref} = \gamma' \varepsilon_{ref} \tag{19}$$

where γ' is a dimensionless function derived from the FE results

$$\gamma' = \begin{cases} 0.0025\exp(9.2\frac{2a}{t}) & \text{for } 2a/t < 0.15 \text{ and } \mathrm{p^A/a} < 1.5 \\ g(\varepsilon_{app})^f & \text{otherwise} \end{cases} \tag{20}$$

where

$$g = \alpha_{ijk}(2c/\pi\, D)^i(p^A/a)^j(2a/t)^k \tag{21}$$

$$f = \beta_{ijk}(2c/\pi\, D)^i(p^A/a)^j(2a/t)^k \tag{22}$$

The constants α_{ijk} and β_{ijk} in Eqns. 21 and 22 are given in Tables 3 and 4.

J values obtained using analytical solutions are normalised by the FE predictions of J^A in Figs. 13 to 15. The results, obtained with the BS7910 limit load solution for embedded flaws and with the surface flaw solution proposed by the authors in [12] (labelled DNV-TTK), are indicated by circles and triangles, respectively. Those obtained with the solution proposed in this work are indicated by rectangles. The predictions for short and long crack lengths are indicated by open and solid symbols, respectively. A ratio in excess of 1 indicates that the analytical solution is non-conservative.

The results in Figs. 13 to 15 show that the BS7910 J-scheme is consistently too conservative when the Willoughby [8] limit load solution is used. The level of conservatism reduces when p^A increases. In contrast, a reasonable approximation of J^A is obtained for the near surface flaws when the Tkaczyk [12] limit load solution is used (i.e. DNV-OS-F101 approach with improved limit load solution). However, unlike surface breaking flaws, embedded flaws grow in two directions. Consequently, the DNV approach may significantly underestimate the crack growth for the near surface flaws in pipes subjected to elastic (e.g. during S-lay) or plastic (e.g. during reel-lay) strains during installation. Finally, the proposed J-scheme provides a good approximation of J^A for all cases considered here. The accuracy is generally within -5%/+10%.

Application Range

The range of application of the proposed J-scheme is summarised in Table 5. On-going research aims at extending the applicability to materials with a yield plateau.

Copyright © 2015 by ASME

TABLE 3. VALUES OF α_{ijk} FOR n = 16.8.

		k		
i	j	0	1	2
0	0	-0.0818	0.7358	-0.9719
0	1	0.0639	-0.6379	0.1972
0	2	-0.0032	0.0960	0.5235
1	0	0.0374	-1.1925	12.5370
1	1	-0.1416	4.3401	-34.9503
1	2	0.1177	-3.4417	23.8306

TABLE 4. VALUES OF β_{ijk} FOR n = 16.8.

		k		
i	j	0	1	2
0	0	-0.3275	0.4911	-0.8057
0	1	0.0285	-0.1199	0.5237
0	2	-0.0014	0.0169	-0.0202
1	0	0.1505	-5.6746	6.2449
1	1	-0.1002	2.1754	1.3680
1	2	-0.0057	0.2375	-2.6416

TABLE 5. RANGE OF APPLICATION

D/t	p^A/a	$2a/t$	$2c/W$	n	$\varepsilon_{app}(\%)$
$\geq$15	$\geq$1.0	$\leq$0.40	$\leq$0.10	16.8	0.50-2.50

CONCLUSION

In this work, a limit load solution has been developed for embedded girth weld flaws in pipelines subjected to tension. The accuracy of the solution is +/-5%. Since bending is less severe than tension, the solution can be safely applied to pure bending and combined tension and bending load modes. In addition, a CDF estimation scheme has been proposed, whereby the reference strain calculated using the developed limit load solution is adjusted to obtain an accurate prediction of J in the shorter ligament of an embedded flaw. The error is generally in the order of -5%/+10% when the K-solution provided in [6] is used. It is recommended that the proposed J-scheme is used for the DNV-OS-F101 – BS7910 Option 2 reeling ECA of embedded flaws in pipeline girth welds, assuming the same amount of ductile tearing at both crack tips.

It was also shown that the current DNV-OS-F101 approach, where the acceptable flaw sizes determined for the surface breaking flaws apply also to embedded flaws, may not be conservative for some cases. This is because crack growth may occur in two directions for embedded flaws, as opposed to one direction for surface breaking flaws, when the pipe is subjected to elastic (e.g. during S-lay) or plastic (e.g. during reel-lay) strains during installation. Nevertheless, there is other significant conservatism inherent in the DNV approach.

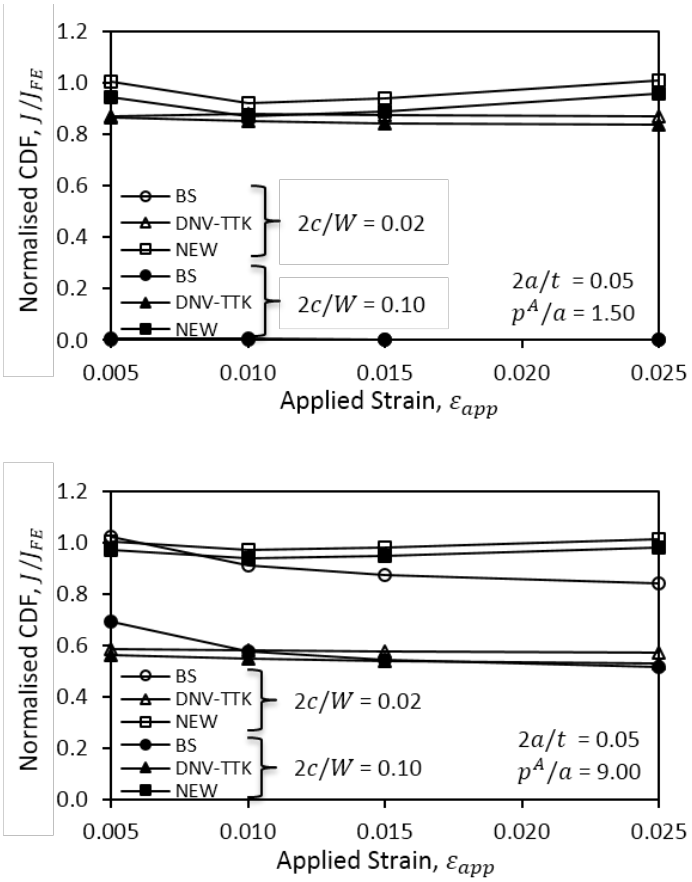


FIGURE 13. COMPARISON OF J-ESTIMATION SCHEMES for $2a/t = 0.05$

ACKNOWLEDGMENT

The authors wish to thank Sylvain Denniel from Technip for his contribution.

REFERENCES

[1] Det Norske Veritas, 2013, *DNV-OS-F101 2013: Submarine Pipeline Systems*.

[2] British Standard Institution, 2013, *BS7910: Guide to Methods for Assessing the Acceptability of Defects in Metallic Structures*.

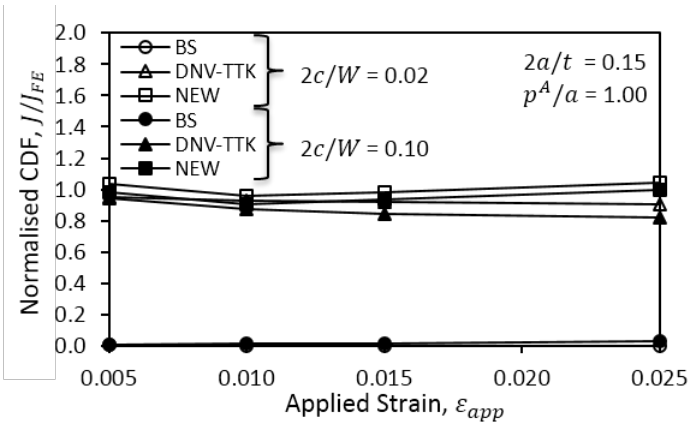
[3] R6, 2013, "Assessment of the integrity of structures containing defects", EDF Energy Nuclear Generation Ltd, R6-Revision4.

[4] Olsø, E., Berg, E., Holthe, K., Nyhus, B., Skallerud, B., Thaulow, C. and Østby, E., 2008, "Effect of embedded defects in pipelines subjected to plastic strains during operation", International Offshore and Polar Engineering Conference, ISOPE 2008.

[5] Newman, J.C. and Raju, I.S., 1984, "Stress intensity factor equations for cracks in three-dimensional finite bodies subjected to tension and bending loads", NASA Technical Memorandum 85793.

[6] Marie, S., Chapuliot, S., Kayser, Y., Lacire, M.H., Drubay, B., Barthelet, B., Le Delliou, P., Rougier, V., Naudin, C., Gilles, P. and Triay, M. (2007)., 2007, "French RSE-M and RCC-MR code appendices for flaw analysis: Presentation of the fracture parameters calculation–Part II: Cracked plates", International Journal of Pressure Vessels and Piping 84, 614 – 658.

Copyright © 2015 by ASME



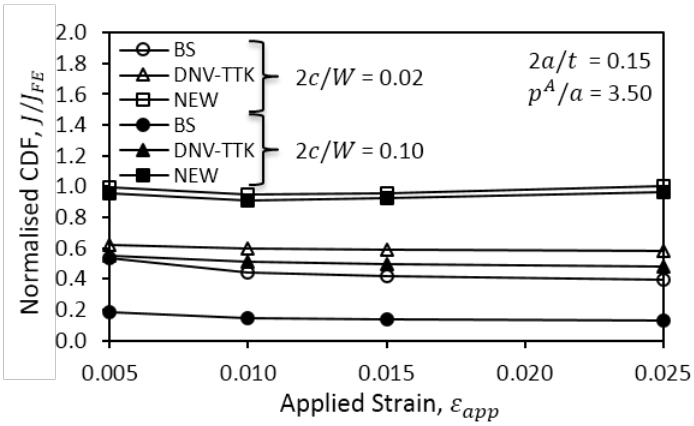
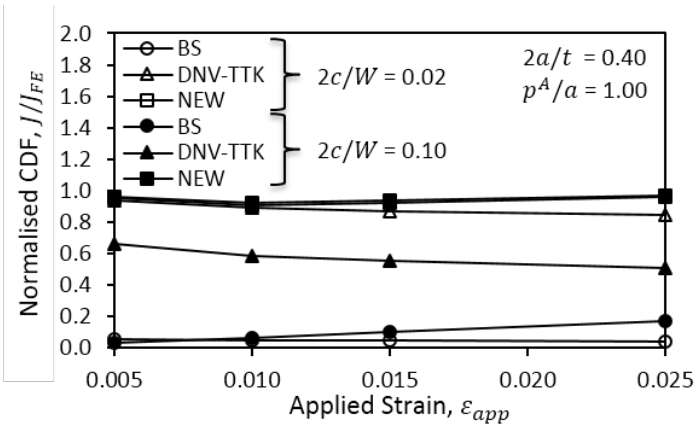


FIGURE 14. COMPARISON OF J-ESTIMATION SCHEMES for $2a/t = 0.15$



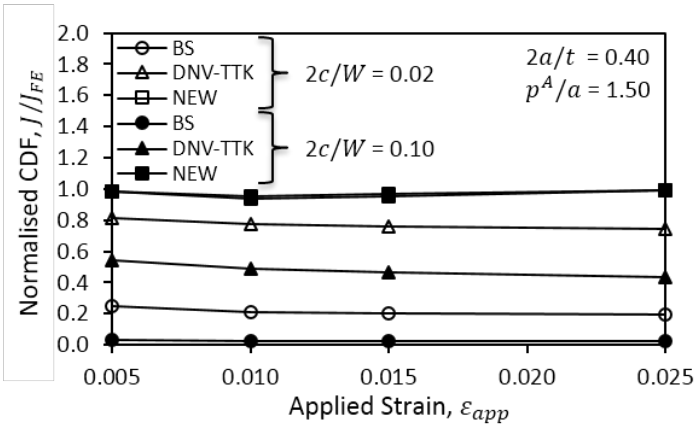


FIGURE 15. COMPARISON OF J-ESTIMATION SCHEMES for $2a/t = 0.40$

[7] Lei, Y. and Budden P.J., 2004, "Limit load solutions for plates with embedded cracks under combined tension and bending", International Journal of Pressure Vessels and Piping 81, 589 – 597.

[8] Willoughby, A.A. and Davey, T.G., 1989, "Plastic Collapse in Part-Wall Flaws in Plates", Fracture mechanics: perspectives and directions. Proceedings of the 20th national symposium. ASTM STP 1020. Bethlehem, PA, 1989, 390 – 409.

[9] Kastner, W.E., Rohrich, E., Schmitt, W., and Steinbuch, R., 1981, "Critical crack sizes in ductile piping", International Journal of Pressure Vessels and Piping 09, 197 – 219.

[10] Tkaczyk, T., O'Dowd, N.P. and Howard, B.P., 2007, "Comparison of Crack Driving Force Estimation Schemes for Weld Defects in Reeled Pipelines", International Offshore and Polar Engineering Conference, ISOPE 2007.

[11] Kim, Y.-J., and Budden, P. J., 2002, "Reference stress approximations for J and COD of circumferential throughwall cracked pipes", International Journal of Fracture 116, 195 – 218.

[12] Tkaczyk, T., O'Dowd, N.P., and Nikbin, K., 2009, "Fracture Assessment Procedures for Steel Pipelines using a Modified Reference Stress Solution", Journal of Pressure Vessel Technology - Transactions of the ASME Volume 131, Issue 3, Article Number 031409.

[13] Østby, E., 2005, "Fracture Control, Offshore Pipelines JIP - New strain-based fracture mechanics equations including the effects of biaxial loading, mismatch and misalignment", International Conference of Offshore Mechanics and Arctic Engineering, OMAE2005-67518.

[14] Østby, E., 2007, "Fracture Control, Offshore Pipelines JIP - Proposal for strain-based fracture assessment procedure", International Offshore and Polar Engineering Conference, ISOPE 2007.

[15] Parise, L.F.S., Ruggieri, C. and O'Dowd, N.P., 2013, "FULLY-PLASTIC STRAIN-BASED J ESTIMATION SCHEME FOR CIRCUMFERENTIAL SURFACE CRACKS IN PIPES SUBJECTED TO REELING", ASME 2013 Pressure Vessels and Piping Conference, PVP2013-97794.

[16] Yi, D., Xiao, Z.M., Idapalapati, S. and Kumar, S.B., 2012, "Fracture analysis of girth welded pipelines with 3D embedded cracks subjected to biaxial loading conditions", Engineering Fracture Mechanics 96, 570 – 587.

[17] Zhang, Y.M., Xiao, Z.M. and Zhang, W.G., 2013, "Fracture analysis of girth welded pipelines with 3D embedded cracks subjected to biaxial loading conditions", Theoretical and Applied Fracture Mechanics 67-68, 22 – 28.

[18] *Abaqus Version 6.13 Documentation*.

[19] American Petroleum Institute, 2007, *API 5L 2007: Specification for Line Pipe, 44th edition*.

Copyright © 2015 by ASME

Appendix C

Paper No. 3 – Qualification of Reeled Mechanically Lined Pipes for Fatigue Service

International Journal of Offshore and Polar Engineering (ISSN 1053-5381)
Copyright © by The International Society of Offshore and Polar Engineers
Vol. 26, No. 3, September 2016, pp. 296–303; http://dx.doi.org/10.17736/ijope.2016.bn09

http://www.isope.org/publications/publications.htm

Qualification of Reeled Mechanically Lined Pipes for Fatigue Service

Aurelien Pepin and Tomasz Tkaczyk
Offshore Engineering Division, Technip UK
Westhill, Aberdeenshire, UK

Noel O'Dowd
Materials and Surface Science Institute, University of Limerick
Limerick, Ireland

Kamran Nikbin
Department of Mechanical Engineering, Imperial College
London, UK

To meet an increasing demand for conveying corrosive fluids in the subsea oil and gas sector, the authors have proposed a design of mechanically lined pipe (MLP) that enables reel-lay installation under atmospheric pressure without the risk of wrinkling of the corrosion resistant alloy (CRA) lining. The novel design was qualified for reeling and subsequent service life in accordance with DNV-RP-A203. To provide further evidence that a high fatigue performance can be achieved before a carbon steel backing pipe is exposed to corrosive constituents, a qualification programme, detailed in this paper, was undertaken. In addition, a 3D finite element (FE) study was performed on MLPs with interface flaws between the liner and clad overlay weld, and recommendations for the fatigue assessment of MLPs with interface flaws were made.

INTRODUCTION

An increasing demand for the transport of corrosive constituents in the subsea oil and gas sector is creating a growing demand for high-strength pipelines with enhanced corrosion resistance such as bimetal pipes. These include hot roll bonded (HRB) clad pipes and mechanically lined pipes (MLPs). The latter are made of a corrosion resistant alloy (CRA) liner adhering to a backing carbon steel pipe by means of an interference fit. MLPs are generally more readily available and cheaper than both solid stainless steel and HRB clad pipes.

Reel-lay is a highly effective installation method, which is an alternative to S-lay and J-lay, for the installation of small to medium-sized subsea pipelines. Reeled pipes are subjected to plastic straining during installation. Although it has been suggested that such plastic straining may reduce the fatigue performance of reeled pipes, no detrimental effect was found in recent works, e.g., Gray et al. (2009). However, plastic straining of the MLP during reeling may trigger wrinkling of the CRA liner if reeling is not properly managed.

Technip has developed and patented a design of the MLP with an increased liner thickness that enables reel-lay installation at atmospheric pressure without the risk of liner wrinkling, thus combining an economically attractive MLP product with a very efficient reel-lay method (Pepin and Tkaczyk, 2011). In accordance with the guidance provided in DNV-RP-A203 (2011), the novel design was qualified for reeling and a subsequent static service in 2011 (Tkaczyk et al., 2011; Pepin et al., 2011). Subsequently, six API 5L X65 (API 5L, 2007) carbon steel pipes lined with alloy 625 with a nominal outer diameter $D = 10.75"$ (273.1 mm) and a total wall thickness $t = 26.5$ mm were qualified for fatigue service (Tkaczyk et al., 2012a). Clad overlay and girth welding were carried out through the use of alloy 625 (ERNiCrMo-3) consumables. Overlay cladding was internally machined, whereas girth weld caps were ground flush. The test strings were subjected to two bending cycles in one plane followed by two bending cycles in a perpendicular plane to simulate perpendicular reeling. Visual inspection carried out on completion of the bending trials confirmed no signs of damage to the liner. Subsequently, the test strings were fatigue tested at positive stress ratios until failure (loss of internal pressure) occurred or until the run-out condition (the DNV class C target curve) was achieved. Fatigue cracks were initiated from lack of fusion flaws, similar to that shown in Fig. 1, in three test pipes. The lack of fusion flaws were approximately 1 mm in height. The post-mortem examination of fracture faces suggested that the anti-corrosion barrier was not breached until after the crack had reached the carbon steel outer surface. The fourth failure initiated from a blemish at the outer surface of the pipe. Specimens tested at the lowest stress range reached the run-out condition without failure. Overall, the fatigue life was above the DNV class D target curve (DNV-RP-C203, 2011). Following this study, DNV endorsed the design of MLPs reeled at atmospheric pressure for dynamic service.

Toguyeni and Banse (2012) tested three API 5L X65 carbon steel pipes lined with alloy 625 to qualify MLPs reeled under internal pressure for steel catenary riser (SCR) service. The MLPs had a nominal outer diameter $D = 8.625"$ (219.1 mm) and a total wall thickness $t = 21.3$ mm. Each test string had 50-mm-long machined clad overlay welds on either side of a central CRA girth weld. Girth weld caps were ground flush. Clad overlay and girth welding were carried out through the use of alloy 625 consumables. The test strings were internally pressurised to 30 bar and subjected to bending to simulate pressurised reeling. Subsequently, the pipes were fatigue tested at positive stress ratios until the DNV class F1 target curve (DNV-RP-C203, 2011) was

Received July 18, 2015; updated and further revised manuscript received by the editors February 5, 2016. The original version (prior to the final updated and revised manuscript) was presented at the Twenty-fifth International Ocean and Polar Engineering Conference (ISOPE-2015), Kona, Hawaii, June 21–26, 2015.

KEY WORDS: Mechanically lined pipe, reel-lay installation, steel catenary riser, fatigue strength, stress intensity factor.

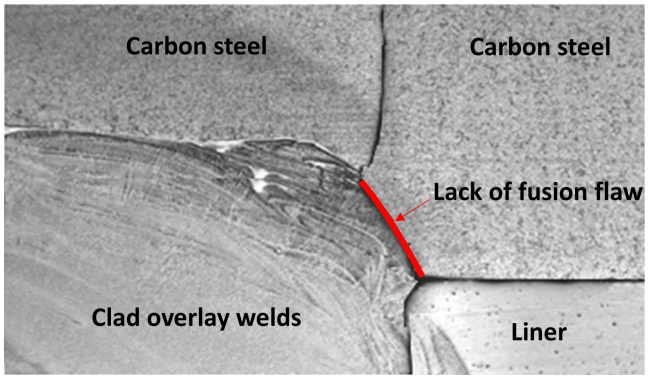


Fig. 1 Flaw between carbon steel pipe and clad overlay weld

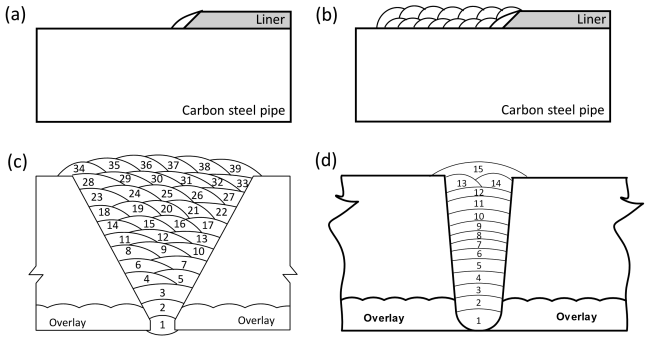


Fig. 2 Weld profiles: (a) Seal, (b) Clad overlay, (c) Manual girth weld, and (d) Mechanised girth weld

achieved. No failure (pressure loss) occurred in the test. Post-test examination confirmed that no through-thickness cracks had developed in the CRA layer.

In the current work as part of a programme to qualify a new supplier of reelable MLPs, Technip undertook full-scale bending and fatigue testing. Nondestructive examination (NDE) was carried out at various stages of fatigue testing to provide further evidence that MLPs reeled at atmospheric pressure can achieve a high fatigue performance without breaching the anti-corrosion barrier. In addition, a 3D finite element (FE) study was performed on MLPs with interface flaws between the liner and clad overlay weld. Finally, on the basis of the results of these studies, recommendations for the fatigue assessment of MLPs with interface flaws were made.

EXPERIMENTAL PROCEDURES

Approach

An approach similar to that detailed in Tkaczyk et al. (2012a) was followed in this work. The liner thickness was designed and MLP joints were manufactured in accordance with the Technip specification that builds on API 5LD (2009). Subsequently, 12 MLP strings were subjected to two symmetrical bending cycles at atmospheric pressure to simulate reeled installation. After pre-straining, the specimens were subjected to fatigue testing in a resonant rig under a positive stress ratio at three constant stress ranges.

Statistically-based target S-N curves, which depend on the number of specimens tested ($n = 6$ in this work), were derived in accordance with recommendations in BS7608 (2014). To meet the DNV design curve at the 95% confidence interval, the specimens had to achieve lives at least $f = 1.36$ times higher than those corresponding to a respective DNV mean curve.

Manufacturing of Test Strings

MLP joints with a nominal outer diameter $D = 8.625"$ (219.1 mm) and a total wall thickness $t = 32.1$ mm were manufactured through the use of API 5L X65 host pipes and alloy 625 liners. The joints were split into 12 pup pieces, each 2.6 m long. One end of each pup piece was terminated with a seal weld and a 150-mm-long clad overlay weld. The liner at the other end was sealed 400 mm away from the pup piece end, which left a bare backing steel pipe. Seal welding was carried out in a single pass through the use of a mechanised pulsed gas tungsten arc welding (GTAW) process with a single wire in the 2F position (see Fig. 2a). In contrast, clad overlay welding was performed in two passes through the use of a mechanised pulsed GTAW process with a twin wire in the 1G position (see Fig. 2b). Alloy 625 (ERNiCrMo-3) consumables were used for both procedures. Subsequently, each overlay clad pipe end was counterbored to a constant inner diameter and flapped to leave a smooth transition between the liner and clad overlay weld. The pup pieces were then heated in a furnace to 250 °C for five minutes to simulate the application of insulation coating. On completion of the nondestructive examination (NDE), the pup pieces were shipped to the Technip spoolbase in Evanton, UK for girth welding.

Each overlay clad pipe end was first scanned with a laser tool, and 2D cross-sectional profiles of the inner and outer pipe surfaces were produced. The profiles were then analysed and matched together to achieve a target internal hi-lo (a mismatch at the pipe inner surface) of 0.5 mm, which is typical of SCRs or flowlines designed for fatigue service. Subsequently, 12 couples of pup pieces were girth welded together in the 5G position to produce six strings with manual welds and six strings with mechanised welds. The manual welds were deposited in 39 passes through the use of a GTAW process with ERNiCrMo-3 (alloy 625) consumables (see Fig. 2c). The mechanised welds' root, hot, and first fill passes were deposited through the use of a pulsed gas tungsten arc welding (P-GTAW) process with ERNiCr22Mo-20 (alloy 660) consumables. The following 11 passes (including strips) were laid through the use of a P-GMAW process with ERNiCrMo-3 consumables, and finally the cap was deposited through the use of a P-GTAW process with ERNiCrMo-3 consumables (see Fig. 2d). After the flush grinding of CRA weld caps, 3-m-long carbon steel pup pieces were girth welded to each end of each fatigue string to produce 11.2-m-long bending strings. Finally, NDE of girth welds was carried out. The maximum allowed flaw sizes were representative of the acceptance criteria for a typical SCR.

Simulation of Reel-Lay Installation

The test strings were bend tested at atmospheric pressure at Heriot-Watt University in the UK. The bending rig was equipped with an 8.23-m-radius reeling former corresponding to the smallest reel hub radius of the Technip reel-lay fleet, and the strings were subjected to two symmetrical bending cycles to simulate reeled installation. The corresponding bending strain was 1.63%. On completion of bending, visual inspection was carried out. No signs of wrinkling, buckling, or other damage to the liner were observed. Subsequently, the sacrificial carbon steel pup pieces were cut off to produce 12 5-m-long fatigue test strings labelled FS01 to FS12, which were shipped to TWI in Cambridge, UK for fatigue testing.

Fatigue Test Procedure

After end caps were welded at both ends of each string, a vent hole, indicated in Fig. 3, was drilled through the carbon steel layer to allow air to escape when the pipe was filled with water. Subsequently, the specimens were instrumented with two rings of eight TML-type PFL-20-11 strain gauges and connected to a data logging system. The gauges, which were located 300 mm apart and above the transitions between the liner and clad overlay weld, were equispaced around the pipe circumference, as shown in Fig. 3. In order to detect potential liner cracking before a through-wall crack developed in the carbon steel backing pipe, the escape ports, shown in Fig. 3, were drilled through the carbon steel at each end of the test string. In addition, a colorant was added to the water to ease detection of a leak should this occur.

The test strings were mounted in a resonance test machine filled with water and pressurised to achieve an axial mean stress of 90 MPa. Then they were fatigue tested at ambient temperature at a frequency of approximately 30 Hz. Two specimens were tested at 80 MPa, 120 MPa, and 175 MPa constant amplitude stress ranges, as detailed in Table 1.

The results of the fatigue tests, which were undertaken earlier by the authors and summarised in the introduction, suggested that girth welded MLPs should not fail before reaching the DNV class D and C target curves when tested at the medium/high and low stress ranges, respectively. Therefore, the specimens FS03 to FS06 and FS09 to FS12 were first fatigue tested until the DNV class D target curve was reached. Testing was then stopped, and the specimens were slowly depressurised to allow water to travel to the escape ports if a through-thickness crack had developed in the CRA layer. Subsequently, the end cap on the drive end side was cut off, and the specimens were dewatered and internally inspected as detailed in the following section. After inspection and rewelding of the end cap, the specimens were filled with water and pressurised. Finally, fatigue testing was resumed; all 12 specimens (FS01 to FS12) were tested until failure (pipe leakage) or the run-out condition (the DNV class C target curve) was reached.

On completion of testing, a central section of each specimen was cut out. The exposed inner region containing the girth and clad overlay welds was subjected to NDE. Any cracks discovered were then cut longitudinally and extracted, chilled in liquid nitrogen, and broken open to expose the fracture faces for fractographic examination.

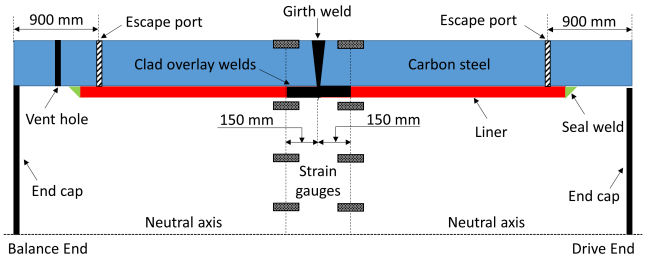


Fig. 3 Preparation of fatigue test string

String Number	Mean Stress (MPa)	Stress Range (MPa)	Stress Ratio R
FS01, 02, 07, 08	90	80	0.38
FS03, 04, 09, 10	90	120	0.20
FS05, 06, 11, 12	90	175	0.01

Table 1 Fatigue test regime

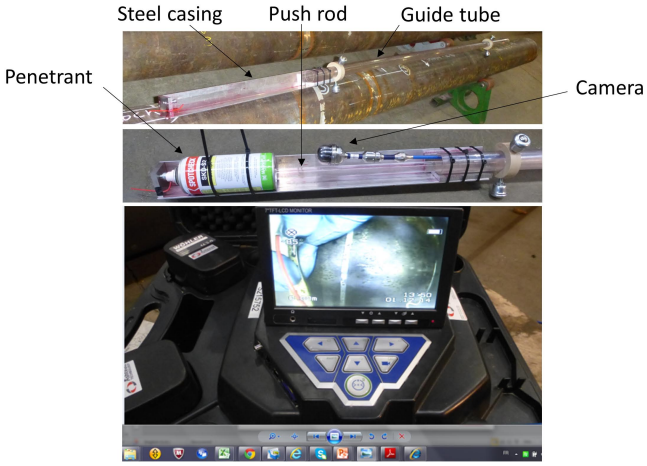


Fig. 4 DPI inspection tool

Nondestructive Examination

A dedicated inspection tool, shown in Fig. 4, was built to allow Dye Penetrant Inspection (DPI) of the interface between the liner and clad overlay weld located 2.5 m away from the pipe end. The DPI was undertaken in three stages: (1) prior to fatigue testing; (2) after the DNV class D target curve was reached; and (3) after the test completion.

After the internal surface of the specimen was verified to be clean, the specimen was rotated while the penetrant was sprayed and allowed to set for approximately 30 minutes. Then the penetrant was removed through the use of a cloth dampened with a solvent, and a developer was sprayed on the surface. It was allowed to set for approximately seven minutes. Finally, a video inspection was carried out to note the position and length of any indication found.

When suspicious indications were found through the intermediate DPI after the DNV class D target curve was reached, a supplementary Eddy Current Testing (ECT) was carried out through the use of a 700 kHz Hocking locator probe, type 29P106, linked

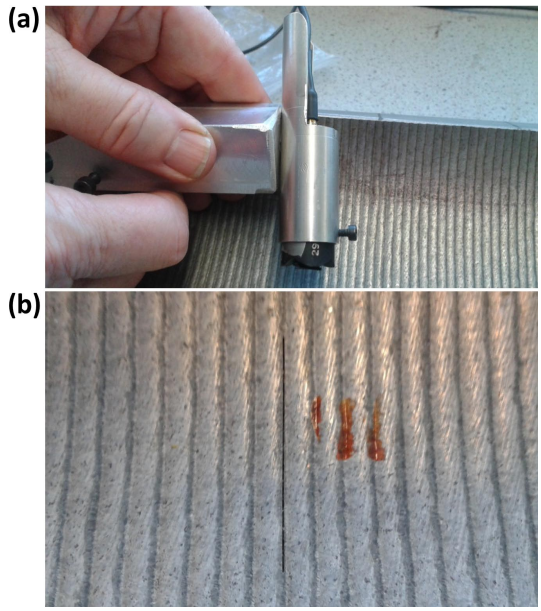


Fig. 5 Eddy current testing: (a) Probe and (b) Calibration block with 3-mm-deep notch

to a Phasec 2200 acquisition system. The Hocking 29P106 locator probe, shown in Fig. 5a, was calibrated against notches introduced in unmachined clad overlay welds shown in Fig. 5b. The ECT probe was first run by hand across a 1-mm notch in the calibration block to verify that it was set up properly. Subsequently, the ECT probe was mounted on the leading edge of the DPI inspection tool that was positioned over the area to be inspected. The probe was then balanced and finally moved forward to scan the indication. The setup was such that the probe was slightly pressed against the inner pipe surface.

Fatigue Test Results

Although the DPI of the liner to clad overlay weld transition revealed the presence of linear indications, shown in Fig. 6a, in all six specimens, the DNV class C target curve was achieved for specimens tested at a low stress range (FS01-FS02, FS07-FS08) without any signs of pressure loss or leak.

Similar indications were found in the medium (FS03, FS04, FS09, FS10) and high (FS05, FS06, FS11, FS12) stress range specimens during the intermediate DPI after the DNV class D target curve was reached. The response amplitude measured by the ECT was below the threshold, corresponding to a 1-mm-high notch for all the aforementioned test strings except FS05. In the case of FS05, the response amplitude was less than the threshold, corresponding to a 2 mm notch height. This indicates that the DNV class D target curve was reached for all specimens without breaching the anti-corrosion barrier.

When fatigue testing was resumed, the test string FS05 failed at the location indicated by the ECT before reaching the DNV class C target curve. The fractographic examination revealed that the failure initiated from flaws between the carbon steel and clad overlay weld and between the liner and clad overlay weld. The cracks grew in both the carbon steel pipe towards the pipe's outer surface and the CRA layer towards the pipe's inner surface, seemingly reaching the inner surface before the pipe leakage. The examination of the strain gauge histograms suggested that the

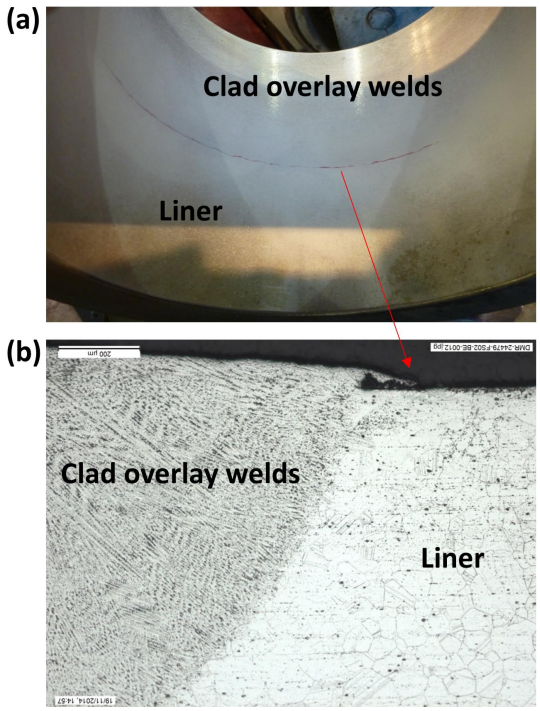


Fig. 6 Post-mortem examination: (a) DPI indication and (b) Macro-section

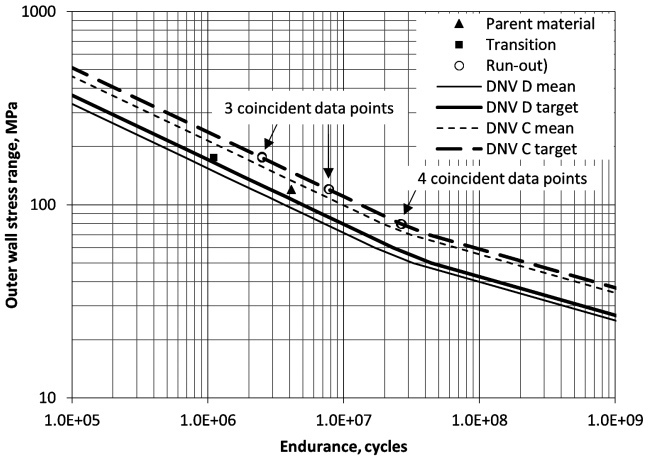


Fig. 7 Fatigue test results vs. DNV-RP-C203 SN curves (DNV-RP-C203, 2011)

anti-corrosion barrier was breached after 1.2 million cycles, i.e., 75% of the total life, were reached. The test string FS04 failed 300 mm away from the girth weld, i.e., 150 mm away from the nearest liner to clad overlay weld transition, before the DNV class C target curve was reached. An inspection of the fracture faces revealed that cracking initiated from a blemish at the outer surface of the pipe. In contrast, for the test strings FS03, FS06, and FS09-FS12, the DNV class C target curve was reached without any signs of pressure loss or leak. The post-mortem examination confirmed that all indications found through the DPI during the initial and intermediate NDE were cold laps, similar to the one shown in Fig. 6b, that were not completely removed when clad overlay welds were flapped after machining. No fatigue failure initiated from these features.

The fatigue test results, in terms of the number of cycles to failure versus the stress range at the pipe's outer surface, are compared in Fig. 7 with the DNV-RP-C203 C (labeled DNV C target) and D (labeled DNV D target) target curves (DNV-RP-C203, 2011). In addition, the DNV C and D mean curves are plotted in Fig. 7 and indicated by the thin dashed lines and thin solid lines, respectively. Stresses at the pipe's outer surface have been calculated through interpolation between strain gauge readings; no Stress Concentration Factor (SCF) has been included. The failure that initiated at the liner to clad overlay weld transition is indicated by the solid square, while the remaining failure is indicated by the solid triangle. Finally, the run-outs are indicated by the open circles.

The fatigue test results for reeled MLP, expressed in terms of outer wall stress ranges, lie above the DNV class D target curve. Furthermore, 10 (four strings with manual girth welds and six strings with mechanised girth welds) out of 12 data points in Fig. 7 are above the DNV class C target curve. This demonstrates that lined pipes reeled at atmospheric pressure are suitable for demanding SCR and fatigue sensitive flowline service.

FATIGUE ASSESSMENT OF MECHANICALLY LINED PIPES WITH INTERFACE FLAWS

General

A methodology for the fracture assessment of MLPs with interface flaws was laid out in Tkaczyk et al. (2012b). However, no guidance on the MLP fatigue design was found in the literature. Therefore, the authors undertook a numerical study, described hereafter, and provided recommendations for carrying out the

fatigue assessment of the MLP with flaws at the interface between the liner and overlay cladding.

Fatigue crack growth assessment of subsea pipeline girth weld flaws can be carried out in accordance with the guidance provided in DNV-OS-F101 (2013). Often, the stress intensity factor solutions (K-solutions) in BS7910 (2013) are used. BS7910 also provides fatigue crack growth curves (FCGCs) for aluminium alloys and austenitic and carbon steels, but none for nickel-based alloys.

DNV-OS-F101 suggests that the Raju and Newman K-solution for surface flaws in plates can be used to estimate K for surface flaws in pipes:

$$K_I = f_w(M_m P_m + M_b P_b)\sqrt{\pi a} \quad (1)$$

where P_m and P_b are the applied membrane and bending stresses, respectively, whereas f_w, M_m, and M_b are dimensionless functions of the geometry and the location along the crack front. A similar formulation is given in the French nuclear codes (FNCs) RSE-M and RCC-MR:

$$K_I = (i_0 P_m + F_{gb} P_b)\sqrt{\pi a} \quad (2)$$

The values of the dimensionless functions i_0 and F_{gb} in Eq. 2 are given in Marie et al. (2007) for internal and external circumferential flaws. The suitability of the K-solutions in Eqs. 1 and 2 for the fatigue assessment of MLPs with interface flaws is investigated in the following sections.

Approach

First, the case of a single pipe (SP) with a surface flaw was analysed through the use of the finite element method, and the obtained K values were compared to the analytical K-solutions given by Eqs. 1 and 2. Subsequently, the case of an MLP with an interface flaw was analysed numerically, and the obtained results were compared with the FE and analytical predictions for an SP. Finally, a fatigue design approach for MLPs with interface flaws was proposed, and a case study was undertaken to evaluate its robustness.

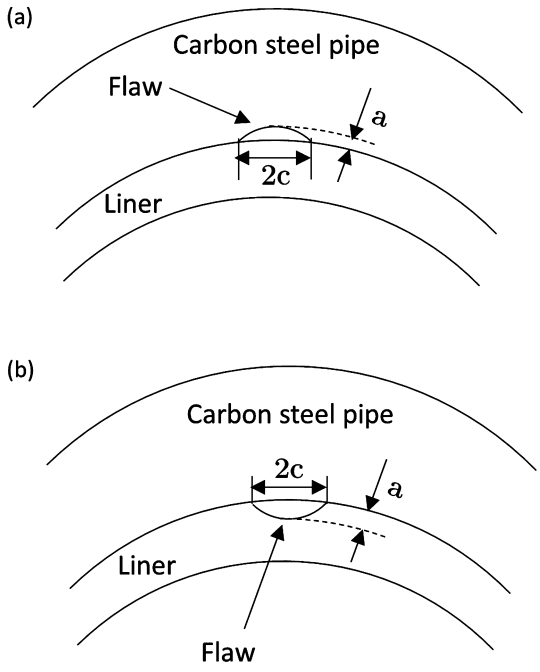


Fig. 8 MLP semi-elliptical interface flaws: (a) Carbon steel flaw and (b) Liner flaw

D (mm)	t_c (mm)	t_l (mm)	a/t	$2c/\pi D$
168.3 219.1 323.9	14.3, 25.4	3.0	0.035, 0.10, 0.30	0.02, 0.07, 0.20

Table 2 FE case matrix: Carbon steel crack geometries

D (mm)	t_c (mm)	t_l (mm)	a/t	$2c/\pi D$
168.3 219.1 323.9	25.4	3.0, 4.1	0.035, 0.10, 0.30	0.02, 0.07, 0.20

Table 3 FE case matrix: CRA crack geometries

Pipe and Crack Geometry

MLPs with the nominal outer diameter, D, in the range between 168.3 mm and 323.9 mm, the carbon steel wall thickness, t_c, in the range between 14.3 mm and 25.4 mm, and the liner thickness, t_l, in the range between 3.0 mm and 5.0 mm were considered. The normalised crack depth, a/t, in the range between 0.035 and 0.300 and the normalised crack length, $2c/\pi D$, in the range between 0.02 and 0.10 were assumed. Semi-elliptical, part-circumferential interface cracks between the carbon steel and clad overlay weld and between the liner and clad overlay weld, illustrated in Fig. 8, were analysed. In total, 48 crack geometries detailed in Tables 2 and 3 were considered.

Material Flow Behaviour

The carbon steel and CRA materials were assumed to be elastic, with Young's modulus $E = 207$ GPa and 200 GPa, respectively.

Finite Element Analysis

A parametric FE study was performed through the use of ABAQUS (2013). Figure 9 depicts a typical FE mesh of an MLP with a semi-elliptical interface flaw composed of up to 300,000 eight-node linear hexahedral elements with reduced integration (C3D8R in ABAQUS). Due to symmetry, only a quarter model of the pipe was built. The model length was three times the pipe outer diameter, and the overlay welds were 150 mm long for all cases. The crack tip region, shown in Fig. 9c, had a focused mesh composed of five to seven rings and 17 to 51 layers depending on crack and pipe geometries. The smallest element size at the crack tip was of the order of 3% of the crack depth, a. A tie contact was used to simulate the metallurgical bond between carbon steel and overlay cladding. In contrast, a frictionless (with negligible effect on K), finite-sliding contact formulation with hard

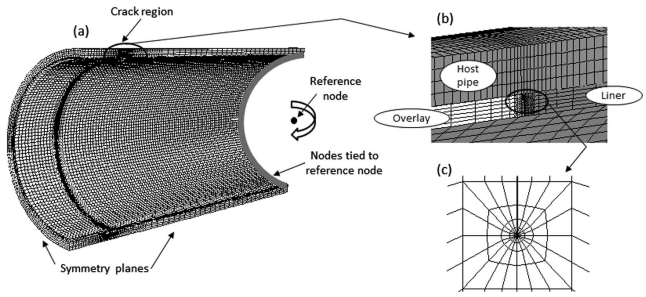


Fig. 9 Finite element model: (a) and (b) Typical mesh and (c) Liner crack tip mesh (adapted from Tkaczyk et al., 2012b)

D (mm)	t_c (mm)	a (mm)	$2c$ (mm)	K_{SP}/K_{BS}	K_{SP}/K_{FNC}
168.3	14.3	0.50	10.6	0.85	1.03
		0.50	105.7	0.85	1.04
		1.43	37.0	0.85	1.03
		4.29	105.7	0.83	1.03
323.9	25.4	0.89	20.4	0.86	1.02
		0.89	203.5	0.86	1.04
		2.54	71.2	0.86	1.03
		7.62	203.5	0.84	1.03

Table 4 Selected results for cracks in single carbon steel pipe

d (mm)	t_l (mm)	a (mm)	$2c$ (mm)	K_{SP}/K_{BS}	K_{SP}/K_{FNC}
117.5	3.0	0.11	10.6	1.02	1.06
		0.11	26.4	1.02	1.06
		0.30	37.0	1.03	1.09
		0.90	105.6	0.98	1.03
168.3	4.1	0.14	13.8	1.02	1.06
		0.14	41.4	1.01	1.06
		0.41	48.2	1.02	1.08
		1.23	137.6	0.99	1.05

Note: d is the outer diameter of the liner.
Table 5 Selected results for cracks in single liner pipe

surface behavior was used to model the interaction between the liner and carbon steel pipe. A radial gap of 0.1 mm was assumed between the liner and carbon steel pipe to simulate the loss of interference stress resulting from the coating application and/or plastic deformation during reeling. Symmetry boundary conditions were applied to the nodes on the left-hand side of the model. The nodes on the right-hand side of the model were coupled to a reference node. Rotation was applied to the reference node to impose bending. Single pipe (either carbon steel or CRA liner) and MLP configurations were considered. A total of 96 FE analyses (48 geometries and two pipe configurations) were performed, and the K values at the deepest point of the crack were extracted through the use of the contour integral method.

Results

Single Pipe. The FE predictions obtained for an SP subjected to bending (K_{SP}) are normalised in Tables 4 and 5 by the BS7910 (K_{BS}) and FNC (K_{FNC}) analytical results for the bending load mode. A ratio less than 1 indicates that the analytical solution overestimates the FE predictions. The Raju-Newman solution generally overestimates the FE predictions. Not surprisingly, there is better agreement between the FE results and the predictions obtained through a more recent FNC solution that was derived by the fitting of polynomial functions to the results of FE analyses. When the FNC solution is used, the maximum error (underestimation) is 10% for all cases considered in this study. (It should be noted that the case with 10% error is not shown in the tables.)

Mechanically Lined Pipe. The FE predictions obtained for interface flaws in MLPs subjected to bending are normalised by the numerical and analytical results for SPs with surface flaws listed in Tables 6 and 7. The normalised K lower than 1 indicates that either an SP FE or an SP analytical solution is conservative. The level of conservatism varies between 4% and 15% for all cases considered in this study. (It should be noted that the case with 15% error is not shown in the tables.) Lower K values are

D (mm)	t (mm)	a (mm)	$2c$ (mm)	K_{MLP}/K_{SP}	K_{MLP}/K_{BS}	K_{MLP}/K_{FNC}
168.3	14.3 + 3.0	0.50	10.6	0.88	0.75	0.88
		0.50	105.7	0.92	0.78	0.92
		1.43	37.0	0.92	0.78	0.92
		4.29	105.7	0.93	0.77	0.93
323.9	25.4 + 3.0	0.89	20.4	0.89	0.77	0.89
		0.89	203.5	0.93	0.80	0.93
		2.54	71.2	0.93	0.80	0.93
		7.62	203.5	0.95	0.80	0.95

Table 6 Selected results for cracks in carbon steel pipe of MLP

D (mm)	t (mm)	a (mm)	$2c$ (mm)	K_{MLP}/K_{SP}	K_{MLP}/K_{BS}	K_{MLP}/K_{FNC}
168.3	25.4 + 3.0	0.11	10.6	0.86	0.88	0.92
		0.11	26.4	0.87	0.88	0.93
		0.30	37.0	0.88	0.91	0.96
		0.90	105.6	0.84	0.83	0.88
323.9	25.4 + 4.1	0.14	13.8	0.87	0.88	0.92
		0.14	41.4	0.88	0.88	0.92
		0.41	48.2	0.89	0.91	0.96
		1.23	137.6	0.85	0.83	0.89

Table 7 Selected results for cracks in liner of MLP

predicted for the MLP configuration compared to the SP configuration because the metallurgical bond between the carbon steel and overlay cladding restricts the opening of the crack.

The FE predictions for MLPs subjected to bending and the FNC solutions for bending are in good agreement for all cases considered in this study. Somewhat worse agreement was obtained between the BS7910 solution and the FE results, especially for cracks in the carbon steel backing pipe. Therefore, the fatigue assessment of MLPs with interface flaws can be conservatively performed through the use of the FNC K-solutions for an SP with a surface flaw under bending.

Most failures in the fatigue test programme detailed in Tkaczyk et al. (2012a) initiated from interface flaws approximately 1 mm high. In addition, the NDE detectability limit was near 1 mm for interface flaws. For example, Zumpano et al. (2012) speculated that 1-mm flaws with a length of 20 mm could be found by radiography testing. Consequently, the crack depth of 1 mm was assumed in this study, while the crack length varied from 15 mm to 25 mm. Interface flaws in both the carbon steel pipe and liner were considered.

The fatigue crack growth assessment was carried out through the use of the FNC K-solution for semi-elliptical circumferential cracks in pipes subjected to bending. The mean BS7910 FCGC for steel in air at $R > 0.5$, shown in Fig. 10, was used. The FCGC at $R > 0.5$ was considered to account for residual stresses in the fatigue strings. The failure criterion was defined as $a/t = 0.8$.

Results and Discussions

The predicted number of cycles to failure is normalised in Fig. 11 by the number of cycles required to achieve the DNV class D target curve. The fatigue life predicted for MLP flaws in the carbon steel pipe, which is indicated by thick solid lines in Fig. 11, is between 30% to 60% of the life obtained during testing. This is a relatively good agreement. The difference is most likely

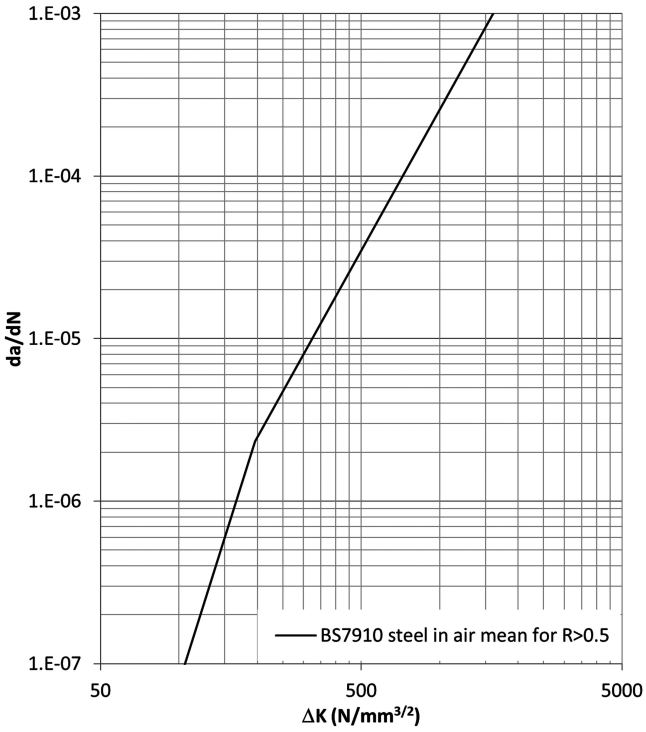


Fig. 10 Fatigue crack growth curve

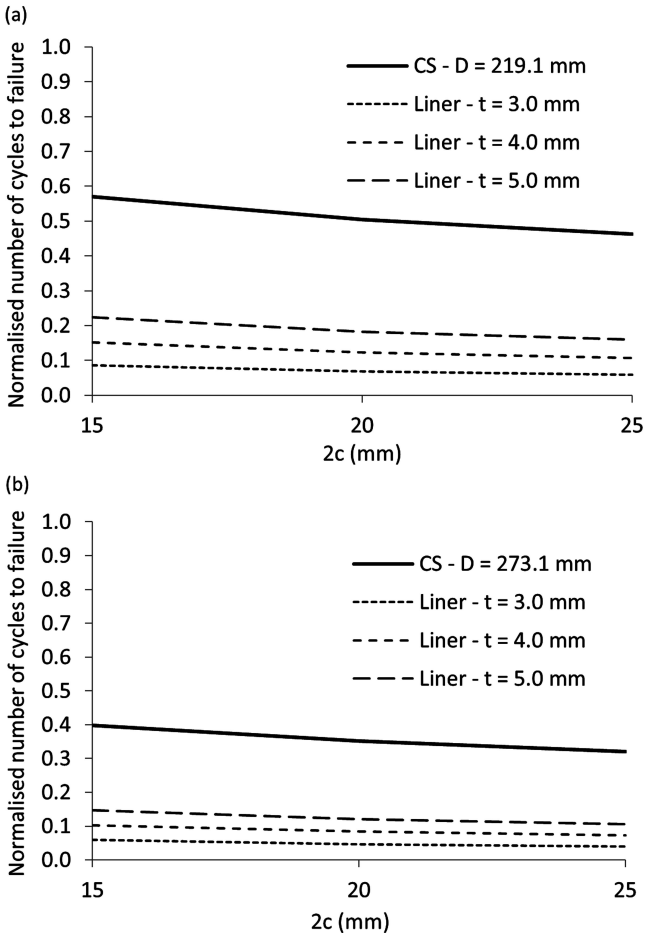


Fig. 11 Number of cycles to failure

due to not accounting for the crack initiation/sharpening time in the analysis. In contrast, the life predicted for MLP flaws in the CRA layer, which is indicated by the dotted lines for $t_l = 3.0$ mm, the short dashed lines for $t_l = 4.0$ mm, and the long dashed lines for $t_l = 5.0$ mm in Fig. 11, is very low compared to that obtained during testing. The inherent conservatism of the analytical K-solution and not accounting for the crack initiation time cannot explain such significant disagreement. The application of the BS7910 FCGC to steel in air is very conservative when used for the prediction of fatigue crack growth in nickel-based alloys. It is recommended that the industry make an effort to develop suitable FCGCs for commonly used nickel-based alloys such as alloy 625.

Finally, the case study results clearly show that it is extremely beneficial to increase the liner thickness as per the Technip reelable MLP philosophy. Reeling does not adversely affect the fatigue performance of MLPs as good fatigue performance was achieved during large-scale testing; however, increasing the liner thickness to suppress wrinkling during reeling at atmospheric pressure significantly improves the fatigue performance of the liner compared to that of the standard MLPs, which have a thinner liner that can be installed by either S-lay, J-lay, or reel-lay under internal pressure. The fatigue life of the liner can increase by over 50% when its thickness is increased by 1 mm.

SUMMARY AND CONCLUSIONS

In this work, large-scale bending and resonant fatigue tests were carried out on 32.1-mm-thick MLPs with 8.625" outer diameter and alloy 625 liner, clad overlay, and girth welds. Prior to fatigue testing, the MLPs were subjected to simulated reeling at atmospheric pressure. The authors have previously shown in Tkaczyk et al. (2012a) that reeled MLPs can achieve a high fatigue performance. The current fatigue programme focused on demonstrating that damage to the anti-corrosion barrier in reeled MLPs does not occur much earlier than the final fatigue failure defined as the pipe burst. This was achieved by (1) constantly monitoring any potential leak into the annulus between the carbon steel backing pipe and the liner; and (2) undertaking DPI and ECT at various stages during the test.

The findings of this work can be summarized as follows:

First, all fatigue test pipes reached the DNV class D target curve on the basis of the outer wall stress ranges without breach of the anti-corrosion barrier. Further fatigue testing showed that 10 (four strings with manual girth welds and six strings with mechanised girth welds) out of 12 specimens reached the DNV class C target curve without failure. This demonstrates that MLPs reeled at atmospheric pressure are suitable for demanding fatigue sensitive flowline and SCR service. The failure of the fifth test string with a manual girth weld, which occurred before the DNV C target curve was reached, initiated from a blemish on the carbon steel pipe's outer surface. Fatigue cracks in the last specimen started from flaws between the liner and clad overlay weld and between the carbon steel and clad overlay weld. The embedded flaws grew in both the CRA layer towards the MLP inner surface and the carbon steel pipe towards the MLP outer surface. The former seemingly broke at the MLP inner surface before the pipe burst. It was estimated that the breach of the anti-corrosion barrier occurred after 75% of the total life had elapsed.

Second, a parametric FE study showed that the K-solution proposed in Marie et al. (2007) for semi-elliptical flaws in single pipes under bending provides a good but slightly conservative approximation of K for interface flaws in MLPs under bending. Therefore, this K-solution can be conveniently used for the fatigue assessment of MLPs with interface flaws.

Third, to allow reeled installation of MLPs at atmospheric pressure, the liner thickness may be increased. The liner thickness required to avoid the risk of liner wrinkling under compressive strains depends on the MLP outer diameter. Although the MLP cost increases with the liner thickness, the fatigue performance of MLPs also increases. It was shown in this work that an increase of 1 mm in the liner thickness can increase the MLP fatigue life by more than 50% in the case of flaws in the CRA layer.

Fourth, the industry is encouraged to develop fatigue crack growth curves suitable for the assessment of flaws in alloy 625 CRA materials such as clad overlay welds.

Finally, the world's first MLP reeled at atmospheric pressure was installed at the end of 2015 in the Gulf of Mexico. Building on the work outlined herein, the Deep Gulf Energy Kodiak project involved ambient reel-lay of 7.625" outer diameter MLP flowlines and SCR sections.

ACKNOWLEDGEMENTS

The authors thank Proclad for their contribution towards the manufacturing of MLP joints. Thanks also go to Mrs. Emilie Buennagel and Mr. Allan Day from TWI and Mr. David Haldane from Heriot-Watt University for their assistance in carrying out tests.

REFERENCES

ABAQUS (2013). Users Manual, version 6.13-1, Dassault Systémes Simulia Corp, Providence, RI, USA. http://www.3ds.com/products-services/simulia/products/abaqus.

API 5L (2007). *ANSI/API Specification 5L: Specification for Line Pipe*, American Petroleum Institute, Washington, DC, USA.

API 5LD (2009). *API Specification 5LD: Specification for CRA Clad or Lined Steel Pipe*, American Petroleum Institute, Washington, DC, USA.

BS7608 (2014). *Guide to Fatigue Design and Assessment of Steel Products*, Standard, British Standards Institution, London, UK.

BS7910 (2013). *Guide to Methods for Assessing the Acceptability of Defects in Metallic Structures*, Standard, British Standards Institution, London, UK.

DNV-OS-F101 (2013). *Submarine Pipeline Systems*, Offshore Standard, Det Norske Veritas, Høvik, Norway.

DNV-RP-A203 (2011). *Qualification Procedures for New Technology*, Recommended Practice, Det Norske Veritas, Høvik, Norway.

DNV-RP-C203 (2011). *Fatigue Design of Steel Offshore Structures*, Recommended Practice, Det Norske Veritas, Høvik, Norway.

Gray, F, Howard, B, Pieton, A, and Gallart, R (2009). "The Qualification and Continued Evolution of Reeled Steel Catenary Risers," *Proc 28th Int Conf Ocean Offshore Arct Eng*, Honolulu, HI, USA, ASME, 3, 97–110. http://dx.doi.org/10.1115/OMAE2009-79176.

Marie, S, et al. (2007). "French RSE-M and RCC-MR Code Appendices for Flaw Analysis: Presentation of the Fracture Parameters Calculation–Part III: Cracked Pipes," *Int J Press Vessels Pip*, 84(10–11), 614–658. http://dx.doi.org/10.1016/j.ijpvp.2007.05.005.

Pepin, A, and Tkaczyk, T (2011). *Methods of Reel-Laying a Mechanically Lined Pipe*, Patent No WO 2011048430 A1.

Pepin, A, Tkaczyk, T, and Denniel, S (2011). "Cost Efficient Solution for the Transport of Highly Corrosive Fluids," *Proc 34th Offshore Pipeline Technol Conf (OPT2011)*, Amsterdam, Netherlands. Available from http://www.ibcenergy.com/.

Tkaczyk, T, Pepin, A, and Denniel, S (2011). "Integrity of Mechanically Lined Pipe Subjected to Multi-Cycle Plastic Bending," *Proc 30th Int Conf Ocean Offshore Arct Eng*, Rotterdam, Netherlands, ASME, 4, 255–265. http://dx.doi.org/10.1115/OMAE2011-49270.

Tkaczyk, T, Pepin, A, and Denniel, S (2012a). "Fatigue and Fracture of Mechanically Lined Pipes Installed by Reeling," *Proc 31st Int Conf Ocean Offshore Arct Eng*, Rio de Janeiro, Brazil, ASME, 3, 9–18. http://dx.doi.org/10.1115/OMAE2012-83050.

Tkaczyk, T, Pepin, A, and Denniel, S (2012b). "Fatigue and Fracture Performance of Reeled Mechanically Lined Pipes," *Proc 21st Int Offshore Polar Eng Conf*, Rhodes, Greece, ISOPE, 4, 603–612.

Toguyeni, GA, and Banse, J (2012). "Mechanically Lined Pipe: Installation by Reel-Lay," *Proc Offshore Technol Conf*, Houston, TX, USA, OTC23096. http://dx.doi.org/10.4043/23096-MS.

Zumpano, PJ, et al. (2012). "Challenges About Testing, Welding and NDT of CRA Pipelines in Brazilian Pre-Salt," *Proc 31st Int Conf Ocean Offshore Arct Eng*, Rio de Janeiro, Brazil, ASME, 6, 145–151. http://dx.doi.org/10.1115/OMAE2012-83461.

Appendix D

Paper No. 4 – Low Cycle Fatigue of Subsea Mechanically Lined Pipeline with Liner Imperfections

Proceedings of the ASME 2017 36th International Conference on Ocean, Offshore and Arctic Engineering
OMAE 2017
June 25-30, 2017, Trondheim, Norway

OMAE2017-62487

LOW CYCLE FATIGUE OF SUBSEA MECHANICALLY LINED PIPELINE WITH LINER IMPERFECTIONS

Aurélien Pépin*
Offshore Engineering Division
TechnipFMC
Westhill, Aberdeen, AB32 6TQ
United Kingdom
Email: aurelien.pepin@technipfmc.com

Tomasz Tkaczyk
Offshore Engineering Division
TechnipFMC
Westhill, Aberdeen, AB32 6TQ
United Kingdom
Email: tomasz.tkaczyk@technipfmc.com

Noel O'Dowd
Bernal Institute
University of Limerick
Limerick, V94 T9PX
Ireland
Email: noel.odowd@ul.ie

Kamran Nikbin
Department of Mechanical Engineering
Imperial College
London, SW7 2AZ
United Kingdom
Email: k.nikbin@imperial.ac.uk

ABSTRACT

There is an ever-increasing demand for subsea transport of corrosive constituents which requires the use of corrosion resistant pipelines. This has generated interest in mechanically lined pipe (MLP) which consists of carbon steel pipe lined with a thin layer of corrosion resistant alloy (CRA), typically stainless steel. The CRA liner is adhered to the backing pipe by means of an interference fit.

MLPs have been traditionally installed subsea using low strain methods such as towing, S-lay or J-lay. More recently, the efficient reel-lay method, typically used for pipelines up to 18" (457.2 mm) in diameter, has also been considered. To prevent damage to the MLP during high strain bending (i.e. wrinkling of CRA the liner) and thus allow reel-lay installation, TechnipFMC has qualified reeling of MLPs at ambient and elevated pressures. The ambient reeling approach, where the liner thickness is increased to prevent wrinkling during reeling, is appropriate for smaller diameter MLPs. For larger pipelines, it is generally more cost-effective to pressurise the MLP during reeling.

Concerns have been expressed that liner imperfections such as small dents or wrinkles, introduced during manufacturing, installation or service, may compromise the integrity of the MLP subjected to high in-service cyclic loading. Therefore, this study was undertaken to examine the criticality of such flaws and determine the low cycle fatigue endurance of reeled MLPs with imperfections. First, a numerical study was undertaken to estimate in-service stress/strain ranges in the MLPs with liner flaws. Subsequently, small scale tests were carried out to quantify the fatigue performance of such MLPs. The obtained results confirmed that there is a negligible risk of failure of MLP flowlines due to crack initiation at liner imperfections and subsequent breach of the CRA layer, even for pipelines subjected to very severe in-service cyclic loading.

INTRODUCTION

Subsea transmission of corrosive petroleum fluids requires the use of pipelines with enhanced corrosion performance such as solid stainless steel or hot-roll bonded clad pipelines. Recently, mechanically lined pipes (MLP) have been used instead

*Address all correspondence to this author.

Copyright © 2017 by ASME

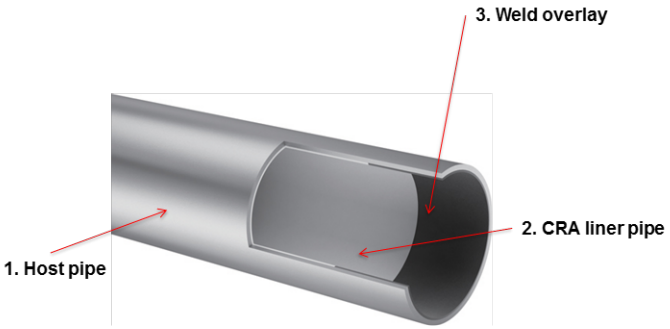


FIGURE 1. SCHEMATIC OF MECHANICALLY LINED PIPE

because they are generally more readily available and more cost effective than other corrosion resistant pipes.

MLP, illustrated in Fig. 1, is made of thin corrosion resistant alloy (CRA) liner adhered to backing carbon steel (CS) pipe by means of an interference fit. The MLP manufacturing process requires the liner (manufactured to API 5LC [1], for example) and the backing pipe (manufactured to API 5L [2], for instance). First, the liner is inserted into the host pipe and expanded by applying internal pressure until it contacts the host pipe. Then, expansion of both pipes continues until a target expansion level is achieved. Once pressure is released, the liner and the host pipe spring back so that grip (mechanical bond) develops between the two pipes. Subsequently, the liner ends are cut back to leave a required length of unlined CS pipe and clad overlay welding is carried out to seal the liner ends.

To enable insertion of the liner into the CS host pipe, a radial gap is required between the liner outer diameter (OD) and the host pipe inner diameter (ID). A large gap makes insertion easier but increases hoop strain in the liner during expansion which renders the liner seam weld prone to fracture. Since a small insertion gap is generally specified, some amount of liner scoring is inherent to the MLP manufacturing process. Light scoring, shown in Fig. 2(a), is typical of a well-controlled insertion process. Uncontrolled galling of the liner, shown in Fig. 2(b), may occur if: (i) the host pipe and the CRA liner are axially misaligned during liner insertion or (ii) the pipe diameter or straightness tolerances are too high. Liner galling may result in the build-up of CRA material (nugget) in the annulus between the liner and the host pipe, see Fig. 2(b). Those nuggets can indent the liner during expansion (see Fig. 3).

MLPs have been traditionally installed subsea using low-strain methods such as towing, S-lay or J-lay [3]. More recently, TechnipFMC has qualified MLP installation by the high strain reel-lay method. The reel-lay installation process involves four plastic bending events. First, the pipeline is spooled onto the reel. Then, the reel-lay vessel travels to the installation site where unreeling takes place. The pipeline is straightened in the free span between the reel and the aligner, passes over the aligner and is finally straightened in the straightener, see Fig. 4.

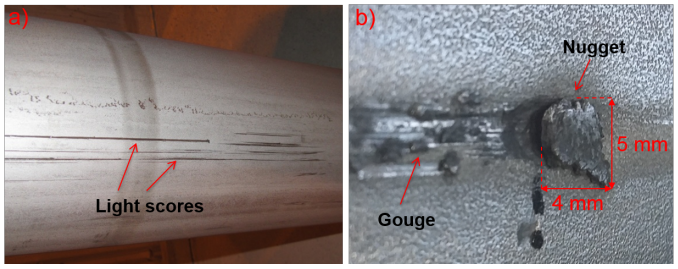


FIGURE 2. LINER SCORING DURING MANUFACTURING: (a) LIGHT SCORING, (b) DEEP SCORING AND BUILD-UP OF CRA MATERIAL (NUGGET)

Wrinkling of the liner during plastic bending of the MLP is prevented by either increasing the liner thickness above a typical thickness of 2.5–3.0 mm [4–8] or pressurising the MLP [9]. Reeling of MLPs with increased liner thickness at ambient pressure is well-suited for pipelines up to 10.75”–14” (273.1–355.6 mm) in diameter. The first ever MLPs (7.625” (193.7 mm) OD flowlines and steel catenary risers), reeled at atmospheric pressure, were installed by TechnipFMC in the Gulf of Mexico in 2015. For larger MLPs, it is generally more economical to implement pressurised reeling due to a lower cost of the MLP with a nominal liner thickness of 2.5–3.0 mm. This approach was implemented offshore Brazil and in the Norwegian sector of the North Sea.

Concerns have been raised that liner imperfections introduced during manufacturing, installation or service may compromise the integrity of the MLP which is subjected to varying pressure, temperature and bending strain during operation. This study examines the criticality of such flaws. Finite-element (FE) analyses are carried out to determine cyclic stress/strain in liners containing wrinkles/dents, associated with in-service loading. Subsequently, it is shown that the liner stress/strain condition in the MLP under in-service loading can be replicated in a simple liner strip geometry subjected to cyclic axial loading. Finally, small scale fatigue testing on a liner with imperfections is undertaken. The fatigue endurance, defined as the number of high strain cycles applied before breach of the CRA liner occurs, is shown to be high enough to deem the risk of loss of the MLP integrity to be very low.

NUMERICAL ANALYSIS

Approach

Three MLPs, suitable for reel-lay installation at ambient pressure, are considered in this work: 8.625” (219.1 mm), 10.75” (273.1 mm), and 12.75” (323.9 mm) OD. The 8” and 12” CS pipes are lined with alloy 316L whereas the 10” pipe is lined with alloy 625. The average measured stress-strain curves for the CS (API 5L X65) and the liners (ASTM 316L and 625) are shown in Fig. 5.

Copyright © 2017 by ASME

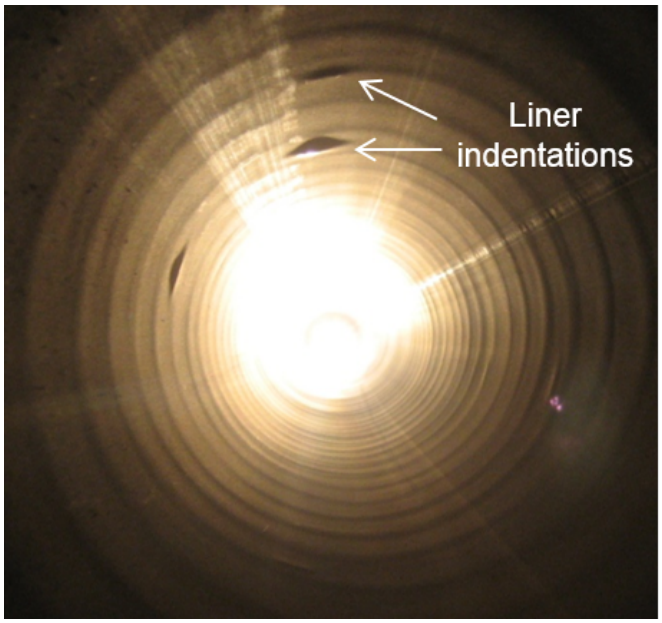


FIGURE 3. LINER IMPERFECTIONS INTRODUCED DURING MANUFACTURING

First, a wrinkling parametric study is undertaken using small scale 3D FE models. Buckling of a standalone liner is simulated to generate eigenmodes, then radial displacements corresponding to a given mode are scaled and imposed to a perfect liner in an MLP. Subsequently, sensitivity analyses are carried out to determine which initial imperfection is appropriate to correctly predict liner wrinkling during bending of the MLP.

Then, the appropriate initial imperfection is introduced into a liner in a full scale 3D MLP model. Manufacturing, installation and operation of the MLP are simulated to produce large residual imperfections (dents/wrinkles) and determine the corresponding stress/strain ranges in the liner during subsea operation of the MLP. Liner wrinkles, up to 6 mm in height, are considered in this work in order to conservatively assess the fatigue endurance of MLPs with imperfections. Such wrinkles are unlikely to be caused by galling and denting of the liner during manufacturing. Equally, in practice it is not possible to introduce such wrinkles during ambient installation of reelable MLPs (i.e. those designed for reeling at atmospheric pressure). Therefore, bending of MLPs on a tight bending former is carried out experimentally and simulated in the FE analysis - the bending radius required to achieve the desired wrinkle height is much smaller than the reel hub radius of a typical reel-lay vessel.

Finally, a liner strip with a wrinkle, extracted from the full scale 3D FE model which accounts for the strain history, is subjected to cyclic axial loading. The applied axial cyclic loading is altered in an iterative manner until the stress/strain ranges in the strip FE model correspond to those in the full scale FE model where the MLP is subjected to in-service loading.

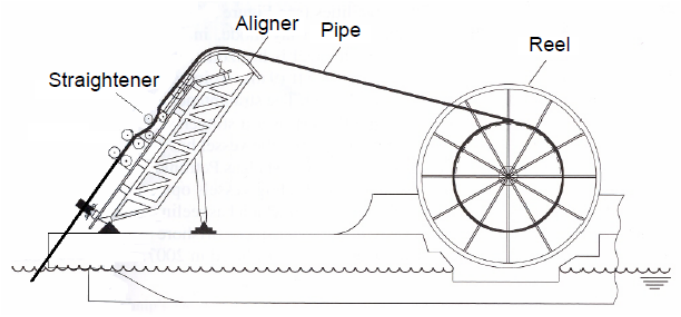


FIGURE 4. ILLUSTRATION OF REEL-LAY INSTALLATION

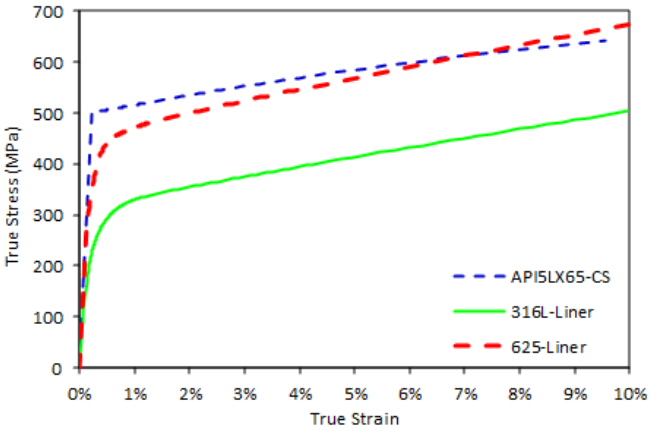


FIGURE 5. ASSUMED TRUE STRESS-STRAIN CURVES

A standard kinematic hardening plasticity model (i.e. with no cyclic isotropic hardening/softening component) associated with the stress-strain behaviour illustrated in Fig. 5, is used throughout.

Wrinkling Parametric Study

Buckling/wrinkling of tubes has been the subject of numerous studies over the past decades. Most studies focused on the behaviour of slender single skinned pipes under axial compression or bending, see [10–14] for example. More recently, liner wrinkling during monotonic bending of the MLP has been studied, see [15–19] for example. Buckling/wrinkling behaviour is strongly influenced by tube/liner imperfections. Most liner imperfections are introduced during manufacturing of the MLP when the liner conforms to the shape of the backing steel pipe ID. Seamless backing pipes are characterised by a spiral surface topology (visible on the pipe ID) which is introduced during the piercing process. This topology is transferred to the liner as shown in Fig. 3. In addition, any CRA material build-up may cause liner indentations during expansion, see Fig. 3. (It should be noted that shadows cast by backlit imperfections make them appear, in Fig. 3, larger than they actually are.)

Copyright © 2017 by ASME

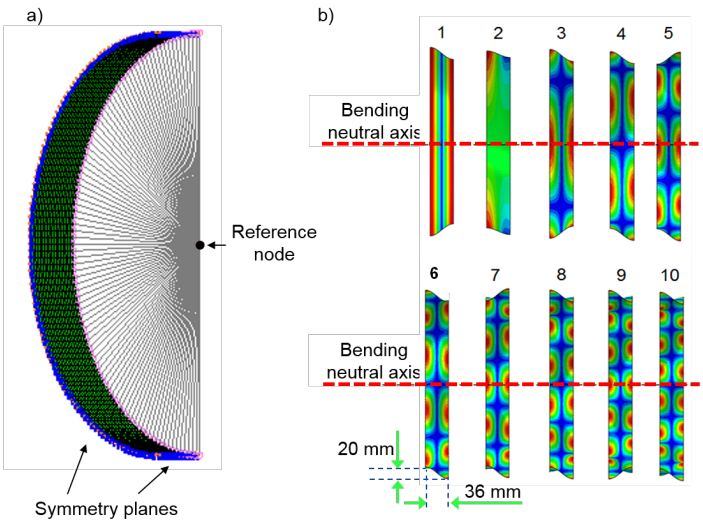


FIGURE 6. LINER BUCKLING ANALYSIS: (a) FE MODEL, (b) CONTOUR PLOT OF EIGENMODE RADIAL DISPLACEMENTS

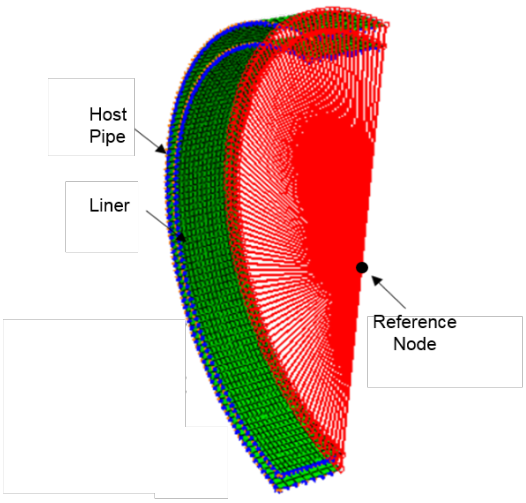


FIGURE 7. FE MODEL FOR WRINKLING PARAMETRIC STUDY

Vasilikis and Karamanos, showed in [19], that applying liner imperfections from an eigenmode buckling analysis allows accurate prediction of wrinkle initiation and growth during bending. Later, Harrison *et al.* [20] established that idealised harmonic imperfections have a similar effect on liner wrinkling behaviour as those introduced by the seamless backing pipe. Therefore, imperfections derived from a buckling/wrinkling eigenmode analysis are applied to the liner in this study. The length of the liner model in the eigenmode analysis is equal to half of the wave length of a liner wrinkle under axial compression [3]

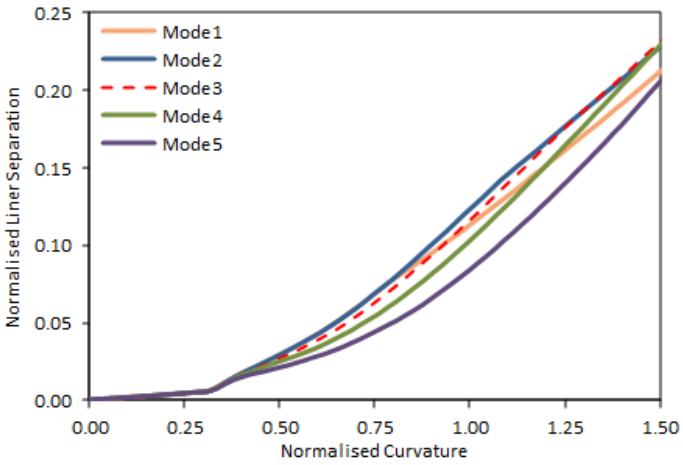


FIGURE 8. EFFECT OF EIGENMODE SHAPE ON LINER WRINKLING

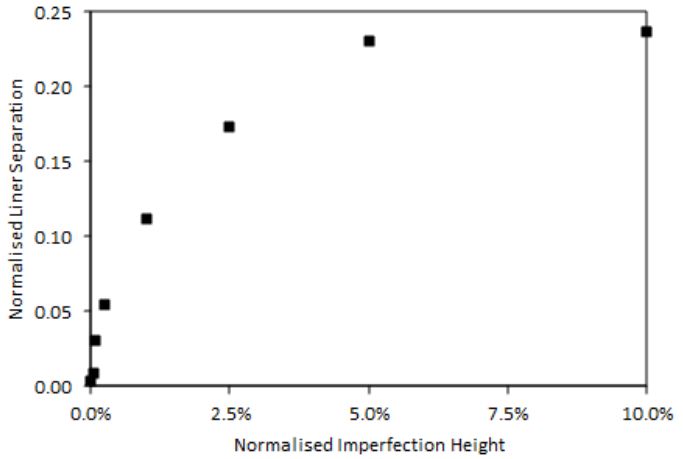


FIGURE 9. EFFECT OF IMPERFECTION HEIGHT ON LINER WRINKLING

$$\lambda = \frac{\pi(rt)^{0.5}}{(12(1-\nu^2))^{0.25}} \tag{1}$$

where t, r and ν are the thickness, the mid-wall radius and Poisson's ratio of the liner. A quarter of the liner is modelled with first-order shell elements with reduced integration (S4R in ABAQUS [21]) and appropriate symmetry boundary conditions, see Fig. 6(a). A compression load mode is preferred over a bending load mode because it yields eigenmodes that are symmetrical with respect to the pipe axis. These are suitable for modelling reverse bending as experienced during the reeling process. Fig. 6(b) shows ten eigenmodes obtained from this analysis.

Copyright © 2017 by ASME

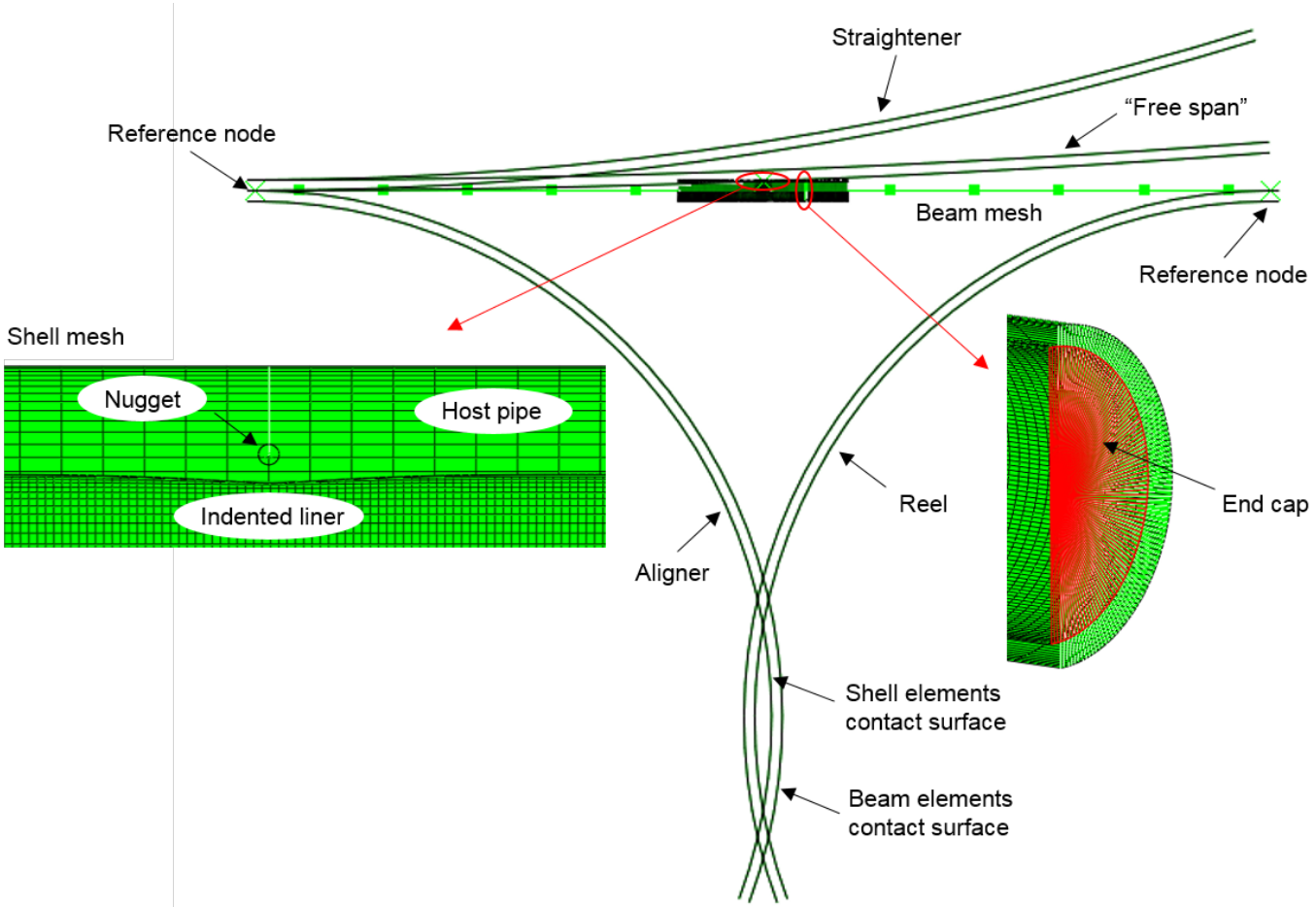


FIGURE 10. 3D FE MODEL FOR SIMULATION OF MANUFACTURING AND REELING OF MLP

The FE model proposed in [18] is used to determine which imperfection shape (eigenmode in Fig. 6(b)) and height is appropriate to correctly predict liner wrinkling during bending of MLP. The model length is the same as that in the eigenmode analysis. Both the liner and the backing pipe are modelled with first-order shell elements with reduced integration (S4R in ABAQUS). A quarter of the MLP with appropriate symmetry boundary conditions is modelled. A finite-sliding contact formulation with Coulomb friction (friction coefficient of 0.1) is employed to model interaction between the liner and the backing pipe. A selected eigenmode is scaled so that the required initial imperfection height is seeded onto the liner. The nodes to the right hand side of the model in Fig. 7 are connected to a reference node through kinematic coupling. The MLP is bent by applying rotation to the reference node. The FE results, shown in Fig. 8, are expressed in terms of the liner separation from the host pipe normalised by the liner thickness versus the normalised bending curvature, κ/κ_0,

$$\kappa/\kappa_0 = \kappa \times d^2/t \tag{2}$$

where d is the liner mid-wall diameter. Eigenmode 3 in Fig. 6(b) is the best suited imperfection shape, because it is symmetrical with respect to the neutral bending axis, and yields separation no lower than the other modes. Figure 9 shows the effect of the normalised imperfection height, h/t, on the liner separation at $\kappa/\kappa_0 = 1.5$. The predicted liner separation is very sensitive to the imperfection height for h/t up to 5% only. Consequently, eigenmode 3 with $h/t = 5\%$ is adopted in the next section.

Manufacturing, Reeling and Operation

A simulation of liner expansion during manufacturing, reel-lay installation and in-service operation is performed with a half-symmetrical 3D FE model, shown in Fig. 10, to determine in-service cyclic loading in the liner. First-order shell elements with reduced integration and first-order pipe/beam elements (respectively S4R and PIPE31 in ABAQUS [21]) are used to model both the liner and the backing pipe. (It should be noted that beam elements are only used to extend the model length to a pipe joint, i.e. 12 m, at low computational cost.) The beam mesh is con-

Copyright © 2017 by ASME

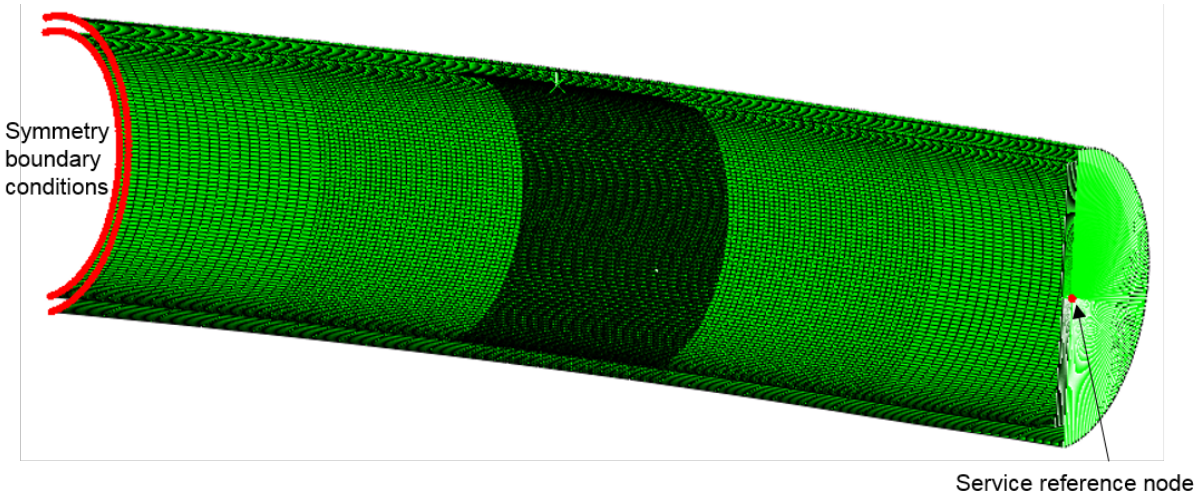


FIGURE 11. 3D FE MODEL FOR SIMULATION OF IN-SERVICE OPERATION OF MLP

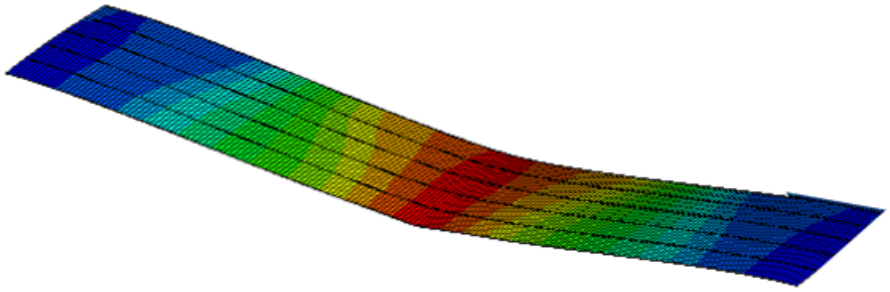


FIGURE 12. LINER STRIP MODEL EXTRACTED FROM 3D FE MODEL OF MLP

nected to the shell mesh with kinematic couplings at either end of the model. The liner shell mesh has a refined central section where the eigenmode 3 imperfection (shown in Fig. 6) is seeded as detailed in the previous section. This central region is indented during simulated manufacturing with a rigid nugget to create a wrinkle/indent similar to those shown in Fig. 3. The end cap, which allows application of the end cap load in-service, is modelled using elastic shell elements (S3 in ABAQUS). Rigid bending formers are utilised to replicate the reel, the aligner, the straightener and the free span between the reel and the aligner. These formers are connected through their reference nodes to the beam mesh end nodes with kinematic couplings. The finite-sliding contact formulation and Coulomb friction model is again used to model the liner-to-host pipe and pipe-to-former interactions. Frictionless contact is assumed between the host pipe and the formers. Finite strain theory is assumed in the analysis.

The liner with a typical insertion gap of 3–4 mm is first subjected to internal pressure to simulate manufacturing of the MLP. This creates an interference fit between the liner and the host pipe while the liner is indented at its central section which is seeded with the eigenmode 3 imperfections, $0.05\times t$ in height. After releasing the pressure, reel-lay installation is simulated by bending the pipe onto the reel, the "free span" former, the aligner and finally onto the straightener before the pipe is relaxed. The radius of the bending former is chosen so that the target wrinkle height (up to 6 mm in height) is obtained. On completion of the installation phase, all surfaces and elements, except from those shown in Fig. 11, are removed from the model in Fig. 10. After applying symmetry boundary conditions to the nodes on the left hand side of the model, shown in Fig. 11, subsea operation is simulated. The MLP is hydrotested to simulate pre-commissioning and bent to 1% strain to simulate a lateral bucking event. Then, the pipe is relaxed to 0.7% residual bending strain. Finally, a severe in-service loading sequence is simulated. The pipe is pressurised from 0 to a pressure corresponding to a hoop stress utilisation ratio of 0.8. Its temperature is increased by 150°C and the bending strain is increased from 0.7% to 1%. Subsequently, the pipe is depressurised, cooled to ambient and relaxed to 0.7% bending strain. The results in terms of operational stress/strain ranges at the crown of the wrinkle are used in the next section.

Copyright © 2017 by ASME

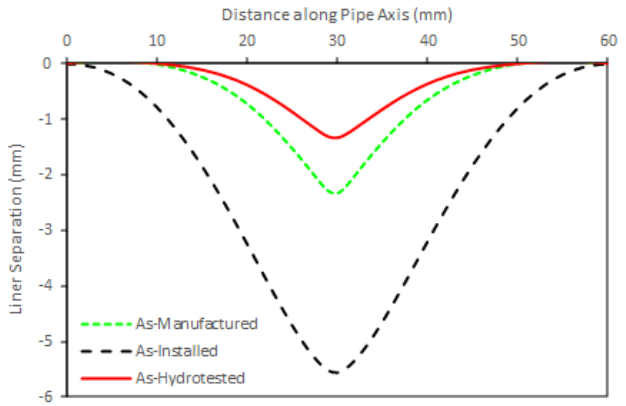


FIGURE 13. 8" MLP WITH 316L LINER: WRINKLE HEIGHT

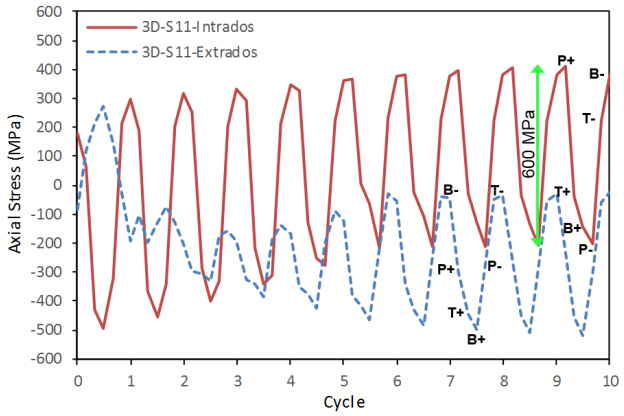


FIGURE 14. 8" MLP WITH 316L LINER: IN-SERVICE STRESS RANGES

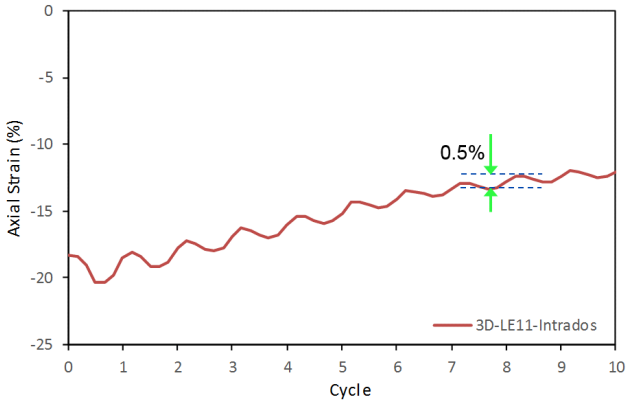


FIGURE 15. 8" MLP WITH 316L LINER: IN-SERVICE STRAIN RANGES

Fatigue Test Simulation

Figure 12 shows a half-symmetrical liner strip model extracted from the central section of the 3D FE model (Fig. 11) after simulated manufacturing, installation, and hydrotest (to account for the strain history). The size of the liner strip is representative of a dumbbell test specimen in a small scale fatigue test. Cyclic axial displacement is applied at the right end of the model, shown in Fig. 12, while the left end is fully constrained, to simulate a small scale fatigue test. The magnitude of displacement is altered in an iterative manner until the stress/strain range at the crown of the wrinkle in the strip FE analysis matches that obtained from the FE analysis of the MLP under operational cyclic loading.

Results of Numerical Study

Large and conservative wrinkle imperfections, up to 6 mm in height, are considered in this paper to assess the fatigue performance of MLPs. To achieve such imperfections in the FE analysis, a 2 mm high indent (double the height of the maximum allowable manufacturing imperfection for a project pipe), indicated with a short-dashed line in Fig. 13, is created during manufacturing and the MLP is bent on a very tight reeling former to maximise bending strain. The bending radius required to achieve the desired wrinkle height of 6 mm (indicated with a long-dashed line in Fig. 13) is smaller than the reel hub radius of a typical reel-lay vessel by the factor of 2. The residual wrinkle after hydrotest of just over 1 mm in height is indicated with a solid line in Fig. 13.

Figure 14 shows the evolution of axial stress at the wrinkle crown during operation, obtained from the model illustrated in Fig. 11. It may be seen that it takes approximately 7 cycles for the stress range to stabilise although peak stresses continue to rise slightly. The maximum stress range, $\Delta\sigma = 600$ MPa, is predicted to occur at the liner intrados, see Fig. 14. The three contributors to stress variations, bending, pressure and temperature, are denoted in this figure by "B", "P" and "T", respectively. The sign "+" in Fig. 14 indicates that bending strain, pressure or temperature increases while the opposite is indicated with the sign "–". It can be seen that temperature variations have the largest effect on the stress range at the liner intrados. Figure 15 shows the evolution of the corresponding axial strain at the liner intrados. It also takes approximately 7 cycles for the strain range to stabilise. The maximum (stable) strain range is $\Delta\varepsilon = 0.5\%$. It is to be noted that the mean axial strain also slowly increases with the number of cycles due to ratcheting.

Figures 16 and 17 compare the results, in terms of axial stress and strain at the liner intrados, obtained from the 3D MLP model (indicated by a dashed line) and the simple strip model (indicated by a solid line). It can be seen that the applied cyclic displacement in the strip FE model can be selected so that the stress/strain range in the MLP is conservatively reproduced. This demonstrates that the complex behaviour of the MLP in-service can be well captured in a small scale displacement-controlled fatigue test.

Copyright © 2017 by ASME

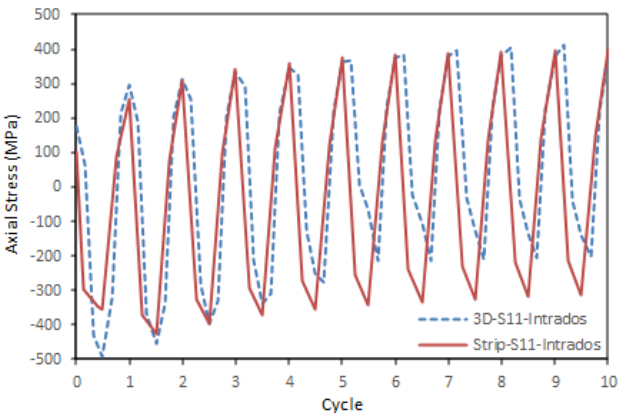


FIGURE 16. STRESS RANGES IN ALLOY 316L LINER: 3D PIPE MODEL VS STRIP MODEL

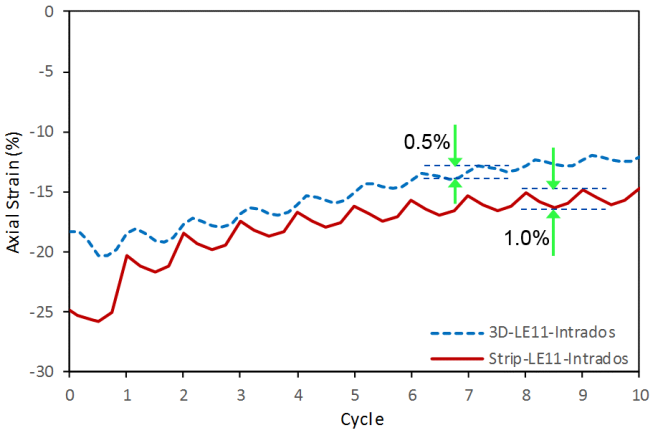


FIGURE 17. STRAIN RANGES IN ALLOY 316L LINER: 3D PIPE MODEL VS STRIP MODEL

It may be noted that a strain range, on the order of twice that predicted with the full scale MLP model, is applied to the strip model to achieve similar stress range in both models. Higher strain range must be applied in the strip model to compensate for biaxial loading (and to some extent plastic deformation due to lateral buckling) in the MLP model.

The results presented in this section are for the 8" MLP. Similar results are obtained for the 10" and 12" pipes.

EXPERIMENTAL WORK

Approach

The 8", 10" and 12" MLPs, detailed in the previous section, were manufactured and bent in a rig, shown in Fig. 18, to simulate reel-lay installation. The MLP is then bent on an increasingly tight former until the required wrinkle height is achieved.

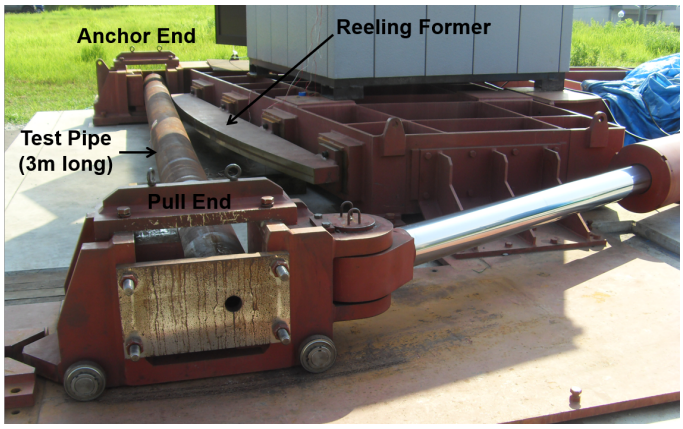


FIGURE 18. BENDING RIG EQUIPPED WITH 8.23 METRE REELING FORMER

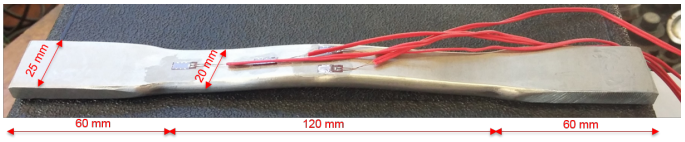


FIGURE 19. SMALL SCALE TEST SPECIMEN

Following hydrotest, the pipes are sectioned to remove the liner. Subsequently, dumbbell specimens are extracted from the liner so that the wrinkle is located centrally along the specimen. Finally, small scale tests are carried out to assess the low cycle fatigue performance of MLPs with imperfect liners. The cyclic axial displacement is selected from the numerical results presented in the previous section.

Bending Trials and Hydrotest

The MLP test strings are conservatively subjected to five reverse bending cycles (i.e. 2.5 times a standard reel-lay installation cycle). The pipe is mounted in the rig, shown in Fig. 18, and bent onto an 8.23 m radius reeling former. After relaxing, it is rotated through 180° while the reeling former is replaced with the straightening former with a 34 m radius. The pipe is then bent onto the straightening former, the load is removed and the pipe turned 180°. This process continues until a total of five reverse bending cycles is applied. Visual inspection carried out during the bending trial revealed no wrinkles after simulated reeling. Therefore, the MLPs are subjected to bending on an increasingly tight former (down to 0.5 of the original bending radius) until a wrinkle height of 3–6 mm is achieved. The height of wrinkles drops to 1–2 mm following hydrotest (at a pressure of 64 MPa). After hydrotesting, the test strings are sectioned to remove the liner and fabricate specimens for small scale fatigue testing.

Copyright © 2017 by ASME

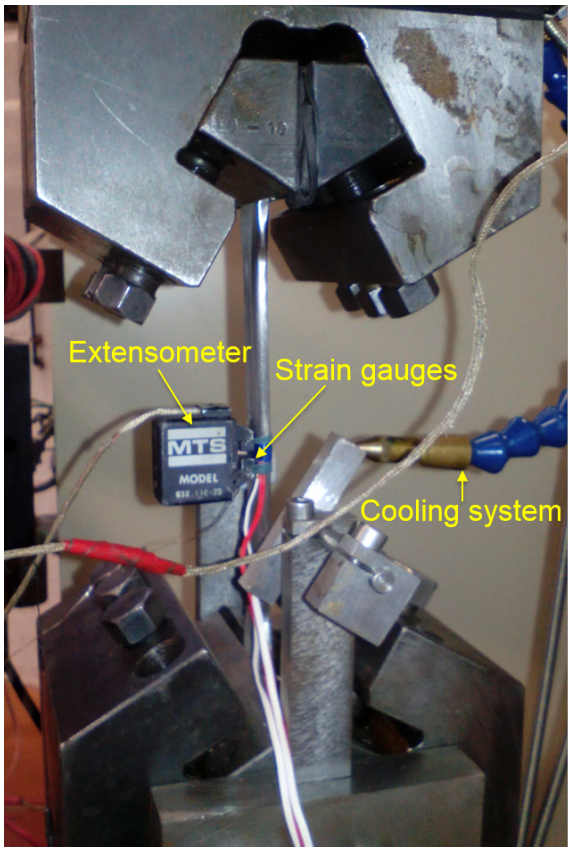


FIGURE 20. SMALL SCALE TEST MACHINE

Small Scale Fatigue Tests

Dumbbell test specimens (Fig. 19) are machined from the corrosion resistant alloy 316L and 625 liners which are removed from the 8", 10" and 12" MLPs after simulated reeling and hydrotest. Before fatigue testing, the specimens are buckled in the test machine, shown in Fig. 20, to increase the wrinkle height back to 3–6 mm. Subsequently, the samples are instrumented with biaxial strain gauges. A transverse gauge is used to compensate for temperature effects. After mounting the specimen in the test machine and installing the cooling system, an extensometer with a 12.5 mm gauge length is affixed to the specimen around the crown of the wrinkle (see Fig. 20). The extensometer is used to control the cross-head displacement of the test machine so that the gauge length is subjected to a global strain range of +/−0.5%. This is conservative and results in a higher strain range at the wrinkle crown compared to that reported in Fig. 17.

Eighteen dumbbell specimens, six for each pipe size, are fatigue tested at a frequency of 2 Hz to determine the fatigue endurance of MLPs with imperfect liners. Although the maximum service temperature can be high (100–150°C or above), testing is conveniently undertaken at room temperature as fatigue cracks generally grow slower at elevated temperature [22].

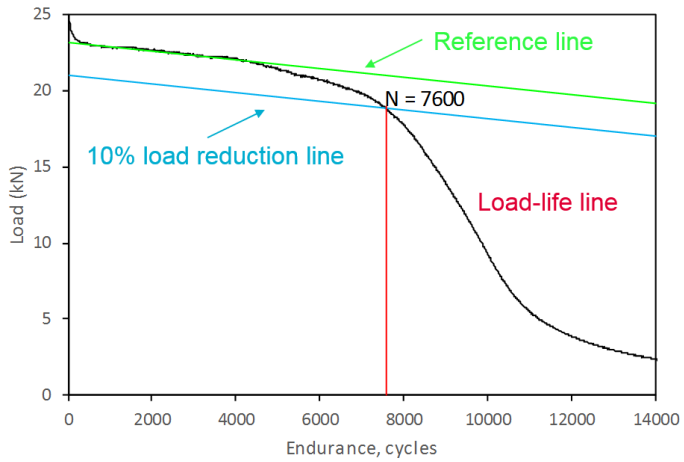


FIGURE 21. LOAD-LIFE LINE

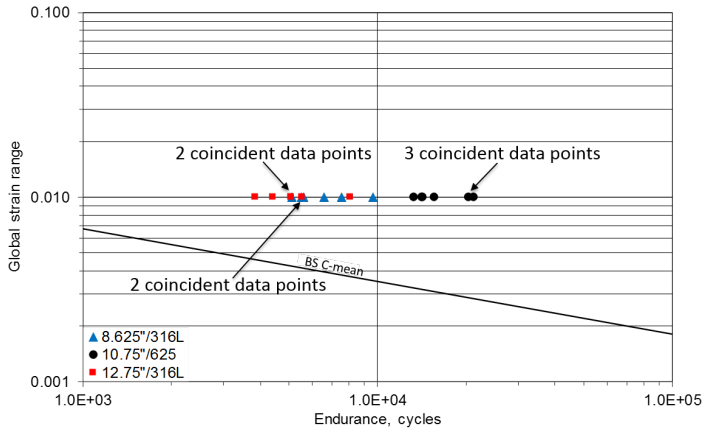


FIGURE 22. SMALL SCALE FATIGUE TEST RESULTS

Results and Discussions

Figure 21 shows an example of the maximum load-life line for the alloy 316L sample tested in this programme. At the beginning of the fatigue test, a rapid decrease in peak load is observed but after a few hundred cycles the rate of load decrease stabilises at a constant low value, most likely due to ratcheting. When cracking initiates, at ca. 7600 cycles in Fig. 21, the load decreases rapidly again. Fatigue failure is deemed to occur when the applied load reduces by 10%, as indicated by the blue line in Fig. 21, which can be considered as crack initiation.

The test results for the 8"/316L, 10"/625 and 12"/316L MLPs (indicated respectively by the triangles, circles and squares in Fig. 22) are compared in Fig. 22 to the BS 7608 class C mean curve [23]. It can be seen that all test results exceed the BS7608 class C mean curve. Furthermore, fatigue life of the alloy 625 liner is higher than that of the alloy 316L liner. This is in line with other studies, where it has been shown that crack initiation and growth is slower in alloy 625 than in alloy 316L [22].

Copyright © 2017 by ASME

CONCLUSIONS

Deep scoring of the liner, when its insertion into the backing pipe during MLP manufacturing process is not well controlled, may result in the build-up of the CRA material in the annulus between the liner and the host pipe. Consequently, the liner may be indented when it is expanded during manufacturing. Furthermore, imperfections such as wrinkles may be introduced during installation or service. As flowlines are often subjected in-service to high pressure and temperature fluctuations and cyclic bending strain, concerns have been expressed that the presence of liner wrinkles/indents may reduce the fatigue performance of MLPs.

A numerical study was undertaken to quantify the stress/strain ranges associated with imperfect liners when MLPs are subjected to onerous in-service loading. It was found that the axial strain range in the liner does not exceed 1% for a pressure range equal to a hoop stress utilisation ratio of 0.8, a temperature range of 150°C and a bending strain range of 0.3%. It was further demonstrated that the stress/strain range in the liner subjected to in-service loading can be reproduced in a strip geometry under cyclic axial displacement. Therefore, a simple small scale test set-up can be used in place of expensive and time consuming large scale testing to determine the fatigue endurance of the MLP in-service.

Liner dumbbell specimens were extracted from the 8", 10" and 12" MLP strings which underwent simulated reeling (bending on the former) and pre-commissioning (hydrotest). The liner specimens had wrinkles, up to 6 mm in height, introduced halfway along their length prior to fatigue testing. The fatigue life obtained from these specimens was between 4,000 and 22,000 cycles, and was significantly higher for alloy 625 (13,000 to 22,000 cycles) compared to that for alloy 316L (4,000 to 10,000 cycles). The predicted life for MLPs with large imperfections and subjected to high cyclic loading is well in excess of 3000 cycles, which corresponds to one shut-down cycle every month, for 25 years with a safety factor of 10. This demonstrates that liner imperfections (indents/wrinkles) in the range considered in this work (up to 6 mm in height) are not detrimental to the in-service integrity of MLP flowlines.

ACKNOWLEDGMENT

The authors wish to thank Gilles Maitres from A2MI, and Ludovic Krauss, Daniil Vasilikis and Paul Sicsic from TechnipFMC for their valuable contribution.

REFERENCES

[1] American Petroleum Institute, 2015, *API 5LC 2015: Specification for CRA Line Pipe, 4th edition*.

[2] American Petroleum Institute, 2015, *API 5L 2015: Specification for Line Pipe, 45th edition*.

[3] Kyriakides, S. and Corona, E., 2007, "Mechanics of Offshore Pipeline, Volume 1: Buckling and Collapse", Elsevier.

[4] Tkaczyk, T., Pépin, A. and Denniel, S., 2011, "Integrity of Mechanically Lined Pipes Subjected to Multi-Cycle Plastic Bending", Proceedings of the 30th International Conference on Offshore Mechanics and Arctic Engineering, OMAE2011-49270.

[5] Tkaczyk, T., Pépin, A. and Denniel, S., 2012, "Fatigue and Fracture of Mechanically Lined Pipes Installed by Reeling", Proceedings of the 31st International Conference on Offshore Mechanics and Arctic Engineering, OMAE2012-83050.

[6] Tkaczyk, T., Pépin, A. and Denniel, S., 2012, "Fatigue and Fracture Performance of Reeled Mechanically Lined Pipes", Proceedings of the 21st International Offshore and Polar Engineering Conference, ISOPE2012-TPC-0143.

[7] Pépin, A., Tkaczyk, T., O'Dowd, N. and Nikbin, K., 2015, "Qualification of Reeled Mechanically Lined Pipes for Fatigue Service", Proceedings of the 25th International Offshore and Polar Engineering Conference, ISOPE2015-TPC-0481.

[8] Pépin, A., Tkaczyk, T., O'Dowd, N. and Nikbin, K., 2016, "Qualification of Reeled Mechanically Lined Pipes for Fatigue Service", International Journal of Offshore and Polar Engineering, ISSN 1053-5381, Vol. 26, No. 3, September 2016, pp. 296 – 303.

[9] Tkaczyk, T., Chalmers, M. and Pépin, A., 2016, "Reel-Lay Installation Approaches for Mechanically Lined Pipes", Proceedings of the 2016 Offshore Technology Conference, OTC Asia 2016, OTC-26440-MS.

[10] Kyriakides, S. and Ju, G.T., 1992, "Bifurcation and Localization Instabilities in Cylindrical Shells under Bending: Part I - Experiments", International Journal of Solids and Structures 29, pp. 1117 – 1142.

[11] Kyriakides, S. and Ju, G.T., 1992, "Bifurcation and Localization Instabilities in Cylindrical Shells under Bending: Part II - Predictions", International Journal of Solids and Structures 29, pp. 1143 – 1171.

[12] Bardi, F.C. and Kyriakides, S., 2006, "Plastic Buckling of Circular Tubes under Axial Compression: Part I - Experiments", International Journal of Mechanical Sciences 48, pp. 830 – 841.

[13] Bardi, F.C. and Kyriakides, S., 2006, "Plastic Buckling of Circular Tubes under Axial Compression: Part II - Analysis", International Journal of Mechanical Sciences 48, pp. 842 – 854.

[14] Hilberink, A., Gresnigt, A.M. and Sluys, L.J., 2010, "Liner Wrinkling of Lined Pipe under Compression, a Numerical and Experimental Investigation", Proceedings of the 29th International Conference on Offshore Mechanics and Arctic Engineering, OMAE2010-20285.

[15] Focke, E.S., Karjadi, E., Gresnigt, A.M., Meek, J., 2007, "Reeling of Tight Fit Pipe (TFP)", Proceedings of the 26th International Conference on Offshore Mechanics and Arctic Engineering, OMAE2007-29100.

[16] Focke, E.S., 2007, "Reeling of Tight Fit Pipe", PhD Thesis, Delft University of Technology, The Netherlands.

[17] Hilberink, A., Gresnigt, A.M. and Sluys, L.J., 2011, "Mechanical Behaviour of Lined Pipe during Bending, Numerical and Experimental Results Compared", Proceedings of the 30th International Conference on Offshore Mechanics and Arctic Engineering, OMAE2011-49434.

[18] Vasilikis, D. and Karamanos, S.A., 2011, "Buckling of Clad Pipes under Bending and External Pressure", Proceedings of the 30th Int. Conference on Offshore Mechanics and Arctic Engineering, OMAE2011-49470.

[19] Vasilikis, D. and Karamanos, S.A., 2012, "Mechanical Behaviour and Wrinkling of Lined Pipe", International Journal of Solids and Structures, Volume 49, Issues 23-24, 3432 – 3446.

[20] Harrison B., Yuan, L. and Kyriakides, S., 2016, "Measurement of Lined Pipe Liner Imperfections and the Effect on Wrinkling and Collapse under Bending", Proceedings of the 35th International Conference on Offshore Mechanics and Arctic Engineering, OMAE2016-54539.

[21] ABAQUS version 6.13.1, www.3ds.com/products-services/simulia.

[22] Johnston, C., Nageswaran, C. and London, T., 2016, "Investigations into the Fatigue Strength of CRA Lined Pipe", Proceedings of the 2016 Offshore Technology Conference, OTC 2016, OTC-27141-MS.

[23] British Standard Institution, 2014, *BS7608: Guide to Fatigue Design and Assessment of Steel Products*.

Copyright © 2017 by ASME

Appendix E

ASME and ISOPE Permissions to Reproduce Published Work from Author and Others

Aurelien Pepin

From: Beth Darchi <DarchiB@asme.org>
Sent: 22 February 2019 16:40
To: Aurelien Pepin
Subject: RE: Permission to Re-Publish Work in PhD Thesis

Dear Mr. Pépin,
It is our pleasure to grant you permission to use **all or any part of** the following ASME papers:

- Low Cycle Fatigue of Subsea Mechanically Lined Pipeline With Liner Imperfections, by Aurélien Pépin, Tomasz Tkaczyk, Noel O'Dowd and Kamran Nikbin, Paper No. OMAE2017-62487
- Limit Load Solution and Crack Driving Force Estimation Scheme for Embedded Flaws in Pipeline Girth Welds, by Aurélien Pépin, Tomasz Tkaczyk, Noel O'Dowd and Kamran Nikbin, Paper No. PVP2015-45702
- Methodology for Assessment of Surface Defects in Undermatched Pipeline Girth Welds, by Aurélien Pépin; Tomasz Tkaczyk; Noel O'Dowd; Kamran Nikbin, J. Pressure Vessel Technol. 2015; 137(5)
- Integrity of Mechanically Lined Pipes Subjected to Multi-Cycle Plastic Bending, by Tomasz Tkaczyk, Aurélien Pépin and Sylvain Denniel, Paper No. OMAE2011-49270
- Fatigue and Fracture of Mechanically Lined Pipes Installed by Reeling, by Tomasz Tkaczyk, Aurélien Pépin and Sylvain Denniel, Paper No. OMAE2012-83050

cited in your letter for inclusion in a doctoral dissertation entitled Design of Mechanically Lined Pipe for Reel-Lay Installation and Subsea Service to be published by Imperial College London.

Permission is granted for the specific use as stated herein and does not permit further use of the materials without proper authorization. Proper attribution must be made to the author(s) of the materials. **Please note**: if any or all of the figures and/or Tables are of another source, permission should be granted from that outside source or include the reference of the original source. ASME does not grant permission for outside source material that may be referenced in the ASME works.

As is customary, we request that you ensure full acknowledgment of this material, the author(s), source and ASME as original publisher. Acknowledgment must be retained on all pages where figure is printed and distributed.

As per ASME policy, we cannot grant permission to use any or all of the works of your ASME paper **OMAE2019-95511** until after presentation at the **OMAE2019** conference. Once your paper has been presented, you can then send a request for permission to use this paper. **PLEASE NOTE**, that we do not keep these requests on file. Once you have presented your paper then send the request for permission.

Many thanks for your interest in ASME publications.

Sincerely,

Beth Darchi
Publishing Administrator
ASME
2 Park Avenue

New York, NY 10016-5990
Tel 1.212.591.7700
darchib@asme.org

From: Aurelien Pepin [mailto:aurelien.pepin@technipfmc.com]
Sent: Friday, February 22, 2019 4:18 AM
To: permissions@asme.org
Subject: Permission to Re-Publish Work in PhD Thesis

This Message Came From Outside of ASME

Hello,

I am completing a Phd at Imperial College London and would like to include the papers I have published in ASME conferences and journals as per the attached form.

In addition, few figures from papers presented by other authors are also reproduced and duly referenced.

Can you please grant me copyrights for this purpose?

Thanks in advance,

Kind Regards,

Aurelien Pepin

Reply all | Delete Junk | •••

RE: Request for Permission to Reproduce Figures from Other Authors in PhD Thesis - ASME

BD

Beth Darchi <DarchiB@asme.org>
Yesterday, 19:36
Aurelien Pepin

Reply all |

Inbox

Label: Technip - 10 years Delete (10 years and 2 days) Expires: 05/03/2029 19:36

Dear Mr. Pepin:
It is our pleasure to grant you permission to use the following material:

1. **Figures 2,3,4,6** from "Wrinkling Failure of Lined Pipe Under Bending," by Lin Yuan and Stelios Kyriakides, Paper No. OMAE2013-11139
2. **Figures 11,14** from "Measurement of Lined Pipe Liner Imperfections and the Effect on Wrinkling and Collapse Under Bending," by Benjamin Harrison, Lin Yuan and Stelios Kyriakides, Paper No. OMAE2016-54539
3. **Figure 11** from "The Effect of Pre-Strain on Ductile Fracture Toughness of Reeled Pipeline Steels," by Tomasz Tkaczyk, Noel P. O'Dowd, Kamran Nikbin and Brett P. Howard, Paper No. PVP2009-77684
4. **Figures 20,22,24** from "Reeling of Tight Fit Pipe (TFP)," by E. S. Focke, E. Karjadi, A. M. Gresnigt, J. Meek and H. Nakasugi, Paper No. OMAE2007-29100
5. **All or any part of** "Integrity of Mechanically Lined Pipes Subjected to Multi-Cycle Plastic Bending," by Tomasz Tkaczyk, Aurélien Pépin and Sylvain Denniel, Paper No. OMAE2011-49270
6. **Figures 9,28** from "Mechanical Behaviour of Lined Pipe During Bending: Numerical and Experimental Results Compared," by A. Hilberink, A. M. Gresnigt and L. J. Sluys, Paper No. OMAE2011-49434
7. **Figures 2,13,14,15,17** from "Buckling of Clad Pipes Under Bending and External Pressure," by Daniel Vasilikis and Spyros A. Karamanos, Paper No. OMAE2011-49470
8. **Figures 17,21** from "Wrinkling of Lined Steel Pipes Under Bending," by Daniel Vasilikis and Spyros A. Karamanos, Paper No. OMAE2013-11122

cited in your letter for inclusion in a doctoral dissertation entitled Design of Mechanically Lined Pipe for Reel-Lay Installation and Subsea Service to be published by Imperial College London.

As is customary, we request that you ensure full acknowledgment of this material, the author(s), source and ASME as original publisher.

Many thanks for your interest in ASME publications.

Sincerely,

Beth Darchi
Publishing Administrator
ASME
2 Park Avenue
New York, NY 10016-5990
Tel 1.212.591.7700

Reply all | Delete Junk | •••

From: Aurelien Pepin [mailto:aurelien.pepin@technipfmc.com]
Sent: Monday, March 4, 2019 10:19 AM
To: permissions@asme.org
Subject: Request for Permission to Reproduce Figures from Other Authors in PhD Thesis - ASME

This Message Came From Outside of ASME

Hello,

I'm currently completing a PhD thesis at Imperial College London. In the literature review section I would like to reproduce and duly reference figures from other authors, as detailed in the attached files.

Can you please grant me permission for this?

Thanks,

Kind Regards,

Aurelien PEPIN

Aurelien Pepin

From: isope-2@sbcglobal.net
Sent: 25 February 2019 20:35
To: Aurelien Pepin
Subject: RE: Permission to Re-Publish Work in PhD Thesis

We cannot grant you a Copyright Right, since ISOPE holds the copyright for these papers. But according to the following standard permission, you may reference these papers by quoting the original full publication information:

Verbatim reproduction or republication of the papers or articles or part of the articles (e.g., figures or tables) by their authors, after the publication or presentation at the ISOPE meetings and journal, is permitted by the International Society of Offshore and Polar Engineers (ISOPE), provided the full credit is given to the authors, to the publisher, The International Society of Offshore and Polar Engineers (ISOPE), and to the Conference, Symposium or Journal — more specifically not to remove the copyright imprint on page 1 of the paper. The permission does not extend to copying for resale and to re-copyrighting the whole or part of the papers.

Posting on your organization's website of the paper(s) you specified is allowed only where only your organization's employees including the students can view free of charge the paper authored or co-authored by your organization's employees, and www.isope.org is provided for the paper(s) in the ISOPE proceedings or journals.

Janice
ISOPE, 495 North Whisman Road, Suite 300
Mountain View, California 94043, USA
T 1-650-254-1871; F 1-650-254-2038; isope-2@sbcglobal.net; isope-2@isope.org
www.isope.org

From: Aurelien Pepin <aurelien.pepin@technipfmc.com>
Sent: Monday, February 25, 2019 2:15 AM
To: info@isope.org; support@isope.org
Subject: Permission to Re-Publish Work in PhD Thesis

Hello,

I am completing a Phd at Imperial College London and would like to include the below papers I have published in ISOPE conference and journal.

Pepin, A., Tkaczyk, T., O'Dowd, N. and Nikbin, K., 2015, "Qualification of Reeled Mechanically Lined Pipes for Fatigue Service", Proceedings of the Twenty-fifth (2015) International Offshore and Polar Engineering Conference, Kona, Big Island, Hawaii, USA, ISOPE2015-TPC-0481.

Pepin, A., Tkaczyk, T., O'Dowd, N. and Nikbin, K., 2015, "Qualification of Reeled Mechanically Lined Pipes for Fatigue Service", International Journal of Offshore and Polar Engineering, Vol. 26, No. 3, September 2016, pp. 296–303.

In addition, few figures from papers presented by other authors are also reproduced and duly referenced.

Can you please grant me copyrights for this purpose?

Thanks in advance,

Kind Regards,

Aurelien Pepin

Aurelien Pepin
Senior Rigid Pipelines Engineer | Rigid Pipeline & Installation Technologies | Subsea GBU
P +44 1224 271106 | Switchboard +44 1224 271000
aurelien.pepin@technipfmc.com

TechnipFMC | UK
Enterprise Drive | Westhill, Aberdeenshire | AB32 6TQ
TechnipFMC.com

This email has been sent by or on behalf of TechnipFMC plc, a company registered in England and Wales with registered no. 09909709, and with its registered office address at One St. Paul's Churchyard, London, EC4M 8AP, or one of its subsidiaries.

Reply all | Delete Junk | •••

Re: Request for Permission to Reproduce Figures from Other Authors in PhD Thesis - ISOPE

Aurelien Pepin
Today, 11:55
isope-2@sbcglobal.net

Reply all |

Sent Items

Hello,

Thanks very much,

I will do as advised.

Warm Regards,

Aurelien PEPIN

From: isope-2@sbcglobal.net <isope-2@sbcglobal.net>
Sent: 02 March 2019 00:07
To: Aurelien Pepin
Subject: RE: Request for Permission to Reproduce Figures from Other Authors in PhD Thesis - ISOPE

Be sure to list the source publication info such as author(s), conference name, publisher, year and place, page number, etc. in the References, and cite it in brief format in the text.

The following is ISOPE standard permission:

Verbatim reproduction or republication of the papers or articles or part of the articles (e.g., figures or tables) by their authors, after the publication or presentation at the ISOPE meetings and journal, is permitted by the International Society of Offshore and Polar Engineers (ISOPE), provided the full credit is given to the authors, to the publisher, The International Society of Offshore and Polar Engineers (ISOPE), and to the Conference, Symposium or Journal— more specifically not to remove the copyright imprint on page 1 of the paper. The permission does not extend to copying for resale and to re-copyrighting the whole or part of the papers.
Posting on your organization's website of the paper(s) you specified is allowed only where only your organization's employees including the students can view free of charge the paper authored or co-authored by your organization's employees, and www.isope.org is provided for the paper(s) in the ISOPE proceedings or journals.

Regards,
Janice
ISOPE, 495 North Whisman Road, Suite 300
Mountain View, California 94043, USA
T 1-650-254-1871; F 1-650-254-2038; isope-2@sbcglobal.net; isope-2@isope.org
www.isope.org

Reply all | Delete Junk | •••

To: isope-2@sbcglobal.net; info@isope.org; support@isope.org
Subject: Request for Permission to Reproduce Figures from Other Authors in PhD Thesis - ISOPE

Hello,

I'm currently completing a PhD thesis at Imperial College London. In the literature review section I would like to reproduce figures from other authors, as detailed below.

Can you please grant me permission for this?

Thanks,

Kind Regards,

Aurelien PEPIN

Paper	Figure Numbers
E.S. Focke, A.M. Gresnigt, J. Meek, H. Nakasugi, "Experimental Research on Local Buckling Behaviour of Tight Fit Pipe", Proceedings of ISOPE 2005 Conference	12, 14, 18
E.S. Focke, A.M. Gresnigt and J. Meek, "Experimental Research on Local Buckling Behaviour of Tight Fit Pipe", Proceedings of ISOPE 2006 Conference	15, 16
T. Tkaczyk, N. P. O'Dowd, K.Nikbin, and B. P. Howard, "A non-linear fracture assessment procedure for pipeline materials with a yield plateau", ISOPE2009-TPC-165	6, 7
A. Hilberink, A.M. Gresnigt, L.J. Sluys, "A Finite Element Method Approach on Liner Wrinkling of Lined Pipe during Bending", ISOPE2011-TPC-792	18